

Instabilities and optimization of elastic structures interacting with laminar flows

Thèse de doctorat de l'Université Paris-Saclay
préparée à l'École polytechnique et
à l'Office National d'Études et de Recherches Aérospatiales

Ecole doctorale n°579 Sciences mécaniques et énergétiques,
matériaux et géosciences (SMEMAG)
Spécialité de doctorat: Mécanique des fluides

Thèse présentée et soutenue à MEUDON, le 12 juin 2019, par

Jean-Lou Pfister

Composition du Jury :

Emmanuel DE LANGRE

Professeur, École polytechnique (Laboratoire d'Hydrodynamique) Président du Jury

Matthew JUNIPER

Professeur, University of Cambridge (Engineering Department) Rapporteur

Thomas WICK

Professeur, Leibniz Universität Hannover (Institute of Applied Mathematics) Rapporteur

David FABRE

Maître de conférences, Université Paul Sabatier (Institut de Mécanique des Fluides) Examinateur

François GALLAIRE

Professeur associé, École Polytechnique Fédérale de Lausanne (Laboratory of Fluid Mechanics and Instabilities) Examinateur

Denis SIPP

Directeur de recherche, ONERA (Département Aérodynamique, Aéroélasticité, Acoustique) Directeur de thèse

Olivier MARQUET

Maître de recherche, ONERA (Département Aérodynamique, Aéroélasticité, Acoustique) Encadrant de thèse

REMERCIEMENTS

J'aimerais d'abord remercier les membres du jury. Merci à David FABRE et à François GALLAIRE d'avoir pris le temps d'examiner mes travaux, à Emmanuel DE LANGRE d'avoir de plus accepté de présider le jury — et pour la dédicace ! J'ai été très honoré par votre présence. Merci beaucoup à Matthew JUNIPER et à Thomas WICK d'avoir accepté la lourde tâche de relire ce manuscrit effectivement « pas infiniment digeste » (Gallaire, 2019). Vos deux sensibilités complémentaires ont je crois permis de couvrir au mieux les thématiques abordées dans cette thèse. Merci à Denis SIPP d'avoir accepté d'en assumer la direction — et de m'avoir sauvé par là même de bien des tracasseries administratives. Au-delà de cela, la qualité de la soutenance doit beaucoup à tes commentaires pertinents lors de la répétition, et toute cette aventure doit finalement beaucoup à ton cours de Master sur le contrôle d'écoulement, qui m'avait littéralement bluffé à l'époque, et ainsi attiré vers l'ONERA.

Que de chemin parcouru depuis ces premiers jours de thèse où, perplexe devant un fichier texte vide, je me demandais bien par où commencer pour parvenir à le remplir de lignes de codes à la fois solides et fluides... Olivier, merci infiniment de m'avoir permis de mener à bien ce travail dans les meilleures conditions possibles, à savoir : de nombreux échanges avec les autres membres de ton projet ERC AEROFLEX¹, quelques voyages et conférences mémorables, et bien sûr et avant tout ton suivi personnel. Ta capacité à creuser au fond des problèmes jusqu'à ce qu'en jaillissent des idées nouvelles n'a pas fini de me surprendre. En plus de tes nombreuses suggestions, la qualité du travail réalisé doit aussi beaucoup à ton exigence constante de rigueur et de clarté, notamment dans l'exercice difficile mais formateur de la rédaction d'articles. Enfin, merci pour ta gestion d'AEROFLEX, que tu as dirigé en laissant une grande liberté dans les orientations de recherche de chacun, tout en donnant des impulsions décisives lorsque c'était nécessaire.

Je dois ainsi beaucoup aux nombreux échanges avec les membres de la « team ERC » : des psychothérapies de groupe aux passionnantes discussions scientifiques, je me serais senti bien seul sans vous. Marco, merci pour ton aide et tes conseils au début de la thèse, alors que rien ne voulait encore converger, et pour tes lumières sur le contrôle actif par piézoélectriques. Nicolò, merci d'avoir partagé avec moi ta science des couches limites au profit de nos plaisirs viscoélastiques, et pour les discussions passionnantes qui s'en sont ensuivies. Tristan, merci d'avoir trouvé à peu près un bug retors par ligne de mes codes et de m'avoir posé tant de questions pertinentes. Luis, merci pour ton enthousiasme communicatif, j'espère que tu finiras ta thèse comme un poisson dans l'eau. Enfin, une mention spéciale à Johann, maître *ès* préconditionneurs et calcul parallèle, avec qui j'ai partagé tant de perplexité devant la magie noire FREEFEM++, de nœuds au cerveau, mais aussi quelques-uns de ces rares moments où quelque chose de net semble enfin se dégager de la brume épaisse des SPAKLAIR ; de Meudon jusqu'en Louisiane, en passant par les Alpes et un centre spatial. Mes Sincères et Amicaux Encouragements pour la suite des événements ! J'ai aussi eu la chance de travailler avec des stagiaires enthousiasmants : merci Georg, *mein Superpraktikant*, d'avoir débroussaillé l'analyse de résolvant, toujours dans la bonne humeur bien qu'on se soit finalement un peu éloigné des hélicoptères... Merci Romain L. d'avoir testé mon petit modèle réduit, bravo à Pauline d'avoir courageusement essayé quelques plâtres numériques. Enfin merci Marie et Rémi, vous m'avez fait rêver avec vos allées de von Kármán savonneuses, que j'ai pu immortaliser grâce à Caroline et Cédric I. qui m'ont ouvert les portes de cette formidable armoire à matériel photo.

¹<https://w3.onera.fr/erc-aeroflex/home>

Les excellentes conditions de travail dont jouit un doctorant à l'ONERA de Meudon doivent aussi beaucoup à l'atmosphère chaleureuse qui y règne, je tiens ainsi à remercier l'ensemble des collègues et personnels que j'y ai côtoyé. Merci à la fine équipe « ONERA dream team » puis « 3-1 » — bientôt « 0-4 » ? — d'avoir égayé le quotidien. Carlos, tu as été un collègue de bureau de grande valeur. Nos discussions croisées sur le féminisme, le vélo et la contrainte énergie-climat vont bien me manquer. Edo, merci d'avoir apporté tout le soleil d'Italie et des histoires incroyables à chacune de tes visites. Quentin, merci d'avoir sauvé mon séjour à Cambridge grâce à ta veste, et pour tes comptes-rendus sur les bizarreries expérimentales. Johann, merci d'avoir établi un nouveau standard en matière de calembours. Les conférences ont aussi été l'occasion de participer à de joyeuses colonies de vacances ONERA, je garde ainsi un excellent souvenir du séjour à Séville, et du week-end prolongé à Stockholm en compagnie de Léopold, Lucas et Edoardo.

Évidemment, je ne suis pas prêt d'oublier le cérémonial de la pause café, d'abord chez les « anciens », Damien, Holly, Nicolas, Robin, Samir et Ye-Bonne ; puis autour de notre brave machine et du mur de capsules. En plus des membres des diverses factions sus-nommées, notre bureau s'est ainsi trouvé périodiquement et sympathiquement envahi par Arnaud, Armand, Camille, Gaétan, Guillaume, Julien, Romain P., Matthieu... Les conversations du bureau AY-00-21 ayant été d'un commun accord classées confidentiel défense (des bonnes mœurs), guère davantage n'en sera dévoilé ici. Merci aussi à Alexandre, Anthony, Arnold, Benjamin (x2), Colin, Catherine, Cédric U., Denis B., Diogo, François, Jahnvi, Juan, Ilias, Navrose, Simon, Tobias, Toni, ne serait-ce que pour m'avoir attendu (ou pas) à la cantine... Enfin, merci à Claire, Dominique et Tanya pour m'avoir bien aidé pour les démarches administratives et l'organisation de la soutenance.

Je ne peux conclure sans penser à mes amis et soutiens de plus longue date, de Strasbourg, Paris ou ailleurs. Merci d'avoir été là lorsque c'était nécessaire, merci pour ce que l'on a vécu ensemble. Merci Lætitia d'avoir supporté sans broncher cette longue quête en terres hostiles peuplées d'équations $\mathfrak{w} \, \mathfrak{z} \, \mathfrak{v} \, \mathfrak{u} \, \mathfrak{t} \, \mathfrak{s} \, \mathfrak{r} \, \mathfrak{q} \, \mathfrak{p} \, \mathfrak{o} \, \mathfrak{n} \, \mathfrak{m} \, \mathfrak{l} \, \mathfrak{k} \, \mathfrak{j} \, \mathfrak{i} \, \mathfrak{h} \, \mathfrak{g} \, \mathfrak{f} \, \mathfrak{e} \, \mathfrak{d} \, \mathfrak{c} \, \mathfrak{b} \, \mathfrak{a}$ et de symboles abscons, et pour ta bienveillance au quotidien. Enfin, merci à ma sœur et à mes parents, sans qui rien n'aurait été possible. Je vous dois beaucoup pour en être arrivé jusque là.

ABSTRACT

Large static and dynamic deformations arise when elastic solids interact with viscous flows. They may accurately be captured by considering a strong numerical coupling between the Lagrangian solid dynamics and the Eulerian fluid dynamics, especially when large added-mass effects are at play. Besides running unsteady non-linear simulations, linearised modal approaches are useful to identify hydro-elastic instabilities at the origin of those vibrations. They can also be used to design passive control strategies aiming at attenuating or even suppressing the structural vibrations. The objectives of this thesis are to develop and apply methods, first to accurately describe the linear dynamics of strongly coupled fluid-solid systems, and then to optimize the shape or the elastic properties of the solid so as to control the linear dynamics.

The first part of this thesis presents the theoretical and numerical methods developed to investigate the linear dynamics of fluid-solid perturbations around non-linear steady states. The fluid dynamics is governed by the incompressible Navier-Stokes equations, while the solid is described by hyperelastic models. An Arbitrary Lagrangian Eulerian coupling is chosen, resulting in a conformal description of the fluid-solid interface in a time-independent reference configuration. An exact linearisation of this formulation is derived, and two analyses of the resulting fully coupled, linearised fluid-solid operator are considered. An eigenvalue analysis allows to determine self-sustained fluid-solid instabilities responsible, for instance, for the vortex-induced vibrations of bluff bodies or the flutter of slender bodies. The resolvent analysis, i.e. a singular value analysis of the fluid-solid operator, allows to determine the linear response of the fluid-solid system to external forcings, such as gusts.

The second part is devoted to the analysis and control of the vibrations of elastic plates attached behind a rigid circular cylinder, and immersed in a uniform incoming flow. First, complex eigenmodes, related to vortex-induced vibrations, are identified by means of the eigenvalue analysis. These modes become unstable when reducing the stiffness. A further decrease of stiffness yields to the destabilization of a real eigenmode, characteristic of a symmetry-breaking divergence instability. Non-linear steady and unsteady simulations are performed to elucidate the non-linear interactions between the unstable modes. Secondly, an adjoint-based shape optimization of the rigid body supporting the elastic plate is proposed to control the unstable complex modes, aiming either at decreasing the growth rate or varying the frequency. A stabilization of the complex mode is achieved by a thinning of the rigid body. More exotic shapes are obtained when considering the variation of the frequency. A frequency decrease is achieved by “D-shaped” cylinders, while a frequency increase is obtained with “C-shaped” cylinders.

The last part of the thesis is dedicated to the delay of laminar/turbulent transition in two-dimensional boundary-layer flows thanks to visco-elastic, finite-length coatings. A resolvent analysis of the fluid-solid operator is used to quantify the attenuation of low-frequency Tollmien-Schlichting instability waves when the stiffness of the coating is reduced. On the other hand, the eigenvalue analysis shows that high-frequency solid-based modes are destabilized when the solid viscous damping is too low. A gradient-based strategy to optimize the stiffness distribution of the coating with respect to the energy amplification of both instabilities is eventually proposed. The optimized coatings have an overall structure organized in layers aligned with the flow, with a much stronger anisotropy in both the streamwise and transverse directions close to the edges, and make it possible both to attenuate Tollmien-Schlichting waves and to limit the development of solid-based instabilities.

TABLE OF NOTATIONS

$\hat{\Omega}$	stress-free reference domain: quantities $\hat{\mathbf{q}}(\hat{\mathbf{x}}, t)$
Ω	steady deformed reference domain: quantities $\mathbf{q}(\mathbf{x}, t)$
$\tilde{\Omega}_t$	instantaneous, time-dependent deformed domain: quantities $\tilde{\mathbf{q}}(\tilde{\mathbf{x}}_t, t)$
\mathbf{i}	imaginary number
$\lambda = \lambda^r + \mathbf{i}\lambda^i$	complex eigenvalue
ω	forcing frequency
$\Re(\cdot), \Im(\cdot)$	real, imaginary part
$(\cdot)^*$	complex conjugate
$\mathbf{Q}(\mathbf{x})$	steady, base field
$\mathbf{q}'(\mathbf{x}, t)$	perturbation field
$\mathbf{q}^\circ(\mathbf{x})$	eigenmode or optimal forcing/response
$\mathbf{q}^\dagger(\mathbf{x})$	adjoint perturbation field
$\mathbf{Q}^\dagger(\mathbf{x})$	adjoint steady base field
\mathbf{u}	fluid velocity
p	fluid pressure
ξ	solid displacement (capital letter: Ξ)
\mathbf{u}_s	solid velocity
ξ_e	extension displacement
λ	interface stress (capital letter: Λ)
λ_e	interface extension pseudo-stress
$\tilde{\nabla} = \partial/\partial\tilde{\mathbf{x}}_t$	differentiation operator in the instantaneous domain
$\nabla = \partial/\partial\mathbf{x}$	differentiation operator in the steady deformed reference domain
$\hat{\nabla} = \partial/\partial\hat{\mathbf{x}}$	differentiation operator in the stress-free reference domain
$\hat{\mathbf{P}}$	first Piola-Kirchhoff stress tensor in stress-free configuration (Eq. (1.1.6) page 18)
$\hat{\mathbf{P}}', \mathbf{P}'$	linearised Piola-Kirchhoff stress tensor (Eq. (2.1.6) page 45 and Eq. (2.1.16) page 48)
$\hat{\mathbf{S}}$	second Piola-Kirchhoff stress tensor in stress-free configuration (Eq. (1.1.7) page 18)
$\hat{\mathbf{S}}', \mathbf{S}'$	linearised second Piola-Kirchhoff stress tensor (Eq. (2.1.7) page 45 and Eq. (2.1.17) page 48)
$\hat{\mathbf{E}}$	Green-Lagrange strain tensor in stress-free configuration (Eq. (1.1.8) page 18)
$\hat{\mathbf{E}}', \mathbf{E}'$	linearised Green-Lagrange strain tensor (Eq. (2.1.8) page 45 and Eq. (2.1.18) page 48)
$\hat{\mathbf{F}}$	deformation gradient in stress-free configuration (Eq. (1.1.9) page 18)
$\hat{J} = \det(\hat{\mathbf{F}})$	transformation Jacobian (Eq. (1.1.27) page 22)
$\hat{\Phi} = \hat{J} \hat{\mathbf{F}}^{-1}$	deformation operator in stress-free configuration (Eq. (1.1.27) page 22)
$\hat{\Phi}', \Phi'$	linearised deformation operator (Eq. (2.1.9) page 45 and Eq. (2.1.19) page 48)
$\tilde{\sigma}$	fluid Cauchy stress tensor (Eq. (1.1.15) page 19)
$\hat{\Sigma}$	fluid stress tensor in the stress-free reference configuration (Eq. (1.1.28) page 22)
$\hat{\Sigma}', \Sigma'$	linearised fluid stress tensor (Eq. (2.1.11) page 45 and Eq. (2.1.21) page 48)
$\hat{\mathbf{D}}$	velocity gradients tensor (Eq. (1.1.29) page 22)
$\hat{\mathbf{D}}', \mathbf{D}'$	linearised velocity gradients tensor (Eq. (2.1.10) page 45 and Eq. (2.1.20) page 48)

CONTENTS

Remerciements	iii
Abstract	v
Table of notations	vii
Introduction	1
Fluid-structure instabilities	1
Description of linear fluid-structure instabilities	6
Passive control of linear fluid-structure instabilities	9
Organisation of the manuscript	12
1 Nonlinear methods for fluid-structure problems	15
1.1 Equations for a viscous fluid interacting with an elastic structure	16
1.1.1 Non-dimensional parameters describing a fluid-solid system	16
1.1.2 Equations for an elastic solid with large deformations	17
1.1.3 Navier-Stokes equations in ALE coordinates	19
1.1.4 Interface & boundary conditions	22
1.1.5 Monolithic weak formulation	23
1.1.6 Summary	28
1.2 Implicit scheme for solving the non-linear ALE equations	29
1.2.1 Coupling schemes for ALE problems	29
1.2.2 Time discretization	30
1.2.3 (Quasi)-Newton iterations & space discretization	31
1.2.4 Extension problem for non-linear computations	32
1.3 Handling the large-scale resulting linear systems	34
1.3.1 Direct <i>vs.</i> iterative methods	34
1.3.2 Preconditioning the fully coupled fluid-structure problem	34
1.4 Turek's benchmark cases	36
1.4.1 Solid mechanics cases	37
1.4.2 Fluid mechanics cases	37
1.4.3 Fluid-structure coupled cases	38
2 Eigenvalue analysis of fluid-structure steady-states	41
2.1 Fluid-structure linear perturbation equations	42
2.1.1 Steady-state solutions	42
2.1.2 Lagrangian-based perturbation equations	44
2.1.3 Link with flutter derivatives & aeroelasticity	49
2.1.4 Link with Eulerian-based perturbation equations	51
2.2 Numerical formulation for an eigenvalue analysis	52
2.2.1 Modal decomposition of the perturbations	52
2.2.2 Implementation of the eigenvalue solver	52
2.2.3 Reduced eigenvalue problem	53
2.3 Numerical testing of the Lagrangian-based approach	54
2.3.1 Test case with a vortex-induced-deformation instability	54
2.3.2 Test case with a flutter instability	57

2.3.3	Influence of the extension operator and domain	60
2.3.4	Results for the reduced eigenvalue-problem	61
2.3.5	Test-case with a 3d flexible plate in a cross-flow	62
2.4	Comparison of Lagrangian-based and Eulerian-based approaches	66
2.4.1	Poiseuille flow between flexible membranes	66
2.4.2	Flag in a channel flow	67
2.5	Conclusion	70
3	Fluid-structure stability analysis of an elastic plate clamped behind a rigid cylinder	73
3.1	Introduction	74
3.2	Problem setting	75
3.3	Non-linear simulations	77
3.3.1	Numerical settings	77
3.3.2	Non-linear simulation results	77
3.4	Stability analysis of the symmetric state	84
3.4.1	Steady solutions	84
3.4.2	Coupled fluid-structure stability analysis	85
3.4.3	Comparison with non-linear results	90
3.4.4	Neutral stability curves	92
3.5	Steady deviated states and secondary instability	93
3.5.1	Computation of the non-linear deviated branches	93
3.5.2	Linear stability analysis of the deviated supercritical branch	94
3.6	Analysis in terms of solid vibration modes	97
3.6.1	Analysis of the high-frequency modes dynamics	97
3.6.2	Analysis of the low-frequency and steady mode dynamics	100
3.7	Conclusion	104
4	Control of fluid-structure linear instabilities with shape optimisation	105
4.1	Introduction	106
4.2	Optimization problem setting	107
4.2.1	Fluid-structure model	107
4.2.2	Time-linearised perturbations of a non-linear steady flow	107
4.2.3	Optimization cost-function	108
4.3	Shape gradient computation & optimization loop	109
4.3.1	Lagrangian approach for shape optimization	109
4.3.2	Governing equations	110
4.3.3	Shape gradient computation	114
4.3.4	Practical gradient evaluation & optimization loop	115
4.4	Application to the cylinder splitter-plate case	116
4.4.1	Description of the unstable modes	117
4.4.2	Adjoint modes & abstract sensitivity analysis	119
4.4.3	Shape gradients	121
4.4.4	Shape optimization for controlling the growth-rate of the modes	124
4.4.5	Shape optimization for controlling the frequency of the modes	128
4.5	Conclusion	132
5	Boundary-layer instabilities over a finite-length compliant coating	133
5.1	Introduction	134
5.1.1	A phenomenology of skin-friction drag-reducing mechanisms	134
5.1.2	Theoretical studies	137
5.2	Physical modelling & numerical model	140
5.2.1	Non-dimensional parameters	140
5.2.2	Navier-Stokes flow	141
5.2.3	Viscoelastic solid	142

5.2.4	Coupled problem and numerical settings	144
5.3	Eigenvalue analysis	145
5.3.1	Free solid dynamics	145
5.3.2	Fluid-elastic eigenvalue analysis	150
5.4	Elastic response to optimal fluid perturbations	155
5.4.1	Resolvent analysis in the rigid-wall case	156
5.4.2	Fluid-elastic response to an optimal rigid-wall forcing	158
5.4.3	Mechanism of wave attenuation/amplification	161
5.5	Fluid-elastic resolvent analysis	165
5.5.1	Fully coupled resolvent analysis	165
5.5.2	Results	165
5.6	Conclusion	166
6	Compliant coating structure optimization for boundary-layer instabilities mitigation	169
6.1	Introduction	170
6.2	Fully coupled resolvent analysis for the fluid-structure problem	171
6.3	Gradient of the energy gain with respect to structural parameters	172
6.3.1	Lagrangian formulation	172
6.3.2	Structural gradients	173
6.4	Optimization of the stiffness distribution	175
6.4.1	Optimisation for TWF instabilities attenuation	176
6.4.2	Combined optimization for TSW/TWF attenuation	180
6.5	Conclusion	183
7	Conclusion & perspectives	185
7.1	Summary and main results	185
7.2	Perspectives	188
A	Resolvent <i>vs</i> eigenvalues	191
A.1	Temporal, modal stability analysis	192
A.2	Frequency response analysis	194
B	Fluid-solid block operators expression	197
B.1	Non-linear fluid-solid equations	197
B.2	Linearised fluid-solid equations	198
C	Technical formulas	201
C.1	Transport formulas between the different configurations	201
C.2	From Lagrangian-based to Eulerian-based perturbation equations	207
C.3	Lagrange identities for adjoint ALE equations	208
D	Derivation of the fluid-elastic shape gradient	213
D.1	Lagrangian formulation with C��a’s method	213
D.2	Explicit formula for the shape gradient	221
	Bibliography	224

INTRODUCTION

FLUID and solid mechanics are traditionally treated as two different subjects. Their coupling, leading to *fluid-structure interactions*, is consequently a challenging issue. Large benefits could be retrieved from a deeper, and more precise understanding of the mutual interaction of fluids and solids. On one hand, this can help to prevent the appearance of undesirable vibrations, for they often come with an increased energy dissipation, materials fatigue and even failure. The most well-known example being probably the flow-induced torsional vibrations that lead to the destruction of the Tacoma Narrows bridge. On the other hand, the large-amplitude deformations that spontaneously appear in fluid-elastic systems might be exploited for designing new, bio-inspired locomotion modes (Gadelha *et al.*, 2010) or energy-harvesting devices (Abdelkefi, 2016). The present work follows this path, by looking upon both the analysis of fluid-solid *instabilities* and their control.

Fluid-structure instabilities

The notion of *stability* is of paramount importance in engineering sciences. The pre-sizing of mechanical structures is often carried out under an assumption of a steady-state equilibrium, in order to be able to quickly determine which loads apply and which material properties are required. In many cases, the assumption of stationarity unfortunately gives completely erroneous results, because the hypothetical stationary state on which they have relied is *unstable* with respect to small disturbances: any small perturbation triggers a reconfiguration towards a new, often more complex equilibrium.

Fluid, solid and coupled instabilities

A major topic in fluid mechanics is to understand how steady, “gentle” flows degenerate towards complex, unsteady, three-dimensional turbulent flows when intrinsic (size of the obstacle, velocity, viscosity, etc.) or external (acoustic noise, heat source, etc.) characteristic parameters are varied. The route to turbulence is not straightforward at all to follow, but the early stages are often characterized by *linear* instability mechanisms that make the transition between the steady flow and an unsteady flow with a relatively simple structure.

It is for instance well-known that the fluid flow about an obstacle suddenly ceases to be stationary when the velocity is increased: the shear layers generated by the presence of the obstacle give birth to unsteady vortices that detach periodically from the object and are advected in the wake, which results in oscillatory loads on the obstacle and an increased mixing downstream. For the flow about a rigid circular cylinder, a bifurcation occurs at a Reynolds number slightly below 50 (Tritton, 1959; Sipp & Lebedev, 2007). Below this threshold, the flow is steady. Above the critical Reynolds number, the so-called bi-dimensional, unsteady von Kármán vortex wake is observed, as represented in Fig. 1a where a soap-film visualization is shown. This unsteady wake appears under the form of localized disturbances that spread upstream and downstream, following the mechanism of an *absolute* instability (Huerre & Monkewitz, 1990). In that case, the convection by the steady flow is not sufficient to prevent from a temporal amplification of the instability. These type of flows are often referred to as *oscillator* flows, for they are associated to dominant frequency peaks. Increasing further the Reynolds number results in secondary instabilities leading to three-dimensional vortices (Williamson, 1996), then to more and more irregular structures and eventually, a turbulent flow.

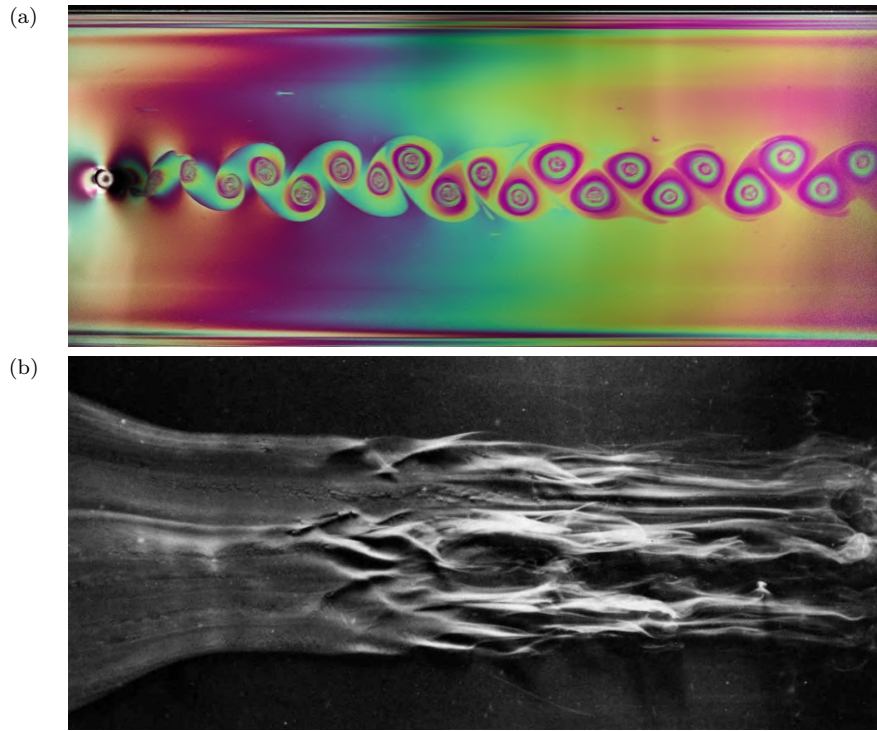


Figure 1 – Two typical fluid instabilities. (a) The von Kármán vortex wake behind a fixed circular cylinder that results from a flow instability. Pictures taken by the author, on a soap-film flow experiment at ONERA set-up by Rémi Allandrieu and Marie Couliou. Visualisation by white-light interferometry: visible colours are related to the local thickness of the film, which itself is related to the local flow velocity (Zhang *et al.*, 2000). The mean flow is from the left to the right. (b) Boundary-layer flow on an inclined plate in a water channel, picture from H. Werlé taken from Van Dyke (1982)

Boundary-layers are another typical example of unstable flows. For the simple case of a flat plate without any adverse pressure gradient, while the flow remains stationary near the leading edge when the free-stream turbulence level is low, unsteady structures appear under the form of the so-called Tollmien-Schlichting waves (Schubauer & Skramstad, 1947) as one moves away from the leading edge. The instability mechanism is however different from the case of the cylinder. The dynamics is of the *amplifier* type: instabilities appear in the flow when it is subjected to an external forcing which allows to maintain the appearance of disturbances. These perturbations are first advected by the flow without being amplified, up to a critical point where an amplification sets in. The region where an amplification occurs is qualified as *convectively unstable* (Huerre & Monkewitz, 1990). These amplified convective waves eventually trigger secondary bifurcations when they reach a sufficient amplitude (Kachanov, 1994), that then degenerate into a cascade of bifurcations and a turbulent flow farther downstream. A visualization of a boundary-layer flow in a water channel is reproduced in Fig. 1b, that illustrates the successive transition steps — Tollmien-Schlichting waves are observed on the form of the small variations of the contrast on the left, while more and more complex structures appear as one moves to the right, downstream. On the contrary to oscillator flows, noise-amplifier flows are particularly sensitive to external perturbations. Note that for the boundary-layer flow, in addition to the transition through Tollmien-Schlichting waves, many other laminar-turbulent transition scenarios may also happen depending on the level of free-stream turbulence (Saric *et al.*, 2002).

The study of hydrodynamic instabilities thus represents an active domain of research (Drazin & Reid, 2004; Charru, 2007; Schmid & Henningson, 2012). Despite a constant interest for these questions dating back to the nineteenth century, many questions stay however unanswered, especially because of the very large numerical power needed for computational fluid mechanics (Slotnick

et al., 2014) and the difficulty for investigating experimentally the behaviour of fluid flows.

Elastic solids are also subject to instabilities. For instance, when an elongated structure is subjected to a compressive stress, a sudden sideways deflection of a structural member may occur. This self-developing instability can lead to structural failure.

Starting especially with the study of the buckling instability of columns by Leonhard Euler as early as the year 1757, the study of the stability of elastic structures has greatly flourished until today, where for instance basically every computer-aided design software has a linear buckling prediction module. An introduction to the domain can be found in the classical book by [Timoshenko & Gere \(1961\)](#). Compared to fluids, solids linear instabilities are simpler to analyse, for their kinematics remains often more easily tractable (both experimentally, numerically and conceptually). Furthermore, the computational power involved in numerical simulations is dramatically reduced. For these reasons, recent developments are essentially devoted to non-linear solid instabilities ([Audoly & Pomeau, 2010](#)).

When coupled together, fluids and solids present on one hand typical pre-existent fluid and solid instabilities, but with features modified by the interaction: for instance, the vortex-shedding past bluff-bodies is altered by solid vibrations that might develop in the solid ([Williamson & Govardhan, 2004](#)). On the other hand, new classes of instabilities appear, resulting from an unstable coupling of the solid and fluid dynamics.

For instance, the flow past a rigid cylinder behind which a flexible filament is attached is reported in [Fig. 2a](#). The pre-existing instability in the wake generates unsteady loads on the structure that are amplified, resulting in the large-amplitude oscillations of the filament. The development of the boundary-layer instabilities are also affected by the flexibility of the underlying surface. Static reconfigurations as those observed in solids might also be produced by the loads exerted by the surrounding fluid: an apparent negative stiffness can appear, that can ultimately trigger a buckling instability usually referred to as the divergence instability in aeroelasticity ([Bisplinghoff et al., 1955](#)). Studying the interaction of a boundary-layer flow with a flexible compliant viscoelastic coating, [Gad-El-Hak et al. \(1984\)](#) observed quasi-steady ripples developing at the surface of the coating, as reported in [Fig. 2b](#). The development of boundary-layer instabilities is then greatly affected by the waves travelling in the solid, that can interact with the flow and generate new types of instabilities ([Carpenter & Garrad, 1986, 1985](#)). Even if the flow by itself and the elastic solid do not present intrinsic instability mechanisms, their mutual interaction may result in unstable situations. The most classical instability of such type is probably the coupled-mode flutter instability of wing profiles, that arises when the flexion and torsion modes of vibration of the solid interact favourably under the action of the fluid ([de Langre, 2002](#)).

Linear stability analyses

Even if the world is deeply non-linear, in some cases it is nevertheless useful and relevant to forget about this inherent complexity. Close to the onset of the instability, one can indeed hope that the perturbation amplitudes are small, and small things usually grow exponentially before they become too big to grow. This reasoning forms the basis of the *linear stability analysis*: how will the “small thing” grow or decay (exponentially, as a solution of a linearised problem) in space and time? This approach is of great practical interest, for linear problems are considerably easier to solve than non-linear problems. In the most general case, the fluid-structure system can be described by a dynamical system of type

$$\mathcal{T}_{\text{fsi}}(\mathbf{q}) \frac{\partial \mathbf{q}}{\partial t} - \mathcal{N}_{\text{fsi}}(\mathbf{q}) = 0$$

where \mathbf{q} is a state vector containing the fluid velocity field, the solid displacement field, etc. Depending on the models chosen for the fluid and the structure, its dimension can range from a few degrees of freedom, like for the introductory spring-mounted flutter model found in every good aeroelasticity textbook ([Bisplinghoff et al., 1955](#); [de Langre, 2002](#); [Dowell et al., 2004](#)), to more than 10^8 for numerical three-dimensional models of non-linear elasticity coupled with the Navier-Stokes equations ([Deparis et al., 2016](#)). As mentioned above, rather than trying to solve this equation



Figure 2 – Fluid-structure instabilities. (a) The von Kármán vortex wake behind a fixed circular cylinder is strongly modified when a flexible filament is attached behind the cylinder. Pictures taken by the author, on a soap-film flow experiment at ONERA set-up by Rémi Allandrieu and Marie Couliou, visualisation by white-light interferometry. The mean flow is from the left to the right. (b) Boundary-layer flow over a viscoelastic patch (view from the top), from [Gad-El-Hak et al. \(1984\)](#).

and determine the full history of $\mathbf{q}(\mathbf{x}, t)$ as a function of the time t and the space coordinate \mathbf{x} , one could instead try to determine only *one* steady, non linear state and then investigate whether an unsteady *perturbation* $\mathbf{q}'(\mathbf{x}, t)$ of steady state non-linear solution $\mathbf{Q}(\mathbf{x})$ is likely to grow or not in time and/or space. Setting

$$\mathbf{q}(\mathbf{x}, t) = \mathbf{Q}(\mathbf{x}) + \varepsilon \mathbf{q}'(\mathbf{x}, t)$$

with $\varepsilon \ll 1$, a linearised equation for the fully coupled fluid-structure perturbation is found by injecting the above decomposition in the non-linear equation and expanding up to the order ε :

$$\left\{ \mathcal{T}_{\text{fsi}}(\mathbf{Q}) \frac{\partial}{\partial t} - \mathcal{N}'_{\text{fsi}}(\mathbf{Q}) \right\} \mathbf{q}' = \mathbf{f}', \quad (\star)$$

where $\partial \mathcal{N}_{\text{fsi}} / \partial \mathbf{q} | \mathbf{Q}$ is the linearised fluid-structure operator. In this linearised problem, a forcing term \mathbf{f}' has been added in the right-hand side so as to model small external perturbations akin for instance to free-stream turbulence or gusts, vibrations in the solid, etc. Once the linear perturbation problem (\star) is derived, there is still to analyse the behaviour of the perturbation field \mathbf{q}' in time and space. Several questions can be raised at this point, for instance: what is the asymptotic behaviour of \mathbf{q}' as $t \rightarrow \infty$? How is \mathbf{q}' affected if some components of the system are forced by the external noise signal \mathbf{f}' ? What would be the most detrimental type of signal for the stability of the system? What initial condition results in the maximum amplification of the perturbation energy? When is this maximal value reached? Where is the energy located? Does the evolution of the perturbation give interesting information on the behaviour of the full non-linear system? etc.

Depending on the nature of the physical problem, different classes of analyses are appropriate to describe the linear regime of all of these instabilities. As exemplified before, while some systems tend to spontaneously evolve towards an oscillating state, some other systems are on the other hand rather known to amplify external perturbations. This distinction is usually made in fluid mechanics ([Huerre & Monkewitz, 1990](#)) where the low-Reynolds number flow behind a cylinder is probably the most famous example of an oscillator flow, while a boundary layer represents a

typical noise-amplifier flow. It is thus appropriate to conceptually and mathematically split the linear behaviour between a self-sustained part and a second part that depends on external forcings.

The eigenvalue analysis of the linearised operator is appropriate for characterizing the self-developing dynamics (Sipp *et al.*, 2010; Theofilis, 2011; Juniper *et al.*, 2014): the long-term evolution of the perturbation can indeed be characterized by the evolution of *normal modes* $\Re\{q^\circ(\mathbf{x}) \exp(\lambda t)\}$, $\lambda \in \mathbb{C}$, determined by solving the complex eigenvalue problem

$$\left\{ \lambda \mathcal{T}_{\text{fsi}}(\mathbf{Q}) - \mathcal{N}'_{\text{fsi}}(\mathbf{Q}) \right\} q^\circ = 0.$$

We then obtain *modes* of instability, oscillating at the frequency $\Im(\lambda)$ and growing or decaying exponentially with time according to $\Re(\lambda)$, and having the spatial structure $q^\circ(\mathbf{x})$. These modes are representative of the long-term evolution of the perturbation, since at large times the least stable mode dominates over the other modes and is representative of the perturbation q' . In the context of fluid dynamics, the predictions of eigenvalue analysis were found to match the experiments in several cases. For instance, it can predict the onset for Rayleigh-Bénard convection (Bodenschatz *et al.*, 2000), or the von Kármán vortex street behind a cylinder (Tritton, 1959; Sipp & Lebedev, 2007) evoked above. This approach is typically adapted for oscillator flows that exhibit one single dominant instability mode. The onset of solid buckling is also well characterized by an eigenvalue analysis (Audoly & Pomeau, 2010). In the context of fluid-solid instabilities, it is for instance appropriate to determine the onset of vortex-induced vibrations (Mittal & Singh, 2005) or some flag instabilities (de Langre, 2002; Dowell *et al.*, 2004; Shoele & Mittal, 2016).

The eigenvalue analysis however overshadows an important effect: if eigenvalues give the asymptotic behaviour when $t \rightarrow \infty$, large amplifications of e.g. an initial condition, external noise, etc. can occur at a *finite* time-horizon (Trefethen *et al.*, 1993; Schmid, 2007). This *transient growth* of perturbations may then be sufficient to trigger non-linear bifurcations not anticipated by the eigenvalue analysis. The non-orthogonal superposition of the eigenmodes representing the perturbation q' may indeed produce, at finite time-horizon, a considerable growth of the norm — that is usually chosen so as to represent an energy — of the perturbation. This can occur even when *all* eigenvalues are stable (i.e. with a negative real part). In some situations, the spectrum thus completely fails to explain the experiments. For instance, a Poiseuille flow is found to be unstable experimentally for Reynolds numbers above about 1000 (Carlson *et al.*, 1982), while an eigenvalue analysis (Orszag, 1971) predicts a critical Reynolds number of 5772 ! Mathematically, the *non-normality* of the linearised Navier-Stokes equations leads actually in some cases to a large transient growth of energy, as reported in the landmark paper by Trefethen *et al.* (1993). The corresponding operator is indeed far from having orthogonal eigenmodes. Physically, this is because of advection that allows for the perturbations to be transported, stretched and spatially amplified. For a comprehensive overview of non-normality effects in fluid dynamics, the reader is referred to the review by Schmid (2007) and the book by Schmid & Henningson (2012). In the context of coupled fluid-structure problems, in addition to the intrinsic non-normality of the solid or the fluid alone, extra causes of non-normality may arise because of non-normal couplings. In particular, it has been shown that large transient growth may occur below the onset (as predicted by eigenvalues) for coupled-mode flutter (Schmid & de Langre, 2002), but also that non-linear transitions could be triggered by the amplification of the energy of gusts (Schwartz *et al.*, 2009; Amandolese *et al.*, 2013). Rather than the eigenvalues, it is thus more appropriate to determine which forcings result in the largest energy amplification. Assuming an harmonic forcing at the frequency ω , the *resolvent* analysis consists in determining the *optimal forcing* f° that produces the largest *response* q° , solution to the optimization problem

$$\max_{\|f^\circ\|=1} \|q^\circ\| \quad \text{such that} \quad q^\circ = \left\{ i\omega \mathcal{T}_{\text{fsi}}(\mathbf{Q}) - \mathcal{N}'_{\text{fsi}}(\mathbf{Q}) \right\}^{-1} f^\circ.$$

Depending on the physical mechanisms at play, one should therefore favour one or the other approach. For the reader not familiar with these concepts, a more detailed, practical introduction is reported in Appendix A, on an example of a very simplified fluid-structure system represented by two coupled oscillators. Let us now introduce more specifically how fluid-structure instabilities may be described.

Description of linear fluid-structure instabilities

Classical approaches for studying fluid-solid vibrations often reduce the problem to a solid mechanics analysis, where vibration modes of the structure are coupled through models for aerodynamic forces (Bisplinghoff *et al.*, 1955; Dowell *et al.*, 2004). For instance, the spanwise deformation of the wing is often modelled by a spring-mounted two-dimensional airfoil section, and the so-called *generalized aerodynamic forces* are proportional to the displacement and/or the velocity of the solid. This approach is well adapted for studying classical aeroelastic phenomena: the characteristic time-scale for the flow (transit time of the fluid particles over the wing) is usually much smaller than the characteristic time-scale for the solid (wing vibration period), and the intrinsic dynamic in the flow (turbulent wake, vortex shedding) has no influence. The aerodynamic forces then only depend on the *static* position of the wing and the aeroelastic analysis reduces to the computation of the steady aerodynamic forces at different angles of attack (de Langre, 2002).

The complexity dramatically increases when it is no longer possible to separate the solid from the fluid dynamics. In that case, the dynamical reaction of the flow to geometry changes is of a much more complicated nature, and may depend on the type of flow as well as on the type of geometry. These cases are referred to as being *strongly coupled*. More evolved models for the aerodynamic forces can in some extent integrate unsteady effects when the flow is assumed potential (Theodorsen, 1949), while semi-empirical models with parameters estimated from experiments or time-marching numerical simulations are used where the flow features are more complex (Karpel, 1982). In some cases, the flow itself has its own — possibly unstable — dynamics, as is for instance the case for the vortex shedding past bluff bodies (Williamson & Govardhan, 2004). In this case, no general approaches are available. If phenomenological models are available (Facchinetti *et al.*, 2004), they often lack of generality.

Thanks to recent progress in fluid mechanics, new developments can be however considered today. One of the goals of the present thesis is to elaborate such new methods. Because of the special nature of fluid-solid interactions, there are primarily three axes according to which we can progress: the solid modelling, the fluid modelling, and the fluid-solid coupling. These axes are not strictly orthogonal, since the coupling between models depends also on their content — for instance, the coupling between a potential flow to any elasticity model would never exhibit the complicated time-delay effects between the fluid and the solid dynamics, since they are provoked by the momentum diffusion by the viscosity of the flow. On the other hand, very fine models can also interact weakly, as would be the case in a simulation of the fully turbulent flow about a non-linear, anisotropic elastic wing in standard flight conditions. Generally speaking, as the models are refined, it is possible (but not necessary) to take into account of more and more feedback loops between the solid and the fluid.

Developments along the two first axes are illustrated in Fig. 3. As evoked before, the classic wing flutter analysis (a) can be carried out on a spring-damper model where the two oscillators are coupled by means of aerodynamic forces proportional to the translation/rotation variables. Panel flutter (b) can be studied using simple aerodynamic models and plate equations for the solid. The flapping dynamics of a rigid wing is well reproduced with vortex methods, while the flag flutter instability has been characterized with point vortices interacting with a vibrating string model. Aeroelastic analyses (e,g) are today commonly carried out using an Euler flow and beam elements or a finite-element elasticity structural model. The laminar vortex-induced vibrations (f) of a circular cylinder are reproduced using a spring-mounted rigid object interacting with a Navier-Stokes flow. Aeroelastic computations of a wind turbine (h) can be carried out by combining beam-elements for the blades and a turbulent flow. Finally, the large elastic deformations provoked by the blood flow through arteries is simulated by coupling the Navier-Stokes equations to a non-linear elasticity model. Note that these examples show how phenomenon are currently modelled rather than how complicated the real configuration is: the scale of an airplane make it mandatory to resort to a simplified flow model, while the Navier-Stokes equations can today be used for modelling a small portion of a deformable artery.

When it comes to the third axis of modelization, recent developments dealing with structures undergoing possible transitions towards large-amplitude oscillations in a viscous flow have empha-

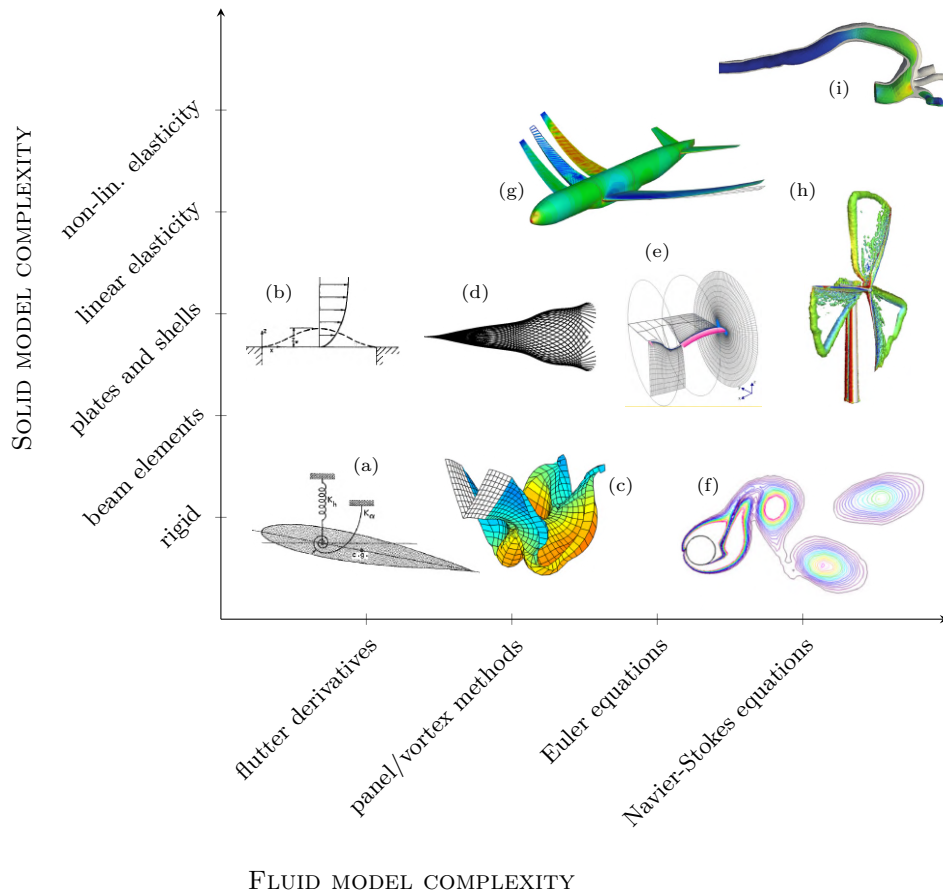


Figure 3 – Fluid-structure interactions models. The few examples shown include (a) the academic spring-mounted wing flutter problem (Bisplinghoff *et al.*, 1955), (b) panel flutter for an elastic plate (Dowell, 1970), (c) vortex-lattice simulation of a rigid flapping wing (Stanford & Beran, 2010), (d) vortex-shedding model of a flapping flag (Michelin *et al.*, 2008), (e) design of a joined-wing aircraft (Hur *et al.*, 2004), (f) vortex-induced vibrations of a spring-mounted cylinder in a Navier-Stokes flow (Placzek *et al.*, 2009), (g) aeroelastic simulation of an aircraft in Euler flow (Kenway *et al.*, 2014), (h) aeroelastic wind-turbine simulation in turbulent flow (Bazilevs *et al.*, 2013), (i) blood flow simulation (Crosetto *et al.*, 2011).

sized the need for a more accurate treatment of the complex coupled dynamics between solids and fluids. Many examples are found in industrial and biology processes. In a recent review, Farhat (2017) insists for instance on the need for taking into account elastic wing deformations for efficient aeroelastic computations. Sørensen (2011) identifies the development of strongly coupled aeroelastic models for wind turbine modelling as a major future research area. In sail or parachute simulations, the lightness of the canopy compared to the air masses is another computational challenge (Takizawa & Tezduyar, 2012). The simulation of the cardiovascular system has led to the development of new computational techniques so as to cope with the large deformations of arteries or aortic valves subject to blood flow (Peskin, 2002). In ocean engineering, vortex-induced vibrations of tubes, pipes and other marine risers is a major concern that comes with large-amplitude vibrations and a complex wake flow (Williamson & Govardhan, 2004). In nature, the elastic reconfiguration of plants in the wind (de Langre, 2008) is another example where significant deformation effects occur, as well as in the flapping dynamics of insects, fishes or birds (Wu, 2011).

In this thesis, we therefore follow a general modelling approach, which investigates the temporal evolution of small fluid-structure perturbations developing around steady solutions of fully coupled fluid-structure equations, i.e. no approximation is made regarding to the kinematic and dynamic

couplings between the solid and the fluid. Unlike the flutter analysis previously described, the linearisation of the governing equation is thus performed prior to any model reduction. The equations governing the dynamics of infinitesimal flow perturbations developing around steady flows are determined by linearisation of the Navier-Stokes equations written in a fixed spatial domain. In the context of fluid-structure interaction, an additional difficulty arises in the linearisation process because of the Lagrangian motion of the fluid-solid interface, that we shall describe in the following.

Linearised, strongly coupled fluid-structure problems

In the early nineties, a substantial effort had been set on solving linearised flow equations coupled to an elastic solid model using the so-called *transpiration approach*, very popular in aeronautics. Derived from the work of Lighthill (1958) for simulating the changes in airfoil thickness, the infinitesimal motion of the fluid-solid interface is taken into account in the linearised equation *via* a simple modification of the velocity boundary condition applied at the equilibrium position of the fluid-solid interface. This *transpiration* velocity condition allows one to easily adapt a flow solver to treat the fluid-structure problem and to effectively perform unsteady aeroelastic simulations. The transpiration approach was first applied to inviscid flows (Raj & Harris, 1993; Mortchewicz, 1997; Fisher & Arena, 1996), for instance in the work by Fisher & Arena (1996), who predicted flutter characteristics of an AGARD wing by coupling a modal solid dynamics solver to a compressible Euler solver. More recently, this transpiration approach was also extended to viscous turbulent flows, like in the work by Bekka *et al.* (2015) who performed aeroelastic computations of the nozzle of a rocket launcher engine using a Reynolds-Averaged Navier-Stokes solver coupled to a beam-element solid solver.

Although the transpiration approach (as derived in the early nineties) sounds quite attractive from a computational point of view, it entirely neglects an important physical effect, namely the coincidence of fluid and solid normal stresses at the interface. Indeed, a generic perturbation in the position of the fluid-solid interface does not only modify the velocity continuity condition but also the normal stress condition. A few exact derivations of linearised fluid-structure problems have therefore been achieved. There are basically two approaches for deriving the perturbative equation of a physical problem governed by a non-linear equation defined in a moving domain (Allaire & Schoenauer, 2007). The perturbations are defined either in a fixed reference configuration — Lagrangian-based perturbations — or in the instantaneous, deformed configuration — Eulerian-based perturbations — (Sokolowski & Zolesio, 1992). These two approaches result eventually to two different descriptions of the *same* physical problem. Considering a stationary Stokes flow interacting with a string model, Van der Zee *et al.* (2011) applied the two linearization approaches in order to derive the adjoint steady fluid-structure equations. In the formulation obtained for the Lagrangian-based perturbations, the coupling conditions at the fluid-solid interface are straightforward, but non-local couplings also exist in the fluid domain and result in significant modifications of the original equations. In the formulation obtained for the Eulerian-based perturbations, the linearised conservation equations are “simpler”, while the coupling conditions, localized at the interface, are more complicated due to the presence of higher-order derivative terms. In the context of time-dependant fluid-structure problems, an Eulerian-based linearisation was proposed by Fernández & Le Tallec (2003a,b), based on the Arbitrary Lagrangian Eulerian (ALE) formulation of the fluid-structure problem (Hughes *et al.*, 1981). They found that in addition to the classical transpiration velocity, the linearised stress coupling results in an *added-stiffness* term that depends on higher-order derivatives of the stationary fluid velocity and pressure, as well as on a deformation operator involving the derivatives of the interface displacement. However, the numerical examples proposed in the paper did not highlight the role of the added stiffness terms and the requirements needed for the proper and accurate capture of the second-order spatial derivatives. For these reasons, we rather follow the Lagrangian-based approach in this thesis, that results in a lower-order differential problem.

The first objective of this thesis is thus to contribute to the definition of a **consistent description of linear fluid-structure instabilities, in a framework that allows an efficient**

numerical resolution, and extend the tools developed for fluid flows to the fluid-structure case. This linear approach is validated by **comparisons with non-linear results** obtained with more classical solvers.

Application cases

The methods developed are used to analyse physically two configurations representative of the two mechanisms of instability described previously. A first study is thus devoted to the **physical analysis of a typical fluid-solid oscillator configuration**: namely, we study how a flexible splitter plate attached behind a circular cylinder surrounded by a laminar flow influences the vortex-shedding mechanisms. This problem is a model for the passive control of wake instabilities (Kwon & Choi, 1996; Assi *et al.*, 2009) or, conversely, for energy-harvesting devices trying to exploit the energy carried by the instabilities (Abdelkefi, 2016; Carini *et al.*, 2017). It is also of interest for the understanding of some locomotion mechanisms found in nature (Lacis *et al.*, 2014): self-developing symmetry-breaking instabilities indeed result in states with non-zero lift that could be exploited for locomotion. Because of the dominant viscous effects and a solid-to-fluid density ratio close to unity, the fully coupled approach introduced above is mandatory if one wants to capture accurately the dynamics of this system.

In a second step, we conduct a **physical analysis of a typical fluid-solid noise-amplifier configuration**. We study the delay of the laminar/turbulent transition by Tollmien-Schlichting waves in a two-dimensional boundary layer by means of a viscoelastic, finite-length compliant coating, a quest that has been the subject of research since the 1960s and the surprising experimental observations of Kramer (1960) on drag-reducing capabilities of flexible surfaces. Delaying the transition is definitely of practical interest, in that it reduces the overall drag. In addition to the low-frequency dynamics associated with Tollmien-Schlichting waves (Carpenter & Garrad, 1985), the interaction between fluid and solid results in possibly globally unstable *travelling-wave flutter* instabilities at higher frequency (Carpenter & Garrad, 1986). A combination of the eigenvalue and resolvent analysis is then adapted to describe this complex dynamics.

For each of these application cases, a more detailed introduction will be made at the beginning of the dedicated chapters.

Passive control of linear fluid-structure instabilities

Once instabilities are characterized, they gain at being controlled. Generally speaking, a simple idea to suppress a non-linear phenomenon, which occurs via the saturation of a linear instability, is to act at the source of this linear instability. Such idea has been systematically formalized for hydrodynamics instabilities, by introducing for instance the concept of *structural sensitivity* of flow instabilities (Giannetti & Luchini, 2006) and, later on, the concept of sensitivity to base flow modifications (Marquet *et al.*, 2008; Brandt *et al.*, 2011). This work highlighted the role of specific regions of the flow in the development of instabilities, and gave hints on *how* these areas should be perturbed — by some rather abstract and general, unspecified practical mechanism — so as to drive the instability in a prescribed way. The key ingredient for these analyses is the *adjoint* equation (Errico, 1997), whose solution allows to compute the sensitivity maps. If the adjoint Navier-Stokes equations are now commonly used for theoretical analyses (Luchini & Bottaro, 2014a) and in engineering applications (Jameson & Ou, 2011), the same is not true concerning the fluid-structure equations. Based on this observation, **local adjoint fluid-structure equations** are determined, and used to build adjoint-based control strategies.

From these theoretical developments, inspiration was taken so as to design control strategies where the structure itself, that deforms under the action of the flow, is used as the *passive* control parameter. On the engineering point of view, there is indeed evidence that the easiest way to modify a fluid flow without having to spend energy during the process is to modify the mechanical

properties of the object that interacts with the flow. These ideas are executed through two complementary approaches, applied to the control of the two main mechanisms of linear instabilities introduced previously.

Shape optimization for controlling self-developing instabilities

With their high operating costs, severe environments and high sensitivity to small geometry changes, aeronautic applications provide obvious applications to *shape optimization*. As early as in the context of the two-dimensional potential flow theory, an effort was put on solving the inverse problem of finding a wing profile that corresponds to a specified pressure distribution (Lighthill, 1945). Some decades after, ideas from the control theory (Lions, 1971) were applied for minimizing the drag of a profile in a Stokes flow by Pironneau (1973) using an adjoint-based approach, and extended a few years later to the viscous, laminar case by Glowinski & Pironneau (1976). The adjoint approach for the shape optimization of a wing in a flow modelled by the compressible Euler equations was first addressed by Jameson (1988). It has since then also been extended to the design of a complete aircraft (Reuther *et al.*, 1996). The viscous case has also been considered (Jameson *et al.*, 1998), as well as the turbulent case (Anderson & Bonhaus, 1999; Nemec *et al.*, 2004). In the broader context of hydrodynamic flow optimization, these methods have now reached maturity: modules for performing adjoint-based geometric shape optimization and sensitivity analyses are now available in engineering CFD softwares, and are promoted as viable alternatives to parametric optimization (ANSYS, 2016).

All of the above approaches however relay on the assumption of a steady regime and a *rigid* structure. When the flow features are simple (typically for cruise regimes), aeroelastic effects can actually be added in a relatively simple way by considering a quasi-static approach (Dowell *et al.*, 2004). In that case, the shape optimization problem reduces to a structural optimization problem with external loads that model the influence of the flow (Haftka, 1977). When the flow features are more complex, this approach is unfortunately no longer accurate. More recently, strongly coupled approaches have therefore been also addressed, but limited to cases where only a few design parameters are used to represent the shape to be optimized. For instance Hur *et al.* (2004) computed design sensitivities of a joined-wing aircraft represented by a beam model, by taking into account the feedback of airloads to the structure, while Lund *et al.* (2003) computed the minimal drag shapes of a flexible object parametrized by NURBS curves in a steady viscous flow using a fully coupled approach. The same approach was followed more recently by Aghajari & Schäfer (2015). For all these cases, the gradient is computed using finite-differences.

When the number of shape parameters increases, the adjoint-based approach becomes more efficient. The key point is then to obtain the adjoint fluid-solid problem at the continuous level, for it allows to obtain an explicit formula for the shape gradient (Allaire & Schoenauer, 2007). This is a particularly tedious task in the fluid-elastic context, which pushed for considering approximate approaches where the geometrical couplings are neglected (Faller *et al.*, 2016; Feppon *et al.*, 2018). To our knowledge, the first attempt for deriving then solving a fully coupled fluid-structure adjoint problem in an Eulerian-based approach was done by Manzoni & Ponti (2016), who derived a continuous adjoint fluid-structure problem for an unsteady Stokes flow interacting with a one-dimensional Koiter solid model. Their derivation resulted in an unsteady Stokes problem backward in time and expressed in the deformed configuration, coupled with the solid model through a rather complicated forcing term. This term was found to depend on the adjoint flow field and on the geometric properties of the interface (for instance, the expression involves the tangential gradient of the normals). The authors used then the adjoint equations to solve a shape optimization problem inspired by haemodynamics concerns. In the present work, we rely on the Lagrangian-based formalism for deriving a shape gradient formula in the fully coupled case.

Turning now on the unsteady effects in coupled flow-structure optimization, they have for instance been considered by Nadarajah & Jameson (2007), who used an adjoint-based method coupled with an Euler solver to optimize the shape of a rigid airfoil undergoing a prescribed oscillation, in order to minimize its time-average coefficient of drag. Drag reductions as high as 46 % have been obtained while maintaining the time-averaged lift coefficient. In the context of micro-air

vehicle design, [Stewart et al. \(2016\)](#) used a vortex-lattice aerodynamic model coupled with a plate finite-element model to compute optimal forced flapping wing design. To our knowledge, only few attempts for taking into account a *self-developping* unsteadiness in the flow about a structure to be optimized were done. In the context of pure hydrodynamics, one can mention the work by [Heuveline & Strauß \(2009\)](#) where the geometry is parametrized by a few points, and that by [Nakazawa & Azegami \(2016\)](#) who used an adjoint-based approach without an *a-priori* parametrization of the shape. For both cases, efforts are put on the stabilization of an unstable mode developing on the steady viscous Navier-Stokes solution, in the case of a rigid geometry.

Shape optimization is considered here as a way for controlling self-developping fluid-elastic instabilities on a steady equilibrium. We show, to our knowledge for the first time in the context of unsteady, strongly coupled fluid-structure instabilities, that an appropriate modification of the geometry can achieve a control of these instabilities. These optimal geometries are computed using a gradient-based approach where an analytic formula is derived for the sensitivity with respect to a modification of the geometry.

Structural optimization for controlling noise-driven instabilities

Another way of controlling fluid-solid instabilities is to act, rather than on the shape, at the level of the material properties themselves (local stiffness, density, etc.).

This approach is particularly adapted for the application case of the transition delay by the use of compliant coatings. Following the early attempts by [Kramer \(1960\)](#), many experimental approaches have indeed tried to reduce the drag with compliant surfaces with different material properties, both in the context of turbulent ([Choi et al., 1997](#); [Bandyopadhyay et al., 2005](#)) and laminar ([Gaster, 1988](#); [Gad-El-Hak et al., 1984](#)) boundary-layer flows. These studies highlighted the need for highly compliant coatings, often made practically as a combination of polymeric materials. As early as in the work by [Benjamin \(1960\)](#), suggestions have been made so as to design appropriate coatings for delaying the boundary-layer transition. Based on numerical computations, [Carpenter \(1993\)](#) estimated the potential benefits, in terms of transitional Reynolds number, that could be retrieved from the use of soft walls. His best-performing compliant panel gave an increase of the transitional Reynolds number by a factor 4.6. Considering two panels mounted in series, the gain reached a factor 6. Based on this observation, he suggested that using a multi-panel wall, each tailored for a specific range of Reynolds numbers, would probably produce the largest transition delay. [Carpenter & Morris \(1990\)](#) investigated the effect of material anisotropy, by adding a term that breaks the isotropy of the plate response with respect to a flow reversal. This approach was intended for mimicking a fibre-composite anisotropic compliant wall. They observed an almost ten-fold rise in transitional Reynolds number. There have also been a few approaches considering a 2d model (but homogeneous in the streamwise direction) for the coating, for instance by [Duncan \(1988\)](#), who showed that a stiff upper layer delays the appearance of the instabilities, or by [Dixon et al. \(1994\)](#), who observed an increase of the transition Reynolds number by a factor 2.5 for a single-layer coating and by a factor 5 for a two-layer coating.

The optimization approaches performed in the aforementioned papers all relied on an assumption of homogeneity in at least one direction: homogeneity in the transverse direction for 1d coatings models, or homogeneity in the streamwise direction for models using the Navier elasticity equation. For both cases, layering (in streamwise or transverse direction) showed an increase in the transition Reynolds number. From these observations, one can expect that a fully non-homogeneous optimized coating would show even greater transition-delaying properties.

The framework developed during the thesis allows to **compute and describe the structural gradients that indicate how to modify the solid properties so as to lower the perturbation amplification gains of a noise-induced fluid-solid instability**, and then to carry out an adjoint-based gradient optimization. This approach is applied to the boundary-layer flow, and will hopefully open new perspectives in the already long story of transition-delaying materials.

Organisation of the manuscript

The rest of the dissertation is divided in three parts, each consisting of two chapters. A first part is devoted to the general methodology while the next parts are devoted to applications.

1. The first part is devoted to a general overview of the numerical methods developed for non-linear and linear fluid-structure simulations.
 - The **Chapter 1** first introduces the general fluid-structure framework that will be used throughout the subsequent chapters. The Arbitrary Lagrangian Eulerian formulation is introduced, formulation that allows to manage the coupling between the solid and the fluid in a consistent fashion. Then, a fully coupled formulation of the non-linear fluid-structure problem is derived. In a second part, we present and validate the numerical methods developed to compute non-linear steady solutions in the aforementioned problem. A fully implicit approach using a Newton method to treat the non-linearities is used, and implemented practically using finite-elements within the programming language FREEFEM++. Apart from the numerical implementation, this introductory chapter does not come with original, new results.
 - The stability analysis of elastic structures strongly coupled to incompressible viscous flows is investigated in the **Chapter 2**, based on a Lagrangian-based exact linearisation of the governing equations introduced previously. The leading eigenvalues/eigenmodes are computed for three configurations representative of classical fluid-structure interaction instabilities, and further analysed. In a second step, the Lagrangian-based approach is compared to the Eulerian-based approach on two representative benchmark cases.
2. The second part is dedicated to the physical analysis and shape optimization of a model problem exhibiting self-developing fluid-structure instabilities: an elastic splitter plate clamped behind a rigid cylinder in a laminar flow.
 - The linear and non-linear dynamics of the aforementioned system is analysed in **Chapter 3**, by performing linear, modal stability analyses and unsteady non-linear simulations. Varying the elasticity of the plate, different regimes of fluid-elastic coupled dynamics are observed in the non-linear simulations. These results are first described, and then analysed in the light of the linear stability analysis.
 - We address in the **Chapter 4** the problem of the passive control of these instabilities using shape optimization. An adjoint-based method for obtaining an explicit formula for the shape gradient of a cost-function based on the coupled fluid-structure eigenvalue is first presented. These results are applied on two types of modes found in the cylinder splitter-plate case previously studied. Deforming the cylinder's surface according to what is prescribed by the shape optimization algorithm, we show to what extent it is possible to control the modes by this means.
3. The last part is dedicated to the physical analysis and structural optimization of a typical noise-amplifier flow: a boundary-layer developing over a flexible coating.
 - In the **Chapter 5**, we analyse the zero adverse pressure gradient, laminar boundary-layer flow over a flat plate in which a viscoelastic, finite-length compliant coating is embedded. Using a resolvent analysis, we investigate how the flexibility of the coating helps in reducing the growth of low-frequency Tollmien-Schlichting waves, but also triggers higher-frequency, solid-based instabilities. These latter waves are globally unstable for purely elastic coatings and are stabilized by viscoelastic damping, but may still result in large energy amplifications, which are analysed.
 - An adjoint-based approach for structural optimization is presented and applied in the shorter and last **Chapter 6** so as to design a compliant material that damps the Tollmien-Schlichting waves, and in the same time mitigates the development of travelling-flutter waves.

The final **Conclusion** summarizes the work and the obtained results, then presents perspectives on further developments. Some technical results, formulas and sketches for proofs are reported in the **Appendices**, as well as a short introduction to the eigenvalue and resolvent analyses.

1

NONLINEAR METHODS FOR FLUID-STRUCTURE PROBLEMS

This chapter first introduces the general fluid-structure framework that will be used throughout the subsequent chapters. The Arbitrary Lagrangian Eulerian formulation is introduced, formulation that allows to manage the coupling between the solid and the fluid in a consistent fashion. Then, a fully coupled formulation of the non-linear fluid-structure problem is derived. In a second part, we present and validate the numerical methods developed to compute non-linear solutions in the aforementioned problem. A fully implicit approach using a Newton method to treat the non-linearities is used, and implemented practically using finite-elements within the programming language FREEFEM++. Details are also given on the techniques that are used, at the algebraic level, to handle the resulting large-scale linear systems. Eventually, the methods are validated on classical fluid-structure benchmark problems. Apart from the numerical implementation, this introductory chapter does not come with original, new results.

Contents

1.1 Equations for a viscous fluid interacting with an elastic structure . . .	16
1.1.1 Non-dimensional parameters describing a fluid-solid system	16
1.1.2 Equations for an elastic solid with large deformations	17
1.1.3 Navier-Stokes equations in ALE coordinates	19
1.1.4 Interface & boundary conditions	22
1.1.5 Monolithic weak formulation	23
1.1.6 Summary	28
1.2 Implicit scheme for solving the non-linear ALE equations	29
1.2.1 Coupling schemes for ALE problems	29
1.2.2 Time discretization	30
1.2.3 (Quasi)-Newton iterations & space discretization	31
1.2.4 Extension problem for non-linear computations	32
1.3 Handling the large-scale resulting linear systems	34
1.3.1 Direct <i>vs.</i> iterative methods	34
1.3.2 Preconditioning the fully coupled fluid-structure problem	34
1.4 Turek's benchmark cases	36
1.4.1 Solid mechanics cases	37
1.4.2 Fluid mechanics cases	37
1.4.3 Fluid-structure coupled cases	38

1.1 Equations for a viscous fluid interacting with an elastic structure

In this section, we introduce the models for the fluid and the structure, which we shall use throughout the rest of the manuscript. In continuum mechanics, flowing fluids and elastic solids are one side very similar: whatever the media, they can be described by momentum, mass and energy conservation equations (Chadwick, 1999), supplemented by continuity conditions at interfaces (in absence of fracture, the media remains indeed continuous, and thus quantities such as velocity or stress must be continuous). On the other hand, we are constantly experiencing the differences between fluids and solids. On the point of view of the modelling, this difference lies in the constitutive relations: while stress in solids depends on the gradients of the *displacement* between adjacent material points, in fluids the shear stress is provoked by the gradients of *velocity*. This discrepancy implies fundamental differences in terms of kinematics. Solid material points present very often reasonably small relative displacements during their movement, that make it easy to follow them independently with a so-called Lagrangian approach. Fluids however usually present large displacements and swirling motions that make it easier to abandon the Lagrangian approach in favour of a fixed-point observer, the so-called Eulerian description. Note that these are however completely arbitrary choices that must be inspired by the case under study: for instance, the elastic-plastic behaviour of solids in forming processes is sometimes better described through an Eulerian point of view (Dawson, 1978), while some gasdynamics problems are more easily treated with a Lagrangian description of the fluid (Zel'Dovich & Raizer, 2012). When finally a system involves a solid region *and* a fluid region, which is the case here, there is no evidence of which point of view is the most appropriate.

In the next sections, after having briefly introduced non-dimensional numbers that are convenient for describing coupled fluid and solid systems, present the governing equations for elastic solids and viscous fluids, and then the Arbitrary Lagrangian Eulerian (ALE) method adopted for tackling the fluid-structure interaction problem will be presented more into details. A reader already familiar with these concepts, and not interested by the details of the derivation, might jump directly to page 28 where all the governing equations are recalled.

1.1.1 Non-dimensional parameters describing a fluid-solid system

In this thesis, we investigate the motion of an elastic solid immersed in an incompressible Newtonian fluid. Unless otherwise stated, the solid is supposed to be homogeneous with a uniform density¹ ρ_s^* in absence of external forces, and its elastic properties are governed by the Poisson coefficient ν_s and the Young modulus E_s^* under the assumption of isotropy. The Newtonian fluid is characterized by its (constant) density ρ_f^* and its kinematic viscosity $\nu_f^* = \eta_f^* / \rho_f^*$, where η_f^* is the dynamic viscosity. We also consider a reference length L^* and a reference velocity U^* , that will be specified later depending on the configuration studied. From these parameters, four non-dimensional numbers can be defined. The flow features will be measured by the Reynolds number

$$\mathcal{R}_e = \frac{L^* U^*}{\nu_f^*} \quad (1.1.1)$$

that evaluates the ratio between convective forces and viscous dissipation. A physically relevant Reynolds number is obtained by taking U^* and D^* representative of characteristic scales for the fluid flow. The fluid-solid interaction is evaluated first through the density ratio

$$\mathcal{M}_s = \frac{\rho_s^*}{\rho_f^*} \quad (1.1.2)$$

that measures the strength of the inertia coupling between the solid and the fluid. When $\mathcal{M}_s \ll 1$, all goes as if a “heavy” solid was moving in a “light” fluid, in such a way that the fluid inertia

¹We adopt the following writing convention: the dimensional quantities are noted with an * superscript, while the non-dimensional quantities are noted without.

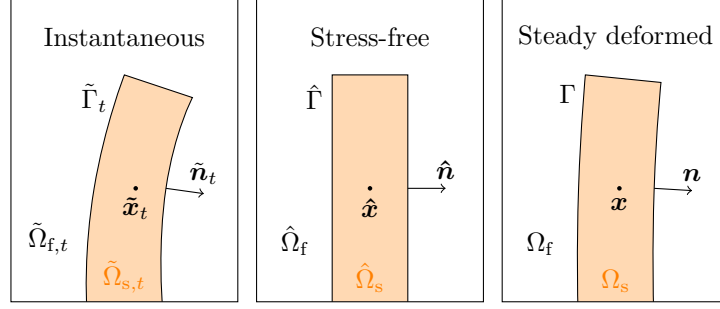


Figure 1.1 – Definitions of notations and spatial domains occupied by the fluid (white) and the solid (orange) in the instantaneous configuration (left), the stress-free reference configuration (middle) and the steady deformed configuration (right). Unlike in the instantaneous configuration, the stress-free and steady deformed configurations are independent of time.

is almost negligible and cannot modify significantly the solid momentum. When $\mathcal{M}_s \simeq 1$, for instance in the case of a structure immersed in water, for blood flow in arteries but also for light structures in air like parachutes (Bazilevs *et al.*, 2013), strong couplings are expected. Apart from the mass ratio, the geometry of the interface in common between the fluid and the solid plays also an important role in the coupling: the coupling is all the stronger as a large mass of fluid is displaced by the movement of the solid. For that reason, depending on the applications, a mass ratio that also integrates geometry constants might more representative of the coupling than the density ratio by itself. Finally, the isotropic solid is characterized by two coefficients. Various couples might be considered, for instance one can use the Poisson coefficient ν_s together with the Cauchy number or its inverse the non-dimensional Young modulus, i.e.

$$\mathcal{E}_s = \frac{E_s^*}{\rho_f^* U^{*2}}. \quad (1.1.3)$$

The strain-stress relations might also be more conveniently written with the non-dimensional Lamé coefficients

$$\lambda_s = \frac{\mathcal{E}_s \nu_s}{(1 + \nu_s)(1 - 2\nu_s)}, \quad \mu_s = \frac{\mathcal{E}_s}{2(1 + \nu_s)}. \quad (1.1.4)$$

Depending on the applications, we will consider one or another set of parameters, possibly supplemented with geometric non-dimensional parameters.

1.1.2 Equations for an elastic solid with large deformations

At time t , the solid occupies the geometric domain $\tilde{\Omega}_{s,t}$, represented on the left side in Fig. 1.1. The motion of the elastic solid is classically defined in a Lagrangian framework: the position of any material point $\tilde{\mathbf{x}}_t$ is identified with respect to its position in a *reference configuration*. A natural choice for this reference configuration is the spatial domain occupied by the structure when *no external stresses* (gravity, fluid load,...) are applied on it, referred to as the *stress-free reference configuration* $\hat{\Omega}_s$ and represented in Fig. 1.1 in the middle. Therefore, unlike the actual configuration $\tilde{\Omega}_{s,t}$, the stress-free reference configuration has usually no experimental evidence and serves only as a convenient mathematical object. In many cases however, for instance if external loads are applied incrementally, the configuration at $t = 0$ can be assimilated as a stress-free configuration. The case of a reference configuration in which there are non-zero *pre-stresses* will be considered in §2.1.2 (steady deformed configuration, represented in Fig. 1.1 in the right side). The solid *displacement field* $\hat{\boldsymbol{\xi}}$ is defined as the difference between the positions in the instantaneous configuration and in the stress-free reference configuration, i.e.

$$\hat{\boldsymbol{\xi}}(\hat{\mathbf{x}}, t) = \tilde{\mathbf{x}}_t - \hat{\mathbf{x}} \quad \text{for } \hat{\mathbf{x}} \in \hat{\Omega}_s. \quad (1.1.5)$$

Quantities related with this configuration will be noted with a hat (^) symbol, whereas quantities defined in the actual configuration will be noted with a tilde (~) symbol.

For sake of simplicity, we limit ourselves to hyperelastic solid models, for which the strain-stress relation derives from a strain energy density function (Ogden, 1997). The following tensors are introduced:

$$\hat{\mathbf{P}}(\hat{\boldsymbol{\xi}}) = \hat{\mathbf{F}}(\hat{\boldsymbol{\xi}}) \hat{\mathbf{S}}(\hat{\boldsymbol{\xi}}), \quad (1.1.6)$$

$$\hat{\mathbf{S}}(\hat{\boldsymbol{\xi}}) = \frac{\mathcal{E}_s}{1 + \nu_s} \left\{ \frac{\nu_s}{1 - 2\nu_s} \text{tr}(\hat{\mathbf{E}}(\hat{\boldsymbol{\xi}})) \mathbf{I} + \hat{\mathbf{E}}(\hat{\boldsymbol{\xi}}) \right\}, \quad (1.1.7)$$

$$\hat{\mathbf{E}}(\hat{\boldsymbol{\xi}}) = \frac{1}{2} \left(\hat{\mathbf{F}}(\hat{\boldsymbol{\xi}})^T \hat{\mathbf{F}}(\hat{\boldsymbol{\xi}}) - \mathbf{I} \right) = \frac{1}{2} \left(\hat{\boldsymbol{\nabla}} \hat{\boldsymbol{\xi}}^T \hat{\boldsymbol{\nabla}} \hat{\boldsymbol{\xi}} + \hat{\boldsymbol{\nabla}} \hat{\boldsymbol{\xi}} + \hat{\boldsymbol{\nabla}} \hat{\boldsymbol{\xi}}^T \right), \quad (1.1.8)$$

$$\hat{\mathbf{F}}(\hat{\boldsymbol{\xi}}) = \mathbf{I} + \hat{\boldsymbol{\nabla}} \hat{\boldsymbol{\xi}}. \quad (1.1.9)$$

The *first Piola-Kirchhoff* stress tensor $\hat{\mathbf{P}}$ relates the force acting in the current configuration $\hat{\Omega}_{s,t}$ to the surface element in the reference configuration $\hat{\Omega}_s$. This tensor writes as a function of the *second Piola-Kirchhoff* stress tensor $\hat{\mathbf{S}}$, that is written here (without dimensions) for a Saint-Venant Kirchhoff (STVK) model. This is the simplest hyperelastic material, for which only geometric non-linearities are considered. The *Green-Lagrange* strain tensor $\hat{\mathbf{E}}$ is a measure of strain, while the *deformation gradient* $\hat{\mathbf{F}}$ characterizes the local deformation of the material. In all these notations, $\hat{\boldsymbol{\nabla}} = \partial/\partial \hat{\mathbf{x}}$ is the differentiation operator with respect to the coordinates in the reference configuration and “T” is the transpose operator. In the stress-free configuration, the solid dynamics is described by the momentum conservation equation that writes as follows (Ogden, 1997) without dimensions:

$$\mathcal{M}_s \frac{\partial^2 \hat{\boldsymbol{\xi}}}{\partial t^2} - \hat{\boldsymbol{\nabla}} \cdot \hat{\mathbf{P}}(\hat{\boldsymbol{\xi}}) = \mathbf{0} \quad \text{in } \hat{\Omega}_s. \quad (1.1.10)$$

Remark. When the strains are small, i.e. $\|\hat{\boldsymbol{\nabla}} \hat{\boldsymbol{\xi}}\| \ll 1$, the quadratic terms in the strain tensor can be neglected and the equations written reduce to much simpler expressions. The Green-Lagrange stress tensor reduces to

$$\hat{\mathbf{E}}(\hat{\boldsymbol{\xi}}) \simeq \frac{1}{2} \left(\hat{\boldsymbol{\nabla}} \hat{\boldsymbol{\xi}} + \hat{\boldsymbol{\nabla}} \hat{\boldsymbol{\xi}}^T \right) \quad (1.1.11)$$

and the first Piola-Kirchhoff stress tensor reduces to the linearised elasticity stress tensor

$$\hat{\boldsymbol{\sigma}}_s(\hat{\boldsymbol{\xi}}) = \frac{\mathcal{E}_s}{1 + \nu_s} \left\{ \frac{\nu_s}{1 - 2\nu_s} (\hat{\boldsymbol{\nabla}} \cdot \hat{\boldsymbol{\xi}}) \mathbf{I} + \frac{1}{2} \left(\hat{\boldsymbol{\nabla}} \hat{\boldsymbol{\xi}} + \hat{\boldsymbol{\nabla}} \hat{\boldsymbol{\xi}}^T \right) \right\}. \quad (1.1.12)$$

In that case, no distinction is made between the reference and deformed configurations.

Turning now on the mass conservation equation, a distinction has to be done between compressible and incompressible solids. Unless otherwise stated, we make the assumption of a uniform density ρ_s^* in absence of forces in the solid. When loads are applied, the density is modified in compressible solids through the relation

$$\rho_s^*(t) = \hat{J}(\hat{\boldsymbol{\xi}}) \rho_s^*(0)$$

where $\hat{J} = \det \hat{\mathbf{F}}$ is the deformation gradient determinant, i.e. a measure of volume changes in the solid. Incompressible materials keep the same density over time, which results into a constraint on \hat{J} , that can be written as

$$\hat{J}(\hat{\boldsymbol{\xi}}) = 1. \quad (1.1.13)$$

A typical nearly incompressible material is for instance rubber. Compressible materials will be considered in the present chapter and in chapters 2, 3 and 4. An incompressible neo-Hookean model will be adopted in chapters 5 and 6.

Remark. The Saint-Venant Kirchhoff modelling is also consistent with thin plate models such as the Föppl-von Kármán or Euler-Bernoulli (in the linear case) models, that are commonly adopted for modelling thin elastic structures, such as airfoils (Hur *et al.*, 2004), flags (Michelin *et al.*, 2008), elastic filaments (Lee *et al.*, 2014), pillars (Leclercq & de Langre, 2018), etc., that are part of

some usual aeroelastic models. These models can actually be derived from the Saint-Venant Kirchhoff elasticity by using appropriate asymptotic developments, taking the plate thickness or aspect ratio as a small parameter (Ciarlet, 1980; Audoly & Pomeau, 2010).

1.1.3 Navier-Stokes equations in ALE coordinates

In the context of fluid-structure interactions, a consistent modelling must ensure that both velocity and stresses are continuous across the interface. A way for achieving this consists in using an *Arbitrary Lagrangian Eulerian* (ALE) formulation for the Navier-Stokes equations.

Navier-Stokes equations in a moving domain

Unlike the structure, the motion of the incompressible, viscous fluid is naturally defined in an Eulerian framework. The Eulerian velocity $\tilde{\mathbf{u}}(\tilde{\mathbf{x}}_t, t)$, defined as the velocity of the fluid at the spatial position $\tilde{\mathbf{x}}_t$ in the instantaneous fluid configuration $\tilde{\Omega}_{f,t}$ (represented in Fig. 1.1 on the left side), satisfies the Navier-Stokes momentum and mass conservation equations

$$\left. \frac{\partial \tilde{\mathbf{u}}}{\partial t} \right|_{\tilde{\mathbf{x}}_t} + (\tilde{\nabla} \tilde{\mathbf{u}}) \tilde{\mathbf{u}} - \tilde{\nabla} \cdot \tilde{\boldsymbol{\sigma}}(\tilde{\mathbf{u}}, \tilde{p}) = \mathbf{0}, \quad \tilde{\nabla} \cdot \tilde{\mathbf{u}} = 0 \quad \text{in } \tilde{\Omega}_{f,t}. \quad (1.1.14)$$

Here \tilde{p} is the pressure field scaled with $\rho_f^* U^{*2}$, and $\tilde{\mathbf{u}}$ the velocity field scaled by the reference velocity U^* . Unlike for the Lagrangian formulation of the structure, the Eulerian formulation implies the presence of a non-linear advection term $(\tilde{\nabla} \tilde{\mathbf{u}}) \tilde{\mathbf{u}}$. The Cauchy stress tensor writes as a function of the pressure and the velocity gradients,

$$\tilde{\boldsymbol{\sigma}}(\tilde{\mathbf{u}}, \tilde{p}) = -\tilde{p} \mathbf{I} + \frac{1}{\mathcal{R}_e} \left(\tilde{\nabla} \tilde{\mathbf{u}} + \tilde{\nabla} \tilde{\mathbf{u}}^T \right), \quad (1.1.15)$$

where the Reynolds number \mathcal{R}_e is defined in (1.1.1). The differentiation operator $\tilde{\nabla} = \partial/\partial \tilde{\mathbf{x}}_t$ refers here to the derivatives with respect to the spatial position $\tilde{\mathbf{x}}_t$ (i.e. the position of the Eulerian observer of the flow) in the moving fluid domain $\tilde{\Omega}_{f,t}$.

As it is, we see that equation (1.1.14) is not straightforward to handle in moving domains: there is no easy way for determining practically the modification of $(\tilde{\mathbf{u}}, \tilde{p})$ resulting from a modification of $\tilde{\Omega}_{f,t}$. For pure fluid problems, $\tilde{\mathbf{x}}_t$ can be kept fixed, since the domain does not move. When the domain moves, if $\tilde{\mathbf{x}}_t$ can be still kept fixed in regions that are never swept by the moving boundaries, something has to be done when it is not the case — otherwise the observer will be like “jostled” by the domain borders. Numerous techniques have therefore been proposed to handle equations defined on moving domains. We will concentrate on the so-called *Arbitrary Lagrangian Eulerian* (ALE) approach for reasons that will appear more clearly in the following. Let us first briefly review other types of strategies.

In the *immersed boundary method* (IBM) proposed by Peskin (1977), the Eulerian coordinate system is kept in the fluid, the Lagrangian system in the solid, and the movement of interfaces is represented in Lagrangian coordinates by a Dirac delta function that can be seen as a source term in the fluid equations. Consequently, a fixed computational grid is used for the fluid and the support of the deformable solid is represented on another grid. This class of methods is referred to as *non-conforming*, because the solid and the fluid computational grids do not conform (Fig. 1.2a). A closely related approach is the *fictitious domain* (FD) approach (Glowinski *et al.*, 1994a, 2001), where the boundary condition for the fluid at the deformable interfaces is enforced through Lagrange multipliers. The level-set method (Chang *et al.*, 1996) also consists in combining an Eulerian representation in the fluid and a Lagrangian description of the solid movement, coupled through an interface-capturing method (level-set, see in Fig. 1.2c). Another approach consists in adopting a fully Eulerian representation (Richter & Wick, 2010): this strategy is also related to the previous approaches, but in that case the solid dynamics is treated with Eulerian coordinates like the fluid. One should also mention other types of approaches, for instance the space-time approach (Tezduyar *et al.*, 1992), the isogeometric analysis (Bazilevs *et al.*, 2008). Lattice-Boltzmann methods have also been applied to fluid-structure interaction problems (Ladd, 1994).

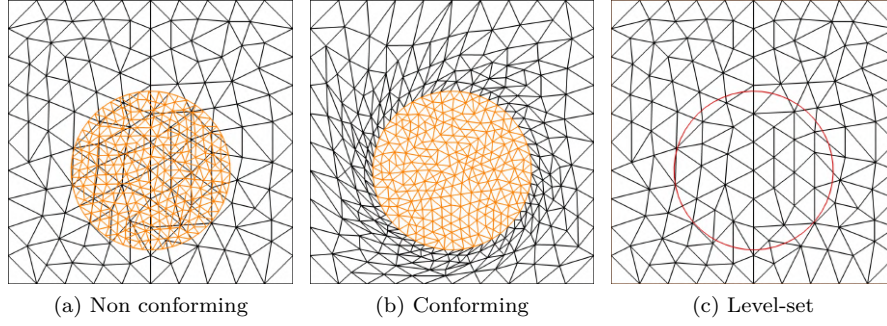


Figure 1.2 – Domain deformation techniques. The orange disk is moved (combined translation/rotation) inside a square domain whose edges are kept fixed.

Non-conforming approaches are found to be computationally efficient, but may lack of robustness in the description of wall-based quantities. This has pushed for considering mesh-conforming approaches, where a consistent description at the interfaces is provided. With the Arbitrary Lagrangian Eulerian formulation, whose early finite-element applications are presented for example in the paper by [Hughes *et al.* \(1981\)](#), the advantages of the Lagrangian representation for solids and of the Eulerian representation for fluids are combined in an elegant generalization ([Donea *et al.*, 2004](#)). The fluid domain $\tilde{\Omega}_{f,t}$ is deformed in order to conform with the solid domain $\tilde{\Omega}_{s,t}$ at the fluid-structure boundary (see Fig. 1.2b). This provides a great precision of the interface description, at the price of having to use a supplementary ingredient to deform practically the fluid domain, as we will see later.

ALE formulation of the Navier–Stokes equations

Let us then focus on the ALE formulation of the Navier–Stokes equations. Given the interface solid displacement $\hat{\xi}|_{\hat{\Gamma}}$, an *extension operator* is introduced, that expresses the position of the actual fluid domain $\tilde{\Omega}_{f,t}$ with respect to a reference fluid domain $\hat{\Omega}_f$ (represented in Fig. 1.1 in the middle):

$$\hat{\mathcal{A}}_t : \begin{cases} \hat{\Omega}_f \times \mathbb{R}^+ & \longrightarrow \tilde{\Omega}_{f,t} \times \mathbb{R}^+ \\ (\hat{\mathbf{x}}, t) & \longmapsto (\tilde{\mathbf{x}}_t, t) \end{cases} . \quad (1.1.16)$$

The coordinates in the actual configuration $\tilde{\Omega}_{f,t} \cup \tilde{\Omega}_{s,t}$ are then deduced from the coordinates in the solid stress-free reference configuration $\hat{\Omega}_s$ and the fluid reference configuration $\hat{\Omega}_f$ as follows,

$$\tilde{\mathbf{x}}_t = \begin{cases} \hat{\mathcal{A}}_t(\hat{\mathbf{x}}, t) & \hat{\mathbf{x}} \in \hat{\Omega}_f \\ \hat{\mathbf{x}} + \hat{\xi}(\hat{\mathbf{x}}, t) & \hat{\mathbf{x}} \in \hat{\Omega}_s \end{cases} . \quad (1.1.17)$$

From this definition, a so-called extension displacement field is defined in the reference fluid domain $\hat{\Omega}_f$ as

$$\hat{\xi}_e(\hat{\mathbf{x}}, t) = \tilde{\mathbf{x}}_t - \hat{\mathbf{x}} = \hat{\mathcal{A}}_t(\hat{\mathbf{x}}, t) - \hat{\mathbf{x}} \quad \text{for } \hat{\mathbf{x}} \in \hat{\Omega}_f. \quad (1.1.18)$$

Unlike the solid displacement, the extension displacement is not governed by a physical equation. Instead, an arbitrary *extension operator* is introduced so as to propagate the solid displacement at the fluid-structure boundary into the fluid domain. In general the extension operator — that will be written $\hat{\Sigma}_e$ — is assumed to follow an elliptic equation that propagates smoothly the deformations — such as the Laplace equation or a linear elasticity equation ([Stein *et al.*, 2003](#)). Enhanced models that confer an increased regularity to the extension field, such as the biharmonic equation, are also used ([Helenbrook, 2003](#)), but will not be considered here because they come with an increased numerical cost. The extension displacement field is thus assumed to be governed by

$$\begin{aligned} -\hat{\nabla} \cdot \hat{\Sigma}_e(\hat{\xi}_e) &= \mathbf{0} && \text{in } \hat{\Omega}_f, \\ \hat{\xi}_e(\hat{\mathbf{x}}, t) - \hat{\xi}(\hat{\mathbf{x}}, t) &= \mathbf{0} && \text{on } \hat{\Gamma}, \\ \hat{\xi}_e(\hat{\mathbf{x}}, t) &= \mathbf{0} && \text{on } \partial\hat{\Omega}_f \setminus \hat{\Gamma}, \end{aligned} \quad (1.1.19)$$

where $\hat{\Gamma}$ is the fluid-solid interface recasted in the reference configuration. We do not precise yet any special expression for $\hat{\Sigma}_e$ since this tensor is arbitrary, but for simplicity we however assume that it defines a linear, first-order differential operator. A discussion on the regularity conditions required for this mapping at the continuous and discrete levels is done in the paper by [Formaggia & Nobile \(1999\)](#). Basically a one-to-one relation has to be preserved between the nodes in the reference configuration and the nodes in the actual configuration. A more detailed discussion about practical choices for the extension operator is done in §1.2.4.

Let us then derive a first ALE formulation of the Navier–Stokes equations. Using the chain rule, the time-derivative in (1.1.14) can be expanded as follows,

$$\left. \frac{\partial \tilde{\mathbf{u}}}{\partial t} \right|_{\tilde{\mathbf{x}}_t} = \left. \frac{\partial \tilde{\mathbf{u}}}{\partial t} \right|_{\hat{\mathbf{x}}} - (\tilde{\nabla} \tilde{\mathbf{u}}) \tilde{\mathbf{w}}, \quad (1.1.20)$$

where $\tilde{\mathbf{w}}$ is the Lagrangian velocity of the fluid domain expressed in the actual domain $\tilde{\Omega}_{f,t}$, *i.e.*

$$\tilde{\mathbf{w}} = \left. \frac{\partial \hat{\mathcal{A}}_t}{\partial t} \right|_{\hat{\mathbf{x}}} \circ \hat{\mathcal{A}}_t^{-1}. \quad (1.1.21)$$

The composition by $\hat{\mathcal{A}}_t^{-1}$ maps the fluid domain velocity, naturally expressed in the reference configuration, to its expression in the actual configuration. Replacing (1.1.20) in (1.1.14) yields to the ALE formulation of the Navier–Stokes equations

$$\left. \frac{\partial \tilde{\mathbf{u}}}{\partial t} \right|_{\hat{\mathbf{x}}} + (\tilde{\nabla} \tilde{\mathbf{u}}) (\tilde{\mathbf{u}} - \tilde{\mathbf{w}}) - \tilde{\nabla} \cdot \tilde{\sigma}(\tilde{\mathbf{u}}, \tilde{p}) = \mathbf{0}, \quad \tilde{\nabla} \cdot \tilde{\mathbf{u}} = 0 \quad \text{in } \tilde{\Omega}_{f,t}. \quad (1.1.22)$$

In the momentum equation, a convective-type term related to the domain movement has appeared. In a fixed Eulerian setting, we have $\tilde{\mathbf{w}} = 0$ and the domain is fixed. In a Lagrangian description, $\tilde{\mathbf{w}} = \tilde{\mathbf{u}}$ and the domain is moving with the velocity $\tilde{\mathbf{u}}$. For that reason, the ALE description lies somewhere “arbitrarily” in between: at the interface the description is purely Lagrangian, far away it is Eulerian, while in between both the Eulerian and Lagrangian representation are used, with a smooth transition between them. For the derivation of the conservative form of this equation, we refer to the Ph.D. manuscript of [Nobile \(2001\)](#), section 1.1. In this formulation the domain movement is still partly embedded in the support domain $\tilde{\Omega}_{f,t}$ of the equation.

Let us now derive a second ALE formulation that depends only on quantities evaluated in the reference fluid domain $\hat{\Omega}_f$. We introduce for that purpose the fluid velocity $\hat{\mathbf{u}}$ in the reference configuration through the identity

$$\hat{\mathbf{u}}(\hat{\mathbf{x}}, t) = \tilde{\mathbf{u}}(\tilde{\mathbf{x}}_t, t) \quad \text{or} \quad \hat{\mathbf{u}} = \tilde{\mathbf{u}} \circ \hat{\mathcal{A}}_t, \quad (1.1.23)$$

and the same for the pressure. The fluid velocity at the reference position $\hat{\mathbf{x}}$ is equal to the Eulerian fluid velocity at the instantaneous position $\tilde{\mathbf{x}}_t = \hat{\mathcal{A}}_t(\hat{\mathbf{x}}, t)$. Following [Le Tallec & Mouro \(2001\)](#), changing the variables in (1.1.22) using the variable change (1.1.17), we obtain the non-conservative ALE formulation of the incompressible Navier–Stokes equations

$$\hat{J}(\hat{\xi}_e) \left. \frac{\partial \hat{\mathbf{u}}}{\partial t} \right|_{\hat{\mathbf{x}}} + \left(\hat{\nabla} \hat{\mathbf{u}} \hat{\Phi}(\hat{\xi}_e) \right) (\hat{\mathbf{u}} - \hat{\mathbf{w}}) - \hat{\nabla} \cdot \hat{\Sigma}(\hat{\mathbf{u}}, \hat{p}, \hat{\xi}_e) = \mathbf{0} \quad \text{in } \hat{\Omega}_f \quad (1.1.24)$$

$$\hat{\nabla} \cdot \left(\hat{\Phi}(\hat{\xi}_e) \hat{\mathbf{u}} \right) = 0. \quad \text{in } \hat{\Omega}_f \quad (1.1.25)$$

Details on the formulas used to express the gradient and divergence operators in the stress-free reference configuration are given in Appendix C.1. We refer the reader to the paper by [Fernández & Le Tallec \(2003a\)](#) for the expression of the conservative form of the equation. In the reference configuration, the fluid domain velocity is simply given by

$$\hat{\mathbf{w}} = \left. \frac{\partial \hat{\mathcal{A}}_t}{\partial t} \right|_{\hat{\mathbf{x}}} = \left. \frac{\partial \hat{\xi}_e}{\partial t} \right|_{\hat{\mathbf{x}}}. \quad (1.1.26)$$

A more visual point of view of this variable change is represented in Fig. 1.3. On the left, a snapshot of the flow about an elastic plate (Turek & Hron, 2006) is represented, and shows the plate bent under the action of the flow. The bending is dynamical and this geometry would actually evolve with time. The flow recasted in the stress-free reference configuration is represented on the right. The change of variable corresponds visually to the orange arrows, that map the reference and actual configurations in a dynamical way. In this configuration, as time goes on, the geometry stays fixed but the arrows are constantly changing so as to represent the movement of the domains. In equations (1.1.24) and (1.1.25), the variable change (1.1.23) has introduced new geometric operators, a *deformation operator* $\hat{\mathbf{F}}$ and \hat{J} the Jacobian of the deformation gradient which are respectively defined as

$$\hat{\mathbf{F}}(\hat{\xi}_e) = \hat{J}(\hat{\xi}_e) \hat{\mathbf{F}}(\hat{\xi}_e)^{-1}, \quad \hat{J}(\hat{\xi}_e) = \det(\hat{\mathbf{F}}(\hat{\xi}_e)) \quad (1.1.27)$$

with $\hat{\mathbf{F}}(\hat{\xi}_e) = \mathbf{I} + \hat{\nabla} \hat{\xi}_e$. The determinant \hat{J} is a scalar field measuring the local volume deformation between the actual and reference configuration, and should remain positive to ensure that (1.1.16) is one-to-one. The deformation operator $\hat{\mathbf{F}}(\hat{\xi}_e)$ expresses how an infinitesimal surface in the instantaneous configuration is transformed in the reference configuration – for instance the normal vectors are transformed following the Nanson’s formula $\tilde{\mathbf{n}}_t = \hat{\mathbf{F}}(t)^T \hat{\mathbf{n}}$ (see Aris (1989) and the Appendix C.1). Note that in the two-dimensional case, $\hat{\mathbf{F}}$ is an affine operator in a Cartesian frame, while there is a quadratic non-linearity in the 3d case. We refer again the reader to the Appendix C.1 for more technical details, in particular the developed expressions. When the fluid domain does not move, these deformation operators are $\hat{\mathbf{F}} = \mathbf{I}$, $\hat{J} = 1$ and $\hat{\mathbf{F}} = \mathbf{I}$. The fluid stress tensor $\hat{\Sigma}$ in the reference configuration writes as

$$\hat{\Sigma}(\hat{\mathbf{u}}, \hat{p}, \hat{\xi}_e) = \hat{\sigma}(\hat{\mathbf{u}}, \hat{p}, \hat{\xi}_e) \hat{\mathbf{F}}(\hat{\xi}_e)^T \quad (1.1.28)$$

where $\hat{\sigma}$ is the Cauchy stress tensor expressed back in the reference configuration. It therefore depends on the geometric operators and writes as $\hat{\sigma}(\hat{\mathbf{u}}, \hat{p}, \hat{\xi}_e) = -\hat{p} \mathbf{I} + 2/\mathcal{R}_e \hat{\mathbf{D}}(\hat{\mathbf{u}}, \hat{\xi}_e)$, where $\hat{\mathbf{D}}$ is the viscous dissipation tensor that writes as

$$\hat{\mathbf{D}}(\hat{\mathbf{u}}, \hat{\xi}_e) = \frac{1}{2} \frac{1}{\hat{J}(\hat{\xi}_e)} \left((\hat{\nabla} \hat{\mathbf{u}}) \hat{\mathbf{F}}(\hat{\xi}_e) + \hat{\mathbf{F}}(\hat{\xi}_e)^T (\hat{\nabla} \hat{\mathbf{u}})^T \right). \quad (1.1.29)$$

Clearly, the deformation of the fluid domain induces extra non-linearities in the governing equations. If the non-linearity arising from the velocity advection is still quadratic, a rational non-linearity arises in the geometric terms due to the factor $1/\hat{J}$ in the stress tensor. Of course, in the rigid case, this expression reduces to the classical expression used in hydrodynamics, and the ALE formulation (1.1.24)–(1.1.25) then reduces to the Eulerian formulation (1.1.14) of the incompressible Navier–Stokes equations.

Remark – continuity equation. Using the Piola identity (C.1.2) and a few tensor indices manipulations, the continuity equation (1.1.25) can be written $\hat{\nabla} \cdot (\hat{\mathbf{F}}(\hat{\xi}_e) \hat{\mathbf{u}}) = \hat{\mathbf{F}}(\hat{\xi}_e)^T : \hat{\nabla} \hat{\mathbf{u}} = 0$. This second writing comes with a lower differentiation order for the displacement unknown. For that reason, it will be used in the variational forms given in §1.1.5.

1.1.4 Interface & boundary conditions

The fluid and solid dynamics are coupled at the fluid-structure interface, where the stresses and velocities on both sides have to match. In the reference configuration, the velocity continuity condition writes as

$$\hat{\mathbf{u}}(\hat{\mathbf{x}}, t) - \frac{\partial \hat{\xi}}{\partial t}(\hat{\mathbf{x}}, t) = \mathbf{0} \quad \text{for} \quad \hat{\mathbf{x}} \in \hat{\Gamma}. \quad (1.1.30)$$

We see here how using the ALE formulation defines without any ambiguity the position of the common interface in a unified coordinate system, and thus makes it straightforward to write the interface conditions. Note that in the solid the (Lagrangian) velocity is everywhere defined as

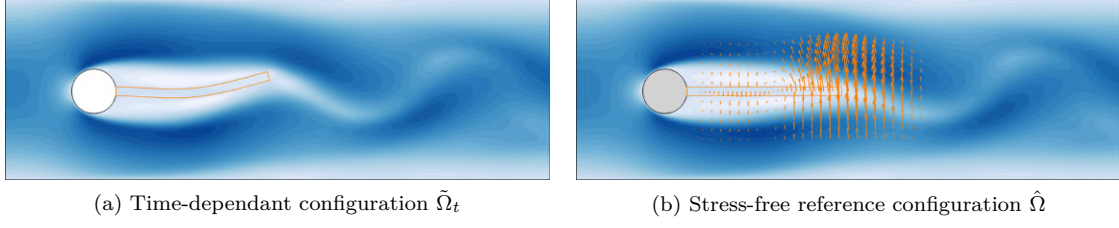


Figure 1.3 – Actual and reference configurations. Snapshot extracted from a non-linear simulation, showing (a) the fluid and the structure domains in their actual configuration, i.e. the one visible in a laboratory experiment (the interface is materialized with the solid orange line, while the streamwise velocity is depicted in blue color), and (b) the same physical state recasted in a reference configuration where the solid is fixed, the fluid domain motion $\hat{\xi}_e$ and the solid displacement $\hat{\xi}$ being represented by the orange arrows.

$\hat{\mathbf{u}}_s = \partial \hat{\xi} / \partial t$, and also matches the fluid geometrical domain velocity $\hat{\mathbf{w}} = \partial \hat{\xi}_e / \partial t$ on the interface. The continuity of the normal stresses writes as

$$\hat{\Sigma}(\hat{\mathbf{u}}, \hat{p}, \hat{\xi}_e) \hat{\mathbf{n}} = \hat{\mathbf{F}}(\hat{\xi}) \hat{\mathbf{S}}(\hat{\xi}) \hat{\mathbf{n}} \quad \text{on} \quad \hat{\Gamma}. \quad (1.1.31)$$

The interface continuity conditions are supplemented by conditions on the other boundaries that enclose the fluid-structure domain. Unless otherwise stated, we assume for simplicity that the solid boundary is divided between $\hat{\Gamma}$ and a fixed boundary Γ_s^D where a zero displacement Dirichlet boundary condition is applied (i.e. the solid is clamped on Γ_s^D). The fluid domain is bounded by the fluid-structure interface $\hat{\Gamma}$, a fixed boundary Γ_f^D , where Dirichlet boundary conditions are given for the fluid on the form $\hat{\mathbf{u}} = \mathbf{u}_\infty$ (where \mathbf{u}_∞ is an inflow velocity or the no-slip boundary condition $\mathbf{u}_\infty = \mathbf{0}$), and a fixed boundary Γ_f^N where a stress-free condition $\hat{\Sigma}(\hat{\mathbf{u}}, \hat{p}, \mathbf{0}) \hat{\mathbf{n}} = \mathbf{0}$ is applied. A discussion on the impact of different outflow conditions for shear flow is available in the paper by Heywood *et al.* (1996). Finally, the extension displacement is set to zero in $\partial \hat{\Omega}_f \setminus \hat{\Gamma}$.

Remark. There is actually no need for defining the extension field in a region that coincides with the fluid region: for practical applications a sub-region $\hat{\Omega}_e \subset \hat{\Omega}_f$ containing $\hat{\Gamma}$ is defined, and we rather impose $\hat{\xi}_e = \mathbf{0}$ on $\partial \hat{\Omega}_e \setminus \hat{\Gamma}$ and set the extension displacement to zero elsewhere, which allows to get rid of the extension problem far away from the solid and spares computational resources. For simplicity, the equations will be however written in the case where $\hat{\Omega}_e = \hat{\Omega}_f$.

1.1.5 Monolithic weak formulation

Instead of considering the local equations, it will be useful to consider the associated weak formulations — also referred to as the virtual work principle in the solid mechanics terminology. This point of view has several advantages. First, it is closely related to the numerical treatment of the equations and their associated boundary conditions by the finite element method, that we will use for solving numerically the equations. It also allows a reasoning in terms of well-defined abstract operators, which considerably simplifies the writing of the equations and also includes the interface conditions (stress, displacement, velocity) in a natural way.

Functional setting

We follow here a standard approach for the representation of the ALE variables (Wick, 2013a; Deparis *et al.*, 2016), by introducing the spaces

$$\begin{aligned} \hat{\mathcal{U}}_f &= \left\{ \mathbf{f} \in \mathcal{H}^1(\hat{\Omega}_f), \mathbf{f} = \mathbf{0} \text{ on } \Gamma_f^D \right\}, \quad \text{and} \quad \hat{\mathcal{U}}_s = \left\{ \mathbf{f} \in \mathcal{H}^1(\hat{\Omega}_s), \mathbf{f} = \mathbf{0} \text{ on } \Gamma_s^D \right\}, \\ \hat{\mathcal{U}}_e &= \left\{ \mathbf{f} \in \mathcal{H}^1(\hat{\Omega}_f), \mathbf{f} = \mathbf{0} \text{ on } \partial \hat{\Omega}_f \setminus \hat{\Gamma} \right\}, \\ \hat{\mathcal{P}} &= \mathcal{L}^2(\hat{\Omega}_f), \end{aligned}$$

defined respectively for the fluid velocity, the solid displacement, the extension displacement and the fluid pressure fields whatever t in some interval $[0, T]$. $\mathcal{L}^2(\Omega)$ is the space of Lebesgue square-integrable functions over some space Ω , while $\mathcal{H}^1(\Omega)$ is the space of functions in $\mathcal{L}^2(\Omega)$ for which the derivatives are also in $\mathcal{L}^2(\Omega)$, see [Ciarlet \(2013\)](#). The Dirichlet boundary conditions other than those at the interface are embedded in these spaces. Practically, these conditions will be imposed by penalization at the algebraic level.

The specificity of the fluid-structure setting (and more generally for any multiphysics problem) lies in the presence of several problems linked by coupling conditions. Several approaches are available for adding these conditions within a consistent functional setting. A common one consists in adding supplementary variables to the problem, seen as Lagrange multipliers introduced so as to enforce the interface constraints. Each new variable is known *a priori* and represents the variable dual to the imposed constraint ([Babuška, 1973](#); [Barbosa & Hughes, 1991](#)). In the context of the Navier–Stokes equations for instance, [Bazilevs & Hughes \(2005\)](#) used a Lagrange multiplier method to enforce the well-known no-slip Dirichlet boundary condition, through the addition of a supplementary variable representing the interface stress. This was found to result in an improved overall quality of the solution. In particular, the interface loads are obtained directly from the Lagrange multipliers variables, which avoids having to differentiate the velocity to get the stresses. This approach has also been successfully applied for imposing boundary conditions at moving interfaces in fixed computational grids, for instance in the fictitious domain method evoked before ([Glowinski et al., 1994b](#); [Court et al., 2010](#)). The same kind of strategy will be used here to enforce velocity and displacement continuity conditions. In the context of fluid-structure interaction in the ALE setting, the representation of the problem by an unique set of equations allows however for a completely implicit treatment of the stress interface condition in the coupled weak formulation, as proposed by [Le Tallec & Mouro \(2001\)](#). More precisely, a boundary Lagrange multiplier $\hat{\lambda} \in \hat{\mathcal{U}}_{\hat{\Gamma}}$ with $\hat{\mathcal{U}}_{\hat{\Gamma}} = \mathcal{H}^{-1/2}(\hat{\Gamma})$ is introduced, such that

$$\hat{\lambda} = \hat{\mathbf{F}}(\hat{\xi})\hat{\mathbf{S}}(\hat{\xi})\hat{\mathbf{n}} = \hat{\Sigma}(\hat{\mathbf{u}}, \hat{p}, \hat{\xi}_e)\hat{\mathbf{n}}, \quad (1.1.32)$$

The variable $\hat{\lambda}$ represents the stress on the fluid *and* the solid side (since from (1.1.31) the two have to match). This allows for the stress continuity condition to be automatically satisfied in a weak sense, provided that the test-functions for the fluid and the solid momentum equations coincide at the interface. We use this Lagrange multiplier to enforce the velocity interface condition. By the same way, a Lagrange multiplier is introduced so as to satisfy the displacement interface condition of the extension problem (1.1.19),

$$\hat{\lambda}_e = \hat{\Sigma}_e(\hat{\xi}_e)\hat{\mathbf{n}}. \quad (1.1.33)$$

This new variable represents the extension pseudostress, i.e. the artificial load that is applied at the interface as a result of the presence of the extension operator. Since it does not have any physical meaning, this quantity is not equilibrated by any solid stress. This Lagrange multiplier $\hat{\lambda}_e \in \hat{\mathcal{U}}_{\hat{\Gamma}}$ will be used to enforce the displacement continuity condition.

In the next sections, we begin by writing the coupled weak formulation. Then, we present a block formulation decomposed in three fields (fluid, solid and extension). The notations with ψ 's symbols used for instance by [Wick \(2013a\)](#) are adopted for noting the test-functions, while we take the notations introduced by [Fernández & Moubachir \(2005\)](#) for the expression of the different abstract operators.

Single-field coupled weak formulation

After integration by parts of solid momentum equation (1.1.10) multiplied by $\hat{\psi}_s^u \in \hat{\mathcal{U}}_s$, the supplementary interface variable $\hat{\lambda}$ defined in (1.1.32) appears in the only remaining interface integral on $\hat{\Gamma}$, namely

$$\mathcal{M}_s \int_{\hat{\Omega}_s} \frac{\partial^2 \hat{\xi}}{\partial t^2} \cdot \hat{\psi}_s^u \, d\hat{\Omega} + \int_{\hat{\Omega}_s} \hat{\mathbf{P}}(\hat{\xi}) : \hat{\nabla} \hat{\psi}_s^u \, d\hat{\Omega} - \int_{\hat{\Gamma}} \hat{\lambda} \cdot \hat{\psi}_s^u \, d\hat{\Gamma} = 0 \quad \forall \hat{\psi}_s^u \in \hat{\mathcal{U}}_s,$$

where we recall that $\hat{\mathbf{P}} = \hat{\mathbf{F}}\hat{\mathbf{S}}$. In order to obtain a solid problem that is first-order in time, a supplementary solid velocity variable $\hat{\mathbf{u}}_s$ is further introduced, such as

$$\hat{\mathbf{u}}_s - \frac{\partial \hat{\boldsymbol{\xi}}}{\partial t} = \mathbf{0}. \quad (1.1.34)$$

Remark. Although convenient for our purpose of deriving linear stability problems on the form of generalized, linear eigenvalue problems, this augmented solid formulation is not mandatory. In the context of strongly coupled non-linear simulations, while the augmented approach has been adopted for instance by [Richter & Wick \(2010\)](#), other authors like for instance [Deparis et al. \(2016\)](#) kept a formulation with the solid displacement variable alone.

Now introducing the test-functions $\hat{\boldsymbol{\psi}}^u \in \hat{\mathcal{U}}_f$, integrating by parts the fluid momentum equation (1.1.24) multiplied by $\hat{\boldsymbol{\psi}}^u$, then using (1.1.28) to express the fluid stress tensor, we arrive after integration by parts to

$$\begin{aligned} & \int_{\hat{\Omega}_f} \hat{J}(\hat{\boldsymbol{\xi}}_e) \frac{\partial \hat{\mathbf{u}}}{\partial t} \cdot \hat{\boldsymbol{\psi}}^u \, d\hat{\Omega} - \int_{\hat{\Omega}_f} \hat{\nabla} \hat{\mathbf{u}} \hat{\boldsymbol{\Phi}}(\hat{\boldsymbol{\xi}}_e) \frac{\partial \hat{\boldsymbol{\xi}}_e}{\partial t} \cdot \hat{\boldsymbol{\psi}}^u \, d\hat{\Omega} \dots \\ & + \int_{\hat{\Omega}_f} \left(\hat{\nabla} \hat{\mathbf{u}} \hat{\boldsymbol{\Phi}}(\hat{\boldsymbol{\xi}}_e) \hat{\mathbf{u}} \cdot \hat{\boldsymbol{\psi}}^u + \frac{2}{\mathcal{R}_e} \hat{\mathbf{D}}(\hat{\mathbf{u}}, \hat{\boldsymbol{\xi}}_e) \hat{\boldsymbol{\Phi}}(\hat{\boldsymbol{\xi}}_e)^T : \hat{\nabla} \hat{\boldsymbol{\psi}}^u \right) d\hat{\Omega} \dots \\ & - \int_{\hat{\Omega}_f} \hat{p} \hat{\boldsymbol{\Phi}}(\hat{\boldsymbol{\xi}}_e)^T : \hat{\nabla} \hat{\boldsymbol{\psi}}^u \, d\hat{\Omega} + \int_{\hat{\Gamma}} \hat{\boldsymbol{\lambda}} \cdot \hat{\boldsymbol{\psi}}^u \, d\hat{\Gamma} = 0 \quad \forall \hat{\boldsymbol{\psi}}^u \in \hat{\mathcal{U}}_f. \end{aligned}$$

Like for the solid equation, using (1.1.31) and (1.1.32), the term $\hat{\boldsymbol{\lambda}}$ appears in the remaining interface integral (with an opposite sign because the normals are reversed). Similarly, weak formulations for the continuity equation are obtained by integrating (1.1.25) multiplied by $\hat{\psi}^p \in \hat{\mathcal{P}}$ over $\hat{\Omega}_f$. A weak formulation of the extension problem is obtained by multiplying (1.1.19) by $\hat{\boldsymbol{\psi}}_e^\xi \in \hat{\mathcal{U}}_e$, which make the supplementary variable $\hat{\boldsymbol{\psi}}^\lambda \in \hat{\mathcal{U}}_{\hat{\Gamma}}$, defined in (1.1.33), appear in the remaining interface integral. The velocity and displacement boundary conditions still remain, which are treated in a weak form: the interface velocity and displacement equations (1.1.30) and (1.1.5) are multiplied by $\hat{\boldsymbol{\psi}}^\lambda \in \hat{\mathcal{U}}_{\hat{\Gamma}}$ and $\hat{\boldsymbol{\psi}}^\lambda \in \hat{\mathcal{U}}_{\hat{\Gamma}}$ respectively, then integrated over $\hat{\Gamma}$. Putting all together, we obtain

$$\begin{aligned} \left\langle \hat{\boldsymbol{\psi}}, \hat{\mathcal{T}}_{\text{fsi}}(\hat{\mathbf{q}}) \partial_t \hat{\mathbf{q}} \right\rangle &= \int_{\hat{\Omega}_s} \left\{ \frac{\partial \hat{\boldsymbol{\xi}}}{\partial t} \cdot \hat{\boldsymbol{\psi}}^\xi + \mathcal{M}_s \frac{\partial \hat{\mathbf{u}}_s}{\partial t} \cdot \hat{\boldsymbol{\psi}}_s^u \right\} d\hat{\Omega} \\ &+ \int_{\hat{\Omega}_f} \left\{ \hat{J}(\hat{\boldsymbol{\xi}}_e) \frac{\partial \hat{\mathbf{u}}}{\partial t} - (\hat{\nabla} \hat{\mathbf{u}}) \hat{\boldsymbol{\Phi}}(\hat{\boldsymbol{\xi}}_e) \frac{\partial \hat{\boldsymbol{\xi}}_e}{\partial t} \right\} \cdot \hat{\boldsymbol{\psi}}^u \, d\hat{\Omega} \\ &- \int_{\hat{\Gamma}} \frac{\partial \hat{\boldsymbol{\xi}}}{\partial t} \cdot \hat{\boldsymbol{\psi}}^\lambda \, d\hat{\Gamma}, \end{aligned} \quad (1.1.35)$$

defining the operator $\hat{\mathcal{T}}_{\text{fsi}}$ acting on time-derivatives, and where $\hat{\mathbf{q}} = [\hat{\boldsymbol{\xi}}, \hat{\mathbf{u}}_s, \hat{\boldsymbol{\xi}}_e, \hat{\boldsymbol{\lambda}}_e, \hat{\mathbf{u}}, \hat{p}, \hat{\boldsymbol{\lambda}}]$ is the fully coupled fluid-structure state variable. The second-member $\hat{\mathcal{N}}_{\text{fsi}}$ is defined by

$$\begin{aligned}
\langle \hat{\boldsymbol{\psi}}, \hat{\mathcal{N}}_{\text{fsi}}(\hat{\mathbf{q}}) \rangle &= \int_{\hat{\Omega}_s} \left\{ \hat{\mathbf{u}}_s \cdot \hat{\boldsymbol{\psi}}^\xi - \hat{\mathbf{P}}(\hat{\boldsymbol{\xi}}) : \hat{\boldsymbol{\nabla}} \hat{\boldsymbol{\psi}}_s^u \right\} d\hat{\Omega} \\
&\quad - \int_{\hat{\Omega}_f} \left\{ \hat{\boldsymbol{\Sigma}}_e(\hat{\boldsymbol{\xi}}_e) : \hat{\boldsymbol{\nabla}} \hat{\boldsymbol{\psi}}_e^\xi \right\} d\hat{\Omega} \\
&\quad - \int_{\hat{\Omega}_f} \left\{ (\hat{\boldsymbol{\nabla}} \hat{\mathbf{u}}) \hat{\boldsymbol{\Phi}}(\hat{\boldsymbol{\xi}}_e) \hat{\mathbf{u}} \cdot \hat{\boldsymbol{\psi}}^u + \frac{2}{\mathcal{R}_e} \hat{\mathbf{D}}(\hat{\mathbf{u}}, \hat{\boldsymbol{\xi}}_e) \hat{\boldsymbol{\Phi}}(\hat{\boldsymbol{\xi}}_e)^T : \hat{\boldsymbol{\nabla}} \hat{\boldsymbol{\psi}}^u \right\} d\hat{\Omega} \\
&\quad + \int_{\hat{\Omega}_f} \left\{ \hat{\boldsymbol{\Phi}}(\hat{\boldsymbol{\xi}}_e)^T : \left(\hat{p} \hat{\boldsymbol{\nabla}} \hat{\boldsymbol{\psi}}^u + \hat{\boldsymbol{\psi}}^p \hat{\boldsymbol{\nabla}} \hat{\mathbf{u}} \right) \right\} d\hat{\Omega} \\
&\quad - \int_{\hat{\Gamma}} \left\{ \hat{\boldsymbol{\lambda}} \cdot \hat{\boldsymbol{\psi}}^u + \hat{\mathbf{u}} \cdot \hat{\boldsymbol{\psi}}^\lambda \right\} d\hat{\Gamma} \\
&\quad - \int_{\hat{\Gamma}} \left\{ \hat{\boldsymbol{\lambda}}_e \cdot \hat{\boldsymbol{\psi}}_e^\xi + \hat{\boldsymbol{\xi}}_e \cdot \hat{\boldsymbol{\psi}}_e^\lambda \right\} d\hat{\Gamma} \\
&\quad + \int_{\hat{\Gamma}} \hat{\boldsymbol{\lambda}} \cdot \hat{\boldsymbol{\psi}}_s^u d\hat{\Gamma} + \int_{\hat{\Gamma}} \hat{\boldsymbol{\xi}} \cdot \hat{\boldsymbol{\psi}}_e^\lambda d\hat{\Gamma}.
\end{aligned} \tag{1.1.36}$$

Then, by construction, noting $\hat{\mathbf{q}} = [\hat{\boldsymbol{\xi}}, \hat{\mathbf{u}}_s, \hat{\boldsymbol{\xi}}_e, \hat{\boldsymbol{\lambda}}_e, \hat{\mathbf{u}}, \hat{p}, \hat{\boldsymbol{\lambda}}]$ the coupled state variable and $\hat{\boldsymbol{\psi}} = [\hat{\boldsymbol{\psi}}^\xi, \hat{\boldsymbol{\psi}}_s^u, \hat{\boldsymbol{\psi}}_e^\xi, \hat{\boldsymbol{\psi}}_e^\lambda, \hat{\boldsymbol{\psi}}^u, \hat{\boldsymbol{\psi}}^p, \hat{\boldsymbol{\psi}}^\lambda]$ the coupled test-function, solving the fluid-structure problem amounts to finding $\hat{\mathbf{q}} \in \hat{\mathcal{U}}_s \times \hat{\mathcal{U}}_s \times \hat{\mathcal{U}}_e \times \hat{\mathcal{U}}_{\hat{\Gamma}} \times (\hat{\mathcal{U}}_f + \mathbf{u}_\infty) \times \hat{\mathcal{P}} \times \hat{\mathcal{U}}_{\hat{\Gamma}}$, such that

$$\left\langle \hat{\boldsymbol{\psi}}, \hat{\mathcal{T}}_{\text{fsi}}(\hat{\mathbf{q}}) \frac{\partial \hat{\mathbf{q}}}{\partial t} - \hat{\mathcal{N}}_{\text{fsi}}(\hat{\mathbf{q}}) \right\rangle = 0 \quad \forall \hat{\boldsymbol{\psi}} \in \hat{\mathcal{U}}_s \times \hat{\mathcal{U}}_s \times \hat{\mathcal{U}}_e \times \hat{\mathcal{U}}_{\hat{\Gamma}} \times \hat{\mathcal{U}}_f \times \hat{\mathcal{P}} \times \hat{\mathcal{U}}_{\hat{\Gamma}}. \tag{1.1.37}$$

Remark. The notations $\langle \cdot, \cdot \rangle$ appearing in (1.1.35), (1.1.36) and (1.1.37) is a shorthand notation for the scalar products defined over the different functional spaces involved. For conciseness of the notation, in the following we keep the same writing for all the scalar products involved.

Three-fields decomposition

Eventually, the single-field problem (1.1.37) can be turned into a three-field problem, following an idea applied by [Lesoinne & Farhat \(1993\)](#) to an ALE formulation of the Euler equations. In this decomposition, the problem is written for a solid variable $\hat{\mathbf{q}}_s$, a fluid variable $\hat{\mathbf{q}}_f$ and an extension variable $\hat{\mathbf{q}}_e$, in such a way that

$$\begin{aligned}
\hat{\mathbf{q}}_s &= (\hat{\boldsymbol{\xi}}, \hat{\mathbf{u}}_s) \in \hat{\mathcal{U}}_s \times \hat{\mathcal{U}}_s, \\
\hat{\mathbf{q}}_e &= (\hat{\boldsymbol{\xi}}_e, \hat{\boldsymbol{\lambda}}_e) \in \hat{\mathcal{U}}_e \times \hat{\mathcal{U}}_{\hat{\Gamma}}, \\
\hat{\mathbf{q}}_f &= (\hat{\mathbf{u}}, \hat{p}, \hat{\boldsymbol{\lambda}}) \in \hat{\mathcal{U}}_f + \mathbf{u}_\infty \times \hat{\mathcal{P}} \times \hat{\mathcal{U}}_{\hat{\Gamma}},
\end{aligned}$$

which clarifies the respective roles and the couplings between the solid, extension and fluid problems. Deriving such formulation practically simply amounts to split (1.1.35) and (1.1.36) into as many pieces as needed. All things done, this gives the following non-linear problem, written in an operator notation:

$$\underbrace{\begin{pmatrix} \hat{\mathcal{T}}_s & 0 & 0 \\ 0 & 0 & 0 \\ 0 & -\hat{\mathcal{T}}_{fe}(\hat{\mathbf{q}}_f, \hat{\mathbf{q}}_e) & \hat{\mathcal{T}}_f(\hat{\mathbf{q}}_e) \end{pmatrix}}_{\hat{\mathcal{T}}_{\text{fsi}}(\hat{\mathbf{q}})} \frac{\partial}{\partial t} \begin{pmatrix} \hat{\mathbf{q}}_s \\ \hat{\mathbf{q}}_e \\ \hat{\mathbf{q}}_f \end{pmatrix} = \underbrace{\begin{pmatrix} \hat{\mathcal{S}}(\hat{\mathbf{q}}_s) + \hat{\mathcal{I}}_{fs}^T \hat{\mathbf{q}}_f \\ -\hat{\mathcal{S}}_e \hat{\mathbf{q}}_e + \hat{\mathcal{I}}_{es} \hat{\mathbf{q}}_s \\ \hat{\mathcal{I}}_{fs} \hat{\mathbf{q}}_s + \hat{\mathcal{N}}_f(\hat{\mathbf{q}}_f, \hat{\mathbf{q}}_e) \end{pmatrix}}_{\hat{\mathcal{N}}_{\text{fsi}}(\hat{\mathbf{q}})}.$$

In the above notation, we have used (1.1.34) to write the interface velocity condition as $\hat{\mathbf{u}}_s = \hat{\mathbf{u}}$, the velocity coupling then appears only in the right-hand side. This block-equation involves several

operators acting on the different variables. The structure of the ALE fluid-solid problem is now more clear: the solid problem (first line, augmented stiffness operator \mathcal{S}) is forced by the fluid problem by means of a load transfer operator $\hat{\mathcal{T}}_{fs}^T$. The extension problem (second line) is a pure static problem that takes the solid interface displacement as an input, by means of the interface operator $\hat{\mathcal{T}}_{es}$, and propagates it onto the whole domain through the extension operator $\hat{\mathcal{A}}_e$. Finally, the geometric transformation of the fluid equations results in a problem where each variable is coupled with the extension problem, except for the velocity coupling with the solid that occurs through $\hat{\mathcal{T}}_{fs}$. The detail of the different operators involved is given in Appendix B.

Remark – a note on “truly monolithic” formulations. Since both velocity and displacement are required to be continuous across the interface, it is tempting to define single displacement and velocity fields over the whole domain $\hat{\Omega}_f \cup \hat{\Omega}_s$, resulting in what could be called “truly monolithic” formulations (Turek & Hron, 2006; Dunne et al., 2010; Richter & Wick, 2015). For instance, considering one single velocity field $\hat{\mathbf{u}} \in \{\mathbf{f} \in \mathcal{H}^1(\hat{\Omega}), \mathbf{f} = \mathbf{0} \text{ on } \partial\hat{\Omega} \setminus \Gamma_f^N\} + \mathbf{u}_\infty$ such that

$$\frac{\partial \hat{\mathbf{u}}}{\partial t} = \begin{cases} \frac{1}{\mathcal{M}_s} \hat{\nabla} \cdot (\hat{\mathbf{F}}(\hat{\xi}) \hat{\mathbf{S}}(\hat{\xi})) & \text{in } \hat{\Omega}_s \\ \frac{1}{\hat{J}(\hat{\xi})} \left(\hat{\nabla} \cdot \hat{\Sigma}(\hat{\mathbf{u}}, \hat{p}, \hat{\xi}) - \left(\hat{\nabla} \hat{\mathbf{u}} \hat{\Phi}(\hat{\xi}) \right) \left(\hat{\mathbf{u}} - \frac{\partial \hat{\xi}}{\partial t} \right) \right) & \text{in } \hat{\Omega}_f \end{cases},$$

and one single displacement field $\hat{\xi} \in \{\mathbf{f} \in \mathcal{H}^1(\hat{\Omega}), \mathbf{f} = \mathbf{0} \text{ on } \partial\hat{\Omega}\}$ such that

$$\frac{\partial \hat{\xi}}{\partial t} = \begin{cases} \mathbf{u} & \text{in } \hat{\Omega}_s \\ \alpha \hat{\nabla} \cdot \hat{\Sigma}_e(\hat{\xi}) & \text{in } \hat{\Omega}_f \end{cases},$$

and taking accordingly global (i.e. defined over the whole fluid-solid domains) test-functions $\hat{\psi}^u$ and $\hat{\psi}^\xi$ for building the weak formulation, the stress continuity equation is again automatically satisfied and there is furthermore no need anymore for introducing interface Lagrange multipliers. Namely, we have then

$$\begin{aligned} \int_{\hat{\Omega}_s} \mathcal{M}_s \frac{\partial \hat{\mathbf{u}}}{\partial t} \cdot \hat{\psi}^u \, d\hat{\Omega} + \int_{\hat{\Omega}_f} J(\hat{\xi}) \frac{\partial \hat{\mathbf{u}}}{\partial t} \cdot \hat{\psi}^u \, d\hat{\Omega} = \\ - \int_{\hat{\Omega}_s} \hat{\mathbf{F}}(\hat{\xi}) \hat{\mathbf{S}}(\hat{\xi}) : \hat{\nabla} \hat{\psi}^u - \int_{\hat{\Omega}_f} \left(\hat{\Sigma}(\hat{\mathbf{u}}, \hat{p}, \hat{\xi}) : \hat{\nabla} \hat{\psi}^u + \left(\hat{\nabla} \hat{\mathbf{u}} \hat{\Phi}(\hat{\xi}) \right) \left(\hat{\mathbf{u}} - \frac{\partial \hat{\xi}}{\partial t} \right) \cdot \hat{\psi}^u \right) d\hat{\Omega} \end{aligned}$$

that defines a fluid-solid momentum equation, a displacement equation

$$\int_{\hat{\Omega}} \frac{\partial \hat{\xi}}{\partial t} \cdot \hat{\psi}^\xi \, d\hat{\Omega} = \int_{\hat{\Omega}_f} \hat{\mathbf{u}} \cdot \hat{\psi}^\xi \, d\hat{\Omega} - \alpha \int_{\hat{\Omega}} \hat{\Sigma}_e(\hat{\xi}) : \hat{\nabla} \hat{\psi}^\xi \, d\hat{\Omega} + \alpha \int_{\hat{\Gamma}} \hat{\Sigma}_e(\hat{\xi}) \hat{\mathbf{n}} \cdot \hat{\psi}^\xi \, d\hat{\Gamma},$$

while the continuity equation remains unchanged. This other three-fields formulation — velocity, displacement, pressure — was not considered for two main reasons. First, in the displacement equation, there is an additional interface term (the last one) coming from the fact that on the contrary to what happens between the fluid and the solid, the extension “stress” is not balanced at the fluid-structure interface. It is then observed that this makes the problem being *dependent* from this feedback extension pseudo-stress. Wick (2013a) compensates this drawback by adding the tuning parameter α in front of the load coupling term and setting it to a sufficiently small value so as to make the spurious stress feedback negligible. If this approach is found to be relevant for the purpose of an implicit non-linear solver, we did not want to introduce a tuning parameter in our linearised problems. Secondly, the structure of this “truly monolithic” problem is also different from the above three-fields formulation, as it is rather decomposed in terms of velocity, displacement and pressure fields than in terms of solid, fluid and extension problems. Numerically, this structure is often handled with multigrid methods (Richter & Wick, 2015), while our chosen approach allows for using more easy-to-implement methods, as will be detailed in section 1.2.

1.1.6 Summary

Regrouping together the equations detailed in §1.1.2, §1.1.3 and §1.1.4 we arrive to a self-consistent formulation of the local non-linear fluid-structure problem written in reference configuration:

Problem 1.1.1 – Non-linear ALE fluid-structure equations in the stress-free reference configuration. *The ALE formulation of the fluid-structure equations written in the stress-free reference configuration in the fluid domain $\hat{\Omega}_f$ and solid domain $\hat{\Omega}_s$, coupled through the interface conditions on $\hat{\Gamma}$, write as follows:*

$$\begin{aligned}
 \mathcal{M}_s \frac{\partial^2 \hat{\xi}}{\partial t^2} - \hat{\nabla} \cdot (\hat{\mathbf{F}}(\hat{\xi}) \hat{\mathbf{S}}(\hat{\xi})) &= \mathbf{0} \quad \text{in } \hat{\Omega}_s, \\
 -\hat{\nabla} \cdot \Sigma_e(\hat{\xi}_e) &= \mathbf{0} \quad \text{in } \hat{\Omega}_f, \\
 \hat{J}(\hat{\xi}_e) \frac{\partial \hat{\mathbf{u}}}{\partial t} + (\hat{\nabla} \hat{\mathbf{u}} \hat{\Phi}(\hat{\xi}_e)) \left(\hat{\mathbf{u}} - \frac{\partial \hat{\xi}_e}{\partial t} \right) - \hat{\nabla} \cdot \hat{\Sigma}(\hat{\mathbf{u}}, \hat{p}, \hat{\xi}_e) &= \mathbf{0} \quad \text{in } \hat{\Omega}_f, \\
 -\hat{\nabla} \cdot (\hat{\Phi}(\hat{\xi}_e) \hat{\mathbf{u}}) &= 0 \quad \text{in } \hat{\Omega}_f, \\
 \hat{\mathbf{u}} - \frac{\partial \hat{\xi}}{\partial t} &= \mathbf{0} \quad \text{and} \quad \hat{\xi}_e - \hat{\xi} = \mathbf{0} \quad \text{on } \hat{\Gamma}, \\
 \hat{\Sigma}(\hat{\mathbf{u}}, \hat{p}, \hat{\xi}_e) \hat{\mathbf{n}} - \hat{\mathbf{F}}(\hat{\xi}) \hat{\mathbf{S}}(\hat{\xi}) \hat{\mathbf{n}} &= \mathbf{0} \quad \text{on } \hat{\Gamma}.
 \end{aligned}$$

These equations govern the evolution of the fluid velocity and pressure fields $\hat{\mathbf{u}}$ and \hat{p} , the solid displacement field $\hat{\xi}$ and the extension displacement field $\hat{\xi}_e$. The solid stress tensor $\hat{\mathbf{S}}(\hat{\xi})$ is defined in (1.1.7). The fluid stress tensor $\hat{\Sigma}(\hat{\mathbf{u}}, \hat{p}, \hat{\xi}_e)$ is defined in (1.1.28). Finally, the deformation operator $\hat{\Phi}(\hat{\xi}_e)$ for the fluid domain and the determinant $\hat{J}(\hat{\xi}_e)$ of the deformation gradient tensor are defined in (1.1.27). The first equation is the solid momentum equation, the second equation defines the extension problem, the third and fourth equations are the Navier–Stokes equations in the reference configuration, and the last equations define the interface conditions (velocity, displacement and stress continuity). The associated weak formulation is written for $\hat{\mathbf{q}}_s = (\hat{\xi}, \hat{\mathbf{u}}_s)$, $\hat{\mathbf{q}}_e = (\hat{\xi}_e, \hat{\lambda}_e)$ and $\hat{\mathbf{q}}_f = (\hat{\mathbf{u}}, \hat{p}, \hat{\lambda})$, in operators notations and writing the interface velocity condition $\hat{\mathbf{u}} = \hat{\mathbf{u}}_s$, as

$$\underbrace{\begin{pmatrix} \hat{\mathcal{T}}_s & 0 & 0 \\ 0 & 0 & 0 \\ 0 & -\hat{\mathcal{T}}_{fe}(\hat{\mathbf{q}}_f, \hat{\mathbf{q}}_e) & \hat{\mathcal{T}}_f(\hat{\mathbf{q}}_e) \end{pmatrix}}_{\hat{\mathcal{T}}_{fsi}(\hat{\mathbf{q}})} \frac{\partial}{\partial t} \begin{pmatrix} \hat{\mathbf{q}}_s \\ \hat{\mathbf{q}}_e \\ \hat{\mathbf{q}}_f \end{pmatrix} = \underbrace{\begin{pmatrix} \hat{\mathcal{S}}(\hat{\mathbf{q}}_s) + \hat{\mathcal{I}}_{fs}^T \hat{\mathbf{q}}_f \\ -\hat{\mathcal{A}}_e \hat{\mathbf{q}}_e + \hat{\mathcal{I}}_{es} \hat{\mathbf{q}}_s \\ \hat{\mathcal{I}}_{fs} \hat{\mathbf{q}}_s + \hat{\mathcal{N}}_f(\hat{\mathbf{q}}_f, \hat{\mathbf{q}}_e) \end{pmatrix}}_{\hat{\mathcal{N}}_{fsi}(\hat{\mathbf{q}})}$$

where the definition of the different operators involved is detailed in Appendix B. The supplementary variables $\hat{\lambda}$ (interface stress) and $\hat{\lambda}_e$ (interface pseudostress) are introduced in (1.1.32) and (1.1.33) respectively, while $\hat{\mathbf{u}}_s = \partial_t \hat{\xi}$ is the solid velocity.

This general problem has to be completed with boundary conditions. The “default” boundary conditions that we will use here are detailed in §1.1.4.

The problem (1.1.1) defines a very general fluid-structure interaction problem. Depending on the physical situation considered, stationary, time-dependant, laminar or turbulent, small-displacement or large-displacement solutions might be found by solving it. It would therefore be an understatement to say that this is a problem numerically difficult to solve. The Navier–Stokes equations alone represent a computational challenge (Slotnick *et al.*, 2014), and the coupling with the structure adds even more complexity. Details on the numerical algorithms used here for solving (1.1.1) are given in the next section.

1.2 Implicit scheme for solving the non-linear ALE equations

In this section, we introduce the numerical scheme used for determining non-linear fluid-structure states — both stationary and time-dependent — solution of (1.1.1). Namely, a fully implicit scheme solved by a Newton method is adopted.

1.2.1 Coupling schemes for ALE problems

The more straightforward approach for solving fluid-structure problems consists in adopting a *partitionned* approach (Hou *et al.*, 2012) — also often referred to as *weakly coupled* or *staggered* approach. In this class of methods, at each time step the fluid, extension and solid equations are solved separately, then the output loads/displacements/velocities obtained by one single-physics solver are transmitted as input boundary-conditions to the other one (represented schematically in Fig. 1.4a). The velocity, displacement and stress interface conditions are never satisfied exactly in each time step. Typically, the fluid-solid variables at time-step $n + 1$ are determined through the following sequence of operations (Fernández, 2011):

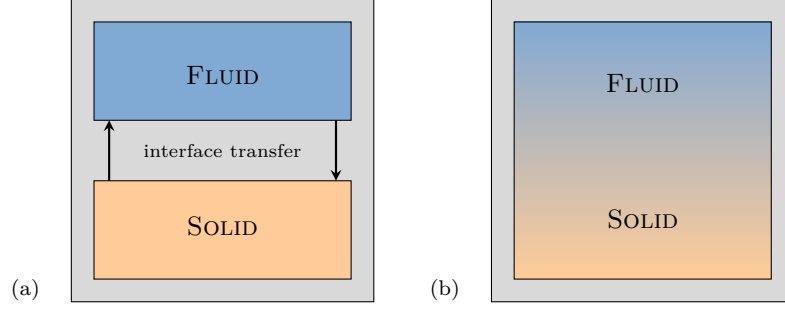
1. Solve an extension problem with a prescribed interface displacement $\hat{\xi}_e^{n+1}|_{\hat{\Gamma}} = \hat{\xi}^n|_{\hat{\Gamma}}$, compute the mesh deformation $\hat{\xi}_e^{n+1}$.
2. Solve a fluid mechanics problem on the deformed grid (according to $\hat{\xi}_e^{n+1}$) with a prescribed interface velocity $\hat{\mathbf{u}}^{n+1}|_{\hat{\Gamma}} = \hat{\mathbf{u}}_s^n|_{\hat{\Gamma}}$, compute the resulting fluid interface load $(\hat{\mathbf{S}}\hat{\mathbf{n}})^{n+1}$.
3. Solve a solid mechanics problem with a prescribed interface load $(\hat{\mathbf{F}}\hat{\mathbf{S}}\hat{\mathbf{n}})^{n+1}|_{\hat{\Gamma}} = (\hat{\mathbf{S}}\hat{\mathbf{n}})^{n+1}|_{\hat{\Gamma}}$, compute the resulting solid displacement and velocity.
4. Go to the next step.

This approach would for instance amount to solve sequentially the extension problem (1.1.19), the Navier-Stokes equations (1.1.22) and the elasticity equation (1.1.10) with transmission boundary conditions on $\hat{\Gamma}$. Partitioned approaches benefit from a great modularity, because they allow for re-using existing, optimized fluid and structural solvers. Furthermore, the cost of the coupled computation is only the cost of solving three single-physics problems and transfer informations at the interface. These solvers have therefore been widely used, in particular in the context of aeroelasticity (Lesoinne & Farhat, 1998; Piperno & Farhat, 2001; Farhat *et al.*, 2006).

The appropriate treatment of the non-linear coupling and the transmission of the informations between the different solvers is however not an easy task (Badia *et al.*, 2008; Breuer *et al.*, 2012). Furthermore, as the density ratio approaches unity and/or for specific geometries (typically blood flow or wing/sails simulations), numerical instabilities, known as “added-mass instabilities”, develop in partitioned solvers (Causin *et al.*, 2005). *Strongly coupled* partitioned solvers improving the overall convergence have therefore been established so as to overcome these stability issues (Matthies & Steindorf, 2002; Badia *et al.*, 2008; Kassiotis *et al.*, 2011; Breuer *et al.*, 2012). The basic idea is to add sub-iterations within the partitioned loop until the interface conditions are satisfied up to the prescribed tolerance and thus realize a “strong” coupling. Unfortunately, many sub-iterations are often required within each time-step (Heil *et al.*, 2008). Note that semi-implicit schemes have also been proposed, in which the added mass effect is treated implicitly while the other contributions are treated explicitly (Fernández *et al.*, 2007; Fernández, 2011). These solvers however come with strong restrictions regarding the size of the time steps.

Starting in the early 2000’s, *monolithic* (or *fully coupled*) solvers for ALE fluid-structure interaction problems have been developed to overcome these difficulties. In this approach, the fluid, the solid and the interface conditions are treated as one single mathematical framework (Fig. 1.4b), and the entire system is solved by a unified implicit algorithm (Hou *et al.*, 2012), in which case the strong coupling is naturally enforced. Fully implicit couplings (Hübner *et al.*, 2004; Heil, 2004; Hron & Turek, 2006), provide indeed the most interesting convergence and robustness properties

Figure (1.4) Two popular fluid-structure coupling schemes. (a) Partitioned (staggered) and (b) monolithic formulation.



— in particular, the added mass instability is completely avoided, and large time steps do not necessarily compromise stability. However, fully implicit algorithms also come with an increased computational effort, because an highly non-linear, large-dimension multiphysics problem has to be solved at each time-step. Provided that good solvers are designed, monolithic approaches however seem to be promising: Heil *et al.* (2008) compared segregated to monolithic approaches on several test-cases. When the density ratio is low, it is found that the monolithic approach clearly outperforms segregated algorithms, whereas at higher ratios the performances were found to be equivalent. The recent developments in the field are primarily focused on the design of efficient algorithms (Gee *et al.*, 2011; Richter, 2015; Deparis *et al.*, 2016) for solving each linear iteration inside the non-linear loop.

In the following, we adopt therefore the fully implicit, monolithic approach, where the problem that has to be solved writes on the form of the augmented first-order problem (1.1.1). In the next paragraphs, we detail first how it is discretized in time and space. The non-linear Newton loop used to handle the non-linearities is presented in §1.2.3. Details specific to the ALE mesh deformation are presented in §1.2.4. Finally, details on the numerical treatment of the resulting large-scale algebraic linear systems are given in section 1.3. With respect to this latter concern, note that the same issues arise with the linear problems presented in the chapter 2.

1.2.2 Time discretization

The temporal discretization is achieved by using an implicit one-step θ -method, allowing to choose between an implicit Euler method and a (eventually shifted) Crank-Nicholson scheme. This time discretization method is appealing because it is adapted both for computing stationary and time-dependant solutions, depending on the choice of θ . Considering a generic equation, the one-step θ -method amounts to solving for the time-step $n + 1$

$$\left[\frac{\partial \mathbf{q}}{\partial t} + f(\mathbf{q}) \right]^{n+1} = 0 \quad \rightarrow \quad \frac{\mathbf{q}^{n+1} - \mathbf{q}^n}{\Delta t} + \theta [f(\mathbf{q})]^{n+1} + (1 - \theta) [f(\mathbf{q})]^n = 0.$$

A stationary solver can be obtained very easily from this time discretization, by simply choosing the Euler scheme ($\theta = 1$) and setting $\Delta t \rightarrow +\infty$ — typically, $\Delta t = 10^{12}$. The Euler method is unconditionally stable but is only of order one in time, whereas the Crank-Nicholson scheme ($\theta = 1/2$) offers a second-order time accuracy at the price of only conditional stability. In particular, Richter & Wick (2015); Wick (2013b) showed that the Crank-Nicholson scheme may come with numerical instabilities in the context of fluid-structure computations. Using a *shifted* ($\theta = 1/2 + \Delta t$) Crank-Nicholson scheme then offers a overall gain in terms of stability, at the price of loosing the second-order accuracy. We apply the θ -method for the time discretization of the stress terms in the solid augmented equations — first line in the three-fields formulation (1.1.1) — that gives (keeping the load transfer term fully implicit)

$$\hat{\mathcal{J}}_s \frac{\hat{\mathbf{q}}_s^{n+1}}{\Delta t} - \theta \hat{\mathcal{J}}(\hat{\mathbf{q}}_s^{n+1}) - \hat{\mathcal{I}}_{fs}^T \hat{\mathbf{q}}_f^{n+1} = (1 - \theta) \hat{\mathcal{J}}(\hat{\mathbf{q}}_s^n) + \hat{\mathcal{J}}_s \frac{\hat{\mathbf{q}}_s^n}{\Delta t}.$$

The static extension equation is kept fully implicit. From the second equation we obtain:

$$-\hat{\mathcal{A}}_e \hat{\mathbf{q}}_e^{n+1} + \hat{\mathcal{I}}_{es} \hat{\mathbf{q}}_s^{n+1} = 0.$$

Finally, in the fluid equations, the pressure and interface terms are kept fully implicit, while the θ -method is used for the stress and advection terms, as well as for the time-derivative term $\hat{\mathcal{T}}$. From the momentum, continuity and interface velocity equations, we have then

$$\begin{aligned}
& \left(\theta \hat{\mathcal{T}}(\hat{\xi}_e^{n+1}) + (1-\theta) \hat{\mathcal{T}}(\hat{\xi}_e^n) \right) \frac{\hat{\mathbf{u}}^{n+1} - \hat{\mathbf{u}}^n}{\Delta t} - \theta \hat{\mathcal{T}}(\hat{\xi}_e^{n+1}) \frac{\hat{\mathbf{u}}^n}{\Delta t} - \hat{\mathcal{N}}(\hat{\xi}_e^{n+1}, \hat{\mathbf{u}}^{n+1}) \frac{\hat{\xi}_e^{n+1} - \hat{\xi}_e^n}{\Delta t} \dots \\
& + \theta \hat{\mathcal{N}}(\hat{\xi}_e^{n+1}, \hat{\mathbf{u}}^{n+1}) \hat{\mathbf{u}}^{n+1} - \hat{\mathcal{B}}(\hat{\xi}_e^{n+1})^T \hat{p}^{n+1} + \frac{2\theta}{\mathcal{R}_e} \hat{\mathcal{D}}(\hat{\xi}_e^{n+1}) \hat{\mathbf{u}}^{n+1} + \hat{\mathcal{I}}_f^T \hat{\lambda}^{n+1} \dots \\
& = (1-\theta) \left[-\hat{\mathcal{N}}(\hat{\xi}_e^n, \hat{\mathbf{u}}^n) \hat{\mathbf{u}}^n + \hat{\mathcal{T}}(\hat{\xi}_e^n) \frac{\hat{\mathbf{u}}^n}{\Delta t} - \frac{2}{\mathcal{R}_e} \hat{\mathcal{D}}(\hat{\xi}_e^n) \hat{\mathbf{u}}^n \right], \\
& - \hat{\mathcal{B}}(\hat{\xi}_e^{n+1}) \hat{\mathbf{u}}^{n+1} = 0, \\
& \hat{\mathcal{I}}_f \hat{\mathbf{u}}^{n+1} - \hat{\mathcal{I}}_s \hat{\mathbf{u}}_s^{n+1} = 0.
\end{aligned}$$

The combination of these three sub-problems yields to a non-linear problem that has to be solved at each time step,

$$\begin{aligned}
\hat{\mathbf{r}}_S(\hat{\mathbf{q}}_s^{n+1}, \hat{\mathbf{q}}_f^{n+1}) &= \hat{\mathbf{b}}_S(\hat{\mathbf{q}}_s^n) && + \text{penalization b.c.'s on } \partial\hat{\Omega}_s \setminus \hat{\Gamma}, \\
\hat{\mathbf{r}}_E(\hat{\mathbf{q}}_s^{n+1}, \hat{\mathbf{q}}_e^{n+1}) &= 0 && + \text{penalization b.c.'s } \partial\hat{\Omega}_f \setminus \hat{\Gamma}, \\
\hat{\mathbf{r}}_F(\hat{\mathbf{q}}_s^{n+1}, \hat{\mathbf{q}}_e^{n+1}, \hat{\mathbf{q}}_f^{n+1}) &= \hat{\mathbf{b}}_F(\hat{\mathbf{q}}_e^n, \hat{\mathbf{q}}_f^n) && + \text{penalization b.c.'s } \partial\hat{\Omega}_f \setminus \hat{\Gamma}.
\end{aligned}$$

1.2.3 (Quasi)-Newton iterations & space discretization

A standard and simple strategy for solving the above non-linear problem $\hat{\mathbf{r}}(\hat{\mathbf{q}}^{n+1}) = \hat{\mathbf{b}}$ is to use a fixed-point algorithm, but unfortunately this approach is often expensive, even though acceleration techniques might improve its efficiency (Deparis *et al.*, 2003). These limitations have pushed for using Newton-like methods for solving each time-step. In the best-case scenario (exact Jacobian evaluated at each iteration), this method achieves indeed a quadratic convergence — if any — to the solution. The basic Newton method consists in computing a sequence $\hat{\mathbf{q}}^{n+1,1}, \dots, \hat{\mathbf{q}}^{n+1,k}, \dots$ such that $\hat{\mathbf{q}}^{n+1,k+1} = \hat{\mathbf{q}}^{n+1,k} + \delta\hat{\mathbf{q}}$ where $\delta\hat{\mathbf{q}}$ is solution of the linear problem

$$\left\{ \frac{\partial \hat{\mathbf{r}}}{\partial \hat{\mathbf{q}}} \bigg|_{\hat{\mathbf{q}}^{n+1,k}} \right\} \delta\hat{\mathbf{q}} = \hat{\mathbf{b}} - \hat{\mathbf{r}}(\hat{\mathbf{q}}^{n+1,k}).$$

Provided that the initial guess $\hat{\mathbf{q}}^{n+1,0}$ is not too far away from the final solution, this sequence converges and is stopped when a relevant norm of the residuals $\|\hat{\mathbf{b}} - \hat{\mathbf{r}}(\hat{\mathbf{q}}^{n+1,k})\|$ is small enough. Since the Jacobian matrix is expensive to compute numerically, it is interesting to use instead a quasi-Newton method, where the same Jacobian matrix is used in several iterations. In all cases, the cornerstone of the Newton method is the computation of the Jacobian operator $\partial\hat{\mathbf{r}}/\partial\hat{\mathbf{q}}$.

A common approach consists in using finite-differences to evaluate the Jacobian operator (Heil, 2004; Matthies & Steindorf, 2002). However, the finite difference step can hardly be chosen *a priori*, which might lead to non-consistent Jacobians and degrade the overall performances. Another strategy consists in computing analytically the linearised operator, and possibly neglect some of the cross-Jacobian terms (Ghattas & Li, 1995; Gerbeau *et al.*, 2003), for instance the so-called shape derivatives that evaluate the sensitivity of the fluid equations with respect to the fluid domain deformation. These terms are indeed not straightforward to compute analytically. This method reduces the cost of building the Jacobian matrix of the problem, but using an approximate Jacobian results in lower convergence rates (Heil, 2004). For that reason, despite of their increased complexity, Newton methods with an exact Jacobian are attractive (Fernández & Moubachir, 2005; Dettmer & Perić, 2008).

The tangent problem for the Newton iteration k of the time-step $n + 1$ writes as

$$\begin{pmatrix} \frac{\partial \hat{\mathbf{r}}_S}{\partial \hat{\mathbf{q}}_s} & 0 & \frac{\partial \hat{\mathbf{r}}_S}{\partial \hat{\mathbf{q}}_f} \\ \frac{\partial \hat{\mathbf{r}}_E}{\partial \hat{\mathbf{q}}_s} & \frac{\partial \hat{\mathbf{r}}_E}{\partial \hat{\mathbf{q}}_e} & 0 \\ \frac{\partial \hat{\mathbf{r}}_F}{\partial \hat{\mathbf{q}}_s} & \frac{\partial \hat{\mathbf{r}}_F}{\partial \hat{\mathbf{q}}_e} & \frac{\partial \hat{\mathbf{r}}_F}{\partial \hat{\mathbf{q}}_f} \end{pmatrix} \begin{pmatrix} \delta \hat{\mathbf{q}}_s \\ \delta \hat{\mathbf{q}}_e \\ \delta \hat{\mathbf{q}}_f \end{pmatrix} = \begin{pmatrix} \hat{\mathbf{b}}_S(\hat{\mathbf{q}}_s^n) - \hat{\mathbf{r}}_S(\hat{\mathbf{q}}_s^{n+1,k}, \hat{\mathbf{q}}_f^{n+1,k}) \\ -\hat{\mathbf{r}}_E(\hat{\mathbf{q}}_s^{n+1,k}, \hat{\mathbf{q}}_e^{n+1,k}) \\ \hat{\mathbf{b}}_F(\hat{\mathbf{q}}_e^n, \hat{\mathbf{q}}_f^n) - \hat{\mathbf{r}}_F(\hat{\mathbf{q}}_s^{n+1,k}, \hat{\mathbf{q}}_e^{n+1,k}, \hat{\mathbf{q}}_f^{n+1,k}) \end{pmatrix} \quad (1.2.1)$$

where it is understood that the block-Jacobian operator in the left-hand side is evaluated about the variables $\hat{\mathbf{q}}_s^{n+1,k}, \hat{\mathbf{q}}_e^{n+1,k}, \hat{\mathbf{q}}_f^{n+1,k}$ in an exact fashion. More details on the linearisation will be given in the chapter 2, and can also be found in the book by [Richter \(2017\)](#).

The velocity and displacement fields are projected onto the space of P_2 finite elements, while the pressure is projected onto the space of P_1 finite elements so as to satisfy at the discrete level the Ladyzenskaya-Babuška-Brezzi condition arising from the Stokes problem ([Girault & Raviart, 1985](#)). P_1 elements are used to represent the Lagrange multipliers.

Note that the extension problem is set in a sub-domain $\hat{\Omega}_e \subset \hat{\Omega}_f$, because the solid movement generally occurs in a limited region. There is therefore no need for solving the extension problem in regions that are unlikely to be affected by its movement. Outside from the extension region, the fluid equations reduce in particular to the Navier-Stokes equations.

The Jacobian matrix and the residual vector are assembled in parallel using `mpi`. The global, conforming fluid-structure mesh is first split by the mesh partitioner SCOTCH ([Pellegrini, 2008](#)) called within the FREEFEM environment. Then, the matrix and the residual vector are assembled locally on each processor. After the assembly part, the size of the different matrices is reduced so that the solid, extension and fluid matrices have the size deduced from the discretization of the sub-domains $\hat{\Omega}_s$, $\hat{\Omega}_e$ and $\hat{\Omega}_f$. Finally, the algebraic problem that has to be solved at each step of the non-linear loop writes

$$\begin{bmatrix} \mathbf{A}_{ss} & \mathbf{0} & \mathbf{A}_{sf} \\ \mathbf{A}_{es} & \mathbf{A}_{ee} & \mathbf{0} \\ \mathbf{A}_{fs} & \mathbf{A}_{fe} & \mathbf{A}_{ff} \end{bmatrix} \begin{bmatrix} \mathbf{x}_s \\ \mathbf{x}_e \\ \mathbf{x}_f \end{bmatrix} = \begin{bmatrix} \mathbf{b}_s \\ \mathbf{b}_e \\ \mathbf{b}_f \end{bmatrix} \quad (1.2.2)$$

where only the matrices emphasized with the red color (solid stiffness matrix, shape derives matrix and fluid matrix) have to be reassembled at each time step (the other matrices are constant). Practically, the Jacobian matrix is assembled at the first iteration (full Newton iteration), and is then re-used for the subsequent iterations if the residuals decrease (quasi-Newton iteration). A reassembly is performed only if the residuals are found to stagnate or increase.

1.2.4 Extension problem for non-linear computations

The practical choice of the extension problem is driven by the requirement for the ALE mapping to be one-to-one, i.e. that $\hat{J}(\hat{\mathbf{x}}) > 0$. Practically, this corresponds to the requirement that the ALE deformation field applied on the reference mesh should not generate reversed triangles. Following [Stein et al. \(2003\)](#), the extension problem (1.1.19) is defined here as a weighted Laplace problem, where the space-dependent weighting coefficient $\mathcal{E}_e(\hat{\mathbf{x}})$ defines a local fluid mesh “stiffness”:

$$\hat{\Sigma}_e(\hat{\xi}_e) = \mathcal{E}_e(\hat{\mathbf{x}}) \hat{\nabla} \hat{\xi}_e. \quad (1.2.3)$$

Several choices are possible for \mathcal{E}_e . Noting h a measure of the local mesh s (for instance the largest edge length of the current triangle in the mesh, the radius of the in or excircle), and $p > 0$ a tuning parameter, a straightforward approach consists in using $\mathcal{E}_s(\hat{\mathbf{x}}) = 1/h(\hat{\mathbf{x}})^p$. Since h usually gets smaller when one gets closer to the fluid-solid boundary $\hat{\Gamma}$, this has for effect to stiffen the transformation of the elements close to the fluid-solid boundary. This effect is represented in the Fig. 1.5, for integer values of p varying between 0 (pure Laplace equation) to 2. A solid-body displacement composed of a translation along the vertical axis plus a rotation around the center of

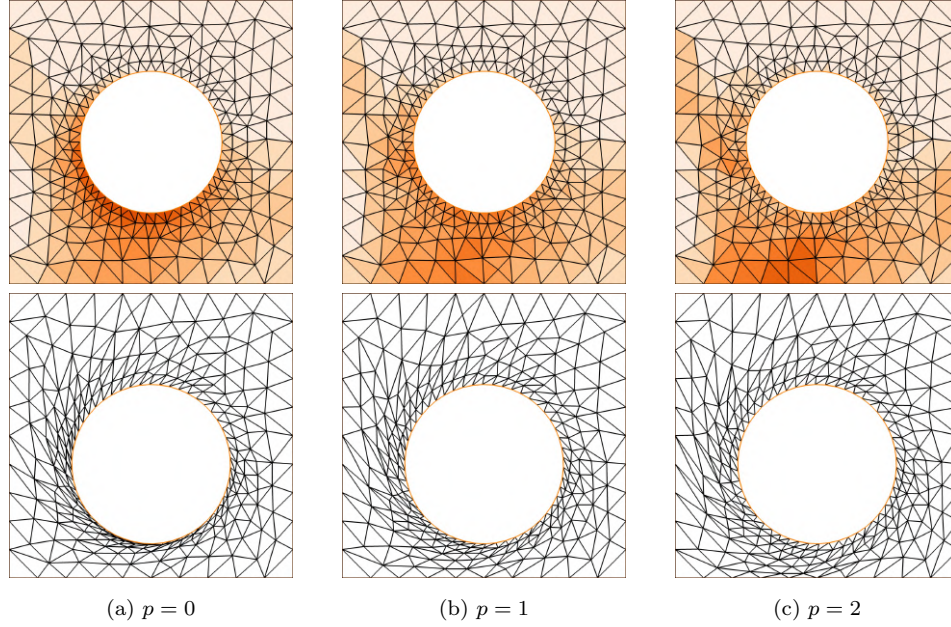


Figure 1.5 – Extension field. Influence of the pseudo-stiffening parameter p on the extension displacement field features. An top, plot of the Jacobian of the transformation in the reference domain. At the bottom, plot of the deformed configuration for a solid-body combined translation/rotation of the cylinder while keeping fixed the position of the edges of the square.

the cylinder is imposed at the surface of the cylinder. The exterior boundaries are kept fixed. The reference configuration is represented on top, while the deformed configuration is at the bottom. The Jacobian of the transformation is represented on top with an orange colormap, where light orange means large \hat{J} (i.e. cells with an increasing area) while the darker regions correspond to values closer to zero. For the case $p = 0$, we have $\min \hat{J} = 0.00811$ in the vicinity of the lower cylinder interface. The corresponding deformed configuration, visible in Fig. 1.5a at the bottom present very stretched triangles: the maximal skewness reaches 0.98. For the case $p = 1$ represented in Fig. 1.5b, the cells are artificially made stiffer regarding to the transformation: as a result, the minimal Jacobian value is increased up to 0.31 and the skewness in the actual domain reduced to 0.81. The deformation is actually reported to larger cells farther away from the interface, that can deform more before getting too stretched. However, a too large value of p can also become detrimental, as visible in Fig. 1.5c. In that case, the cells close to the fixed boundaries get elongated and the minimum of the Jacobian falls down to 0.03. The skewness is however still better and decreases down to 0.7, as it can be seen on the bottom of the figure. Obviously, a trade-off has to be found, that depends on the magnitude of the deformations.

Another possibility that we have adopted consists in computing the signed distance d to $\hat{\Gamma}$ and set $\mathcal{E}_e(\hat{\mathbf{x}}) = 1/(\alpha + d(\hat{\mathbf{x}}))^p$ with $\alpha > 0$. This method has the advantage to be mesh-size independent, and can for instance be used if the cells density does not vary much between the interface and the farfield region.

Note that other types of extension operators are found in the literature, see for instance the work by Wick (2011), where harmonic, linear-elastic and biharmonic operators are compared. It is found that the biharmonic operator provides the smoothest results, but since it also involves an higher computational cost, it has not been considered here.

1.3 Handling the large-scale resulting linear systems

1.3.1 Direct *vs.* iterative methods

Nearly every problem based on partial differential equations usually ends, after time and space discretization, by a linear algebra problem where linear systems of size $N \gg 1$ have to be solved once or several times. In the case of a finite-element discretization, the problem is *sparse* (i.e. only a few entries per line are non-zero).

The most general and computationally feasible procedure for solving the linear system (1.2.2) in a finite number of operations (also referred to as a *direct* solver) is known at least since the nineteenth century and the Gauss elimination method. Modern computational packages such as MUMPS (Amestoy *et al.*, 2013), PARDISO (Schenk & Gärtner, 2004) or SUPERLU (Li, 2005) provide robust routines for solving sparse linear systems of type $\mathbf{Ax} = \mathbf{b}$. The basic idea exploited by these solvers consists in variations about the Gauss elimination method, that consists in particular to compute the LU decomposition of the matrix, i.e. find a lower-triangular matrix \mathbf{L} and an upper-triangular matrix \mathbf{U} , such that $\mathbf{A} = \mathbf{LU}$. Once these matrices are computed and stored, the resolution of the original system amounts to solving two triangular systems $\mathbf{Ly} = \mathbf{b}$ and then $\mathbf{Ux} = \mathbf{y}$. These are very simple problems that are easily solved by forward and backward substitution. Computing explicitly \mathbf{A}^{-1} is practically never done because \mathbf{A}^{-1} is generally not a sparse matrix. The most expensive part (in terms of computational time and, even more dramatically, in memory requirements) is by far the LU decomposition, which scales barely better than $\mathcal{O}(N^3)$ operations and is therefore not well suited for large-dimension linear systems. Considering the easily-accessible computational power today, this limits the reasonable use of direct solvers to problems not very much larger than $N \simeq 10^6$ when the sparsity (ratio between the number of non-zero entries in the matrix and N) is of order 50 – typically, for 2d problems.

Another class of methods consist in computing a sequence of vectors that, under certain hypotheses, are found to converge towards the solution of the linear system, i.e. compute

$$\mathbf{x}^{k+1} = \mathbf{F}(\mathbf{A}, \mathbf{x}^k) \mathbf{b}^k$$

for $k = 1, 2, \dots$ and a certain function \mathbf{F} in which only *cheap* matrix-vector operations on \mathbf{A} and \mathbf{b} are done. These iterative methods are much less demanding in terms of memory (and are thus mandatory for solving large-scale problems), and also faster than direct methods when N is greater than some value. The drawback is that they are usually problem-dependant, converge slowly or even might fail to converge in some cases. For that reason, a vast literature is devoted to the derivation of robust and efficient solvers. We refer the reader to the book by Saad (2003) and the review by Benzi (2002) for an extended overview of the field. Basically, the convergence properties of iterative methods depend on the condition number of \mathbf{A} : the larger the condition number, the slower the convergence (Benzi, 2002). Even the most advanced Krylov-based iterative schemes, such as for instance GMRES (Saad & Schultz, 1986), thus usually display a very slow convergence without *preconditioning*. A (left) preconditioner is a matrix \mathbf{P} , such that the spectral properties (hence the condition number) of $\mathbf{P}^{-1}\mathbf{A}$ are enhanced. Depending on the side of the multiplication by \mathbf{P} , left, right or symmetric preconditioning can be obtained. The iterative method applied to the system $\mathbf{P}^{-1}\mathbf{Ax} = \mathbf{P}^{-1}\mathbf{b}$ has then chances to converge much faster. The difficult part consists in finding a matrix $\mathbf{P} \simeq \mathbf{A}$ but that is nevertheless easy to invert, since the operation $\mathbf{x} \mapsto \mathbf{P}^{-1}\mathbf{x}$ will have to be called a number of times during the iterative process.

In the next paragraph, the block-Gauss-Seidel/SIMPLE iterative algorithm that was used to handle the inversion of the coupled fluid-structure problem is presented.

1.3.2 Preconditioning the fully coupled fluid-structure problem

Since it groups a solid problem, the extension problem and a fluid problem, the matrix in (1.2.2) growth very quickly as the mesh is refined. Typically for a 2d mesh with about 65 000 points and a P_2/P_1 discretization, \mathbf{A}_{ss} has a size of order 45 000, \mathbf{A}_{ee} a size of order 145 000 and \mathbf{A}_{ff} a size of order 275 000, i.e. $N = 465\,000$. Even if the parallelization allows to distribute the required memory between many computational nodes, it is thus critical to reduce the overall size of the

matrices handled by direct solvers. The present adopted strategy allows for having to inverse only \mathbf{A}_{ff} , \mathbf{A}_{ss} and \mathbf{A}_{ee} . It is based on using a first loop of a preconditioned parallel GMRES iterative method to decouple the three fluid, solid and extension problems (with a so-called block Gauss-Seidel preconditioner). Inside this loop, a second loop of either direct or iterative methods is used for solving each single-physics problem (i.e. \mathbf{A}_{ff} , \mathbf{A}_{ss} and \mathbf{A}_{ee}).

The outer iterative loop is achieved by using a GMRES algorithm with a left block Gauss-Seidel preconditioner (BGS) for \mathbf{P}_{fsi} , that writes as

$$\mathbf{P}_{fsi} = \begin{bmatrix} \mathbf{A}_{ss} & \mathbf{0} & \mathbf{0} \\ \mathbf{A}_{es} & \mathbf{A}_{ee} & \mathbf{0} \\ \mathbf{A}_{fs} & \mathbf{A}_{fe} & \mathbf{A}_{ff} \end{bmatrix}, \quad (1.3.1)$$

which is the matrix \mathbf{A}_{fsi} without the upper-right corner block (representing the action of the fluid load on the solid). The triangular structure of the matrix results in an expression for \mathbf{P}_{fsi}^{-1} that only involves the inverses of the diagonal blocs. More precisely, the application $\mathbf{x}_{fsi} = [\mathbf{x}_s, \mathbf{x}_e, \mathbf{x}_f]^T \mapsto \mathbf{P}_{fsi}^{-1} \mathbf{x}_{fsi}$ writes:

$$\begin{cases} \mathbf{x}_s^{\text{new}} = \mathbf{A}_{ss}^{-1} \mathbf{x}_s^{\text{old}} \\ \mathbf{x}_e^{\text{new}} = \mathbf{A}_{ee}^{-1} (\mathbf{x}_e^{\text{old}} - \mathbf{A}_{es} \mathbf{x}_s^{\text{new}}) \\ \mathbf{x}_f^{\text{new}} = \mathbf{A}_{ff}^{-1} (\mathbf{x}_f^{\text{old}} - \mathbf{A}_{fs} \mathbf{x}_s^{\text{new}} - \mathbf{A}_{fe} \mathbf{x}_e^{\text{new}}) \end{cases}.$$

Each application of the BGS preconditioner thus requires to invert \mathbf{A}_{ss} , \mathbf{A}_{ee} and \mathbf{A}_{ff} . Using the block Gauss-Seidel/GMRES approach is quickly competitive as N increases. The convergence of the preconditioned GMRES loop is typically achieved down to 10^{-8} in less than ten iterations for the cases we considered. Let us now concentrate of the resolution of the three sub-problems that appear in each call to a BGS iteration.

As pointed before, the solid problem is a relatively small-scale problem compared to the fluid problem and was thus primarily handled with the direct LU solver MUMPS. The extension problem is larger, but as long as there is no remeshing operation, the extension matrix \mathbf{A}_{ee} remains *constant*. For that reason, the direct LU solver MUMPS was also used to handle this problem – recall that once the LU decomposition of a matrix \mathbf{A} is computed and stored, the map $\mathbf{x} \mapsto \mathbf{A}^{-1} \mathbf{x}$ is very quick to compute, as many times as needed.

On the contrary to the solid and extension problems, the fluid problem has a much greater size, and presents in addition a fairly poor sparsity (in 2d, about 25–30, worse in 3d). We therefore gain in using an iterative method for inverting \mathbf{A}_{ff} . The special *saddle-point* nature of the linearised fluid problem calls for specific methods. More precisely, the linearised fluid operator has the structure

$$\mathbf{A}_{ff} = \begin{bmatrix} \mathbf{A} & \mathbf{B}^T & \mathbf{I}_\Gamma^T \\ \mathbf{B} & \mathbf{0} & \mathbf{0} \\ \mathbf{I}_\Gamma & \mathbf{0} & \mathbf{0} \end{bmatrix} \quad (1.3.2)$$

where \mathbf{A} is a convection-diffusion operator, \mathbf{B} and \mathbf{B}^T are respectively the divergence and gradient operators (modified by the change of reference configuration), while \mathbf{I}_Γ is the interface transfer matrix. The saddle-point structure consists in this arrangement with a zero block in the lower-right corner of the matrix, typical of a constrained problem (here by the fluid incompressibility and the interface velocity continuity condition). A vast literature is devoted to the numerical solution of saddle-point problems, that has been summarized for instance in the review by [Benzi et al. \(2005\)](#).

As far as the design of a preconditioner for \mathbf{A}_{ff} is concerned, stationary problems have to be distinguished from time-dependant cases. Indeed, the large factors $1/\Delta t$ that appear in the diagonal of \mathbf{A} confer a special structure to the matrix that can be profitably operated. In time-dependent algorithms, following [Debaris et al. \(2014\)](#), the SIMPLE preconditioner ([Patankar & Spalding, 1972](#); [Patankar, 1981](#)) was implemented, associated to a GMRES loop. Using the preconditioner SIMPLE for \mathbf{A}_{ff} , only an approximation of its Schur complement $-(\bar{\mathbf{B}} \mathbf{A}^{-1} \bar{\mathbf{B}}^T)$ has to be inverted,

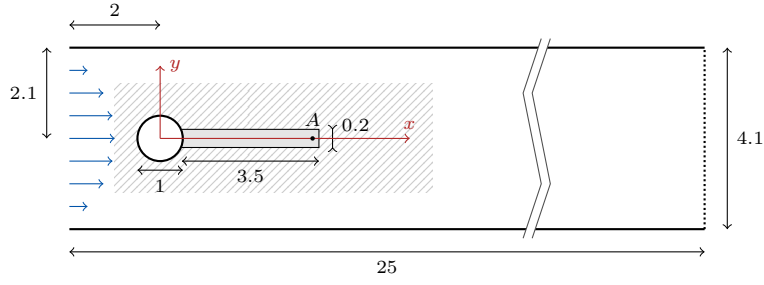


Figure 1.6 – Reference configuration for the vortex-induced elastic-deformation instability.. Sketch of the geometry proposed by Turek & Hron (2006) with the associated non-dimensional lengths. Point A is located in the elastic plate at the position $(x_A, y_A) = (3.95, 0)$ in the reference configuration. The extension box is depicted with the oblique lines and has dimensions $x \in [-1, 7]$, $y \in [-1.5, 1.5]$.

where $\bar{\mathbf{B}}^T = [\mathbf{B}^T \ \mathbf{I}_\Gamma^T]$. Namely, this approximation consists in replacing the convection-diffusion operator \mathbf{A} by its diagonal. One can also further avoid from having the interface terms related to \mathbf{I}_Γ^T and \mathbf{I}_Γ appearing in the Schur complement, by means of the so-called *static condensation*, we refer the reader to Deparis *et al.* (2016) where this method is detailed.

Due to the rather crude approximation of the matrix \mathbf{A} , SIMPLE is competitive only when \mathbf{A} is diagonally dominant, i.e. for sufficiently small time-steps Δt (Benzi *et al.*, 2005). For steady cases ($\Delta t \rightarrow +\infty$) or in eigenvalue problems solved using a shift-and-invert spectral transformation ($1/\Delta t$ is basically replaced by a complex number that depends on the problem eigenvalue plus the chosen shift value — these problems will be considered in the chapter 2 —, other approaches are found to cope more efficiently with the saddle-point problem, such as the Stokes preconditioning (Tuckerman & Barkley, 2000), the pressure-convection-diffusion preconditioner (Kay *et al.*, 2002) or Augmented Lagrangian preconditioners (Benzi & Olshanskii, 2006; Olshanskii & Benzi, 2008; Heister & Rapin, 2013; Moulin *et al.*, 2019).

1.4 Turek’s benchmark cases

In this section, the non-linear solver is validated on the well-known 2D benchmark problems proposed by Turek & Hron (2006), that consists in variations on the flow-induced vibrations of an elastic bar attached behind a circular cylinder in a channel flow. The configuration of the physical problem is shown in Fig. 1.6, where all lengths were taken relatively to the cylinder diameter. The origin of the axes is taken at the cylinder centre, which is slightly moved downwards so as to break the symmetry of the problem. The plate (with straight corners) is attached behind the cylinder and made with a Saint-Venant Kirchhoff material of non-dimensional Young modulus \mathcal{E}_s and Poisson coefficient ν_s , while a viscous flow of Reynolds number \mathcal{R}_e (based on the cylinder’s diameter and the mean inflow velocity) is considered in the channel. A parabolic inflow velocity profile is imposed at the inlet, which writes without dimensions as $u(y) = 0.357(2 + y)(2.1 - y)$. No-slip boundary conditions are imposed on the top and bottom walls as well as on the bluff-body surface. A zero normal stress boundary condition is taken at the outflow.

In the paper by Turek & Hron (2006), different benchmarks are proposed. The physical parameters for the different cases are reported in Tab. 1.1. The case CSM1 consists in the steady deviation of the plate alone in a gravity field \mathcal{G} , while the case CSM2 considers the unsteady case. In our case, this problem is solved by simply retaining the terms related to the solid in the matrices obtained after time and space discretization. The fluid sub-problem CFD1 consists in the steady flow about the rigid geometry at a low Reynolds number $\mathcal{R}_e = 20$, while in the case CFD2 the higher Reynolds number $\mathcal{R}_e = 200$ comes with an unsteady vortex shedding behind the obstacle. These cases can be solved practically by using the fluid-structure solver and setting the stiffness to a very high value, or by considering the fluid solver only. In our case, like for the solid bench-

	<i>solid alone</i>		<i>fluid alone</i>		<i>fluid-structure</i>	
	CSM1	CSM3	CFD1	CFD3	FSI1	FSI3
\mathcal{R}_e	-	-	20	200	20	200
\mathcal{M}_s	1	1	-	-	1	1
ν_s	0.4	0.4	-	-	0.4	0.4
\mathcal{E}_s	1400	1400	(∞)	(∞)	35 000	1400
\mathcal{G}	0.2	0.2	0	0	0	0
type	forced steady	unsteady	steady	unsteady	steady	unsteady

Table 1.1 – Non-dimensional parameters for the benchmark of Turek & Hron (2006). The Reynolds number \mathcal{R}_e is built on the cylinder's diameter and the mean inflow velocity \bar{U}^* , $\mathcal{M}_s = \rho_s^*/\rho_f^*$ is the density ratio, ν_s is the structure Poisson coefficient, \mathcal{E}_s is the non-dimensional Young modulus obtained by dividing by $\rho_f^* \bar{U}^{*2}$ the coefficient with dimensions, and \mathcal{G} is the non-dimensional gravity number obtained by multiplying the dimensioned characteristic external force magnitude by D^*/\bar{U}^{*2} .

mark we simply retain the fluid-related matrices. Finally, the fluid-structure benchmark FSI1 is a stationary case where the plate bends through its interaction with the flow but remains steady, while the case FSI3 is an unsteady case.

The values of interest are the displacement (whose components x and y are written ξ_x and ξ_y respectively) at the point A of coordinates $(4, 0)$ measured from the cylinder centre, the aerodynamic drag and lift coefficients C_D and C_L of the full bluff-body (including the rigid part), and the vortex shedding frequencies f_1 and f_2 . Both the mean displacement and the displacement amplitude are measured using the convention from Turek & Hron (2006):

$$\begin{aligned} \langle \cdot \rangle &= \frac{1}{2} \left(\max(\cdot) + \min(\cdot) \right) && \text{(mean)} \\ \delta \cdot &= \frac{1}{2} \left(\max(\cdot) - \min(\cdot) \right) && \text{(amplitude)} \end{aligned}$$

A set of various meshes are used to test the algorithms, labelled M0 to M4 from the coarsest to the finest. Their characteristics are reported in Tab. 2.1 page 55.

1.4.1 Solid mechanics cases

Some results for the unsteady case CSM3 are reported in Fig. 1.7. The energy-preserving properties of the Crank-Nicholson scheme are clearly visible in (a) where the total kinetic energy in the solid is represented as a function of time for mesh M1 and a time step $\Delta t = 0.05$. The implicit Euler scheme is associated with a strong damping of energy (although there is no physical source of damping) whereas the Crank-Nicholson scheme is able to keep it almost constant. When the time-step is decreased, the Euler scheme becomes less dissipative but never outperforms the Crank-Nicholson scheme both in terms of energy conservation and — to a lesser extent — precision. However, when the time-step is increased, the conditional stability of the Crank-Nicholson scheme results in a blow up for time steps above $\Delta t \simeq 0.2$, as reported in (b). The Euler scheme is unconditionally stable but the precision suffers much of an increase of the time-step because it is only first-order accurate. The Euler scheme is however appropriate for computing the stationary case CSM1, which is solved by setting a large time-step in the Euler scheme. With $\Delta t = 10$ the solution stabilizes to a steady regime after $t \simeq 50$. For the mesh M1, the x and y displacements are found to -0.070 and 0.648 respectively, in good agreement (deviation less than 2%) with the values -0.072 and 0.661 reported by Turek & Hron (2006).

1.4.2 Fluid mechanics cases

Taking the plate as a rigid object, subtests focusing on the fluid dynamics part of the problem can be performed. Practically, we only consider in the code the submatrices and subvectors corresponding

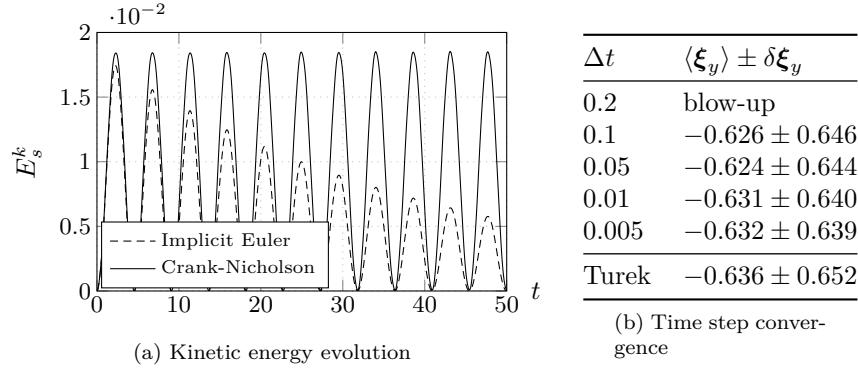


Figure 1.7 – CSM3 benchmark. (a) Comparison of the total solid kinetic energy E_s^k , for a time-step $\Delta t = 0.05$ and $\theta = 1$ (implicit Euler scheme) and $\theta = 0.5$ (Crank-Nicholson scheme), on mesh M1. (b) Evolution of the transverse mean displacement and displacement amplitude for different time-step sizes. Results from Turek & Hron (2006) are reported in the last line.

Δt	$\langle C_D \rangle \pm \delta C_D$	$\langle C_L \rangle \pm \delta C_L$	Δt	$\langle C_D \rangle \pm \delta C_D$	$\langle C_L \rangle \pm \delta C_L$
0.4	2.181	-0.5470 ± 0.002	0.4	2.174 ± 0.0259	-0.0316 ± 2.122
0.2	2.181	-0.5470 ± 0.002	0.2	2.175 ± 0.0277	-0.0571 ± 2.180
0.1	2.181	-0.5390 ± 0.007	0.1	2.176 ± 0.0281	-0.0654 ± 2.194
0.05	2.178 ± 0.0181	-0.3428 ± 1.571	0.05	2.175 ± 0.0282	-0.0678 ± 2.197
0.01	2.175 ± 0.0255	-0.0944 ± 2.097	0.01	2.176 ± 0.0282	-0.0683 ± 2.197
0.005	2.175 ± 0.0267	-0.0794 ± 2.149	0.005	2.176 ± 0.0282	-0.0683 ± 2.197
Turek	2.197 ± 0.0281	-0.0595 ± 2.189	Turek	2.197 ± 0.0281	-0.0595 ± 2.189

(a) Implicit Euler

(b) Crank-Nicholson

Table 1.2 – CFD benchmark, aerodynamic coefficients. Values of the mean and amplitude aerodynamic coefficients for the two time schemes. Mesh M1. Results from Turek & Hron (2006) are reported in the last line.

to the fluid part of the problem. For the stationary case CFD1, the implicit Euler scheme is used with a time-step 1, that allows to reach the steady-state solution. With mesh M2, the drag coefficient is found to 7.133 (Turek: 7.145) and the lift coefficient to 0.558 (Turek: 0.559). The time-step convergence in the case CFD3, for the mesh M1, is reported on table 1.2 for the implicit Euler (a) and Crank-Nicholson scheme (b). The period of the flow is $T \simeq 4.5$ so the coarsest discretization corresponds to about 10 times steps per period. In (a) the solution is stationary for time-steps greater than $\Delta t = 0.05$. As already observed previously, the first-order Euler scheme comes logically with a stronger dependency of the integrated quantities with respect to the time step, while the second-order properties of the Crank-Nicholson scheme provides converged results from $\Delta t = 0.05$. For the sake of comparison, the reference values given by Turek & Hron (2006) for the benchmark case CFD3 are also reported. The overall agreement is good, except perhaps for the mean lift. This is perhaps due to the weak imposition of the no-slip boundary conditions, that allows to get the interface loads as a supplementary unknown. Tests with the same time discretization, the same mesh but velocity boundary conditions enforced by penalization gave, for $\Delta t = 0.1$, a lift coefficient of 0.056 ± 2.197 , and no significant evolution for smaller time steps.

1.4.3 Fluid-structure coupled cases

We finally validate the coupled fluid-structure solver on the case FSI3. After a short transient regime, self-sustained, periodic oscillations are observed in the plate from $t \simeq 70$, as reported in Fig. 1.9. Snapshots of the flow at different non-dimensional times, in the actual configuration $\tilde{\Omega}_t$,

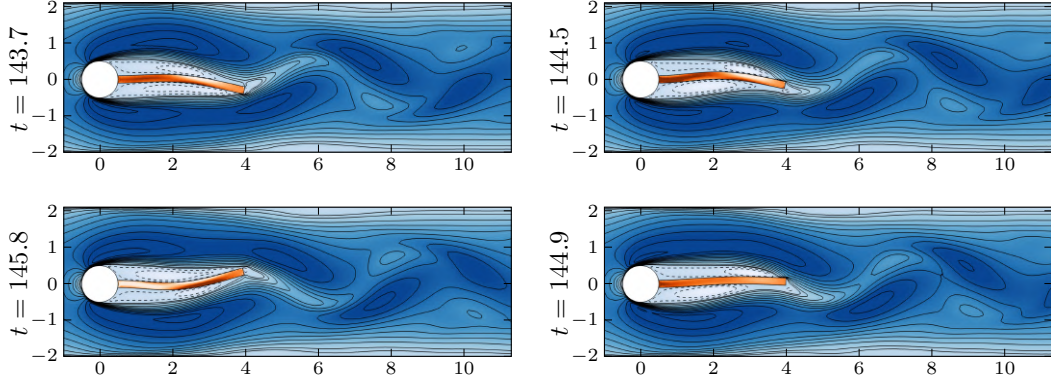


Figure 1.8 – Turek's case FSI3. Plot of the fluid streamwise velocity in the fluid and of the xx component of the solid stress tensor.

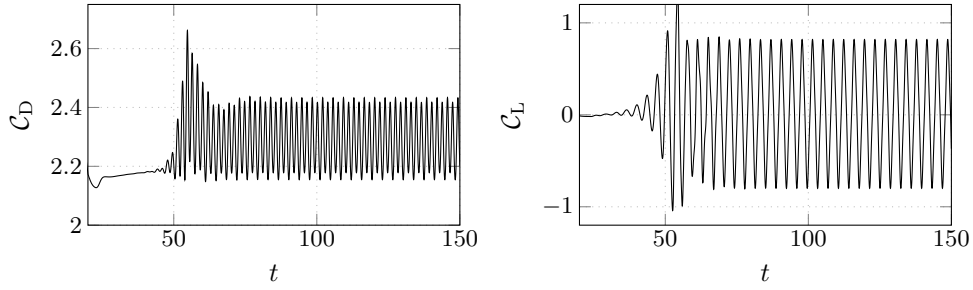


Figure 1.9 – Lift and drag time-series for the fluid-structure benchmark case FSI3.

are depicted in Fig. 1.8, showing large deformations and the vortex wake further downstream to the plate.

The time-step convergence is displayed in Tab. 1.3, where the Crank-Nicholson scheme is compared with the shifted Crank-Nicholson scheme. We see how shifting the scheme allows to gain in numerical stability at large time-steps. Only small deviations are observed with the Crank-Nicholson scheme for time-steps smaller than 0.01. Quantities such as the streamwise displacement or the lift coefficient are found to evolve in the same manner (not represented here).

Finally, the influence of the mesh resolution is reported in Tab. 1.4. We choose to perform this study using the shifted Crank-Nicholson scheme which is found to be the most stable, at the converged time-step size $\Delta t = 0.01$. The evolution of different measured quantities is displayed for different mesh resolutions, and show converged results from mesh M2. These results can be compared with those obtained by various groups using different strongly coupled methods, as

Δt	$\langle \psi(A) \rangle \pm \delta \psi(A)$	$\langle C_D \rangle \pm \delta C_D$	Δt	$\langle \psi(A) \rangle \pm \delta \psi(A)$	$\langle C_D \rangle \pm \delta C_D$
0.2	blow-up	blow-up	0.2	0.016 ± 0.257	2.227 ± 0.094
0.1	blow-up	blow-up	0.1	0.015 ± 0.327	2.264 ± 0.130
0.05	blow-up	blow-up	0.05	0.014 ± 0.344	2.272 ± 0.138
0.01	0.014 ± 0.342	2.274 ± 0.134	0.01	0.014 ± 0.349	2.274 ± 0.140
0.005	0.014 ± 0.350	2.274 ± 0.139	0.005	0.014 ± 0.350	2.274 ± 0.140

(a) Crank-Nicholson
(b) Shifted Crank-Nicholson

Table 1.3 – FSI3 benchmark, time-step convergence. Values of the mean and amplitude solid y displacement and aerodynamic drag coefficients, for different time-steps, the mesh M1, and (a) the Crank-Nicholson and (b) the shifted Crank-Nicholson schemes.

Mesh	$\langle \hat{\xi}(A)_x \rangle \pm \delta \hat{\xi}(A)_x$	$\langle \hat{\xi}(A)_y \rangle \pm \delta \hat{\xi}(A)_y$	$\langle \mathcal{C}_D \rangle \pm \delta \mathcal{C}_D$	$\langle \mathcal{C}_L \rangle \pm \delta \mathcal{C}_L$
M0	blow-up	blow-up	blow-up	blow-up
M1	-0.029 ± 0.027	0.014 ± 0.350	2.274 ± 0.140	0.014 ± 0.813
M2	-0.029 ± 0.027	0.014 ± 0.344	2.294 ± 0.141	0.011 ± 0.807
M3	-0.028 ± 0.027	0.014 ± 0.342	2.301 ± 0.141	0.010 ± 0.806
Schäfer	-0.029 ± 0.027	0.015 ± 0.349	2.293 ± 0.136	0.010 ± 0.767
Turek	-0.027 ± 0.025	0.015 ± 0.344	2.286 ± 0.113	0.011 ± 0.749
Rannacher	-0.028 ± 0.027	0.012 ± 0.346	2.262 ± 0.131	0.012 ± 0.764
Wall	-0.020 ± 0.019	0.014 ± 0.290	2.170 ± 0.088	0.013 ± 0.881

Table 1.4 – FSI3 benchmark, mesh convergence. Values of the mean and amplitude solid x and y displacements (two first columns) and aerodynamic coefficients (two last columns), for different meshes and a time-step $\Delta t = 0.01$. For the sake of comparison, results from different groups gathered in the review paper by [Turek *et al.* \(2011\)](#) are added.

summarized in the review paper by [Turek *et al.* \(2011\)](#). All these results were obtained with the same time-step $\Delta t = 0.01$, using an implicit partitioned approach (Schäfer), a monolithic approach (Turek, Rannacher) and a strongly coupled, iterative staggered scheme (Wall). The obtained results compare well with the data obtained by these groups.

2

EIGENVALUE ANALYSIS OF FLUID-STRUCTURE STEADY-STATES

The stability analysis of elastic structures strongly coupled to incompressible viscous flows is investigated in this chapter, based on a Lagrangian-based exact linearisation of the governing equations introduced previously. The leading eigenvalues/eigenmodes are computed for three configurations representative of classical fluid-structure interaction instabilities. Results are in very good agreement with instability thresholds reported in the literature and obtained with time-marching simulations. The present, new method, is also compared with an Eulerian-based linearised fluid-structure problem found in the literature.

Contents

2.1 Fluid-structure linear perturbation equations	42
2.1.1 Steady-state solutions	42
2.1.2 Lagrangian-based perturbation equations	44
2.1.3 Link with flutter derivatives & aeroelasticity	49
2.1.4 Link with Eulerian-based perturbation equations	51
2.2 Numerical formulation for an eigenvalue analysis	52
2.2.1 Modal decomposition of the perturbations	52
2.2.2 Implementation of the eigenvalue solver	52
2.2.3 Reduced eigenvalue problem	53
2.3 Numerical testing of the Lagrangian-based approach	54
2.3.1 Test case with a vortex-induced-deformation instability	54
2.3.2 Test case with a flutter instability	57
2.3.3 Influence of the extension operator and domain	60
2.3.4 Results for the reduced eigenvalue-problem	61
2.3.5 Test-case with a 3d flexible plate in a cross-flow	62
2.4 Comparison of Lagrangian-based and Eulerian-based approaches	66
2.4.1 Poiseuille flow between flexible membranes	66
2.4.2 Flag in a channel flow	67
2.5 Conclusion	70

2.1 Fluid-structure linear perturbation equations

We proceed in this chapter as summarized in the Fig. 2.1. First, we define in §2.1.1 the *base* state (i.e. stationary solutions to (1.1.1)) whose linear stability will be investigated. Then, the linearised equations are derived in §2.1.2. This results in a first set of perturbation equations for the fluid-structure problem. Using a variable change from the stress-free reference configuration to a steady deformed configuration, it is possible to rewrite this perturbation problem in a simpler form, referred to as the Lagrangian-based linear perturbation equations. We will also recall in §2.1.4 the Eulerian-based perturbation equations and show how they are related to the Lagrangian-based linear perturbation equations. The modal analysis associated to the linearised problem is introduced in §2.2.1. Then, in section 2.3 three fluid-structure configurations are studied more specifically: an elastic plate clamped on a rigid cylinder immersed in a viscous channel flow (Turek & Hron, 2006), a flag placed in a viscous channel flow (Cisonni *et al.*, 2017) and a plate positioned perpendicular to an incoming flow (Marquet & Larsson, 2015). The first configuration is representative of a vortex-induced-vibration instability, while the second accounts for a flutter-induced-vibration instability. The last case shows, in a three-dimensional setting, how static reconfiguration of a flexible obstacle affects the instabilities in the wake (see also Leclercq & de Langre (2018)). Obtained stability results are validated on these cases, and the specific features that come with our formulation are further assessed. Finally, in section 2.4, the previously validated Lagrangian-based approach is compared to the Eulerian-based approach.

2.1.1 Steady-state solutions

Steady-state solutions of the fluid-structure interaction problem are solutions for which the fluid loads exactly balance the elastic restoring force so that the fluid-structure interface position does not change with time. The steady fluid-structure equilibrium $\hat{\mathbf{Q}} = (\hat{\mathbf{Q}}_s, \hat{\mathbf{Q}}_e, \hat{\mathbf{Q}}_f)$ is found by seeking for time-independent solutions to the problem (1.1.1), resulting in the non-linear problem

$$-\mathcal{N}_{\text{fsi}}(\hat{\mathbf{Q}}) = 0. \quad (2.1.1)$$

More explicitly, the steady *base* fluid velocity $\hat{\mathbf{U}}(\hat{\mathbf{x}})$, pressure field $\hat{P}(\hat{\mathbf{x}})$, solid $\hat{\mathbf{\Xi}}(\hat{\mathbf{x}})$ and extension $\hat{\mathbf{\Xi}}_e(\hat{\mathbf{x}})$ displacements satisfy

$$\begin{aligned} -\hat{\nabla} \cdot (\hat{\mathbf{F}}(\hat{\mathbf{\Xi}}) \hat{\mathbf{S}}(\hat{\mathbf{\Xi}})) &= \mathbf{0} & \text{in } \hat{\Omega}_s, \\ -\hat{\nabla} \cdot \hat{\mathbf{\Sigma}}_e(\hat{\mathbf{\Xi}}_e) &= \mathbf{0} & \text{in } \hat{\Omega}_f, \\ (\hat{\nabla} \hat{\mathbf{U}} \hat{\mathbf{\Phi}}(\hat{\mathbf{\Xi}}_e)) \hat{\mathbf{U}} - \hat{\nabla} \cdot \hat{\mathbf{\Sigma}}(\hat{\mathbf{U}}, \hat{P}, \hat{\mathbf{\Xi}}_e) &= \mathbf{0} & \text{in } \hat{\Omega}_f, \\ -\hat{\nabla} \cdot (\hat{\mathbf{\Phi}}(\hat{\mathbf{\Xi}}_e) \hat{\mathbf{U}}) &= 0 & \text{in } \hat{\Omega}_f, \\ \hat{\mathbf{U}} = \mathbf{0} \quad \text{and} \quad \hat{\mathbf{\Xi}}_e - \hat{\mathbf{\Xi}} &= \mathbf{0} & \text{on } \hat{\Gamma}, \\ \hat{\mathbf{\Sigma}}(\hat{\mathbf{U}}, \hat{P}, \hat{\mathbf{\Xi}}_e) \hat{\mathbf{n}} - \hat{\mathbf{F}}(\hat{\mathbf{\Xi}}) \hat{\mathbf{S}}(\hat{\mathbf{\Xi}}) \hat{\mathbf{n}} &= \mathbf{0} & \text{on } \hat{\Gamma}. \end{aligned} \quad (2.1.2)$$

Remark. Looking for stationary solutions to the augmented solid problem results in the local equations $-\hat{\nabla} \cdot (\hat{\mathbf{F}}(\hat{\mathbf{\Xi}}) \hat{\mathbf{S}}(\hat{\mathbf{\Xi}})) = \mathbf{0}$ and $\hat{\mathbf{U}}_s = \mathbf{0}$ in $\hat{\Omega}_s$. This latter equation for the solid base velocity $\hat{\mathbf{U}}_s$ has been explicitly replaced in the above system.

Although this problem is much simpler than (1.1.1) in the sense that there is no longer any time-dependence, there are still difficulties. First, the resulting problem is highly non-linear and thus requires to use an appropriate iterative method such as the Newton method, as done for instance by Ghattas & Li (1995). Secondly, the presence of possibly large deformations in the solid can lead to degenerated extension fields in some cases. Specific methods such as the so-called *updated Lagrangian formulation* are adapted for handling such cases (Etienne & Pelletier, 2005).

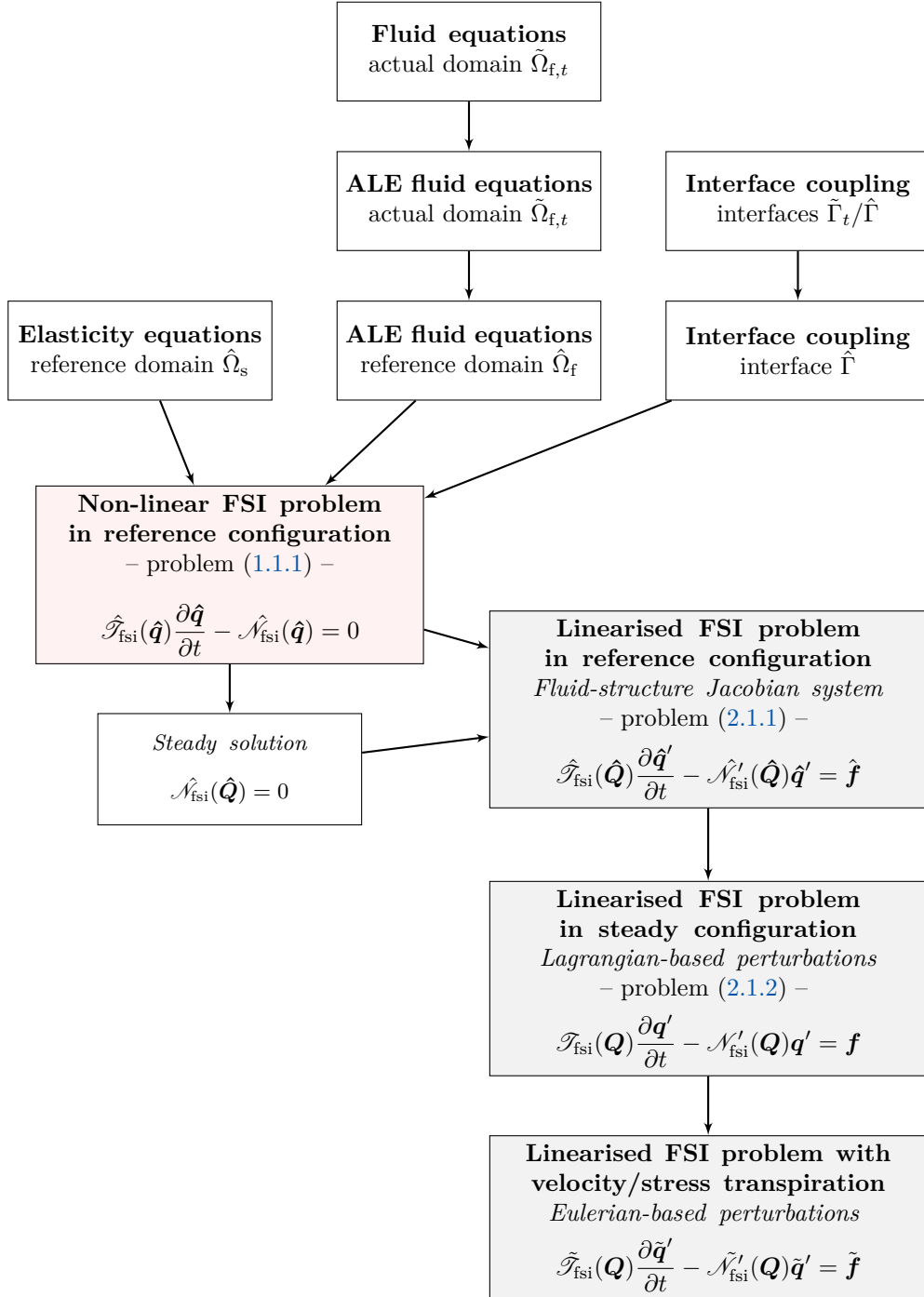


Figure 2.1 – Overall view. Classification of the different formulations of non-linear and linear formulations of the fluid-structure problem used throughout this manuscript. Symbols with a hat indicate variables or operators expressed in the stress-free reference configuration, while symbols with a tilde indicate quantities defined in the actual configuration. Non accentuated symbols are related to the steady deformed configuration.

2.1.2 Lagrangian-based perturbation equations

We present here the derivation of the linearised equations. For the reader not interested in the technical details, the resulting problems are summarized under the form of the problems (2.1.1) page 46 (expression in the reference configuration) and (2.1.2) page 49 (expression in the steady deformed configuration).

In the stress-free reference configuration

Once a steady solution $\hat{\mathbf{Q}}$ is determined, it is possible to investigate the linearised dynamics about the steady base solution, that describe the evolution of small-amplitude perturbations. To that aim, for $\varepsilon \ll 1$, we state the following splitting of the variables $\hat{\mathbf{q}}(\hat{\mathbf{x}}, t) = \hat{\mathbf{Q}}(\hat{\mathbf{x}}) + \varepsilon \hat{\mathbf{q}}'(\hat{\mathbf{x}}, t)$, that is,

$$\begin{aligned}\hat{\mathbf{u}}(\hat{\mathbf{x}}, t) &= \hat{\mathbf{U}}(\hat{\mathbf{x}}) + \varepsilon \hat{\mathbf{u}}'(\hat{\mathbf{x}}, t), \\ \hat{p}(\hat{\mathbf{x}}, t) &= \hat{P}(\hat{\mathbf{x}}) + \varepsilon \hat{p}'(\hat{\mathbf{x}}, t), \\ \hat{\xi}_e(\hat{\mathbf{x}}, t) &= \hat{\Xi}_e(\hat{\mathbf{x}}) + \varepsilon \hat{\xi}'_e(\hat{\mathbf{x}}, t), \\ \hat{\xi}(\hat{\mathbf{x}}, t) &= \hat{\Xi}(\hat{\mathbf{x}}) + \varepsilon \hat{\xi}'(\hat{\mathbf{x}}, t).\end{aligned}\tag{2.1.3}$$

The decomposition between $\hat{\mathbf{Q}}$ and the perturbation $\hat{\mathbf{q}}'$ is then introduced in the non-linear equations of the problem (1.1.1), and after having subtracted the stationary equation $\hat{\mathcal{N}}_{\text{fsi}}(\hat{\mathbf{Q}}) = 0$, we obtain at first order a perturbation problem that only depends on the linearised operators about the stationary base flow $\hat{\mathbf{Q}}$. For $\hat{\mathbf{q}}' \in \hat{\mathcal{U}}_s \times \hat{\mathcal{U}}_s \times \hat{\mathcal{U}}_e \times \hat{\mathcal{U}}_{\hat{\Gamma}} \times \hat{\mathcal{U}}_{\hat{\Gamma}} \times \hat{\mathcal{P}} \times \hat{\mathcal{U}}_{\hat{\Gamma}}$,

$$\left\langle \hat{\psi}, \hat{\mathcal{N}}'_{\text{fsi}}(\hat{\mathbf{Q}}) \frac{\partial \hat{\mathbf{q}}'}{\partial t} - \hat{\mathcal{N}}'_{\text{fsi}}(\hat{\mathbf{Q}}) \hat{\mathbf{q}}' \right\rangle = 0 \quad \forall \hat{\psi} \in \hat{\mathcal{U}}_s \times \hat{\mathcal{U}}_s \times \hat{\mathcal{U}}_e \times \hat{\mathcal{U}}_{\hat{\Gamma}} \times \hat{\mathcal{U}}_{\hat{\Gamma}} \times \hat{\mathcal{P}} \times \hat{\mathcal{U}}_{\hat{\Gamma}}.$$

After a few tedious derivations whose detail is reported in Appendix C.1, the corresponding linearised fluid-solid operator (designated with a prime symbol) reads as follows:

$$\begin{aligned}\left\langle \hat{\psi}, \hat{\mathcal{N}}'_{\text{fsi}}(\hat{\mathbf{Q}}) \hat{\mathbf{q}}' \right\rangle &= \dots \\ &\int_{\hat{\Omega}_s} \left\{ \hat{\mathbf{u}}'_s \cdot \hat{\psi}^\xi - \hat{\mathbf{P}}'(\hat{\Xi}; \hat{\xi}') : \hat{\nabla} \hat{\psi}_s^u \right\} d\hat{\Omega} \\ &- \int_{\hat{\Omega}_f} \left\{ \hat{\Sigma}_e(\hat{\xi}'_e) : \hat{\nabla} \hat{\psi}_e^\xi \right\} d\hat{\Omega} \\ &- \int_{\hat{\Omega}_f} \left\{ (\hat{\nabla} \hat{\mathbf{U}}) \hat{\Phi}(\hat{\Xi}_e) \hat{\mathbf{u}}' + (\hat{\nabla} \hat{\mathbf{u}}') \hat{\Phi}(\hat{\Xi}_e) \hat{\mathbf{U}} + (\hat{\nabla} \hat{\mathbf{U}}) \hat{\Phi}'(\hat{\Xi}_e, \hat{\xi}'_e) \hat{\mathbf{U}} \right\} \cdot \hat{\psi}^u d\hat{\Omega} \\ &- \frac{2}{\mathcal{R}_e} \int_{\hat{\Omega}_f} \left\{ \hat{\mathbf{D}}(\hat{\mathbf{u}}', \hat{\Xi}_e) \hat{\Phi}(\hat{\Xi}_e)^T + \hat{\mathbf{D}}(\hat{\mathbf{U}}, \hat{\Xi}_e) \hat{\Phi}'(\hat{\Xi}_e, \hat{\xi}'_e)^T + \hat{\mathbf{D}}'(\hat{\mathbf{U}}, \hat{\Xi}_e; \hat{\xi}'_e) \hat{\Phi}(\hat{\Xi}_e)^T \right\} : \hat{\nabla} \hat{\psi}^u d\hat{\Omega} \\ &+ \int_{\hat{\Omega}_f} \left\{ \hat{\Phi}(\hat{\Xi}_e)^T : (\hat{p}' \hat{\nabla} \hat{\psi}^u + \hat{\psi}^p \hat{\nabla} \hat{\mathbf{u}}') + \hat{\Phi}'(\hat{\Xi}_e, \hat{\xi}'_e)^T : (\hat{P} \hat{\nabla} \hat{\psi}^u + \hat{\psi}^p \hat{\nabla} \hat{\mathbf{U}}) \right\} d\hat{\Omega} \\ &- \int_{\hat{\Gamma}} \left\{ \hat{\lambda}' \cdot \hat{\psi}^u + \hat{\mathbf{u}}' \cdot \hat{\psi}^\lambda \right\} d\hat{\Gamma} \\ &- \int_{\hat{\Gamma}} \left\{ \hat{\lambda}'_e \cdot \hat{\psi}_e^\xi + \hat{\xi}'_e \cdot \hat{\psi}_e^\lambda \right\} d\hat{\Gamma} \\ &+ \int_{\hat{\Gamma}} \hat{\lambda}' \cdot \hat{\psi}_s^u d\hat{\Gamma} + \int_{\hat{\Gamma}} \hat{\xi}' \cdot \hat{\psi}_e^\lambda d\hat{\Gamma}.\end{aligned}\tag{2.1.4}$$

In the above identity, colors have been added so as to identify the hydrodynamics part (blue), the elastic part (red) and the ALE geometry terms (orange). When solving the above variational formulation, the perturbation Lagrange multiplier associated to the extension problem is $\hat{\lambda}'_e = \hat{\Sigma}_e(\hat{\xi}'_e) \hat{\mathbf{n}}$, while the one associated to the velocity interface condition gives the linearised interface

stresses, namely

$$\hat{\lambda}' = \hat{\mathbf{P}}'(\hat{\mathbf{\Xi}}; \hat{\xi}') \hat{\mathbf{n}} = \left[\hat{\mathbf{\Sigma}}(\hat{\mathbf{u}}', \hat{p}', \hat{\mathbf{\Xi}}_e) + \hat{\mathbf{\Sigma}}'(\hat{U}, \hat{P}, \hat{\mathbf{\Xi}}_e; \hat{\xi}'_e) \right] \hat{\mathbf{n}}, \quad (2.1.5)$$

where the expression of the different linearised tensors is given hereafter. For the Saint-Venant Kirchhoff solid model chosen, all solid non-linearities are polynomial and the linearisation does not present any special difficulty. The linearised first Piola-Kirchhoff solid stress tensor, second Piola-Kirchhoff stress tensor and Green-Lagrange stress tensor writes respectively as

$$\hat{\mathbf{P}}'(\hat{\mathbf{\Xi}}, \hat{\xi}') = \hat{\mathbf{F}}(\hat{\mathbf{\Xi}}) \hat{\mathbf{S}}'(\hat{\mathbf{\Xi}}, \hat{\xi}') + \hat{\nabla} \hat{\xi}' \hat{\mathbf{S}}(\hat{\mathbf{\Xi}}), \quad (2.1.6)$$

$$\hat{\mathbf{S}}'(\hat{\xi}'; \hat{\mathbf{\Xi}}) = \lambda_s \text{tr} \left(\hat{\mathbf{E}}'(\hat{\xi}'; \hat{\mathbf{\Xi}}) \right) \mathbf{I} + 2\mu_s \hat{\mathbf{E}}'(\hat{\xi}'; \hat{\mathbf{\Xi}}) \quad (2.1.7)$$

$$\hat{\mathbf{E}}'(\hat{\xi}'; \hat{\mathbf{\Xi}}) = \frac{1}{2} \left(\hat{\nabla} \hat{\mathbf{\Xi}}^T \hat{\nabla} \hat{\xi}' + \hat{\nabla} \hat{\xi}'^T \hat{\nabla} \hat{\mathbf{\Xi}} + \hat{\nabla} \hat{\xi}' + \hat{\nabla} \hat{\xi}'^T \right). \quad (2.1.8)$$

Turning now to the fluid equations, in addition to the quadratic convective terms, more complex geometric non-linearities are present in the Navier-Stokes equations. Considering the steady fluid domain deformation $\hat{\mathbf{\Xi}}_e$, the linearised fluid domain deformation Jacobian, fluid domain deformation operator, viscous diffusion gradient and viscous stress tensor write as follows (we refer again the reader to the Appendix C.1 for further details):

$$\hat{\Phi}'(\hat{\mathbf{\Xi}}_e; \hat{\xi}'_e) = \frac{1}{\hat{J}(\hat{\mathbf{\Xi}}_e)} \left[\left(\hat{\Phi}(\hat{\mathbf{\Xi}}_e)^T : \hat{\nabla} \hat{\xi}'_e \right) \hat{\Phi}(\hat{\mathbf{\Xi}}_e) - \hat{\Phi}(\hat{\mathbf{\Xi}}_e) \hat{\nabla} \hat{\xi}'_e \hat{\Phi}(\hat{\mathbf{\Xi}}_e) \right], \quad (2.1.9)$$

$$\hat{\mathbf{D}}'(\hat{U}, \hat{\mathbf{\Xi}}_e; \hat{\xi}'_e) = \frac{-1/2}{\hat{J}(\hat{\mathbf{\Xi}}_e)^2} \left[\hat{\nabla} \hat{U} \hat{\Phi}(\hat{\mathbf{\Xi}}_e) \hat{\nabla} \hat{\xi}'_e \hat{\Phi}(\hat{\mathbf{\Xi}}_e) + \left(\hat{\nabla} \hat{U} \hat{\Phi}(\hat{\mathbf{\Xi}}_e) \hat{\nabla} \hat{\xi}'_e \hat{\Phi}(\hat{\mathbf{\Xi}}_e) \right)^T \right], \quad (2.1.10)$$

$$\hat{\mathbf{\Sigma}}'(\hat{U}, \hat{P}, \hat{\mathbf{\Xi}}_e; \hat{\xi}'_e) = \hat{\sigma}(\hat{U}, \hat{P}, \hat{\mathbf{\Xi}}_e) \hat{\Phi}'(\hat{\mathbf{\Xi}}_e; \hat{\xi}'_e)^T + \frac{2}{\mathcal{R}_e} \hat{\mathbf{D}}'(\hat{U}, \hat{\mathbf{\Xi}}_e; \hat{\xi}'_e) \hat{\Phi}(\hat{\mathbf{\Xi}}_e)^T. \quad (2.1.11)$$

Local perturbation equations are eventually obtained using integration by parts in (2.1.4) and expressing the solid velocity as $\hat{\mathbf{u}}'_s = \partial \hat{\xi}' / \partial t$, or by linearising directly the non-linear, local equations given in (1.1.1). The following problem is obtained:

Problem 2.1.1 – linearised fluid-structure equations in the stress-free reference configuration. *The evolution of small-amplitude perturbations of fluid velocity $\hat{\mathbf{u}}'$, fluid pressure \hat{p}' , solid displacement $\hat{\xi}'$, in the stress-free reference configuration where the stationary flow is given by the velocity \hat{U} and pressure \hat{P} and the stationary displacement by $\hat{\mathbf{\Xi}}$, writes as follows:*

$$\begin{aligned} \mathcal{M}_s \frac{\partial^2 \hat{\xi}'}{\partial t^2} - \hat{\nabla} \cdot \hat{\mathbf{P}}'(\hat{\mathbf{\Xi}}; \hat{\xi}') &= \mathbf{0} & \text{in } \hat{\Omega}_s \\ -\hat{\nabla} \cdot \hat{\mathbf{\Sigma}}_e(\hat{\xi}'_e) &= \mathbf{0} & \text{in } \hat{\Omega}_f, \\ \hat{J}(\hat{\mathbf{\Xi}}_e) \frac{\partial \hat{\mathbf{u}}'}{\partial t} + \left(\hat{\nabla} \hat{U} \hat{\Phi}(\hat{\mathbf{\Xi}}_e) \right) \left(\hat{\mathbf{u}}' - \frac{\partial \hat{\xi}'_e}{\partial t} \right) + \left(\hat{\nabla} \hat{\mathbf{u}}' \hat{\Phi}(\hat{\mathbf{\Xi}}_e) \right) \hat{U} \dots \\ + \left(\hat{\nabla} \hat{U} \hat{\Phi}'(\hat{\mathbf{\Xi}}_e; \hat{\xi}'_e) \right) \hat{U} - \hat{\nabla} \cdot \left[\hat{\mathbf{\Sigma}}(\hat{\mathbf{u}}', \hat{p}', \hat{\mathbf{\Xi}}_e) + \hat{\mathbf{\Sigma}}'(\hat{U}, \hat{P}, \hat{\mathbf{\Xi}}_e; \hat{\xi}'_e) \right] &= \mathbf{0} & \text{in } \hat{\Omega}_f, \\ -\hat{\nabla} \cdot \left[\hat{\Phi}(\hat{\mathbf{\Xi}}_e) \hat{\mathbf{u}}' + \hat{\Phi}'(\hat{\mathbf{\Xi}}_e; \hat{\xi}'_e) \hat{U} \right] &= \mathbf{0} & \text{in } \hat{\Omega}_f, \\ \hat{\mathbf{u}}' - \frac{\partial \hat{\xi}'}{\partial t} &= \mathbf{0} & \text{on } \hat{\Gamma} \\ \hat{\xi}'_e - \hat{\xi}' &= \mathbf{0} & \text{on } \hat{\Gamma}, \\ \left[\hat{\mathbf{\Sigma}}(\hat{\mathbf{u}}', \hat{p}', \hat{\mathbf{\Xi}}_e) + \hat{\mathbf{\Sigma}}'(\hat{U}, \hat{P}, \hat{\mathbf{\Xi}}_e; \hat{\xi}'_e) \right] \hat{\mathbf{n}} - \hat{\mathbf{P}}'(\hat{\mathbf{\Xi}}; \hat{\xi}') \hat{\mathbf{n}} &= \mathbf{0}, & \text{on } \hat{\Gamma}, \end{aligned}$$

where the perturbation extension displacement $\hat{\xi}'_e$ serves for propagating the solid deformation onto the fluid domain. In this system, the first equation is the solid momentum equation, the extension equation is written in the second line, the third and fourth equations represent the linearised fluid momentum and continuity equations respectively. The last three equations represent the interface velocity, displacement and stress continuity conditions. Using the velocity equation (1.1.34) to write the interface velocity as $\hat{\mathbf{u}}' - \hat{\mathbf{u}}'_s$, the block notation reads:

$$\underbrace{\begin{pmatrix} \hat{\mathcal{T}}_s & 0 & 0 \\ 0 & 0 & 0 \\ 0 & -\hat{\mathcal{T}}_{fe}(\hat{\mathbf{Q}}_f, \hat{\mathbf{Q}}_e) & \hat{\mathcal{T}}_f(\hat{\mathbf{Q}}_e) \end{pmatrix}}_{\hat{\mathcal{T}}_{fsi}(\hat{\mathbf{Q}})} \begin{pmatrix} \frac{\partial \hat{\mathbf{q}}'_s}{\partial t} \\ \frac{\partial \hat{\mathbf{q}}'_e}{\partial t} \\ \frac{\partial \hat{\mathbf{q}}'_f}{\partial t} \end{pmatrix} = \underbrace{\begin{pmatrix} \hat{\mathcal{J}}'(\hat{\mathbf{Q}}_s) & 0 & \hat{\mathcal{I}}_{fs}^T \\ \hat{\mathcal{I}}_{es} & -\hat{\mathcal{A}}_e & 0 \\ \hat{\mathcal{I}}_{fs} & \hat{\mathcal{N}}'_{fe}(\hat{\mathbf{Q}}_e, \hat{\mathbf{Q}}_f) & \hat{\mathcal{N}}'_{ff}(\hat{\mathbf{Q}}_e, \hat{\mathbf{Q}}_f) \end{pmatrix}}_{\hat{\mathcal{N}}'_{fsi}(\hat{\mathbf{Q}}) = \left. \frac{\partial \hat{\mathcal{N}}_{fsi}}{\partial \hat{\mathbf{q}}} \right|_{\hat{\mathbf{Q}}}} \begin{pmatrix} \hat{\mathbf{q}}'_s \\ \hat{\mathbf{q}}'_e \\ \hat{\mathbf{q}}'_f \end{pmatrix}.$$

where the colors are related to (2.1.4), $\hat{\mathcal{N}}'_{ff}(\hat{\mathbf{Q}}_e, \hat{\mathbf{Q}}_f) = \partial \hat{\mathcal{N}}_f / \partial \hat{\mathbf{q}}_f|_{\hat{\mathbf{Q}}_e, \hat{\mathbf{Q}}_f}$ is the linearised Navier-Stokes equations and $\hat{\mathcal{N}}'_{fe}(\hat{\mathbf{Q}}_e, \hat{\mathbf{Q}}_f) = \partial \hat{\mathcal{N}}_f / \partial \hat{\mathbf{q}}_e|_{\hat{\mathbf{Q}}_e, \hat{\mathbf{Q}}_f}$ is a shape derivative term that represents the effect of a perturbation of the fluid domain on the fluid equations.

The above formulation gives in particular the linearised operators used in the Jacobian matrix that appears in (1.2.1).

In the steady deformed configuration

In the previous section, we have formulated a linearised fluid-structure interaction problem in the stress-free reference configuration (problem (2.1.1) written page 46). This formulation is used for designing efficient steady and unsteady fluid-structure solvers, as evoked in the previous chapter. However, it results in heavy expressions in which each fluid operator depends on the steady extension field. In this section, we derive a much simpler expression of the linearised problem. The basic idea is to use the stationary displacement field to define a new formulation in a steady deformed configuration where the stationary base displacement is *zero* by construction. This alternative point of view is illustrated in Fig. 2.2.

Mathematically, this amounts to perform a change of variable so as to rewrite the whole problem as a function of $\mathbf{x} = \hat{\mathbf{x}} + \hat{\mathbf{\Xi}}(\hat{\mathbf{x}})$ instead of $\hat{\mathbf{x}}$, in domains Ω_f and Ω_s such that $\Omega_f = (\text{Id} + \hat{\mathbf{\Xi}}_e)(\hat{\Omega}_f)$ and $\Omega_s = (\text{Id} + \hat{\mathbf{\Xi}})(\hat{\Omega}_s)$. These mappings coincide at the fluid-solid interface but are not continuously differentiable there, as can be seen in Fig. 2.2. The perturbation problem in the steady deformed configuration is obtained by changing the variables as

$$\begin{aligned} \hat{\mathbf{u}}' &= \mathbf{u}' \circ (\text{Id} + \hat{\mathbf{\Xi}}_e) \\ \hat{p}' &= p' \circ (\text{Id} + \hat{\mathbf{\Xi}}_e) \\ \hat{\xi}'_e &= \xi'_e \circ (\text{Id} + \hat{\mathbf{\Xi}}_e) \\ \hat{\xi}' &= \xi' \circ (\text{Id} + \hat{\mathbf{\Xi}}) \end{aligned} \tag{2.1.12}$$

where the transformation only applies to the space variable. Furthermore, we introduce $\mathbf{U} = \hat{\mathbf{U}} \circ (\text{Id} + \hat{\mathbf{\Xi}}_e)^{-1}$ and $P = \hat{P} \circ (\text{Id} + \hat{\mathbf{\Xi}}_e)^{-1}$ the steady fluid velocity and pressure fields, transported in the steady deformed configuration. By construction, the steady displacements are zero in the steady deformed configuration, i.e. the *Lagrangian-based* decomposition for the variables writes as

$$\begin{aligned} \mathbf{u}(\mathbf{x}, t) &= \mathbf{U}(\mathbf{x}) + \varepsilon \mathbf{u}'(\mathbf{x}, t), \\ p(\mathbf{x}, t) &= P(\mathbf{x}) + \varepsilon p'(\mathbf{x}, t), \\ \xi_e(\mathbf{x}, t) &= \mathbf{0} + \varepsilon \xi'_e(\mathbf{x}, t), \\ \xi(\mathbf{x}, t) &= \mathbf{0} + \varepsilon \xi'(\mathbf{x}, t). \end{aligned} \tag{2.1.13}$$

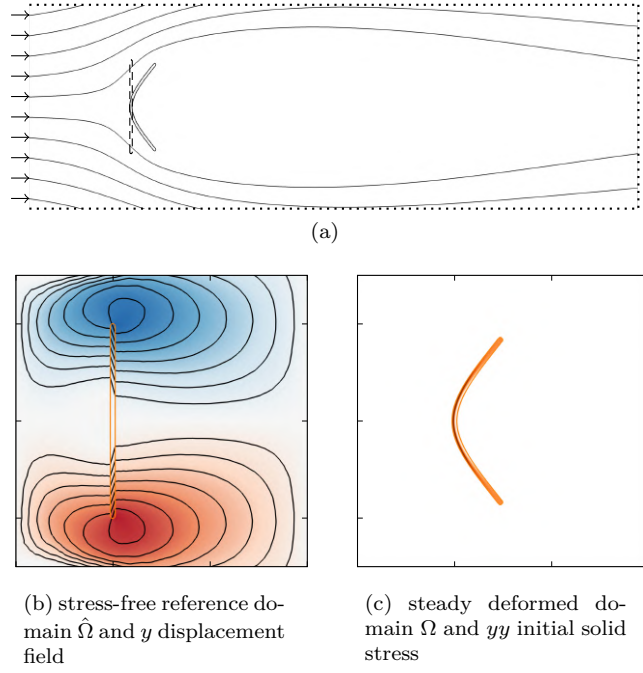


Figure 2.2 – Two equivalent descriptions. (a) Representation of a steady flow that bends an elastic plate. The steady deformed solid is represented by the solid line while the stress-free (not deformed) solid is represented by the dashed line. (b) Description in the stress-free reference configuration $\hat{\Omega}$. (c) Description in the steady deformed configuration $\Omega = (\text{Id} + \hat{\xi})(\hat{\Omega})$.

This way of introducing the perturbations in the steady deformed configuration simplifies the equations, but does not change the general structure of the problem. Changing the variables in (1.1.35) and in (2.1.4), with

$$\mathbf{q}' = \begin{pmatrix} \hat{\xi}' \circ (\text{Id} + \hat{\Xi})^{-1} \\ \hat{\mathbf{u}}_s' \circ (\text{Id} + \hat{\Xi})^{-1} \\ \hat{\xi}_e' \circ (\text{Id} + \hat{\Xi}_e)^{-1} \\ \hat{\lambda}_e' \circ (\text{Id} + \hat{\Xi}_e)^{-1} \\ \hat{\mathbf{u}}' \circ (\text{Id} + \hat{\Xi}_e)^{-1} \\ \hat{p}' \circ (\text{Id} + \hat{\Xi}_e)^{-1} \\ \hat{\lambda}' \circ (\text{Id} + \hat{\Xi}_e)^{-1} \end{pmatrix} \quad \text{and} \quad \boldsymbol{\psi} = \begin{pmatrix} \hat{\psi}^\xi \circ (\text{Id} + \hat{\Xi})^{-1} \\ \hat{\psi}_s^u \circ (\text{Id} + \hat{\Xi})^{-1} \\ \hat{\psi}_e^\xi \circ (\text{Id} + \hat{\Xi}_e)^{-1} \\ \hat{\psi}_e^\lambda \circ (\text{Id} + \hat{\Xi}_e)^{-1} \\ \hat{\psi}^u \circ (\text{Id} + \hat{\Xi}_e)^{-1} \\ \hat{\psi}^p \circ (\text{Id} + \hat{\Xi}_e)^{-1} \\ \hat{\psi}^\lambda \circ (\text{Id} + \hat{\Xi}_e)^{-1} \end{pmatrix},$$

we obtain expressions of the transformed operators (on the left side, the scalar products are taken in the stress-free reference domain while they are taken in the steady deformed domain in the right side):

$$\langle \hat{\psi}, \hat{\mathcal{T}}_{\text{fsi}}(\hat{\mathbf{Q}}) \hat{\mathbf{q}}' \rangle = \langle \boldsymbol{\psi}, \mathcal{T}_{\text{fsi}}(\mathbf{Q}) \mathbf{q}' \rangle \quad \text{and} \quad \langle \hat{\psi}, \hat{\mathcal{N}}'_{\text{fsi}}(\hat{\mathbf{Q}}) \hat{\mathbf{q}}' \rangle = \langle \boldsymbol{\psi}, \mathcal{N}'_{\text{fsi}}(\mathbf{Q}) \mathbf{q}' \rangle.$$

We refer again the reader to the Appendix C.1 for more detail about the practical computations, that result in the following expressions,

$$\begin{aligned} \langle \boldsymbol{\psi}, \mathcal{T}_{\text{fsi}}(\mathbf{Q}) \partial_t \mathbf{q}' \rangle &= \int_{\Omega_s} \left\{ \frac{\partial \xi'}{\partial t} \cdot \boldsymbol{\psi}^\xi + \frac{\mathcal{M}_s}{J(\Xi)} \frac{\partial \mathbf{u}_s'}{\partial t} \cdot \boldsymbol{\psi}_s^u \right\} d\Omega \\ &\quad + \int_{\Omega_f} \left\{ \frac{\partial \mathbf{u}'}{\partial t} - (\nabla U) \frac{\partial \xi_e'}{\partial t} \right\} \cdot \boldsymbol{\psi}^u d\Omega \\ &\quad - \int_{\Gamma} \frac{\partial \xi'}{\partial t} \cdot \boldsymbol{\psi}^\lambda d\Gamma, \end{aligned} \tag{2.1.14}$$

defining the operator \mathcal{T}_{fsi} acting on time-derivatives, and

$$\begin{aligned}
\langle \psi, \mathcal{N}'_{\text{fsi}}(\mathbf{Q})\mathbf{q}' \rangle = & \int_{\Omega_s} \left\{ \mathbf{u}'_s \cdot \psi \boldsymbol{\xi} - \mathbf{P}'(\boldsymbol{\Xi}; \boldsymbol{\xi}') : \nabla \psi_s^{\mathbf{u}} \right\} d\Omega \\
& - \int_{\Omega_f} \left\{ \boldsymbol{\Sigma}_e(\boldsymbol{\xi}'_e) : \nabla \psi_e^{\boldsymbol{\xi}} \right\} d\Omega \\
& - \int_{\Omega_f} \left\{ (\nabla \mathbf{U})\mathbf{u}' + (\nabla \mathbf{u}')\mathbf{U} + (\nabla \mathbf{U})\boldsymbol{\Phi}'(\boldsymbol{\xi}'_e)\mathbf{U} \right\} \cdot \psi^{\mathbf{u}} d\Omega \\
& - \frac{2}{\mathcal{R}_e} \int_{\Omega_f} \left\{ \mathbf{D}(\mathbf{u}') + \mathbf{D}(\mathbf{U})\boldsymbol{\Phi}'(\boldsymbol{\xi}'_e)^T + \mathbf{D}'(\mathbf{U}; \boldsymbol{\xi}'_e) \right\} : \nabla \psi^{\mathbf{u}} d\Omega \\
& + \int_{\Omega_f} \left\{ p' \nabla \cdot \psi^{\mathbf{u}} + \psi^p \nabla \cdot \mathbf{u}' + \boldsymbol{\Phi}'(\boldsymbol{\xi}'_e)^T : (P \nabla \psi^{\mathbf{u}} + \psi^p \nabla \mathbf{U}) \right\} d\Omega \\
& - \int_{\Gamma} \left\{ \boldsymbol{\lambda}' \cdot \psi^{\mathbf{u}} + \mathbf{u}' \cdot \psi \boldsymbol{\lambda} \right\} d\Gamma \\
& - \int_{\Gamma} \left\{ \boldsymbol{\lambda}'_e \cdot \psi_e^{\boldsymbol{\xi}} + \boldsymbol{\xi}'_e \cdot \psi_e^{\boldsymbol{\lambda}} \right\} d\Gamma \\
& + \int_{\Gamma} \boldsymbol{\lambda}' \cdot \psi_s^{\mathbf{u}} d\Gamma + \int_{\hat{\Gamma}} \boldsymbol{\xi}' \cdot \psi_e^{\boldsymbol{\lambda}} d\Gamma,
\end{aligned} \tag{2.1.15}$$

for $\mathcal{N}'_{\text{fsi}}(\mathbf{Q})$, where the same conventions as before hold: red for the solid operator, blue for the Navier-Stokes operator, and orange for the shape derivatives. The corresponding three-fields representation has of course the same structure as before. There is no longer any explicit dependency to the steady extension displacement field $\hat{\boldsymbol{\Xi}}_e$, for this information is now embedded in the deformed domain itself. The solid however depends on the non-zero stains that are present in the steady deformed configuration. Namely, the linearised first and second Piola-Kirchhoff solid stress tensor, and Green-Lagrange strain tensor in the steady deformed configuration, write respectively as

$$\mathbf{P}'(\boldsymbol{\Xi}; \boldsymbol{\xi}') = \frac{1}{J(\boldsymbol{\Xi})} \left\{ \nabla \boldsymbol{\xi}' \mathbf{F}(\boldsymbol{\Xi}) \mathbf{S}(\boldsymbol{\Xi}) + \mathbf{F}(\boldsymbol{\Xi}) \mathbf{S}'(\boldsymbol{\xi}'; \boldsymbol{\Xi}) \right\} \mathbf{F}(\boldsymbol{\Xi})^T, \tag{2.1.16}$$

$$\mathbf{S}'(\boldsymbol{\Xi}; \boldsymbol{\xi}') = \lambda_s \text{tr}(\mathbf{E}'(\boldsymbol{\xi}'; \boldsymbol{\Xi})) \mathbf{I} + 2\mu_s \mathbf{E}'(\boldsymbol{\xi}'; \boldsymbol{\Xi}), \tag{2.1.17}$$

$$\mathbf{E}'(\boldsymbol{\Xi}; \boldsymbol{\xi}') = \frac{1}{2} \mathbf{F}(\boldsymbol{\Xi})^T (\nabla \boldsymbol{\xi}' + \nabla \boldsymbol{\xi}'^T) \mathbf{F}(\boldsymbol{\Xi}). \tag{2.1.18}$$

In these expressions, we have written $J(\boldsymbol{\Xi}) = \hat{J}(\hat{\boldsymbol{\Xi}}) \circ (\text{Id} + \hat{\boldsymbol{\Xi}})^{-1}$ the transported Jacobian, and $\mathbf{F}(\boldsymbol{\Xi}) = \hat{\mathbf{F}}(\hat{\boldsymbol{\Xi}}) \circ (\text{Id} + \hat{\boldsymbol{\Xi}})^{-1}$ the transported deformation gradient, from the stress-free reference configuration to the steady deformed configuration. In the fluid, the different operators involved are

$$\boldsymbol{\Phi}'(\boldsymbol{\xi}'_e) = \nabla \cdot \boldsymbol{\xi}'_e \mathbf{I} - \hat{\nabla} \boldsymbol{\xi}'_e, \tag{2.1.19}$$

$$\mathbf{D}'(\mathbf{U}; \boldsymbol{\xi}'_e) = -\frac{1}{2} \left(\nabla \mathbf{U} \nabla \boldsymbol{\xi}'_e + (\nabla \boldsymbol{\xi}'_e)^T (\nabla \mathbf{U})^T \right), \tag{2.1.20}$$

$$\boldsymbol{\Sigma}'(\mathbf{U}, P; \boldsymbol{\xi}'_e) = \boldsymbol{\sigma}(\mathbf{U}, P) \boldsymbol{\Phi}'(\boldsymbol{\xi}'_e)^T + \frac{2}{\mathcal{R}_e} \mathbf{D}'(\mathbf{U}; \boldsymbol{\xi}'_e). \tag{2.1.21}$$

In the above expression, $\boldsymbol{\sigma}(\mathbf{U}, P) = -P \mathbf{I} + 2/\mathcal{R}_e \mathbf{D}(\mathbf{U})$ with $\mathbf{D}(\mathbf{U}) = 1/2 (\nabla \mathbf{U} + \nabla \mathbf{U}^T)$. Again, details on the derivation are reported in Appendix. The corresponding local equations write as follows:

Problem 2.1.2 – linearised fluid-structure problem in the steady deformed configuration with a Lagrangian decomposition of the perturbations. *The evolution of small-amplitude perturbations of fluid velocity \mathbf{u}' , fluid pressure p' , solid displacement $\boldsymbol{\xi}'$, about a steady deformed solid configuration (Ω_s obtained from the stress-free reference configuration $\hat{\Omega}_s$ by the steady base displacement field $\hat{\boldsymbol{\Xi}}$) where the stationary flow is given by the velocity \mathbf{U}*

and P , writes as follows:

$$\begin{aligned}
\frac{\mathcal{M}_s}{J(\Xi)} \frac{\partial^2 \xi'}{\partial t^2} - \nabla \cdot \mathbf{P}'(\Xi; \xi') &= \mathbf{0} & \text{in } \Omega_s, \\
-\nabla \cdot \Sigma_e(\xi'_e) &= \mathbf{0} & \text{in } \Omega_f, \\
\frac{\partial \mathbf{u}'}{\partial t} + (\nabla \mathbf{U}) \left(\mathbf{u}' - \frac{\partial \xi'_e}{\partial t} \right) + (\nabla \mathbf{u}') \mathbf{U} - \nabla \cdot \boldsymbol{\sigma}(\mathbf{u}', p') + \dots \\
(\nabla \mathbf{U}) \boldsymbol{\Phi}'(\xi'_e) \mathbf{U} - \nabla \cdot \Sigma'(U, P; \xi'_e) &= \mathbf{0} & \text{in } \Omega_f, \\
-\nabla \cdot \mathbf{u}' - \nabla \cdot (\boldsymbol{\Phi}'(\xi'_e) \mathbf{U}) &= 0 & \text{in } \Omega_f, \\
\mathbf{u}' - \frac{\partial \xi'}{\partial t} &= \mathbf{0} & \text{on } \Gamma, \\
\xi'_e - \xi' &= 0 & \text{on } \Gamma, \\
[\boldsymbol{\sigma}(\mathbf{u}', p') + \Sigma'(U, P, \xi'_e)] \mathbf{n} - \mathbf{P}'(\Xi; \xi') \mathbf{n} &= \mathbf{0} & \text{on } \Gamma.
\end{aligned}$$

where the perturbation extension displacement ξ'_e is used to propagate the solid deformation onto the fluid domain. In this system, the first equation is the solid momentum equation, the extension equation is written in the second line, the third and fourth equations represent the linearised fluid momentum and continuity equations respectively. The last three equations represent the interface velocity, displacement and stress continuity conditions.

In the above system, the first line in the momentum equation gathers the terms linearised with respect to the fluid (and fluid domain) velocity and pressure (and thus obtained by keeping $\xi'_e = \mathbf{0}$). They are very similar to the linearised equation obtained in a purely hydrodynamic case, except for the second term that includes the advection by the extension domain velocity perturbation. The second line gathers additional terms that represent how the stationary equilibrium (U, P) is affected by the domain displacement perturbation (these terms are part of the shape derivative $\mathcal{N}'_{fe}(\mathbf{Q}_f)$). The first term is related to the modification of the velocity gradients due to the domain motion, while the second expresses how the displacement of the domain modifies the stress. An extra term related to the geometry modification is also present in the mass conservation equation.

2.1.3 Link with flutter derivatives & aeroelasticity

Let us consider another writing of the three-fields perturbation problem (2.1.1). When the solid velocity variable is eliminated (i.e. we do not consider an augmented solid problem) by writing explicitly $\hat{\mathbf{u}}_s = \partial_t \hat{\xi}$, a second-order problem is obtained. It is convenient here to introduce the modal decomposition

$$\begin{aligned}
\hat{\xi}'(\hat{\mathbf{x}}, t) &= \hat{\xi}^\circ(\hat{\mathbf{x}}) \exp(\lambda t) + \text{c.c.}, \\
\hat{\mathbf{q}}'_e(\hat{\mathbf{x}}, t) &= \hat{\mathbf{q}}_e^\circ(\hat{\mathbf{x}}) \exp(\lambda t) + \text{c.c.},
\end{aligned}$$

with $\lambda \in \mathbb{C}$. We then obtain a complex, quadratic eigenvalue problem that writes as follows (note that we have integrated the density ratio \mathcal{M}_s in the operator $\hat{\mathcal{M}}_s$):

$$\lambda^2 \begin{pmatrix} \hat{\mathcal{M}}_s & 0 & 0 \\ 0 & 0 & 0 \\ 0 & 0 & 0 \end{pmatrix} \begin{pmatrix} \hat{\xi}^\circ \\ \hat{\mathbf{q}}_e^\circ \\ \hat{\mathbf{q}}_f^\circ \end{pmatrix} + \lambda \begin{pmatrix} 0 & 0 & 0 \\ 0 & 0 & 0 \\ -\hat{\mathcal{I}}_{f\xi} - \hat{\mathcal{J}}_{fe} & \hat{\mathcal{J}}_f & \end{pmatrix} \begin{pmatrix} \hat{\xi}^\circ \\ \hat{\mathbf{q}}_e^\circ \\ \hat{\mathbf{q}}_f^\circ \end{pmatrix} = \begin{pmatrix} -\hat{\mathcal{K}}' & 0 & \hat{\mathcal{I}}_{f\xi}^\top \\ \hat{\mathcal{I}}_{e\xi} & -\hat{\mathcal{A}}_e & 0 \\ 0 & \hat{\mathcal{N}}'_{fe} & \hat{\mathcal{N}}'_{ff} \end{pmatrix} \begin{pmatrix} \hat{\xi}^\circ \\ \hat{\mathbf{q}}_e^\circ \\ \hat{\mathbf{q}}_f^\circ \end{pmatrix}. \quad (2.1.22)$$

As seen in the second row and already evoked before, the extension problem is subordinated to the solid problem in a static way. The extension variable \mathbf{q}'_e can therefore be expressed as a function of the solid displacement by

$$\hat{\mathbf{q}}'_e = \hat{\mathcal{A}}_e^{-1} \hat{\mathcal{I}}_{e\xi} \hat{\xi}'.$$

Now expanding the blocks in the above three-fields, non-augmented formulation, and replacing the extension variable, results in

$$\begin{aligned} (\lambda^2 \hat{\mathcal{M}}_s + \hat{\mathcal{K}}') \hat{\xi}^\circ &= \hat{\mathcal{I}}_{\text{fe}}^T \hat{\mathbf{q}}_f^\circ, \\ (\lambda \hat{\mathcal{T}}_f - \hat{\mathcal{N}}_{\text{ff}}') \hat{\mathbf{q}}_f^\circ &= (\hat{\mathcal{N}}_{\text{fe}}' \hat{\mathcal{A}}_e^{-1} \hat{\mathcal{I}}_{\text{e}\xi}) \hat{\xi}^\circ + (\hat{\mathcal{I}}_{\text{fe}} + \hat{\mathcal{T}}_{\text{fe}} \hat{\mathcal{A}}_e^{-1} \hat{\mathcal{I}}_{\text{e}\xi}) (\lambda \hat{\xi}^\circ). \end{aligned} \quad (2.1.23)$$

We have obtained here two coupled problems: a pure solid equation (left-hand side in the first line) forced by the fluid variable through the load transfer term $\hat{\mathcal{I}}_{\text{fe}}^T \hat{\mathbf{q}}_f^\circ$, and a pure fluid equation (left-hand side of the second line) forced by the solid displacement and displacement velocity in a more complex way, that involves the shape derivatives $\hat{\mathcal{T}}_{\text{fe}}$ and $\hat{\mathcal{N}}_{\text{fe}}'$. Further eliminating the fluid equation, we can write (2.1.23) as a problem that depends on the solid variable only:

$$\underbrace{(\lambda^2 \hat{\mathcal{M}}_s + \hat{\mathcal{K}}')}_{\text{solid oscillator}} \hat{\xi}^\circ = \underbrace{\hat{\mathcal{A}}_{\text{sfs}}(\lambda)}_{\text{effect of the fluid}} \hat{\xi}^\circ. \quad (2.1.24)$$

We recover here a solid free solid vibration problem when the right-hand-side is zero. This right-hand side is a “solid-to-fluid-to-solid” operator that writes as follows:

$$\hat{\mathcal{A}}_{\text{sfs}}(\lambda) = \underbrace{\hat{\mathcal{I}}_{\text{fe}}^T (\lambda \hat{\mathcal{T}}_f - \hat{\mathcal{N}}_{\text{ff}}')^{-1}}_{(1)} \underbrace{\left(\lambda (\hat{\mathcal{I}}_{\text{fe}} + \hat{\mathcal{T}}_{\text{fe}} \hat{\mathcal{A}}_e^{-1} \hat{\mathcal{I}}_{\text{e}\xi}) + (\hat{\mathcal{N}}_{\text{fe}}' \hat{\mathcal{A}}_e^{-1} \hat{\mathcal{I}}_{\text{e}\xi}) \right)}_{(2)}. \quad (2.1.25)$$

The linear (or quadratic) eigenvalue problem obtained from the linearised, fully coupled fluid-structure problem (2.1.2), can thus be rewritten as a *non-polynomial* eigenvalue problem, where the only source of non-linearity is the coupling between the solid and the fluid. $\hat{\mathcal{A}}_{\text{sfs}}$ represents how a linear solid deformation influences back the solid modal problem after having “travelled” in the fluid.

In classical aeroelasticity, as evoked in the introduction, a forced solid problem of type (2.1.24) is often considered, but the special form of the right-hand side (2.1.25) is usually not known. Depending on the physical case considered, several different forms are commonly used to model the solid-to-fluid-to-solid feedback: for instance, flutter derivatives terms proportional to the solid displacement (constant $\hat{\mathcal{A}}_{\text{sfs}}$, quasi-static approach) and/or solid velocity ($\hat{\mathcal{A}}_{\text{sfs}}(\lambda) \propto \lambda$, pseudo-static approach), see de Langre (2002). More evolved models also involve rational terms (Karpel, 1982), for instance $\hat{\mathcal{A}}_{\text{sfs}}(\lambda) \propto \sum_i \mathcal{A}_i / (\lambda - \sigma_i)$ where the coefficients σ_i and operators \mathcal{A}_i are estimated from experiments or time-marching simulations.

All of these aeroelasticity models can actually be recovered on the form of approximations of (2.1.25). Far from the resonances with the fluid eigenvalues, as is typically the case for flutter or divergence instabilities (since the fluid by itself has only stable eigenvalues), the action of the fluid *resolvent operator* (1) is likely to be almost independent from λ (Kato, 1995). In such case, the dynamic fluid-solid feedback coupling reduces to the static action of the fluid $(\hat{\mathcal{N}}_{\text{ff}}')^{-1}$, times (2), resulting in an *added stiffness* term $(\hat{\mathcal{N}}_{\text{ff}}')^{-1} (\hat{\mathcal{N}}_{\text{fe}}' \hat{\mathcal{A}}_e^{-1} \hat{\mathcal{I}}_{\text{e}\xi})$ (proportional to the solid displacement) and an *added damping* term $(\hat{\mathcal{N}}_{\text{ff}}')^{-1} (\hat{\mathcal{I}}_{\text{fe}} + \hat{\mathcal{T}}_{\text{fe}} \hat{\mathcal{A}}_e^{-1} \hat{\mathcal{I}}_{\text{e}\xi})$ (proportional to the solid velocity $\lambda \hat{\xi}^\circ$). Dynamic effects related to the fluid dynamics are recovered when the term (1) is expanded in a Laurent series truncated at first order: an *added mass* term appears in the expansion of $\hat{\mathcal{A}}_{\text{sfs}}$ (term proportional to the solid acceleration $\lambda^2 \hat{\xi}^\circ$). When the dynamical fluid effects become important (as is for instance the case for vortex-induced vibrations), the fluid resolvent cannot be approximated by a convergent series in λ . On the other hand — at least after space discretization of the different operators — it is also possible to decompose the fluid resolvent (Kato, 1995; Trefethen & Embree, 2005) on the form of

$$(\lambda \hat{\mathcal{T}}_f - \hat{\mathcal{N}}_{\text{ff}}')^{-1} = \sum_i \frac{1}{\lambda - \lambda_i} \mathcal{A}_i,$$

where the complex numbers λ_i are the eigenvalues of the fluid operators $(\hat{\mathcal{T}}_f, \hat{\mathcal{N}}_{\text{ff}}')$. With this respect, rational models presented by Karpel (1982) appear as a way to integrate the dominant poles of the fluid resolvent operator in the fluid-solid dynamics.

2.1.4 Link with Eulerian-based perturbation equations

The previous decomposition of the flow fields is natural when considering the ALE formulation of the fluid-structure problem. Following [Fernández & Le Tallec \(2003a\)](#), the equality (1.1.23) of the ALE and Eulerian velocities, i.e. $\mathbf{u}(\mathbf{x}, t) = \tilde{\mathbf{u}}(\tilde{\mathbf{x}}_t, t)$, also suggests to decompose the velocity from the Eulerian point of view, and thus to take into account of the position modification in the definition of the perturbation, by setting

$$\begin{aligned}\tilde{\mathbf{u}}(\tilde{\mathbf{x}}_t, t) &= (\tilde{\mathbf{U}} + \varepsilon \tilde{\mathbf{u}}')(\mathbf{x} + \varepsilon \boldsymbol{\xi}'_e(\mathbf{x}, t), t), \\ \tilde{p}(\tilde{\mathbf{x}}_t, t) &= (\tilde{P} + \varepsilon \tilde{p}')(\mathbf{x} + \varepsilon \boldsymbol{\xi}'_e(\mathbf{x}, t), t),\end{aligned}\tag{2.1.26}$$

where $(\tilde{\mathbf{U}}, \tilde{P})$ and $(\tilde{\mathbf{u}}', \tilde{p}')$ are the steady-state and perturbation of the Eulerian velocity and pressure fields. The instantaneous spatial position is also decomposed in the above expression as $\tilde{\mathbf{x}}_t = \mathbf{x} + \varepsilon \boldsymbol{\xi}'_e$, with $\boldsymbol{\xi}'_e$ the perturbation of the extension displacement. After developing the above expression in ε and comparing with the Lagrangian decomposition (2.1.13), one obtains at order zero the equality of the steady-state base solutions

$$\mathbf{U}(\mathbf{x}) = \tilde{\mathbf{U}}(\mathbf{x}), \quad P(\mathbf{x}) = \tilde{P}(\mathbf{x})\tag{2.1.27}$$

and at first-order in ε the following relation between the Lagrangian and Eulerian perturbations,

$$\begin{aligned}\mathbf{u}'(\mathbf{x}, t) &= \tilde{\mathbf{u}}'(\mathbf{x}, t) + (\nabla \mathbf{U}) \boldsymbol{\xi}'_e(\mathbf{x}, t), \\ p'(\mathbf{x}, t) &= \tilde{p}'(\mathbf{x}, t) + (\nabla P) \cdot \boldsymbol{\xi}'_e(\mathbf{x}, t).\end{aligned}\tag{2.1.28}$$

These relations can be used to derive another set of equations describing the evolution of fluid-structure perturbations.

Replacing the decomposition (2.1.28) in the problem (2.1.2), it can be shown that the linear stability equations given in [Fernández & Le Tallec \(2003a\)](#) are recovered. The derivation is essentially technical and is reported in Appendix C.2. The following fluid equations are obtained:

$$\frac{\partial \tilde{\mathbf{u}}'}{\partial t} + (\nabla \mathbf{U}) \tilde{\mathbf{u}}' + (\nabla \tilde{\mathbf{u}}') \mathbf{U} - \nabla \cdot \boldsymbol{\sigma}(\tilde{\mathbf{u}}', \tilde{p}') = \mathbf{0}, \quad \Omega_f \tag{2.1.29}$$

$$-\nabla \cdot \tilde{\mathbf{u}}' = 0. \quad \Omega_f \tag{2.1.30}$$

These are exactly the linearised Navier-Stokes equations obtained for a purely hydrodynamics flow problem ([Sipp et al., 2010](#)). In particular, the extension field has disappeared from the equations. However, the boundary conditions at the fluid/solid interface Γ are different from the hydrodynamics case. The linearization of the equality of fluid and solid velocities yields the so-called *transpiration* condition

$$\tilde{\mathbf{u}}' = \frac{\partial \boldsymbol{\xi}'_e}{\partial t} - (\nabla \mathbf{U}) \boldsymbol{\xi}'_e \quad \text{on} \quad \Gamma \tag{2.1.31}$$

which states that the Eulerian velocity perturbation is equal to the Lagrangian velocity perturbation of the interface corrected by the velocity induced by the displacement of the interface on the steady-state solution. While this expression of the linearised velocity continuity at the fluid-solid interface is relatively simple, the linearization of the normal-stress continuity condition yields to a much more complex expression, namely

$$[\boldsymbol{\sigma}(\tilde{\mathbf{u}}', \tilde{p}') + \nabla \boldsymbol{\sigma}(\mathbf{U}, P) \boldsymbol{\xi}'_e + \boldsymbol{\sigma}(\mathbf{U}, P) \boldsymbol{\Phi}'(\boldsymbol{\xi}'_e)^T] \mathbf{n} = \mathbf{P}'(\boldsymbol{\xi}'_e; \hat{\mathbf{E}}) \mathbf{n}. \tag{2.1.32}$$

The left-hand side operator is the linearised fluid stress that writes as the sum of a classical Cauchy stress for the Eulerian perturbation and two *added-stress* terms ([Fernández & Le Tallec, 2003a](#); [de Langre, 2002](#)) proportional to the interface displacement and its derivatives. The first added-stress term is a second-order tensor whose components write in index notation (using Einstein's rule for repeated indices) as

$$[\nabla \boldsymbol{\sigma}(\mathbf{U}, P) \boldsymbol{\xi}'_e]_{ij} = \frac{\partial [\boldsymbol{\sigma}(\mathbf{U}, P)]_{ij}}{\partial [\mathbf{x}]_k} [\boldsymbol{\xi}'_e]_k. \tag{2.1.33}$$

It represents the transport of the interface stress by the interface displacement. Note in particular that second-order derivatives of the steady flow are involved in this expression — and remain second-order in the weak formulation. The second added-stress term $\sigma(\mathbf{U}, P)\Phi'(\xi')^T$ is a *form-stiffness* term which accounts for the modification of the normal-stress induced by a geometrical modification of the interface. While non-local couplings (by means of the extension operator) are present in the Lagrangian-based equations, we observe here local (i.e. concentrated at the fluid-solid interface), higher-order couplings. These two different structures are related to the way we have defined the disturbances.

As already mentioned in the introduction, the fact that there are two equivalent formulations (Eulerian-based and Lagrangian-based) of the stability problem comes more fundamentally from the fact that the derivative of an equation with respect to its domain of definition can be defined in two ways. For more details, the reader is referred to the book by [Allaire & Schoenauer \(2007\)](#), section 6.3, where these two equivalent notions of differentiation are introduced and discussed.

2.2 Numerical formulation for an eigenvalue analysis

2.2.1 Modal decomposition of the perturbations

To investigate the long-term behaviour of the linearised problem (2.1.2), as mentioned in the introduction, the eigenvalue analysis is appropriate. The perturbation variable is then decomposed in modes

$$\mathbf{q}'(\mathbf{x}, t) = \mathbf{q}^\circ(\mathbf{x}) \exp(\lambda t) + \text{c.c.} \quad (2.2.1)$$

where $\lambda = \lambda^r + \mathbf{i}\lambda^i$ is a complex eigenvalue and $\mathbf{q}^\circ(\mathbf{x})$ is the spatial structure of the coupled fluid-structure eigenmode. The discrete generalized eigenvalue problem obtained from the finite-elements discretization of the modal problem obtained by introducing (2.2.1) in (2.1.2) writes as

$$\lambda \begin{bmatrix} \mathbf{B}_s & 0 & 0 \\ 0 & 0 & 0 \\ 0 & \mathbf{B}_{fe} & \mathbf{B}_f \end{bmatrix} \begin{bmatrix} \mathbf{q}_s^\circ \\ \mathbf{q}_e^\circ \\ \mathbf{q}_f^\circ \end{bmatrix} = \begin{bmatrix} \mathbf{A}_s & 0 & \mathbf{A}_{fs}^T \\ \mathbf{A}_{es} & \mathbf{A}_e & 0 \\ \mathbf{A}_{fs} & \mathbf{A}_{fe} & \mathbf{A}_f \end{bmatrix} \begin{bmatrix} \mathbf{q}_s^\circ \\ \mathbf{q}_e^\circ \\ \mathbf{q}_f^\circ \end{bmatrix}, \quad (2.2.2)$$

where the different matrices are the discrete counterparts of the operators present in the three-fields formulation of the problem. The left-hand side matrix is not symmetric due to the off-diagonal term \mathbf{B}_{fe} , obtained from the temporal derivative of the extension displacement. A symmetric formulation can nevertheless be obtained at the price of introducing an additional extension velocity variable $\mathbf{u}_e^\circ = \lambda \xi_e^\circ$. In the first line (solid equation), the off-diagonal term \mathbf{A}_{fs}^T results from the continuity of the fluid and solid velocities at the interface and expresses the coupling with the fluid. In the second line (extension equation), the off-diagonal term \mathbf{A}_{es} results from the continuity of the extension and solid displacements at the fluid-solid interface. In the last line (fluid equation), the off-diagonal term \mathbf{A}_{fs} also results from the continuity of the fluid and solid velocities at the interface, while \mathbf{A}_{fe} represents the shape derivatives of the fluid equation. Finally, it should be noted that the eigenmodes are normalized so that $\mathbf{q}_s^{\circ H} \mathbf{B}_s \mathbf{q}_s^\circ = 1$, where the superscript H denotes the transconjugate operation.

2.2.2 Implementation of the eigenvalue solver

The matrices presented above are constructed with the finite-element software FREEFEM++ ([Hecht, 2012](#)). An Implicitly Restarted Arnoldi Method ([Arnoldi, 1951](#); [Saad, 2011](#)) is used, associated with a shift-and-invert spectral transformation that enables to get a set of eigenvalues in the vicinity of a given complex shift. For small problems, a sequential solver that uses a direct LU solver and the library ARPACK ([Lehoucq et al., 1997](#)) has been developed. For larger-scale problems, a parallel version using domain decomposition methods has also been developed. In order to handle the multiples inversions of the shifted matrices required by the eigenvalue solver within the IRAM method we use the iterative BGS algorithm presented in §1.3.2, where only each diagonal sub-block (fluid, solid and extension) is inverted by the direct LU solver MUMPS ([Amestoy et al., 2013](#)). This considerably lowers the total amount of memory needed to handle the problem. Another

approach, based on a modal projection of the solid-extension problem, is presented in the next section.

2.2.3 Reduced eigenvalue problem

To reduce the size of the eigenvalue problem, it is tempting in (2.2.2) to eliminate the extension displacement, that depends only on the solid displacement according to

$$\mathbf{q}_e^\circ = -\mathbf{A}_e^{-1} \mathbf{A}_{es} \mathbf{q}_s^\circ \quad (2.2.3)$$

By introducing this expression into the above eigenvalue problem, one obtains the reduced eigenvalue problem

$$\lambda \begin{bmatrix} \mathbf{B}_f & -\mathbf{B}_{fe} \mathbf{A}_e^{-1} \mathbf{A}_{es} \\ 0 & \mathbf{B}_s \end{bmatrix} \begin{bmatrix} \mathbf{q}_f^\circ \\ \mathbf{q}_s^\circ \end{bmatrix} = \begin{bmatrix} \mathbf{A}_f & \mathbf{A}_{fs} - \mathbf{A}_{fe} \mathbf{A}_e^{-1} \mathbf{A}_{es} \\ \mathbf{A}_{fs}^T & \mathbf{A}_s \end{bmatrix} \begin{bmatrix} \mathbf{q}_f^\circ \\ \mathbf{q}_s^\circ \end{bmatrix}, \quad (2.2.4)$$

in which the extension variable has disappeared, at the price of the inverted operator \mathbf{A}_e^{-1} appearing in the upper right corners of the block matrices that form the reduced problem. Consequently, the matrices in the above reduced eigenvalue problem cannot be assembled and their inversion cannot be performed with a sparse LU factorization, since \mathbf{A}_e^{-1} is in general a full matrix. To circumvent this difficulty, one possibility is to resort to a projection of the solid equations onto the free-vibration modal basis.

The free-vibration modes, denoted $\phi_{s,k}^\circ$ for $k = 1, 2, \dots$, are the vibration modes of the solid structure in absence of dynamic coupling with the fluid – the static coupling resulting from the steady deformed equilibrium is however embedded in the matrices \mathbf{B}_s and \mathbf{A}_s . They are obtained as eigenvectors of the eigenvalue problem

$$\mathbf{i}\omega_{s,k} \mathbf{B}_s \phi_{s,k}^\circ = \mathbf{A}_s \phi_{s,k}^\circ \quad (2.2.5)$$

that corresponds to the solid sub-problem extracted from (2.2.2), and where the coupling \mathbf{A}_{fs}^T with the fluid is cancelled out. In this problem (and in the supposed case where there are no unstable static buckling modes), the associated eigenvalues $\mathbf{i}\omega_{s,k}$ are purely imaginary, where $\omega_{s,k}$ is the vibration circular frequency of the mode k . By normalizing the free-vibrations modes as $\phi_{s,k}^\circ{}^T \mathbf{B}_s \phi_{s,k}^\circ = 1$, they form an orthonormal basis that is used to decompose the solid component of the eigenvectors \mathbf{q}_s° onto a finite number N_s of free-vibration modes, as

$$\mathbf{q}_s^\circ = \sum_{k=1}^{N_s} \alpha_{s,k} \phi_{s,k}^\circ = \mathbf{\Phi}_s \boldsymbol{\alpha}_s. \quad (2.2.6)$$

The columns of the rectangular matrix $\mathbf{\Phi}_s = [\phi_{s,1}^\circ, \phi_{s,2}^\circ, \dots, \phi_{s,N_s}^\circ]$ are the free-vibration modes and $\boldsymbol{\alpha}_s = (\alpha_{s,1}, \alpha_{s,2}, \dots, \alpha_{s,N_s})^T$ denotes the vector of modal amplitudes. Introducing this decomposition into (2.2.4) and projecting orthogonally onto the free-vibration basis, one obtains the reduced eigenvalue problem

$$\lambda \begin{bmatrix} \mathbf{B}_f & \mathbf{B}_{fs}^r \\ 0 & \mathbf{B}_s^r \end{bmatrix} \begin{bmatrix} \mathbf{q}_f^\circ \\ \boldsymbol{\alpha}_s \end{bmatrix} = \begin{bmatrix} \mathbf{A}_f & \mathbf{A}_{fs}^r \\ \mathbf{A}_{fs}^r & \mathbf{A}_s^r \end{bmatrix} \begin{bmatrix} \mathbf{q}_f^\circ \\ \boldsymbol{\alpha}_s \end{bmatrix}, \quad (2.2.7)$$

where the reduced matrices $\mathbf{B}_s^r = \mathbf{\Phi}_s^T \mathbf{B}_s \mathbf{\Phi}_s$ and $\mathbf{A}_s^r = \mathbf{\Phi}_s^T \mathbf{A}_s \mathbf{\Phi}_s$ are diagonal matrices of size $N_s \times N_s$, that form the solid eigenvalue problem in the free-vibration modal basis. The off-diagonal reduced matrices are rectangular matrices defined as $\mathbf{B}_{fs}^r = -\mathbf{B}_{fe} \mathbf{A}_e^{-1} \mathbf{A}_{es} \mathbf{\Phi}_s$, $\mathbf{A}_{fs}^r = \mathbf{A}_{fs} \mathbf{\Phi}_s - \mathbf{A}_{fe} \mathbf{A}_e^{-1} \mathbf{A}_{es} \mathbf{\Phi}_s$ and $\mathbf{A}_{sf}^r = (\mathbf{A}_{fs} \mathbf{\Phi}_s)^T$. These matrices are small dense matrices and can be assembled explicitly, since the extension displacement modes can be computed from the solid modes $\phi_{s,k}^\circ$ using (2.2.3).

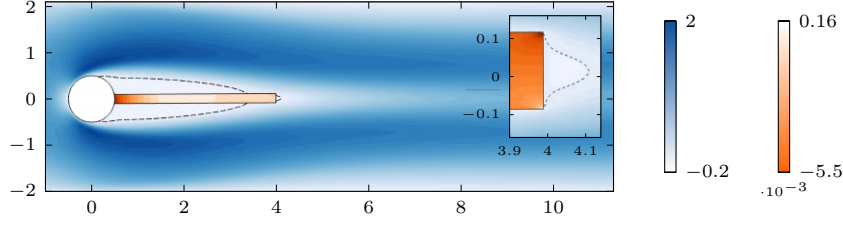


Figure 2.3 – Steady-state solution for the vortex-induced-deformation test case (shown in the steady configuration). The streamwise component of the velocity \mathbf{U} of the steady flow is depicted in blue, while the shear component $[\hat{\mathbf{F}}(\hat{\mathbf{\Xi}})]_{xy}$ of the strain tensor is depicted in orange in the elastic plate. The dashed lines delimit the recirculating flow regions (a zoom on the tip end of the plate is represented in the insert on the right, where the orange color has also been modified to emphasize the peaks at the corners, compared to the full picture).

2.3 Numerical testing of the Lagrangian-based approach

In this section, we first present numerical results obtained for two significant two-dimensional test-cases corresponding to the flow induced vibrations of an elastic bar, and of the flutter instability of a flag in a channel flow. In the first case, the fluid-structure instability is essentially driven by the fluid wake instability, whereas in the second configuration the fluid-solid interaction is essential for the development of the instability. A three-dimensional configuration is also considered, that consists in the vortex shedding instability in the wake of a plate deflected by the stationary flow.

2.3.1 Test case with a vortex-induced-deformation instability

The first test case considered here is similar to the fluid-configuration proposed and used by [Turek & Hron \(2006\)](#) for benchmarking steady and unsteady nonlinear fluid-structure interaction solvers. As shown in the Fig. 1.6, an elastic plate is clamped at the rear of a rigid circular cylinder of diameter D^* , which is placed in a channel flow. As in their benchmark study, the center of the cylinder is not located on the symmetry axis of the channel, but is slightly shifted downwards, thus creating an asymmetry in the fluid-solid solution. Details of the geometry are indicated in the Fig. 1.6, where all lengths have been made non-dimensional using the cylinder's diameter as reference length ($L^* = D^*$). Furthermore, the mean velocity \bar{U}^* of the parabolic velocity profile imposed at the inlet is chosen as the reference velocity (i.e. $U^* = \bar{U}^*$). The four non-dimensional parameters governing this problem are defined with these reference quantities and are chosen as

$$\mathcal{E}_s = 1400, \nu_s = 0.4, \mathcal{M}_s = 1, \mathcal{R}_e = 120 \quad (2.3.1)$$

These values correspond to the test-case denoted FSI3 in [Turek & Hron \(2006\)](#) except for the Reynolds number $\mathcal{R}_e = \bar{U}^* D / \nu_f^* = 120$, which is here smaller so as to design a test-case with only one unstable eigenvalue, as detailed later. At the inlet of the channel, the parabolic velocity profile $(u, v) = (0.357(2 + y)(2.1 - y), 0)$ is imposed. No-slip boundary conditions are imposed on the top and bottom walls, as well as on the surface of the rigid cylinder (denoted Γ_{cyl}) and at the fluid-elastic interface Γ . At the outlet of the channel, a zero normal-stress boundary condition is imposed. When solving the unsteady non-linear fluid-structure equations for the above values of the non-dimensional parameter, one obtains a periodic solution characterized by the unsteady shedding of vortices in the flow and an unsteady deformation of the elastic plate. Such a configuration can be referred to as a *vortex-induced deformation* configuration ([de Langre, 2002](#)), since the vortex-shedding that develop in the wake of the rigid cylinder induces the deformation of the elastic plate.

The steady-state fluid-structure solution is computed by solving the non-linear steady equations written in the stress-free reference configuration. The fluid velocity (blue) and the shear component

mesh	N_t	Δy	C_D	$\xi_y^s(A)$	eigenvalue	time-march
M_0	3264	0.113	2.440	0.0163	$-0.023 + 1.674i$	(0.0159, 1.690)
M_1	8788	0.051	2.516	0.0158	$0.0226 + 1.689i$	(0.0228, 1.688)
M_2	15 716	0.030	2.528	0.0152	$0.0237 + 1.688i$	(0.0238, 1.688)
M_3	32 732	0.018	2.531	0.0155	$0.0238 + 1.688i$	(0.0238, 1.687)
M_4	59 689	0.012	2.533	0.0154	$0.0238 + 1.688i$	–

Table 2.1 – Vortex-induced deformation test-case. The total number of elements and the minimal size of the elements are indicated in the second and third columns respectively. The drag coefficient is given in the fourth columns. The fifth column reports the transverse solid displacement at point A located in $x_A = 3.95$, $y_A = 0$ in the reference configuration. The sixth column reports the value of the leading eigenvalue, while the last column reports the growth-rate and angular frequency extracted from time-marching non-linear simulations in the linear phase.

$[\hat{\mathbf{F}}(\hat{\mathbf{\Xi}})]_{xy}$ of the solid strain tensor (orange) are shown in Fig. 2.3. Although barely visible due to the small deformation of the solid, the visualization is done in the steady deformed configuration, obtained after having deformed the domain using the stationary displacement field. The steady flow separates on the rigid cylinder and reattaches on the elastic plate, as indicated by the black dashed curves which represent the isocontours of zero streamwise velocity. The two recirculation regions formed on the upper and lower sides of the elastic plate are not symmetric with respect to the symmetry axis of the channel, due to the slight asymmetry of the cylinder's position in this channel. The recirculation velocity is slightly larger in the upper region than in the lower region, thus creating a resultant pressure force that moves the elastic plate upward. The y -displacement of the point A (located at $y = 0$ in the reference configuration) is around 0.015, as reported in Tab. 2.1. The flow recirculation also generates viscous shear forces oriented upstream and resulting in a slight compression of the elastic plate. The x -displacement is however two orders of magnitude lower than the y -displacement and is therefore not reported here. Finally, the drag and lift coefficients of the rigid cylinder plus the elastic plate are computed as

$$C_D = 2 \int_{\hat{\Gamma} \cup \Gamma_{cyl}} \hat{\mathbf{\Sigma}}(\hat{\mathbf{U}}, \hat{\mathbf{P}}, \hat{\mathbf{\Xi}}_e) \hat{\mathbf{n}} \cdot \mathbf{e}_x d\hat{\Gamma} \quad \text{and} \quad C_L = 2 \int_{\hat{\Gamma} \cup \Gamma_{cyl}} \hat{\mathbf{\Sigma}}(\hat{\mathbf{U}}, \hat{\mathbf{P}}, \hat{\mathbf{\Xi}}_e) \hat{\mathbf{n}} \cdot \mathbf{e}_y d\hat{\Gamma},$$

where Γ denotes the fluid-elastic plate boundary and Γ_{cyl} the rigid cylinder surface. They are equal to $C_D = 2.533$ and $C_L = 8.38 \times 10^{-3}$, the weak positive lift being induced by the slight asymmetry of the configuration. The influence of the mesh resolution on the computed steady-state solution is reported in Tab. 2.1, which shows the drag coefficient and the y -displacement of the elastic plate at point A . The drag coefficient as well as the plate displacement reach converged values for the mesh labelled M_3 .

The linear stability analysis of the steady-state solution is investigated by solving the eigenvalue problem (2.2.2). The resulting spectrum is displayed in Fig. 2.4a. One unstable pair of complex eigenvalues ($\lambda^r > 0, \lambda^i \neq 0$) is obtained. The real and imaginary parts of the corresponding eigenvector are displayed in Fig. 2.4b. The transverse solid displacement field inside the elastic plate is depicted in orange, while the arrows represent the centreline displacement vectors. The mode presents a spatial structure in the solid with one vibration node at the clamped end of the plate. When the phase of the mode is varied between 0 and 2π , a second vibration minima moves back and forth along the centreline of the plate.

The influence of the spatial resolution on the unstable eigenvalues is reported in the sixth column in Tab. 2.1. A converged eigenvalue is reached as the mesh resolution is increased. The unstable eigenvalues are compared with estimations of the growth rate and frequency (reported in the last column of the table) obtained by time-marching the non-linear ALE formulation in the reference configuration. To estimate the growth rate and frequency of the *linear* perturbation using the non-linear solver, the initial solution is chosen as the superposition of the steady-state and of the Lagrangian perturbation mode, scaled with a small amplitude $a = 0.005$ here. The amplitude

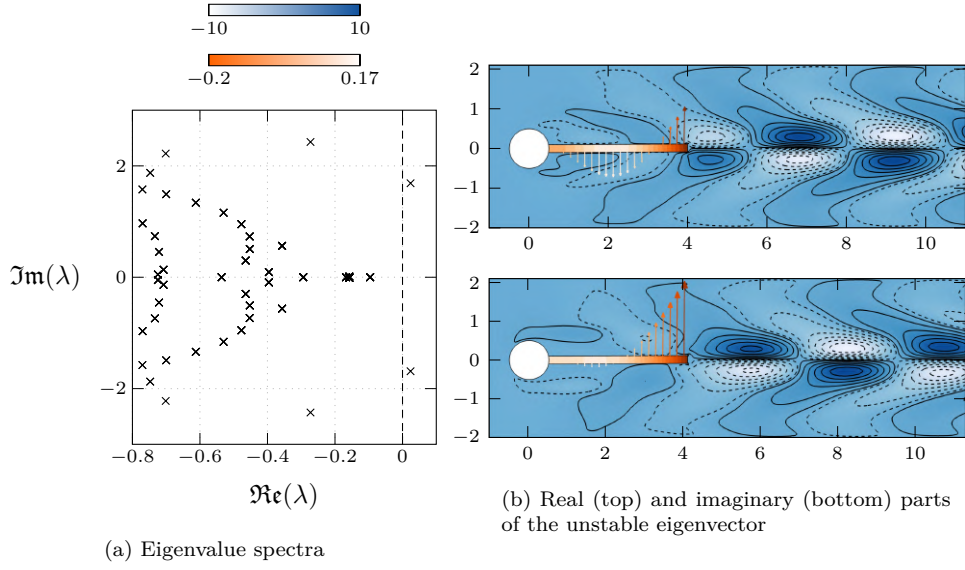


Figure 2.4 – Stability analysis for the vortex-induced elastic-deformation configuration. (a) Eigenvalue spectra. The vertical dashed line delimits the stable half-plane (left) from the unstable half-plane (right). Numerical values of the unstable eigenvalues are reported in Tab. 2.1 for different mesh resolutions. (b) Snapshots of the unstable mode eigenvector for the real (top) and imaginary (bottom) parts, depicted with the streamwise component of the fluid velocity (blue, dashed negative contours), and the transverse solid displacement (orange). The centreline displacement in the solid is represented by the orange arrows. Results obtained with the mesh M_4 .

of the perturbation is expected to grow exponentially as long as the non-linear terms are negligible. Fig. 2.5 depicts the absolute value of the lift coefficient of the fluctuation as a function of time, equal to the lift coefficient of the unsteady solution corrected by the steady lift coefficient $C_{Lstat.}$. For $t < 200$, the fluctuating lift coefficient grows exponentially (straight envelope in the log-scale) and the estimated growth rate is in good agreement with the growth-rate λ^r of the eigenvalue analysis, given by the slope of the red line in the figure. The Fourier spectra of the signal in the linear phase shows one largely predominant peak. The resulting frequencies are reported in the last column of Tab. 2.1, showing a good agreement.

As a conclusion for this test-case, we observe that a proper eigenvalue convergence is achieved when the mesh is refined. Furthermore, a good agreement is found between the linear stability analysis and features extracted from a time-marching simulation. The next test case is devoted to a configuration where the fluid-solid coupling is essential for the development of the instability.

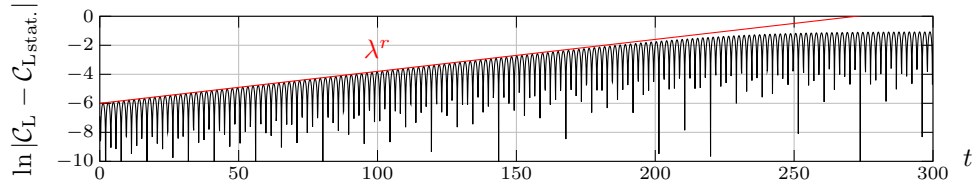


Figure 2.5 – Results obtained with temporal simulation where the initial condition is the superposition of the steady solution and the unstable eigenmode found in Fig. 2.4a with an amplitude $a = 0.005$. Representation of the absolute value of the lift coefficient for the cylinder and the plate as a function of time, and superimposed growth rate λ^r given by the eigenvalue analysis.

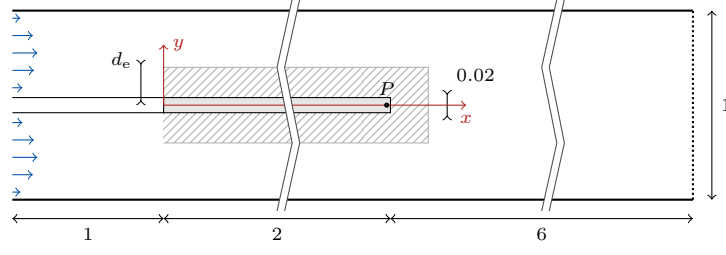


Figure 2.6 – Reference configuration for the flutter instability. Sketch of the geometry investigated by Cisonni *et al.* (2017). The dashed rectangular box is the extension domain Ω^e , and the reference point P is located at the position $(1.95, 0)$.

2.3.2 Test case with a flutter instability

The test case considered in this paragraph is shown in Fig. 2.6 and is similar to the configuration investigated by Cisonni *et al.* (2017). A thin elastic plate, denoted “flag” hereinafter, is clamped at the rear of a rigid plate of same thickness, and placed at the center of a channel flow. All lengths have been made non-dimensional using the height of the channel H^* as the reference length ($L^* = H^*$). Identical parabolic velocity profiles are imposed at the two inlets of the channel, and their mean velocity is chosen as the reference velocity (*i.e.* $U^* = U^*$). Following the original paper, we impose $u(y) = 12y(1 - 2y)$ at the upper inlet and $u(y) = -12y(1 + 2y)$ at the lower inlet. The four non-dimensional parameters governing this problem are defined with these reference quantities and their values are

$$\mathcal{E}_s = 13766, \quad \nu_s = 0.4, \quad \mathcal{M}_s = 25, \quad \mathcal{R}_e = 100 \quad (2.3.2)$$

These values of the non-dimensional elastic Young modulus \mathcal{E}_s , Poisson coefficient ν_s , density ratio ρ and Reynolds number \mathcal{R}_e correspond to the reduced velocity $U = 13.53$ and the inertia ratio $M = 4$ used as a set of non-dimensional parameters in the study. The non-dimensional lengths are indicated in Fig. 2.6, in particular the aspect ratio of the flag is $h_L = 1/100$ (corresponding to the case labelled (vii) on the Figure 7a in Cisonni *et al.* (2017)). The relations between the different parametrizations is given by $\mathcal{M}_s = 1/(Mh_L)$ and $\mathcal{E}_s = 12(1 - \nu_s^2)/(h_L^3 MU^2)$. No-slip boundary conditions are imposed on the top and bottom walls, as well as on the surface of the rigid and elastic plates. At the outlet of the channel, a zero normal-stress boundary condition is imposed. When solving the unsteady non-linear fluid-structure equations for these values of the non-dimensional parameters, the flag oscillates around its mean deformed position and unsteady flow oscillations develop downstream. The onset of the oscillations is attributed to a flutter instability which is triggered by the energy transfer from the fluid to the solid (de Langre, 2002).

The steady-state solution is computed with the methodology already described in the previous paragraph with an additional ingredient: the symmetry of the present configuration with respect to channel’s axis is used to determine the steady-state solution, by imposing a zero transverse displacement condition along the centreline of the solid. The steady-state solution is depicted in Fig. 2.7 with the streamwise fluid velocity (blue) and the axial component $[\mathbf{\hat{F}}(\mathbf{\hat{E}})]_{xx}$ of the solid strain tensor (orange). The main difference with the vortex-induced deformation configuration investigated before is that the steady flow does not separate from the solid surface, except at the trailing edge of the flag where a tiny recirculation region appear (its length is less than the thickness of the flag). The viscous fluid forces produce a slight stretching of the flag. This can be observed in Fig. 2.7 where the axial stress is maximal at the clamped end of the flag, then decreases as we move closer to the tip. The drag coefficient exerted on the flag \mathcal{C}_D^f , and the solid axial displacement $(\mathbf{\Xi}_P \cdot \mathbf{e}_x)$ of point $P(1.95, 0)$, are reported in Tab. 2.2 for various mesh resolutions. Both the drag coefficient and the solid displacement, which is of order of magnitude of 10^{-3} , do not display significant evolution for meshes finer than M_2 .

The linear stability of this steady-state solution is now investigated. A converged eigenvalue

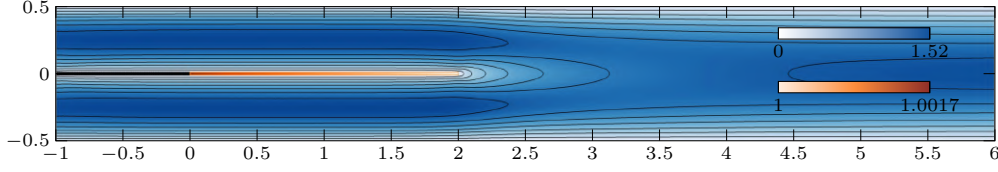


Figure 2.7 – Steady-state solution in the flutter instability configuration. Streamwise fluid velocity is depicted in blue while the component $[\hat{\mathbf{F}}(\hat{\mathbf{E}})]_{xx}$ of the solid strain tensor is shown in orange.

mesh	N_t	Δ^{\max}	Δ^{\min}	C_D^f	$\Xi_P \cdot \mathbf{e}_x$	eigenvalue
M_0	3675	0.1649	0.0164	1.016	1.663×10^{-3}	$0.0210 + 3.530 \mathbf{i}$
M_1	8899	0.1335	0.0109	1.017	1.668×10^{-3}	$0.0294 + 3.534 \mathbf{i}$
M_2	16105	0.0942	0.0081	1.015	1.670×10^{-3}	$0.0280 + 3.542 \mathbf{i}$
M_3	35272	0.0720	0.0038	1.016	1.671×10^{-3}	$0.0297 + 3.545 \mathbf{i}$
M_4	67602	0.0517	0.0025	1.016	1.672×10^{-3}	$0.0305 + 3.546 \mathbf{i}$

Table 2.2 – Flutter-induced elastic-deformation test-case. The total number of elements N_t and the minimal/maximal size of the elements are indicated in the second and third/-fourth columns. The fifth and sixth columns display the drag coefficient of the flag and the streamwise displacement at point P . The leading eigenvalue is reported in the last column.

spectra is depicted in Fig. 2.8a. A pair of complex unstable eigenvalues is found close to the imaginary axis. The spatial structure of the corresponding eigenvector is shown in Fig. 2.8b. It displays four vibration minimas in the solid, which are emphasized in Fig. 2.8c where the y component of the transverse displacement perturbation $\xi'(y, 0) = \Re(\xi^o(y, 0) \exp i\phi)$ is represented for different phases ϕ varying between 0 and 2π . The resulting superposition shows the vibration envelope. A first vibration node is obviously located at the clamped end $x_0 = 0$. Then, a second vibration node is clearly noticeable at a position x_1 . The third and fourth vibration minimas in x_2 and x_3 (see the positions in Tab. 2.8d) cannot be assimilable to vibration nodes, since the position of zero transverse displacement varies with the phase (see in supplementary material an animation showing the mode). In Tab. 2.8d the position of the vibration minimas of the leading eigenmode are reported, together with measurements made on the modal shapes extracted from non-linear simulations in Cisonni *et al.* (2017), also represented by orange dots in Fig. 2.8c. A very good agreement is found concerning the position x_1 . Since the other vibration minima are less marked (and thus less identifiable as vibration nodes), the evaluation of their position is less relevant. An estimate is nevertheless given in Tab. 2.8d. The influence of the spatial resolution on the leading eigenvalue is reported in Tab. 2.2. Compared to the vortex-induced-deformation test-case, the spatial resolution needs to be finer for converging the growth rate and the frequency.

We compare now the instability thresholds predicted with the eigenvalue analysis to those reported by Cisonni *et al.* (2017) and obtained with time-marching simulations. In this study, the authors vary different parameters such as the plate aspect ratio, the mass ratio M or the reduced velocity U . Then, neutral curves are determined by running non-linear time-marching simulations in which a small-amplitude perturbation is applied at the flag at the beginning of the computation. The growth (resp. decay) of the oscillations is measured so as to estimate an unstable (resp. stable) growth-rate of the perturbations. The vibration frequencies are estimated using a Fast Fourier Transform of the oscillation signal at the tip end of the flag. In what follows, the Reynolds number, Poisson coefficient and inertia ration are fixed to the values used previously, (i.e. $\mathcal{R}_e = 100$, $\nu_s = 0.4$ and $M = 4$), while the reduced velocity U is varied. The results are reported in Fig. 2.9. On the left side, the growth-rate of the leading eigenvalue is displayed as a function of the reduced velocity U , while the angular frequency is reported on the right side. The case $(U, M) = (13.53, 4)$, or equivalently $(\mathcal{E}_s, \mathcal{M}_s) = (13766, 25)$ is the reference flutter case presented in Fig. 2.6, and is materialized by the dashed vertical line. The linear stability analysis predicts an instability threshold ($\lambda^r = 0$) for $U^{\text{crit}} = 13.35 \pm 0.05$, which is very close to the one

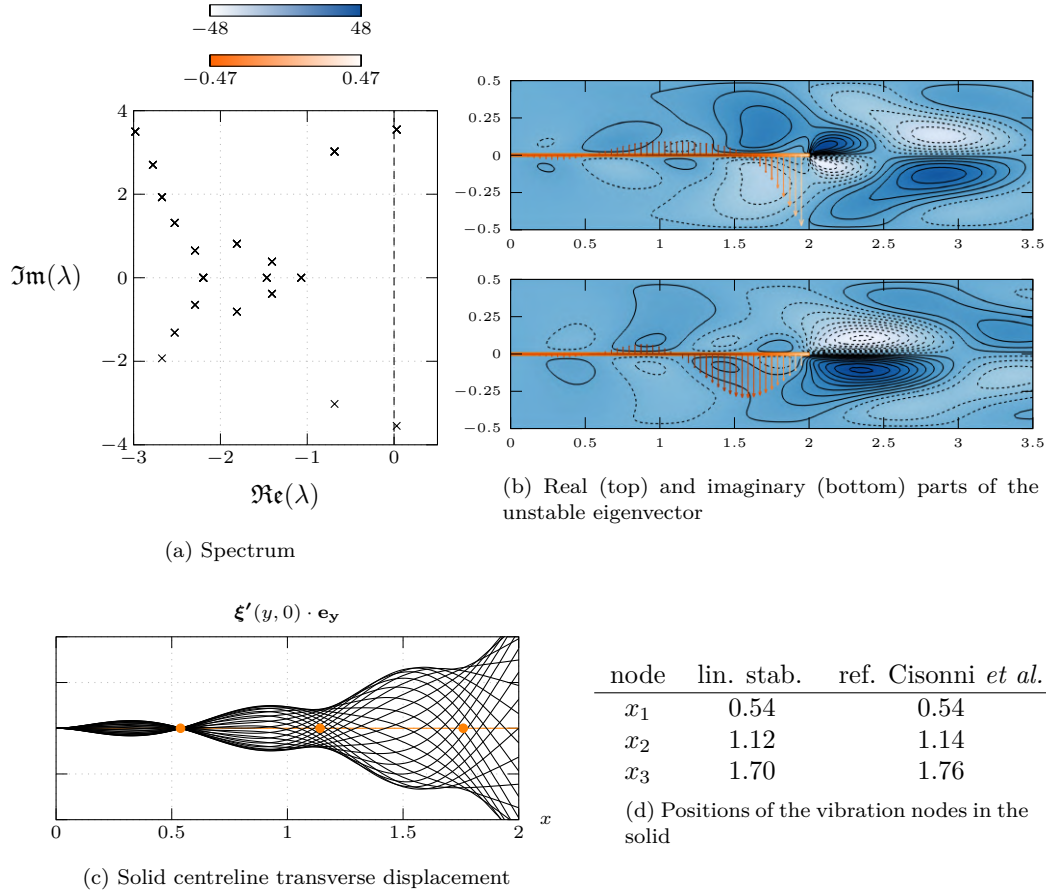


Figure 2.8 – Flutter-induced vibrations case. (a) Eigenvalue spectrum. (b) Real and imaginary parts of the leading eigenmode depicted with the streamwise fluid velocity (blue, dashed negative contours) and the transverse solid velocity (orange). (c) Solid transverse displacement extracted along the centreline ($y = 0$) of the solid, for 25 phases varying between 0 and 2π . Orange dots represent the vibrations minimas found in Cisonni *et al.* (2017) also reported in (d). Results are shown for the finest mesh.

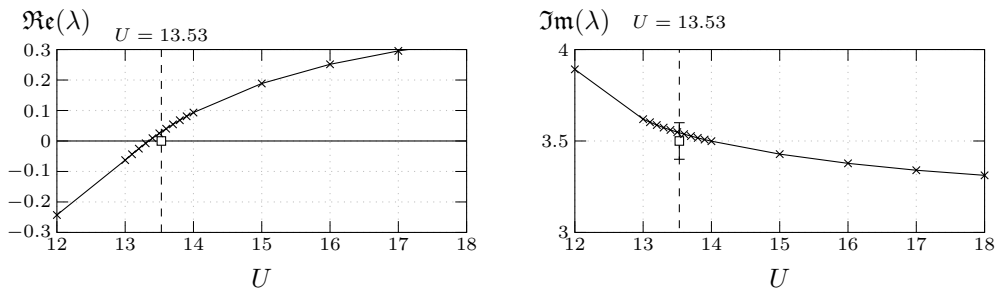


Figure 2.9 – Flutter-induced vibrations, evolution of the leading eigenvalue for a mass ratio $M = 4$, Reynolds number $\mathcal{R}_e = 100$ and Poisson coefficient $\nu_s = 0.4$ when the reduced velocity U is varied, with mesh M_3 . The values obtained by Cisonni *et al.* are reported with squares symbols: the instability onset is found to $U = 13.53$ (left), with a vibration frequency estimated around 3.5 ± 0.1 (right).

Table 2.3 – Characteristics of the extension domain and influence on the leading eigenmodes. d_e is the thickness of the extension domain Ω_e , while N_L and N_{Ω_e} are the numbers of layers of triangles and the total number of triangles in the extension region, respectively. The leading eigenvalue is reported in the last column.	d_e	N_L	N_{Ω_e}	eigenvalue
	0.500	> 15	17 475	$0.0297 + 3.545 \mathbf{i}$
	0.380	> 15	15 721	$0.0297 + 3.545 \mathbf{i}$
	0.199	12	13 829	$0.0301 + 3.544 \mathbf{i}$
	0.041	6	8421	$0.0320 + 3.541 \mathbf{i}$
	0.018	3	5444	$0.0341 + 3.536 \mathbf{i}$
	0.010	2	3531	$0.0364 + 3.530 \mathbf{i}$
	0.005	1	1793	$0.0419 + 3.515 \mathbf{i}$

obtained by Cisonni *et al.* (2017) at $U = 13.53$. The frequency at the threshold is estimated by the authors to $(\lambda^i)^{\text{crit}} = 3.5 \pm 0.1$ (their values are reported in a logarithmic scale on a figure). Once again, the frequency prediction obtained with the linear approach is in good agreement. It is interesting to notice that the computational time for the characterization of one case is estimated to about 1.2 hours on an Intel Xeon X5660 2.8 Ghz processor (CPUmark score 7622 according to www.cpubenchmark.net, where it is claimed that the score roughly scales linearly with the amount of data that the processor can handle in a given period of time). In our sequential computations, performed with one core of an Intel Xeon E5-1620 v3 3.5 Ghz processor (CPUmark score 9758), it takes about 2 minutes to compute a stationary flow and then about 4 minutes to compute 20 eigenvalues on the mesh M_3 with the Lagrangian approach (without the modal projection evoked in §2.3.4). This clearly shows the advantage of running linear analyses for thresholds identifications.

As a conclusion, our linear eigenvalue analysis, tested in a strongly coupled case where the instability arises primarily from the fluid-structure coupling, is able to reproduce at much lower costs the instability thresholds obtained with non-linear time-marching simulations. It remains now to investigate, if any, the influence of the extension equation, and use modal projection to further reduce the overall computational cost.

2.3.3 Influence of the extension operator and domain

The ALE formulation introduces a non-physical variable, the extension displacement, to propagate the solid displacement field at the fluid-solid boundary into the fluid domain with the extension operator. In the present linear stability analysis, the perturbation of the extension displacement ξ_e^o is by definition infinitesimal and is thus never used to explicitly move the fluid domain, unlike in non-linear simulations. Nevertheless, we investigate here the influence of the extension domain size on the results of the linear stability analysis.

Due to the infinitesimal size of the extension displacement, we expect that the extension domain can be reduced to a few layers of elements around the elastic solid, as depicted in the sketch of Fig. 2.6. The extension region, depicted with dashed lines, extends over a layer of thickness d_e around the solid. For a given mesh, we define the signed distance function $\delta(\mathbf{x})$ of any point $\mathbf{x} \in \Omega_f$ from the fluid-solid boundary Γ . The extension mesh Ω_e is then defined as the set of elements whose centroids satisfy the relation $\delta(\mathbf{x}) < d_e$. Thus d_e controls the thickness of the extension domain and the number N_L of layers of elements, without changing the distribution of the elements in the fluid mesh. This way of proceeding allows one to study only the influence of the size of the extension domain, without changing the overall mesh resolution.

The characteristics of the extension regions and their influence on the leading eigenmode are reported in Tab. 2.3. The extension region does not influence the leading eigenvalue provided its size is sufficiently large, $d_e > 0.2$ in the present case. Note also the greater sensitivity of the growth-rate: while the frequency varies by about 0.03 % between the case $d_e = 0.199$ and $d_e = 0.38$, the variation is by 1.3 % for the growth-rate. For the case with only one layer, the discrepancy compared to the converged values is by 41 % for the growth-rate, and a remarkably small 0.84 % for the frequency. We have also performed the same tests on the vortex-induced elastic deformation case, and observed the same behaviour, with even smaller variations, probably due to the fact that the instability mechanism is essentially linked with the wake located further downstream to the interface.

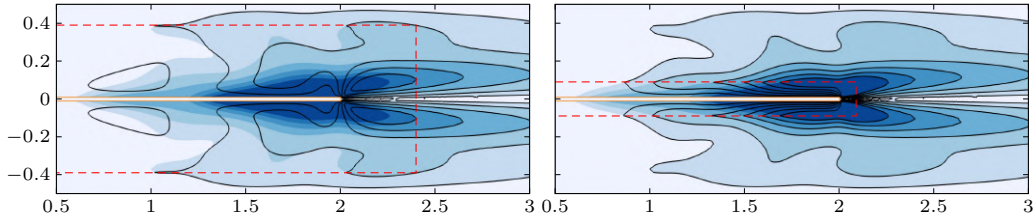


Figure 2.10 – Influence of the extension domain on the spatial structure of the leading eigenmode for (left) $d = 0.4$ and (right) $d = 0.1$. The limit of the extension region is marked with the red dashed line. Contours correspond to the module of the streamwise Lagrangian velocity ($|\mathbf{u}^o \cdot \mathbf{e}_x|$) while colors represents the Eulerian velocity $|\tilde{\mathbf{u}}^o \cdot \mathbf{e}_x|$, defined in (2.3.3).

Let us now examine the eigenvectors, and more specifically the absolute value of the streamwise fluid velocity. This quantity is displayed in Fig. 2.10 with solid lines, for two sizes of the extension domain, $d_e = 0.4$ (top) and $d_e = 0.01$ (bottom). A strong difference is observed inside the extension domain, while the isocontours look the same outside this region. This is expected since \mathbf{u}^o is the Lagrangian velocity perturbation that depends on the extension displacement ξ_e^o . To display a quantity independent on the extension displacement, we follow Fernández & Le Tallec (2003a) and define the Eulerian-based velocity perturbation as

$$\tilde{\mathbf{u}}^o = \mathbf{u}^o - \nabla U \xi_e^o \quad (2.3.3)$$

that includes the effect of the transport by the domain movement of the steady flow. Such Eulerian-based perturbation is displayed with colors in Fig. 2.10. A comparison between the two figures shows that the spatial structure of the Eulerian velocity does not depend on the size of the extension domain.

To conclude, the size of the extension domain cannot be reduced to very few layers around the solid domain, without modifying significantly the results of the stability analysis. The critical size of the extension region depends on the mesh resolution at the interface but also on the problem investigated: all things being equal, it is for instance smaller in the vortex-induced-deformation problem than in the flutter problem, probably because the origin of the instability is more critically the fluid-solid interaction in the latter case. As explained and detailed in §2.3.4, the extension displacement field variable can also be eliminated from the discrete eigenvalue problem, to the price of projecting the solid dynamics on a reduced basis composed of free-vibration modes. Results obtained with the resulting reduced eigenvalue problem are presented in the next paragraph.

2.3.4 Results for the reduced eigenvalue-problem

Rather than solving the full eigenvalue problem (2.2.2), we consider here the resolution of the reduced eigenvalue problem (2.2.7) obtained after projection of the solid dynamics onto free-vibrations modes. More specifically, we investigate how the number of free-vibrations modes influence the accuracy of the leading eigenvalue.

For our test-cases with elongated structures, the free-vibration mode with the lowest frequency is a flexion mode with one vibration node at the clamped end, as represented on top in Fig. 2.11a. Then as the frequency increases, the number of vibration nodes in the corresponding mode increases as well (see Fig. 2.11a modes 2 and 3). For higher frequencies, compression modes also appear. Note that taking into account the initial stationary strains has a significant influence on the computed frequencies: while the four first *in-vacuo* circular frequencies are 0.130, 0.842, 2.227 and 4.458, due to the presence of the pre-strains that tends to elongate the solid, the vibration frequencies are higher when the steady deformation $\hat{\mathbf{\Xi}} \neq 0$ is taken into account for computing the uncoupled solid vibration frequencies. Namely, the four first pre-stressed frequencies are 0.602, 1.577, 3.421 and 5.579. In all what follows, the free vibration basis is therefore computed by taking into account

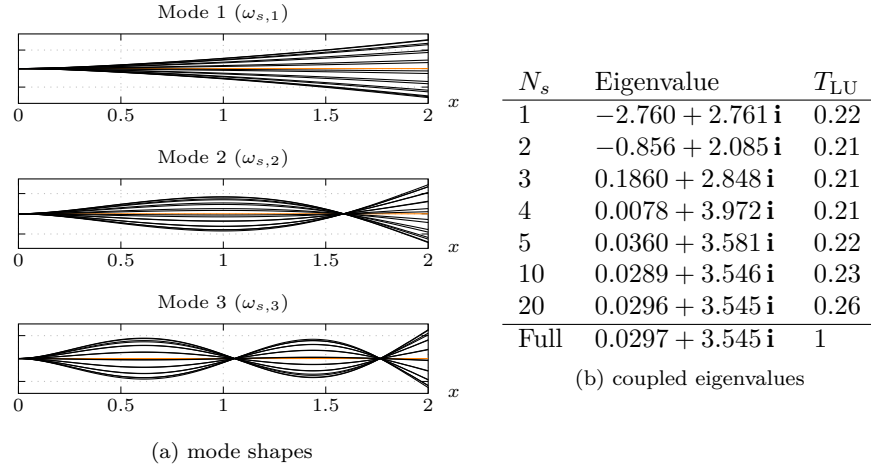


Figure 2.11 – Flutter-induced case, free vibration modes. (a) snapshots of the transverse centreline displacement in the solid for different phases, for the three lowest frequency solid modes with pre-stress ($\hat{\mathbf{e}} \neq 0$). (b) Eigenvalues obtained with a projection on a basis with N_s modes, and associated time T_{LU} for the LU decomposition of the corresponding reduced matrix. The case without modal projection is reported in the last line.

these pre-stresses. Also note that the free vibration frequencies without initial strains that we have computed are in good agreement with those obtained in [Cisonni et al. \(2017\)](#) (respectively 0.820, 2.287 and 4.498 for the second, third and fourth *in-vacuo* circular frequencies, re-normalized according to the reference scales used in this paper).

The results obtained with mesh M_3 are reported in Fig. 2.11b. For $N_s = 5$, the basis for the flutter-induced case is constituted of five modes, the first one with $\omega_{s,1} = 0.602$ and the last one with $\omega_{s,5} = 8.584$. As the number of modes in the free vibration basis is increased, the leading eigenvalue of the approximate eigenvalue problem become closer to the leading eigenvalue of the full problem (reported in the last row). One notices that the approximate results become fairly good from $N_s = 5$. This is no real surprise, since the mode obtained with the full solver seems to be a combination of the bending modes 1, 2 and 3 (see for instance the solid displacement extracted from a cut $y = 0$ on Fig. 2.8c). Note that fewer modes are required to reconstruct correctly the frequency than to reconstruct the growth-rate. For $N_s = 5$, the deviation compared to the eigenvalue obtained with the full problem is of about 23% for the growth-rate and less than 2% for the frequency. In all cases the interest of the modal decomposition in terms of computing performance is clear. Even when a solid basis of 20 modes is considered, a speedup of at least about $4\times$ is observed for the LU factorization of the shifted system matrix (using a direct LU solver like MUMPS). The gain in terms of memory depends on the initial extension box size.

2.3.5 Test-case with a 3d flexible plate in a cross-flow

The last test-case is a three-dimensional flexible plate facing a uniform incoming flow of velocity U_∞ . The stability of the three-dimensional flow around the *rigid* plate was previously investigated by [Marquet & Larsson \(2015\)](#). Following them, we define the Reynolds number as $\mathcal{R}_e = U_\infty h^* / \nu$ where the height of the plate h^* is used to non-dimensionalize all lengths. The non-dimensional thickness of the plate being fixed to 0.04, they varied the non-dimensional spanwise length L in the range $1 \leq L \leq 6$ and determined the critical Reynolds number for various eigenmodes. These unstable eigenmodes break one of the reflectional symmetries with respect to the planes $y = 0$ and $z = 0$ that are satisfied by the steady flow. Here, we focus on the longest plate $L = 6$ and set the Reynolds number to $\mathcal{R}_e = 60$. For this value an unsteady eigenmode breaking the reflectional symmetry with respect to the plane $y = 0$ is unstable. Such eigenmode leads to the shedding of vortices whose axis is aligned with the z direction. Here, we consider that the flexible plate is clamped along its axis Oy and investigate the effect of the flexibility on the unsteady properties of

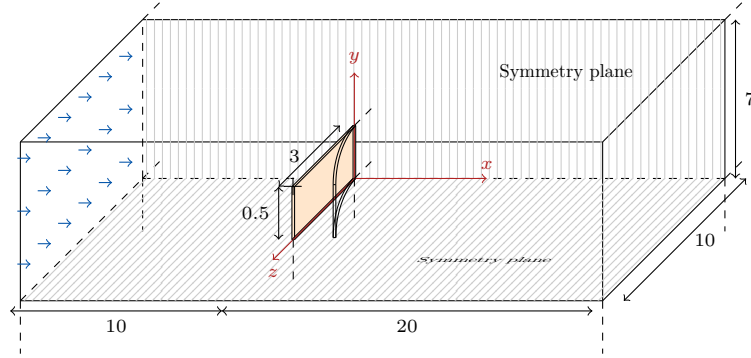


Figure 2.12 – Computational domain of the three-dimensional flexible plate (orange) immersed in an incoming uniform flow sketched with blue arrows. The plate is of (non-dimensional) height 1, length 6 and thickness 0.04. Only a quarter of the physical domain is used for the computation, exploiting the reflectional symmetries of the problem. The boundary conditions applied on the symmetry planes are specified in the text. A probe point P is placed in the free corner of the plate at position $(0, 0.5, 3)$ marked with a + symbol.

the wake flow. As the stiffness is reduced, the plate bends in the streamwise direction as a result of the load exerted by the incoming flow. After computing the steady flow balancing the deformation of the plate for various stiffness, we determine its stability by computing the largest eigenmodes.

The plate is made of an elastic material characterized by a fixed Poisson coefficient $\nu_s = 0.35$ and a non-dimensional Young modulus varying in the range $5 \times 10^5 \leq \mathcal{E}_s \leq 1 \times 10^{10}$. The fluid-to-solid density ratio is set to $\mathcal{M}_s = 1$. The computational domain, sketched in Fig. 2.12, is a quarter of the physical domain, taking advantage of the reflectional symmetries, specified hereinafter, to reduce the computational cost. Dirichlet conditions are applied to the velocities at the inlet ($x = -10$), a stress-free boundary condition is applied at the outlet ($x = 20$) and slip boundary conditions are applied on the lateral planes ($z = 10$ and $y = 7$). The boundary conditions applied along the symmetry planes ($y = 0$ and $z = 0$) depend on the type of computations. The steady flow velocity and solid displacement fields exhibit the following reflectional symmetries

$$\begin{aligned} (\mathcal{S}_y) : (U_x, U_y, U_z, \Xi_x, \Xi_y, \Xi_z)(x, -y, z) &= (U_x, -U_y, U_z, \Xi_x, -\Xi_y, \Xi_z)(x, y, z) \\ (\mathcal{S}_z) : (U_x, U_y, U_z, \Xi_x, \Xi_y, \Xi_z)(x, y, -z) &= (U_x, U_y, -U_z, \Xi_x, \Xi_y, -\Xi_z)(x, y, z) \end{aligned}$$

where (U, V, W) are the components of the steady flow velocity and $(\Xi_x^s, \Xi_y^s, \Xi_z^s)$ are the components of the steady solid displacement. For the steady-state computations, the following boundary conditions are thus applied on the symmetry planes

$$\begin{aligned} (\partial_y U_x, U_y, \partial_y U_z, \partial_y \Xi_x, \Xi_y, \partial_y \Xi_z)(x, 0, z) &= (0, 0, 0, 0, 0, 0) \\ (\partial_z U_x, \partial_z U_y, U_z, \partial_z \Xi_x, \partial_z \Xi_y, \Xi_z)(x, y, 0) &= (0, 0, 0, 0, 0, 0). \end{aligned}$$

The eigenmode of interest satisfies the symmetry (\mathcal{S}_z) but breaks the symmetry (\mathcal{S}_y) . For the eigenvalue computations, the following boundary conditions are therefore applied on the symmetry planes,

$$\begin{aligned} (u_x^\circ, \partial_y u_y^\circ, u_z^\circ, \xi_x^\circ, \partial_y \xi_y^\circ, \xi_z^\circ)(x, 0, z) &= (0, 0, 0, 0, 0, 0) \\ (\partial_z u_x^\circ, \partial_z u_y^\circ, u_z^\circ, \partial_z \xi_x^\circ, \partial_z \xi_y^\circ, \xi_z^\circ)(x, y, 0) &= (0, 0, 0, 0, 0, 0) \end{aligned}$$

where $(\xi_x^\circ, \xi_y^\circ, \xi_z^\circ)$ are the solid components of an eigenmode. More details about the various combination of symmetries satisfied by the eigenmodes can be found in [Marquet & Larsson \(2015\)](#). The computations are performed using a mesh made of 268 562 tetrahedra that yields to 1 830 560 degrees of freedom for the steady-state problem and 1 916 836 for the eigenvalue problem. For

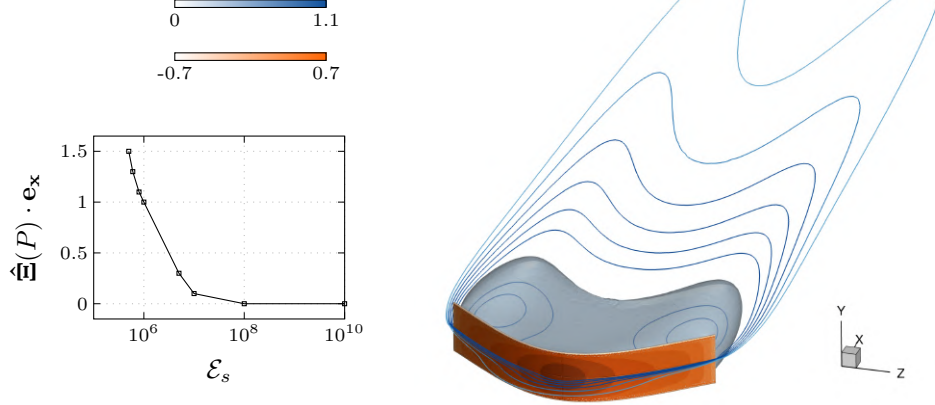


Figure 2.13 – Steady fluid-structure equilibrium for the three-dimensional flexible plate facing an incoming uniform flow. The pictures on the right-hand side display top and side views of the steady solution obtained for $\mathcal{E}_s = 5 \times 10^5$ in the symmetry planes $y = 0$ (top) and $z = 0$ (bottom). Velocity magnitude contours in the $y = 0$ plane are depicted with the blue color, and the pressure at the surface of the plate is depicted with the orange color. The back-flow region in the wake of the plate is delimited with the gray translucent surface for which the streamwise velocity is -0.05 . The left-hand side graph represents the streamwise displacement of the point P as a function of the stiffness \mathcal{E}_s .

both the stationary computations and eigenvalue problems investigated here, the block Gauss-Seidel preconditioner requires on the order of ten iterations to converge. Combined with direct LU decompositions for each sub-block, this provides relatively fast and robust computations for moderately large 3d problems. To compute large steady deformations of the plate achieved when the stiffness \mathcal{E}_s is reduced, an updated Lagrangian approach (Etienne & Pelletier, 2005) is used together with a continuation on the Young modulus, so as to deform progressively the computational domain.

The steady-state solutions are described in Fig. 2.13. Contours of the flow velocity magnitude (blue) in the plane $y = 0$ and the pressure at the surface of the plate (orange) computed for $\mathcal{E}_s = 5 \times 10^5$ are shown. The pressure is maximum in the center of the plate, then decreases as one moves towards the edges thanks to the streamlining effect induced by the deformation of the plate. For the above value of the stiffness, the displacement of the plate in the streamwise direction is of the same order of magnitude as the height of the plate. The shape of the back-flow region in the wake of the plate is modified by the bending of the plate, as emphasized by the translucent gray interface that delimits the back-flow region. The larger back-flow velocities are obtained near the tip of the plate. The streamwise displacement of the tip (point P shown in Fig. 2.12) is reported in the left-hand side picture as a function of the stiffness. Small displacements of the plate are obtained down to $\mathcal{E}_s = 10^7$. Further decreasing the stiffness yields to a linear increase of the displacement up to 1, the (non-dimensional) height of the plate.

The largest eigenvalues are computed for a stiff ($\mathcal{E}_s = 1 \times 10^{10}$) and a flexible ($\mathcal{E}_s = 5 \times 10^5$) plate. The eigenvalue spectra are reported in Fig. 2.14a with symbols \square and \times , respectively. The unstable pair of eigenvalues obtained for the stiff plate compares well with results given in Fig. 5 in Marquet & Larsson (2015) where an angular frequency of 0.529 is reported for the unstable mode. In the case where $\mathcal{E}_s = 1 \times 10^{10}$, an angular frequency of 0.518 is found (deviation of about 2%). Considering now the flexible plate, one clearly see that the pair of complex eigenvalues is stabilized and its frequency is increased ($0.003 \pm 0.797i$). The vibrating motion given by the solid component

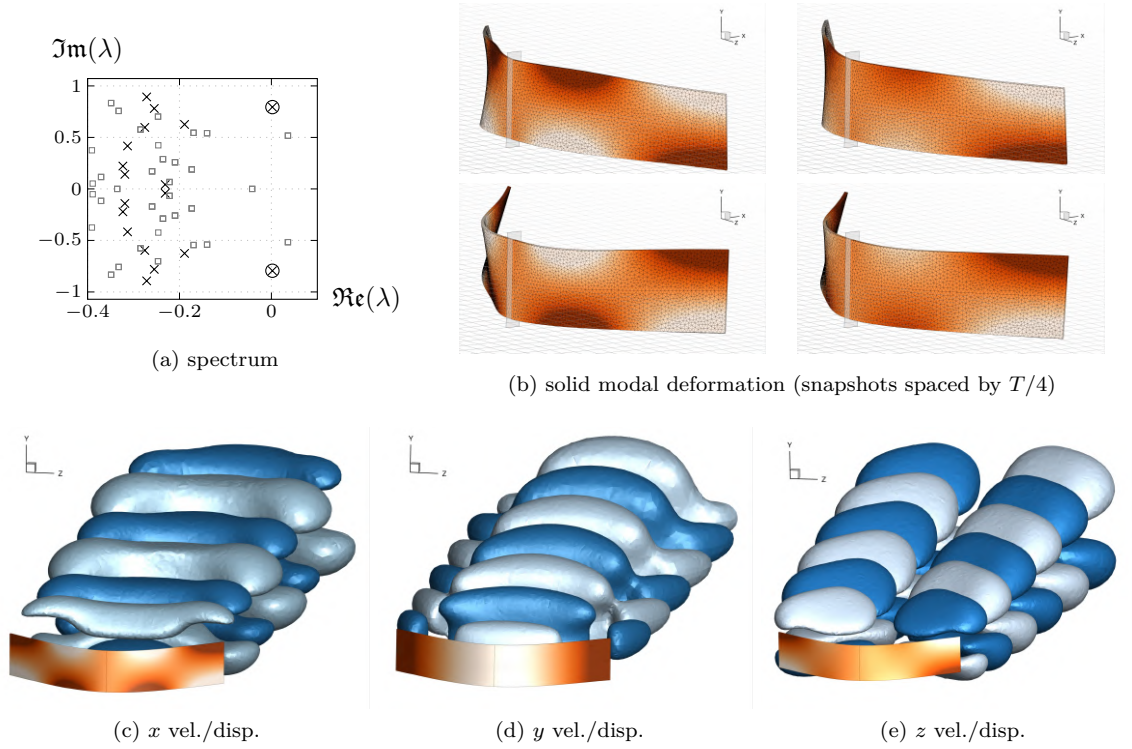
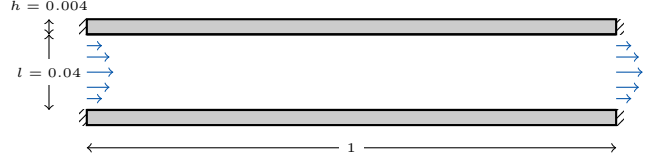


Figure 2.14 – Linear stability analysis of steady solutions computed for flexible plates of various stiffness \mathcal{E}_s . (a) Eigenvalue spectra for a stiff plate (\square , $\mathcal{E}_s = 10^{10}$) and a flexible plate (\times , $\mathcal{E}_s = 5 \times 10^5$) where the unstable eigenvalue is circled. (b) Three-dimensional view of the instantaneous deformation of the flexible plate induced by the solid component of the eigenmode associated to the pair of marginal complex eigenvalues (\times). Snapshots are displayed (in the clockwise direction) at times $1/4, 1/2, 3/4$ and 1 of the oscillation period $T = 2\pi/\omega$, ω being the imaginary part of the eigenvalue. The colors indicate the deformation magnitude. The rectangle placed in the plane $z = 0$ materializes the clamped position of the plate. (c,d,e) Plots of the x , y and z components of the flow velocity (blue) and solid displacement (orange) of the real part of the unstable eigenmode. For the fluid, iso-contours are shown for a positive (light blue) and a negative (dark blue) values.

of the eigenmode that corresponds the marginal pair of eigenvalues is shown in Fig. 2.14b for the flexible plate. Four snapshots in the period of oscillation are depicted. The displacement is a combination of torsional motion about the z axis and a smaller-amplitude up-and-down flexion along the y axis. As shown in Figs. 2.14c–2.14e, the flow velocity components exhibit an oscillating pattern in the streamwise direction, typical of the vortex-shedding pattern also observed for the rigid plate (Marquet & Larsson, 2015). The spatial structure is mainly modified by the streamlining effect induced by the bending of the plate. For instance, the transverse size of the region where the largest y velocity perturbations occur is reduced.

This three-dimensional test-case shows that the present approach allows to compute steady fluid-solid configurations for which the solid is strongly deformed by the fluid loads and to determine the three-dimensional fluid and solid modal perturbations that are responsible for the destabilization of this steady state.

Figure 2.15 – Poiseuille flow between flexible plates. Representation of the configuration (not to scale) with dimensions in m.



2.4 Comparison of Lagrangian-based and Eulerian-based approaches

Let us now compare our new Lagrangian-based approach introduced in section 2.1.2 to the Eulerian-based approach recalled in section 2.1.4. Even if these two approaches are equivalent at the continuous level (see Appendix C.2), they do not necessarily behave similarly at the discrete level.

2.4.1 Poiseuille flow between flexible membranes

We first consider the case of a two-dimensional Poiseuille flow in a channel 1 m long and $l = 0.04$ m high, between two elastic membranes of 4 mm thickness, as represented in the sketch in the Fig. 2.15. This case is convenient, for it allows to compute analytically the components of the steady equilibrium if the steady displacements are neglected. Then, the two linear stability formulations can be compared in a case where the steady flow as well as the added stresses are explicitly known. In particular, in that case the stress-free and steady deformed configuration strictly coincide, because the steady displacement is identically zero.

This benchmark problem is close to that considered by Fernández & Le Tallec (2003b), with the following discrepancies: the authors considered the first three modes of a beam model as a reduced solid model, while we consider an elastic 2d solid without modal basis reduction. They also considered a simple-cantilevered case, while we assume that both ends of the solid are clamped. We made this choice in order to avoid having to consider the stress variation at a mobile outflow, which is not possible in the Eulerian-based approach without modal projection. The geometric parameters (with dimensions in m) are reported in Fig. 2.15. In the present case, the fluid density is set to $\rho_f = 1000 \text{ kg/m}^3$ and the solid density to $\rho_s = \rho_f$. The fluid viscosity is $\nu_f = 5 \times 10^{-5} \text{ m}^2/\text{s}$. The Poisson coefficient for the linear elastic solid is $\nu_s = 0.4$, and the Young modulus $E_s = 5 \times 10^8 \text{ Pa}$. Finally, the mean parabolic inflow flow velocity is set to $U_0 = 3.5 \text{ m/s}$.

Under the assumption of a negligible steady displacement $\Xi = \mathbf{0}$, the stationary solution reduces to a Poiseuille flow of velocity $\mathbf{U}(x, y)$ and pressure $P(x, y)$ solution to the Navier-Stokes equations in a channel made with rigid walls:

$$\mathbf{U}(x, y) = \left[6U_0 \frac{y}{l} \left(1 - \frac{y}{l} \right), 0 \right], \quad P(x, y) = -12 \frac{U_0 \nu_f \rho_f}{l^2} x.$$

Furthermore, the components of the added stiffness term appearing in (2.1.32) can be computed explicitly, since in particular the components of the stationary fluid stress tensor is known. Noting $\alpha = 12 U_0 \nu_f \rho_f / l^2$, they write $\sigma_{xx} = \sigma_{yy} = \alpha x$ and $\sigma_{xy} = \sigma_{yx} = \alpha(l/2 - y)$ while the only non-zero stress derivatives are constant, namely

$$\frac{\partial \sigma_{xx}}{\partial x} = \frac{\partial \sigma_{yy}}{\partial x} = \alpha \quad \text{and} \quad \frac{\partial \sigma_{xy}}{\partial y} = \frac{\partial \sigma_{yx}}{\partial y} = -\alpha.$$

This allows to write explicit expressions for the transpiration velocity condition (2.1.31) and the added stiffness term (2.1.32), as well as for the steady flow that appears in the linearised Navier-Stokes equations.

Once the steady flow is determined, its stability is investigated, by solving on the one hand the Lagrangian-based problem (2.2.2), and on the other hand the Eulerian-based problem that writes

N_t	Lagrangian-based	Eulerian-based
1200	$2.34518 + 5.85571 \mathbf{i}$	$2.34203 + 5.85409 \mathbf{i}$
2400	$1.47758 + 7.19049 \mathbf{i}$	$1.47672 + 7.19151 \mathbf{i}$
7000	$0.93877 + 7.47793 \mathbf{i}$	$0.93878 + 7.47785 \mathbf{i}$
28 000	$0.99725 + 7.42718 \mathbf{i}$	$0.99774 + 7.42694 \mathbf{i}$
63 000	$1.00867 + 7.42059 \mathbf{i}$	$1.00866 + 7.42058 \mathbf{i}$

Table 2.4 – Eigenvalue analysis for the Poiseuille flow between flexible walls. For the case of an analytic steady flow between rigid walls, leading eigenvalues obtained with the Lagrangian-based and Eulerian-based approaches with fluid-elastic perturbations, as a function of the number of triangles N_t in the mesh.

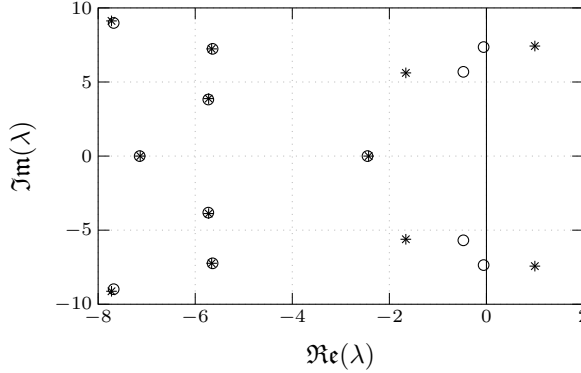


Figure 2.16 – Eigenvalue spectrum for the Poiseuille flow between flexible walls. Eigenvalues obtained with the Lagrangian-based approach (\times), exact Eulerian-based ($+$) and approximate Eulerian-based (O) approach where the added stiffness terms are neglected.

after space discretization with finite elements

$$\lambda \begin{bmatrix} \mathbf{B}_s & \mathbf{0} \\ \mathbf{0} & \mathbf{B}_f \end{bmatrix} \begin{bmatrix} \mathbf{q}_s^\circ \\ \tilde{\mathbf{q}}^\circ \end{bmatrix} = \begin{bmatrix} \mathbf{A}_s + \mathbf{K} & \mathbf{A}_{fs}^T \\ \mathbf{A}_{fs} + \mathbf{T} & \mathbf{A}_f \end{bmatrix} \begin{bmatrix} \mathbf{q}_s^\circ \\ \tilde{\mathbf{q}}^\circ \end{bmatrix} \quad (2.4.1)$$

where the matrices \mathbf{T} and \mathbf{K} are obtained from the transpiration velocity condition (2.1.31) and the added stiffness term (2.1.32) respectively. The other matrices are the same than that obtained with the Lagrangian-based approach. Since the steady displacement is zero, the solid problem reduces to the linear elasticity equations. A perfect agreement is found between both stability approaches, as reported in Tab. 2.4 where the leading eigenvalues are reported as a function of the number of triangles in the (structured) mesh used to discretize the channel and the surrounding elastic walls. For all mesh resolutions, the deviation between both the real and imaginary parts of the leading eigenvalue do not exceed 0.05 %

This example furthermore allows to investigate the importance of the added-stiffness terms: we can evaluate the error that is made when they are neglected. In Fig. 2.16 the spectra obtained with the Lagrangian-based (\times) and exact Eulerian-based ($+$) approaches are represented, showing the excellent agreement mentioned above. In addition, the spectra obtained by setting the added terms to zero (i.e. set \mathbf{K} to zero) is shown with O symbols. In this latter case, the only remaining coupling between the fluid and the structure is the interface transpiration velocity condition $\mathbf{u}_s^\circ = \tilde{\mathbf{u}}^\circ + (\nabla \mathbf{U}) \boldsymbol{\xi}^\circ$. We observe in that case that although the leading eigenvalue has roughly the same frequency as that obtained from the exact formulations, it has a slightly negative growth-rate and thus completely misses to predict the instability.

On this simple example, it is thus illustrated that the (equivalent at the continuous level) Lagrangian-based and Eulerian-based approaches are also *equivalent* at the discrete level when the stationary solution whose stability is investigated is provided in an *exact* fashion. Furthermore, the critical role of the added-stress terms has been shown.

2.4.2 Flag in a channel flow

We now come back to the more complicated case of a flag in a channel flow, already described in §2.3.2. Like in the previous paragraph, the Lagrangian-based and Eulerian-based approaches are compared. In the present case it is *much* harder to obtain converged results with the Eulerian-based approach. In particular, the eigenvalues are found to be extremely mesh-sensitive, especially

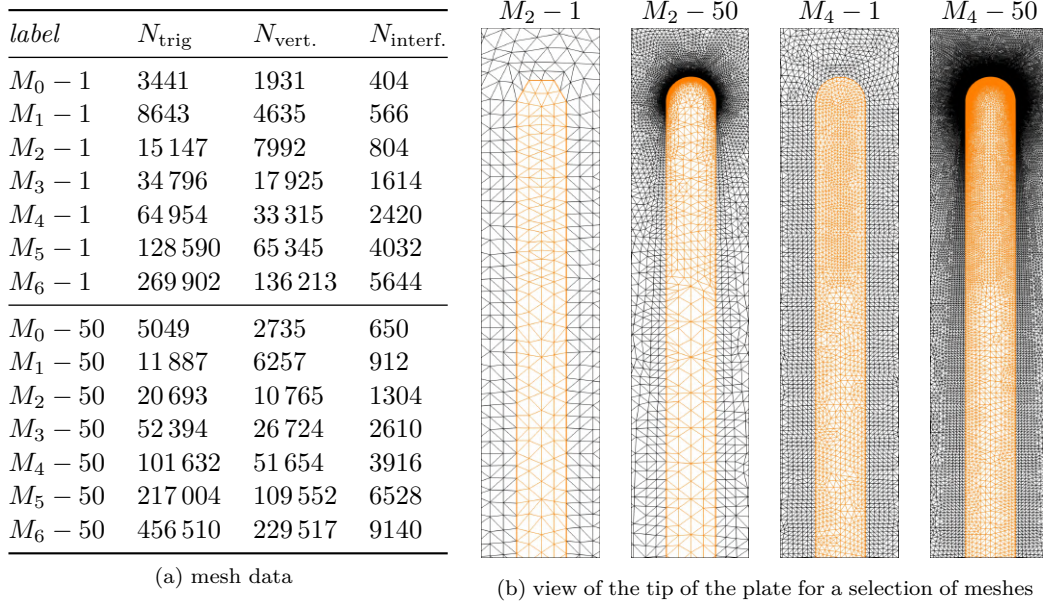


Figure 2.17 – Mesh for a rounded flag. (a) For the set of meshes considered, number of triangles and vertices in the total mesh, N_{trig} , and $N_{\text{vert.}}$, and number of vertices $N_{\text{interf.}}$ on the fluid-structure interface. (b) Region of different meshes in the vicinity of the tip of the plate.

with respect to the discretization close to the tip of the plate. For that reason, a set of meshes with a rounded tip is considered, as reported in Fig. 2.17.

Steady flow & stresses computation

The computation of the steady flow is done by the very same way as in §2.3.2. Let us give details about the computation of interface stresses, that enter as an input of the Eulerian-based stability formulation. They are computed here in the steady deformed configuration, as a post-processing from the velocity and pressure fields. Noting $\mathbf{U} = (U, V)$, the xx component of the fluid stress tensor is for instance computed by solving numerically the variational problem

$$\int_{\Omega_f} \sigma_{xx} \psi \, d\Omega_f = \int_{\Omega_f} \left\{ -P + \frac{2}{\mathcal{R}_e} \frac{\partial U}{\partial x} \right\} \psi \, d\Omega_f,$$

by projecting the test-function ψ and the stress component σ_{xx} in the basis of P_1 finite-elements. The same kind of approach is used for computing the partial derivatives of the interface stress, that again are represented as P_1 fields. This approach necessarily comes with degraded fields: the higher the differentiation order, the higher the differentiation “noise”. Note that this problem can be partially overcome by using mixed-hybrid formulations for the Navier-Stokes equations, where in addition to the usual velocity and pressure variables, the velocity *gradient* itself is considered as an unknown (Farhloul & Fortin, 2002). This way of proceeding allows in a certain sense to save one step of differentiation, but has some drawbacks either: these formulations require special elements (Raviart & Thomas, 1977) or numerical stabilization (Behr *et al.*, 1993), and result in a larger numerical problem because of the additional unknowns. Furthermore, to our knowledge the method has never been applied to fluid-structure problems. Its adaptation might not be that obvious: for instance, gradients are not necessarily continuous at the interface in this latter case. For all of these reasons, we kept a more classical formulation for computing the steady flow and the stresses where systematically computed *a posteriori*.

The three components of the viscous stress tensor along the flag’s surface (the upper portion $y > 0$, in the steady deformed configuration) are represented in Fig. 2.18. The graph on the left

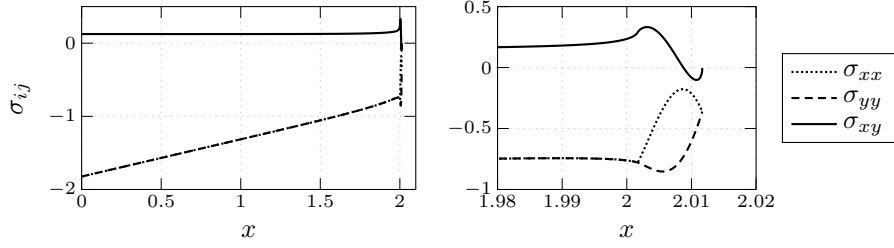


Figure 2.18 – Interface stresses. Representation of the three components of the viscous stress tensor along the flag's interface ($y > 0$ side), computed in the steady deformed configuration, as a function of the x -position, for the mesh $M_3 - 50$.

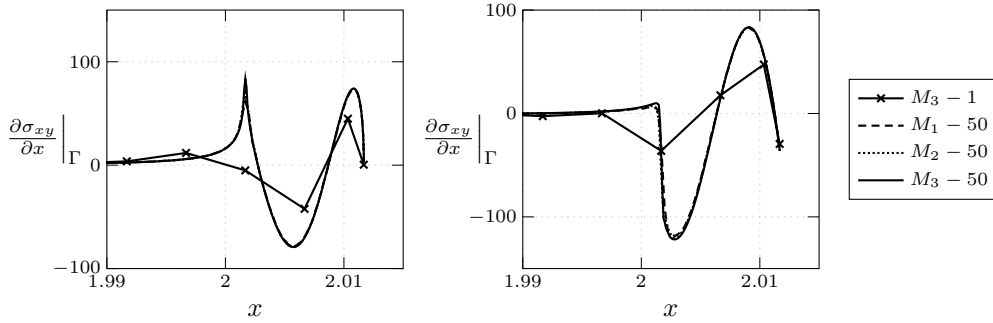


Figure 2.19 – Interface shear stress derivatives. Representation of the three components of the viscous stress tensor along the flag's interface ($y > 0$ side), computed in the steady deformed configuration, as a function of the x -position, for different mesh resolutions.

shows the evolution over the whole span of the flag, where nothing of great interest is happening. The shear stress is almost constant for $x < 2$, because the flow is almost a pure Poiseuille flow (see also Fig. 2.7 showing the steady flow) without great variations in the streamwise direction. For the same reason, the xx and yy component involve principally the pressure that varies almost linearly with x . Larger variations occur close to the tip of the flag, as represented in the graph in the right side, that displays a zoom in this region. Due to the change of curvature, the stress components are found to vary much more rapidly there. In particular, the sharp transition shortly after $x = 2$ is caused by the curvature discontinuity that results from the transition between a straight line (infinite curvature) and the circle that makes the tip (finite curvature equal to the radius of the circle). The transition does not occur exactly at the position $x = 2$ (recall that the plate length is 2 and the origin of the axis is at the clamped end) because of the slight elongation of the elastic plate provoked by the steady flow.

The evolution of the shear stress derivatives in the vicinity of the tip is displayed in Fig. 2.19. Without surprise, an extra mesh refinement has to be prescribed close to the tip so as to capture the sharp variations. When a factor 50 is applied, the variations are properly captured from mesh M_1 .

Linear stability analysis

We now move on to the results of the linear stability analysis. There is no surprise as far as the Lagrangian-based approach is concerned, as reported in Fig. 2.20. For sake of comparison, the case with a tip refinement is reported as well as the case without.

The same is not true when considering the Eulerian-based approach, for which the mesh convergence is reported in Fig. 2.21. In these graphs, the dashed line identifies the real and imaginary parts of the converged leading eigenvalue obtained with the Lagrangian-based approach, while the shaded area depicts the min/max y -axis limits applied in Fig. 2.20. Like before, both refined and regular meshes are considered. No convergence at all is observed with the regular mesh. This is

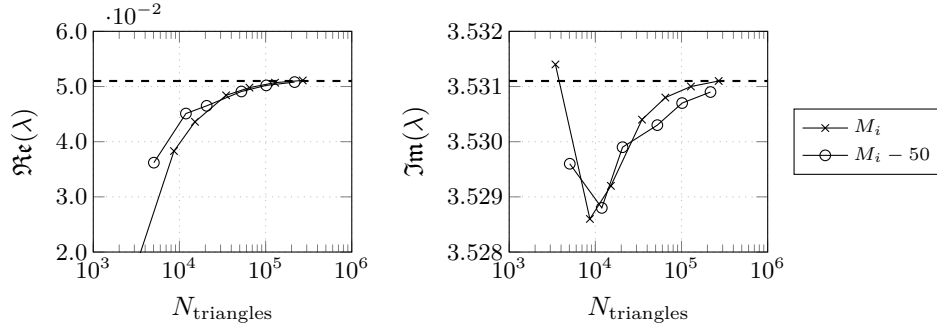


Figure 2.20 – Mesh convergence for the Lagrangian-based approach.

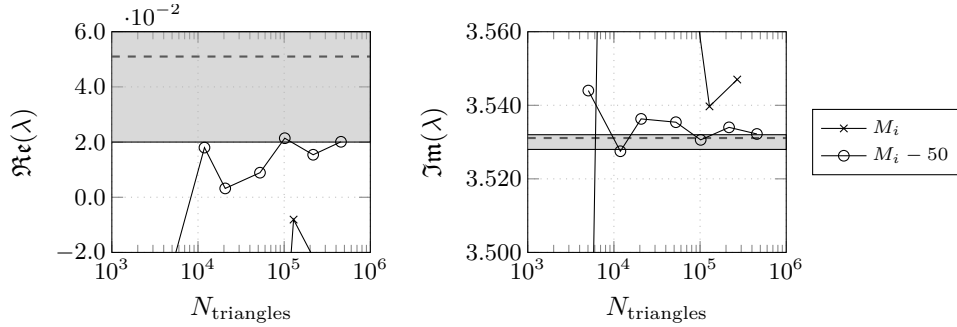


Figure 2.21 – Mesh convergence for the Eulerian-based approach.

not surprising, because in that case the steady stresses are not properly captured in the vicinity of the tip. What is more surprising is that when considering the set of meshes refined $50\times$, there is still a fairly bad convergence. Even for the most refined mesh, the growth-rate stays far away from the value obtained with the Lagrangian-based approach, while the frequency oscillates quite erratically.

In order to identify more precisely what terms cause trouble, mesh convergence for cases with and without the added stiffness terms is reported in Fig. 2.21. Like above, the dashed line represents the values obtained using the Lagrangian-based approach. Note also the much wider range for the y -axis compared to the previous graphs. The case with all the added terms (+) yields to the best agreement when it comes to both the growth-rate and the frequency (for this latter case, the curve collapses onto the dashed line because of the scale, but a close-up view displays what is reported in Fig. 2.21). On the other hand, neglecting the added terms (O) results in a dramatic underestimation for both the growth-rate and the frequency. Note also that both of them does not seem to be converged even with the finest mesh. When only the term $\sigma(\mathbf{U}, P)\Phi(\xi^\circ)^T$ is considered (\square), there is still an underestimation of the growth-rate, but an overestimation of the frequency. Note that in that case, a converged eigenvalue seems to be eventually obtained. Finally, when only the term $\nabla\sigma(\mathbf{U}, P)\xi^\circ$ is considered (\diamond), the situation is reversed: the growth-rate is overestimated while the frequency is underestimated. The convergence is also less good.

We see here first that, like before, it is necessary to consider the full added term to capture the instability. However, on this example, the mesh convergence properties of the method are fairly bad. Especially, the method seems to be extremely dependent from the regularity of the mesh in the vicinity of the fluid-structure interface.

2.5 Conclusion

Let us also now summarize the three different formulations available for the fluid-structure linear perturbations problem: in the sketch below, an orange color refers to the stress-free reference

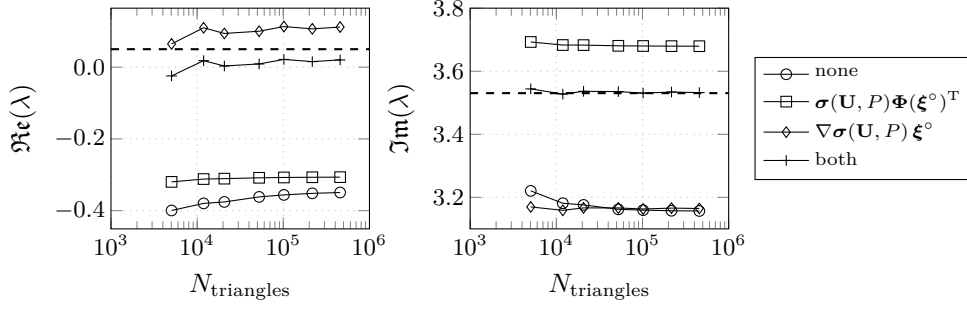
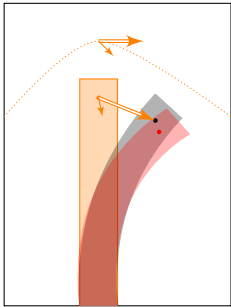


Figure 2.22 – Influence of the added terms on the Eulerian-based formulation. Plot of the real (left) and imaginary (right) parts for the leading eigenvalue obtained with the Eulerian-based approach, as a function of the number of triangles in the mesh (series $M_i - 50$), for the velocity transpiration case where the added-stiffness terms are removed (\circ symbols), the case where only the part $\sigma(\mathbf{U}, P)\Phi(\xi^\circ)^T$ is considered (\square), the case where only the term $\nabla\sigma(\mathbf{U}, P)\xi^\circ$ is considered (\diamond) and finally the case with all the terms ($+$).

configuration (rigid solid), a gray color refers to the steady deformed configuration (by the steady fluid-solid equilibrium) and the red color refers to the actual, perturbed configuration. The dotted line represents schematically a fluid flow streamline. Steady fields are materialized with double arrows (\Rightarrow) and perturbation fields with a simple arrow (\rightarrow).

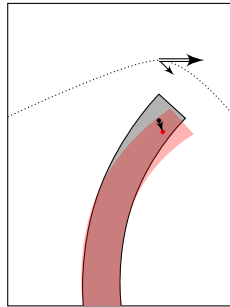
With the Lagrangian-based approach in the stress-free reference configuration, all fields are evaluated in the same fixed configuration. This approach is used for computing the exact Jacobian of our non-linear time-dependant solver. With the Lagrangian-based approach in the steady deformed configuration, the steady flow is used to deform the solid and generate the aforementioned steady deformed configuration. The perturbation problem is written there. This is the preferred approach for fluid-solid stability analyses: it is found to be numerically consistent, and gives accurate predictions of instability thresholds at a very moderate cost compared to non-linear simulations. Finally, the Eulerian-based approach also starts with a base-perturbation decomposition written in the steady deformed configuration, both that integrates the transport of the fluid velocity and pressure by the perturbation of the domain. This formulation is conceptually appealing, but comes sadly with numerical difficulties. For this reason, in the next chapters, all the computations will be done using the Lagrangian-based approach.

Lagrangian-based
(stress-free configuration)



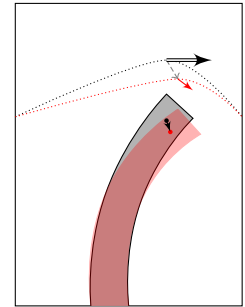
$$\begin{aligned}\hat{\mathbf{u}}(\hat{\mathbf{x}}, t) &= \hat{\mathbf{U}}(\hat{\mathbf{x}}) + \varepsilon \hat{\mathbf{u}}'(\hat{\mathbf{x}}, t) \\ \hat{p}(\hat{\mathbf{x}}, t) &= \hat{P}(\hat{\mathbf{x}}) + \varepsilon \hat{p}'(\hat{\mathbf{x}}, t) \\ \hat{\xi}(\hat{\mathbf{x}}, t) &= \hat{\Xi}(\hat{\mathbf{x}}) + \varepsilon \hat{\xi}'(\hat{\mathbf{x}}, t) \\ \hat{\xi}_e(\hat{\mathbf{x}}, t) &= \hat{\Xi}_e(\hat{\mathbf{x}}) + \varepsilon \hat{\xi}'_e(\hat{\mathbf{x}}, t)\end{aligned}$$

Lagrangian-based
(steady deformed configuration)



$$\begin{aligned}\mathbf{u}(\mathbf{x}, t) &= \mathbf{U}(\mathbf{x}) + \varepsilon \mathbf{u}'(\mathbf{x}, t) \\ p(\mathbf{x}, t) &= P(\mathbf{x}) + \varepsilon p'(\mathbf{x}, t) \\ \xi(\mathbf{x}, t) &= \mathbf{0} + \varepsilon \xi'(\mathbf{x}, t) \\ \xi_e(\mathbf{x}, t) &= \mathbf{0} + \varepsilon \xi'_e(\mathbf{x}, t)\end{aligned}$$

Eulerian-based
(steady deformed configuration)



$$\begin{aligned}\mathbf{u}(\mathbf{x}, t) &= \mathbf{U}(\mathbf{x}) + \varepsilon (\nabla \mathbf{U} \xi' + \tilde{\mathbf{u}}')(\mathbf{x}, t) \\ p(\mathbf{x}, t) &= P(\mathbf{x}) + \varepsilon (\nabla P \cdot \xi' + \tilde{p}')(\mathbf{x}, t) \\ \xi(\mathbf{x}, t) &= \mathbf{0} + \varepsilon \xi'(\mathbf{x}, t) \\ \xi_e(\mathbf{x}, t) &= \mathbf{0} + \varepsilon \xi'_e(\mathbf{x}, t)\end{aligned}$$

3

FLUID-STRUCTURE STABILITY ANALYSIS OF AN ELASTIC PLATE CLAMPED BEHIND A RIGID CYLINDER

Instabilities developing in a configuration constituted by an elastic plate clamped behind a rigid cylinder are analysed in this chapter. The interaction between the wake flow generated by the cylinder and the elastic plate leads to self-developing vortex-induced vibrations. Depending on the stiffness, the plate may oscillate about a non-deviated or a deviated mean transverse position. After having presented non-linear results computed using the methods detailed in the chapter 1, the instabilities are analysed in terms of the eigenvalue analysis introduced in the chapter 2. We show that the deviation of the plate can be interpreted as a divergence mode that appears at zero frequency in the eigenvalue spectrum. Further analyses show in which extent the linear analyses explain the non-linear limit-cycles observed.

Contents

3.1 Introduction	74
3.2 Problem setting	75
3.3 Non-linear simulations	77
3.3.1 Numerical settings	77
3.3.2 Non-linear simulation results	77
3.4 Stability analysis of the symmetric state	84
3.4.1 Steady solutions	84
3.4.2 Coupled fluid-structure stability analysis	85
3.4.3 Comparison with non-linear results	90
3.4.4 Neutral stability curves	92
3.5 Steady deviated states and secondary instability	93
3.5.1 Computation of the non-linear deviated branches	93
3.5.2 Linear stability analysis of the deviated supercritical branch	94
3.6 Analysis in terms of solid vibration modes	97
3.6.1 Analysis of the high-frequency modes dynamics	97
3.6.2 Analysis of the low-frequency and steady mode dynamics	100
3.7 Conclusion	104

3.1 Introduction

The well-known laminar, incompressible cylinder flow, that is representative for most of the mechanisms that occur in low-Reynolds number wake flows (Roshko, 1993), loses its stability above a diameter-based Reynolds number of about 47, the new stable attracting state consisting in an unsteady, time-periodic wake resulting from an alternate shedding of vortices from the obstacle. This is a typical self-developing instability that is well characterized by eigenvalue analyses (Sipp & Lebedev, 2007). We focus here on the flow about the circular cylinder with a passive flexible appendage attached in the rear side, referred hereafter to as a *splitter plate*, with the aim to analyse the mechanisms at play in the development of the flow-induced vibrations of the system.

This configuration has been used for instance to increase the stability of the wake and decrease the drag: experiments conducted at Reynolds numbers between 5×10^3 and 5×10^4 by Roshko (1954), Apelt & West (1974) and Cimbalá & Garg (1991) showed for instance that when the splitter plate is rigid and has a length L that is greater than $5D$, where D is the diameter of the cylinder, then the vortex shedding completely disappears and the drag is significantly reduced. This observation has also been reproduced numerically by Kwon & Choi (1996) at lower Reynolds numbers between 80 and 160. In the flexible case, using numerical simulations at a Reynolds number of 150 and plate lengths between D and $3D$, Wu *et al.* (2014) also observed drag-reductions as well as a damping of the unsteady aerodynamic forces, compared to the rigid case. We will investigate here this short-length regime, that shows complex coupling dynamics. When the plate is flexible, an oscillatory deformation induced by the wake flow develops in the splitter plate, that can in return significantly affect the flow, and thus further modify the vortex shedding mechanisms on the form of *vortex-induced vibrations* (Williamson & Govardhan, 2004).

The coupled fluid-solid dynamics of the cylinder-splitter plate dynamics were investigated numerically primarily using time-dependent non-linear simulations, assuming a freely rotatable rigid plate (Xu *et al.*, 1990; Kwon & Choi, 1996; Lu *et al.*, 2016) or a flexible plate (Turek & Hron, 2006; Gomes *et al.*, 2011; Lee & You, 2013; Shukla *et al.*, 2013). Depending on the parameters (typically the Reynolds number, the density ratio between the solid and the fluid, the flexibility and the length of the plate), different regimes are observed non-linearly. At sufficiently high Reynolds numbers and low flexibility, vibrations are observed in the plate and a vortex wake sets in downstream to the obstacle. If these unsteady simulations provide the limit-cycles and the associated non-linear features such as the vibration amplitudes, they provide only a limited overview of the underlying destabilization mechanisms at play. Furthermore, the high computational cost (which increases all the more as the mass ratio is close to unity) prevents from obtaining a comprehensive characterization of the regions where unsteady oscillations occur, since each point in the parameter space requires a lot of numerical effort to be characterized. This pushes for using a linearised, faster approach, that in addition gives the linear *modes* of instability. Namely, we consider here the eigenvalue analysis introduced in the previous chapter, that is appropriate for that purpose.

One of the most striking effect on the vortex shedding dynamics that emerges from the coupling with a flexible structure is that of *frequency lock-in*: in a certain range of parameters, the Strouhal number of the flow has the tendency to get “locked” to the structural natural frequencies (Williamson & Govardhan, 2004). This effect has been evidenced experimentally, numerically and theoretically in many configurations such as the well-known spring-mounted cylinder (Zhang *et al.*, 2015; Navrose & Mittal, 2016) but also in the cylinder-splitter plate configuration (Jia & Yin, 2009; Kim *et al.*, 2017) that is studied here more specifically. Frequency lock-in was explained in a very simple way by de Langre (2006) in terms of coupled-mode flutter. In his analysis, the flow is reduced to a wake oscillator model (Facchinetti *et al.*, 2004) that is further linearised, then coupled to a one degree-of-freedom spring-mounted solid. By varying the reduced velocity, it is observed that an unstable mode appears, whose frequency deviates from the Strouhal law. Instead of the coupling between plunging and torsion that is at play in classical wing coupled mode flutter (Dowell *et al.*, 2004), frequency lock-in is caused here by a coupling between the solid displacement and the fluid wake oscillation. Strikingly, in presence of flexibility, coupled-mode flutter and frequency lock-in can occur in sub-critical conditions (Mittal & Singh, 2005), that-is, at a Reynolds number that corresponds to a stationary, stable flow when the system is rigid.

A second effect that appears because of the flexibility is that of *symmetry-breaking reconfigura-*

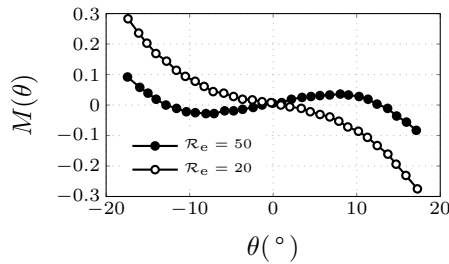


Figure 3.1 – Flow with freely rotatable cylinder-splitter plate. Total moment $M(\theta)$ acting on the body as a function of imposed deviation angles θ varying between -20° and 20° , for a plate length such that $L/D = 1$ and at Reynolds numbers 20 and 50. Reproduced from the FIG. 2 in [Xu et al. \(1990\)](#).

tion: for some parameters, the configuration where the mean position of the splitter plate remains aligned with the mean flow is unstable, and the observed configuration is that of an oscillation about a deviated mean position. For the case of a rigid splitter plate mounted on a freely rotatable cylinder, this deviation was first observed experimentally by [Cimbala et al. \(1988\)](#), [Cimbala & Garg \(1991\)](#) at Reynolds numbers between 5×10^3 and 2×10^4 , [Cimbala & Chen \(1994\)](#), and more recently by [Gu et al. \(2012\)](#) in wind tunnel experiments in a range of Reynolds number from 3×10^4 to 6×10^4 . On the other hand, [Xu et al. \(1990\)](#) conducted numerical simulations in a Reynolds number range 1 – 100 and plate lengths between 0.5 and 2. They found that above a critical Reynolds number that depends on the ratio L/D , a symmetry-breaking bifurcation appears and the splitter plate migrates to an asymmetric equilibrium position where the total moment $M(\theta)$ as a function of the deviation angle θ is zero. The equilibrium is stable when $dM/d\theta < 0$. As reported in Fig. 3.1 for the case $L/D = 1$, only the position $\theta = 0$ is stable at $\mathcal{R}_e = 20$, whereas at $\mathcal{R}_e = 50$ the position $\theta = 0$ is unstable and two stable equilibria (on either side of the wake with equal probability of being reached) are found. A semi-empirical expression for the moment $M(\theta)$ was given by [Lacis et al. \(2014\)](#), who then constructed a model of the deviation in terms of an “inverse-pendulum instability”. This model could then reproduce the deviations observed in soap-film experiments as well as numerical simulations. Spontaneous deviations have also been observed with flexible splitter plates, for instance by [Bagheri et al. \(2012\)](#) and [Wu et al. \(2014\)](#). On the occasion of Rémi Allandrieu’s graduation internship (2018) at ONERA under the supervision of Marie Couliou, such deviations have also been reproduced, the role of the flexible splitter plate being played by a silk fiber clamped behind a rigid cylinder, and placed in a vertical soap-film driven by gravity. A quick preview of the obtained results is displayed in Fig. 3.2 and we refer the reader to the report by [Allandrieu \(2018\)](#) for more details.

The cylinder-flexible splitter plate is analysed here in the context of both non-linear simulations and linear stability analysis. By varying the rigidity of the plate, we will highlight both vortex-induced vibrations instabilities and symmetry-breaking bifurcations. In particular, we will show that the symmetry-breaking reconfiguration appears as an unstable stationary mode, and thus can be interpreted in terms of a *divergence* instability, that is simply provoked by the apparition of a negative added-stiffness fluid force that balances the elastic restoring force. The plan of the study is the following: after having introduced the configuration, time-series extracted from non-linear simulations at different values of the plate stiffness are presented. Then, a linear stability analysis of the stationary, symmetric fluid-structure equilibrium is performed in the range of stiffness investigated previously, showing the different types of instabilities evoked before. Added-mass, frequency lock-in and divergence phenomena are analysed into details. The stationary symmetry-breaking instability is then used to compute a steady deformed, non-linear fluid-structure equilibrium, whose linear stability is further investigated. The results of the linear stability analysis are compared to the non-linear results: insights available from the linear analyses are emphasized, as well as the intrinsically non-linear properties.

3.2 Problem setting

The geometry of the present fluid-structure configuration is taken from a study by [Lee & You \(2013\)](#) and is reproduced in Fig. 3.3, where we have indicated the non-dimensional lengths. An elastic

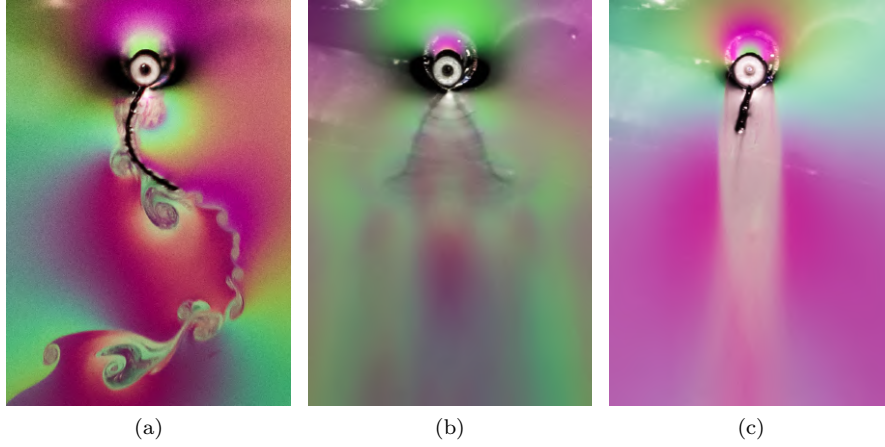


Figure 3.2 – Experimental deviations in a soap-film. Pictures taken by the author, on a soap-film flow experiment conducted at ONERA, set-up by Rémi Allandrieu and Marie Couliou. Visualisation by white-light interferometry: visible colours are related to the local thickness of the film, which itself is related to the local flow velocity (Zhang *et al.*, 2000). The mean flow is from the top to the bottom with an average velocity of the order of 2 m s^{-1} while the diameter of the cylinder is about 5 mm. For a ratio $L/D \simeq 4$, (a) short-exposure time snapshot (exposure time $1/3200 \text{ s}$) and (b) longer-exposure ($1/10 \text{ s}$) showing the filament vibration envelope. For a ratio $L/D \simeq 1.5$ and the same exposure time $1/10 \text{ s}$, (c) shows a case with a steady deviation. Pictures taken with a 105 mm f/2.8 lens mounted on a NIKON D750 camera. More details available in the Master’s thesis report by Allandrieu (2018)

Figure 3.3 – Geometry of the problem. Represented with dimensionless lengths relative to the cylinder’s diameter.

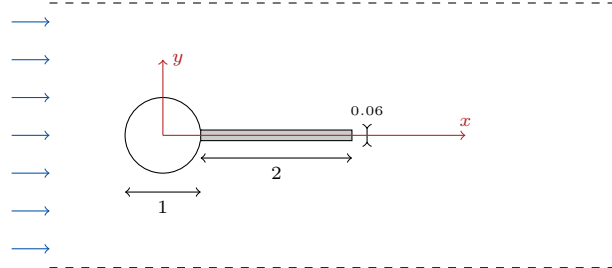


plate is clamped on the rear side of a *rigid* circular cylinder of diameter D^* . The non-dimensional length of the plate is set to $L^*/D^* = 2$ and the thickness to $H^*/D^* = 0.06$

A uniform flow field of velocity U_∞^* is applied at the inlet of the domain. We assume that the flow of density ρ_f^* and viscosity η_f^* is incompressible. For short splitter plates, the cylinder diameter D^* is an appropriate measure of the characteristic length scale in the flow, while the inflow velocity is taken as the characteristic velocity. The flow is governed by the Navier-Stokes equations, while a Saint-Venant Kirchhoff elasticity model is taken for the solid with a Poisson coefficient ν_s of 0.35. The Reynolds number and the non-dimensional stiffness parameter then read as follows:

$$\mathcal{R}_e = \frac{\rho_f^* U_\infty^* D^*}{\eta_f^*} \quad \text{and} \quad \mathcal{E}_s = \frac{E_s^*}{\rho_f^* (U_\infty^*)^2}.$$

The governing equations are written under the form of the fully coupled three-fields problem (1.1.1), while the eigenvalue problem will be written for convenience without the velocity augmentation (we refer the reader to the chapter 1 for further details).

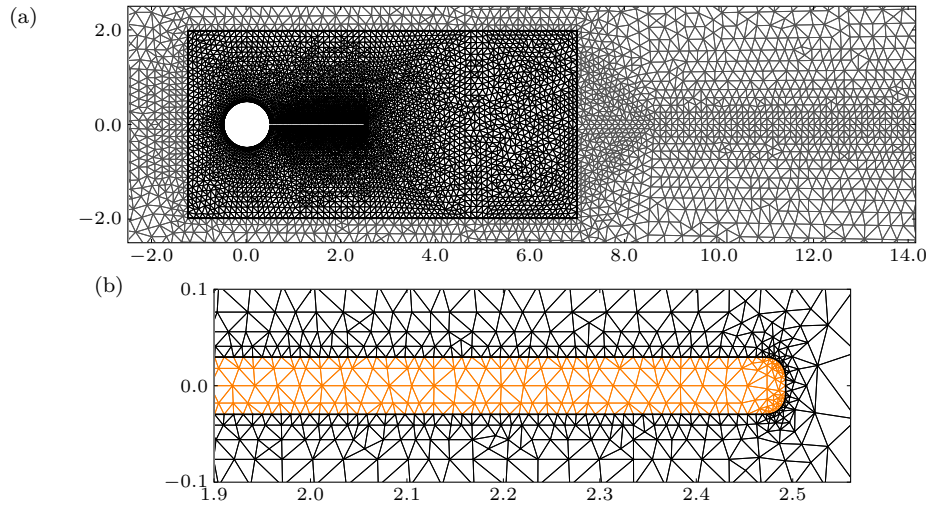


Figure 3.4 – Mesh. Plot of the computational mesh, showing (a) a portion of the farfield fluid region (light gray) and the extension region (black), and (b) close-up view in the vicinity of the tip of the splitter plate (solid mesh represented in orange color).

3.3 Non-linear simulations

3.3.1 Numerical settings

The computational domain has dimensions $x \in [-15, 50]$ and $y \in [-25, 25]$. The unstructured mesh is made of 29 976 triangles and 15 297 vertices, among which 1376 and 1007 are located in the solid region (see in Fig. 3.4 a representation of the mesh). At the conforming fluid-solid interface, the grid spacing in the x and y direction is set to 0.0067, while the largest spacing of 1.67 is set in the farfield region. Refinement is applied in the wake up to $x = 26$ so as to capture properly the near-wake vortices, and the edges of the tip of the splitter plate are rounded. The extension region is taken as a sub-region of the fluid region enclosing the splitter plate, of dimensions $x \in [-1.5, 7]$ and $y \in [-2, 2]$. An inflow velocity is prescribed at the inlet boundary $x = -15$, slip conditions are taken at the top and bottom farfield boundaries $y = \pm 25$, and a stress-free outflow condition is taken for the outflow at $x = 50$. No-slip conditions are prescribed at the surface of the bluff-body (cylinder and plate).

Several non-linear simulations have been performed for various rigidities \mathcal{E}_s of the plate. Details on the non-linear solver used as well as its validation are given in the chapter 1. A shifted Crank-Nicholson scheme is used for the time discretization, and finite-elements are used for space discretization. For all computations, the time-step is set to $\Delta t = 0.01$ which was found to result in converged time series. More details about the validation of the non-linear solver are given in section 1.2. Unless otherwise stated, the simulations are initialised by a uniform, zero flow. Between the non-dimensional time units $t = 0$ and $t = 20$ the inlet velocity is smoothly increased following the law $u_{\text{in}}(t) = 0.5(1 - \cos(\pi/20t))$. For $t > 20$ the inflow velocity is set to 1.

As time goes on, two symmetric (with respect to the $y = 0$ axis) recirculating bubbles appear behind the cylinder, above and below the splitter plate. These recirculating regions tend to slightly compress the splitter plate in the direction $x < 0$. After some time (function of the rigidity) and for rigidities less than $\mathcal{E}_s = 119\,900$, self-developing instabilities set in, that result in different types of limit-cycles, characterized by periodic movements for the fluid and the splitter plate.

3.3.2 Non-linear simulation results

In the following, we vary the stiffness and keep the other physical parameters to fixed values. More precisely,

$$\mathcal{E}_s \in [2 \times 10^2, 2 \times 10^5] \quad \mathcal{R}_e = 80, \quad \mathcal{M}_s = 1, \quad \nu_s = 0.35.$$

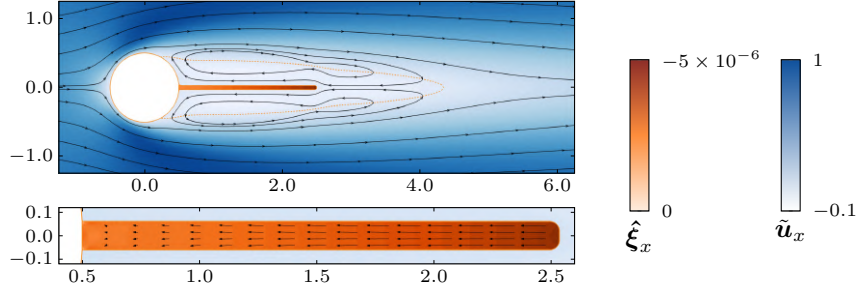


Figure 3.5 – Stationary flow (region n_1). For the case at $\mathcal{R}_e = 80$ and $\mathcal{E}_s = 2 \times 10^5$, plot of the streamwise velocity (blue color), streamlines (solid lines) and limits of the recirculating region (orange dashed line). The figure at the bottom presents a close-up view of the solid deformation, where its direction is materialized by the arrows and the magnitude by the orange color shade.

In the following, we first detail a few representative cases (in the order of a decreasing stiffness). The observations are then summarized in Fig. 3.12 and Tab. 3.1, where a more comprehensive classification is reported.

A stationary symmetric case ($\mathcal{E}_s = 2 \times 10^5$, region n_1)

The computations at high rigidities show a steady behaviour: no unsteadiness is observed. A steady wake develops downstream to the cylinder, while the plate is kept aligned with the wake without oscillating. The steady flow computed at $\mathcal{E}_s = 2 \times 10^5$ is shown in Fig. 3.5. The fluid flow is represented on top, where the black solid lines indicate a few streamlines. The flow detaches symmetrically (with respect to the x axis) from the cylinder surface and forms two symmetric recirculating regions above and below the splitter plate. The limit of this back-flow region is depicted by the dotted orange line, and extends downstream up to the non-dimensional position $x \simeq 4.4$. Since the splitter plate surface completely lies inside the backflow region, the shear stress generated by the fluid are directed upstream. As a consequence, the solid is slightly compressed, as shown at the bottom. The displacement field is oriented almost exclusively along the x axis, but a slight flare in the direction of the $\pm y$ axis is observed as one moves closer to the clamped edge of the plate, due to the positive Poisson effect ($\nu_s = 0.35$). The amplitude of the compression is rather small: for the case considered, the tip end streamwise displacement is only -5×10^{-6} .

An oscillating, symmetric periodic case ($\mathcal{E}_s = 88\,678$, region n_2)

Cases with a rigidity lower than 119 900 show a completely different behaviour. Unsteady velocity oscillations are observed in the wake as well as in the splitter plate. Fluctuating lift and drag coefficients are therefore observed. A typical time-series for these type of flows ($\mathcal{E}_s = 88\,678$) is reported in Fig. 3.6a where the transverse tip displacement of the splitter plate and the lift coefficient of the cylinder plus splitter plate are represented, showing the development of unsteadiness from $t \simeq 175$, and then the non-linear saturation from $t \simeq 300$. Clearly, the fluid-structure solution evolves towards a limit-cycle that oscillates at one single dominant circular frequency: as displayed in Fig. 3.11a, the frequency spectrum computed for the lift signal has only one very dominant peak (evaluated to $\omega_{n.l.} \simeq 1.02$). The plate displacement reaches a noticeable amplitude (more than half the diameter of the cylinder in the tip). Looking at the lift coefficient, this time-series is similar from what could have been monitored for a cylinder flow without any splitter plate, once the Hopf bifurcation marking the onset (with respect to the Reynolds number) of vortex shedding is passed (Sreenivasan *et al.*, 1987). In particular, the lift oscillation amplitude smoothly decays to zero when the stiffness is increased.

Let us detail the structure of the flow. Snapshots of the limit-cycle are reported in Fig. 3.6b, where the z vorticity is represented clockwise at four instants T , $T + T/4$, $T + T/2$ and $T + 3T/4$, where T is the period of the flow. These instants are marked by the white circles in Fig. 3.7, where the normalized (by the maximum value) aerodynamic coefficients for the cylinder and splitter plate

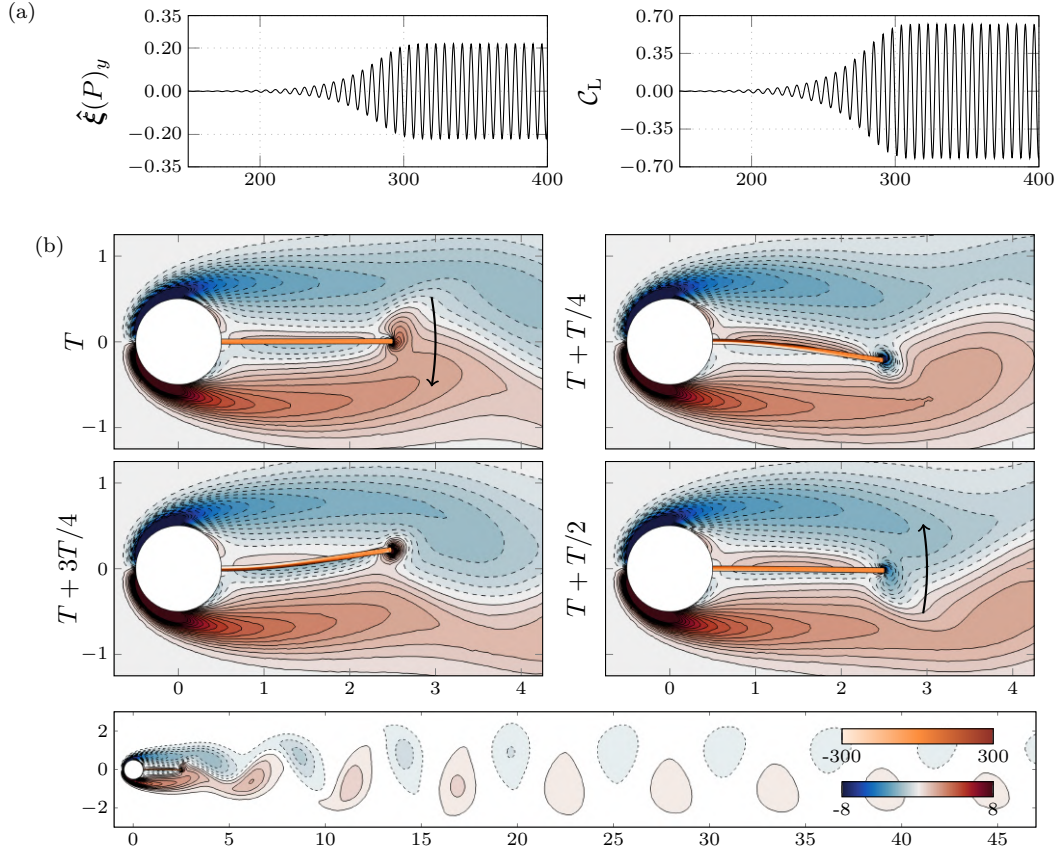


Figure 3.6 – Non-linear simulation for $\mathcal{E}_s = 88678$ (region n_2). (a) Time-series for the transverse tip displacement $\hat{\xi}(P)_y$ and for the lift coefficient C_L . (b) Plot of the z vorticity (blue-red colours, dashed negative contours) in the fluid and of the yy stress in the solid (orange color). The black arrow indicate the direction of the velocity vector in the solid.

as well as the tip displacement of the plate are reported over one period. It is observed that the cylinder generates two vortices of opposite sign on the top and bottom faces, that are eventually released in the wake (see the overall view in the bottom). As mentioned before, at higher rigidity the flow is stable, and flexibility thus necessarily acts as a destabilizing effect here. If ones look closer to the four pictures, it is clear that secondary, smaller vortices are generated at the tip of the plate. A vortex with a positive sign is generated as the plate goes downwards (upper left picture) and *vice-versa* (lower right picture). They do not have a sufficient strength to be released in the wake and stay attached, but the resulting downwash (or upwash) effect is sufficient to affect the larger, surrounding vortices, which might cause them to detach: the detachment zone is precisely located near the tip of the plate (this is particularly visible in the bottom picture) that acts sort as a “vortex-cutter” that favours the vortex shedding.

As visible in Fig. 3.7 — and can be deduced from the snapshots in Fig. 3.6 —, the period of

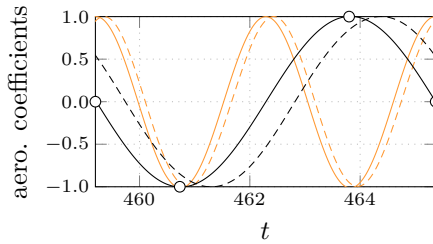


Figure 3.7 – Evolution during one period. For the case $\mathcal{E}_s = 88678$, plot of the normalized (mean set to zero and amplitude scaled between ± 1) lift (—) and drag (—) coefficients (splitter plate and cylinder), y (—) and x (—) tip displacement, over one oscillation period in the limit-cycle.

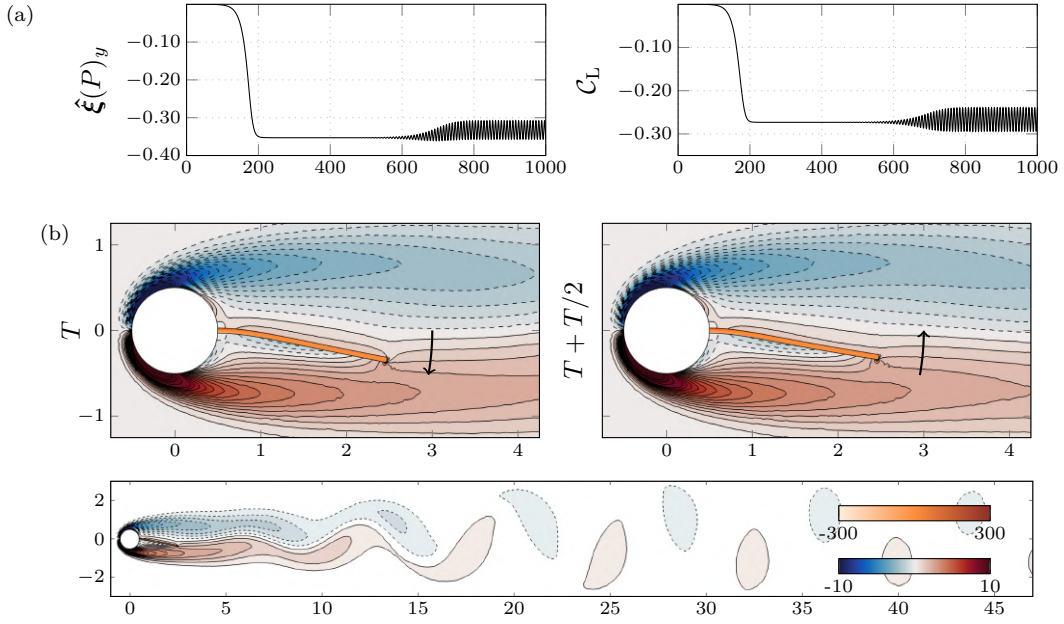


Figure 3.8 – Non-linear simulation for $\mathcal{E}_s = 2804$ (region n_3). (a) Time-series for the transverse tip displacement $\xi(P)_y$ and for the lift coefficient C_L . (b) Plot of the z vorticity (blue-red colours, dashed negative contours) in the fluid and of the yy stress in the solid (orange color). The black arrow indicate the direction of the velocity vector in the solid.

oscillation in the transverse direction is twice that in the streamwise direction. The same is true for the aerodynamic coefficients, with a small phase delay. The transverse (lift/ y displacement) components thus define odd functions over one period and only odd harmonics appear in the Fourier spectra. Conversely, even harmonics appear in the spectra of streamwise (drag/ x displacement) quantities.

An oscillating, deviated case ($\mathcal{E}_s = 2804$, region n_3)

When rigidity is further decreased down below about $\mathcal{E}_s = 12\,000$, a new regime appears. The mean position of the plate tip end ceases to be zero: unsteady oscillations about a *deviated* mean position for the plate are observed. The plate deviates towards the bottom in the present case. For other settings (initial condition or repartition of the points in the mesh) a deviation towards the top can also be obtained. For the case $\mathcal{E}_s = 2804$, a time-series for the plate transverse tip displacement and lift coefficient is reported in Fig. 3.8a. After the development of the wake behind the plate in the period of time where the inflow velocity is progressively increased and a short steady regime, the tip of the plate slowly deviates towards the bottom between $t \simeq 100$ and $t \simeq 200$. As seen in the graph in the right side, the lift is also directed towards the bottom. Then, from $t \simeq 600$, unsteady oscillations appear, that again saturate in a periodic limit-cycle from $t \sim 750$. The spectra for the lift signal, reported in Fig. 3.11b, shows one fundamental circular frequency at $\omega_{n.l.} = 0.79$ and one harmonic peak at $2\omega_{n.l.}$, while higher-order harmonic frequencies are not visible in the spectrum. A peak at $2\omega_{n.l.}$ (instead of $3\omega_{n.l.}$ like for the previous case) is found because the plate ceases to oscillate about a zero mean and thus lift and drag have the same periodicity.

The amplitude of the vibrations is much smaller than in the symmetric oscillating regime — for instance, the tip vibration amplitude is barely more than 0.05. The mean deviation has thus a strong stabilizing effect on the wake oscillation. This latter effect can be made more visible by looking to a field representation of the flow. In Fig. 3.8b, snapshots of vorticity in the deviated limit-cycle are reported. The mean position of the plate is always maintained in the $y < 0$ region, on top of which small oscillations are superimposed. We clearly see how reduced is the amplitude of the oscillations (only snapshots at T and $T + T/2$ are represented, because the flow in the near-

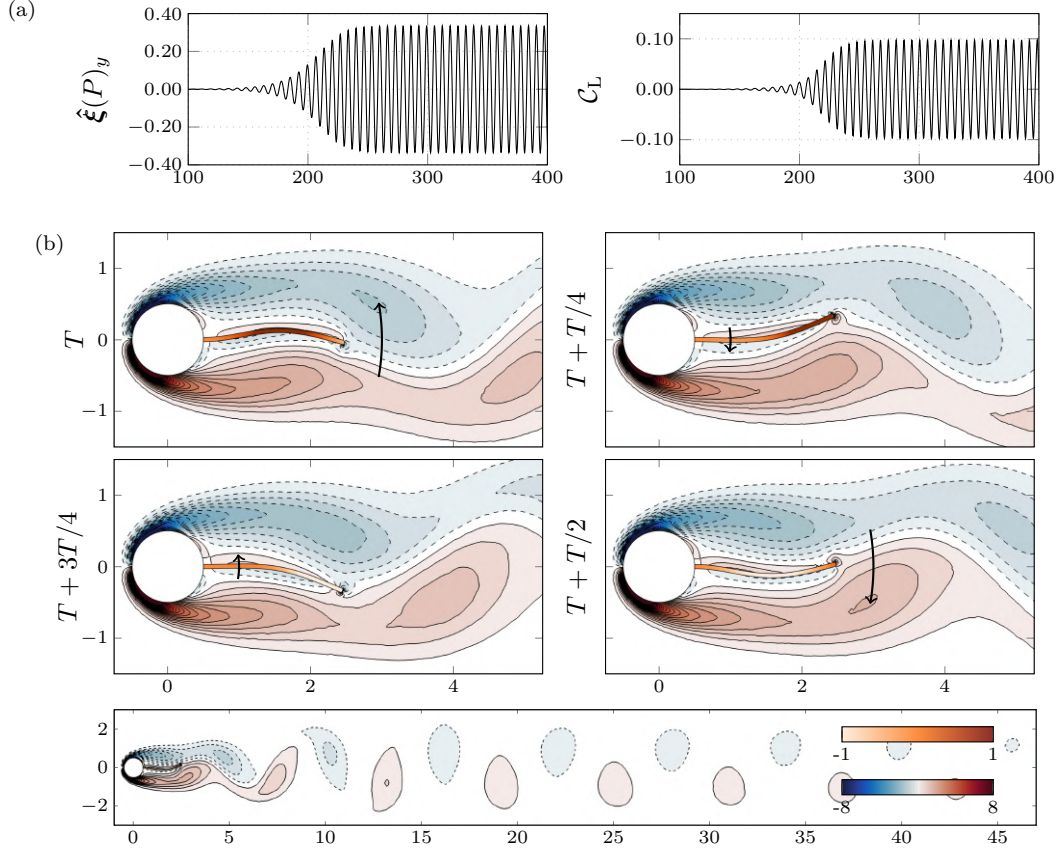


Figure 3.9 – Non-linear simulation for $\mathcal{E}_s = 560$ (region n_4). (a) Time-series for the transverse tip displacement $\hat{\xi}(P)_y$ and for the lift coefficient C_L . (b) Plot of the z vorticity (blue-red colours, dashed negative contours) in the fluid and of the yy stress in the solid (orange color). The black arrow indicate the direction of the velocity vector in the solid.

solid region does not vary much during a period of oscillation). These oscillations comes with tiny secondary vortices at the tip of the plate (not visible in Fig. 3.8b), that have only a limited influence on the flow. The reversed vorticity signs close to the plate mark the presence of a recirculating region, that does actually not evolve a lot. That is not to say that the wake remains steady: as shown in the bottom figures, vortices are nevertheless shed, but with a smaller intensity as before, and further away from the plate (the detachment zone is located at about $x \simeq 10$, as against $x \simeq 5$ in the previous case). All goes as if the seemingly more streamlined overall shape prevents from the release of vortices in the wake.

An oscillating, symmetric, low-stiffness, periodic case ($\mathcal{E}_s = 560$, region n_4)

The main features for a case with a smaller rigidity $\mathcal{E}_s = 560$ are reported in Fig. 3.9. In the contrary to the previous case, the plate again oscillates about a non deviated mean position. The deformation of the plate follows however a different pattern from what is displayed in Fig. 3.6. An inflexion point appears in the centreline deformation of the plate, as visible in Fig. 3.9b, and the maximal transverse deviation is increased (± 0.35 compared to ± 0.25 for the case $\mathcal{E}_s = 88678$). Despite this increase of the oscillation amplitude, the lift amplitude is reduced compared to the case $\mathcal{E}_s = 88678$, probably because the kinematics of the plate decreases the strength of the vortex release.

The spectra of the lift coefficient is reported in Fig. 3.11c. The largest peak of response is located at $\omega_{n.l.} \simeq 0.95$. Because of the recovered symmetry, a sequence of type $\{\omega_{n.l.}, 3\omega_{n.l.}, 5\omega_{n.l.}, \dots\}$ is again found — with amplitudes that are greater than in the high-stiffness case $\mathcal{E}_s = 88678$ displayed

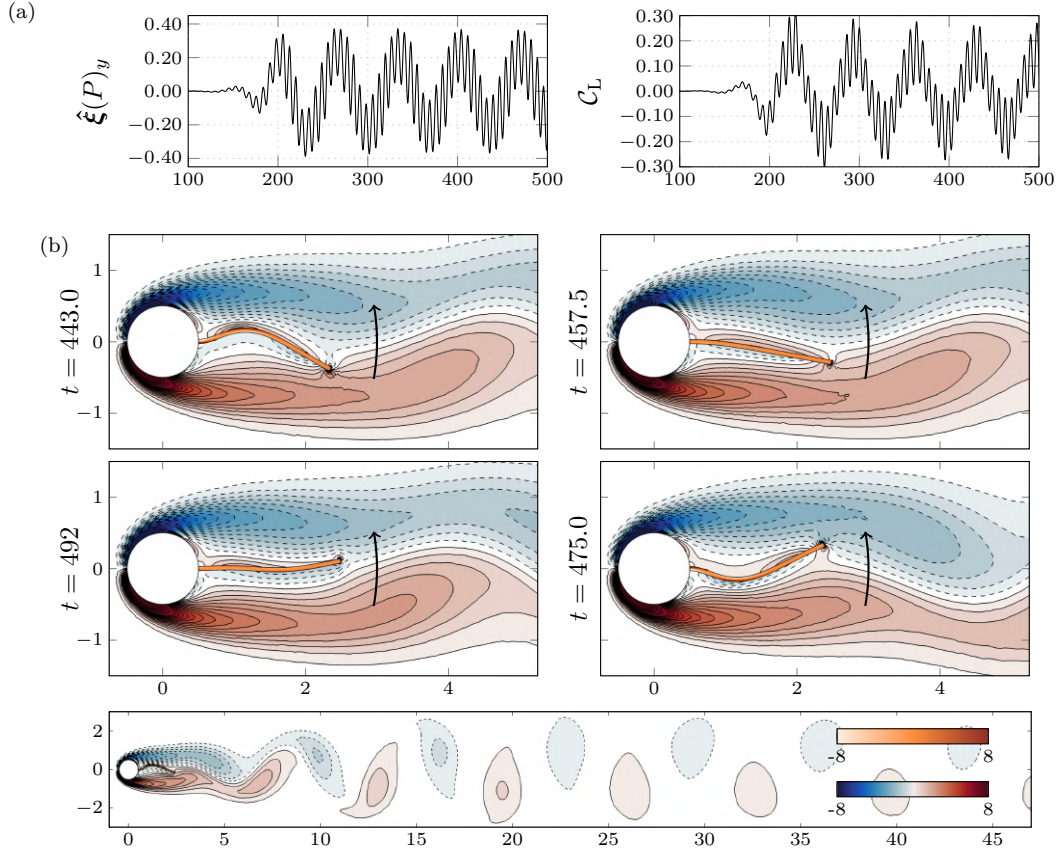


Figure 3.10 – Non-linear simulation for $\mathcal{E}_s = 223$ (region n_5). (a) Time-series for the transverse tip displacement $\hat{\xi}(P)_y$ and for the lift coefficient C_L . (b) Plot of the z vorticity (blue-red colours, dashed negative contours) in the fluid and of the yy stress in the solid (orange color). The black arrow indicate the direction of the velocity vector in the solid, averaged over the high-frequency period.

in (a).

A quasi-periodic case ($\mathcal{E}_s = 223$, region n_5)

Finally, for smaller rigidities, yet another regime is found. In this case, oscillations develop about a mean position that is again symmetric, but in that case a secondary frequency appears in the spectrum of the flow (Fig. 3.11d), resulting in a quasi-periodic limit-cycle. While the high, main frequency has still roughly the same value as for the other cases (non-dimensional angular frequency of $\omega_{n.l.} = 0.89$), a lower frequency ($\omega_{n.l.}^{(2)} = 0.09$) enters in the spectrum and modulates the vibration history, as shown in Fig. 3.10a and in the spectra displayed in Fig. 3.11d. Snapshots of the flow in a phase where the tip globally moves upwards are depicted in Fig. 3.10b. The vibration pattern in the solid is very different from what was observed previously: its movement is now composed of a combination of a pure bending with one vibration node at the clamped, and bending with two vibration nodes. The detachment region is also again located closer to the cylinder ($x \simeq 5$).

Summary

Depending on the stiffness, several categories are to be distinguished, established from the behaviour of the solid. These observations are summarised in Fig. 3.12, that shows (a) the total drag and (b) total lift coefficients for the plate and the cylinder, (c) the transverse displacement of the tip of the plate and (d) the fundamental vibration frequencies. The mean values are represented

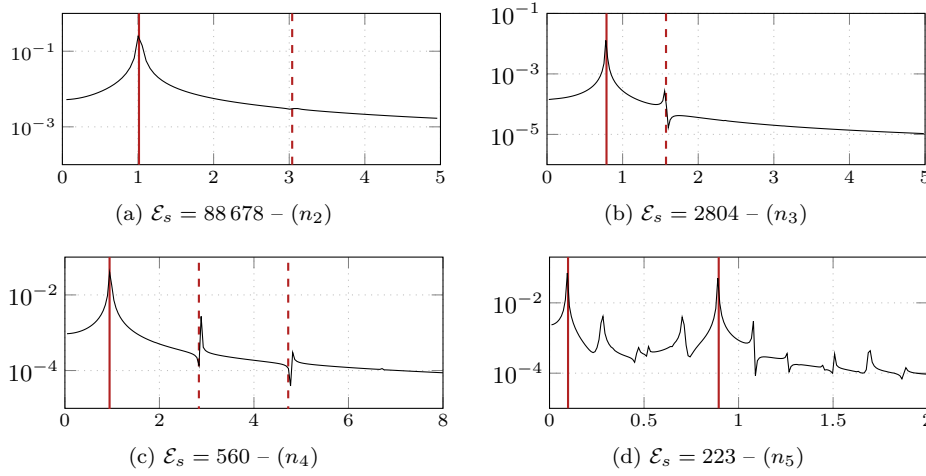


Figure 3.11 – Frequency spectra. Plot of the Fast Fourier Transform spectra of the lift coefficient C_L . Fundamental frequencies are marked with the solid vertical line, harmonics with the dashed lines.

<i>region</i>	<i>range</i>	<i>main features</i>
n_1	$\mathcal{E}_s > 119\,900$	steady-state with a straight plate position
n_2	$119\,900 > \mathcal{E}_s > 12\,000$	oscillations about a straight mean plate position
n_3	$12\,000 > \mathcal{E}_s > 1100$	oscillations about a deviated mean plate position
n_4	$1100 > \mathcal{E}_s > 255$	oscillations about a straight mean plate position
n_5	$255 > \mathcal{E}_s$	quasi-periodic oscillations

Table 3.1 – Summary of the different regimes reported from the non-linear simulations. The labels n_i for $1 \leq i \leq 5$ refer to the different regions of interest and are also reported in Fig. 3.12.

with a circle symbol, while the vertical bars account for the oscillation amplitudes about the mean value.

Steady states are found at large values of the non-dimensional Young modulus \mathcal{E}_s (right end, region n_1 , typical case $\mathcal{E}_s = 2 \times 10^5$): in this region, the plate slightly deforms but the flow remains steady. Decreasing the rigidity below $\mathcal{E}_s = 119\,900$ results in the apparition of oscillating states (region n_2 , typical case $\mathcal{E}_s = 88\,678$) with a zero mean y displacement (first gray region). In this region, very large-amplitude lift fluctuations are observed, while the mean drag is increased compared to the stationary case. Decreasing further the rigidity results in oscillating states with a deviated mean transverse displacement (region n_3 , typical case $\mathcal{E}_s = 2804$), starting from $\mathcal{E}_s = 12\,000$. This region comes with much smaller oscillation amplitudes. This region suddenly ceases to exist from $\mathcal{E}_s = 1100$. A symmetric oscillating state is recovered in this region n_4 (lighter gray shaded area in the left sides in Fig. 3.12, typical case $\mathcal{E}_s = 560$) but with other flapping features than previously. Very high vibrations amplitudes are reached (greater than the diameter of the cylinder), but the lift fluctuation amplitudes are smaller than in the first unsteady symmetric region. Drag fluctuations are however of the same order of magnitude as in the first region. Finally, below $\mathcal{E}_s = 255$, quasi-periodic limit-cycles are observed (region n_5 , typical case $\mathcal{E}_s = 223$).

We see here that by simply varying the rigidity coefficient of the plate, several limit-cycles can be reached. The transient behaviour observed in Fig. 3.8a and the coexistence of two vibration frequencies in Fig. 3.10a clearly indicate that several instability *modes* that are likely to coexist and compete non-linearly. It is thus appealing to compute the linear modes for the studied configuration, for they give a better picture of the instability mechanisms at play. In the next section, we therefore pursue on linear stability analyses of steady solutions of the fluid-structure equilibrium.

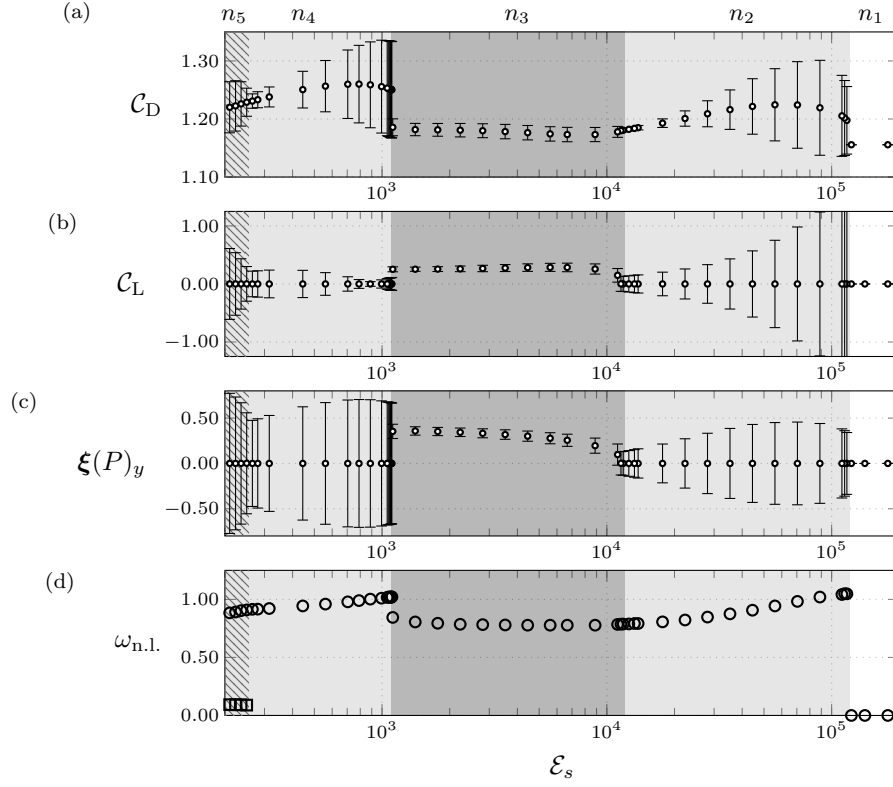


Figure 3.12 – Limit-cycles features. For different values of \mathcal{E}_s , plot of the (a) drag and (b) lift coefficient of the plate and cylinder, and (d) transverse tip displacement, in the limit-cycle regime. The mean value is indicated by a circle (○) symbol and is computed as $1/2(\max + \min)$ while the amplitude ($\max - \min$) is indicated by the errorbar and centred about the mean. The dominant plate oscillation frequency (○) is reported in (d) as well as (if any) a second, non-harmonic frequency (□). Regions n_2 and n_4 that show an unsteady behaviour and a zero mean plate deviation are highlighted with a gray color, while region n_3 coming with deviated mean oscillations is emphasized by a darker gray color. Region n_5 with quasi-periodic limit-cycles is hatched with oblique lines.

3.4 Stability analysis of the symmetric state

3.4.1 Steady solutions

Steady solutions, whose linear stability will be investigated, can be computed by seeking for time-independent solutions in the non-linear problem 1.1.1. Since we are interested in determining the linear stability of the symmetric (with respect to the x axis), steady deformed state, we enforce the symmetry by applying a zero transverse displacement condition along the neutral line in the solid. The steady fluid-structure solutions computed have a very similar aspect as what is shown in the Fig. 3.5. As \mathcal{E}_s is decreased, the compression effect increase almost linearly over the whole range of rigidities. The maximal deviation from linearity, reached at small rigidities, does not exceed 0.5%. The drag coefficient, computed as twice the non-dimensional integrated interface fluid stress about the fluid-solid boundary, is found to be $\mathcal{C}_D = 1.155$ and varies less than 0.1% over the whole range of rigidities. The net drag is actually essentially generated by the rigid cylinder, whose position does obviously not depend on the rigidity: the evolution of the drag coefficient for the plate only shows very small variations (less than 1.5% over the whole range of rigidities). In average, a net drag of magnitude about 6×10^{-2} and directed upstream is generated by the recirculation region.

3.4.2 Coupled fluid-structure stability analysis

Let us now investigate the linear stability of the steady symmetric solutions presented above, using the method presented in the chapter 2. For each considered value of \mathcal{E}_s , after having computed the corresponding steady equilibrium, its stability is investigated in the steady deformed domain $\Omega_f \cup \Omega_s$, by solving the quadratic eigenvalue problem (Eq. (2.1.22) deduced from the problem (2.1.1))

$$\lambda^2 \begin{pmatrix} \mathcal{M}_s & 0 & 0 \\ 0 & 0 & 0 \\ 0 & 0 & 0 \end{pmatrix} \begin{pmatrix} \xi^\circ \\ \mathbf{q}_e^\circ \\ \mathbf{q}_f^\circ \end{pmatrix} + \lambda \begin{pmatrix} 0 & 0 & 0 \\ 0 & 0 & 0 \\ -\mathcal{I}_{f\xi} - \mathcal{T}_{fe} & \mathcal{T}_f & 0 \end{pmatrix} \begin{pmatrix} \xi^\circ \\ \mathbf{q}_e^\circ \\ \mathbf{q}_f^\circ \end{pmatrix} = \begin{pmatrix} -\frac{\mathcal{E}_s}{\mathcal{M}_s} \mathcal{K}' & 0 & \frac{1}{\mathcal{M}_s} \mathcal{I}_{f\xi}^T \\ \mathcal{I}_{e\xi} & -\mathcal{A}_e & 0 \\ 0 & \mathcal{N}'_{fe} & \mathcal{N}'_{ff} \end{pmatrix} \begin{pmatrix} \xi^\circ \\ \mathbf{q}_e^\circ \\ \mathbf{q}_f^\circ \end{pmatrix} \quad (3.4.1)$$

where we have rescaled the solid stiffness operator \mathcal{K}' in order to emphasize its dependency with respect to the solid stiffness \mathcal{E}_s and mass ratio \mathcal{M}_s (recall that for the Saint-Venant Kirchhoff model, the solid stress, Eq. (1.1.7), is proportional to the Young modulus and hence to \mathcal{E}_s). In this problem, the first line

$$\left\{ \lambda^2 \mathcal{M}_s + \frac{\mathcal{E}_s}{\mathcal{M}_s} \mathcal{K}'(\mathbf{Q}) \right\} \xi^\circ = \frac{1}{\mathcal{M}_s} \mathcal{I}_{f\xi}^T \mathbf{q}_f^\circ$$

is the solid modal problem (which is second-order in time), where the elasticity equation (operators \mathcal{M}_s and \mathcal{K}') acting on the solid displacement ξ° are forced by the fluid loads (left-hand side term). The second line is the static, geometric ALE mapping acting on $\mathbf{q}_e^\circ = [\xi_e^\circ, \lambda^\circ]$ (extension displacement and extension interface Lagrange multiplier), while the Navier-Stokes equations written within the linearised ALE framework are in the last line, with $\mathbf{q}_f^\circ = [\mathbf{u}^\circ, p^\circ, \lambda^\circ]$ — velocity, pressure, interface stress. In particular, this sub-problem is coupled the geometric ALE problem (effect of the domain displacement) and the solid problem (velocity/stress continuity). Unstable modes are couples of eigenvectors $[\xi^\circ, \mathbf{q}_e^\circ, \mathbf{q}_f^\circ]$ and complex eigenvalues $\lambda = \lambda^r + i\lambda^i$ such that $\Re(\lambda) = \lambda^r > 0$.

As in the previous section, we start by analysing in detail some characteristic examples, then a more comprehensive summary is presented.

High-frequency, high stiffness unstable modes

When the rigidity is decreased, the first unstable modes to appear are unsteady modes at a frequency close to unity. They are found for $\mathcal{E}_s < 119900$. For the case $\mathcal{E}_s = 88678$ (same stiffness as for the characteristic non-linear computation in the region n_1), the resulting eigenvalue spectrum is displayed in Fig. 3.13a, that shows a pair of complex-conjugate unstable modes $\lambda = 0.0436 \pm 0.929i$, emphasized with the ○ symbol. The governing operators being real-valued, recall that the spectrum is necessarily symmetric with respect to the real axis (Golub & van Loan, 2013). A representation of the real part of the eigenvector for the most unstable mode ○ is reported in Fig. 3.13b. Contour lines represent the real part of the streamwise Eulerian velocity perturbation $\tilde{\mathbf{u}}^\circ = \mathbf{u}^\circ - \nabla \mathbf{U} \xi_e^\circ$. Recall that this quantity does not depend upon the choice of the extension operator, and represents the velocity perturbation in the perturbed domain (see a discussion in §2.3.3). This representation is actually a snapshot of the perturbation at a certain phase: when the phase is varied, one sees the vortex wake being advected downstream, while the solid deformation alternates up and down. The dynamical deformation is made more clear for the solid with a superposition of the plate's position (the displacement being arbitrary scaled) at different phases (dark lines). The perturbed position of the solid, deduced by applying the real part of the mode to its position in the steady deformed configuration, is represented by the orange line.

It is observed that the downwards deformation of the structure tends to induce a positive streamwise velocity in the very close vicinity of the splitter plate, while the flow goes in the other direction further away in the transverse direction. The streamwise deformation of the plate is almost zero, which indicates that, at the linear level, the coupling with the solid occurs essentially through a pressure effect rather than through shear stresses. In the fluid, the characteristic features for an unstable vortex wake are found (Hill, 1992), i.e. alternant lobes of positive and negative streamwise velocity that mark the early stages of development of the unsteady von Kármán vortex wake.

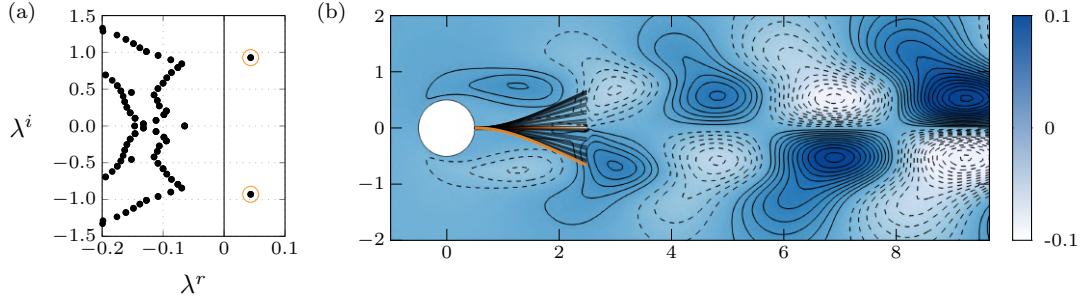


Figure 3.13 – High-frequency, high stiffness unstable mode, $\mathcal{E}_s = 88\,678$. (a) Eigenvalue spectrum showing one unstable pair of complex-conjugate modes ($\lambda^r > 0$) emphasized by the \circ symbol. (b) Spatial representation of the real part of the Eulerian velocity component of the unstable mode (blue gradient and contours, dashed negative) and snapshots of the solid deformation.

Steady, deviated modes

Let us now consider a value of the Young modulus corresponding to a case where a mean deviation was observed in the non-linear simulations. For the case $\mathcal{E}_s = 2804$ (same stiffness as for the characteristic non-linear computation in the region n_2), the results are reported in Fig. 3.14. The spectrum displayed in (a) shows one unstable ($\lambda^r > 0$), steady ($\lambda^i = 0$) mode emphasized by the \square symbol. This type of mode thus describes a static instability that grows exponentially with time without oscillating. The steady modes actually represent a symmetry-breaking bifurcation – or divergence – instability.

The spatial structure of the associated eigenvector is displayed in (b). Unlike for the unsteady modes, we do not have here a static vision of an unsteady process: there is no oscillation in the solid (in particular, switching between the real or imaginary part of the mode just amounts to shifting the sign of the considered quantity). No advected structures are observed in the wake. Only a decreasing (predominantly streamwise) velocity field is observed in the downstream direction for $y > 0$ and in the upstream direction for $y < 0$. Another representation of the mode is displayed in Fig. 3.15a, in terms of pressure and velocity streamlines. Looking at the velocity streamlines in the vicinity of the solid, one observes that the flow consists in a counter-clockwise circulation around the object, that evolves more downstream into a quasi-parallel flow, as already noted above. The pressure (represented in a blue-red colour gradient) is a good marker for the deformation processes at play. Namely, one sees that the bending is associated to low-pressure areas that tend to push down the plate. Since the pressure balance (that takes here the major part in the generation of lift) is directed to the bottom, the net lift is also negative.

When the rigidity is decreased, the deformation pattern in the solid evolves. An unstable, steady eigenmode at $\mathcal{E}_s = 700$ is represented in Fig. 3.15b. In that case, the maximal deformation occurs roughly in the middle of the plate. The change of sign of the pressure along the splitter plate is associated to a change of sign of the curvature of the bended plate. This effect is barely visible at high stiffness (Fig. 3.15a), but appears more clearly at lower stiffness (Fig. 3.15b). In any case, the dynamics seems to be dominated by pressure effects, because the deviation follows the pressure difference rather than the fluid velocity perturbation shear stresses, that would rather provoke a bending in the opposite direction and act as a stabilizing effect. This is contrary to what was for instance observed in the context of slender structures interacting with a Stokes flows (Gadelha *et al.*, 2010), i.e. in a much more viscous context.

The velocity perturbation developing on the steady base-flow tends to decrease the size of the lower recirculating region (close to the solid, the signs of the steady base-flow velocity and of the perturbation velocity are opposed) and to increase that of the upper recirculating region. In order to better visualise how the mode influences the total flow, a superposition of the steady flow plus the coupled fluid-structure mode is reported in Fig. 3.16 for two mode amplitudes. The Lagrangian-based mode is considered here, for we can then deform both the solid and the fluid domain according to the solid/extension perturbation field. We see how the asymmetry in the

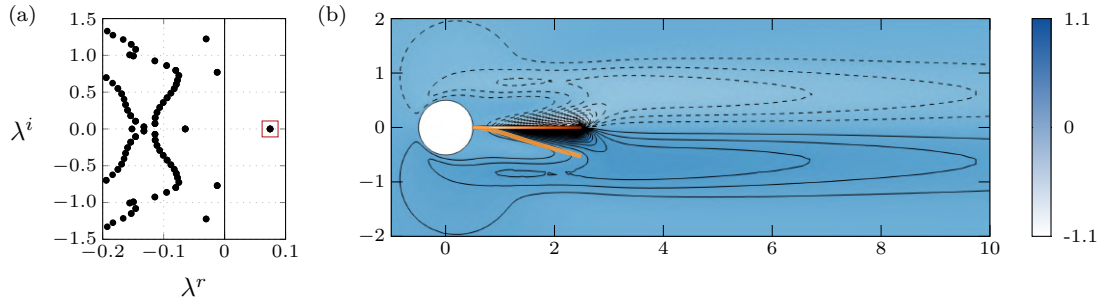


Figure 3.14 – Steady, deviated modes, $\mathcal{E}_s = 2804$. (a) Eigenvalue spectrum showing one unstable steady mode ($\lambda^r > 0, \lambda^i = 0$). (b) Spatial representation of the real part of the Eulerian velocity component of the unstable mode (blue gradient and contours, dashed negative) in the steady deformed configuration, and solid deformation scaled with an amplitude of 0.4 (orange, thick deviated line).

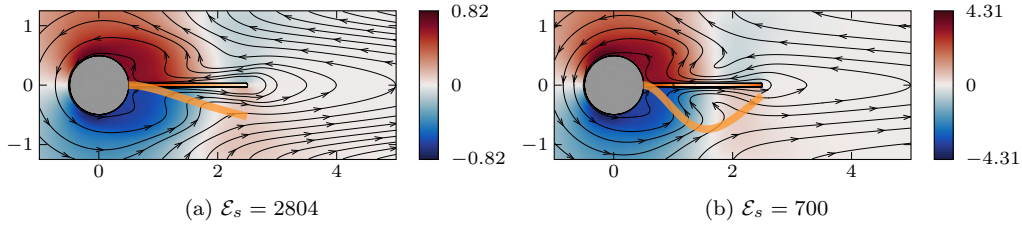


Figure 3.15 – Pressure component of the steady mode and velocity streamlines. For the case (a) $\mathcal{E}_s = 2804$ and (b) $\mathcal{E}_s = 700$, spatial representation of the real part of the Eulerian pressure component of the mode (blue-red gradient) and superimposed velocity streamlines (for the real part of the Eulerian velocity), and plot of the solid deformation scaled with an amplitude of 0.15 (orange thick line).

mode tends to deform the recirculating region as well as to bend the splitter plate.

Low-stiffness, symmetric unstable modes

Let us now finally consider the linear stability analysis for the case $\mathcal{E}_s = 223$ already studied previously by means of a non-linear simulation (region n_5). For this case, two unsteady, unstable pair of complex-conjugate modes are found in the spectrum depicted in Fig. 3.17a. The associated eigenvectors are represented in Fig. 3.17b.

The high-frequency mode (○) is depicted at the top. The real part of the streamwise velocity is represented. It shows similar features than that observed in the oscillating symmetric case, i.e. a vortex shedding velocity pattern in the wake. The solid deformation looks however different, the tip of the plate being bend again in the direction of the centreline.

The low-frequency unstable mode (◇) is depicted at the bottom of Fig. 3.17b. The visualisation

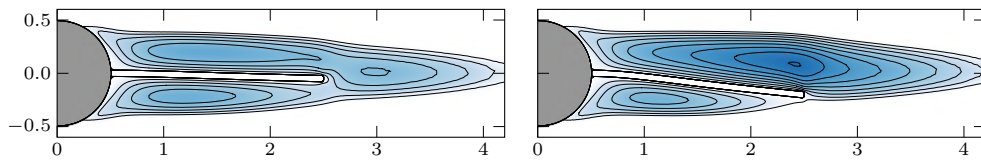


Figure 3.16 – Stationary flow modified by the steady mode. Plot of the sum of the steady baseflow velocity, plus the Lagrangian-based velocity perturbation, scaled by an amplitude 0.1 (left) and 0.4 (right). Contours indicate negative velocity levels between 0 and -0.15 .

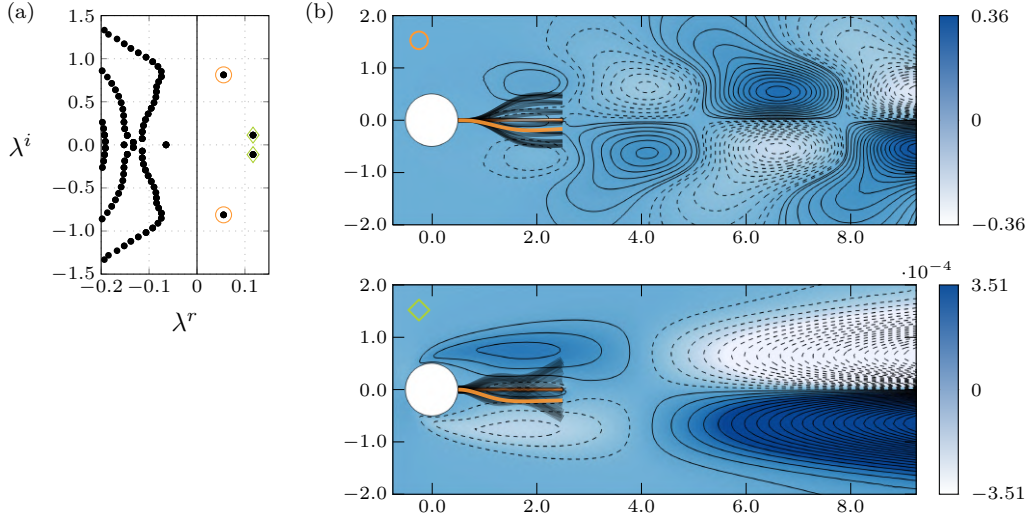
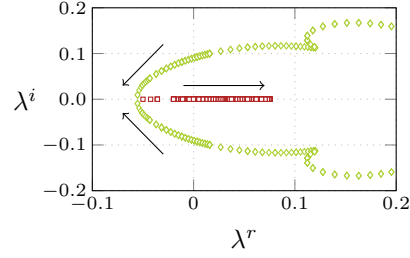


Figure 3.17 – Low-stiffness, symmetric unstable modes, $\mathcal{E}_s = 223$. (a) Eigenvalue spectrum showing low-frequency (\diamond) and higher-frequency (\circ) unstable modes. (b) Spatial representation of the real part of the Eulerian streamwise velocity (blue gradient and contours, dashed negative) in the steady deformed configuration, and snapshots of the solid deformation.

Figure 3.18 – Low frequency and steady modes. Plot of the steady modes (\square) and the low-frequency modes (\diamond) in the complex plane. Arrows indicate the direction of an increasing stiffness.



is again focused on the near-solid region, that present most of the interesting features of the modes. It should nevertheless be noted that advected structure are now found in the wake. Similar features as found for the stationary modes are observed in the near-solid region. In particular, the pressure acts in a similar way as before, by dragging the plate towards lower-pressure zones.

If we follow the position in the complex plane of the two low-frequency unsteady modes (Fig. 3.18), we observe that their frequency decreases as the stiffness increases, until they get stable. Increasing further the stiffness decreases eventually the frequency of the modes down to zero. At this point, the nature of the modes change: the branch of unsteady modes (\diamond) merge and results in the branch of steady modes (\square), that persists alone when the stiffness is increased. At some point, unstable steady modes are then found.

Parametric study in the stiffness range

We investigate here in a more systematic way how the variations of the rigidity coefficient \mathcal{E}_s affect the coupled fluid-structure spectrum. We focus only on the unstable modes, which are physically the most relevant, and forget all the other — stable — modes present in the spectrum of the linearised fluid-structure problem. Different regions (referred to as *linear* regions l_1, \dots, l_7) are observed, whose features are summarized in Tab. 3.2. The real and imaginary parts of the unstable modes are reported in Fig. 3.19. At very high rigidities, the system is found to be stable (no modes with $\lambda^r > 0$, region l_1). At sufficiently high stiffness, the system is actually equivalent to a decoupled fluid problem and the coupled spectrum reduces to that of the decoupled fluid problem, which is stable, as will be shown in Fig. 3.29b. By varying the Reynolds number, we have indeed observed that the flow about a rigid configuration becomes linearly unstable from $\mathcal{R}_e \simeq 92$.

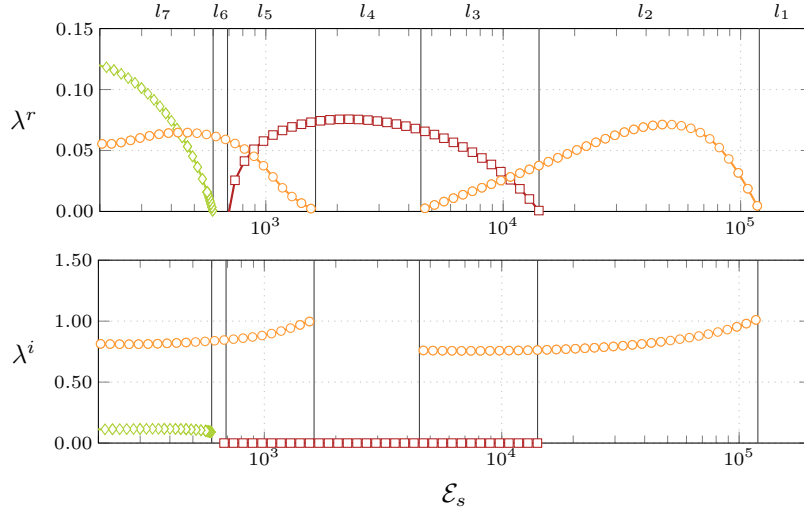


Figure 3.19 – Eigenvalue variation with \mathcal{E}_s . For the case $\mathcal{R}_e = 80$ and $\mathcal{M}_s = 1$, evolution of the unstable eigenvalues noted $\lambda = \lambda^r + i\lambda^i$, as a function of the plate stiffness coefficient \mathcal{E}_s . Unstable, unsteady modes are depicted with orange circles (\circ), steady modes are depicted with a red square symbol (\square) and low-frequency modes with a green diamond symbol (\diamond). The seven regions l_i summarized in Tab. 3.2 are delimited with vertical lines.

region	range	unstable modes
l_1	$\mathcal{E}_s > 119900$	none (stable)
l_2	$119900 > \mathcal{E}_s > 14157$	high-frequency
l_3	$14157 > \mathcal{E}_s > 4500$	high-frequency and steady
l_4	$4500 > \mathcal{E}_s > 1620$	steady
l_5	$1620 > \mathcal{E}_s > 690$	high-frequency and steady
l_6	$690 > \mathcal{E}_s > 600$	high-frequency
l_7	$600 > \mathcal{E}_s$	high-frequency and low-frequency

Table 3.2 – Summary of the different regimes reported from the linear stability analysis. The labels l_i for $1 \leq i \leq 7$ refer to the different regions of interest and are also reported in Fig. 3.12.

For our case with $\mathcal{R}_e = 80$ unstable modes appear when the stiffness is reduced. From $\mathcal{E}_s = 119900$, unstable modes are found (depicted with an orange color, regions l_2 and l_3), with frequencies decreasing from $\lambda^i \simeq 1$ at the upper threshold to $\lambda^i \simeq 0.8$ at the lower threshold at $\mathcal{E}_s = 4500$. A representative eigenvector ($\mathcal{E}_s = 88678$, region l_2) for these modes was presented in Fig. 3.13.

Decreasing the stiffness, a second type of unstable modes (depicted in red color, regions l_3 , l_4 , l_5) appears between $\mathcal{E}_s = 14157$ and $\mathcal{E}_s = 690$, that first coexist with the latter unstable modes (region l_3), then are alone (region l_4), before finally coexisting with another type of unstable modes at lower rigidities (region l_5). These modes are steady modes, as seen in Fig. 3.19 on the right. A representative eigenvector ($\mathcal{E}_s = 2804$, region l_2) for these modes was presented in Fig. 3.14.

Low-stiffness, high frequency modes are found in the regions l_5 , l_6 and l_7 . These modes are the only unstable modes only in the region l_6 . A representative mode eigenvector is displayed in Fig. 3.17b at the top. Finally, from $\mathcal{E}_s = 600$, another type of modes is found, with lower oscillation frequencies close to 0.1. These modes are represented with a green color in Fig. 3.19, and a typical eigenvector was represented in Fig. 3.17b at the bottom (for a mode with $\mathcal{E}_s = 223$ in the region l_7).

While only one unstable mode is found in regions l_2 , l_4 and l_6 , there is a coexistence of two modes in regions l_3 , l_5 and l_7 . Let us now compare these different regimes with what was observed in the non-linear simulations.

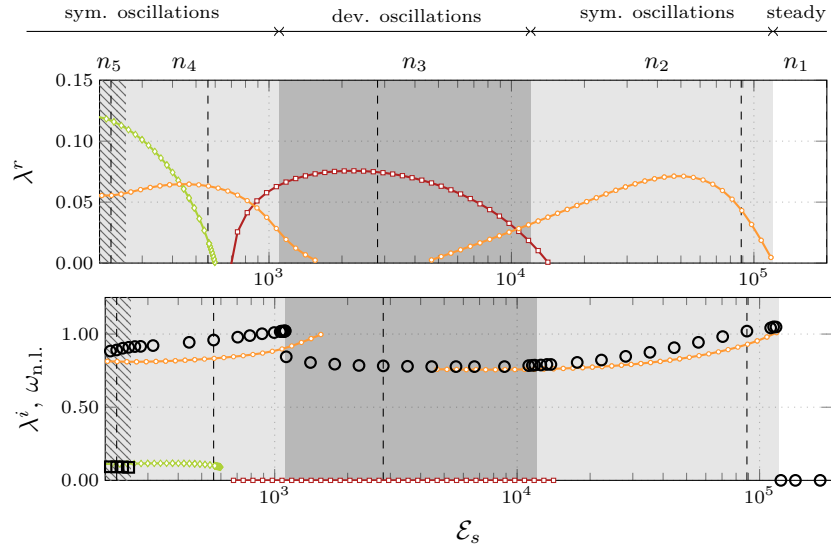


Figure 3.20 – Comparison with non-linear computations. Plot of the real λ^r (top) and imaginary (bottom) part λ^i for the unstable eigenvalues found by investigating the linear stability of the symmetric steady state. The values of the stiffness for the non-linear computations presented in §3.3.2 are reported with a dashed line, as well as the corresponding non-linear regimes n_1, \dots, n_5 . At the bottom, the largest-amplitude frequency peak $\omega_{n,1}$ in a Fourier-transform of the plate's tip end displacement is reported with circles (○) while square symbols (□) report (if any) frequencies with an high spectrum peak that are not harmonics from the previous one.

3.4.3 Comparison with non-linear results

We come back here on the results obtained with the non-linear simulations and presented in §3.3.2. The comparison is shown in Fig. 3.20, where the non-linear regions are superimposed on the graph giving the growth-rate and frequency of the linear modes. The white background indicate the region n_1 (steady cases). The light gray background at high stiffness refers to the region n_2 , and to the region n_4 at low stiffness. The dark gray background corresponds to the region n_3 (deviated oscillations). Finally, the quasi-periodic region n_5 is marked with the hatches. In addition, the vertical dashed lines indicate the position of the different non-linear calculations associated with each region n_i . The graph at the bottom further compares the non-linear frequencies (black circle and square symbols) and the linear frequency obtained as the imaginary part of the unstable eigenvalue (colors).

Transition between stable and unstable regions (n_1/n_2)

The first transition at $\mathcal{E}_s = 88678$ between the regions n_1 and n_2 is perfectly captured by the linear analysis. An oscillating situation is obtained non-linearly as soon as an unsteady mode (○) becomes unstable. Furthermore, close to the threshold the linear vibration frequency λ^i matches exactly the non-linear one, as represented in Fig. 3.20 at the bottom. A fairly good agreement is actually found over the whole range where the unsteady, high-frequency mode is unstable. A deviation not greater than 10 % is observed. The overall picture is clear for the cases where there is only one unstable mode: the instability develops according to this single mode, then eventually saturates non-linearly. Features observed linearly such as the pattern of oscillation in the plate are conserved in the limit-cycle, and the plate's oscillation frequency is only weakly modified non-linearly.

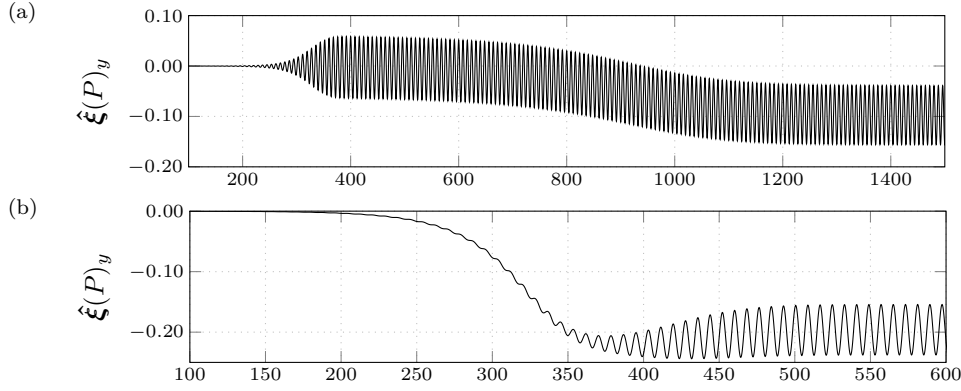


Figure 3.21 – Time-series in the vicinity of high-stiffness threshold n_2/n_3 . Plot of the plate's transverse tip displacement as a function of time for (a) $\mathcal{E}_s = 11164$ and (b) $\mathcal{E}_s = 6667$, both located in region n_3 .

Transition between symmetric and deviated regimes ($n_2/n_3/n_4$)

The steady modes are obviously related to the process that results in the deviated cases, for they indeed describe a deviation (see Fig. 3.16). The presence of unstable steady modes (\square) in the coupled fluid-structure spectrum does however not perfectly coincide with the presence, non-linearly, of a mean deviation (region n_3 , dark gray). If the deviated case is always observed non-linearly when the stationary mode is the only unstable one, the deviated/not deviated transitions occur somewhere in the region where the stationary mode coexists with an unsteady mode. Furthermore, *unsteady* oscillations are always eventually observed non-linearly, even in the region where the *steady* mode is the only unstable mode. This is for instance visible in the time-series in Fig. 3.8a, for a case located in the region l_4/n_3 : a mean deviation first sets in (in agreement with the presence of a single unstable, steady mode in the eigenvalue spectrum), but then unsteady oscillations develop. This pushes for seeking for a secondary instability, which will be the object of the next section.

For the moment, let us examine into more details the upper threshold at $\mathcal{E}_s = 12000$ between regions n_2 and n_3 . The instability threshold is predicted with a deviation of about 20 % by the stability analysis (transition between regions l_2 and l_3 at $\mathcal{E}_s = 14157$). Since two unstable modes coexist in the range $4500 < \mathcal{E}_s < 14157$ (region l_3), they interact non-linearly and might actually lead to different scenarios. For rigidities greater than 12000, the unsteady mode seems to be predominant, and leads to non-deviated oscillations. Below this threshold, the combined growth of the steady and unsteady modes result in oscillations superimposed to the quasi-steady deviation of the plate. For instance, at a stiffness $\mathcal{E}_s = 11164$ (Fig. 3.21a), the growth of the unsteady oscillating mode ($\lambda^r = 0.029$) coexists with that of the steady mode ($\lambda^r = 0.023$), resulting in oscillations that slowly reach a non-zero mean deviation. The deviation nevertheless occurs over a longer timescale than would be expected from the value of the growth-rate of the steady mode only, which emphasizes the non-linear effects at play there. At lower rigidities, the growth of the steady mode overcomes that of the unsteady mode: one observes first the static deviation, then oscillations that seem to appear as a secondary instability (Fig. 3.21b). On the other hand, as noted before, slightly above $\mathcal{E}_s = 12000$ and below $\mathcal{E}_s = 14157$, the growth of the symmetric oscillating mode overcomes that of the steady mode, and no deviation is observed. It is nevertheless also likely that the very small growth-rate of the steady mode prevents it from being visible during the period of time covered by our simulations (just in the case displayed in Fig. 3.21a it takes already 1000 non-dimensional time units for the deviation to take place).

In the vicinity of the lower threshold for the mean deviated cases (transition between regions n_4 and n_3), a less good agreement is found between the non-linear simulations (threshold at $\mathcal{E}_s = 1100$)

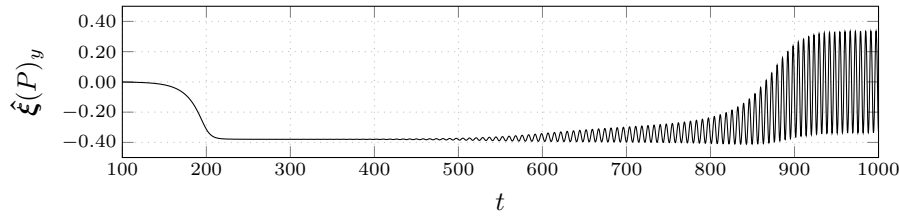


Figure 3.22 – Time-series in the vicinity of the low-stiffness threshold n_4/n_3 . Plot of the plate’s transverse tip displacement as a function of time for and $\mathcal{E}_s = 1091$.

and the linear stability analyses (threshold at $\mathcal{E}_s = 690$). In the vicinity of this transition, another type of behaviour is observed, as reproduced in Fig. 3.22. A deviation following the steady mode ($\lambda^r = 0.063$) first develops (this mode is the leading mode: the growth-rate for the oscillating symmetric mode is $\lambda^r = 0.026$). But then, unsteady oscillations develop from $t \simeq 400$, and eventually “kill” the deviation from $t \simeq 850$, which result in a limit cycle that has again a zero mean transverse displacement. This transition comes with a sudden frequency shift (Fig. 3.20) at $\mathcal{E}_s = 1100$.

Transition towards a quasi-periodic state (n_4/n_5)

Finally, let us examine the transition that leads to the quasi-periodic states. the linear analysis provides only little reliable information as to the threshold at which the quasi-periodic state is reached. It occurs when the low-frequency mode reaches a “very high” growth rate. For cases at higher stiffness, the high-frequency mode seems to dominate the initial growth and the non-linear saturation, like is for instance the case for the non-linear computation at $\mathcal{E}_s = 560$ (Fig. 3.9). On the other hand, as seen in Fig. 3.20 at the bottom, the two non-linear frequencies observed non-linearly match surprisingly fairly well with the frequencies of the two unstable modes.

3.4.4 Neutral stability curves

Before going further, let us briefly give a more general overview of the stability properties of the cylinder-splitter plate configuration. By varying the Reynolds number and the stiffness, we can determine stability regions in the $(\mathcal{E}_s, \mathcal{R}_e)$ plane. Results are displayed in Fig. 3.23, where the neutral curves ($\lambda^r = 0$) are displayed for the different modes evoked before. The general features already reported before are conserved when the Reynolds number is varied in addition to the stiffness, which allows to identify the different types of modes (low-frequency, steady and high-frequency) when both parameters are varied. At low Reynolds numbers, we observe that the configuration is stable: oscillations are damped by the viscosity. For Reynolds numbers greater than 92, a fourth type of mode is identified (its neutral stability curve is displayed with the blue color). This mode is clearly akin to the vortex-shedding, since it is the only unstable mode when the stiffness is high. Moreover, the marginal stability curve forms a line that is all the more horizontal when the Reynolds number is large, which also indicates the hydrodynamic nature of this mode. A typical mode of this kind will be studied more specifically in the next chapter on shape optimization.

At high Reynolds numbers, we observe that the upper limits (in terms of rigidity) of unstable zones for stationary, low-frequency and high-frequency modes form almost vertical lines. Rather than the Reynolds number, the instabilities are driven by the stiffness of the splitter plate. This is particularly the case for the steady mode.

No computations were done for Reynolds numbers higher than 140. When the Reynolds number increases well above the threshold of vortex shedding at $\mathcal{R}_e = 92$, the stationary flow field ceases indeed to be the relevant baseflow on which to perform the linear stability analysis (Sipp & Lebedev, 2007; Barkley, 2006) and other method should be employed.

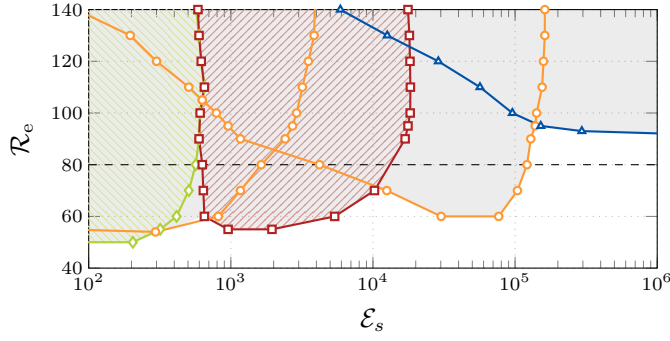


Figure 3.23 – Neutral curves in the $(\mathcal{E}_s, \mathcal{R}_e)$ plane. For a mass ratio $\mathcal{M}_s = 1$, plot of the neutral stability curves for steady modes (—), low-frequency modes (—), high-frequency modes (—) and vortex-shedding modes (—).

3.5 Steady deviated states and secondary instability

We have seen that unstable steady modes are found in the regions $l_3/l_4/l_5$. These modes are related to deviated equilibrium positions for the plate, and we will see that the thresholds are associated to symmetry-breaking pitchfork bifurcations that result in steady, deviated, non-linear equilibrium solutions. It is then possible to test the linear stability of these deviated solutions so as to characterize the secondary instabilities that might develop on the deviated configurations.

3.5.1 Computation of the non-linear deviated branches

The deviated branch that appears at the high-stiffness threshold at $\mathcal{E}_s = 14157$ can be computed using our steady solver. At a stiffness slightly below the threshold, the Newton solver is initialized by the symmetric steady flow plus the real part of the unstable eigenvector found by the linear eigenvalue analysis, scaled with a small amplitude 0.1. With this initial guess, the non-linear solver converges towards the steady deviated solution in a few iterations if the symmetry constraint (a Dirichlet boundary condition enforcing a zero transverse displacement along the centreline of the plate) is relaxed. It is then possible to compute the deviated states along this branch of non-linear solutions, by slightly reducing the stiffness at each step and take as an initial guess the steady deviated solution previously computed.

The corresponding results are reported in Fig. 3.24, where the lift coefficient for the plate and the cylinder is reported as a function of the stiffness. As the stiffness is decreased and crosses the critical value of $\mathcal{E}_s = 14157$, a supercritical pitchfork bifurcation occurs, that is associated with the apparition of two (up or down) steady deviated solutions, depending on the sign of the perturbation in the initial guess used in the Newton method. Just after the critical stiffness had been reached, the plate undergoes a deviation that follows the mechanism already reported in Fig. 3.16. When the stiffness is decreased, the deflection increases while the lower recirculation region shrinks. Along the lower branch, this process is associated with a rapid decrease of the lift coefficient, until it reaches a minimal value that correspond to the point where the tip end of the plate touches the limit between the recirculating and the free-stream region. At lower flexibilities, the plate tends to align with the free-stream streamlines, as visible in the inserts in the middle and at the bottom.

No difficulties have been experienced to follow the deviated branch, even below the second critical value at $\mathcal{E}_s = 690$. Note that even for a stiffness away from the divergence threshold, it is possible to “jump” directly from the steady, symmetric branch to the steady deviated branch, provided that the amplitude for the mode used in the initialisation of the Newton loop is well chosen. This is probably because the sum of the steady flow plus the perturbation is a fairly good approximation of the non-linear, steady deviated solution.

Initializing the Newton solver using the unstable mode was not sufficient to reach the non-linear, deviated branch close to the lower-stiffness threshold at $\mathcal{E}_s = 690$. Using this method, only the symmetric solution, or the deviated solution presented before could be reached. An additional constraint was therefore added in the non-linear loop, taking inspiration from arc-length methods

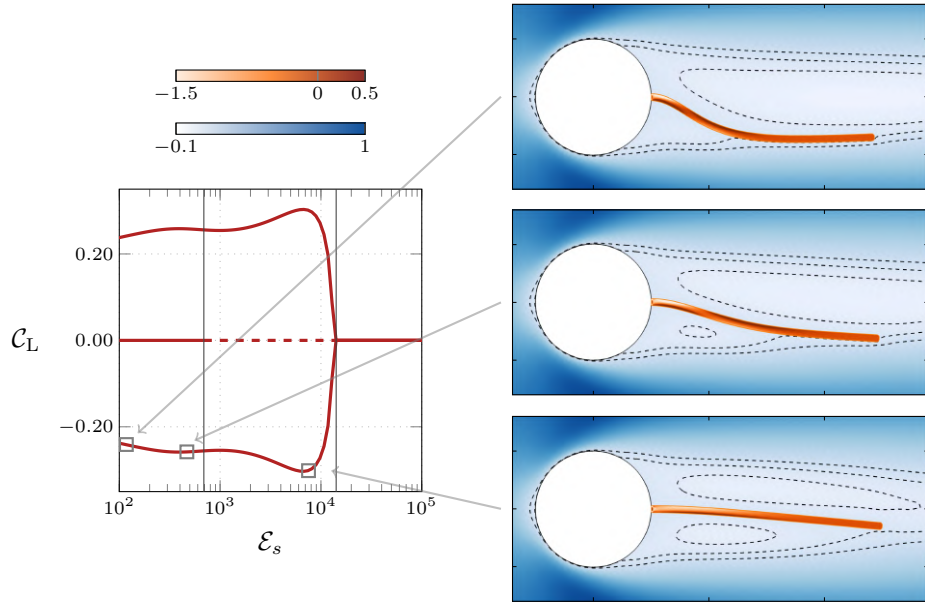


Figure 3.24 – Steady deviated configuration, supercritical branch. The graph on the left displays the bifurcation diagram, where dashed lines indicate unstable states with respect to the steady deviation. Horizontal lines mark the limits l_6/l_5 ($\mathcal{E}_s = 690$) and l_3/l_2 ($\mathcal{E}_s = 14157$) where the steady mode is marginally stable. A few deviated solutions are represented in the right side, for which the lift is directed towards the bottom (negative lift). Dashed lines indicate the contours where the streamwise velocity is zero and ± 0.05 .

(Chan & Keller, 1982). Namely, the solution was forced to be orthogonal (in the space of the state vector $\hat{\mathbf{Q}}$ plus the stiffness parameter \mathcal{E}_s) to the initial guess $\hat{\mathbf{Q}}_{(0)}$ composed of the steady solution plus the mode. The stiffness parameter is then itself an unknown that adapts so as to satisfy the orthogonality constraint. Using this method, it was possible to reach a non-linear, deviated branch, for values of the stiffness *below* the instability threshold. The transition between regions l_5 and l_6 comes therefore with a sub-critical pitchfork bifurcation, as reproduced in Fig. 3.25. The deviated branch is unstable to steady deviations and is thus marked with a dashed line.

3.5.2 Linear stability analysis of the deviated supercritical branch

Once non-linear, steady deviated solutions are computed, it is possible, using the same approach as in §3.4.2, to investigate the linear stability of this new equilibrium. We focus here on the supercritical branch, because it covers the region l_4 that did not exhibit modes that are consistent with the observations made from non-linear computations.

In this case, only one type of unstable, unsteady modes are found, represented in Fig. 3.26 with the cross symbols. For sake of comparison, the modes obtained about the symmetric configuration are also reported in the background, in light colors and following the same nomenclature as in Fig. 3.19.

Close to the high-stiffness threshold for a deviated equilibrium (l_3/l_4), the eigenvalues almost coincide with those obtained from the linear stability analysis of the steady, symmetric solution. Discrepancies appear away from the threshold. It is observed that the region where the steady mode (on the symmetric configuration) is unstable is associated to the modes on the deviated configuration having the lowest growth-rate, and a frequency that is close to that of the high-frequency modes. The frequency is reduced in the region $\mathcal{E}_s \sim 10^3$. Close to the low-stiffness threshold for static divergence and below, the growth-rate of the modes again increases while their frequency slightly decreases.

A representation of a few modes eigenvectors is displayed in Fig. 3.27. The pressure is represented in the fluid region while snapshots of the solid displacement are also displayed, showing the

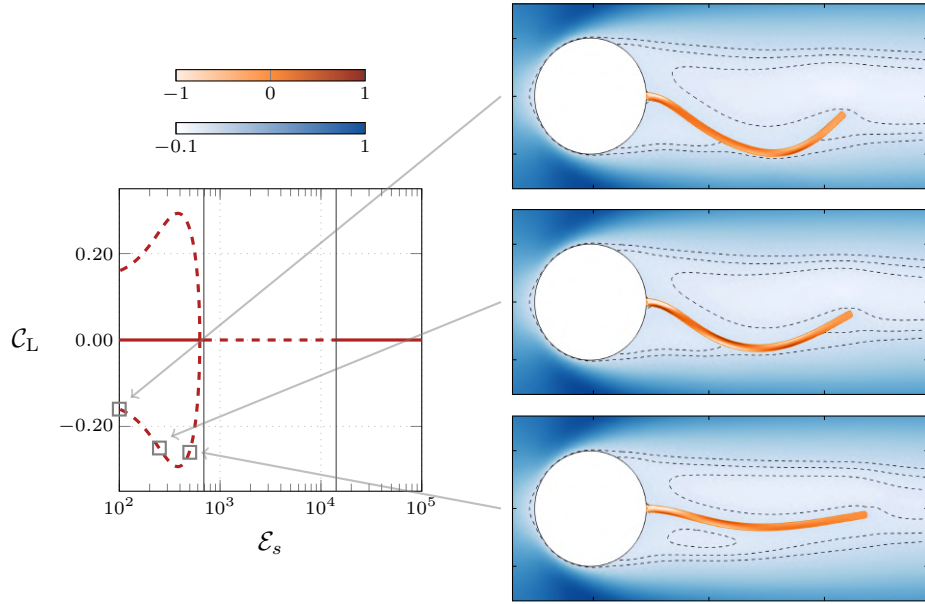


Figure 3.25 – Steady deviated configuration, subcritical branch. The graph on the left displays the bifurcation diagram, where dashed lines indicate unstable states with respect to the steady deviation. Horizontal lines mark the limits l_6/l_5 ($\mathcal{E}_s = 690$) and l_3/l_2 ($\mathcal{E}_s = 14157$) where the steady mode is marginally stable. A few deviated solutions are represented in the right side, for which the lift is directed towards the bottom (negative lift). Dashed lines indicate the contours where the streamwise velocity is zero and ± 0.05 .

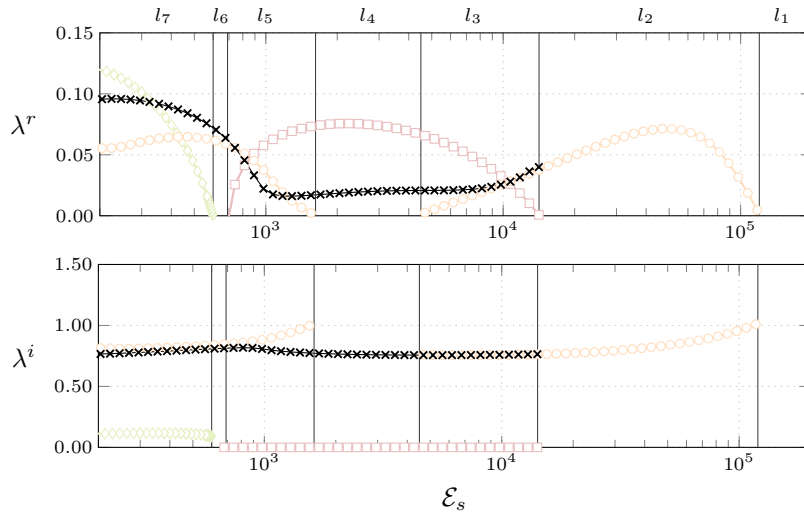


Figure 3.26 – Eigenvalue variation with \mathcal{E}_s on the supercritical deviated branch. For the case $\mathcal{R}_e = 80$ and $\mathcal{M}_s = 1$, evolution of the unstable eigenvalues (\times) noted $\lambda = \lambda^r + i\lambda^i$ computed by investigating the stability of the deviated supercritical branch, as a function of the plate stiffness coefficient \mathcal{E}_s . For comparison, unstable modes obtained in the symmetric case are also represented (\circ , \square , \diamond).

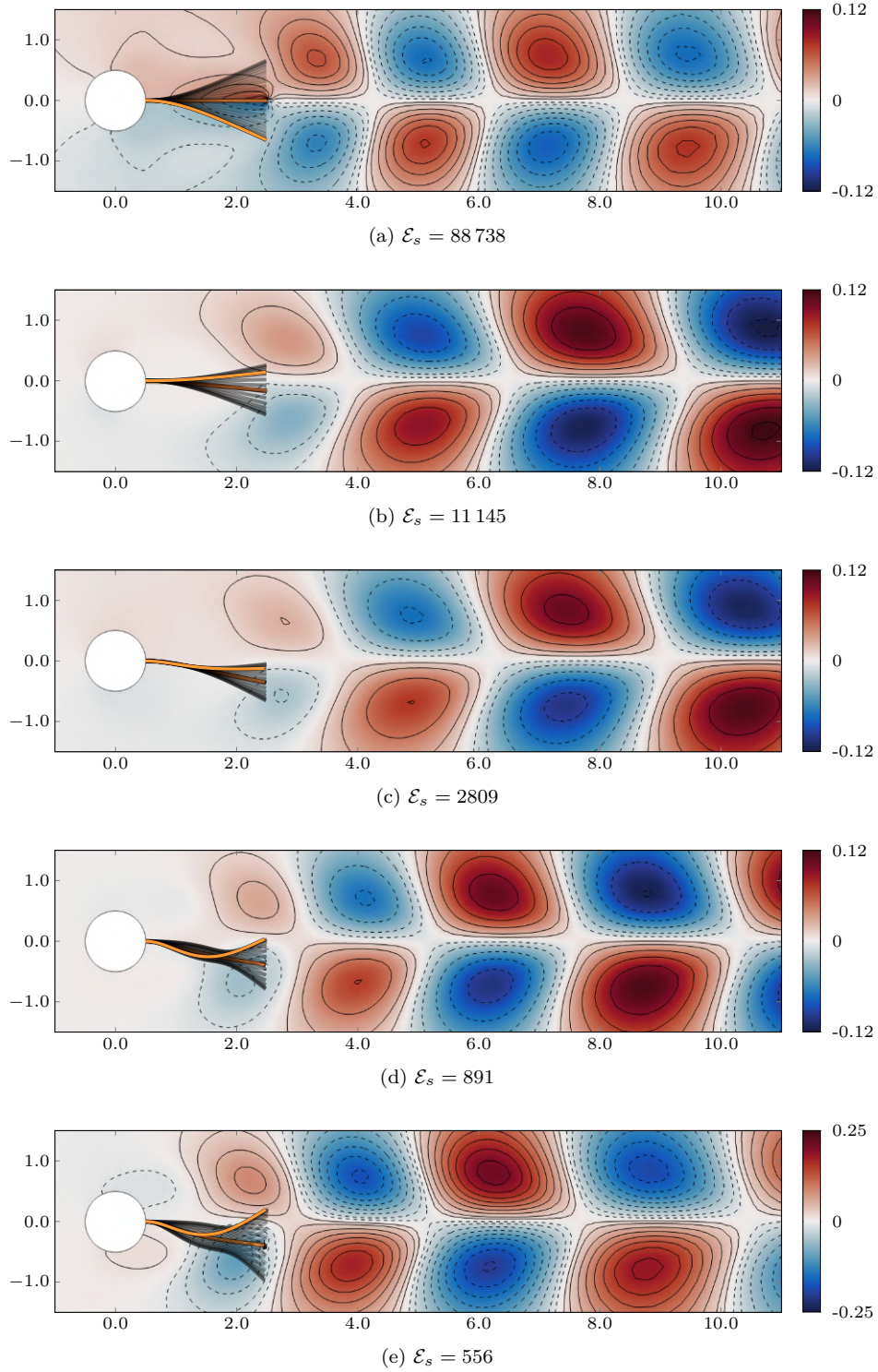


Figure 3.27 – Modes on the steady deformed configuration. Representation of the real part of the pressure component of the fluid-structure mode in the fluid region, and snapshots of the solid deformation (the real part of the displacement being emphasized by the orange color). Contours are the same in all the graphs.

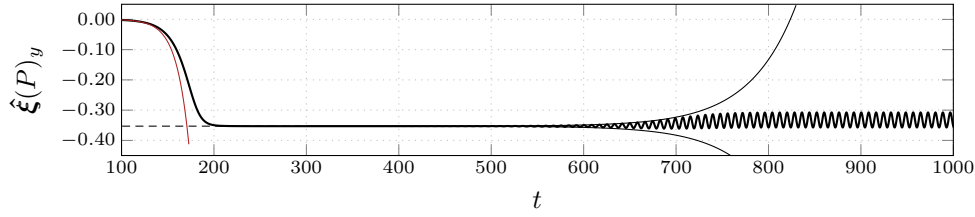


Figure 3.28 – Instability mechanism for the deviated case at $\mathcal{E}_s = 2804$. Plot of the plate's transverse tip displacement as a function of time, and exponential growths deduced from the linear stability analyses.

evolution of the deformation pattern from a pure S_1 mode to a combination of S_1 and S_2 modes when the stiffness is reduced. In (a) a non-deviated case is represented, while in (b-e) the modes on the deformed configuration are displayed. In particular, the case (b) is close to the high-stiffness divergence onset and shows little differences with (a) – except that the mean position of the splitter plate is now slightly deviated towards the bottom. In (c), a solid component S_2 starts to be visible in the solid deformation pattern. The same is observed in cases (d) and (e). Note that in cases (b-e) the unsteady deformation of the tip of the plate is directed towards higher-pressure zones. The real part of the mode is actually found to be close to the point where the maximal deformation occurs, i.e. just before when the low-pressure region will again aspire down the plate. A representation of the solid velocity shows that the transverse component is directed downwards in the vicinity of the tip.

We can finally explain what happens non-linearly in the region l_4 . The deviation first occurs according to the steady mode. The steady deviated state is eventually reached, which itself is unstable. The secondary instability grows on the deviated state and yields to small-amplitude oscillations about this deviated mean position. A time-series corresponding to this scenario is reported in Fig. 3.28, for a stiffness parameter $\mathcal{E}_s = 2804$ located in the region l_4 .

At lower values of the stiffness, other mechanisms than this secondary instability are at play: in particular, the frequency jump between regions n_4 and n_3 (Figs. 3.20 and 3.22) would suggest to study the linear stability of the periodic limit-cycle that develops on the deviated configuration. Other tools such as the Floquet analysis would then be required (Barkley, 1996), which is out of the scope of the present study.

3.6 Analysis in terms of solid vibration modes

In classical aeroelastic analyses, a modal analysis of the solid is first performed so as to project the solid dynamics on the basis of the so-called free vibration modes. This reduced model is then coupled to the fluid through an approximate models such as the well-known flutter derivatives (Dowell *et al.*, 2004). If such a model is sufficient for capturing some classical aeroelastic phenomena, in the case where the solid-to-fluid coupling is stronger, it is unable to predict the fluid-solid coupled dynamics (Mittal & Singh, 2005; Meliga & Chomaz, 2010; Navrose & Mittal, 2016). In our naturally fully coupled formulation, the fluid and solid intrinsic dynamics are coupled in an exact fashion. The decoupled solid and fluid modes can easily be computed, as eigenvalues and eigenvectors of sub-operators extracted from the full operator. Then, we can analyse into more details how the fluid-structure coupling affects these decoupled modes.

3.6.1 Analysis of the high-frequency modes dynamics

We focus here on the analysis of the high-frequency unstable modes obtained by investigating the linear stability of the symmetric steady flow (modes labelled ○ in Fig. 3.19).

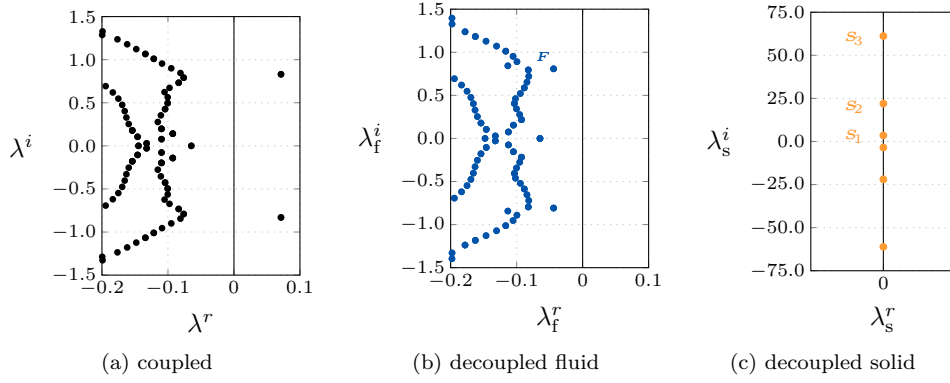


Figure 3.29 – Coupled and decoupled spectra. For the case $\mathcal{E}_s = 46\,800$, plot of the spectrum of (a) the coupled fluid-structure operator, the (b) decoupled fluid operator and (c) the decoupled solid operator (right).

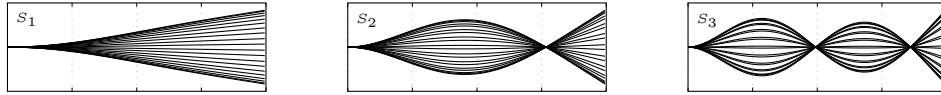


Figure 3.30 – Free vibration modes shapes. For the case $\mathcal{E}_s = 46\,800$, modal shapes S_1 , S_2 and S_3 found in the spectrum presented in Fig. 3.29c.

Decoupled spectra for a typical case in the region l_2

For a case at $\mathcal{E}_s = 46\,800$ (region l_2 with only one unstable, unsteady mode), the spectra for the fully coupled problem is computed in the left side of Fig. 3.29, showing one unstable, unsteady mode, while the spectra for the decoupled fluid ($\mathcal{T}_f, \mathcal{N}'_f$) and decoupled solid ($\mathcal{K}', \mathcal{M}_s$) operators are reported in the middle and right side, respectively.

Remark. A decoupling of the solid from the fluid occurs for instance physically for the solid when $\mathcal{M}_s \gg 1$ and finite values for $\mathcal{E}_s/\mathcal{M}_s$ i.e. for very large mass ratios. In that case all goes as if the solid was oscillating in a nearly vacuum, while the fluid responds to this oscillation (by means of the interface displacement transmitted by the extension operator) with only a weak feedback onto the solid. Under these assumptions, Meliga & Chomaz (2010) performed for instance a weakly non-linear expansion for the case of a spring-mounted cylinder, and could explain the sub-critical (with respect to the Reynolds number threshold) vortex shedding in terms of an interaction between a so-called wake mode and a structure mode. On the other hand, when $\mathcal{E}_s \rightarrow \infty$ then the fluid is decoupled from the solid and we recover the case of fluid instabilities in a rigid geometry.

The spectrum of the fluid operators ($\mathcal{T}_f, \mathcal{N}'_f$), reported in Fig. 3.29b, displays only stable modes and is typical to the spectrum computed for stable wake flows like the flow about a circular cylinder (Sipp & Lebedev, 2007). The least stable of these modes is noted (F), with $\lambda_f = -0.044 \pm 0.808i$. We clearly see on this case that the coupling of the solid and fluid operators through the interface continuity and shape deformation operators strongly affects the overall spectrum, that in particular cannot be obtained as a small deviation from either the decoupled-solid and decoupled-fluid spectra like in some previous works (Meliga & Chomaz, 2010) and thus justifies the need for a fully coupled approach. This makes sense, because the low density ratio $\mathcal{M}_s = 1$ comes with a strong coupling. In the following, we will examine how the coupled, high frequency modes vary, in the frequency range, compared to the free vibration modes.

By considering in the fully coupled problem (3.4.1) only the pair of operators ($\mathcal{K}', \mathcal{M}_s$) describing the solid dynamics, one obtains an eigenvalue problem describing the vibrations modes

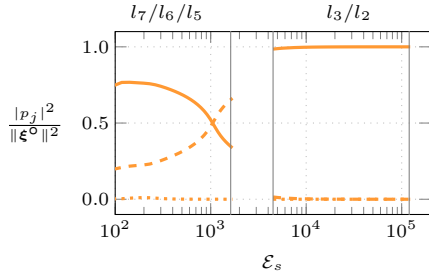


Figure 3.31 – Projection of the high-frequency modes on the free vibration basis. Normalized projection coefficients for the projection of the unstable, high-frequency modes, on the free-vibration modal basis with modes S_1 (solid line), S_2 (dashed line) and S_3 (dotted line). Vertical lines mark the limits of the instability regions reported in Fig. 3.19.

$\phi_{s,j}^o$ of the solid,

$$\left(\lambda_{s,j}^2 \mathcal{M}_s + \frac{\mathcal{E}_s}{\mathcal{M}_s} \mathcal{K}'(\mathbf{Q}) \right) \phi_{s,j}^o = 0. \quad (3.6.1)$$

These modes are that of the pre-stressed (by the steady equilibrium \mathbf{Q}) solid, vibrating at the frequency $\lambda_{s,j}$. The three lowest-frequency modes are labelled S_1 , S_2 and S_3 in Fig. 3.30, their shape is reported in Fig. 3.30. These are the three first bending modes for a beam. The solid problem is self-adjoint in absence of viscoelastic damping (Marsden & Hughes, 1994) and the solutions to (3.6.1) therefore form an orthogonal projection basis (normalization condition $\langle \phi_{s,i}^o, \mathcal{M}_s \phi_{s,j}^o \rangle = \delta_{ij}$). Taking a basis truncated to N modes, we can then write

$$\xi^o(\mathbf{x}) \simeq \sum_{j=1}^N p_j \phi_{s,j}^o(\mathbf{x}),$$

where $p_j = \langle \xi^o, \mathcal{M}_s \phi_{s,j}^o \rangle$ is the projection coefficient on the free vibration mode j . For the case $\mathcal{E}_s = 46\,800$, $|p_1| / \|\xi^o(\mathbf{x})\| \simeq 1$, indicating that the deformation of the coupled fluid-structure mode is almost exclusively that of a mode S_1 . This makes sense, given the shape of the solid deformation for the modes in the region l_2 (Fig. 3.13b).

Evolution with the stiffness: added mass & lock-in effects

Considering the fully coupled eigenmodes ξ^o computed by solving (3.4.1) for various values of \mathcal{E}_s , the evolution of the projection coefficients on the free vibration modal basis is reported in Fig. 3.31. In the regions l_3/l_2 , the coupled mode follows almost exclusively a modal deformation of type S_1 . In the regions, $l_5/l_6/l_5$, the component S_2 is non negligible, but the projection coefficient associated to the mode S_3 remains very low. For all cases, more than 90 % of the deformation energy is contained in the first two modes S_1 and S_2 . In the following, we therefore only retain these two modes for the comparisons.

The vibration frequency of the free vibration modes S_1 and S_2 are reported in Fig. 3.32a (solid and dashed line, respectively), together with the imaginary part of the unstable, high-frequency unsteady fully coupled modes (\circ). We observe that the frequency of the coupled modes is much lower than the frequency of the free-vibration modes. For instance, for $\mathcal{E}_s = 1 \times 10^4$ the coupled mode has a projection almost only on the mode S_1 but its frequency is half as low than that of the free mode S_1 at the same stiffness. On the other hand, comparing in Fig. 3.32c the fully coupled vibration frequencies and the frequency of the decoupled fluid mode (whose frequency corresponds to that of the leading mode λ_f in Fig. 3.29b), one sees that the coupled mode has more or less the frequency of the (stable) hydrodynamic wake mode in the vicinity of the low-stiffness instability threshold.

The significant decrease in frequency is classically attributed to an *added mass* effect (de Langre, 2002): all goes as if the solid had an increased mass and thus a lower eigenfrequency. To isolate the added mass effect from other fluid effects (for instance the shear forces caused by the presence of the bluff-body), it is convenient to determine the solid eigenmodes for a solid immersed in a fluid at rest. Thus, the only remaining effect is that of the momentum transport caused by small movements close to the vibrating solid. Strictly speaking, added mass effects can be reduced to an inertia coefficient only in the case of inviscid flows. For viscous flows, even at rest, viscosity causes

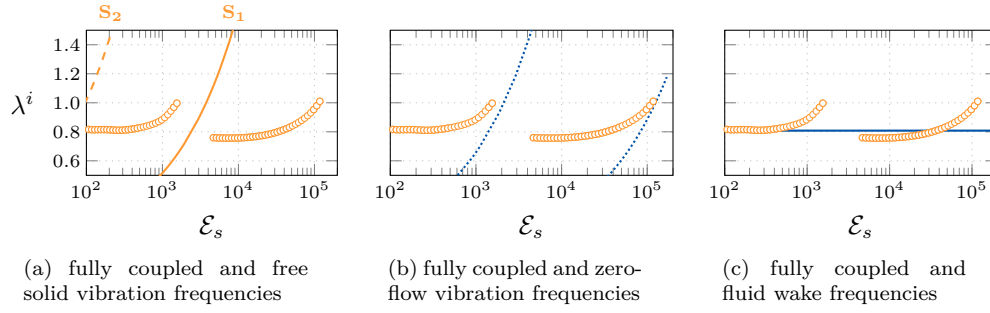


Figure 3.32 – Added-mass effects. Plot of the vibrations frequencies obtained by solving the fully coupled problem (unstable frequencies are marked with the orange circle \circ), together with (a) the free solid vibration frequencies of modes S_1/S_2 (—/—) obtained by computing the eigenvalue of the pair $(\mathcal{K}', \mathcal{M}_s)$, (b) the vibration frequencies (\cdots) computed in a still fluid and (c) the fluid wake frequency (—) obtained by computing the eigenvalues of the fluid operators.

the momentum transport to be delayed in time as it propagates in space, thus resulting in much more complex effects (Maxey & Riley, 1983). Our fully coupled approach can nevertheless be used to evaluate added mass effects, by simply setting to *zero* the solid steady displacement and fluid steady flow: in that case, all goes as if one was looking at the free, small-amplitude vibrations of the fully coupled problem in a still fluid.

The corresponding obtained vibrations frequencies are reported in Fig. 3.32b. The fully coupled frequencies are still reported in orange color (\circ), while the vibration frequencies for a solid in a still fluid are reported with the blue dotted line. One observes that at the right end of the branches, they match fairly well with the fully coupled frequencies, especially close to the high-frequency instability threshold. All goes as if the frequency of the coupled mode was “locked” onto that of the solid *corrected by added mass effects*.

3.6.2 Analysis of the low-frequency and steady mode dynamics

We have seen previously that the low-frequency and steady modes belong to the same branch of modes (Fig. 3.18). They are therefore conveniently studied together. Since the solid is compressed by the load arising from the steady fluid-solid equilibrium and may drive a solid buckling instability, we first investigate if such scenario could have occurred.

Solid buckling induced by the steady fluid-solid flow

We have seen that the solid deformation \mathbf{Q} — although small — is not zero: the steady fluid flow induces axial compression strains in the solid (see Fig. 3.5 where the compression displacement field is represented). We are thus here in the classical case of a long column loaded in compression, that may suddenly spring outward laterally in a bending mode if the load exceeds some threshold (Timoshenko & Gere, 1961). Thanks to the non-linear Saint-Venant Kirchhoff model chosen, this *buckling* instability can be analysed in terms of the eigenvalues of the linearised solid operator about the loaded state. Above the buckling threshold, the pair $(\mathcal{K}'(\mathbf{Q}), \mathcal{M}_s)$ display only pure imaginary eigenvalues $\lambda_{s,j} = \pm i\lambda_{s,j}^i$ that describe the free vibration frequencies of the solid. When the compression load increases, the vibration frequencies are decreased compared to a case without loading (Bokaian, 1990), i.e. the apparent stiffness of the plate is reduced. Increasing further the load, at some point the apparent stiffness is zero and a *divergence*, or buckling instability occurs. The trace for this in the eigenvalue spectrum is the apparition of pure real eigenvalues representing the static growth of an instability. On the other hand, when the stationary solid deformation is set to zero, then \mathcal{K}' does not depend any more on the stationary solution and the Saint-Venant Kirchhoff model reduces to the linear elasticity (recall that it only accounts for geometrical non-linearities), in which case the eigenvalues $\lambda_{s,j}$ are always pure imaginary numbers whatever the stiffness.

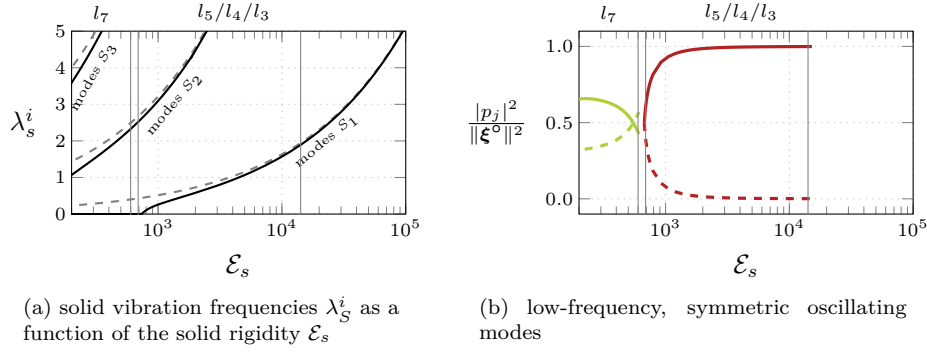


Figure 3.33 – Solid dynamics as a function of \mathcal{E}_s . Plot of (a) the solid vibration frequencies without (solid line) and with (dashed line) the pre-stress generated by the stationary fluid-structure equilibrium, and (b) snapshots of the transverse displacement for the modes 1 (top), 2 (middle) and 3 (bottom), computed without pre-stresses.

The vibration frequencies for the three first lowest-frequency solid modes S_1 , S_2 and S_3 , are represented in Fig. 3.33a as a function of the rigidity coefficient \mathcal{E}_s . The vibration frequencies about the pre-stressed configuration ($\mathbf{Q} \neq \mathbf{0}$) are represented with the solid line while the free vibration frequencies ($\mathbf{Q} = \mathbf{0}$) are displayed with the dashed lines. We see how the pre-stress diminishes the vibration frequency, down to the point that they become zero, which identifies the buckling threshold. Namely, at $\mathcal{E}_s = 755$ the first frequency suddenly decreases down to zero, while a non-zero complex part appears in the eigenvalue (not represented in Fig. 3.33a), which reflects the buckling instability.

The mechanism that drives the apparition of the steady unstable modes from $\mathcal{E}_s = 1460$ when the stiffness is reduced is obviously not a solid buckling instability, for the buckling threshold for the mode S_1 reported in Fig. 3.33a occurs for a stiffness about one order of magnitude lower (recall that the threshold for static instabilities is not affected by added mass effects, which only acts at a dynamical level).

Reduced model for the steady and low-frequency modes dynamics

To further clarify the physical mechanisms at play for the low-frequency/steady modes, a reduced model of the perturbation fluid-structure problem is considered in the following. Eliminating the fluid and extension variables from the coupled fluid-structure modal problem (3.4.1) by the same way as in §2.1.3, one obtains a problem that only depends on the solid displacement mode,

$$\left(\lambda^2 \mathcal{M}_s + \frac{\mathcal{E}_s}{\mathcal{M}_s} \mathcal{K}' \right) \xi^0 = \frac{1}{\mathcal{M}_s} \mathcal{A}_{\text{sfs}}(\mathbf{Q}_{\text{rigid}}; \lambda) \xi^0. \quad (3.6.2)$$

The left-hand side is the solid vibration problem (3.6.1) already studied before, while the fluid dynamics as well as the couplings are now written under the form of a solid-to-fluid-to-solid operator

$$\mathcal{A}_{\text{sfs}}(\mathbf{Q}_{\text{rigid}}; \lambda) = \mathcal{I}_{\text{fe}}^T \mathcal{R}_{\text{f}}(\mathbf{Q}_{\text{rigid}}; \lambda) \left(\mathcal{N}'_{\text{fe}}(\mathbf{Q}_{\text{rigid}}) \mathcal{A}_{\text{e}}^{-1} \mathcal{I}_{\text{e}\xi} + \lambda (\mathcal{I}_{\text{f}\xi} + \mathcal{T}_{\text{fe}}(\mathbf{Q}_{\text{rigid}}) \mathcal{A}_{\text{e}}^{-1} \mathcal{I}_{\text{e}\xi}) \right) \quad (3.6.3)$$

where $\mathcal{R}_{\text{f}}(\mathbf{Q}_{\text{rigid}}; \lambda) = (\lambda \mathcal{T}_{\text{f}}(\mathbf{Q}_{\text{rigid}}) - \mathcal{N}'_{\text{ff}}(\mathbf{Q}_{\text{rigid}}))^{-1}$ is the fluid resolvent operator. Under this form, the fully coupled problem is a solid vibration problem “forced” by a non-linear feedback term: the load response to a displacement perturbation is extracted by means of $\mathcal{I}_{\text{fe}}^T$ from the fluid dynamics, that is embedded in the – non-linear with respect to λ – resolvent operator $\mathcal{R}_{\text{f}}(\mathbf{Q}_{\text{rigid}}; \lambda)$. This part takes as an input three components: a dynamical part $\lambda \mathcal{I}_{\text{f}\xi}$ corresponding to the interface velocity forcing of the fluid, and two other parts that correspond to the influence, at both a static and dynamic level, of the domain deformation – by means of the shape deformation operator and the extension operator.

In the above formulation of the fully coupled fluid-structure modal problem, we have made the following approximation concerning the steady state: $\mathbf{Q} = [\mathbf{0}, \mathbf{0}, \mathbf{Q}_{\text{rigid}}]$, which amount to consider only the steady flow about a *rigid* solid. This is a fairly good approximation, both at the static and dynamical levels as long as we stay not too close from the buckling thresholds (see Fig. 3.33a that shows the vibration frequencies for the solid). Under this assumption, the model only depends on the rigidity through the explicit dependency that appear in front of the (thus assumed constant) solid operator \mathcal{K}' . Furthermore, we have seen in the previous section that the unstable low-frequency and steady mode involve primarily the free structural bending modes S_1 and S_2 . It is therefore convenient to project the modal dynamics of the coupled problem on the basis of these two free-vibration modes obtained by solving (3.6.1), i.e. note $\hat{\xi}^o(\hat{\mathbf{x}}) \simeq \alpha_1 \phi_{s,1}^o(\hat{\mathbf{x}}) + \alpha_2 \phi_{s,2}^o(\hat{\mathbf{x}})$ for some complex modal amplitudes α_i and eigenvectors $\phi_{s,i}^o$, and project the problem onto the free modal basis so as to obtain

$$\left(\lambda^2 + \frac{\mathcal{E}_s}{\mathcal{M}_s} K_i \right) \alpha_i = \frac{1}{\mathcal{M}_s} \sum_{j=1}^2 K_{ij}(\lambda) \alpha_j, \quad i = 1, 2, \quad (3.6.4)$$

where $K_i = \langle \phi_{s,i}^o, \mathcal{K}' \phi_{s,i}^o \rangle$ and $K_{ij}(\lambda) = \langle \phi_{s,i}^o, \mathcal{A}_{\text{sfs}}(\mathbf{Q}; \lambda) \phi_{s,j}^o \rangle$, and using the orthonormalization condition $\langle \phi_{s,i}^o, \mathcal{M}_s \phi_{s,j}^o \rangle = \delta_{ij}$ (recall that on the contrary to the fluid, the solid operator is self-adjoint).

Provided that we are close enough to the static instability threshold, $|\lambda|$ can be chosen arbitrarily small, and thus it can reasonably be assumed that $K_{ij}(\lambda)$ can be expanded by means of a Laurent series with respect to the complex variable λ , of the form

$$K_{ij}(\lambda) \simeq K_{ij}^{(0)} + \lambda K_{ij}^{(1)} + \lambda^2 K_{ij}^{(2)} \quad (3.6.5)$$

in the vicinity of the static instability threshold. In this notation, $K_{ij}^{(0)}$ defines the coefficients of a 2×2 added mass matrix, $K_{ij}^{(1)}$ those for an added damping matrix, and $K_{ij}^{(2)}$ the coefficients of an added mass matrix, that are given by

$$\begin{aligned} K_{ij}^{(0)} &= -\langle \phi_{s,i}^o, \mathcal{I}_{\text{f}\xi}^T \mathcal{A}_{\text{f}}^{-1} \mathcal{N}'_{\text{fe}} \mathcal{A}_{\text{e}}^{-1} \mathcal{I}_{\text{e}\xi} \phi_{s,j}^o \rangle, \\ K_{ij}^{(1)} &= -\langle \phi_{s,i}^o, \mathcal{I}_{\text{f}\xi}^T \mathcal{A}_{\text{f}}^{-1} (\mathcal{T}_{\text{f}} \mathcal{A}_{\text{f}}^{-1} \mathcal{N}'_{\text{fe}} \mathcal{A}_{\text{e}}^{-1} \mathcal{I}_{\text{e}\xi} + \mathcal{T}_{\text{fe}} \mathcal{A}_{\text{e}}^{-1} \mathcal{I}_{\text{e}\xi} + \mathcal{I}_{\text{f}\xi}) \phi_{s,j}^o \rangle, \\ K_{ij}^{(2)} &= -\langle \phi_{s,i}^o, \mathcal{I}_{\text{f}\xi}^T \mathcal{A}_{\text{f}}^{-1} \mathcal{T}_{\text{f}} \mathcal{A}_{\text{f}}^{-1} (\mathcal{T}_{\text{f}} \mathcal{A}_{\text{f}}^{-1} \mathcal{N}'_{\text{fe}} \mathcal{A}_{\text{e}}^{-1} \mathcal{I}_{\text{e}\xi} + \mathcal{T}_{\text{fe}} \mathcal{A}_{\text{e}}^{-1} \mathcal{I}_{\text{e}\xi} + \mathcal{I}_{\text{f}\xi}) \phi_{s,j}^o \rangle. \end{aligned}$$

The added stiffness matrix only depends on the static shape derivative \mathcal{N}'_{fe} , i.e. that expresses the modification of the stresses in the fluid as a result of a modification of the interface position. Added mass and added damping matrices have more complicated expressions, that depend on the direct load transfer through $\mathcal{I}_{\text{f}\xi}$, the static and dynamic shape derivatives, and several applications of the inverse of the static flow operator \mathcal{A}_{f} . Practically, the different coefficients K_{ij} are built at the discrete level, using the matrices resulting from the finite-element discretization of the different operators involved. The inverse matrices for the static fluid and extension problem never have to be explicitly formed since they are only involved in matrix-vector operations. We finally obtain the reduced-order eigenvalue problem

$$\left[\lambda^2 \left(\mathbf{I} - \frac{1}{\mathcal{M}_s} \mathbf{K}^{(2)} \right) - \lambda \frac{1}{\mathcal{M}_s} \mathbf{K}^{(1)} - \left(\frac{1}{\mathcal{M}_s} \mathbf{K}^{(0)} - \frac{\mathcal{E}_s}{\mathcal{M}_s} \mathbf{K} \right) \right] \boldsymbol{\alpha} = \mathbf{0} \quad (3.6.6)$$

where $\boldsymbol{\alpha} = [\alpha_1, \alpha_2]^T$ gathers the modal coefficients for projections on free solid modes S_1 and S_2 . The solid modal matrix \mathbf{K} is diagonal with coefficients 2.659×10^{-4} and 1.034×10^{-2} , \mathbf{I} is the identity matrix while $\mathbf{K}^{(0)}$, $\mathbf{K}^{(1)}$ and $\mathbf{K}^{(2)}$ write as

$$\underbrace{\mathbf{K}^{(0)} = \begin{bmatrix} 3.74 & -5.02 \\ 4.47 & 0.63 \end{bmatrix}}_{\text{added stiffness}}, \quad \underbrace{\mathbf{K}^{(1)} = \begin{bmatrix} -33.1 & -11.4 \\ -25.0 & -23.3 \end{bmatrix}}_{\text{added damping}}, \quad \underbrace{\mathbf{K}^{(2)} = \begin{bmatrix} -73.5 & 5.22 \\ -82.8 & -18.9 \end{bmatrix}}_{\text{added mass}}.$$

In these matrices, diagonal terms represent the actions of the mode on itself, while off-diagonal terms result from the coupling of the modes by the fluid.

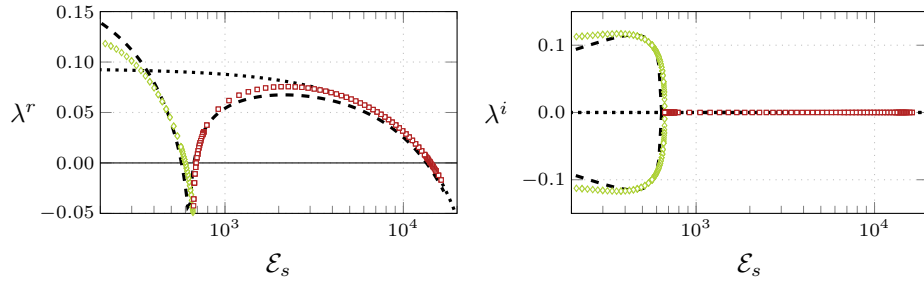


Figure 3.34 – Low frequency modes and reduced models. Plot of the frequency (left) and growth-rate (right) of the steady (\square) and low-frequency modes (\diamond) obtained as solutions of the fully coupled case, as well as from the modes obtained from the 2-degrees-of-freedom S_1/S_2 (—) and one-degree-of-freedom S_1 (\cdots) approximate models, as a function of the rigidity coefficient \mathcal{E}_s .

The unstable eigenvalues from (3.6.6) are represented in the Figure 3.34 as a function of the stiffness \mathcal{E}_s with a dashed line, together with the eigenvalues obtained with the fully coupled fluid-structure eigenvalue problem. The two modal branches are formed first by a pair of steady modes, that suddenly separate into a pair of unsteady modes. One observes that the instability threshold for both the stationary modes and the low-frequency modes is very well predicted by the two degrees-of-freedom reduced model, as well as the frequency and growth-rate. This shows again that the dynamics of these modes is not associated with the buckling instability of the solid, because our model assumes a rigid stationary geometry. Rather, added mass, damping and stiffness effect coming from the coupling with the fluid are at play. Especially, the divergence threshold is marked by a destabilization because of an added stiffness that overcomes that of the solid — when $\lambda = 0$ in (3.6.6) there is indeed an equilibrium between the solid stiffness and the fluid added stiffness.

The first mode S_1 is found to be essentially involved in the destabilization process in the vicinity of the high-rigidity threshold, while the combination of modes S_1 and S_2 drives the lower-stiffness thresholds. This is in accordance with the modal projections depicted in Fig. 3.33b. A reduced model where the projection basis only involves the mode S_1 predicts well the apparition of a static mode at $\mathcal{E}_s = 14160$, but not the re-stabilization at $\mathcal{E}_s = 690$ (dotted line). On the other hand, a model with only the second mode S_2 results in an unsteady, *stable* ($\lambda^r = -0.58$) mode down to $\mathcal{E}_s = 720$ then a steady and still stable mode at lower stiffness. Note also that when both the added mass and added damping matrices are set to zero, the static and low-frequency instabilities are still predicted with the fairly good thresholds, but the growth-rate is completely overestimated (by about a factor 20) as well as the frequency in the low-frequency region. By the same way, neglecting the added-mass matrix still provides a good description of the instabilities, probably because added-mass effect have a limited influence on the low-frequency dynamics.

We can now clarify the low-frequency instability mechanisms. The static instability appears at the high-stiffness threshold as a divergence instability that develops when the negative added stiffness associated to the mode S_1 overcomes the restoring elastic force. The re-stabilization at lower stiffness and the apparition of the low-frequency mode results from the interaction between the modes S_1 and S_2

Remark. One may wonder why the approach presented above was not used also in the case of high frequency modes. Indeed, the coupled dynamics is then reduced to a system with only a few degrees of freedom. The key assumption in the above development was to assume that the solid-to-fluid-to-solid operator can be approximated by a development of the form of (3.6.5). It turns out that this approximation ceases rapidly to be true when $|\lambda|$ is moving away from zero (see also the discussion in §2.1.3).

3.7 Conclusion

The linear stability of a system constituted by a flexible splitter plate attached behind a rigid cylinder has been considered, and compared with non-linear simulations. When the stiffness is reduced, non-linear simulations show that harmonic flow-induced oscillations appear. Decreasing more the stiffness results in harmonic oscillations about a deviated mean position for the splitter plate, while secondary frequencies appear at even lower rigidities. The linear stability analysis is able to predict the onset for the flow-induced vibrations, and results in various types of coupled fluid-structure modes, that have been described. Furthermore, this analysis provides an explanation for the mechanism at the origin of the deviated oscillations, in terms of a static divergence mode superimposed to unsteady fluid-elastic modes. Mechanisms at the origin of the coupled vibration frequency such as lock-in and added mass have also been characterized by this means. It is observed that several features present in the linear modes are actually conserved in the non-linear limit-cycles, when one single unstable mode is dominant. When two mode present about the same growth-rate, other types of analyses such as weakly non-linear expansions would be mandatory to get a more precise description of the non-linear evolution of the perturbations.

4

CONTROL OF FLUID-STRUCTURE LINEAR INSTABILITIES WITH SHAPE OPTIMISATION

In the previous chapter, self-developing fluid-elastic instabilities were described on a model problem constituted by an elastic plate attached to a circular cylinder in a laminar flow. We address here the problem of the passive control of these instabilities by means of shape optimization. An adjoint-based method for obtaining an explicit formula for the shape gradient of a cost-function based on the coupled fluid-structure eigenvalue is first presented. These results are applied on the two types of modes in the cylinder splitter-plate configuration previously studied. Deforming the cylinder's surface according to what is prescribed by the shape optimization algorithm, we show that it is possible to stabilize the modes, but also to design a fluid-structure oscillator beating at a prescribed frequency.

Contents

4.1	Introduction	106
4.2	Optimization problem setting	107
4.2.1	Fluid-structure model	107
4.2.2	Time-linearised perturbations of a non-linear steady flow	107
4.2.3	Optimization cost-function	108
4.3	Shape gradient computation & optimization loop	109
4.3.1	Lagrangian approach for shape optimization	109
4.3.2	Governing equations	110
4.3.3	Shape gradient computation	114
4.3.4	Practical gradient evaluation & optimization loop	115
4.4	Application to the cylinder splitter-plate case	116
4.4.1	Description of the unstable modes	117
4.4.2	Adjoint modes & abstract sensitivity analysis	119
4.4.3	Shape gradients	121
4.4.4	Shape optimization for controlling the growth-rate of the modes	124
4.4.5	Shape optimization for controlling the frequency of the modes	128
4.5	Conclusion	132

4.1 Introduction

We consider here the shape optimization of the cylinder–elastic plate system already considered in the previous chapter. The shape of the rigid cylinder is modified, so as to minimize a cost-function based on the eigenvalues of the fully coupled, unsteady linear fluid-structure modal problem written for perturbations about a steady non-linear state.

In the context of shape optimization, the key ingredient is to compute the sensitivity of the cost-function with respect to a variation of the shape at the continuous level, for it allows to obtain an explicit formula (Allaire & Schoenauer, 2007). This represents then the most efficient approach, since the sensitivity is obtained at a computational cost that is independant from the number of design variables. These ideas from the control theory (Lions, 1971) were applied in the context of hydrodynamics for minimizing the drag of a profile in a Stokes flow by Pironneau (1973) using an adjoint-based approach, and extended a few years later to the viscous, laminar case by Glowinski & Pironneau (1976).

The derivation of adjoint fluid-structure equations is a tedious task, which pushed in the past for considering approximate approaches where the geometrical couplings are neglected (Failer *et al.*, 2016; Feppon *et al.*, 2018). In particular, within the so-called *frozen domain velocity* approximation (Helgason & Krajnović, 2015; Heners *et al.*, 2018), time-dependant ALE adjoint equations are relatively easily obtained by assuming that the time-dynamics of the flow is much faster than the mesh movement dynamics. Under this assumption (whose physical meaning does not seem to be really clear), the sensitivity to the domain displacement is simply obtained as a post-processing (Helgason & Krajnović, 2015), but of course the coupling not considered in a fully consistent way. A continuous adjoint ALE equation was obtained for a stationary Stokes flow coupled with a chord model by Van der Zee *et al.* (2011), for the purpose of goal-oriented error estimation. To our knowledge, the first attempt for deriving then solving a fully coupled fluid-structure adjoint problem was done by Manzoni & Ponti (2016) using an Eulerian-based approach: they derived a continuous adjoint fluid-structure problem for an unsteady Stokes flow interacting with a one-dimensional Koiter solid model. Their derivation resulted in an unsteady Stokes problem backward in time and expressed in the deformed configuration, coupled with the solid model through a rather complicated interface term, that was found to depend on the adjoint flow field and on the geometric properties of the interface (for instance, the expression involves the tangential gradient of the normals). The authors used then the adjoint equations to solve a shape optimization problem inspired by haemodynamics concerns. In this work, we rather adopt the Lagrangian-based approach for deriving a shape gradient formula in the fully coupled case, because of its more favourable numerical properties (see the chapter 2).

Turning now on the unsteady effects, only few attempts for taking into account a *self-developping* unsteadiness in the flow about a structure to be optimized were done. In the context of pure hydrodynamics, one can mention the work by Heuveline & Strauß (2009) where the geometry is parametrized by a few points, and that by Nakazawa & Azegami (2016) who used an adjoint-based approach without an *a-priori* parametrization of the shape. For both cases, efforts are put on the stabilization of an unstable mode developing on the steady viscous Navier-Stokes solution, in the case of a rigid geometry. We continue on this way by considering the time-linearised fluid-solid perturbations developing on the steady equilibrium.

In the following sections, we first state the optimization problem, the governing state and adjoint equations are then presented, and details on the numerical method are given. The approach is then used to control the system studied in the previous chapter. Varying the Reynolds number of the flow and the stiffness of the material, two types of unstable modes can be found, one essentially related to the wake instability and another related more specifically to the fluid-structure coupling. The shape gradients for these two modes are presented and analysed, then the shape optimization is carried out.

4.2 Optimization problem setting

4.2.1 Fluid-structure model

We consider here the interaction between an incompressible fluid and the Saint-Venant Kirchhoff elastic material already considered in the previous chapter. The equations are written in the stress-free reference domain $\hat{\Omega}$ that is constituted by the solid geometry $\hat{\Omega}_s$ taken as not deformed, and the complementary fluid region $\hat{\Omega}_f$. When time goes on, due to the interaction between the fluid and the solid, recall that the actual (observable) domain evolves with time and differs from the reference domain. For sake of clarity, whenever possible the problem will be written under the symbolic operator notation of the problem (1.1.1), that is

$$\hat{\mathcal{T}}_{\text{fsi}}(\hat{\mathbf{q}}) \frac{\partial \hat{\mathbf{q}}}{\partial t} - \hat{\mathcal{N}}_{\text{fsi}}(\hat{\mathbf{q}}) = 0, \quad (4.2.1)$$

where the fluid-solid operator $\hat{\mathcal{T}}_{\text{fsi}}$ is obtained from (1.1.35), and $\hat{\mathcal{N}}_{\text{fsi}}$ from (1.1.36). The state vector $\hat{\mathbf{q}}(\hat{\mathbf{x}}, t)$ contains all the fluid-solid variables, split between a solid variable $\hat{\mathbf{q}}_s$ (containing the solid displacement $\hat{\boldsymbol{\xi}}$ and the solid velocity $\hat{\mathbf{u}}_s$, so as to have a first-order problem in time), an extension variable $\hat{\mathbf{q}}_e$ containing the extension displacement $\hat{\boldsymbol{\xi}}_e$ and the interface Lagrange multiplier $\hat{\boldsymbol{\lambda}}_e$ ensuring the continuity of the displacement at the interface, and a fluid variable $\hat{\mathbf{q}}_f$ composed of the fluid velocity $\hat{\mathbf{u}}$, the fluid pressure \hat{p} and the interface Lagrange multiplier $\hat{\boldsymbol{\lambda}}$ ensuring the continuity of the velocity at the fluid-structure interface.

4.2.2 Time-linearised perturbations of a non-linear steady flow

Like in the previous chapters, we assume that the flow can be approximated by a finite-amplitude steady component, plus a time-dependant perturbation component of infinitesimal amplitude $\varepsilon \ll 1$. The coupled fluid/elastic state vector $\hat{\mathbf{q}}(\hat{\mathbf{x}}, t)$ is thus split as follows:

$$\hat{\mathbf{q}}(\mathbf{x}, t) = \hat{\mathbf{Q}}(\mathbf{x}) + \varepsilon \Re \{ \hat{\mathbf{q}}^\circ(\mathbf{x}) \exp((\lambda^r + \mathbf{i}\lambda^i)t) \} + o(\varepsilon), \quad (4.2.2)$$

where $\hat{\mathbf{Q}}(\mathbf{x})$ is a steady solution of (4.2.1), and $\hat{\mathbf{q}}^\circ(\mathbf{x}) \exp(\lambda t)$, with $\lambda = \lambda^r + \mathbf{i}\lambda^i$, is the complex linear perturbation field taken under the form of a global mode (Sipp *et al.*, 2010). Neglecting the higher-order terms, we obtain a description of the fluid-structure system where the steady, non-linear component of the flow is taken into account, as well as its asymptotic stability when $t \rightarrow \infty$. A case with $\lambda^r < 0$ means that a small perturbation to $\hat{\mathbf{Q}}(\mathbf{x})$ will eventually decay exponentially, while $\lambda^r > 0$ means that this perturbation is exponentially amplified, leading to the development of an unsteady flow with structural vibrations at the frequency λ^i , at least during the linear phase of the instabilities.

Plugging the decomposition (4.2.2) into (4.2.1), the governing equations for the steady (order ε^0) and unsteady (order ε^1) parts then writes as follows:

$$-\hat{\mathcal{N}}_{\text{fsi}}(\hat{\mathbf{Q}}) = 0 \quad \text{in } \hat{\Omega}, \quad (4.2.3)$$

$$\left\{ (\lambda^r + \mathbf{i}\lambda^i) \hat{\mathcal{T}}_{\text{fsi}}(\hat{\mathbf{Q}}) - \hat{\mathcal{N}}'_{\text{fsi}}(\hat{\mathbf{Q}}) \right\} \hat{\mathbf{q}}^\circ = 0 \quad \text{in } \hat{\Omega}. \quad (4.2.4)$$

The first equation represents the steady equilibrium equations (2.1.2), while the second equation is the linear modal perturbation problem about this steady equilibrium. In particular, recall that the linear operator $\hat{\mathcal{N}}'_{\text{fsi}}(\hat{\mathbf{Q}})$ corresponds to the linearisation of $\hat{\mathcal{N}}_{\text{fsi}}$ about the steady stationary solution $\hat{\mathbf{Q}}$,

$$\hat{\mathcal{N}}'_{\text{fsi}}(\hat{\mathbf{Q}}) \hat{\mathbf{q}}^\circ = \left. \frac{\partial \hat{\mathcal{N}}_{\text{fsi}}}{\partial \hat{\mathbf{q}}} \right|_{\hat{\mathbf{q}}=\hat{\mathbf{Q}}} \hat{\mathbf{q}}^\circ.$$

The problem (4.2.4) is an eigenvalue problem, that admits a set of solutions $\{\lambda_1^r + \mathbf{i}\lambda_1^i, \hat{\mathbf{q}}_1^\circ; \lambda_2^r + \mathbf{i}\lambda_2^i, \hat{\mathbf{q}}_2^\circ; \dots\}$ whose size depends on the numerical discretization of the problem and on the spectral properties of the continuous linear operator. However, the only eigenvalue pair that is of interest

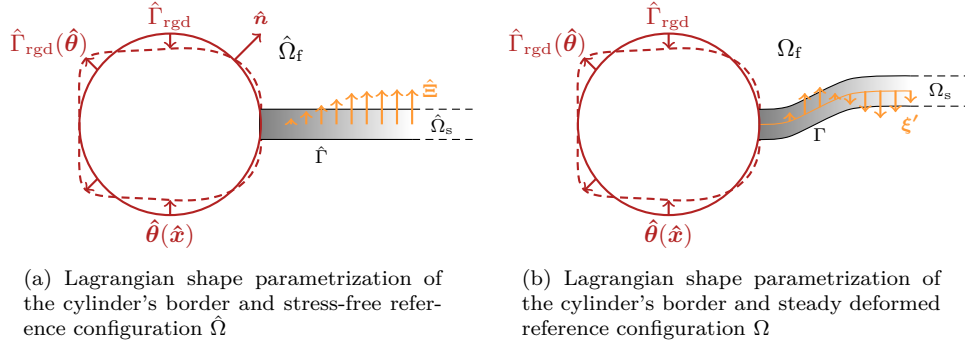


Figure 4.1 – Lagrangian shape parametrization. Sketch representing the Lagrangian parametrization $\hat{\theta}$ of the shape of the cylinder (a) in the stress-free reference configuration and (b) in the steady deformed configuration deduced from the stress-free reference configuration by means of the steady displacement $\hat{\Xi}$. The displacement perturbation field in the steady deformed configuration is represented by ξ' .

here is the one that has the largest growth-rate, because it becomes predominant over the other modes when $t \rightarrow \infty$. For that reason, in all what follows, it should be always understood that the pair $\{\lambda^r + i\lambda^i; \hat{q}^\circ\}$ corresponds to the mode of (4.2.4) having the largest growth-rate (leading mode).

4.2.3 Optimization cost-function

The question is: which *optimal* shape stabilizes or destabilizes the perturbations, or modifies the frequency of unstable fluid-solid oscillations in a prescribed way? We therefore introduce a cost-function based on the most unstable eigenvalue of (4.2.4), and the optimization problem reads

$$\min_{\hat{\Omega} \in \mathcal{W}_{\text{ad}}} \mathcal{J}(\hat{\Omega}), \quad \mathcal{J}(\hat{\Omega}) = \frac{\alpha_r}{2} \left(\lambda^r(\hat{\Omega}) - \lambda_c^r \right)^2 + \frac{\alpha_i}{2} \left(\lambda^i(\hat{\Omega}) - \lambda_c^i \right)^2 \quad (4.2.5)$$

under the constraints (4.2.3) and (4.2.4). In the above notation, λ_c^r and λ_c^i are the control parameters, and α_r and α_i belong to $\{0, 1\}$. For instance when $\alpha_r = 1$ and $\alpha_i = 0$ one tries to control only the growth-rate of the perturbations while the frequency is left free.

Let us now precise what we mean here by “shape”. We will consider in the applications the cylinder splitter-plate configuration already studied in the previous chapter, and deform the **rigid** cylinder (more precisely, the portion $\hat{\Gamma}_{\text{rgd}}$ of the cylinder represented with the red colour in Fig. 4.1, that excludes the portion Γ_s^D where the splitter plate is clamped) through the shape optimization process. In the above formula, \mathcal{W}_{ad} is a set of admissible shapes defined here as the set containing all the shapes that can be obtained by continuously deforming the initial shape made by the circular cylinder (this excludes for instance the creation or coalescence of holes), and such that the farfield boundaries Γ_∞ , Γ_s^D and $\hat{\Gamma}$ are kept fixed.

Special attention should be paid to the different domains in the context of fluid-structure interactions: in addition to the variations of the domain introduced for the purpose of shape optimization, the structure might also deform by itself because it is flexible and is subject to the loads coming from the surrounding fluid (see Fig. 4.1). Like in the chapter 2 we therefore distinguish between (a) the stress-free reference configuration and (b) the steady deformed configuration. Since $\hat{\Gamma}_{\text{rgd}}$ is a portion of the *rigid* part of the domain's boundary, it can however only be deformed during the shape optimization process: spatially, there is no overlap between the deformation induced by the shape optimization and the deformation induced by the fluid-elastic coupling. In the vicinity of $\hat{\Gamma}_{\text{rgd}}$ the stress-free and steady deformed configuration therefore coincide — which is not *a priori* the case close in the neighbourhood of the elastic solid.

4.3 Shape gradient computation & optimization loop

The solution of the optimization problem (4.2.5) is sought using gradient descent. The key point is therefore to derive a formula for the gradient of \mathcal{J} with respect to a modification of $\hat{\Omega}$.

4.3.1 Lagrangian approach for shape optimization

To define the notion of differentiation with respect to a geometrical domain, we presently rely on the boundary variation approach initially developed by Hadamard (1908). Developments of this approach have led to what is now called *geometric* shape optimization (Henrot & Pierre, 2006; Allaire & Schoenauer, 2007; Delfour & Zolésio, 2011). In this framework, the variations of the stress-free reference domain $\hat{\Omega}$ are considered on the form of a Lagrangian parametrization

$$\hat{\Omega}(\hat{\theta}) = (\text{Id} + \hat{\theta})(\hat{\Omega}) \quad (4.3.1)$$

where $\hat{\theta}$ is a smooth, one-to-one field (Henrot & Pierre, 2006) used to deform the interface $\hat{\Gamma}_{\text{rgd}}$, as visualised on the sketches in Fig. 4.1. For $\hat{\Omega}$ to be in \mathcal{W}_{ad} , we set

$$\hat{\theta} : \mathbb{R}^2 \rightarrow \mathbb{R}^2, \quad \hat{\theta} = \mathbf{0} \quad \text{on } \Gamma_{\infty} \cup \Gamma_{\text{s}}^{\text{D}} \cup \hat{\Gamma},$$

that is, $\hat{\theta}$ is allowed to be non-zero only on the interface $\hat{\Gamma}_{\text{rgd}}$ to be optimized. With this respect, taking a derivative with respect to $\hat{\Omega}$ amounts to differentiate with respect to the *field* $\hat{\theta}$ close to zero. Using the Lagrangian parametrization of the domain, the Taylor expansion of the cost-function (4.2.5) with respect to a small domain variation is naturally defined as

$$\mathcal{J}(\hat{\Omega}(\hat{\theta})) = \mathcal{J}(\hat{\Omega}) + \mathcal{J}'(\hat{\Omega})(\hat{\theta}) + o(\|\hat{\theta}\|), \quad (4.3.2)$$

where at the linear order, the function $\hat{\theta} \mapsto \mathcal{J}'(\hat{\Omega})(\hat{\theta})$ defines the sensitivity of the cost-function with respect to $\hat{\theta}$ — usually referred to as the *shape derivative*.

As mentioned in introduction, the most efficient approach for computing the gradient consists in using an adjoint-based approach in which the variations with respect to the domain are obtained in one single step. An explicit formula is obtained by applying the method of C  a (1986), which is based on a Lagrangian approach. Two groups of *adjoint variables* $\hat{\mathbf{Q}}^{\dagger}$ and $\hat{\mathbf{q}}^{\dagger}$ are introduced. These additional variables are Lagrange multipliers used to enforce the state equations (4.2.3) and (4.2.4).

We first consider the general problem of the shape gradient of an eigenvalue, from which we easily deduce the shape gradient for (4.2.5). Noting $\lambda = \lambda^r + \mathbf{i}\lambda^i$, the following complex Lagrangian function is introduced,

$$\begin{aligned} \mathcal{L}(\hat{\Omega}, \hat{\mathbf{Q}}, \hat{\mathbf{Q}}^{\dagger}, \hat{\mathbf{q}}^{\circ}, \hat{\mathbf{q}}^{\dagger}, \lambda) = & \lambda - \left\langle \hat{\mathbf{Q}}^{\dagger}, -\hat{\mathcal{N}}_{\text{fsi}}(\hat{\mathbf{Q}}) \right\rangle \\ & - \left\langle \hat{\mathbf{q}}^{\dagger}, \left(\lambda \hat{\mathcal{T}}_{\text{fsi}}(\hat{\mathbf{Q}}) - \hat{\mathcal{N}}'_{\text{fsi}}(\hat{\mathbf{Q}}) \right) \hat{\mathbf{q}}^{\circ} \right\rangle. \end{aligned} \quad (4.3.3)$$

An explicit form of this Lagrangian function can be obtained from the weak formulations (1.1.35), (1.1.36) and (2.1.4). Extra care has to be taken when it comes to Dirichlet boundary conditions: they should be enforced using Lagrange multipliers, otherwise the variables are not truly independent since their support domain depends on $\hat{\Omega}$ (Allaire & Schoenauer, 2007). Like what was done for the velocity continuity condition on the fluid-elastic boundary $\hat{\Gamma}$ (with the Lagrange multiplier $\hat{\lambda}$), the no-slip velocity condition on $\hat{\Gamma}_{\text{rgd}}$ is therefore also enforced weakly (with a Lagrange multiplier also noted $\hat{\lambda}$). Details are given in Appendix D, where the developed expressions are also available.

Once the Lagrangian is formed with independent variables, classical optimization results are used (Wright & Nocedal, 1999; Allaire, 2012): the governing equations and the gradient are obtained by taking the derivative of the Lagrangian function with respect to the different independent variables. The shape gradient is obtained by seeking for the stationarity conditions for (4.3.3), from which we obtain equations for each unknown as well as the expression of the gradient:

$$\mathcal{L}'_{\hat{\mathbf{Q}}^{\dagger}}(\delta \hat{\mathbf{Q}}^{\dagger}) = 0 \quad \forall \delta \hat{\mathbf{Q}}^{\dagger} \quad (\text{non-linear stationary equation}),$$

$$\begin{aligned}
\mathcal{L}'_{\hat{\mathbf{Q}}}(\delta\hat{\mathbf{Q}}) &= 0 & \forall \delta\hat{\mathbf{Q}} & \quad (\text{linear stationary adjoint equation}), \\
\mathcal{L}'_{\hat{\mathbf{q}}^\dagger}(\delta\hat{\mathbf{q}}^\dagger) &= 0 & \forall \delta\hat{\mathbf{q}}^\dagger & \quad (\text{direct eigenvalue problem}), \\
\mathcal{L}'_{\hat{\mathbf{q}}^\circ}(\delta\hat{\mathbf{q}}^\circ) &= 0 & \forall \delta\hat{\mathbf{q}}^\circ & \quad (\text{adjoint eigenvalue problem}), \\
\mathcal{L}'_{\lambda}(\delta\lambda) &= 0 & \forall \delta\lambda & \quad (\text{direct/adjoint modes normalization}), \\
\mathcal{L}'_{\hat{\Omega}}(\delta\hat{\Omega}) &= \lambda'(\hat{\Omega})(\hat{\theta}) & & \quad (\text{shape sensitivity of } \lambda).
\end{aligned}$$

These are conditions written for the directional derivatives of \mathcal{L} in the direction of the i^{th} group of variables, i.e.

$$\mathcal{L}'_{\hat{\mathbf{Q}}_i}(\delta\hat{\mathbf{Q}}_i) = \lim_{\varepsilon \rightarrow 0} \frac{1}{\varepsilon} \left(\mathcal{L}(\hat{\mathbf{Q}}_1, \dots, \hat{\mathbf{Q}}_i + \varepsilon \delta\hat{\mathbf{Q}}_i, \dots, \hat{\mathbf{Q}}_p) - \mathcal{L}(\hat{\mathbf{Q}}_1, \dots, \hat{\mathbf{Q}}_p) \right).$$

In the following, we keep the abstract notations in the derivations for readability reasons. The local form of the equations are given here without further details, while their derivation is reported in Appendix D.

4.3.2 Governing equations

Non-linear stationary equilibrium

By construction, the variations with respect to the adjoint stationary variable $\hat{\mathbf{Q}}^\dagger$ give the stationary equilibrium equation (4.2.3). The developed equations are written:

$$\begin{aligned}
-\hat{\mathbf{V}} \cdot \hat{\mathbf{P}}(\hat{\mathbf{\Xi}}) &= \mathbf{0} & \text{in } \hat{\Omega}_s, \\
-\hat{\mathbf{V}} \cdot \hat{\mathbf{\Sigma}}_e(\hat{\mathbf{\Xi}}_e) &= 0 & \text{in } \hat{\Omega}_f, \\
(\hat{\mathbf{V}}\hat{\mathbf{U}})\hat{\mathbf{U}} - \hat{\mathbf{V}} \cdot \hat{\mathbf{\Sigma}}(\hat{\mathbf{U}}, \hat{P}, \hat{\mathbf{\Xi}}_e) &= \mathbf{0}, \quad -\hat{\mathbf{V}} \cdot (\hat{\mathbf{\Phi}}(\hat{\mathbf{\Xi}}_e)\hat{\mathbf{U}}) = 0 & \text{in } \hat{\Omega}_f.
\end{aligned} \tag{4.3.4}$$

The first equation represents the solid equilibrium equation, the second line is the extension problem and the last line the ALE Navier-Stokes equations. These equations are completed with fluid-solid interface conditions on $\hat{\Gamma}$, namely $\hat{\mathbf{U}} = \mathbf{0}$ (no-slip velocity), $\hat{\mathbf{\Xi}} - \hat{\mathbf{\Xi}}_e = \mathbf{0}$ (displacement continuity) and $\hat{\mathbf{P}}(\hat{\mathbf{\Xi}})\hat{\mathbf{n}} = \hat{\mathbf{\Sigma}}(\hat{\mathbf{U}}, \hat{P}, \hat{\mathbf{\Xi}}_e)\hat{\mathbf{n}}$ (stress continuity). The (fixed) farfield boundary Γ_∞ is composed of an inflow boundary Γ_{in} , an outflow boundary Γ_{out} and lateral boundaries Γ_{lat} . We take the inflow condition $\hat{\mathbf{U}} = \mathbf{u}_\infty$ on Γ_{in} , the outflow condition $\hat{\mathbf{\Sigma}}(\hat{\mathbf{U}}, \hat{P}, \hat{\mathbf{\Xi}}_e) = \mathbf{0}$ on Γ_{out} , the zero extension displacement $\hat{\mathbf{\Xi}}_e = \mathbf{0}$ on $\partial\hat{\Omega}_f \setminus (\hat{\Gamma} \cup \Gamma_{\text{rgd}})$ and solid displacement $\hat{\mathbf{\Xi}} = \mathbf{0}$ on $\partial\hat{\Omega}_s \setminus \hat{\Gamma}$, and a zero normal velocity condition on the lateral boundary Γ_{lat} . On the rigid boundary Γ_{rgd} , the no-slip velocity condition $\hat{\mathbf{U}} = \mathbf{0}$ is enforced.

The problem (4.3.4) is solved using a Newton method, in the same way than what was already described previously.

Direct and adjoint modes

Like already introduced in the chapter 2, there are two equivalent descriptions for the perturbation problems. They can be written in the stress-free reference configuration $\hat{\Omega}$ — Eq. (4.2.4) — but also in the steady deformed configuration Ω obtained from the stress-free reference configuration through the combined solid-extension displacement $\hat{\mathbf{\Xi}}$, solution of (4.2.3),

$$\Omega = (\text{Id} + \hat{\mathbf{\Xi}})(\hat{\Omega}).$$

It is more convenient to write the perturbation problems in the steady deformed configuration, since the expressions are simpler.

A summary for this process is reported in Fig. 4.2. Changing the variables accordingly in (4.3.3), i.e. $\mathbf{Q} = \hat{\mathbf{Q}} \circ (\text{Id} + \hat{\mathbf{\Xi}})^{-1}$, $\mathbf{q}^\circ = \hat{\mathbf{q}}^\circ \circ (\text{Id} + \hat{\mathbf{\Xi}})^{-1}$ and $\mathbf{q}^\dagger = \hat{\mathbf{q}}^\dagger \circ (\text{Id} + \hat{\mathbf{\Xi}})^{-1}$, and taking the variations

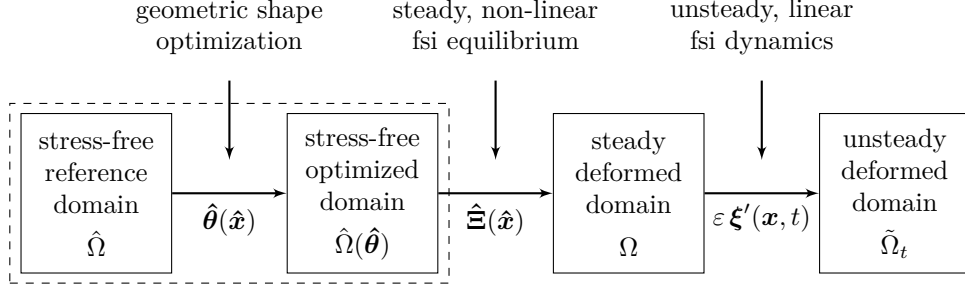


Figure 4.2 – Physical domains flowchart. The shape optimization problem is set at the level of the stress-free reference domain, defining a stress-free optimized domain. The steady deformed domain is deduced from the stress-free, optimized reference domain by means of the steady displacement $\hat{\Xi}$ obtained from (4.2.3), while the unsteady deformed domain — by the fluid-solid linear perturbation solution of (4.2.4) — is deduced from the steady deformed domain by $\varepsilon \xi'(x, t) = \varepsilon \Re\{\xi^\circ(x) \exp(\lambda t)\}$.

with respect to \mathbf{q}^\dagger (that does not depend on the steady deformation), one therefore obtains the direct eigenvalue problem in the steady deformed configuration:

$$\left\{ \lambda \mathcal{T}_{\text{fsi}}(\mathbf{Q}) - \mathcal{N}'_{\text{fsi}}(\mathbf{Q}) \right\} \mathbf{q}^\circ = 0 \quad \text{in } \Omega. \quad (4.3.5)$$

This problem is linear: to set the amplitude of the eigenmodes \mathbf{q}° , we add the normalization condition

$$\langle \mathbf{q}^\circ, \mathcal{T}_{\text{fsi}}(\mathbf{Q}) \mathbf{q}^\circ \rangle = 1. \quad (4.3.6)$$

The direct eigenvalue problem (4.3.5) is the modal problem already derived from the problem (2.1.2). Recall that the corresponding local equations read as follows:

$$\begin{aligned} \lambda \xi^\circ = \mathbf{u}_s^\circ, \quad \lambda \left(\mathcal{M}_s / J(\Xi) \right) \mathbf{u}_s^\circ - \nabla \cdot \mathbf{P}'(\Xi; \xi^\circ) &= \mathbf{0} \quad \text{in } \Omega_s, \\ -\nabla \cdot \Sigma_e(\xi_e^\circ) &= \mathbf{0} \quad \text{in } \hat{\Omega}_f, \\ \lambda \mathbf{u}^\circ + (\nabla U) \left(\mathbf{u}^\circ - \lambda \xi_e^\circ \right) + (\nabla \mathbf{u}^\circ) U + (\nabla U) \Phi'(\xi_e^\circ) U &\dots \\ -\nabla \cdot (\sigma(\mathbf{u}^\circ, p^\circ) + \Sigma'(U, P; \xi_e^\circ)) &= \mathbf{0} \quad \text{in } \Omega_f, \\ -\nabla \cdot \mathbf{u}^\circ - \nabla \cdot (\Phi'(\xi_e^\circ) U) &= \mathbf{0} \quad \text{in } \Omega_f. \end{aligned} \quad (4.3.7)$$

These are the solid equations, the extension equation and the Navier-Stokes momentum and continuity equations, in that order. They are supplemented by interface conditions

$$\begin{aligned} \mathbf{u}^\circ - \mathbf{u}_s^\circ &= \mathbf{0} && \text{on } \Gamma, \\ \mathbf{u}^\circ &= \mathbf{0} && \text{on } \Gamma_{\text{rgd}}, \\ \xi_e^\circ - \xi^\circ &= \mathbf{0} && \text{on } \Gamma, \\ (\sigma(\mathbf{u}^\circ, p^\circ) + \Sigma'(U, P, \xi_e^\circ)) \mathbf{n} - \mathbf{P}'(\Xi; \xi^\circ) \mathbf{n} &= \mathbf{0} && \text{on } \Gamma, \end{aligned}$$

and completed by zero extension displacement farfield conditions, $\xi_e^\circ = \mathbf{0}$ on $\partial\Omega_f \setminus \Gamma$, zero solid displacement $\xi^\circ = \mathbf{0}$ on $\partial\Omega_s \setminus \Gamma$, and the outflow condition $(\sigma(\mathbf{u}^\circ, p^\circ) + \Sigma'(U, P, \xi_e^\circ)) \mathbf{n} = \mathbf{0}$ on Γ_{out} . A zero condition holds for the velocity on Γ_{rgd} , Γ_{in} and Γ , and the slip condition on Γ_{lat} .

The determination of an analytic formula for the shape gradient requires to adopt a continuous approach for deriving the adjoint problem. Quantities such as the adjoint interface stress should indeed be determined. Like previously, it is convenient to write the problem in the steady deformed configuration. Changing the variables and varying the Lagrangian function (4.3.3) with respect to \mathbf{q}° gives the condition

$$\left\langle \mathbf{q}^\dagger, \left(\lambda \mathcal{T}_{\text{fsi}}(\hat{\mathbf{Q}}) - \mathcal{N}'_{\text{fsi}}(\mathbf{Q}) \right) \delta \mathbf{q}^\circ \right\rangle = 0 \quad \forall \delta \mathbf{q}^\circ.$$

To obtain the corresponding local equations, the adjoint operators $\mathcal{T}_{\text{fsi}}(\mathbf{Q})^\dagger$ and $\mathcal{N}'_{\text{fsi}}(\mathbf{Q})^\dagger$ are introduced, such that

$$\left\langle \mathbf{q}^\dagger, \left(\lambda \mathcal{T}_{\text{fsi}}(\mathbf{Q}) - \mathcal{N}'_{\text{fsi}}(\mathbf{Q}) \right) \delta \mathbf{q}^\circ \right\rangle = \left\langle \left(\lambda^* \mathcal{T}_{\text{fsi}}(\mathbf{Q})^\dagger - \mathcal{N}'_{\text{fsi}}(\mathbf{Q})^\dagger \right) \mathbf{q}^\dagger, \delta \mathbf{q}^\circ \right\rangle,$$

from which we obtain the adjoint equation

$$\left\{ \lambda^* \mathcal{T}_{\text{fsi}}(\mathbf{Q})^\dagger - \mathcal{N}'_{\text{fsi}}(\mathbf{Q})^\dagger \right\} \mathbf{q}^\dagger = 0. \quad (4.3.8)$$

Practically, the transformation is achieved using integration by parts and the formulas reported in Appendix C.1. The derivation is detailed in Appendix D. The corresponding developed, local equations write as follows:

$$\begin{aligned} \boldsymbol{\xi}^\dagger &= \lambda^* (\mathcal{M}_s / J(\boldsymbol{\Xi})) \mathbf{u}_s^\dagger, & \lambda^* \boldsymbol{\xi}^\dagger - \nabla \cdot \mathbf{P}'(\boldsymbol{\Xi}; \mathbf{u}_s^\dagger) &= \mathbf{0} \quad \text{in } \Omega_s, \\ -\nabla \mathbf{U}^T \left(\lambda^* \mathbf{u}^\dagger + (\nabla \mathbf{U})^T \mathbf{u}^\dagger - (\nabla \mathbf{u}^\dagger) \mathbf{U} \right) - (\nabla \mathbf{u}^\dagger)^T \nabla \mathbf{U} \mathbf{U} \dots \\ &\quad - \nabla \cdot \left(\boldsymbol{\Sigma}_e(\boldsymbol{\xi}_e^\dagger) + \boldsymbol{\Sigma}_e^\dagger(\mathbf{U}, P, \mathbf{u}^\dagger, p^\dagger) \right) &= \mathbf{0} \quad \text{in } \Omega_f, \\ \boldsymbol{\xi}_e^\dagger &= \mathbf{0} && \text{on } \Gamma, \\ \lambda^* \mathbf{u}^\dagger + (\nabla \mathbf{U})^T \mathbf{u}^\dagger - (\nabla \mathbf{u}^\dagger) \mathbf{U} - \nabla \cdot \boldsymbol{\sigma}(\mathbf{u}^\dagger, p^\dagger) &= \mathbf{0} \quad \text{in } \Omega_f, \\ -\nabla \cdot \mathbf{u}^\dagger &= 0 && \text{in } \Omega_f, \\ \mathbf{u}^\dagger - \mathbf{u}_s^\dagger &= \mathbf{0} && \text{on } \Gamma, \\ \lambda^* \boldsymbol{\sigma}(\mathbf{u}^\dagger, p^\dagger) \mathbf{n} + \left(\boldsymbol{\Sigma}_e(\boldsymbol{\xi}_e^\dagger) + \boldsymbol{\Sigma}_e^\dagger(\mathbf{U}, P, \mathbf{u}^\dagger, p^\dagger) \right) \mathbf{n} - \mathbf{P}'(\boldsymbol{\Xi}; \mathbf{u}_s^\dagger) \mathbf{n} &= \mathbf{0} \quad \text{on } \Gamma. \end{aligned} \quad (4.3.9)$$

The first equation is the adjoint solid vibration problem written under the augmented form. This problem is self-adjoint as is the case for solids in absence of damping (Marsden & Hughes, 1994), except that the adjoint displacement plays the role of the direct solid velocity, and *vice-versa*, because of the formulation on the form of an augmented problem.

The second equation is the adjoint extension equation that takes a rather complicated form, that also involves the tensor

$$\begin{aligned} \boldsymbol{\Sigma}^\dagger(\mathbf{U}, P, \mathbf{u}^\dagger, p^\dagger) &= - \left(P \boldsymbol{\Phi}'(\mathbf{u}^\dagger)^T + P^\dagger \boldsymbol{\Phi}'(\mathbf{U})^T \right) \dots \\ &\quad + \frac{2}{\mathcal{R}_e} \left\{ - \left((\nabla \mathbf{u}^\dagger)^T \mathbf{D}(\mathbf{U}) + (\nabla \mathbf{U})^T \mathbf{D}(\mathbf{u}^\dagger) \right) + \left(\mathbf{D}(\mathbf{U}) : \mathbf{D}(\mathbf{u}^\dagger) \right) \mathbf{I} \right\}. \end{aligned} \quad (4.3.10)$$

The adjoint displacement $\boldsymbol{\xi}_e^\dagger$ is prescribed to be zero at the fluid-solid interface (third line). This makes sense: adjoints can indeed be interpreted as the receptivity to forcings of the direct equations (Luchini & Bottaro, 2014a,b); with this respect the adjoint displacement expresses the receptivity to a forcing of the extension equation, that must be zero on the fluid-solid interface: otherwise, this would signify that the extension equation may influence the physical problem.

The fourth and fifth equations are the adjoint Navier-Stokes equations, that take the same form as would be obtained in a pure hydrodynamic case (Luchini & Bottaro, 2014a,b). Since the adjoint velocities express physically the receptivity to a physical mechanism that would have injected momentum in the system, they are also continuous across the interface (sixth line). The adjoint stress balance however couples in a rather complicated way the adjoint fluid and solid stresses, plus the adjoint extension pseudo-stresses.

Finally, the other boundary conditions are the zero extension displacement farfield conditions, $\boldsymbol{\xi}_e^\dagger = \mathbf{0}$ on $\partial\Omega_f \setminus \Gamma$, the zero solid displacement $\boldsymbol{\xi}^\dagger = \mathbf{0}$ on $\partial\Omega_s \setminus \Gamma$, and finally the outflow condition $\boldsymbol{\sigma}(\mathbf{u}^\dagger, p^\dagger) \mathbf{n} + (\mathbf{U} \cdot \mathbf{n}) \mathbf{u}^\dagger = \mathbf{0}$ on Γ_{out} . A zero condition holds for the velocity on Γ_{rgd} , Γ_{in} and Γ , and the slip condition on Γ_{lat} . The variation of the Lagrangian function (4.3.3) with respect to the eigenvalue λ eventually gives the normalization condition between the direct and adjoint modes,

$$\left\langle \mathbf{q}^\dagger, \mathcal{T}_{\text{fsi}}(\mathbf{Q}) \mathbf{q}^\circ \right\rangle = 1. \quad (4.3.11)$$

Note that the block-formulation of the adjoint problem is obtained by taking the block-transpose of the block formulation (2.1.1).

Let us give some details on the numerical resolution of (4.3.5) and (4.3.8). After space discretization with finite-elements, ARPACK (shift-and-invert mode) is used to find the leading eigenvalues. The complex shift is taken close to the estimated unstable eigenvalue and only the leading mode is retained. Finally, the modes are normalized using (4.3.6) and (4.3.11). The adjoint problem can be discretized directly from (4.3.7), or derived at the discrete level, i.e. by simply taking the hermitian transpose of the direct problem (Thevenin & Janiga, 2008). This latter approach is used practically, for it avoids from having to assemble the matrix of the direct problem first, and then the matrix of the adjoint problem: only the direct problem needs to be assembled. This also ensures that the discrete adjoint mode is the *exact* counterpart of the discrete direct mode, independently from the mesh discretization.

Adjoint stationary equation

The adjoint stationary equation is obtained by differentiating (4.3.3) with respect to the stationary variables $\hat{\mathbf{Q}}$. When $\mathcal{L}'_{\hat{\mathbf{Q}}}(\delta\hat{\mathbf{Q}})$ is set to zero whatever $\delta\hat{\mathbf{Q}}$, we obtain

$$\left\langle \hat{\mathbf{Q}}^\dagger, \hat{\mathcal{N}}'_{\text{fsi}}(\hat{\mathbf{Q}})\delta\hat{\mathbf{Q}} \right\rangle = \left\langle \hat{\mathbf{q}}^\dagger, \left(\lambda \frac{\partial \hat{\mathcal{T}}_{\text{fsi}}}{\partial \hat{\mathbf{Q}}} \bigg|_{\hat{\mathbf{Q}}} \delta\hat{\mathbf{Q}} - \frac{\partial \hat{\mathcal{N}}'_{\text{fsi}}}{\partial \hat{\mathbf{Q}}} \bigg|_{\hat{\mathbf{Q}}} \delta\hat{\mathbf{Q}} \right) \hat{\mathbf{q}}^\circ \right\rangle \quad \forall \delta\hat{\mathbf{Q}}. \quad (4.3.12)$$

Compared to a pure hydrodynamic case, $\hat{\mathcal{T}}_{\text{fsi}}$ depends on the steady variables because of the geometric non-linearities. The same is true for $\hat{\mathcal{N}}'_{\text{fsi}}$, where they have to be considered in addition to the quadratic velocity advection term. Introducing the operators $\hat{\mathcal{N}}''_{\text{fsi}}$ and $\hat{\mathcal{T}}'_{\text{fsi}}$ such that

$$\hat{\mathcal{T}}'_{\text{fsi}}(\hat{\mathbf{Q}}, \hat{\mathbf{q}}^\circ)\delta\hat{\mathbf{Q}} = \left\{ \frac{\partial \hat{\mathcal{T}}_{\text{fsi}}}{\partial \hat{\mathbf{Q}}} \bigg|_{\hat{\mathbf{Q}}} \delta\hat{\mathbf{Q}} \right\} \hat{\mathbf{q}}^\circ \quad \text{and} \quad \hat{\mathcal{N}}''_{\text{fsi}}(\hat{\mathbf{Q}}, \hat{\mathbf{q}}^\circ)\delta\hat{\mathbf{Q}} = \left\{ \frac{\partial \hat{\mathcal{N}}'_{\text{fsi}}}{\partial \hat{\mathbf{Q}}} \bigg|_{\hat{\mathbf{Q}}} \delta\hat{\mathbf{Q}} \right\} \hat{\mathbf{q}}^\circ,$$

and using again the properties of adjoints, we arrive to the adjoint steady fluid-solid equation

$$\hat{\mathcal{N}}'_{\text{fsi}}(\hat{\mathbf{Q}})^\dagger \hat{\mathbf{Q}}^\dagger = \underbrace{\left(\lambda \hat{\mathcal{T}}'_{\text{fsi}}(\hat{\mathbf{Q}}, \hat{\mathbf{q}}^\circ) - \hat{\mathcal{N}}''_{\text{fsi}}(\hat{\mathbf{Q}}, \hat{\mathbf{q}}^\circ) \right)^* \hat{\mathbf{q}}^\dagger}_{\text{sensitivity to steady flow modifications } \nabla_{\hat{\mathbf{Q}}} \lambda}. \quad (4.3.13)$$

In the context of a pure hydrodynamic problem, Marquet *et al.* (2008) showed that the right-hand side of this equation has a physical interpretation in terms of the sensitivity of the eigenvalue λ to steady flow modifications. The exact same interpretation holds in the fluid-elastic case. In the hydrodynamic case, its explicit expression is however way simpler, since $\partial \hat{\mathcal{T}}_{\text{fsi}} / \partial \hat{\mathbf{Q}} = 0$, and $\hat{\mathcal{N}}'_{\text{fsi}}$ only depends on the velocity.

In the fluid-elastic case, there is also a dependency with respect to the deformations of the steady flow. For this reason, the exact expression for the right-hand side of the above expression is particularly tedious to derive: in the stress-free reference configuration, each term of the fluid equation depends on the stationary extension domain displacement (see Eq. (2.1.4) and in Appendix D). We therefore consider an approximate sensitivity to steady flow modifications, where the effect of the displacements are neglected. This approximation is valid when the displacements are small, as is the case for the cylinder-splitter plate configuration in absence of steady deviations that will be studied in what follows. This amounts indeed to assume that the computation of (4.3.13) can be done by assuming that $\hat{\Omega} = \Omega$. The adjoint steady equation then reduces to the adjoint Navier-Stokes equations, forced by sensitivities $\nabla_U(\lambda)$ and $\nabla_P(\lambda)$. All calculations done (see Appendix

D), we have in the steady deformed configuration

$$\begin{aligned}\nabla_U(\lambda) = & -(\nabla \mathbf{u}^{\circ*})^T \mathbf{u}^\dagger + \nabla \mathbf{u}^\dagger \mathbf{u}^{\circ*} \\ & - \Phi'(\xi_e^{\circ*})^T \nabla U^T \mathbf{u}^\dagger + \nabla \mathbf{u}^\dagger \Phi'(\xi_e^{\circ*}) U \\ & - \lambda^* (\nabla \mathbf{u}^\dagger \xi_e^{\circ*} + \nabla \cdot \xi_e^{\circ*} \mathbf{u}^\dagger) \\ & + \nabla \cdot \Sigma'(\mathbf{u}^\dagger, p^\dagger; \xi_e^{\circ*})\end{aligned}\quad (4.3.14)$$

for the sensitivity to variations of the steady flow. The first line is exactly that obtained by [Marquet et al. \(2008\)](#), while the other terms represent the corrections coming from dynamic flexibility effects. In the fluid-elastic case, there is furthermore a sensitivity to pressure variations,

$$\nabla_P(\lambda) = \Phi'(\xi_e^{\circ*})^T : \nabla \mathbf{u}^\dagger. \quad (4.3.15)$$

The approximate adjoint stationary equation with the approximate right-hand side writes as follows in the steady deformed configuration:

$$\begin{aligned}(\nabla U)^T U^\dagger - (\nabla U^\dagger) U - \nabla \cdot \sigma(U^\dagger, P^\dagger) &= \nabla_U(\lambda) \quad \text{in } \Omega_f, \\ -\nabla \cdot U^\dagger &= \nabla_P(\lambda) \quad \text{in } \Omega_f, \\ U^\dagger &= \mathbf{0} \quad \text{on } \Gamma \cup \Gamma_{\text{rgd}},\end{aligned}\quad (4.3.16)$$

completed by the outflow condition $(U \cdot \mathbf{n}_f)U^\dagger + \sigma(U^\dagger, P^\dagger)\mathbf{n}_f - \sigma^\dagger(\mathbf{u}^\dagger, p^\dagger, \xi_e^{\circ*})\mathbf{n} = \mathbf{0}$ on Γ_{out} and the other farfield velocity conditions.

Remark. We have also considered the exact equation deduced from (4.3.12) at the *discrete* level. The left-hand side can indeed be computed at the discrete level using a matrix transpose operation — or at the continuous level by the same manipulations than that used to derive the adjoint eigenvalue problem. When it comes to the right-hand side, once the derivatives $\partial \hat{\mathcal{T}}_{\text{fsi}} / \partial \hat{\mathbf{Q}}$ and $\partial \hat{\mathcal{N}}'_{\text{fsi}} / \partial \hat{\mathbf{Q}}$ are computed, we have actually to our disposal a weak formulation that can be directly used to assemble the discrete right-hand side of the equation. What is missing then is an expression of the *strong* form for the right-hand side in (4.3.13), that should be obtained from direct/adjoint manipulations. When examining the shape gradient, no differences between the exact and approximate approaches were observed on the test-case considered, so that we rather consider here the approximate formula.

4.3.3 Shape gradient computation

It now remains to differentiate (4.3.3) with respect to the Lagrangian domain mapping $\hat{\boldsymbol{\theta}}$ in order to obtain the shape gradient, which basically amounts to differentiating an integral with respect to its support domain. From the so-called *structure theorem* ([Hadamard, 1908](#); [Delfour & Zolésio, 2011](#)), it can be shown that the shape derivative takes then the generic form

$$\mathcal{L}'_{\hat{\Omega}}(\delta \hat{\boldsymbol{\theta}}) = \lambda'(\hat{\Omega})(\delta \hat{\boldsymbol{\theta}}) = \int_{\hat{\Gamma}_{\text{rgd}}} G_\lambda \hat{\mathbf{n}} \cdot \delta \hat{\boldsymbol{\theta}} \, d\Gamma \quad \forall \delta \hat{\boldsymbol{\theta}}, \quad (4.3.17)$$

where the function $G_\lambda \hat{\mathbf{n}}$ is referred to as the *shape gradient* and depends on state and adjoint variables. In (4.3.17), the shape derivative only depends on the normal component $\hat{\mathbf{n}} \cdot \delta \hat{\boldsymbol{\theta}}$ of the boundary variation, reflecting the intuitive idea that variations of the border $\partial \hat{\Omega}$ along the normals affect $\hat{\Omega}$ at first-order, while the tangential variations have only a second-order influence. In the present case, all computations done (see the detail in Appendix D), we obtain the remarkably simple formula

$$G_\lambda = - \underbrace{\frac{2}{\mathcal{R}_e} \hat{\mathbf{D}}(\hat{U}) : \hat{\mathbf{D}}(\hat{U}^\dagger)^*}_{G_{\lambda,s}} - \underbrace{\frac{2}{\mathcal{R}_e} \hat{\mathbf{D}}(\hat{u}^\circ) : \hat{\mathbf{D}}(\hat{u}^\dagger)^*}_{G_{\lambda,u}} \quad \text{on} \quad \hat{\Gamma}_{\text{rgd}}, \quad (4.3.18)$$

where we have noted $G_{\lambda,s}$ and $G_{\lambda,u}$ the so-called *steady* and *unsteady* components of the shape gradient. Recall that on $\hat{\Gamma}_{\text{rgd}}$, $\hat{\mathbf{D}} = 1/2(\hat{\mathbf{\nabla}} + \hat{\mathbf{\nabla}}^T)$, and that $\mathbf{A} : \mathbf{B} = A_{ij}B_{ij}$. In the case where the interface to be optimized would be *elastic*, the expression is however *a priori* much less simple (see again Appendix D). In the above expression, $G_{\lambda,s}$ is related to the stationary part of the problem, with $\hat{\mathbf{U}}$ and $\hat{\mathbf{U}}^\dagger$ being respectively the steady fluid velocity and the adjoint stationary fluid velocity. On the other hand, $G_{\lambda,u}$ represents the contribution of the unsteady part of the problem, where $\hat{\mathbf{u}}^\circ$ is the fluid velocity eigenmode and $\hat{\mathbf{u}}^\dagger$ is the adjoint fluid velocity eigenmode. Eventually, the shape gradient for the parametrized cost-function (4.2.5) is deduced from (4.3.18) simply as follows:

$$G = \alpha_r(\lambda^r - \lambda_c^r) \Re\{G_\lambda\} + \alpha_i(\lambda^i - \lambda_c^i) \Im\{G_\lambda\}. \quad (4.3.19)$$

The decomposition of the gradient between two components results from the fact that the sensitivity of the eigenvalue with respect to a domain variation actually depends on two mechanisms. We can indeed write $\lambda = \lambda(\hat{\Omega}, \hat{\mathbf{Q}}(\hat{\Omega}))$. The first argument refers to the fact that, for a given $\hat{\mathbf{Q}}$, the structure of the eigenvalue problem (4.3.5) is obviously affected by a variation of the domain $\hat{\Omega}$. The second argument expresses that the stationary flow $\hat{\mathbf{Q}}$ is itself a function of $\hat{\Omega}$ through the stationary problem (4.2.3). Considering a variation $\delta\hat{\theta}$ of the domain mapping, a corresponding variation $\delta\lambda$ of the eigenvalue can therefore be formally written, with the appropriate scalar products (\cdot, \cdot) , as

$$\delta\lambda = (\nabla_{\hat{\Omega}}\lambda, \delta\hat{\theta}) + (\nabla_{\hat{\mathbf{Q}}}\lambda, \delta\hat{\mathbf{Q}}).$$

The first term is related to how a modification of the domain influences the cost-function, for a *fixed* stationary flow. This term is thus related to mechanisms that influence the eigenvalue through linear, unsteady mechanisms (term $G_{\lambda,u}$). On the other hand, the second term is related to the influence of the variations of the steady flow through a modification of the geometry (term $G_{\lambda,s}$).

4.3.4 Practical gradient evaluation & optimization loop

From (4.3.2) and (4.3.17), a descent direction that diminishes the cost-function is then for instance

$$\phi = -G \hat{\mathbf{n}}. \quad (4.3.20)$$

An other choice, though similar in principle, is made practically. There is indeed a numerical difficulty to solve here: the gradient is defined only at the fluid-structure interface, that is practically a boundary of the fluid mesh. Using the gradient information to deform the surface vertices is thus likely to result in degenerated neighbouring cells if the update step is too large. A representation of a circular interface (in orange) placed in the middle of a mesh in Fig. 4.3 illustrates this phenomenon: in (a) the descent direction computed from (4.3.20) is represented. One observes that on the top of the circle, mesh reversal will occur because the displacement exceeds the thickness of the first layer of cells, and thus remeshing will be mandatory. On the other hand, a general lack of regularity is observed, notably because the formula (4.3.19) giving the gradient requires to differentiate the previously computed fields, and because the discrete boundary necessarily lacks of smoothness.

For all these reasons, the interface gradient information is propagated onto the whole domain, exactly in the same way as the ALE extension operator does. An efficient method to propagate and regularize the gradient is to use the so-called \mathcal{H}^1 -method (Allaire & Pantz, 2006; Dapogny *et al.*, 2017), where the shape gradient is identified from $\mathcal{J}'(\hat{\Omega})(\theta)$ by means of the \mathcal{H}^1 scalar product on $\hat{\Omega}_f$, *i.e.* $\langle \mathbf{a}, \mathbf{b} \rangle_{\mathcal{H}^1(\hat{\Omega}_f)} = \int_{\hat{\Omega}_f} (\mathbf{a} \cdot \mathbf{b} + \nabla \mathbf{a} : \nabla \mathbf{b}) d\hat{\Omega}$, rather than an usual \mathcal{L}^2 scalar product on $\hat{\Gamma}$. This defines a variational formulation for a Poisson equation. The descent direction is then solution to

$$\begin{aligned} \hat{\mathbf{\nabla}}^2 \phi - \phi &= 0 & \text{in } \hat{\Omega}_f, \\ (\hat{\mathbf{\nabla}} \phi) \hat{\mathbf{n}} &= -G \hat{\mathbf{n}} & \text{on } \hat{\Gamma}_{\text{rgd}}. \end{aligned} \quad (4.3.21)$$

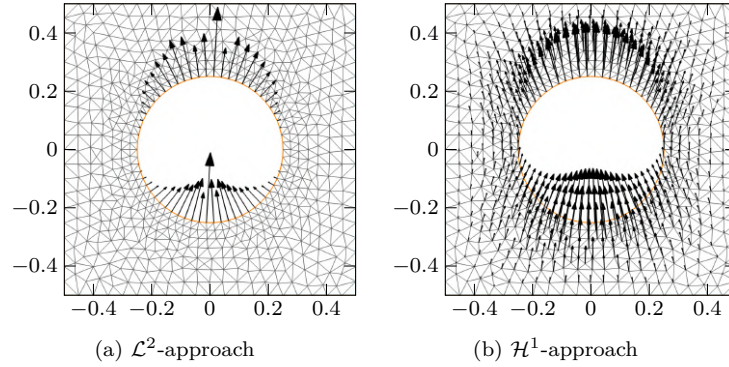


Figure 4.3 – Mesh extension-regularization approaches. Comparison of the \mathcal{L}^2 -based and \mathcal{H}^1 -based approaches, for $G = \cos(2\pi x) \sin(2\pi y)$ around a cylinder of diameter 0.5, showing the superiority of the latter one.

A comparison with the \mathcal{L}^2 -based approach is showed in Fig. 4.3b, showing the clear improvements provided by the latter: first, the interface deformation is now propagated in the whole domain that can thus be deformed without remeshing, and the smoothness is greatly improved. Note that with the \mathcal{H}^1 -based approach, the deformation field is no longer along the normals at the deformable edges.

To address mesh-related issues, once the regularized gradient is computed and the new position of the interface is determined, even if not mandatory, the region around the optimization interface is nevertheless remeshed, in order to prevent from mesh cell degeneracy. For instance on the case depicted in Fig. 4.3b, the updated shape will be moved upwards, resulting in a compression of the cells in the upper region, and a elongation of the cells in the lower region. A remeshing generates a new distribution of cells that have a more regular aspect ratio. For some cases, it is also useful to use a two-level discretization (Allaire & Schoenauer, 2007): one fine grid to resolve the physics and a coarse grid that supports the interface. We have observed that in some specific cases this approach prevents from the apparition of spikes in the optimization surface. Using one single mesh was however sufficient for the applications presented in what follows.

The optimization loop is represented schematically in Fig. 4.4. The procedure only requires an initial shape $\hat{\Omega}^{(0)}$ as an input, which is that with the circular cylinder. Within one iteration of the algorithm, several steps are realized sequentially. First, the non-linear stationary problem (4.2.3) is solved. The steady deformed configuration is then computed, and the direct eigenvalue problem (4.2.4) is assembled, then solved. The adjoint eigenvalue problem (4.3.8) is solved using the discrete transpose-conjugate approach, which avoids having to reassemble the corresponding matrix. The direct and adjoint modes are scaled according to (4.3.6) and (4.3.11). Then, the adjoint stationary equation (4.3.13) is solved. The matrix for this problem is also obtained practically by taking the transpose of the Jacobian matrix used in the Newton loop considered for solving (4.2.3), since the exact Jacobian has been determined. Finally, the shape gradient is computed using the analytic formula (4.3.19). A fixed descent step k is chosen, that sets the magnitude of the shape deformations for the current iteration. The extended-regularized descent direction is computed from (4.3.21), and the mesh is updated accordingly. The stop criterion is set on the magnitude of the deformation of this deformation field. Finally, the non-linear solution at the current step is interpolated on the new mesh and serves as an initial guess for the next step.

4.4 Application to the cylinder splitter-plate case

In this section, following what was introduced before, we consider the problem constituted by an elastic plate attached to a rigid cylinder, already introduced in section 3.2 (see also a sketch of the configuration in the Fig. 3.3). The optimization procedure is applied to the rigid part of the object, as mentioned before and as represented in the Fig. 4.5. In the following, we first describe

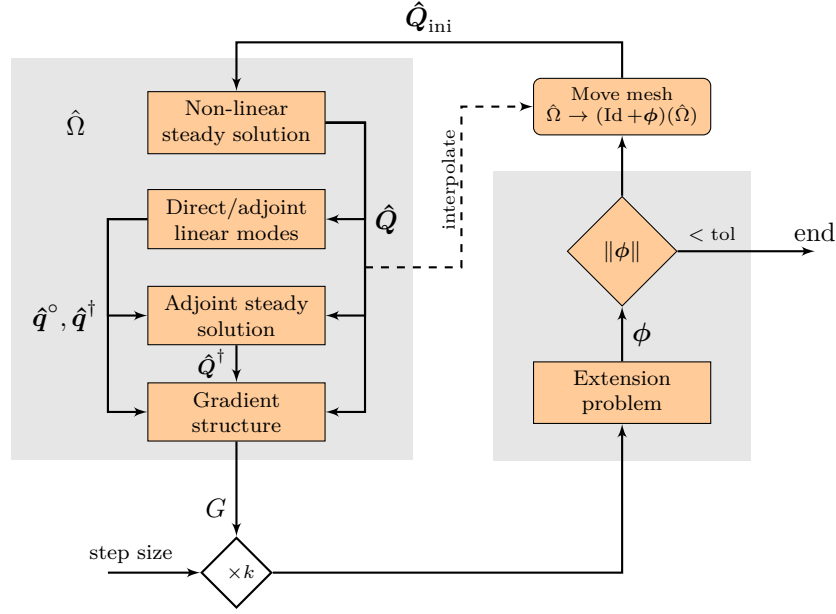


Figure 4.4 – Shape optimization loop.

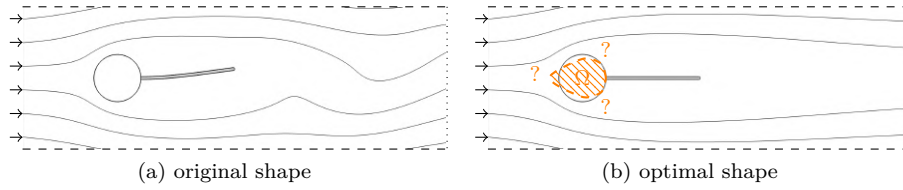


Figure 4.5 – Shape optimization for stabilizing an unstable mode. The shape of the rigid part of the object is optimized so as to stabilize an unsteady mode, as represented in (b), or to modify the frequency of the mode (not represented).

two types of modes found at different values of the stiffness and Reynolds number, and carry out a sensitivity analysis so as to identify the active regions in the development of the instabilities. The general shape gradients for both modes are then introduced and discussed. Results of shape optimization for stabilizing the modes are presented. Finally, we consider a case where one tries to design an unstable configuration oscillating at a prescribed frequency.

4.4.1 Description of the unstable modes

Solving the stationary flow equation (4.2.3) and eigenvalue problem (4.2.4) for different parameters $(\mathcal{E}_s, \mathcal{R}_e)$ results in two regions of unstable, unsteady modes, as represented in Fig. 4.6 that reports the stability regions in the $(\mathcal{E}_s, \mathcal{R}_e)$ plane. The region where unstable modes are found is emphasized by the gray color, while neutral stability curves are drawn with the solid lines. At high rigidities and for Reynolds numbers greater than 92, an unstable region is found, where only one unstable mode is present. These modes are referred to as “fluid” modes, for they remain unstable if the rigidity is increased up to the point that the solid is rigid. Their governing mechanics is thus likely to be related to the unstable vortex wake that develops downstream to the cylinder. Keeping the Reynolds number constant and decreasing the stiffness results in a stabilization of these modes (precisely, when one crosses the boundary depicted with the blue solid line in Fig. 4.6), but another type of unstable modes appear at some point (when one crosses the boundary depicted with the orange solid line in Fig. 4.6). These modes are referred to as “solid” modes, for they do not exist at high rigidity and are thus necessarily related to the fluid-structure interaction. They are also

Figure 4.6 – Study cases before optimization. For a density ratio $\mathcal{M}_s = 1$, the shaded region delimits the parameter space in the Reynolds number \mathcal{R}_e – stiffness parameter \mathcal{E}_s plane, where unstable coupled fluid-structure modes are found. The blue and orange lines depict marginal stability curves obtained by following two different modes. The blue square symbol (■) identifies the reference fluid case ($\mathcal{R}_e = 100$ and $\mathcal{E}_s = 4.68 \times 10^6$), the orange square symbol (■) identifies the reference solid case ($\mathcal{R}_e = 80$ and $\mathcal{E}_s = 105\,000$).

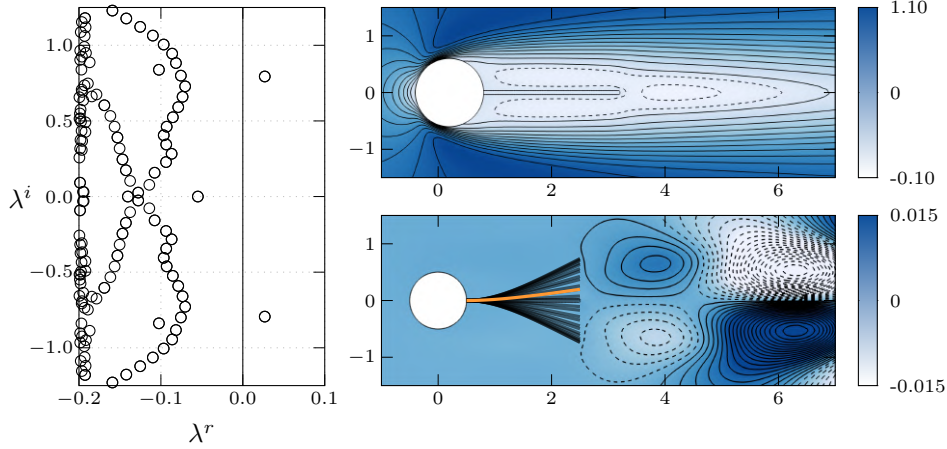
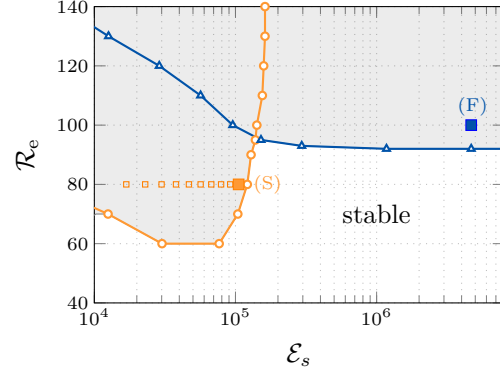


Figure 4.7 – Non-optimized case (F). Eigenvalue spectrum (left), streamwise velocity component of the stationary flow (top right, dashed negative contours, the first solid line in the vicinity of the recirculating region marks the limit of zero velocity), and real part of the streamwise component of the leading mode (bottom right, 40 contours between ± 0.015 , dashed negative). Snapshots of the solid deformation for 25 phases uniformly distributed over a period of oscillation of the mode are depicted with the black solid line, while the real part is represented in orange color.

stabilized by a decrease of the Reynolds number, but however survive down to $\mathcal{R}_e = 60$ — in which case the rigid case yields to a stable flow. In the following, we concentrate on two reference unstable cases, a case (F) in the fluid modes region, at a Reynolds number $\mathcal{R}_e = 100$ and high rigidity $\mathcal{E}_s = 4.68 \times 10^6$, and a case (S) in the solid modes region, having a Reynolds number $\mathcal{R}_e = 80$ and a lower stiffness $\mathcal{E}_s = 105\,000$.

Unstable case (F)

The main features for the case (F) are presented in Fig. 4.7. The streamwise velocity for the stationary flow for the case (F) is reported in the upper right picture. In the fluid region, a wake flow with two symmetric recirculating regions above and below the splitter plate that merge downstream to the plate. This recirculating region extends here down to $x = 5.54$. A very small compression towards $x < 0$ in the solid is observed, that does not exceed -1×10^{-7} . The spectrum that is obtained by solving the coupled fluid-structure eigenvalue problem (4.3.5) for this set of values is reported in the graph on the left side. As mentioned above, one single unstable eigenvalue pair $\lambda_{(F)} = 2.677 \times 10^{-2} \pm 0.794i$ is found. The spatial structure (real part of the streamwise velocity component of the perturbation) of the corresponding eigenvector is represented in the bottom right picture, showing the classical features of an unsteady vortex street wake (Sipp & Lebedev, 2007; Williamson, 1996) associated with a one-node bending vibration of the solid.

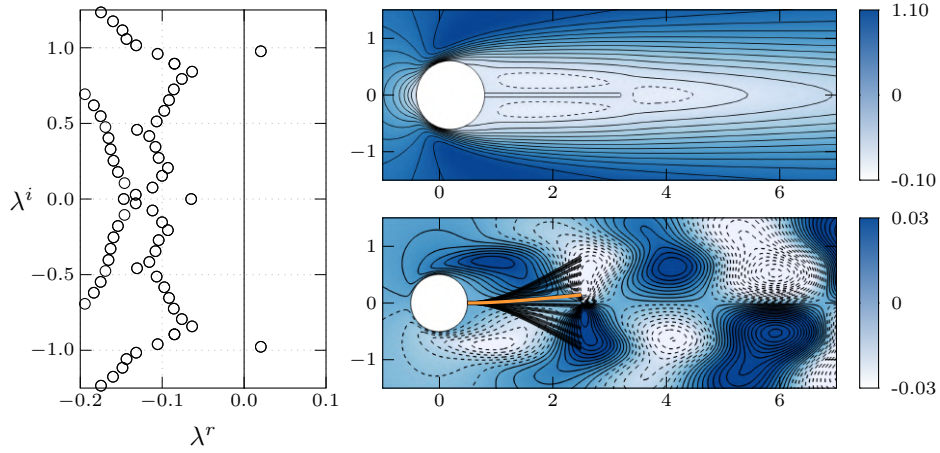


Figure 4.8 – Non-optimized case (S). Eigenvalue spectrum (left), streamwise velocity component of the stationary flow (top right, dashed negative contours, the first solid line in the vicinity of the recirculating region marks the limit of zero velocity), and real part of the streamwise component of the leading mode (bottom right, 40 contours between ± 0.03 , dashed negative). Snapshots of the solid deformation for 25 phases uniformly distributed over a period of oscillation of the mode are depicted with the black solid line, while the real part is represented in orange color.

Unstable case (S)

Computed for a smaller rigidity coefficient $\mathcal{E}_s = 105\,000$, and a slightly lower Reynolds number $\mathcal{R}_e = 80$, the steady flow for the case (S), represented in the upper right picture in Fig. 4.8, displays a shorter recirculation region that extends down to $x = 4.32$. Due to the smaller rigidity, the maximal compression (at the tip of the plate) reaches a slightly higher value of -5×10^{-6} . The fluid-structure eigenvalue spectrum is reported in the graph on the left side and shows one unstable eigenvalue pair $\lambda_{(S)} = 2.039 \times 10^{-2} \pm 0.977i$. A representation of the real part of the streamwise velocity component of the mode is also shown in the bottom right picture. Compared to the case (F), structures are observed closer to the fluid-structure interface (even if the amplitude chosen for the contours is twice as large as in the previous case), while a typical vortex shedding pattern is also present in the wake. In this case, the deformation amplitude in the solid is also about 2500 greater than for the mode (F), while the amplitude in the wake decreases more rapidly in the downstream direction.

The very low values found for the displacement justify the choice for an approximate adjoint stationary flow.

4.4.2 Adjoint modes & abstract sensitivity analysis

We have seen in §4.3.3 that the expression (4.3.18) for the shape gradient depends on the direct and adjoint steady and unsteady velocities. If adjoint fields might be viewed only as a convenient mathematical ingredient that allows to compute the gradient, they have also been interpreted more physically in terms of *sensitivity* (Giannetti & Luchini, 2006; Marquet *et al.*, 2008; Luchini & Bottaro, 2014a). The same kind of analysis is extended here to the fluid-structure case, allowing to get further insights on the dynamics on the modes, and evaluate their overall potential for being controlled, regardless of the specific method used practically. The analysis is divided in two parts, the first focusing on the effect of a modification of the steady flow (steady part), and the second dedicated to the sensitivity to a modification of the structure of the eigenvalue problem (unsteady part).

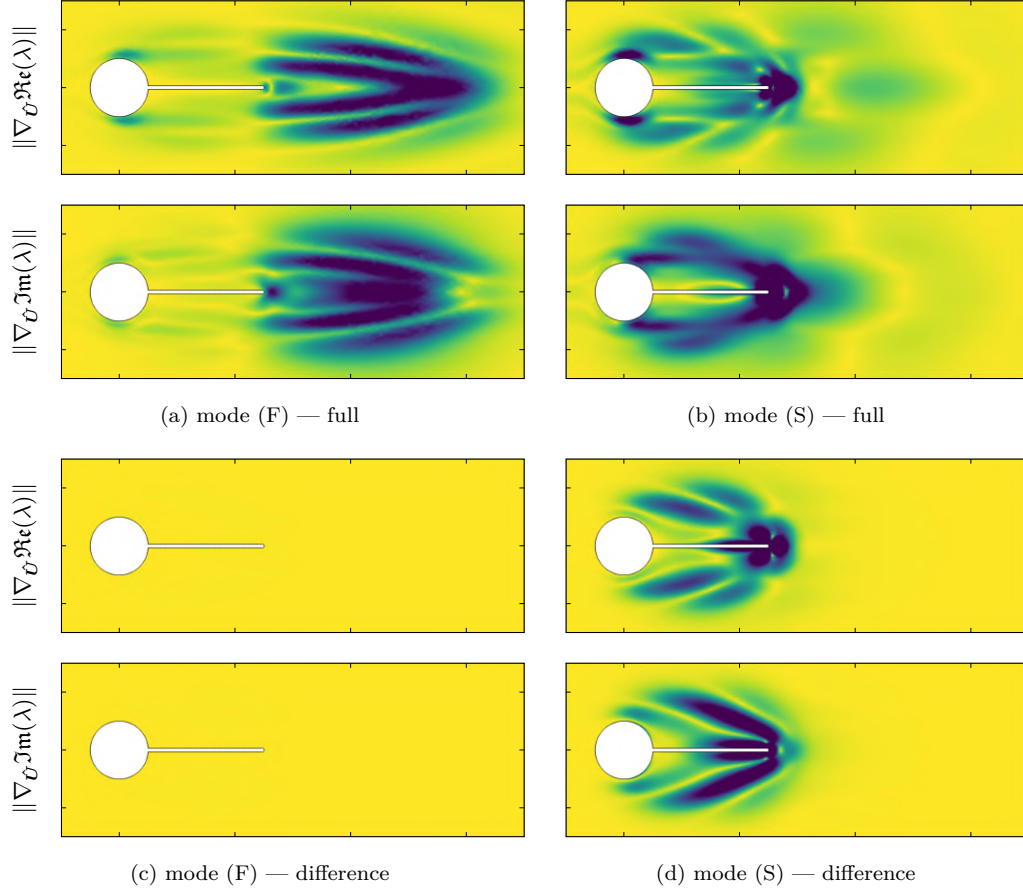


Figure 4.9 – Sensitivity to a stationary flow variation. Maps of the magnitudes for the real and imaginary parts of (a,b) $\nabla_{\mathbf{U}}\lambda$, and (c,d) of $\nabla_{\mathbf{U}}\lambda$ minus the pure hydrodynamic contribution $-(\nabla \mathbf{u}^{\circ*})^T \mathbf{u}^\dagger + \nabla \mathbf{u}^\dagger \mathbf{u}^{\circ*}$. The same levels are taken everywhere.

Sensitivity to steady flow modifications

The sensitivity of the eigenvalue λ to a *steady flow modification* can be evaluated by looking at the gradients $\nabla_{\mathbf{U}}\lambda$ obtained from (4.3.14). The results are reported in Fig. 4.9 where the complete term is represented in (a,b), while the difference between $\nabla_{\mathbf{U}}\lambda$ and the pure hydrodynamic contribution $-(\nabla \mathbf{u}^{\circ*})^T \mathbf{u}^\dagger + \nabla \mathbf{u}^\dagger \mathbf{u}^{\circ*}$ derived by Marquet *et al.* (2008) is represented in (c,d), with the same color levels.

Looking first at the full component (a,b), we see a clear difference between the cases (F) and (S): for the mode (F), there is a large sensitivity in the wake and a smaller sensitivity in the vicinity of the detachment area at the surface of the cylinder. Conversely, structures concentrated all around the solid are found for the mode (S). Notice also the difference in terms of growth-rate and frequency sensitivity close to the cylinder. For the mode (F), the contributions are very similar, while stronger differences are observed for the mode (S). This indicates that for a given modification of the steady flow in the vicinity of the detachment region at the surface of the cylinder, different effects on the frequency/growth-rate are likely occur, depending on the nature of the mode.

On the other hand, looking in (c,d) at the magnitude of the difference between the complete sensitivity map obtained from (4.3.14) and that from Marquet *et al.* (2008), we clearly see the “fluid” nature of the mode (F): all the sensitivity is contained in the pure hydrodynamic term. Conversely, we see in (d) that the corrections induced by the fluid-elastic part are not small, even in the vicinity of the cylinder.

We see here how a modification of the steady flow might influence the eigenvalue. Especially,

shape optimization will certainly act locally (because there are sensitive regions close to the cylinder) but also non-locally, since a modification of the shape of the cylinder is also likely to affect the wake.

Structural sensitivity

A measure of the sensitivity of the eigenvalues to perturbations of the *eigenvalue problem* is the *structural sensitivity*, first introduced by [Giannetti & Luchini \(2006\)](#) in the context of the linear stability analysis for a cylinder flow, as a measure of the sensitivity of the eigenvalues to a modification of the structure of the eigenvalue problem. A generic perturbation $\delta\mathcal{H}$ of the eigenvalue problem (4.2.4) generating perturbations $\lambda + \delta\lambda$ and $\hat{\mathbf{q}}^\circ + \delta\hat{\mathbf{q}}^\circ$,

$$\left\{ (\lambda + \delta\lambda) \hat{\mathcal{T}}_{\text{fsi}}(\hat{\mathbf{Q}}) - \hat{\mathcal{N}}'_{\text{fsi}}(\hat{\mathbf{Q}}) \right\} (\hat{\mathbf{q}}^\circ + \delta\hat{\mathbf{q}}^\circ) = \delta\mathcal{H}(\hat{\mathbf{q}}^\circ),$$

results at first-order, using the properties of the adjoint equation and the normalization condition $\langle \hat{\mathbf{q}}^\dagger, \hat{\mathcal{T}}_{\text{fsi}}(\hat{\mathbf{Q}}) \hat{\mathbf{q}}^\circ \rangle = 1$, to the relation

$$|\delta\lambda| = |\langle \hat{\mathbf{q}}^\dagger, \delta\mathcal{H}(\hat{\mathbf{q}}^\circ) \rangle|$$

An upper bound for the eigenvalue variation can then be obtained if one considers that $\delta\mathcal{H}$ takes the form of a spatially localized force-velocity feedback. According to [Giannetti & Luchini \(2006\)](#), such feedback could practically be produced by introducing small devices exerting a force whose direction and strength depend on the local value of the velocity field. In the fluid-structure case, the greatest eigenvalue drift is thus bounded as $|\delta\lambda| \leq \hat{S}(\hat{\mathbf{x}})$ for a disturbance located in $\hat{\mathbf{x}}$, with

$$\hat{S}(\hat{\mathbf{x}}) = \begin{cases} \|\hat{\mathbf{u}}^\circ(\hat{\mathbf{x}})\| \|\hat{\mathbf{u}}^\dagger(\hat{\mathbf{x}})\| & \text{in } \hat{\Omega}_f \\ \|\hat{\mathbf{u}}_s^\circ(\hat{\mathbf{x}})\| \|\hat{\mathbf{u}}_s^\dagger(\hat{\mathbf{x}})\| & \text{in } \hat{\Omega}_s \end{cases}$$

where $\|\cdot\|$ is the algebraic 2-norm computed pointwise, thus defining $\hat{S}(\hat{\mathbf{x}})$ as a spatial field. The above definition ensures that \hat{S} defines a continuous and smooth field, because both the direct and adjoint fluid and structure velocities have indeed to match at the interface. High sensitivities are associated to an high receptivity to a structural modification of the eigenvalue problem. In the context of fluid dynamics, the sensitivity maps obtained for a cylinder flow could explain how the stability of the wake is affected by the presence of small control cylinders ([Giannetti & Luchini, 2006](#); [Strykowski & Sreenivasan, 1990](#)).

A map of the structural sensitivity is reported in Fig. 4.10 for both modes, and shows great differences. The structure with two symmetrically placed lobes observed in the sensitivity map for the mode (F) is very close to what is also observed in the cylinder flow by [Giannetti & Luchini \(2006\)](#), although it is shifted more downstream because of the presence of the splitter plate. Close to the cylinder's surface, the sensitivity is however very weak. This indicates that a mechanism concentrated at the interface — typically, shape optimization — should act in a non-local way for provoking an eigenvalue drift.

For the mode (S), the sensitivity peaks at the tip end of the plate, as could have been speculated from the mode (Fig. 4.8) that concentrates structures close to the solid. Again, this emphasizes the “solid” nature of the mode: the largest drift of the eigenvalue is obtained by a perturbation in the solid. On the other hand, a relatively large-amplitude sensitivity is also located close to the top and bottom ends of the cylinder. A local effect of the shape optimization of the cylinder can therefore be expected.

At the level of the eigenvalue problem, we again see that different sensitivities are found depending on the nature of the mode. Let us now compute the shape gradients.

4.4.3 Shape gradients

In the following, we use the regularized descent direction ϕ_λ to represent graphically the shape gradient of λ along the cylinder's surface. Recall that it writes as $\phi_\lambda = -G_\lambda \hat{\mathbf{n}}$ when the \mathcal{L}^2 -approach

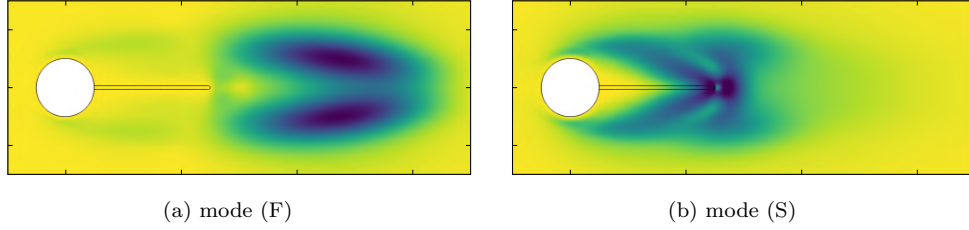


Figure 4.10 – Structural sensitivity. Plot of $\hat{S}(\hat{\mathbf{x}})$ for (a) the mode (S) and (b) the mode (F). Colors scaled with respect to the highest values (darker is higher).

is used. From the shape gradient expression (4.3.18), recall also that we can split the expression as the sum of a steady part $\phi_{\lambda,s}$ and an unsteady part $\phi_{\lambda,u}$. The sensitivity of the eigenvalue to a variation of the shape of the cylinder is then visualized as follows:

$$\begin{aligned} \text{decrease the growth-rate} &\Rightarrow \text{deform according to } \Re\{\phi_{\lambda,s} + \phi_{\lambda,u}\}, \\ \text{decrease the frequency} &\Rightarrow \text{deform according to } \Im\{\phi_{\lambda,s} + \phi_{\lambda,u}\}. \end{aligned}$$

The real parts of the steady and unsteady components of ϕ_λ are related to a modification of the growth-rate, while the imaginary parts are related to a modification of the frequency. In the following graphs, the arrows thus represent the oriented interface displacement (arbitrary scaled) that should be prescribed so as to decrease either the growth-rate or the frequency of the mode. All the components are found to be symmetric with respect to the horizontal axis. This property can easily be deduced from the symmetries of the problem (the stationary flow is symmetric with respect to the horizontal axis). Let us now detail the features of the shape gradient.

Shape gradient for the mode (F)

Let us first turn our attention for deformations of the cylinder's surface that modify the mode (F) in the direction of the decrease of the components of the leading eigenvalue. We immediately notice in Fig. 4.11 the different scale of the two components (that have been magnified for the purpose of the visualization): the steady component is at least 200 times greater than the unsteady one. This means that almost all the controllability of the mode (F) has to do with a modification of the steady flow rather than a modification of the structure of the eigenvalue problem.

Let us then focus on the predominant component whose features are reported at the top in Fig. 4.11a for the growth-rate and at the top in Fig. 4.11b for the frequency. The imaginary part has an amplitude about twice as large as the real part and, interestingly, it is also observed that the two components are almost proportional: they both cross zero at almost the same position (the first crossing occurs at $\theta = 64^\circ$ and the second one at $\theta = 126^\circ$ for both the real and imaginary part). Furthermore, the peaks for both curves are reached at about the same angle. The major peaks are located slightly upstream to the top/bottom of the cylinder ($\theta = 95^\circ$ and $\theta = 97^\circ$ for $\Re(\phi_{\lambda,s})$ and $\Im(\phi_{\lambda,s})$ respectively). The contributions have however opposite signs: a decrease of the growth-rate is associated to a flattening of the shape along the vertical axis — which seems reasonable —, while a decrease of the frequency is associated to a blowing of the shape in the opposite direction.

Shape gradient for the mode (S)

Moving now to the analysis for the mode (S) and focusing first on the real part, it is observed in Fig. 4.12 that both the steady and the unsteady components have roughly the same amplitude. Looking at $\phi_{\lambda,s}$ and $\phi_{\lambda,u}$, it is clear that the two components act in an opposed way. The stationary component is associated with a blowing in the directions $\theta \pm 135^\circ$, while the unsteady component prescribes a crushing of the shape along the vertical axis. If the slendening of the shape, by reduction of the cross-section, has an evident stabilizing effect, the blowing effect observed in

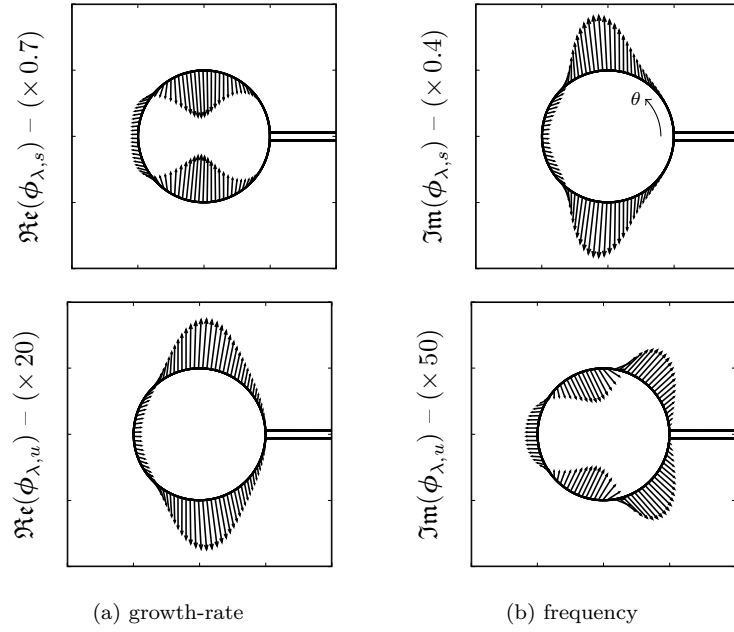


Figure 4.11 – Gradient-based shape modifications for the mode (F). Plot of the real and imaginary parts of the steady and unsteady components of a descent direction that decreases (a) the growth-rate (real part of $\phi_{\lambda,u}$ and $\phi_{\lambda,s}$) and (b) the frequency (imaginary part of $\phi_{\lambda,u}$ and $\phi_{\lambda,s}$) of the mode (F). The angle θ represents the position along the cylinder's surface, counted in anti-clockwise direction from the middle of the boundary where the plate is clamped to the cylinder.

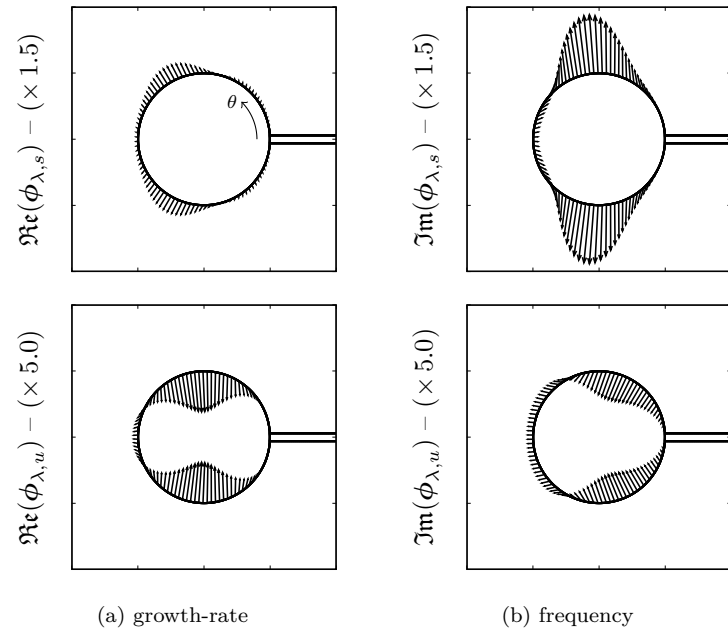


Figure 4.12 – Gradient-based shape modifications for the mode (S). Plot of the real and imaginary parts of the steady and unsteady components of a descent direction that decreases (a) the growth-rate (real part of $\phi_{\lambda,u}$ and $\phi_{\lambda,s}$) and (b) the frequency (imaginary part of $\phi_{\lambda,u}$ and $\phi_{\lambda,s}$) of the mode (F). The angle θ represents the position along the cylinder's surface, counted in anti-clockwise direction from the middle of the boundary where the plate is clamped to the cylinder.

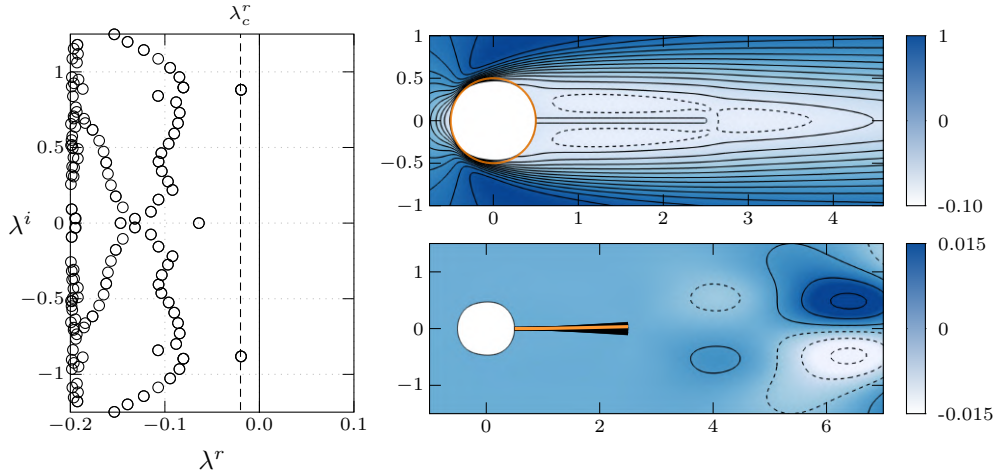


Figure 4.13 – Spectrum and leading eigenmode in the optimized case (F). Eigenvalue spectrum (left), streamwise velocity component of the stationary flow (top right, dashed negative contours, the first solid line in the vicinity of the recirculating region marks the limit of zero velocity, and the initial cylinder’s shape is materialized by the orange circle), and real part of the streamwise component of the leading mode (bottom right, same levels as in Fig. 4.7). Snapshots of the solid deformation are also reported (same nomenclature and scaling as in Fig. 4.7).

ϕ_s is less evident to interpret. The combination of the two seems to generate a more “D-shaped” bluff-body when it comes to decrease the growth-rate of the mode.

The imaginary part is associated to a modification of the frequency and roughly act with the same signs, but with very different amplitudes. The amplitude for steady the component is actually about 10 times higher than the one for unsteady. For instance, decreasing infinitesimally the frequency of the mode (S) therefore essentially requires to deform the shape according to $\Im(\phi_{\lambda,s})$ into an ellipse whose major axis is directed along the vertical axis, while the information in $\phi_{\lambda,u}$ only intervenes as a second-order effect.

4.4.4 Shape optimization for controlling the growth-rate of the modes

We focus in this section on the shape optimization for controlling the growth-rate of the modes. We therefore consider $\alpha_r = 1$ and $\alpha_i = 0$, i.e. in this section the cost-function writes

$$\mathcal{J}(\hat{\Omega}) = \frac{1}{2} \left(\lambda^r(\hat{\Omega}) - \lambda_c^r \right)^2.$$

Using the gradient descent algorithm described in the Fig. 4.4, optimal shapes satisfying $\lambda^r = \lambda_c^r$ (up to a prescribed tolerance) are computed. In particular, setting $\lambda_c^r < 0$ amounts to finding shapes which suppress the instability. On the other hand, taking λ_c^r greater to the initial growth-rate (that found in the non-optimized case) results in shapes that come with a stronger instability. Note also that the frequency is left unconstrained in this case. The case where the a target frequency is set will be considered in §4.4.5.

Optimal shapes

Let us first set the growth-rate control to a slightly negative value $\lambda_c^r = -0.02$. The results of the shape optimization for the mode (F) are reported in Fig. 4.13, with the same nomenclature as that used in Fig. 4.7 (except that a slightly closer view is taken to depict the stationary flow, so as to see more clearly how the shape is modified). In the spectrum on the left, the target growth-rate has been identified with the vertical dashed line, and we see that the optimized eigenvalue has reached the target. Compared to the initial mode, the frequency is increased to 0.88. It is observed that the mode is stabilized through a small flattening of the cylinder. The deformation is not symmetric

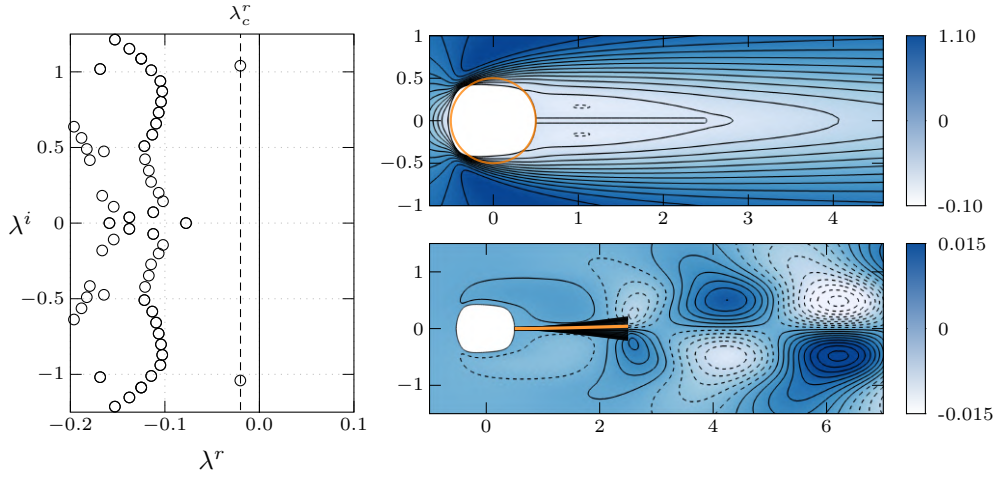


Figure 4.14 – Spectrum and leading eigenmode in the optimized case (S). Eigenvalue spectrum (left), streamwise velocity component of the stationary flow (top right, dashed negative contours, the first solid line in the vicinity of the recirculating region marks the limit of zero velocity), and real part of the streamwise component of the leading mode (bottom right, same levels as in Fig. 4.8). Snapshots of the solid deformation are also reported (same nomenclature and scaling as in Fig. 4.8).

with respect to the $x = 0$ axis: the cylinder is slightly more flattened in the region $x < 0$. Despite this small variation of the geometry, the stationary flow is noticeably modified. For instance, the limit of the recirculating region in the streamwise direction, initially located at $x = 5.54$, is moved upstream up to $x = 4.45$. The reduction of the wake comes with modal structures that are located more downstream, as seen in the lower right picture.

The results for the shape optimization in the case (S) are reported in Fig. 4.14. Although the control value is the same ($\lambda_c^r = -0.02$), the optimal shape that stabilizes the mode (S) notably differs from what was observed previously. If again the cross-section is reduced (which has a stabilizing effect, since it reduces the apparent Reynolds number), there is kind of a growth on the front face of the cylinder, which forms a steeper change of curvature than previously. Like previously, the recirculation region is smaller in the optimized case (limit at $x = 4.35$ in the initial case and $x = 2.81$ in the optimized case).

Let us now vary the value of the target growth-rate λ_c^r . The least stable eigenvalue obtained once the optimization has converged is represented in the complex plane in Fig. 4.15. The vertical axis thus displays the reached growth-rate λ^r as well as the objective growth-rate λ_c^r , which are the same up to the prescribed tolerance. The initial cases are depicted with the ■ symbol for the case (F) and with the ■ symbol for the case (S). In both cases the converged, optimized eigenvalue evolve similarly: the more stable the target growth-rate, the higher the frequency. For the case (S) however, the frequency reach a maxima as λ_c^r is increased up to about 0.05, then decreases again. Note also that for the same value of λ_c^r , the frequency does not reach the same value in both cases (F/S).

A few shapes are represented in the inserts (arrows indicating which is the corresponding eigenvalue). Their properties make sense: a stabilization of the mode is achieved by flattening the shape. This lowers the apparent Reynolds number of the bluff-body, but not down to the point that it reaches the critical Reynolds number of 92: the streamlining effect induced by the decrease of the curvature of the shape indeed also tends to stabilize the flow by favourably positioning the detachment point (the limits of the recirculating region in the optimized shapes are indicated with a dashed line). If the overall trend is the same for both types of modes, the optimal shapes for the modes (F) and (S) is not the same: the shapes associated to the cases (S) they are somewhat sharper.

Rather than targeting a specific value for the growth-rate, it is also interesting to examine, for a fixed target λ_c^r , the influence of the initial state. For that purpose, we consider a set of

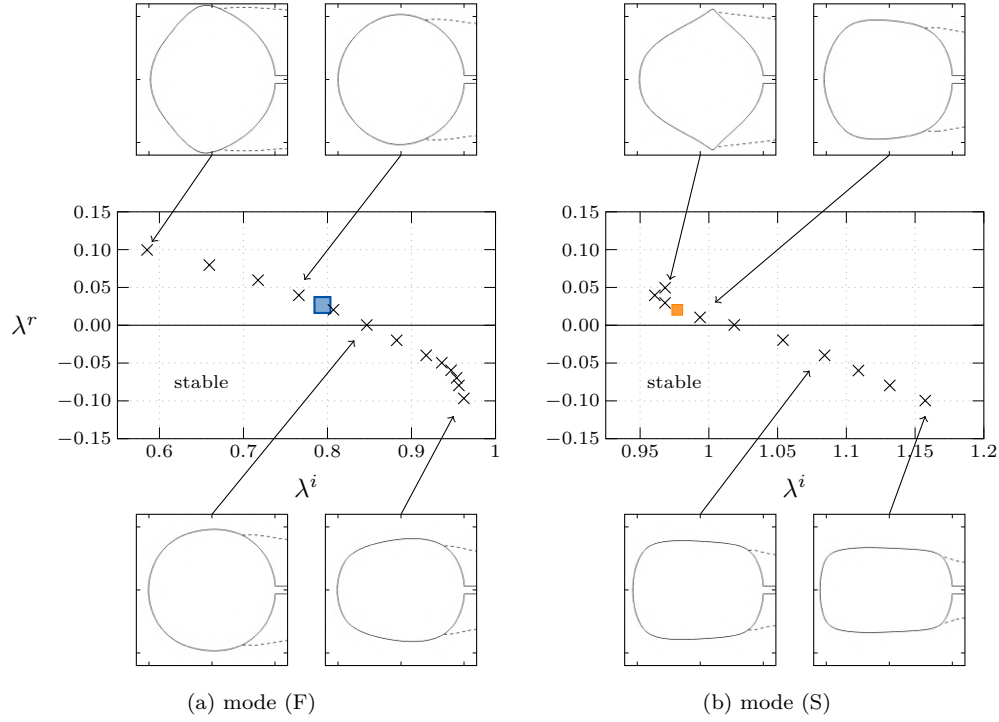


Figure 4.15 – Shape optimization for controlling the growth-rate. Representation, after shape optimization, of the leading coupled fluid-structure eigenvalues for the case where the growth-rate is optimized (the growth-rate satisfies at convergence $|\lambda^r - \lambda_c^r| < \text{tol}$). The square symbols represent the initial location in the spectrum of the leading eigenvalue. A few optimized shapes are indicated with the inserts, where the limits of the back-flow region behind the bluff-body has been marked with a dashed line.

unstable configurations at $\mathcal{R}_e = 80$ with different values of \mathcal{E}_s (represented by the small orange squares in Fig. 4.6), and consider the growth-rate optimization problem with $\lambda_c^r = -0.01$, that is, one tries to stabilize the unstable mode. In all cases it has been checked that the optimized shape yields to only stable eigenvalues in the global spectrum. The corresponding results are reported in Fig. 4.16. We see in Fig. 4.16a that for all the cases considered (the initial, unstable eigenvalues are displayed in the left side of the complex plane, each point representing a different value of the stiffness) a stabilization can be achieved. The stabilized modes have an increased frequency compared to the initial ones, as indicated by the dashed lines that link the initial and the optimized modes leading eigenvalues. Some characteristics of the optimal configuration are reported in the Figs. 4.16b and 4.16c, that show non-monotonic variations. For instance, at moderate stiffnesses, the cross-section of the optimal shape decreases with \mathcal{E}_s , before reaching a minimum and then increasing with the stiffness. The same observation holds for the length of the recirculating region, as represented in Fig. 4.16c. The variation of the cross-section indeed directly influences the length of the recirculation region. The plateau between $\mathcal{E}_s = 0.5$ and 0.8 corresponds to a case where the limit of the two recirculating bubbles touches the tip of the plate.

Algorithm convergence & global fluid-structure spectrum modifications

Let us finally give some technical details about the optimization algorithm. Starting from the initial case where the rigid cylinder is circular, the optimization algorithm results in modified shapes that are no longer circular but present a modified curvature. The convergence of the method is tuned with the update parameter k , that sets the magnitude of the deformation along the direction given by the gradient. We also found that no normalization of the gradient was needed. We did not develop any special feature other than trial-and-error for choosing k . Our selected values were

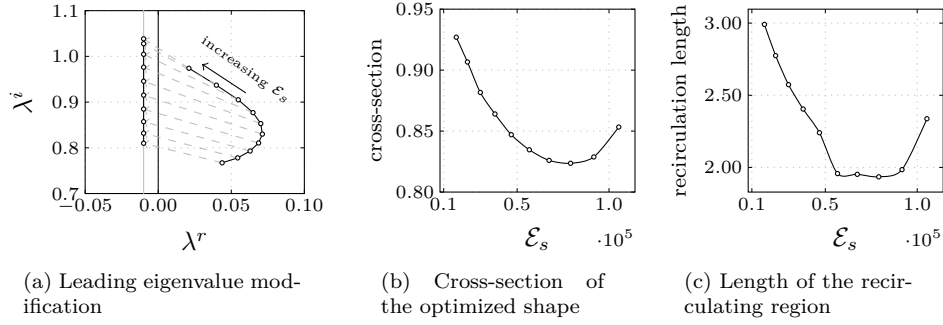


Figure 4.16 – Influence of the initial state for (S)-like modes optimization.

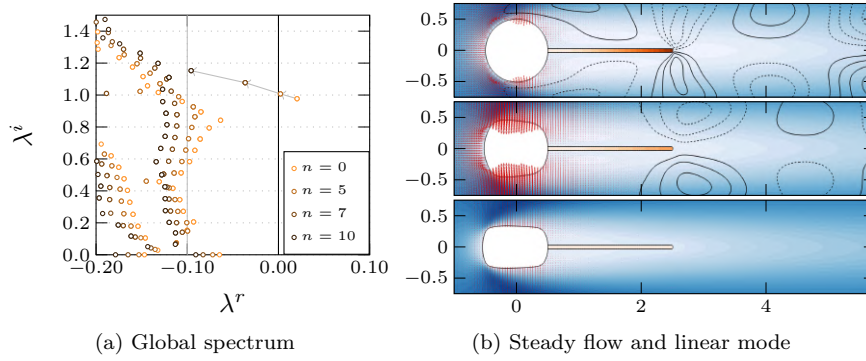


Figure 4.17 – Evolution of the global features during shape optimization. (a) plot of the coupled fluid-structure spectrum for different iterations of the optimization algorithm. (b) snapshots of the fluid-structure mode at iteration 0 (top), 5 (middle) and 10 (bottom). The streamwise steady flow velocity is depicted in blue shade color, the modulus of the transverse displacement in the solid is depicted in orange color, and a snapshot of the streamwise velocity of the fluid-structure mode is represented with the lines (dashed lines indicate negative contours). The phase has been adjusted between the different modes. The \mathcal{H}^1 extended-regularized deformation field obtained from the shape gradient is represented by the red arrows (amplitude magnified 20 times).

between 0.1 and 2 for all the cases tested. The key point is to find a balance between a too small value that comes with a slow convergence, and a too high value. In this latter case, the shape at iteration $n + 1$ might be notably different from the shape at iteration n . In that case, like for every optimization algorithm one could simply miss the minimum of the cost function. Another problem, specific to our eigenvalue tracking procedure, is the following: in the Arnoldi process for solving the eigenvalue problem at step $n + 1$, the eigenvalues are sought in the vicinity of a complex shift that is defined in our case as the eigenvalue at iteration n . If the new shape at iteration $n + 1$ is very different from the previous one, this shift value might lie in a region of the fluid-structure spectrum where the most unstable eigenvalue no longer lie. In that case, the tracking of the eigenvalue might be lost. This is easily observable in an history of the eigenvalues: in that case, a large discontinuity is then observed between two successive iterations.

Although our approach could be easily adapted for handling several eigenvalues, we consider here the case where only one eigenvalue is modified through shape optimization. Therefore, it is relevant to examine how the modification of one eigenvalue affects the entire spectrum through the optimization process. To address this question, let us consider as an example the case where $\mathcal{J}(\hat{\Omega}) = 1/2(\lambda^r + 0.1)^2$ — other cases would lead to the same observations. We take an update step of $k = 2$, in which case 14 iterations are required for $\mathcal{J}(\hat{\Omega})$ to decrease down below 1×10^{-7} . The main features of the evolution of the fluid-structure system are reported in Fig. 4.17. The global spectra at iterations 0 (initial configuration), 5, 7 and 10 are represented in Fig. 4.17a. The

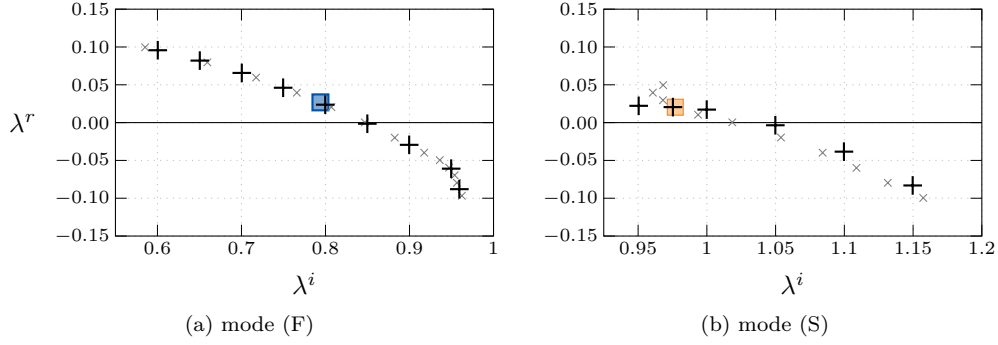


Figure 4.18 – Shape optimization for controlling the frequency. Representation, after shape optimization, of the leading coupled fluid-structure eigenvalues (+) for the case where the frequency is optimized (the frequency satisfies at convergence $|\lambda^i - \lambda_c^i| < \text{tol}$). The square symbols represent the initial location in the spectrum of the leading eigenvalue. For the sake of comparison, the eigenvalues reported in Fig. 4.15 (optimization of the growth-rate only) are also reported (x).

evolution of the leading eigenvalue towards the left side of the complex plane is associated with a global decrease of the growth-rate of the modes. However, at some point (between iterations 7 and 10), the tracked mode (its path is emphasized by the gray arrows) ceases to be the most unstable one for the benefit of a zero-frequency mode. This illustrates the need for an *a-posteriori* computation of the entire spectrum, to ensure that no other mode has become unstable elsewhere. Snapshots of the flow are represented in Fig. 4.17b, together with a representation (red arrows) of the \mathcal{H}^1 deformation field that extends the information of the gradient onto the whole fluid domain. The phase of the streamwise velocity mode at iteration 5 (middle) has been adjusted in such a way that it corresponds to the phase of the mode at iteration $n = 0$, and the same contour levels have been kept between the three pictures.

4.4.5 Shape optimization for controlling the frequency of the modes

Frequency optimization

We now consider the case where the frequency is set to a specified value λ_c^i , while the growth-rate is left free to evolve. In the present case, the cost-function therefore writes as

$$\mathcal{J}(\hat{\Omega}) = \frac{1}{2} \left(\lambda^i(\hat{\Omega}) - \lambda_c^i \right)^2.$$

The obtained eigenvalues at convergence of the algorithm are reported in Fig. 4.18 for both reference cases, as a function of the target frequency λ_c^i . We observe that the converged eigenvalue are clustered in the same region of the complex plane as previously: for comparison, the gray crosses represents the location of the optimized eigenvalues obtained by targeting a specified growth-rate. In particular, for the case (F) it seems that the optimizations with $(\alpha_r, \alpha_i) = (1, 0)$ and $(\alpha_r, \alpha_i) = (0, 1)$ result in modes that collapse on the *same* curve. The same is not true for the case (S), although the same global tendency is observed.

The remarkable link between the frequency/growth-rate optimization for the mode (F) can be interpreted by coming back to the gradients. It has been observed for the mode (F) that (i) the steady component is largely dominant over the unsteady component (Fig. 4.11), and (ii) that the real and imaginary parts of the steady component are almost proportional with opposite signs, $\Im\{G_{\lambda,s}\} \simeq -0.5 \Re\{G_{\lambda,s}\}$, see Fig. 4.11 or Fig. 4.19. Combining these two assumptions, we can simplify (4.3.19) as follows,

$$\begin{aligned} G &= \alpha_r(\lambda^r - \lambda_c^r) \Re\{G_\lambda\} + \alpha_i(\lambda^i - \lambda_c^i) \Im\{G_\lambda\} \\ &\simeq (\alpha_r(\lambda^r - \lambda_c^r) - 0.5 \alpha_i(\lambda^i - \lambda_c^i)) \Re\{G_{\lambda,s}\}. \end{aligned}$$

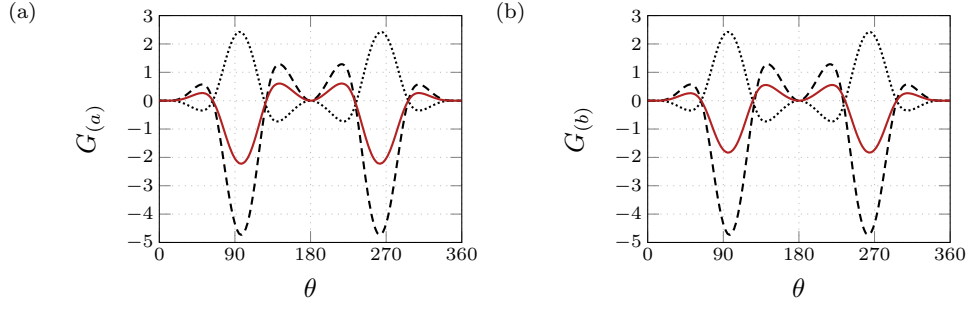


Figure 4.19 – Shape gradients for the mode (F). Representation of the real (\cdots) and imaginary ($---$) parts of the stationary part for the shape gradient $G_{\lambda,s}$, and plot of the composite gradient G (—) for (a) $G_{(a)} = 0.47 \Im(G_{\lambda,s})$ and (b) of $G_{(b)} = -0.76 \Re(G_{\lambda,s})$, as a function of the position θ , in degrees, along the cylinder's surface ($\theta = 0$ corresponds to the side where the splitter plate is clamped).

In other words, the gradients for the frequency-based and growth-rate-based optimizations are almost *proportional*.

Let us for instance consider two optimization cases. The shape gradients are reported in Fig. 4.19, as a function of the angle θ along the cylinder's surface in order to facilitate quantitative comparisons. In the first case (a), we set $(\alpha_r, \alpha_i) = (0, 1)$ with a target frequency set to $\lambda_c^i = 0.7$ (looking in Fig. 4.18a, the optimized eigenvalue is then $0.065 + 0.7i$). As a second case (b), we set $(\alpha_r, \alpha_i) = (1, 0)$ and a target growth-rate to 0.065 — which would result in the *same* eigenvalue $0.065 + 0.7i$ after shape optimization. The associated shape gradients for these two objectives have the same signs and are proportional: with $\lambda_{(F)} = 0.0277 + 0.794i$ being the initial eigenvalue, we have $G_{(a)} \simeq 0.094 \Im(G_{\lambda,s})$ and $G_{(b)} \simeq -0.0373 \Re(G_{\lambda,s})$. Since $\Im(G_{\lambda,s})$ and $\Re(G_{\lambda,s})$ have opposite signs, these two gradients have eventually the same sign, as reported in Fig. 4.19 where the two gradients (scaled differently) are reported with the thick red line.

This property is actually conserved during the optimization steps, which shrinks the set of reachable eigenvalues to a curve passing through the initial (non-optimized eigenvalue). Conversely, because of the richer structure of the gradient for the mode (S), more varied optimal shapes can be reached. In the next section, we perform a combined optimization aiming at specifying both the frequency *and* the growth-rate.

Remark. Note that in the case of a stable flow, changing the target frequency or growth-rate would result in stable flows having different features (drag/lift) depending on the choice of λ_c^i , but there is *a priori* no simple way to connect the objective eigenvalue to integrated quantities such as the drag of the object in the steady flow. In this case, it is more adapted to adopt an approach in which the objective-function is directly the drag like for instance in the work by Lund *et al.* (2003), or a measure of the distance to a prescribed velocity or energy criteria (Pironneau, 2012). This can be relatively easily done within the present framework — the derivation of the shape gradient is in that case by any means simpler as what is needed in the unsteady case.

Combined frequency & growth-rate optimization: design of a fluid-structure oscillator

A practical outcome for the frequency-based optimization would be the ability to design a fluid-structure oscillator, beating at a prescribed frequency. In the case where the flow is slightly unstable, an exponential growth of perturbations oscillating at frequency λ_c^i will be observed (in an experiment or in non-linear simulations) in the linear regime of development of the instabilities if no significant transient growth affects the process (Schmid & de Langre, 2002). Hopefully, some features observed linearly would then persist once the non-linear limit-cycle is reached, as it was already observed in the previous chapter. If all these requirements are fulfilled, the optimized system would behave as a self-sustained oscillator at a frequency close to λ_c^i . Practically, these

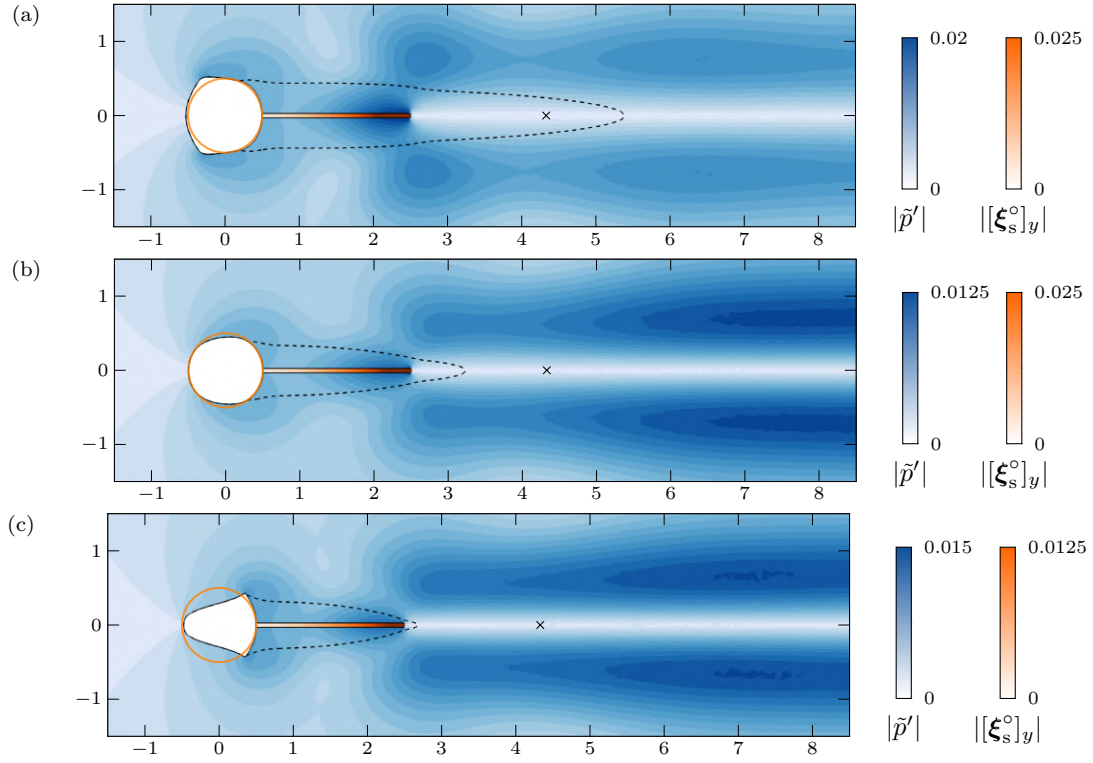


Figure 4.20 – Optimal fluid-structure oscillators. For the cases with $\lambda_c^r = 0.01$ and (a) $\lambda_c^i = 0.95$, (b) $\lambda_c^i = 1.025$ and (c) $\lambda_c^i = 1.1$, plot of the absolute value of the Eulerian pressure perturbation $\tilde{p}' - p' - \nabla P \xi_e'$ (blue colors in the fluid) and of the absolute value of the solid deformation mode ξ_s^o , transverse component (orange color in the solid). The limits of the back-flow region of the steady flow is marked with the dashed black line, while the maximal x extension of the back-flow region for the *initial, non-optimized shape* materialized with the orange circle is marked with a cross (\times).

features could for instance be exploited to design more efficient energy-harvesting devices, by tuning the resonance frequencies of the system in order to maximize the energy transfer (Carini *et al.*, 2017).

To do so, the growth-rate should nevertheless stay positive. The approach where only the frequency is taken as a part of the cost-function is thus not very appropriate, since we have seen above that in that case the flow becomes at some point *stable* when the frequency target is increased. We therefore set here a cost-function that depends on both the growth-rate and the frequency, that is,

$$\mathcal{J}(\hat{\Omega}) = \frac{1}{2} \left(\lambda^r(\hat{\Omega}) - \lambda_c^r \right)^2 + \frac{1}{2} \left(\lambda^i(\hat{\Omega}) - \lambda_c^i \right)^2.$$

On the contrary to the previous case where an high target frequency results in a stable flow, an unstable fluid-structure oscillator at a prescribed frequency can be designed here. In the following, we choose a constant positive growth-rate $\lambda_c^r = 0.01$ for all cases. We consider here the case (S). Probably for the reasons presented above (proportionality of the gradients), for the case (F) it was actually not possible to obtain shapes associated with other values (λ^r, λ^i) than that reported in Fig. 4.18a.

An overview of the optimization results is displayed in Fig. 4.4.5., which is indicated by the dashed line in the figure. As the frequency objective is varied, different shapes are obtained, four of them being displayed in the inserts (top left: $\lambda_c^i = 0.925$, top right: $\lambda_c^i = 0.950$, bottom left: $\lambda_c^i = 1.025$, bottom right: $\lambda_c^i = 1.1$). For the case with $\lambda_c^i = 0.925$, a second unstable mode located at $0.0411 \pm 0.514i$ is found in the spectrum of the linearised problem, after convergence of the algorithm, in addition to the controlled mode located at $0.01 \pm 0.925i$. Since its growth-rate is

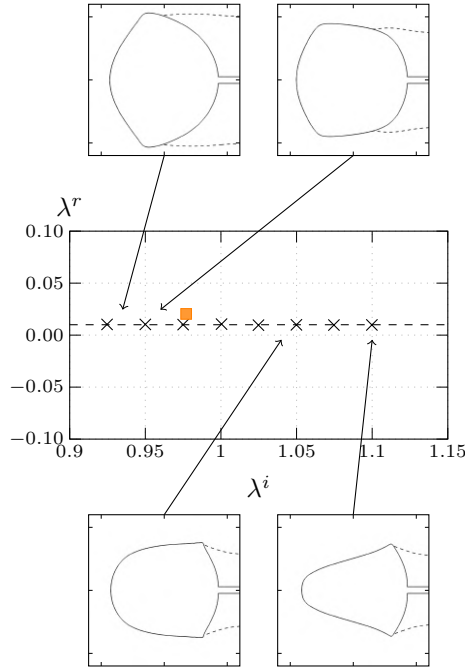


Figure 4.21 – Shape optimization for designing a fluid-structure oscillator. Plot, in the (λ^i, λ^r) plane, of the converged eigenvalues obtained with an optimization for the growth-rate (fixed to $\lambda_c^r = 0.01$) and the frequency (varying between 0.925 and 1.1). A few optimal shapes are represented, with $\lambda_c^i = 0.925$ (upper left), $\lambda_c^i = 0.95$ (upper right), $\lambda_c^i = 1.05$ (below left) and $\lambda_c^i = 1.1$ (below right). The eigenvalue corresponding to the initial shape (circular cylinder) is represented with the orange square symbol.

much larger than the target value of $\lambda_c^r = 0.01$, it overcomes the growth of the optimized mode and is the predominant mode of the flow. A two-points optimization taking into account of these two unstable modes would be mandatory to treat this specific case, but will not be considered here. For all the other cases displayed in Fig. 4.4.5, only one unstable mode is found.

Let us describe more precisely the obtained flow for three cases. The corresponding results are reported in Fig. 4.20 where, for sake of comparison, the initial (i.e. before the optimization process) shape is materialized by the orange circle, and the limit of the recirculating region of the stationary flow along the streamwise axis is marked with a cross symbol. The cases with $\lambda_c^i = 0.95$ (top), $\lambda_c^i = 1.025$ (middle) and $\lambda_c^i = 1.1$ (bottom) are represented. First, we note that even if the three modes have the same growth-rate, they are associated to steady flows having recirculating regions (whose limits are marked with the dashed line) of very different lengths: the maximal extension is reached at $x = 5.39$ for the lowest-frequency case (a), $x = 3.23$ for case (b) and $x = 2.65$ for the higher-frequency case (c). This situation is quite different from what is observed for a rigid case. In the circular cylinder flow for instance, the growth-rate of unstable modes is found to increase with the length of the stationary back-flow region (Giannetti & Luchini, 2006). Here, the shorter the recirculating region, the higher the frequency. A possible mechanism to explain this behaviour is that the ratio between the recirculating region and the splitter plate length might determine the vibration frequency, by specifying at which point vortices should be released so as to interact favourably with the solid. In this sense in (a) the vortex formation region is larger as in the case (c), and this increased half-width makes it longer for a vortex to complete its period of oscillation. Note however that previous studies, in which the length of a flexible splitter attached behind a circular (Lee & You, 2013; Wu *et al.*, 2014) or square (Mat Ali *et al.*, 2011) cylinder was varied, reported that the vortex shedding frequency possible varies non-monotonously, and in any case non-linearly with the length of the splitter plate. Complex mechanisms might therefore be at play.

The pressure mode in the fluid region is depicted with a blue color. The absolute value is represented so as to have a visualisation independent from the phase (real and imaginary parts are symmetric with respect to the axis $y = 0$). The structures close the the solid have roughly the same shape for all cases, indicating that the fluid-structure dynamics close to the solid is not dramatically different between the three cases. In particular, the absolute transverse displacement in the solid indicates that the vibration pattern in the solid is in all cases that of a bending mode with one vibration node at the clamped end.

Finally, the non-linear behaviour of the fluid-structure oscillators can also investigated. How

does the “optimal” linear frequency obtained with the time-linearised shape optimization process relates to the non-linear frequency resulting from a fully non-linear, time-marching simulation ? Except for the case $\lambda_c^i = 0.925$, that comes with another unstable mode (the corresponding non-linear simulation comes with an oscillation frequency of $\omega_{\text{DNS}} = 0.69$), a fairly good agreement is found. For instance, for the case $\lambda_c^i = 1$, the non-linear frequency obtained using a Fast Fourier Transform of the lift signal once the limit cycle has been reached is $\omega_{\text{DNS}} = 1.037$. This is in accordance with the observations in the previous chapter, where we observed that the predictions for the linear frequency are found to match pretty well with that extracted from the non-linear limit-cycles. The time-series exhibits a symmetric flapping regime with an amplitude of oscillation of the tip of the plate of 0.12.

4.5 Conclusion

A shape optimization approach for controlling the growth and the frequency of time-asymptotic linear, strongly coupled fluid-structure instabilities has been proposed. This approach has been applied on a model problem that consists in a flexible splitter plate clamped behind a cylinder and placed in a viscous, laminar flow. The control of two types of modes has been achieved, one first mode truly related to the fluid-structure interaction (i.e. that disappears in the rigid case) and another mode that is essentially related to the instabilities at play in the wake behind the cylinder. It is shown that it is possible to stabilize unstable fluid-structure modes by modifying the shape of the rigid cylinder, or to design an fluid-structure oscillator beating at a prescribed frequency. It has also been shown how the type of mode influences the region of the complex plane that can be eventually reached after the optimization process.

5

BOUNDARY-LAYER INSTABILITIES OVER A FINITE-LENGTH COMPLIANT COATING

We now turn on to the analysis of the second class of instabilities evoked in the introduction. We consider here a laminar boundary-layer flow, which is classically known for amplifying external perturbations such as noise or gusts. Specifically, we analyse the zero adverse pressure gradient boundary-layer flow over a flat plate in which a viscoelastic, finite-length compliant coating is embedded. Using a resolvent analysis of the linearised fluid-structure operator, we show in what extents the flexibility of the coating helps in reducing the growth of low-frequency Tollmien-Schlichting waves, but also triggers higher-frequency, solid-based travelling-wave flutter instabilities. These latter waves are globally unstable for purely elastic coatings and are stabilized by viscoelastic damping, but may still result in a large energy amplifications, which are analysed.

Contents

5.1 Introduction	134
5.1.1 A phenomenology of skin-friction drag-reducing mechanisms	134
5.1.2 Theoretical studies	137
5.2 Physical modelling & numerical model	140
5.2.1 Non-dimensional parameters	140
5.2.2 Navier-Stokes flow	141
5.2.3 Viscoelastic solid	142
5.2.4 Coupled problem and numerical settings	144
5.3 Eigenvalue analysis	145
5.3.1 Free solid dynamics	145
5.3.2 Fluid-elastic eigenvalue analysis	150
5.4 Elastic response to optimal fluid perturbations	155
5.4.1 Resolvent analysis in the rigid-wall case	156
5.4.2 Fluid-elastic response to an optimal rigid-wall forcing	158
5.4.3 Mechanism of wave attenuation/amplification	161
5.5 Fluid-elastic resolvent analysis	165
5.5.1 Fully coupled resolvent analysis	165
5.5.2 Results	165
5.6 Conclusion	166

5.1 Introduction

If the search for drag reduction has already a long history in engineering sciences, in nature billions of years of evolution have endowed both plants and animals with many astute features for decreasing the energy spent for locomotion, which furnishes as many endless sources of fascination and inspiration for engineers and scientists. Bio-inspired flow control mechanisms are indeed a promising way for progressing towards more efficient means of locomotion.

Among the different forms of drag — pressure drag, lift-induced drag and skin-friction drag, we concentrate here on the latter. Skin-friction drag is generally much lower than the pressure drag, except when the flow remains attached, which is the case for streamlined objects. In that case, a strong drag increase is observed when the flow undergoes the laminar-turbulent transition — for instance, depending on the Reynolds number, factors as large as 10 can be reached between the drag in a laminar and a turbulent boundary-layer over a flat plate (Emmons, 1951). Control mechanisms delaying the laminar-turbulent transition could thus provide valuable energy savings. Taking inspiration notably from the surprising ability of flying or swimming animals to move fast without spending too much energy, several devices have therefore been proposed to postpone the laminar-turbulent transition of boundary-layers. Blowing and suction devices, wave cancellation disturbance generators, moving walls or heating/cooling devices have for instance been designed (Gad-El-Hak, 2000). These devices are *active*, in the sense that they require an energy source to feed the actuator. On the other hand, *passive* mechanisms do not require sources of energy other than that from the flow itself.

5.1.1 A phenomenology of skin-friction drag-reducing mechanisms

In nature, marine animals have developed strategies to spend as little energy as possible to move around, that engineers try to reproduce. Both active and passive mechanisms are at play: Barrett *et al.* (1999) showed for instance experimentally that the power required to propel an actively swimming, streamlined, fish-like body is significantly smaller than the power needed to tow the body straight and rigid at the same speed. Even the porpoising movement of dolphins (the swimming mode consisting of alternate leaping and submersion) seems to have power-sparing foundations: in the review by Fish & Rohr (1999), it is emphasized that at high speeds it is more energy-efficient for dolphins to adopt this locomotion mode. In such a regime, the dolphin benefits in particular from the lower air density to reduce the overall drag.

Apart from these dynamical, active effects, passive mechanisms are also at play. With this respect, two basic approaches can be undertaken for reducing skin-friction drag: either maintain the flow laminar as long as possible, or alter the structure of the turbulent near-wall motion. Surface additives provide a large skin-friction drag reduction, through for instance polymers, surfactants or even bubbles (Bushnell & Moore, 1991). Permanent geometrical alterations such as ridges are associated with skin-friction drag reduction in turbulent flows. For instance, dolphins and sharks are found to benefit from ridge features, occurring as dermal denticles, to control the wall-turbulence (Bandyopadhyay & Hellum, 2014). In engineering applications, riblets (Walsh & Lindemann, 1984; Gad-El-Hak, 2000) are now commonly used to reduce the drag of boat hulls, aerofoils and aircrafts. Reductions as large as 12 % have been reported (Itoh *et al.*, 2006).

When the surface is *flexible*, wave propagation effects might also be at play. Some results have been obtained inspired from the study of the dolphins (Kramer, 1961): a typical cross-section of the skin has been reproduced from Carpenter *et al.* (2000) in Fig. 5.2a. The upper epidermal layer forms a dense elastic membrane considered capable of transmitting the pressure fluctuations to the underlying layer. This dermal layer is made of softer, more hydrated tissues, with a strong anisotropy induced by the presence of the dermal ridges, that also act as reinforcing structures (Pavlov, 2006). Note that these ridges are not homogeneous in the transverse direction of the skin but form rather regularly spaced pillars (Carpenter *et al.*, 2000). Wave propagation effects coming with this arrangement of the skin were evidenced for instance by Essapian (1955), who observed skin-induced skin folds at the surface of a high-speed swimming dolphin (Fig. 5.1a). In-vivo measurements have furthermore been performed so as to characterize the surface waves propagating along the skin of dolphins (Madigosky *et al.*, 1986). Apart from dolphins, Aleyev Yu

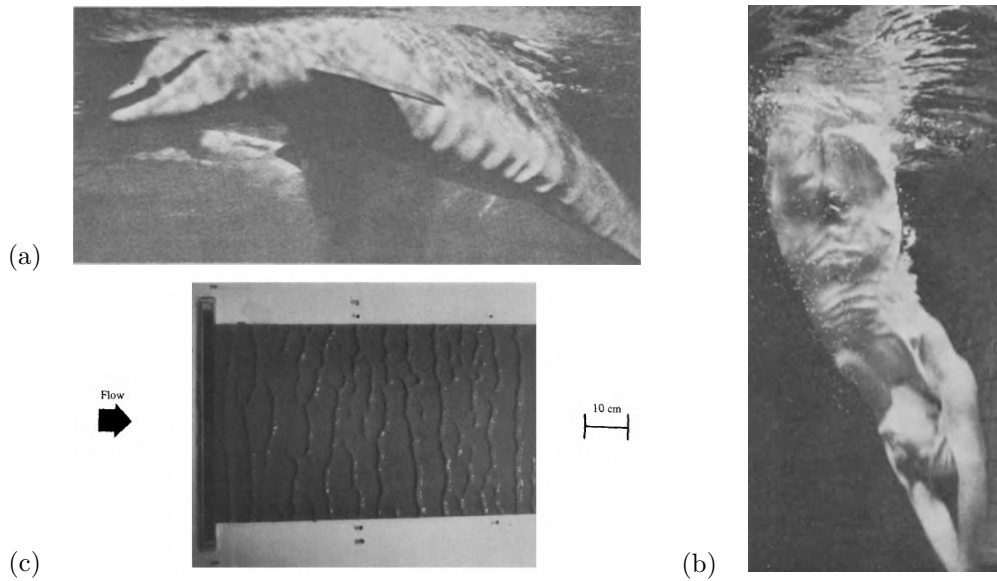


Figure 5.1 – Flow-induced skin folds. Observation of flow-induced elastic deformations (a) on the skin of a fast-swimming dolphin (Essapian, 1955), (b) on the skin of a human diving down (Aleyev Yu, 1977) and (c) at the surface of a viscoelastic coating (Gad-El-Hak *et al.*, 1984)

(1977) also observed deformation waves on the skin of humans diving down, see Fig. 5.1b. The phenomenon has also been reproduced in more controlled environments, for instance by Gad-El-Hak *et al.* (1984) who studied the interaction of a viscoelastic coating with a boundary-layer flow, see (Fig. 5.1c). An immediate question is then to know whether these flow-induced elastic surface deformations may help in reducing the drag.

The dolphin paradox & transition delay with flexible coatings

This question was raised after a controversy that begun with a study by Gray (1936). He asserted that if the resistance of an actively swimming dolphin at 10 m s^{-1} is equal to that of a rigid model towed at the surface, the power requirements would exceed by at least a factor seven the estimated power that the slow fibres of the muscles of a dolphin could generate in a continuous effort. If the boundary layer were to remain laminar, no such discrepancy would exist, hence the so-called “dolphin paradox”. From this statement, some researchers have inferred that dolphins must be able to maintain laminar flow by some process involving the flexibility of their skin (Kramer, 1961). New estimates for the energy balance (Babenko & Carpenter, 2003; Fish, 2006) and the drag reduction that comes with the swimming motion (Bale *et al.*, 2014) showed that there is actually no need to invoke special transition-delaying properties conferred by the elasticity of the dolphin skin. Nevertheless, laminar flow control is very likely to be profitable not for reaching the top velocity but rather for sparing energy during long slower swimming phases: it might be during the glide phase of deep dives that a laminar-flow capability would be the most efficient (Williams *et al.*, 2000). Rather than swimming, marine animals tend actually to glide most of the time of their dive, for it spares energy. The exact fluid-elastic properties conferred by this complex skin arrangement are still debated today (Fish, 2006), but in any case, this initial “paradox” has triggered the study of the drag-reducing properties (if any) of elastic coatings.

Kramer’s coating and transition-delaying compliant walls

Inspired by the “dolphin paradox”, Kramer (1960) proposed a passive drag-reduction engineering device, inspired by his observations of fast moving dolphins (Kramer, 1961). The basic idea consisted in preventing the transition to turbulence of a laminar boundary layer by substituting the decrease of the fluid viscous damping as the Reynolds number increases, with an distributed

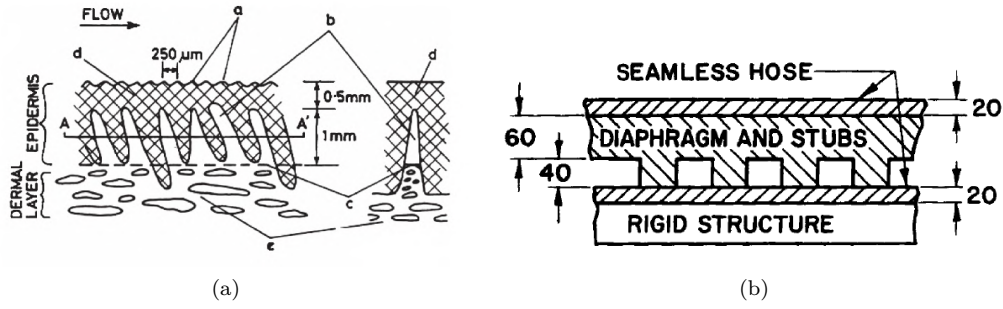


Figure 5.2 – Dolphin-inspired compliant coating. (a) cross-section cut of a typical dolphin skin reproduced from [Carpenter *et al.* \(2000\)](#), showing a. surface cutaneous ridges (upper epidermal layer), b. dermal papillae, c. dermal ridges, d. the upper epidermal layer and e. fatty tissues. (b) Cross-section cut of the compliant coating of [Kramer \(1960\)](#), showing the different layers (dimensions are in $1/1000$ of an inch, *i.e.* 2.54×10^{-3} cm)

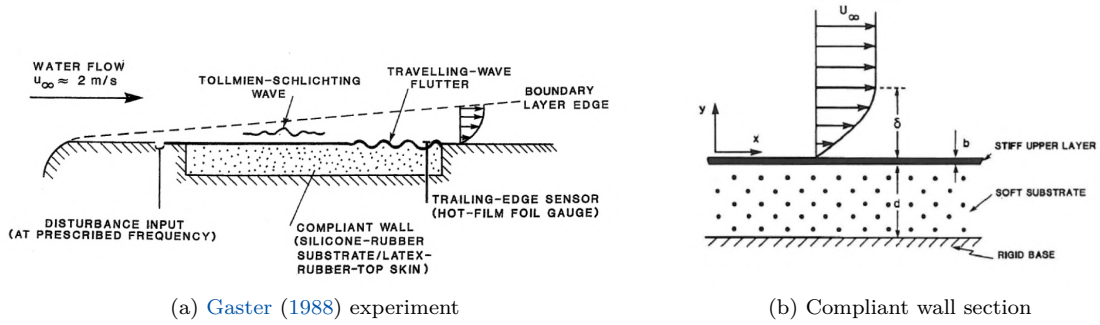


Figure 5.3 – Experiments from Gaster. Reproduced from [Lucey & Carpenter \(1995\)](#).

damping embedded directly into the wetted surface of a flexible coating. Practically, he designed a compliant wall (see in Fig. 5.2b a cross-section cut) made with a heavy rubber diaphragm supported by an array of tiny rubber stubs. The flexible inner skin, the outer diaphragm and the stubs were all made of the same soft natural rubber. The stiffness of the different materials involved was evaluated from 0.4 to 1 MPa. The space between the rubber stubs is filled with a silicone fluid that acts as a damper. Kramer reported an astonishing maximal drag reduction (compared to the rigid case) of about 60 %. However, the best results in terms of drag reduction were obtained at speeds of 18 m s^{-1} , which is twice as much the normally assumed maximum speed for dolphins ([Babenko & Carpenter, 2003](#)). Kramer believed that the drag reductions achieved in his tests were a results of the transition-delaying properties of hies coatings, but this hypothesis has not been confirmed by later works ([Carpenter & Garrad, 1985](#)): it is more likely that the drag reductions observed were a result of a favourable interaction of the wall with a fully turbulent boundary layer. More recent experiments ([Choi *et al.*, 1997](#)) showed that drag reduction of up to 7 % can be achieved in a turbulent flow over a compliant layer (modulus of elasticity of order of 2 MPa).

The two decades that followed the experiments by Kramer offered only limited experimental confirmations of the speculated transition-delaying properties of compliant coatings, as documented in the review paper by [Carpenter & Garrad \(1985\)](#). The transition-delaying and drag-reduction capabilities of compliant surfaces were however again observed in careful experiments conducted by [Gaster \(1988\)](#). He used a compliant wall about 10 mm thick, made with viscoelastic silicon rubber. The elastic moduli was adjusted by adding silicon oil in the rubber and was estimated ranging between 1×10^4 Pa and 3×10^5 Pa, *i.e.* much softer than that used by Kramer. The rubber plate was covered with a very thin (tenth of a millimeter) and stiffer (elastic moduli of 1 MPa) latex rubber membrane, and the ensemble placed in a water channel with an inflow velocity ranging

	Hydrofoil	Torpedo	Nuclear sub.	Dolphin
Length L^* (m)	1	5	100	3
Velocity U_∞^* (m s ⁻¹)	15	20	15	7
Wetted area (m ²)	0.6	3.7	3100	4.7
Reynolds number \mathcal{R}_e	1.5×10^7	1×10^8	1.5×10^9	2×10^7
Initial transition pos. (m)	0.06	0.05	0.07	0.14
Delayed transition pos. (m)	0.40	0.30	0.40	0.86
Overall drag decrease (%)	-33 %	-6 %	-0.5 %	-25 %

Table 5.1 – Estimates for drag reduction. For an initial transition Reynolds number of $\mathcal{R}_e^{\text{trans}} = 10^6$, estimate of the overall drag decrease with a 6-fold increase of $\mathcal{R}_e^{\text{trans}}$ when the relation (5.1.1) is used to compute the overall laminar-turbulent drag.

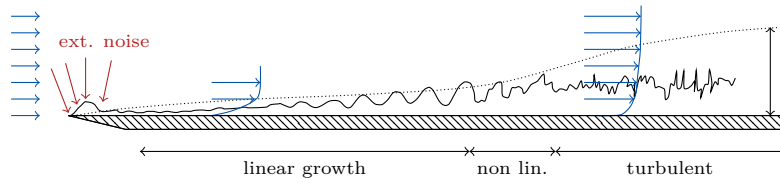


Figure 5.4 – Laminar-turbulent transition scenario in a low-amplitude disturbances environment. Reproduced from Kachanov (1994) for the case of a flat plate boundary-layer without adverse pressure gradient. δ refers to the characteristic thickness of the boundary-layer.

between 1 and 4 m s⁻¹, resulting in an initially laminar boundary-layer flow. A sketch of the experimental setup is reproduced in Fig. 5.3, taken from a paper by Lucey & Carpenter (1995). The best surface tested showed an increase in transition Reynolds number of 30 % over that of a rigid surface. It is then now established that compliant materials can postpone the laminar-turbulent transition. Theoretical studies (more details will be given in the next paragraph) have shown that the transition Reynolds number might be increased by up to a factor 6 (Carpenter, 1993). The practical benefits of such delay can be estimated for various objects, by computing the drag using the Prandtl-Schlichting formula for a mixed laminar-turbulent boundary-layer over a flat plate (Schlichting, 1979): the overall skin-friction drag coefficient can be roughly estimated by

$$C_F = \frac{0.455}{\log(\mathcal{R}_e)^{2.58}} - \frac{\mathcal{R}_e^{\text{trans}}}{\mathcal{R}_e} \left[\frac{0.074}{(\mathcal{R}_e^{\text{trans}})^{1/5}} - \frac{1.328}{(\mathcal{R}_e^{\text{trans}})^{1/2}} \right] \quad (5.1.1)$$

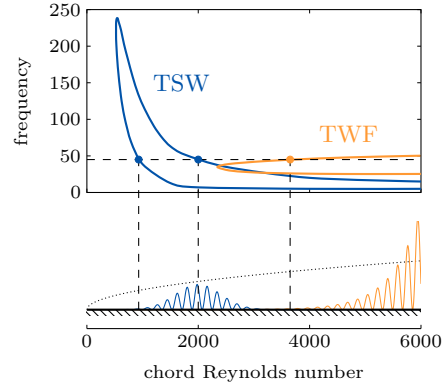
where \mathcal{R}_e is the Reynolds number based on the characteristic length in the streamwise direction, and $\mathcal{R}_e^{\text{trans}}$ is the transition Reynolds number that we take here to $\mathcal{R}_e^{\text{trans}} = 10^6$. The results for a few underwater devices are reported in Tab. 5.1, showing the potential of transition-delaying materials. Of course, the smaller/slower the object, the largest the overall skin-friction drag reduction. We have only considered underwater objects, because the main benefits in terms of laminar-turbulent transition delay would probably be obtained in this context rather than for aeronautic applications (Carpenter *et al.*, 2001), in particular because too soft materials would be mandatory in this case. Note finally that aside from drag-reduction features, compliant surfaces have also other useful applications such as acoustic noise reduction (Gad-El-Hak, 2000), and this technique is relatively easy to apply practically, even if it seems that there are some practical issues about the ageing of the materials (Bandyopadhyay *et al.*, 2005).

Let us now move on to the theoretical description of the interaction between compliant walls and boundary-layer flows, in order to elucidate the different processes at play.

5.1.2 Theoretical studies

The physics of the flow over compliant walls is rather complex. For conciseness of the presentation, we restrict ourselves to the study of low-level disturbances in a boundary layer over a flat plate

Figure 5.5 – Typical neutral curves for Tollmien-Schlichting Waves (TSW, blue) and Travelling-Wave Flutter (TWF, orange) instabilities. Data are taken from Lucey & Carpenter (1995). The chord Reynolds number is actually a measure of the local position along the plate. The boundary layer thickness is represented schematically with the black dotted line.



without adverse pressure gradient. In this case, the transition to turbulence is known to happen *via* amplification of so-called *Tollmien-Schlichting waves*.

Transition by Tollmien-Schlichting waves

As represented in Fig. 5.4, the early stages of the laminar-turbulent transition can be understood by means of the amplification of external perturbations such as acoustic noise, free-stream gusts, etc. Low-amplitude waves generated close to the leading edge are advected by the flow, up to a critical point where an exponential amplification sets in. This exponential growth is well described by the hydrodynamic linear stability theory.

Assuming homogeneity in the streamwise direction x , it is convenient to study the propagation of waves of type $A(y) \exp i(\omega t - kx)$ with temporal stability analyses (Tollmien, 1929; Schlichting, 1933) that show that when the frequency $\omega \in \mathbb{R}$ is varied, the boundary layer amplifies waves ($\Im m(k) > 0$) in some frequency range; provided that the Reynolds number based on the displacement thickness is greater than 520. The streamwise position in the flow where the perturbations are amplified actually also depends on the frequency of the excitation and form kind of a “banana curve” represented in Fig. 5.5. Within the “banana” all disturbances are amplified, while in all other regions the disturbances are damped. The curve itself is called the *neutral curve*. At some point, it may happen that the linear amplification grows too big (“too big” meaning here that the disturbances amplitudes reach a few percents of the free-stream velocity) and triggers non-linear wave interactions, that eventually result in a fully turbulent flow (Kachanov, 1994). Experiments (Schubauer & Skramstad, 1947) confirmed the existence of these unstable, mainly two-dimensional *Tollmien-Schlichting waves*. More recent works focused on the response of the boundary-layer flow to external disturbances, showing that strong transient growth effects are at play, that amplify external noise up to the point that the transition begins (Reddy *et al.*, 1993; Schmid & Henningson, 2012; Åkervik *et al.*, 2008; Sipp & Marquet, 2013). For that reason, the resolvent analysis is adapted to the study of boundary-layer flows. Note that for higher-amplitude initial disturbances, other transition scenarios are likely to occur (Fedorov, 2011), but are not discussed here.

When flexibility is added in the solid, new effects emerge. The Tollmien-Schlichting waves (TSW) are affected by the compliance of the wall and the possibility for waves to travel in the solid favor the emergence of new class of instabilities, in particular the so-called travelling-wave flutter (TWF). A summary of the different instabilities observed in the literature is reported in Fig. 5.6 adapted from Gad-El-Hak (1996). Let us now describe them.

Classification of fluid-solid instabilities in compliant coatings

Thanks to pioneering works by notably Benjamin (1960) and Landahl (1962), it is by now well-known that laminar boundary layers over flexible surfaces are susceptible to at least three main types of instabilities. A vast literature is devoted to the study of linear disturbances evolving on a parallel (local analysis), weakly non-parallel or fully streamwise-evolving flow (global analysis) coupled with an infinite or finite-length panel. When the compliant coating is supposed to be

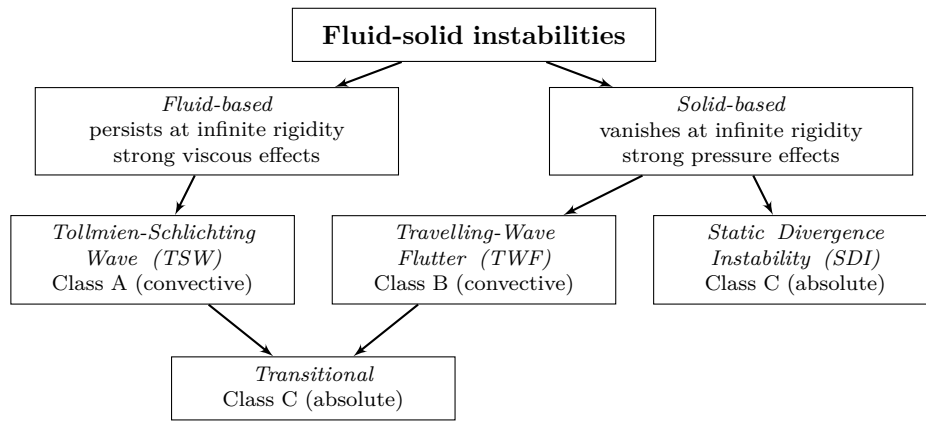


Figure 5.6 – Classification of the instabilities in compliant walls. Inspired by [Gad-El-Hak \(1996\)](#). The classification with letters (A,B,C) is from [Benjamin \(1963\)](#), while the distinction between absolute and convective instabilities refers to the classification by [Huerre & Monkewitz \(1990\)](#) and makes primarily sense in the infinite-length case. The distinction between solid-based and fluid-based instabilities relates back to the work by [Carpenter & Garrad \(1985\)](#).

of infinite extent in the x direction, it is convenient to study the propagation of waves of type $A(y)\exp i(\omega t - kx)$, that allows in particular to determine the dispersion relation of the coupled solid-fluid problem. However, no account is taken for the ends of the coating in that case. Although some studies have been conducted in 3d ([Yeo, 1992](#); [Lucey & Carpenter, 1993](#)), the majority of the approaches deal with 2d geometries, for the instability mechanisms at play at low-amplitude noise level are essentially bi-dimensional ([Schlichting, 1979](#)). The well-documented series of papers by [Carpenter & Garrad \(1985, 1986\)](#) and review papers from [Gad-El-Hak \(1996\)](#) and [Carpenter et al. \(2001\)](#) cover most of the field between the 60's and early 2000's.

In the energy classification by [Benjamin \(1963\)](#), the Tollmien-Schlichting waves (TSW) modified by the wall flexibility have been related to oscillations involving conservative energy-exchanges between the fluid and solid. Travelling-wave analyses in a one-dimensional wall model interacting with disturbances following the Orr-Sommerfeld equation ([Benjamin, 1960](#); [Landahl, 1962](#); [Carpenter & Garrad, 1985](#)) characterized this instability as a slowly convective, downstream-travelling wave in the solid, associated with modified Tollmien-Schlichting waves in the fluid. These waves are found to be stabilized by the flexibility of the coating, but destabilized by viscoelastic damping in the solid. Using a more complex model of the solid (bi-dimensional Navier equations), [Yeo \(1988\)](#) arrived to the same conclusions. Using a weakly non-parallel approximation, [Yeo et al. \(1994\)](#) also observed that the effects of the boundary-layer growth have only a mild influence on TSW, that increases as the Reynolds number is decreased.

If TSW's exist in the rigid case, travelling-wave flutter (TWF) develop only when the wall is flexible. On the basis of the travelling-wave analyses, this instability is classified as another convective instability involving conservative energy-exchanges between the fluid and solid ([Benjamin, 1963](#)), but flexibility and damping play a reversed role: while decreasing the stiffness of the coating destabilizes the TWF, an increase of damping has a stabilizing effect. Travelling-flutter waves are observed as downstream-travelling waves with a velocity close to those of the free-surface waves. As noted by [Carpenter & Garrad \(1986\)](#), the stabilizing effect of damping on TWF is more marked than its destabilizing effect on TSW. These are dangerous instabilities: as noted by [Gad-El-Hak \(1996\)](#), although the frequency band where the instability occurs is narrower than for the TSW, it extends indefinitely as the Reynolds number increases downstream (see an illustration in Fig. 5.5). It is actually believed that the TWF were the main route to transition in the experiments by [Gaster \(1988\)](#), as reported by [Lucey & Carpenter \(1995\)](#). The TWF instabilities are also found to be more sensitive to non-parallel effects than TSW: [Yeo et al. \(1994\)](#) showed that strong destabilization can occur due to boundary-layer growth in some TWF regimes.

A third type of instability occurs in the case of an unidirectional energy-transfer from the fluid to the solid [Benjamin \(1963\)](#), more precisely if the pressure fluctuation amplitude outweighs the

restoring force due to the stiffness of the coating. Due to this negative added stiffness mechanism, the instability has been identified as a static divergence (SD) instability, well known in aeroelasticity (Dowell, 1971). This instability has been observed in water-channel experiments by Gad-El-Hak *et al.* (1984) on the form very slow two-dimensional waves normal to the flow, and also on the skin of dolphins and fast human swimmers (Aleyev Yu, 1977) — see in Fig. 5.1. Yeo *et al.* (1996) showed that static divergence appears when the coating is sufficiently soft, but can be suppressed by decreasing the thickness of the coating. Travelling-wave flutter and standing wave analyses of the static divergence instability in infinite panels arrived to the somewhat surprising conclusion that viscoelastic damping is necessary to trigger the instability (Landahl, 1962; Carpenter & Garrad, 1986; Yeo *et al.*, 1996). The role of damping in finite-length coatings has been studied by Lucey & Carpenter (1992) using a potential flow approach. They showed in that case that damping is not necessary any more for triggering the instability. According to them, in infinite-length panels, the energy transfer that leads to divergence is favoured by the slight wave propagation slowdown caused by damping. For finite-length panels, this role is essentially played by edge boundary conditions. In that case, viscoelastic damping has its more classical role of attenuating the growth of the instability.

Another class of instability, referred to as *transitional*, occurs as a coalescence of TWF and TSW waves (see in Fig. 5.6). This instability has been documented in particular by Sen & Arora (1988). In the work by Wiplier & Ehrenstein (2001), transitional instabilities are also found as a coalescence between an evanescent wave and a TSW.

We focus here on the TWF and TSW instabilities, in the context of a *finite-length* coating. In this case, it is no longer possible to assume streamwise homogeneity. This case has been treated in the past using non-linear time-marching simulations of inviscid flows (Lucey & Carpenter, 1992, 1993) or linearised Navier-Stokes flows (Davies & Carpenter, 1997; Stewart *et al.*, 2009) interacting with a spring-backed solid. More recently, Tsigklifis & Lucey (2017) performed modal and transient growth analyses for the case of a viscous boundary-layer flow interacting with a finite-length coating modelled by a spring/damper-backed plate equation. The analysis is extended here in two ways. First, we consider a fully elastic solid. Secondly, for the first time a resolvent analysis is performed in the context of a finite-length coating.

After having introduced the physical modelling in section 5.2, the complex dynamics of the viscoelastic patch alone is first analyzed (§5.3.1), making it possible to identify which vibration modes are likely to interact with the flow. In particular, the dispersion relation in the case of a patch of infinite length is linked to the vibration modes of a patch of finite length. The fluid-solid coupled modes are then determined for different patch stiffness and viscoelastic damping parameters (§5.3.2). In the case of sufficient viscoelastic damping, all the modes are stable. The resolvent analysis is then adapted. We first evaluate how the fluid-elastic configuration responds to optimal perturbations determined in the fluid-rigid case (section 5.4). Finally, optimal perturbations and responses are determined in the fluid-elastic case (section 5.5).

5.2 Physical modelling & numerical model

5.2.1 Non-dimensional parameters

The solid is characterized by its density ρ_s^* , Young modulus E_s^* and viscoelastic damping coefficient η_s^* . It is assumed to be incompressible, as is often the case for rubber-like materials. The fluid is considered incompressible with a uniform density ρ_f^* and a dynamic viscosity ν_f^* . The coupled problem is non-dimensionalized with respect to the fluid variables, namely the farfield velocity U_∞^* and the boundary-layer displacement thickness δ_i^* at the inlet of the computational domain (see a sketch of the configuration in Fig. 5.7 where the dimensions are included) that is a good reference length for boundary-layer flows. Four non-dimensional parameters govern the physical properties of the system, namely

$$\mathcal{E}_s = \frac{E_s^*}{\rho_f^* U_\infty^{*2}}, \quad \mathcal{D}_s = \frac{\eta_s^*}{\rho_f^* U_\infty^* \delta_i^*}, \quad \mathcal{M}_s = \frac{\rho_s^*}{\rho_f^*} \quad \text{and} \quad \mathcal{R}_e = \frac{\delta_i^* U_\infty^*}{\nu_f^*} \quad (5.2.1)$$

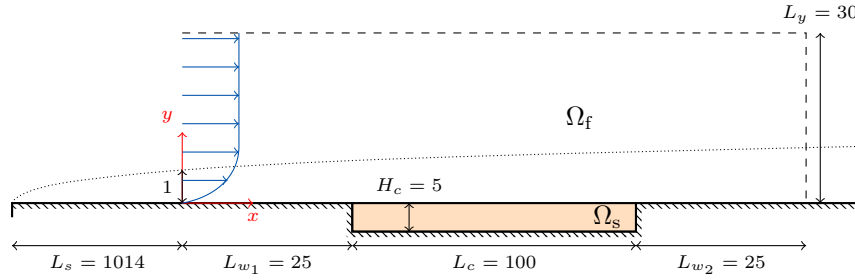


Figure 5.7 – Boundary-layer flow over a compliant coating. Non-dimensional lengths are indicated, the reference length being the boundary-layer displacement thickness at the inflow position. The solid domain is represented in orange color.

for the non-dimensional Young modulus and damping coefficient, density ratio and Reynolds number respectively. In what follows, the density ratio is fixed to $\mathcal{M}_s = 1$ and the Reynolds number (based on the streamwise distance) to $\mathcal{R}_e = 3000$. For this Reynolds number, unsteady Tollmien-Schlichting waves developing on the steady boundary-layer flow are found to be convectively unstable (Schmid & Henningson, 2012; Sipp & Marquet, 2013). With the parameters used here, the Reynolds number based on the boundary-layer thickness evolves between 3036 and 3179 over the compliant coating. For the solid, we consider a stiffness $\mathcal{E}_s = 1$ and a damping coefficient $\mathcal{D}_s = 0.2$ for the reference flexible case.

For a water flow (density $\rho_f^* = 1000 \text{ kg m}^{-3}$ and dynamic viscosity $\eta_f^* = 1.00 \times 10^{-3} \text{ Pa s}$) with $U_\infty = 10 \text{ m s}^{-1}$, $\mathcal{E}_s = 1$ corresponds to a Young modulus of 0.1 MPa, while a flow ten times slower comes with a stiffness reduced by a factor hundred, i.e. on the order of 1000 Pa. For the same flow velocities the thickness of the boundary layer is of the order of 0.3 mm to 3 mm. For comparison, in the experiments by Gad-El-Hak *et al.* (1984) on a laminar boundary-layer (see also the picture (c) in Fig. 5.1), the material (a viscoelastic plastisol gel, obtained from polyvinyl chloride resin combined with a plasticizer and a stabilizer) was found to have a Young modulus between 15 Pa and 37 500 Pa. The materials used in Gaster's experiments is found in the same range (Gaster, 1988; Lucey & Carpenter, 1995). As said before, on the other hand, experiments studying turbulent boundary layers used materials with a stiffness that is more in the range of 1 MPa (Choi *et al.*, 1997; Bandyopadhyay *et al.*, 2005). The parameter $\mathcal{E}_s = 1$ thus seems to be representative of the flexibility of compliant coatings used in laminar boundary-layer flow experiments. Realistic values of the damping coefficient are much harder to determine *a priori*. For instance, low-stiffness, high damping viscoelastic plastisol gels have damping properties that depend strongly on the temperature or the solicitation frequency (Nakajima *et al.*, 1981; Nakajima & Harrell, 2001). The present damping coefficient was thus mainly chosen so as to reproduce earlier results, but should not be considered as being truly representative of a wide range of real coatings.

5.2.2 Navier-Stokes flow

A viscous, incompressible Navier-Stokes flow is considered in the fluid region above the wall. Since it takes a while for the boundary-layer to develop, the computational domain $\Omega_f \cup \Omega_s$ starts at a non-dimensional distance $L_s = L_s^*/\delta_i^* = 1014$ from the leading edge of the plate, in such a way that the Reynolds number based on the displacement thickness is 3000 there. Over this distance, the flow is modelled by a Blasius profile that is then used as an inlet condition. This way of proceeding is relatively common in the literature and comes with very small deviations from a Navier-Stokes solution over the complete plate (Brandt *et al.*, 2011). In particular, the local displacement thickness computed for a Blasius flow is an excellent approximation of the “true” displacement thickness that can be computed from the Navier-Stokes flow. The coating is placed at a non-dimensional distance $L_{w1} = 25$ from the inlet such that the inflow velocity is not influenced by the presence of the coating. The distance between the end of the coating and the outlet is fixed to $L_{w2} = 25$ unless otherwise stated.

Remark – computation of the Blasius inflow condition. In order to avoid from having to solve the Navier-Stokes equation over the whole span of the plate, the development of the boundary-layer flow is assumed to follows a zero pressure gradient Blasius flow in the region $x < 0$. Practically, the self-similar asymptotic boundary-layer Blasius flow

$$\frac{u^*(x^*, y^*)}{U_\infty^*} = f'(\eta), \quad \frac{v^*(x^*, y^*)}{U_\infty^*} = \frac{1}{2} \sqrt{\frac{\nu_f^*}{U_\infty^* x^*}} \left(\eta f'(\eta) - f(\eta) \right)$$

is first computed (Schlichting, 1979), with $\eta = y^*(U_\infty^*/(\nu_f^* x^*))^{1/2}$ the similarity variable (x^* is counted — with dimensions — from the beginning of the plate) and f is the solution of the Blasius equation $f''' + 1/2 f'' f = 0$ with $f'(0) = f(0) = 0$ and $f'(+\infty) = 1$. Then, the local displacement thickness

$$\delta^*(x^*) = \int_0^{+\infty} \left(1 - \frac{u^*(x^*, y^*)}{U_\infty^*} \right) dy \simeq 1.72 \sqrt{\frac{\nu_f^* x^*}{U_\infty^*}}$$

is computed, which allow to determine the different scalings for the non-dimensional problem. For instance, solving $\delta^*(L_s \delta_i^*) = \delta_i^*$ gives $L_c = \mathcal{R}_e / (1.72)^2$, and the non-dimensional displacement thickness for the Blasius flow evolves as

$$\delta(x) = \frac{\delta^*(x)}{\delta_i^*} = \sqrt{1 + 1.72^2 \frac{x}{\mathcal{R}_e}}. \quad (5.2.2)$$

By the same way, the length L_s is fixed by the choice of the Reynolds number.

In the present approach, the steady deformations in the coating are assumed to be zero. We look on how the flexibility of the wall affects the development of these instabilities at the dynamical level only, that is, we neglect the stationary deformation of the coating induced by the shear stresses produced by the steady boundary-layer flow. This is actually found to be a very good approximation, since the steady deformation is very small. In all what follows, we will thus investigate the behaviour of perturbations computed for a fluid-elastic model, in the case where the stationary equilibrium, whose stability is investigated, is assumed to be that of a *rigid* solid surrounded by a viscous flow¹. The stationary base fluid flow (\mathbf{U}, P) then reduces to the solution of the equations in a rigid case, i.e. of the Navier-Stokes equations with a Blasius inlet condition

$$\begin{aligned} (\nabla \mathbf{U}) \mathbf{U} + \nabla P - \mathcal{R}_e^{-1} \nabla^2 \mathbf{U} &= 0 && \text{in } \Omega_f, \\ \nabla \cdot \mathbf{U} &= 0 && \text{in } \Omega_f, \\ \mathbf{U} &= \mathbf{U}_{\text{Blasius}} && \text{in } \Gamma_{\text{in}}, \end{aligned}$$

completed with a no-slip condition on the surface of the plate. On the top boundary ($y = 30$), the streamwise velocity is fixed to that of the Blasius flow (the transverse component being left free), while at the outflow boundary ($x = L_{w_1} + L_c + L_{w_2}$) the transverse velocity is set to that of the Blasius flow (the streamwise component being left free). At the perturbation level, zero-velocity conditions are taken in the inflow boundary, no-slip conditions are taken along the plate and stress-free conditions are considered elsewhere.

5.2.3 Viscoelastic solid

In theoretical studies of compliant coatings, a simple approach commonly adopted consisted in modelling the solid as a spring-backed beam with damping, as represented in the sketch in Fig. 5.8a. Several authors have considered the case of homogeneous panels infinite in the streamwise direction as a convenient way for analysing the limit of a “long” coating — see for instance Carpenter & Garrad (1985) and the many references herein. To investigate edge effects, the spring-backed

¹in that case, the stress-free reference and steady deformed configurations coincide, and we will adopt here the notations related to the steady deformed configuration

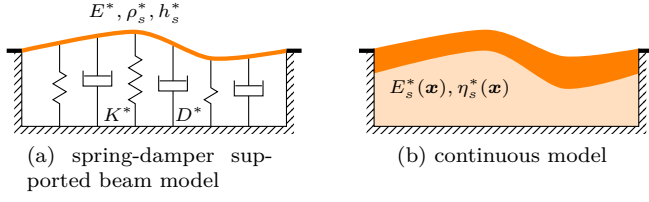


Figure 5.8 – Models for the compliant coating.

model has also been applied for modeling finite-length panels (Davies & Carpenter, 1997; Pitman & Lucey, 2009; Tsigklifis & Lucey, 2017), or an association of finite-length panels with different material properties, as considered by Carpenter (1993). More complex models including material anisotropy have also been studied, for instance by Carpenter & Morris (1990). A more realistic, yet computationally more expensive approach, consists in viewing the solid as a continuous elastic, possibly non-homogeneous media, as represented in Fig. 5.8b. This latter approach was also selected by several authors, assuming either homogeneous one-layer coatings (Duncan *et al.*, 1985) or two-layer (in the transverse direction) coatings (Yeo, 1988; Duncan, 1988; Dixon *et al.*, 1994). Mixed models have also been used, for instance Lucey & Carpenter (1995) considered the combination of an upper, thin layer, governed by a plate equation, with a lower, thick layer, governed by the Navier elasticity equations. To our knowledge, in all these approaches the coating was however assumed to be of infinite extent in the streamwise direction. This motivates the present study, where the case of a two-dimensional, finite-length coating is addressed. Namely, we consider a rectangular coating of dimensions L_c^* in the x direction and H_c^* in the y direction (see the sketch in Fig. 5.7).

We choose to model the solid *elasticity* by an incompressible hyperelastic neo-Hookean model, for it is the simplest physically-based constitutive equation for rubber materials commonly used in compliant-wall experiments (Gad-El-Hak *et al.*, 1984; Gaster, 1988), derived from molecular chain statistics considerations (Treloar, 1943). More involved models such as for instance the semi-empirical Mooney-Rivlin, Ogden or Yeoh materials are more representative for the real behaviour of silicon-rubber and soft tissues (Martins *et al.*, 2006), but as pointed by Marckmann & Verron (2006), for small strains (about 150 % and below), the neo-Hookean solid should be used because of its physically-based origin, its small number of parameters and its robustness with respect to various experimental load configurations. With dimensions, the first Piola-Kirchhoff stress tensor for a general non-linear, incompressible neo-Hookean solid is given (Ogden, 1997) by

$$\hat{\mathbf{P}} = -\hat{p}_s^* \hat{\mathbf{F}}^{-T} + \mu_s^* (\hat{\mathbf{F}} - \hat{\mathbf{F}}^{-T}). \quad (5.2.3)$$

Where $\mu_s^* = E_s^*/(2(1 + \nu_s))$ is the second Lamé coefficient, that is more conveniently written here as $E_s^*/3$ because of the solid's incompressibility ($\nu_s = 0.5$). If one further sets $\hat{\boldsymbol{\xi}}^* = \hat{\boldsymbol{\Xi}}^* + \varepsilon \hat{\boldsymbol{\xi}}'^*$, $\hat{p}_s^* = \hat{P}_s^* + \varepsilon \hat{p}_s'^*$, in the above relation we obtain

$$\begin{aligned} \hat{\mathbf{P}}(\hat{\boldsymbol{\xi}}^*)^* &= -\hat{P}_s^* \hat{\mathbf{F}}(\hat{\boldsymbol{\Xi}}^*)^{-T} + \frac{E_s^*}{3} (\hat{\mathbf{F}}(\hat{\boldsymbol{\Xi}}^*) - \hat{\mathbf{F}}(\hat{\boldsymbol{\Xi}}^*)^{-T}) \\ &+ \varepsilon \left\{ -(\hat{p}_s')^* \mathbf{I} + \hat{P}_s^* \hat{\mathbf{F}}(\hat{\boldsymbol{\Xi}}^*)^{-T} \hat{\boldsymbol{\nabla}} \hat{\boldsymbol{\xi}}' + \frac{E_s^*}{3} (\hat{\boldsymbol{\nabla}} \hat{\boldsymbol{\xi}}' \hat{\mathbf{F}}(\hat{\boldsymbol{\Xi}}^*)^T + \hat{\mathbf{F}}(\hat{\boldsymbol{\Xi}}^*)^{-T} \hat{\boldsymbol{\nabla}} \hat{\boldsymbol{\xi}}'^T) \right\} \hat{\mathbf{F}}(\hat{\boldsymbol{\Xi}}^*)^{-T}. \end{aligned}$$

In the present approach, the steady base displacement is assumed to be zero. Then, setting $\hat{\boldsymbol{\Xi}} = \mathbf{0}$ and $\hat{P}_s = 0$, the above neo-Hookean solid strain-stress relation reduces at the first-order to that of the linear elasticity, namely

$$\sigma_s^{\text{elastic}}(p_s', \boldsymbol{\xi}')^* = -(p_s')^* \mathbf{I} + \frac{E_s^*}{3} (\boldsymbol{\nabla} \boldsymbol{\xi}' + \boldsymbol{\nabla} \boldsymbol{\xi}'^T), \quad (5.2.4)$$

while the incompressibility condition $\hat{J}(\hat{\boldsymbol{\xi}}) = 1$ reduces to $\boldsymbol{\nabla} \cdot \boldsymbol{\xi}' = 0$. Like for incompressible fluids, the solid pressure can be viewed as a Lagrange multiplier that ensures the solid incompressibility.

Compliant materials should also present *viscoelastic* properties (Gad-El-Hak *et al.*, 1984; Gaster, 1988), because the solid viscous damping helps for absorbing the energy produced by wall-based

instabilities. When undergoing deformation, viscoelastic solids exhibit both viscous and elastic characteristics. Unlike pure elastic materials that immediately respond to stress, then immediately return to their original state once the stress is removed (they can only *store* energy), viscoelastic materials show in addition time-delay and memory effects, associated to the rate at which energy is lost (storing and dissipation of energy). In the most general viscoelastic case, the current value of the strain depends upon the complete past history of the components of the stress tensor, which results in models where the strain depends on a convolution integral between the stress and the so-called *creep functions* (Christensen, 2012). However, it can often be considered that only a very short part of the history has an influence on the present material state, in which case the full viscoelastic model can be reduced to the so-called differential relations (Truesdell & Noll, 1992). These models are much easier to manipulate, for strain and stresses are in that case linked by differential relations, and the elastic and viscous responses can be distinguished. In the present case, we adopt the most simple differential material of Kelvin-Voigt type, where the viscoelastic part reduces to the time-derivative of the strain tensor. Combining the elastic and viscoelastic parts for the strain-stress relation and non-dimensionalizing, we obtain the following relation,

$$\sigma_s(p'_s, \xi') = -p'_s \mathbf{I} + \frac{\mathcal{E}_s}{3} (\nabla \xi' + \nabla \xi'^T) + \frac{\mathcal{D}_s}{2} \frac{\partial}{\partial t} (\nabla \xi' + \nabla \xi'^T) \quad (5.2.5)$$

where $\mathcal{D}_s = \eta_s^* / (\rho_f^* U_\infty^* \delta_i^*)$ is the non-dimensional damping parameter build upon the solid kinematic viscosity η_s^* (in $\text{kg m}^{-1} \text{s}^{-1}$). Such model can be seen as the most simple generalization of the one-dimensional spring-damper Kelvin-Voigt model displayed in Fig. 5.8a. The solid equations finally read as follows:

$$\mathcal{M}_s \frac{\partial^2 \xi'}{\partial t^2} = -\nabla p'_s + \frac{\mathcal{E}_s}{3} \nabla^2 \xi' + \frac{\mathcal{D}_s}{2} \frac{\partial \nabla^2 \xi'}{\partial t}, \quad (5.2.6)$$

$$\nabla \cdot \xi' = 0. \quad (5.2.7)$$

The first equation is the small-displacement momentum equation deduced from (1.1.10) and the second equation represents the incompressibility constraint — Eq. 1.1.13 in the case of infinitesimal displacements.

5.2.4 Coupled problem and numerical settings

The linearised fluid-structure problem (2.1.1), slightly modified by the presence of the solid pressure, is written here under the form of the 2×2 problem

$$\underbrace{\begin{pmatrix} \mathcal{B}_s & 0 \\ 0 & \mathcal{B}_f \end{pmatrix}}_{\mathcal{T}_{fsi}(\mathbf{Q})} \underbrace{\begin{pmatrix} \frac{\partial \mathbf{q}'_s}{\partial t} \\ \frac{\partial \mathbf{q}'_f}{\partial t} \end{pmatrix}}_{\mathcal{N}'_{fsi}(\mathbf{Q})} - \underbrace{\begin{pmatrix} \mathcal{A}_s & \mathcal{C}_{sf} \\ \mathcal{C}_{fs} & \mathcal{A}_f(\mathbf{Q}) \end{pmatrix}}_{\mathcal{N}'_{fsi}(\mathbf{Q})} \begin{pmatrix} \mathbf{q}'_s \\ \mathbf{q}'_f \end{pmatrix} = \begin{pmatrix} \mathbf{0} \\ \mathcal{P}_f \mathbf{f}' \end{pmatrix} \quad (5.2.8)$$

In this notation, $(\mathcal{B}_s, \mathcal{A}_s)$ represent the linearised solid operators that only depend on the material parameters \mathcal{D}_s , \mathcal{M}_s and \mathcal{E}_s . The augmented solid variable is $\mathbf{q}'_s = [\xi', \mathbf{u}'_s, p'_s]^T$ that gathers the solid displacement, solid velocity $\mathbf{u}'_s = \partial \xi' / \partial t$ and solid pressure p'_s . The fluid operators $(\mathcal{B}_f, \mathcal{A}_f)$ regroup the linearised Navier-Stokes equations in the ALE framework plus the extension problem, i.e. $\mathbf{q}'_f = [\xi'_e, \lambda'_e, \mathbf{u}', p', \lambda']^T$. The steady flow \mathbf{Q} is a pure hydrodynamic boundary-layer flow of velocity \mathbf{U} and pressure P that thus only depends on the Reynolds number. The off-diagonal operators \mathcal{C}_{sf} and \mathcal{C}_{fs} are the coupling operators. Finally, the right-hand side term accounts for an external volumic forcing in the fluid momentum equation, the operator \mathcal{P}_f being introduced to adjust the dimension of the vector, i.e. $\mathcal{P}_f \mathbf{f}' = [\mathbf{0}, \mathbf{0}, \mathbf{f}', 0, \mathbf{0}]^T$. The different operators involved in the coupled problem (5.2.8) take a form that is similar to what was already described in the chapter 2. The only difference is that the solid model is incompressible.

Remark – coupling with transpiration. We found that in the range of parameters investigated in this study, the approximate Eulerian-based approach (i.e. with a fluid-structure coupling by means of the velocity transpiration only, see in §2.1.4) gives actually results that are very close to that given by the Lagrangian-based approach. Significant differences only arise for much more viscous boundary-layers.

The computational domain of the solid region is discretized with a structured mesh made with 17 982 triangles and 9352 vertices. The computational domain for the fluid region Ω_f is discretized with a structured mesh made of 72 324 triangles and 36 686 vertices. At the fluid-solid interface, that conforms with the solid mesh, the grid resolution in the streamwise direction is $\Delta x = 0.15$ while the transverse resolution is $\Delta y^{\min} = 0.03$. The transverse grid resolution is smoothly decreased in the $y > 0$ direction using a sine law and reaches $\Delta y^{\max} = 0.3$ close to the upper boundary. Finally, the extension region is made as a layer (of width 5) around the solid, and the Laplace operator is taken as the extension operator.

5.3 Eigenvalue analysis

5.3.1 Free solid dynamics

Before analysing the coupled fluid-structure perturbations, it is useful to describe the dynamics of the compliant coating alone, i.e. vibrating in vacuum without the surrounding fluid. This allows for instance to determine what types of solid vibration modes are to be expected in the coupled analysis.

For this free solid vibration analysis, the non-dimensionalization with respect to fluid variables is not the most adapted. In this section, we therefore rewrite the equations by taking as a reference velocity the transverse (shear) elastic waves velocity

$$c_t^* = \sqrt{\frac{E_s^*}{3\rho_s^*}},$$

which is the propagation speed for elastic waves in an infinite, incompressible elastic media, whose vibration direction is perpendicular to the direction of propagation (Landau & Lifchitz, 1967). The width of the coating, H_c^* is naturally taken as the reference length. In this section (and this section only), the solid equations then writes as

$$\frac{\partial^2 \boldsymbol{\xi}'}{\partial t^2} = -\nabla p'_s + \left(1 + \frac{\mathcal{D}'_s}{2} \frac{\partial}{\partial t}\right) \nabla^2 \boldsymbol{\xi}', \quad \nabla \cdot \boldsymbol{\xi}' = 0 \quad (5.3.1)$$

which are simply (5.2.6)–(5.2.7) rewritten with the new scalings. In this analysis, the non-dimensional solid dynamics only depends – apart from the aspect ratio of the plate — from the ratio $\mathcal{D}'_s = \eta_s^*/(\rho_s^* H_c^* c_t^*)$ between the characteristic time for wave propagation H_c^*/c_t^* and the characteristic time for diffusion $\rho_s^* (H_c^*)^2 / \eta_s^*$. The boundary conditions are here

$$\boldsymbol{\sigma}_s(p'_s, \boldsymbol{\xi}') \mathbf{n} = 0 \quad \text{on } \Gamma, \quad (5.3.2)$$

$$\boldsymbol{\xi}' = 0 \quad \text{on } \Gamma_{\text{bottom}}, \quad (5.3.3)$$

$$\boldsymbol{\xi}' = 0 \quad \text{on } \Gamma_{\text{side}}. \quad (5.3.4)$$

We start by the analysis of an infinite-length coating of finite thickness, in which case a dispersion relation for travelling-waves can be determined. For this case, we only consider the boundary conditions (5.3.2) and (5.3.3). Then, we move on to the finite-length case, and show the great variety of vibration patterns that are obtained in this latter case. For this second case, the side edges condition (5.3.4) should be prescribed as well.

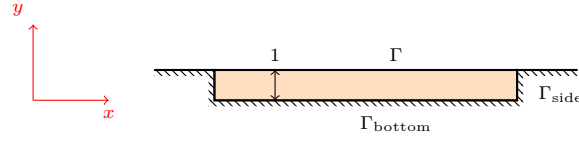


Figure 5.9 – Free, finite-length solid. The solid domain is represented in orange color, with the scaling used for the free-solid analysis.

Infinite-length, finite-thickness coating

The limit case where the length of the coating is assumed to be infinite is convenient, for it allows to compute the dispersion relation of the coating and thus give a clear physical overview of the vibration dynamics in the coating. For that aim it is convenient to introduce a solid stream function ϕ such that

$$[\xi']_x = \frac{\partial \phi}{\partial y} \quad \text{and} \quad [\xi']_y = -\frac{\partial \phi}{\partial x},$$

that enables the incompressibility condition $\nabla \cdot \xi' = 0$ to be automatically satisfied. Then, we obtain the following momentum equations,

$$\begin{aligned} \frac{\partial^3 \phi}{\partial t^2 \partial y} &= -\frac{\partial p_s}{\partial x} + \left(1 + \frac{\mathcal{D}'_s}{2} \frac{\partial}{\partial t}\right) \left(\frac{\partial^3 \phi}{\partial x^2 \partial y} + \frac{\partial^3 \phi}{\partial y^3}\right), \\ -\frac{\partial^3 \phi}{\partial t^2 \partial x} &= -\frac{\partial p_s}{\partial y} - \left(1 + \frac{\mathcal{D}'_s}{2} \frac{\partial}{\partial t}\right) \left(\frac{\partial^3 \phi}{\partial x^3} + \frac{\partial^3 \phi}{\partial y^2 \partial x}\right), \end{aligned}$$

for the x and y components respectively. The pressure can be eliminated from the above equations by considering the difference between the x component differentiated with respect to y and the y component differentiated with respect to x . This results in the fourth-order equation

$$\frac{\partial^2}{\partial t^2} (\nabla^2 \phi) = \left(1 + \frac{\mathcal{D}'_s}{2} \frac{\partial}{\partial t}\right) (\nabla^4 \phi).$$

Seeking there for modes $\phi(x, y, t) = \hat{\phi}(y) \exp \mathbf{i}(\lambda t - kx)$ propagating in the homogeneous x direction, with $k \in \mathbb{R}$ and λ is the frequency — possibly complex when $\mathcal{D}'_s \neq 0$ —, gives

$$\lambda^2 \left(\frac{d^2 \hat{\phi}}{dy^2} - k^2 \hat{\phi} \right) + \left(1 + \mathbf{i} \lambda \frac{\mathcal{D}'_s}{2} \right) \left(\frac{d^4 \hat{\phi}}{dy^4} - 2k^2 \frac{d^2 \hat{\phi}}{dy^2} + k^4 \hat{\phi} \right) = 0. \quad (5.3.5)$$

The modes should satisfy the zero displacement condition (5.3.3) at the bottom at $y = -1$ (recall that the reference length is here H_c^* instead of δ_i^*) and the stress free conditions (5.3.2) at $y = 0$. The first condition writes

$$\left. \frac{d\hat{\phi}}{dy} \right|_{-1} = k \hat{\phi}(-1) = 0 \quad (5.3.6)$$

while the stress-free condition is obtained by evaluating $\sigma_s(p'_s, \xi') \mathbf{n}$ at the interface. The normal vector being aligned with the y axis, we obtain

$$\begin{aligned} \left(1 + \mathbf{i} \lambda \frac{\mathcal{D}'_s}{2} \right) \left. \frac{d^2 \hat{\phi}}{dy^2} \right|_0 + k^2 \hat{\phi}(0) &= 0, \\ \lambda^2 \left. \frac{d\hat{\phi}}{dy} \right|_0 + \left(1 + \mathbf{i} \lambda \frac{\mathcal{D}'_s}{2} \right) \left(\left. \frac{d^3 \hat{\phi}}{dy^3} \right|_0 - 3k^2 \left. \frac{d\hat{\phi}}{dy} \right|_0 \right) &= 0. \end{aligned} \quad (5.3.7)$$

In the second term of the above relation (y component), the pressure appearing in the stress has been eliminated using the x equilibrium equation.

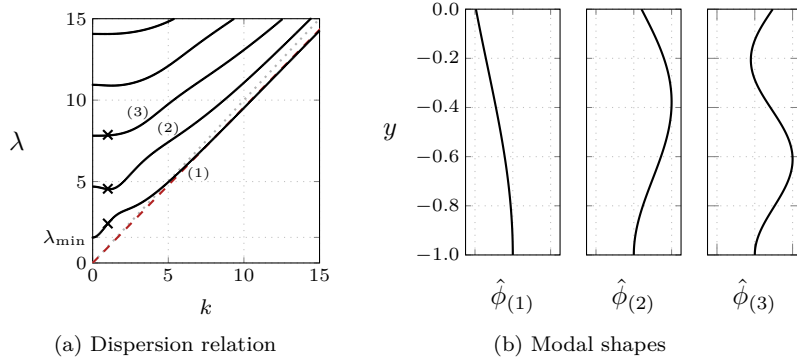


Figure 5.10 – Infinite-length coating without damping. (a) Dispersion relation for an infinite-length coating with $\mathcal{D}_s = 0$. For sake of comparison, the $\lambda - k$ relation for Rayleigh surface waves is depicted with the red dashed line. (b) Modal shapes for the first three lowest-frequency branches with zero damping ($\hat{\phi}_{(1)}$ corresponds to the lowest branch) and a wavenumber $k = 1$ (identified in the dispersion relation by the crosses).

After discretization in the y direction (practically, second-order centred finite-differences in a regularly spaced grid, with ghost cells for handling the boundary condition), equations (5.3.5), (5.3.6) and (5.3.7) form an eigenvalue problem of type $(\lambda^2 \mathbf{A}(k) + i\lambda \mathbf{B}(k) + \mathbf{C}(k))\boldsymbol{\phi} = \mathbf{0}$, that can be solved numerically for various wavenumbers k , yielding to couples $(\lambda, \hat{\phi})$ and to the dispersion relation $(k, \lambda(k))$. Since the problem has a relatively small size (less than 500 unknowns are required for converging the first modes), all the eigenvalues are explicitly computed using dense algebra libraries implemented in the software SCILAB, and the lowest-frequency eigenvalues are then retained.

Remark. Note that it is also possible to derive an explicit equation for the dispersion relation. The fourth-order above differential equation (5.3.5) admits a solution space basis that can be written with trigonometric functions $\{\sin, \cos, \sinh, \cosh\}$. Applying the boundary conditions (5.3.6) and (5.3.7) to an arbitrary element of the solution space results in a 4×4 determinant that should be zero, which gives the dispersion relation in the plane (k, λ) for the elastic waves in the coating,

$$\tilde{k}\Lambda_1(k, \lambda) \cosh(\tilde{k}) \cosh(k) - k\Lambda_2(k, \lambda) \sinh(\tilde{k}) \sinh(k) - \tilde{k}\Lambda_3(k, \lambda) = 0 \quad (5.3.8)$$

where we have noted $\alpha = 1 + i\lambda\mathcal{D}'_s/2$, $\tilde{k} = k(1 - (\lambda/k)^2/\alpha)^{1/2}$, and where the coefficients Λ_i are given by $\Lambda_1(k, \lambda) = 8\alpha^2 k^4 - 4\alpha k^2(\lambda)^2 + (\lambda)^4$, $\Lambda_2(k, \lambda) = 8\alpha^2 k^4 - 8\alpha k^2(\lambda)^2 + (\lambda)^4$ and $\Lambda_3(k, \lambda) = 4\alpha k^2((\lambda)^2 - 2\alpha k^2)$. This equation cannot be solved analytically and a numerical treatment is required. In the context of a compressible material, [Gad-El-Hak et al. \(1984\)](#) or [Duncan et al. \(1985\)](#) obtained a similar formula. We furthermore observed that the graph of (5.3.8) coincides with their dispersion relation when $\nu_s \rightarrow 0.5$. In our case, we rather solved directly (5.3.5) for various values of k , which of course allows to recover the graph of (5.3.8), but also compute the modal shapes (that are not directly available from the dispersion relation).

The obtained dispersion relation is represented in Fig. 5.10a for the case without damping ($\mathcal{D}_s = 0$). λ is then a real number representing the circular frequency. Several branches of increasing vibration frequencies are observed, all located above a cutoff frequency $\lambda_{\min} = 1.57$ reached for small wavenumbers — i.e. large wavelengths. Each branch (labelled by an integer i) in Fig. 5.10) is associated to a particular vibrating pattern, as represented in Fig. 5.10b that displays the modal shapes for three modes at $k = 1$ (identified by crosses in the dispersion relation). Higher-order modes are characterized with an increase of the number of the inflexion points in the modal shapes (an additional one for each branch of higher frequency). The evolution of the deformation in the x direction is represented in Fig. 5.11 where the y displacement deduced from the modes is represented for the three first branches. In the x direction, the wavelength of the structures is

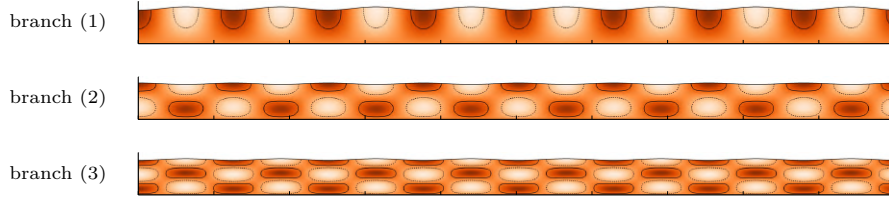
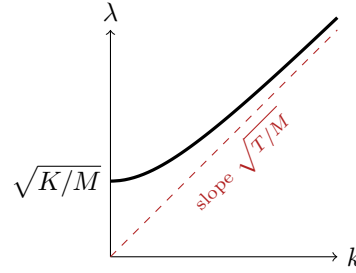


Figure 5.11 – Mode shapes (y displacement) for an infinite-length coating with a fixed wavenumber $k = 0.5$, for the first three modal branches. Contour lines (dashed negative) indicate the levels ± 1 . The interface is deformed according to the y displacement field.

Figure 5.12 – Cutoff frequency. Dispersion relation for the spring-backed string equation (5.3.9), with asymptotic features.



given by $2\pi/k$, while the transverse pattern is that observed in Fig. 5.10b.

At high wavenumbers, the waves are almost non-dispersive (see Fig. 5.10a), and the lowest branch is asymptotic to the dispersion relation $\lambda = 0.955 k$ established by Rayleigh (1885) for the propagation of interface waves in a semi-infinite media $((x, y) \in \mathbb{R} \times \mathbb{R}^-)$. This makes sense, because in that case the small characteristic size for the waves makes as if the rigid wall at the bottom bottom is sent back to infinity.

On the other hand, low wavenumbers come with a stronger dispersion. Furthermore, each branch is marked with a frequency cutoff — the cutoff for the branch (1) being λ_{\min} . No propagation occurs below this limit. When $k \rightarrow 0$, all goes actually as if the coating was experiencing a bulk displacement over its whole length, and the frequency limit is thus the natural frequency for this movement. This phenomenon can be better understood in the case of a spring-backed solid. Considering the model used for instance by Carpenter & Garrad (1985) and neglecting damping and flexural resistance, the transverse displacement ξ_y for the string of linear density M and tension T placed above the bed of springs of stiffness K is given by

$$M \frac{\partial^2 \xi_y}{\partial t^2} = T \frac{\partial^2 \xi_y}{\partial x^2} - K \xi_y. \quad (5.3.9)$$

Then, the dispersion relation for waves of type $\xi_y(x, t) = \hat{\xi}_y \exp \mathbf{i}(\lambda t - k x)$ writes as

$$\lambda = \sqrt{\frac{T}{M} k^2 + \frac{K}{M}}.$$

This dispersion relation is represented in Fig. 5.12. In the limit of very long waves ($k \rightarrow 0$), this relation becomes $\lambda \simeq \sqrt{K/M}$ which is the eigenfrequency for the springs alone, that oscillate as if they were alone. In our more complex elasticity model, the reason for the apparition of the cutoffs is essentially the same, except that in that case there are several modal branches.

Note that a fluid model can be added quite easily to this travelling-wave analysis, by modifying the stress boundary condition: for the case of a compressible material, Duncan *et al.* (1985) determined for instance dispersion relations for a compliant coating interacting with a prescribed pressure wave applied in the upper interface, akin to fluid pressure perturbations coming from the surrounding fluid.

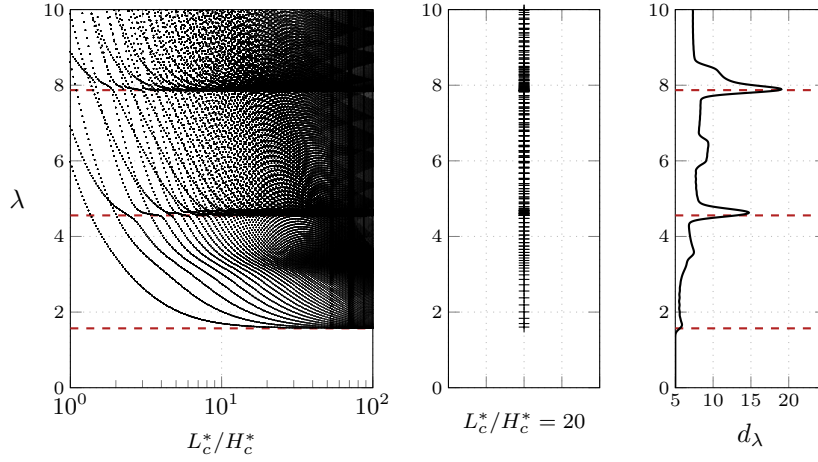


Figure 5.13 – Free vibration frequencies for finite-length coatings. Lowest frequencies obtained in the free vibration problem for a finite-length compliant coating without damping as a function of the coating’s aspect ratio L_c^*/H_c^* . The dashed lines mark the n frequencies obtained in the limits $k \rightarrow 0$ for each branch of the dispersion relation for the infinite-length coating (see Fig. 5.10).

Finite-length, finite-thickness coating

Let us now move on to the case of a finite-length coating of width H_c^* in the y direction and length L_c^* in the x direction, clamped on its bottom side but also on the left and right sides, and free to vibrate in vacuum in the upper side. The travelling-wave analysis performed above is no longer appropriate because of these side conditions. Therefore, the solid displacement field is now decomposed as $\mathbf{q}'_s(\mathbf{x}, t) = \mathbf{q}_{s,\text{free}}^\circ(\mathbf{x}) \exp(\lambda t)$ in the solid equations (5.2.6)–(5.2.7), with $\lambda \in \mathbb{C}$ and $\mathbf{q}_{s,\text{free}}^\circ = [\boldsymbol{\xi}_{\text{free}}^\circ, \mathbf{u}_{s,\text{free}}^\circ = \lambda \boldsymbol{\xi}_{\text{free}}^\circ]$. This now amounts to solve the solid part of (5.2.8) — still with the solid-based non-dimensionalization —, that is,

$$\left\{ \lambda \mathcal{B}_s - \mathcal{A}_s \right\} \mathbf{q}_{s,\text{free}}^\circ = 0. \quad (5.3.10)$$

This eigenvalue problem is solved by a shift-and-invert strategy using the ARPACK library (Lehoucq *et al.*, 1997).

Remark. The free vibration problem (5.3.10) is written on the form of an augmented first-order problem, where $\mathbf{q}_{s,\text{free}}^\circ$ has a velocity and displacement component. In absence of damping ($\mathcal{D}_s = 0$), the eigenvalues are pure imaginary numbers. Physically, because there is no amplification/decay mechanism in this case. Mathematically, because the solid operator \mathcal{K}' in \mathcal{A}_s is positive and symmetric. When $\mathcal{D}_s = 0$, the free vibration modes $\{\mathbf{q}_{s,\text{free}_i}^\circ\}_{i=1,2,\dots}$ form therefore an orthogonal basis.

The lowest-frequency eigenvalues for this problem are represented in Fig. 5.13, for different aspect ratios L_c^*/H_c^* and no damping. We recover the main features obtained from the infinite-case. First, we again notice a cutoff frequency for all coating lengths. For “long” coatings (aspect ratio greater than about 10) the cutoff at $\lambda = \lambda_{\min}$ determined in the infinite-length case is recovered. Shorter coatings come with an increased lowest frequency. Sort of “modes accumulation zones” are also noticed on the spectrum shown in the middle figure, which correspond to the eigenfrequencies prescribed by the dispersion relation for the infinite coating in the limit $k \ll 1$: because the slope of the dispersion relation is almost flat in this region, there are many of modes having different wavenumbers but the same vibration frequency. This is made more visible in the graph on the right side, where the moving average density of modes per unit frequency is displayed, showing peaks close to the location of the frequency cutoffs for the branches (1), (2) and (3) of Fig. 5.10a. Setting a finite length in the x direction amounts in a certain extent to selecting integer wavenumbers in the infinite-length dispersion relation (wavelengths L_c^* , $L_c^*/2$, $L_c^*/3$, etc.).

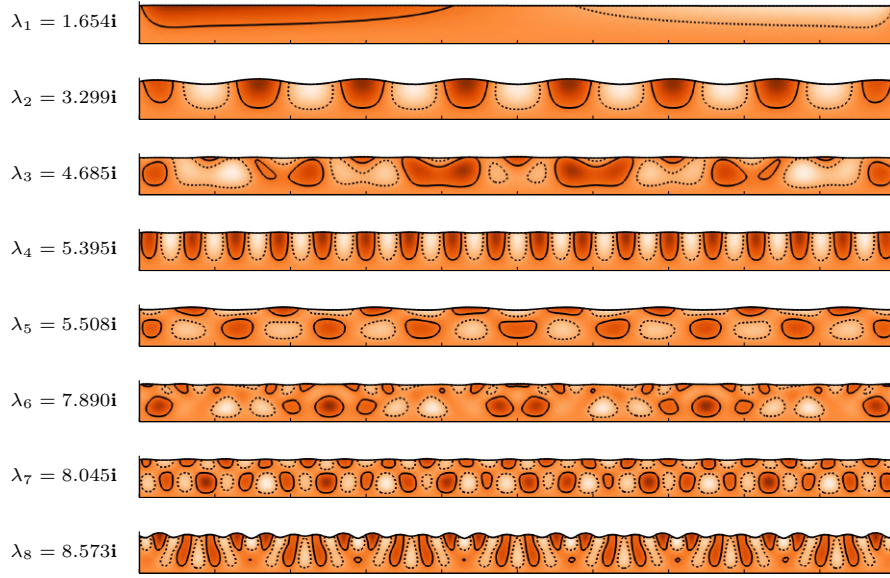


Figure 5.14 – Mode shapes (real part of the transverse displacement, $\Re(\xi_{\text{free}}^{\circ})$) for a finite-length coating of aspect ratio $L_c^*/H_c^* = 20$, ordered by increasing vibration frequency. Contour lines (dashed negative) indicate the levels ± 1 .

A few mode shapes for the case with an aspect ratio 20 are reported in Fig. 5.14, represented in an increasing order in terms of their frequency. The y displacement is shown together with the interface deformation for a better visualisation. This “zoology” of modes shows the great variety of modal behaviours that can be found. The first, second and fourth modes have actually the same transverse distribution than that of the mode $\hat{\phi}_1$ presented above, and almost the same in the x direction (apart from the sides where edge effects alter the deformation, the modal pattern is very similar to the what is shown in Fig. 5.11 for the mode in the branch (1)). Because the length of the coating is finite, the admissible streamwise wavelengths are actually L_c^* , $L_c^*/2$, $L_c^*/3$, etc. and for the same transverse pattern, all possible integer values for the streamwise wavenumber can possibly be found. At higher frequency, the trace of the second modal branch with modes $\hat{\phi}_2$ is found (fifth mode) as well as its x subdivisions (seventh mode). More complex patterns are also found, like the third, sixth mode or last mode. For these cases, the spatial distribution is more specific to the finite-length case.

Finally, the influence of the viscoelastic damping onto the free-vibration eigenvalues is reported in Fig. 5.15. In presence of damping, the eigenvalues are no longer real-valued as it is the case when $\mathcal{D}_s = 0$ but present a negative growth-rate (damped oscillations). The higher the frequency, the more negative the growth rate is, as it is traditionally observed for damped oscillators. From (5.2.6) and (5.2.5), the decay of the growth-rate can be for instance evaluated as $\lambda^r = -3\mathcal{D}_s/(2\mathcal{E}_s)\lambda_0^i$, where λ_0^i is the frequency of the modes without damping.

5.3.2 Fluid-elastic eigenvalue analysis

We now compute the global modes for the fluid-elastic configuration. Considering a finite-length, spring-backed solid interacting with a boundary-layer flow, Tsigklifis & Lucey (2017) showed indeed that the configuration can become globally unstable. In this latter case, the system acts as a self-sustained, self-amplified oscillator, and global modes are appropriate to describe its behaviour. Since the characteristic frequency for the solid is $\sqrt{\mathcal{E}_s/\mathcal{M}_s}$, we should find a trace there for the solid modes described in the previous paragraph, at somewhat lower frequencies compared to the free vibration case, because of added mass effects.

In all what follows, we consider the case of a finite-length coating of aspect ratio 20, and the

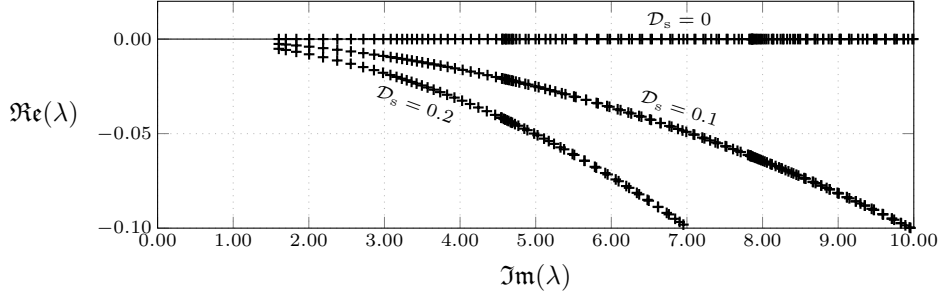


Figure 5.15 – Free vibration frequencies for finite-length coatings, influence of damping. Plot of the eigenvalues for the cases without damping, $\mathcal{D}_s = 0.1$ and $\mathcal{D}_s = 0.2$, for the case $L_c^*/H_c^* = 20$.

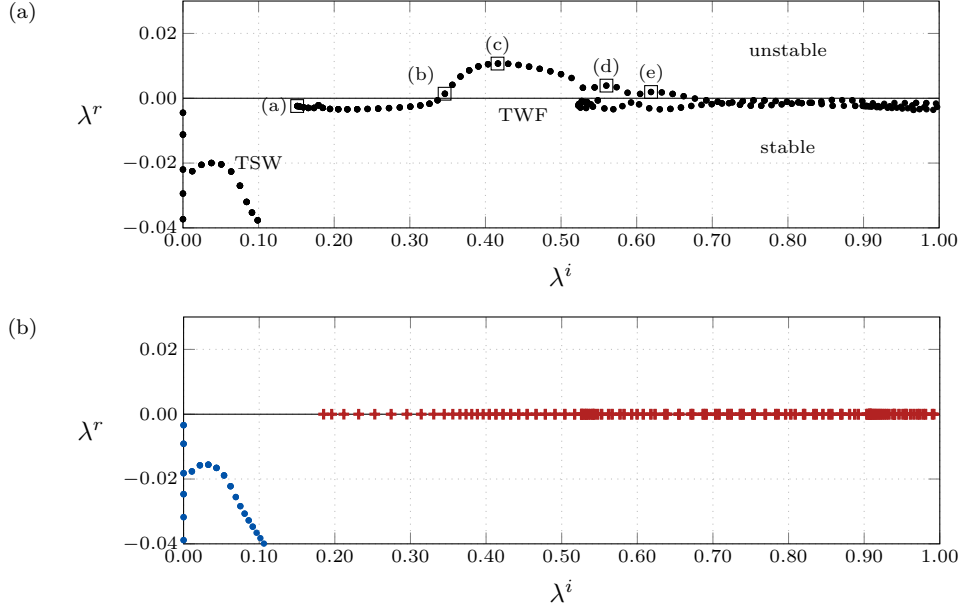


Figure 5.16 – Eigenvalue spectrum for the fluid-elastic configuration without damping ($\mathcal{E}_s = 1, \mathcal{D}_s = 0$). (a) Fully coupled spectrum showing the fluid-elastic eigenvalues (\bullet), and (b) superposition of the hydrodynamic (rigid-wall) spectrum (\bullet) and free solid vibration frequencies ($+$), rescaled according to the fluid-based non-dimensionalization (the non-dimensional width of the coating being 5, all frequencies are $5\sqrt{3} \simeq 8.66$ times smaller as what is shown in §5.3.1).

Reynolds number for the flow is fixed to $\mathcal{R}_e = 3000$. We look here for coupled fluid-elastic modes

$$\begin{pmatrix} \mathbf{q}'_s \\ \mathbf{q}'_f \end{pmatrix}(\mathbf{x}, t) = \begin{pmatrix} \mathbf{q}^\circ_s \\ \mathbf{q}^\circ_f \end{pmatrix}(\mathbf{x}) \exp\left((\lambda^r + \mathbf{i}\lambda^i)t\right)$$

in the linearised fluid-structure problem without any forcing term, where λ^r is the growth-rate of the perturbations and λ^i is the angular frequency. This results in the eigenvalue problem

$$\left\{ (\lambda^r + \mathbf{i}\lambda^i) \begin{pmatrix} \mathcal{B}_s & 0 \\ 0 & \mathcal{B}_f \end{pmatrix} - \begin{pmatrix} \mathcal{A}_s(\mathcal{E}_s, \mathcal{D}_s) & \mathcal{C}_{sf} \\ \mathcal{C}_{fs} & \mathcal{A}_f(Q) \end{pmatrix} \right\} \begin{pmatrix} \mathbf{q}^\circ_s \\ \mathbf{q}^\circ_f \end{pmatrix} = \mathbf{0}. \quad (5.3.11)$$

Solving (5.3.11) for different values of the stiffness and damping parameters allows to determine the region in the parameter space — if any — where the flow is globally unstable.

Pure-elastic case

We consider first the pure-elastic case ($\mathcal{E}_s = 1$ and $\mathcal{D}_s = 0$). The eigenvalue spectrum of the fully coupled, linearised fluid-solid operator is displayed in Fig. 5.16a, while the decoupled spectrums

for the fluid (blue) and the solid (red) is displayed in Fig. 5.16b. In the left side ($\lambda^i < 0.15$) in (a), only stable modes are found. These modes are also found in the rigid-wall configuration, whose eigenvalues are depicted in Fig. 5.16b with dot symbols. These stable modes are associated to the Tollmien-Schlichting waves (Ehrenstein & Gallaire, 2005; Åkervik *et al.*, 2008). Actually, if the individual two-dimensional modes are stable, an appropriate superposition of them may exhibit a transient growth (Ehrenstein & Gallaire, 2005). The dynamics of the Tollmien-Schlichting waves has indeed more to do with receptivity and energy amplification mechanisms than modal behaviour (Schmid, 2007). For that reason, a resolvent analysis will be performed in Section 5.5. Compared to the rigid case (b), in the flexible case, the TSW's are slightly attenuated: the maximum growth-rate decreases from -0.0155 in (b) down to -0.02 in (a).

Unstable modes are found in the pure-elastic case (a) in a frequency range between 0.35 and 0.70. These modes are clearly related to the destabilization of the free vibration solid modes (depicted with $+$ symbols in Fig. 5.16b) through the interaction with the fluid. Note that the frequency of the coupled modes is slightly shifted towards lower frequencies, because of added mass effects. This part of the spectrum is in qualitative agreement with what was observed in the global mode analysis by Tsigklifis & Lucey (2017) in the case without damping: one branch of unstable modes was found in about the same frequencies. In the present case, more than one branch of modes is observed. This makes sense, since our solid model enables to carry many more types of modes than the spring-backed solid considered by Tsigklifis & Lucey. In the following, we refer to these modes as the travelling-wave flutter (TWF) modes.

Remark. It is well-known that the eigenvalues related to the Tollmien-Schlichting waves are sensitive to the location and type of boundary conditions considered (Ehrenstein & Gallaire, 2005). We also observed this phenomenon by varying the distance between the end of the coating and the outflow. With the chosen dimensions for the domain, the region that drives the instability (referred to as the wavemaker region by Giannetti & Luchini (2006)) is indeed not completely covered by the computational grid. This is however not really an issue, because we are rather interested by the effect of variations of the material parameters than by the absolute values. On the other hand, the eigenvalues related to the solid-based instabilities are completely insensitive to the dimensions of the domain.

The spatial structures for the global modes labelled (a) to (e) in Fig. 5.16 are displayed in Fig. 5.17. Large perturbation velocities are observed in the vicinity of the fluid-solid interface. We have kept separate colors to better distinguish the solid from the fluid region, but the contour levels are the same in both regions. In each case, the structures of the mode are concentrated in the vicinity of the solid, and quickly decay in the streamwise direction after the coating's end at $x = 125$ has been reached. For a better visualisation of the transient interface dynamics, snapshots of the interface at different phases of the modes are also reported, as well as the instantaneous position at zero phase (real part of the deformation).

The mode (a) is stable and corresponds to the lowest-frequency mode in the first TWF modal branch that appears in the spectrum. The mode (b) is the lowest-frequency unstable mode. The mode (c) is the most unstable mode, while modes (d) and (e) are higher-frequency, unstable modes. As one evolves toward higher-frequency modes, the vibration pattern becomes more and more complex. In particular, the instantaneous interface deformation counts more and more vibration nodes: in case (a) there are two vibration nodes at the clamped ends, while in case (c) the snapshots of the deformation reveal 22 nodes.

The space-time structure for the mode (c) is reported in Fig. 5.18. The velocity vibration nodes observed in Fig. 5.17 form vertical lines in the space-time diagram, that break periodically the oblique stripes corresponding to the wave propagation. Downstream and upstream directions of propagation are observed here, that correspond to the superposition of two travelling waves that form one standing wave. We clearly see in this representation the spatial amplification of the waves in the streamwise direction, and edge effects close to the clamped side at $x = 125$. Downstream of the coating's end, the cut in the fluid ($y = 1$) shows how the mode recovers a downstream travelling-wave structure, that quickly decays down to zero.

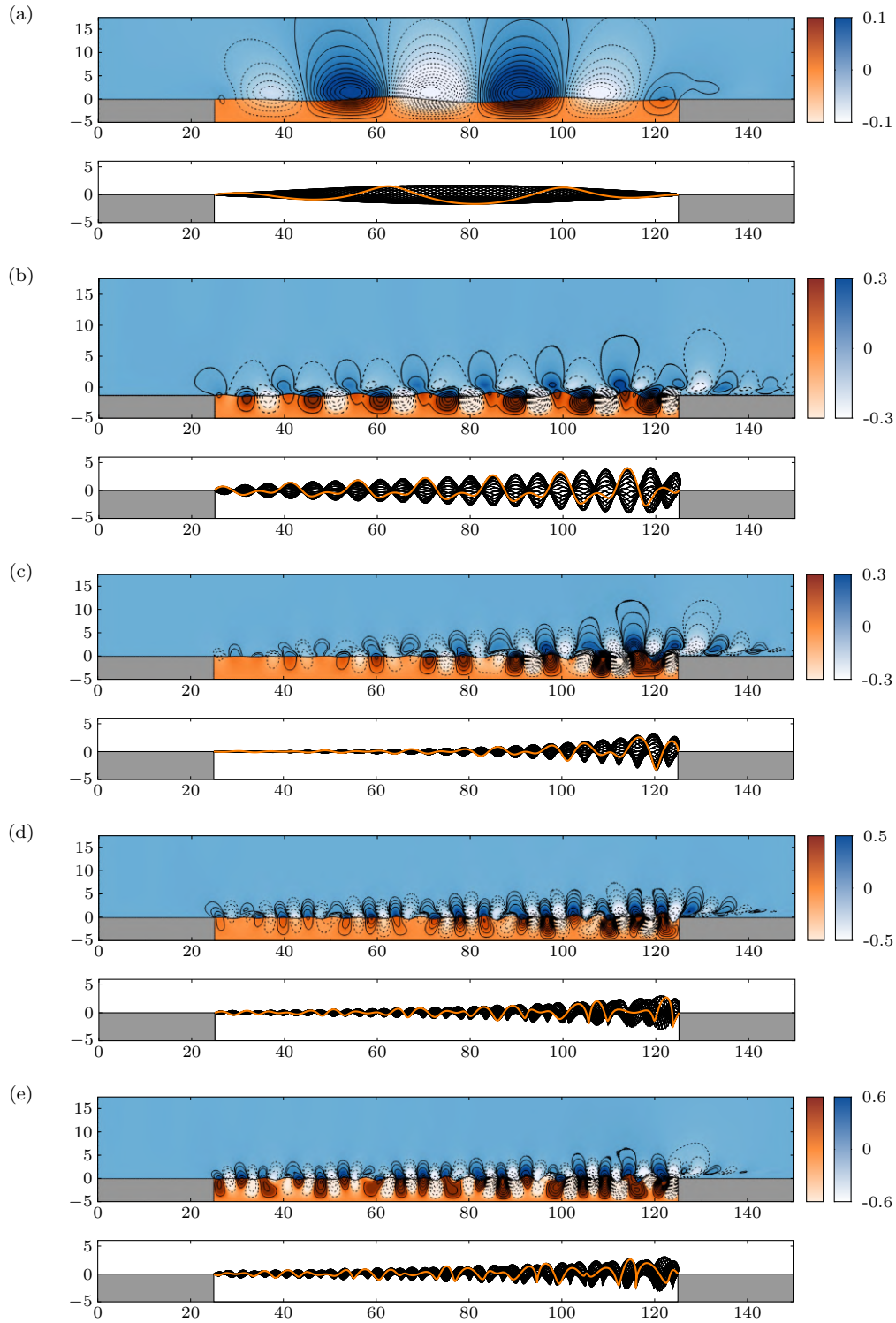


Figure 5.17 – Global modes. For the modes labelled (a,...,e) in Fig. 5.16, plot of the real part of the transverse velocity in the solid (blue color) and in the solid (orange color, same levels). The bottom inserts depict snapshots of the solid interface deformation at different phases, while the orange line depicts the real part (zero phase).

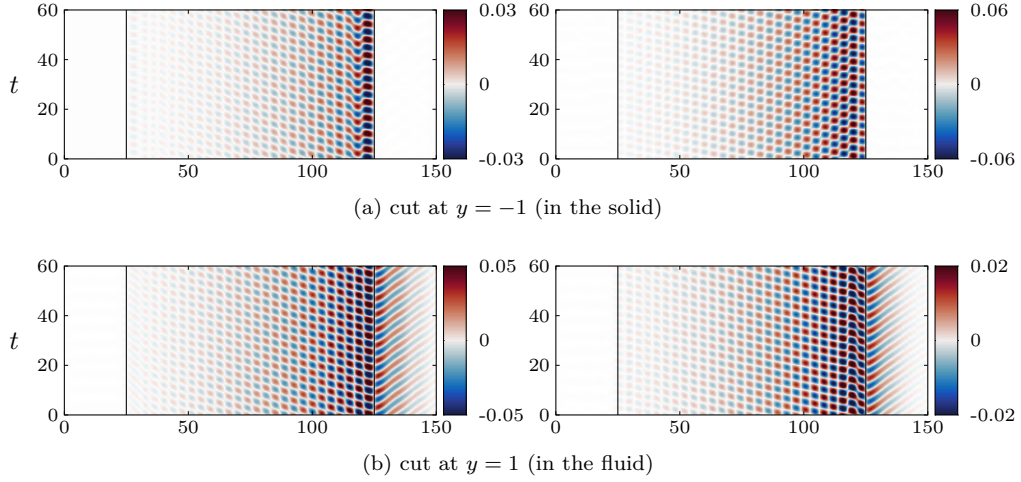
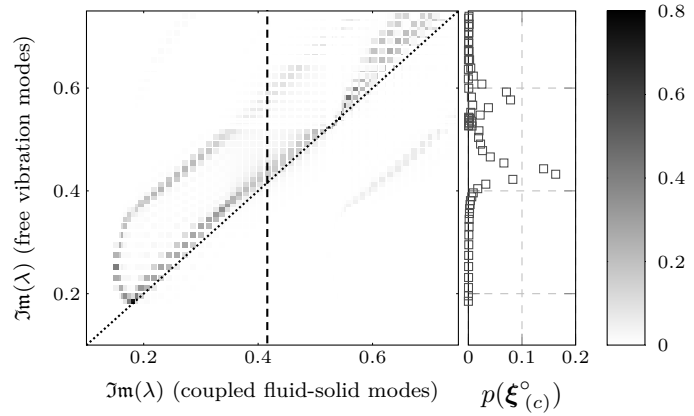


Figure 5.18 – Space-time diagrams. For the unstable global mode (c), plot of streamwise (left) and transverse (right) cuts of the mode $\Re\{u^o(x, y = y_0) \exp(i\lambda t)\}$ in the (x, t) plane, for (a) $y_0 = -1$, (b) $y_0 = 1$ and (c) $y_0 = 2$.

Figure 5.19 – Projection of the fluid-solid modes on the free vibration modal basis. For the case $\mathcal{E}_s = 1$, $\mathcal{D}_s = 0$, plot of the projection coefficients $p(\xi^o)$ of the coupled fluid-solid modes on the free vibration modal basis (grayscale). The graph in the right corresponds to a slice (indicated by the dashed line) at the frequency of the mode (c) in Fig. 5.16.



Analysis in terms of free vibration modes

The coupled modal deformation represented in Fig. 5.17 shows a complex pattern. A projection of the solid component of the coupled fluid-solid mode allows to better understand how the coupled mode is related to the free vibration modes described in §5.3.1. Considering a basis of N free vibration modes $\{\xi_{\text{free},i}^o\}_{i=1,\dots,N}$ (ordered by increasing frequency) and projecting ξ^o on this orthogonal basis gives

$$\sum_{i=1}^N \frac{|\langle \xi^o, \xi_{\text{free},i}^o \rangle|^2}{\|\xi^o\|^2} \simeq 1$$

provided that N is chosen sufficiently large. The coefficients $p_i(\xi^o) = |\langle \xi^o, \xi_{\text{free},i}^o \rangle|^2 / \|\xi^o\|^2$ give how the solid kinetic energy of the coupled fluid-structure mode is distributed on the basis of free vibration modes. For instance, $p_1 = 0.9$ would mean that 90% of the mode's solid kinetic energy is related to the lowest-frequency free vibration mode. The coefficients $p_i(\xi_j^o)$ are reported in the scatter plot in Fig. 5.19, where ξ_j^o is the j^{th} mode in the TWF branch (ordered by an increasing frequency) of fluid-structure modes. The free modal basis consists of all the modes having a frequency smaller than 0.8. Each vertical slice (at some frequency of a coupled mode) thus represents the frequency histogram of the projection on the free vibration basis. Darker points indicate regions with a larger projection coefficient.

A complex pattern is observed. The high projection coefficients are mainly concentrated above

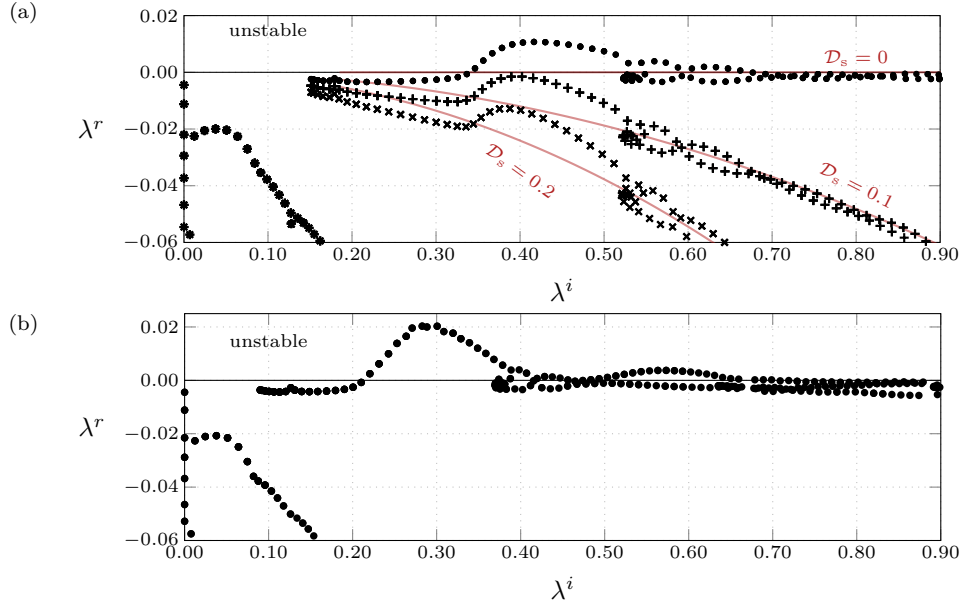


Figure 5.20 – Eigenvalue spectrum for the viscoelastic configuration, effect of damping and stiffness. (a) Plot of the eigenvalues for the case without damping (\bullet), the case $\mathcal{D}_s = 0.1$ ($+$) and the case $\mathcal{D}_s = 0.2$ (\times). The red lines mark the growth-rate of the free-vibration modes. (b) Plot of the eigenvalues for the case $\mathcal{D}_s = 0$ and $\mathcal{E}_s = 0.5$.

the $y = x$ line, because of added mass effects. We see that several free vibration modes contribute to the coupled dynamics.

Effect of viscoelastic damping and stiffness variation

Still considering the case $\mathcal{E}_s = 1$, let us now consider a few cases with viscoelastic damping. The stabilizing effect on the modes is clearly visible in Fig. 5.20a that shows superimposed spectra for $\mathcal{D}_s = 0$, $\mathcal{D}_s = 0.1$ and $\mathcal{D}_s = 0.2$. The TSW modes are almost not affected at all by the viscoelastic damping, on the contrary to the higher-frequency TWF modes that are strongly damped. In particular, from $\mathcal{D}_s = 0.1$ the TWF modes are all stable. The decay of the growth-rate is asymptotic to that of the free solid vibration modes (indicated by the red line) at high frequency: out of the frequency region where there is an interaction with the flow, the decoupled modes are recovered.

Finally, the spectrum of a case without damping and a stiffness $\mathcal{E}_s = 0.5$ is depicted in Fig. 5.20b, and shows a decrease of the minimum frequency attained by the modes in the TWF branch. This makes sense, because the frequency of the solid modes scales as $\sqrt{\mathcal{E}_s/\mathcal{M}_s}$. The same frequency shift is observed when there is viscoelastic damping. Compared to the reference case $\mathcal{E}_s = 1$, the maximal growth for the modes in the TSW branch is decreased by about 9.6 %, but a great increase of the maximal growth-rate of the unstable modes (about a factor 2) is also observed, showing the well-known antagonist behaviour between the TSW/TWF modes with respect to the stiffness (Carpenter & Garrad, 1985, 1986).

5.4 Elastic response to optimal fluid perturbations

It is well known that the development of the Tollmien-Schlichting waves in boundary-layer flows is often more conveniently analysed in terms of the receptivity of the flow to external perturbations (Schmid, 2007) than in terms of eigenmodes. Strong energy amplifications may indeed occur even though the eigenvalues are all stable, because of transient growth (see the Appendix A for an introduction to these notions). We presently apply a resolvent analysis first in the rigid-wall configuration, that allows to determine which perturbation leads to the strongest response in the

flow. Then, considering this optimal, rigid-wall perturbation, the response in the viscoelastic case is computed and analysed.

5.4.1 Resolvent analysis in the rigid-wall case

In our framework, the governing equation for the fluid velocity and pressure perturbation \mathbf{q}'_f developing about the boundary-layer flow past a rigid wall, and excited by some momentum forcing \mathbf{f}' , corresponds to the sub-problem

$$\mathcal{B}_f \frac{\partial \mathbf{q}'_f}{\partial t} - \mathcal{A}_f \mathbf{q}'_f = \mathcal{P}_f \mathbf{f}' \quad (5.4.1)$$

deduced from (5.2.8). In the linear framework, the response to a generic forcing akin to free-stream perturbations (gusts, etc.) can be computed as the sum of independent responses to each harmonic component of the original forcing, thanks to the superposition principle. Hence, we assume an harmonic forcing

$$\mathbf{f}'(\mathbf{x}, t) = \mathbf{f}_{\text{rgd}}(\mathbf{x}) e^{i\omega t} + \text{c.c.}$$

where c.c. stands for the complex-conjugate and the subscript “rgd” stresses the fact that the forcing is taken here in the rigid-wall case. Because of the linearity of (5.4.1), this harmonic forcing leads to an harmonic fluid velocity-pressure-interface stress response

$$\mathbf{q}'_f(\mathbf{x}, t) = \mathbf{q}_{f,\text{rgd}}(\mathbf{x}) e^{i\omega t} + \text{c.c.}$$

Introducing the fluid resolvent operator $\mathcal{R}_f(\omega) = (i\omega \mathcal{B}_f - \mathcal{A}_f)^{-1}$, the fluid velocity response \mathbf{u}_{rgd} to a momentum forcing $\mathbf{f}_{\text{rgd}}(\mathbf{x})$, in the rigid configuration, writes as (the momentum forcing and the velocity response are living in the same space)

$$\mathbf{u}_{\text{rgd}} = \mathcal{P}_f^T \mathcal{R}_f(\omega) \mathcal{P}_f \mathbf{f}_{\text{rgd}}. \quad (5.4.2)$$

The Tollmien-Schlichting waves developing in the rigid-wall configuration can be characterized by looking, at a given frequency ω , for what is the spatial distribution of $\mathbf{f}_{\text{rgd}}(\mathbf{x})$ that gives the greatest amplification $G_f(\omega)$ of the fluid velocity perturbations $\mathbf{u}_{\text{rgd}}(\mathbf{x})$ akin for these unstable waves (Sipp & Marquet, 2013). Namely, we set

$$G_f(\omega)^2 = \max_{\|\mathbf{f}_{\text{rgd}}\|^2=1} \|\mathbf{u}_{\text{rgd}}\|^2 \quad \text{with} \quad \|\mathbf{q}\|^2 = \int_{\Omega_f} |\mathbf{q}|^2 d\Omega, \quad (5.4.3)$$

that is, energy is measured over the whole fluid domain. Using (5.4.2) and the adjoint resolvent operator $\mathcal{R}_f(\omega)^\dagger$, equations giving the solutions to this constrained optimization problem can be obtained by writing the associated Lagrangian function. Looking for the stationarity conditions, the problem then amounts to solve the generalized eigenvalue problem (Brandt *et al.*, 2011)

$$(\mathcal{P}_f^T \mathcal{R}_f(\omega)^\dagger \mathcal{P}_f \mathcal{P}_f^T \mathcal{R}_f(\omega) \mathcal{P}_f) \mathbf{f}_{\text{rgd}} = \sigma^2 \mathbf{f}_{\text{rgd}} \quad (5.4.4)$$

with $G_{f,i}(\omega) = \sigma_i$ — all the eigenvalues $\sigma_0^2 > \sigma_1^2 > \dots$ are positive because the left and right-hand sides of this problem are Hermitian. In the present case, the explicit form of the adjoint resolvent operator does not need to be determined: the discrete adjoint approach is considered. Once the forcing field is determined, the velocity perturbation response can be computed using (5.4.2). The triplet $(G_{f,0}, (\mathbf{f}_{\text{rgd}})_0, (\mathbf{u}_{\text{rgd}})_0)$ is called *optimal* (gain, forcing, response) because $(\mathbf{f}_{\text{rgd}})_0$ is the momentum forcing field that yields to the most amplified (by a factor $G_{f,0}$ according to the kinetic energy norm) velocity perturbation $(\mathbf{u}_{\text{rgd}})_0$. The triplets $(G_{f,i}, (\mathbf{f}_{\text{rgd}})_i, (\mathbf{u}_{\text{rgd}})_i)$ are called the *sub-optimum* of order $i > 0$, and form less amplified couples of forcing and response, that can nevertheless still participate to the instability process if their amplification is not negligible compared to the optimal instability mode. Note that these fields are given for *each* value of the forcing frequency: both the gain, the forcing and the response field depend on ω .

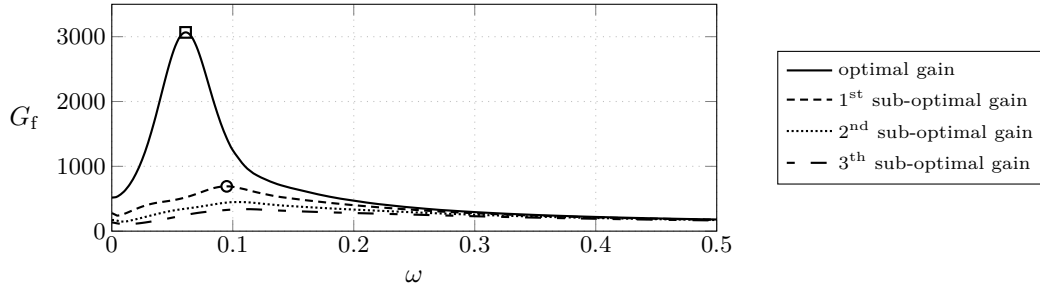


Figure 5.21 – Gain curve in the rigid configuration. Plot of the amplification gain G_f as a function of the forcing frequency (optimal and five first sub-optimum). The forcing and response fields associated to the points \square ($\omega = 0.06$) and \circ ($\omega = 0.095$) are reported in Fig. 5.22.

Remark – practical resolution of (5.4.4). Generalized eigenvalue problems of type $\mathbf{K}\mathbf{x} = \lambda\mathbf{M}\mathbf{x}$ with \mathbf{K} an invertible matrix, \mathbf{M} a symmetric positive matrix and $\lambda \in \mathbb{C}$, are solved in FREEFEM++, using an interface with the library ARPACK, that allows to find the smallest eigenpairs. More specifically, the function `complexEigenValue(...,CFA,CFB,...)` is used, that requires as an input the functions $\mathbf{x} \mapsto \mathbf{K}^{-1}\mathbf{x}$ and $\mathbf{x} \mapsto \mathbf{M}\mathbf{x}$ coded in routines CFA and CFB. This interface is used here to solve (5.4.4). At the discrete level, we have $\mathbf{K} = [\mathbf{P}^T \mathbf{R}(\omega)^H \mathbf{P} \mathbf{P}^T \mathbf{R}(\omega) \mathbf{P}]^{-1}$, $\mathbf{M} = \mathbf{I}$ and $\lambda = (1/\sigma)^2$, and look for the smallest λ (i.e. the largest σ). The following implementation is done:

$$\text{CFA} : \mathbf{x} \mapsto \mathbf{P}^T \mathbf{R}(\omega)^H \mathbf{P} \mathbf{P}^T \mathbf{R}(\omega) \mathbf{P} \mathbf{x},$$

$$\text{CFB} : \mathbf{x} \mapsto \mathbf{x}.$$

This requires to compute the resolvent $\mathbf{R}(\omega)$ and its transconjugate, which is done using a LU decomposition of the operator $(i\omega\mathbf{B} - \mathbf{A})$. Note that only one LU decomposition has to be done, since the transposition of the inverse can be done by transposition of the resultant lower and upper triangular matrices. Then, having found the smallest pairs $(\lambda_i, \mathbf{x}_i)$, the relevant quantities are derived as

$$\sigma_i = \frac{1}{\sqrt{\Re(\lambda_i)}}, \quad (\mathbf{f}^\circ)_i = \mathbf{x}_i, \quad (\mathbf{r}^\circ)_i = \mathbf{P}^T \mathbf{R}(\omega) \mathbf{P} \mathbf{x}_i.$$

For values of the forcing frequency $0 \leq \omega \leq 0.5$, solving the eigenvalue problem (5.4.4) results in the gain curve displayed in Fig. 5.21. A peak of amplification at $G_f(\omega = 0.06) = 3066$ is observed, in the frequency range typical to that of the TS instabilities. The optimal response curve largely dominates over the other: the sub-optimal peak of amplification is found at $G_f(\omega = 0.095) = 690$. From $\omega = 0.2$ to the maximum frequency $\omega = 1$ considered, a monotonic decrease of the gains is observed.

The spatial structure of the forcing and response fields corresponding to the optimal and sub-optimal gain peaks (materialized in Fig. 5.21 by symbols \square and \circ respectively) are represented in Fig. 5.22. They are similar to those shown and described by Sipp & Marquet (2013) at lower Reynolds numbers $0 \leq x^* U_\infty^* / \nu_f^* \leq 1490$, and we refer to this paper for more details. In (a) the real parts for the optimal forcing and response are displayed. The corresponding imaginary parts are similar to the real part but out of phase, thus describing a downstream convection of the perturbations. The response is also amplified in the downstream direction, which is in agreement with the fact that for the Reynolds number chosen, amplified waves are found. The forcing is made of elongated waves inclined against the flow stream, whose maximal amplitude is found upstream to the response. This structure of the forcing indicates that the Orr mechanism is at play (Åkervik et al., 2008). The same features are observed for the first sub-optimal mode (b), but in this case two maxima of forcing/response are observed in the streamwise direction (before and after $x \simeq 100$ for the response and $\simeq 50$ for the forcing).

The analysis performed here characterizes unstable Tollmien-Schlichting waves. In the next section, we discuss the fluid-elastic response to the previously determined optimal forcings.

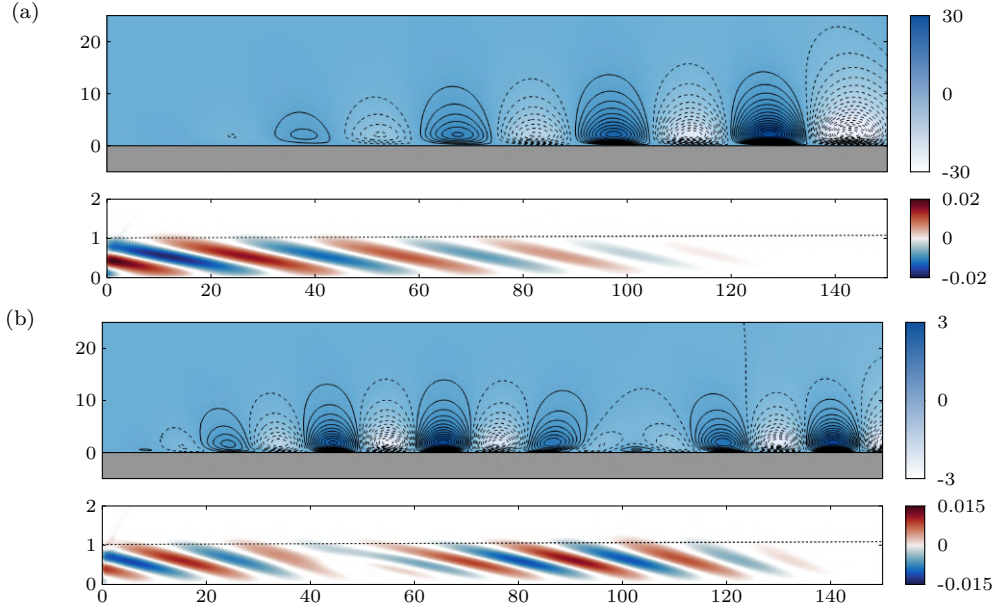


Figure 5.22 – Forcing & response for the rigid configuration. Snapshot of the real part of the transverse velocity response (dashed negative contours, top) and of the real part of the streamwise momentum forcing (blue-red gradient, bottom, the local displacement thickness being materialized with the dotted line), for (a) the optimal case (□) and (b) the first sub-optimal case (○) in Fig. 5.21.

5.4.2 Fluid-elastic response to an optimal rigid-wall forcing

We now investigate the effect of the wall's viscoelastic properties on the response to the optimal fluid momentum forcing determined in the rigid case. Unless otherwise stated, we consider the globally stable case $\mathcal{E}_s = 1$ and $\mathcal{D}_s = 0.2$. Introducing the optimal forcing determined in (5.4.4) as the forcing term in (5.2.8), we have

$$\begin{pmatrix} \mathbf{q}_s \\ \mathbf{q}_f \end{pmatrix} = \left\{ i\omega \begin{pmatrix} \mathcal{B}_s & 0 \\ 0 & \mathcal{B}_f \end{pmatrix} - \begin{pmatrix} \mathcal{A}_s & \mathcal{C}_{sf} \\ \mathcal{C}_{fs} & \mathcal{A}_f(\mathbf{Q}) \end{pmatrix} \right\}^{-1} \begin{pmatrix} \mathbf{0} \\ \mathcal{P}_f \mathbf{f}_{\text{rgd}}(\omega) \end{pmatrix} \quad (5.4.5)$$

where the solid response \mathbf{q}_s and the fluid response \mathbf{q}_f are determined by using the coupled fluid-structure resolvent operator. The amplification in the flexible case can by the same way as before be determined by computing the gain

$$G(\omega) = \|\mathbf{u}\| \quad (5.4.6)$$

where $\mathbf{u} = \mathcal{P}_f^T \mathbf{q}_f$ is the velocity component of the fluid variable. This allows to evaluate the effect of wall viscoelasticity on the response to a *given* forcing. In particular, there is no need for an optimization here, since we simply evaluate the fluid-elastic response to a known forcing field.

For each value of the forcing frequency ω , the viscoelastic response to the optimal and sub-optimum forcings determined in the rigid case is computed. The response curve computed from (5.4.6) is displayed in Fig. 5.23, and shows two distinct regions that are further analysed in the following. At low frequency, we recover an amplification that is related to the Tollmien-Schlichting waves, while higher-frequency amplifications are also observed. This higher-frequency amplifications are obviously related to the travelling-wave flutter of the solid.

Response in the Tollmien-Schlichting waves frequency range

In Fig. 5.23, let us focus first on the low-frequency region $\omega \leq 0.3$. Both the responses to the optimal and first sub-optimum rigid-wall forcings are displayed. It is observed that the maximal amplification for the Tollmien-Schlichting waves is reduced by about 25 %, in qualitative agreement with earlier studies on the impact of lowering the coating's stiffness (Benjamin, 1960; Carpenter &

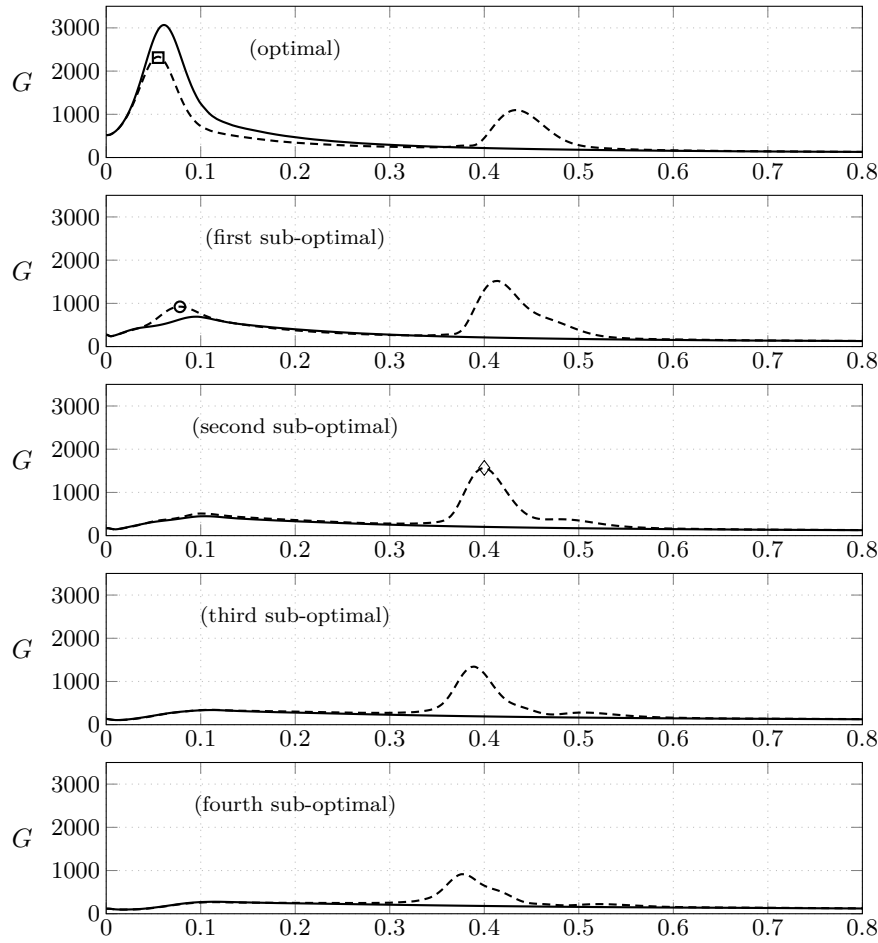


Figure 5.23 – Response curve for the viscoelastic configuration. Plot of the amplification gain G for the case with $\mathcal{E}_s = 1$ and $\mathcal{D}_s = 0.2$, determined as the response to the optimal and four first sub-optimum fluid perturbations. The solid line (—) refers to the rigid-wall amplification, while the dashed (---) line indicates the fluid-elastic response. Points \square ($\omega = 0.055$) and \circ ($\omega = 0.078$) identify the peak of the fluid-elastic response, in the low-frequency TSW region, to optimal and sub-optimal forcings respectively. Point \diamond ($\omega = 0.4$) identifies the peak of the fluid-elastic response, in the higher-frequency TWF region.

(Garrad, 1985): Tollmien-Schlichting instabilities are damped by the flexibility of the wall. Furthermore, the frequency range where large amplifications occur is reduced. Considering the response to the first sub-optimal rigid-wall forcing, we see that the fluid-elastic response results in a larger amplification as what is observed in the rigid-wall case. The amplitude of this secondary response is however still lower (by a factor about 2) than the response to the optimal rigid-wall forcing, and the responses to higher-order sub-harmonics have all even smaller amplitudes.

The spatial structures of the responses corresponding to the peaks materialized in Fig. 5.23 by the square (\square) and circle (\circ) symbols are depicted in Fig. 5.24. The transverse component of the real part of the velocity response \mathbf{u} is represented in the fluid and solid regions. For a better visualisation, the solid has been deformed according to the real part of the solid deformation field (scaled with an arbitrary amplitude). In the fluid, the same features as that observed in the rigid case are observed, namely, out of phase streamwise and transverse (not represented) velocity perturbations travelling downstream while being amplified. Two different scales have been used to represent the solid and fluid velocities, because the solid velocity perturbations are much smaller than in the fluid. In particular, the solid velocity perturbation in the vicinity of the interface is very small compared to the fluid velocity perturbations (about 1% of the maximal velocity

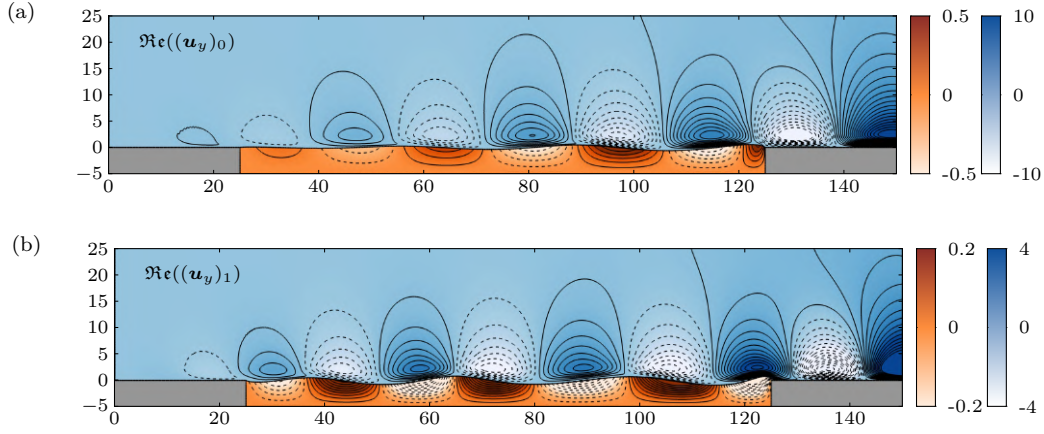


Figure 5.24 – Elastic responses to optimal fluid forcing. Fluid and solid transverse velocity components (real part) for the response to the momentum forcing determined in the rigid case, for (a) the peak of response to the fluid optimum (point \square in Fig. 5.23) and (b) the peak of response to the fluid sub-optimum forcing (point \circ in Fig. 5.23).

fluctuations).

In the solid, the longitudinal wavelength of the deformation is the same as that of the surrounding Tollmien-Schlichting waves. The displacement is in phase quadrature with the velocity, since $\mathbf{u}_s = i\omega\boldsymbol{\xi}$. The deformation history is better visualised in Fig. 5.25. Ten snapshots of the solid deformation during an oscillation period are reported there, showing the temporal evolution of the solid deformations. Arrows indicate the displacement field while the colours indicate the velocity magnitude. Using this representation, we clearly see the wave propagation (and amplification in the $x > 0$ direction) at a constant phase speed, which is also that of the fluid perturbations. Although smaller than that of the transverse deformation, there is a noticeable streamwise deformation in the solid — that is in any case necessary, so as to guaranty the incompressibility of the material.

In Fig. 5.26, two space-time diagrams show the evolution with t of $\Re\{\mathbf{u}(x, y = 1) \exp(i\omega t)\}$ in the fluid and $\Re\{\mathbf{u}_s(x, y = -1) \exp(i\omega t)\}$ in the solid (transverse component). We see here that the fluid wave propagation is not much altered by the presence of the solid (presence of almost straight oblique stripes) between $x = 25$ and $x = 125$. The second cut (right) shows how edge effects alter the wave propagation in the solid, in the vicinity of the coating's ends. On the contrary to what was shown in the modal analysis, the response to the rigid-wall forcing generates only a downstream travelling wave in both media.

Response in the travelling-wave flutter frequency range

Let us now focus on the higher-frequency region $\omega \geq 0.3$ in Fig. 5.23. Large peaks of amplification are found around the forcing frequency $\omega = 0.4$. On the contrary to what was observed for the Tollmien-Schlichting waves, in the present case the optimal forcing computed in the rigid case is no longer that who produces the largest viscoelastic response. Rather, the travelling-flutter waves are amplified with a large magnitude for both the optimal and at least the four first sub-optimum forcings. The higher the order of the forcing, the lower the frequency of the peak of response. For frequencies larger than 0.6, a monotonic decay of the response is again observed.

The mode corresponding to the peak of the response curve to the second sub-optimum (point \diamond in Fig. 5.23) is displayed in Fig. 5.27, together with the fluid forcing computed from (5.4.4), displayed with the blue-red gradient. The mode takes the form of a downstream travelling-wave that vanishes after the coating's end. Like for the global modes, the perturbations have the same order of magnitude in the solid and in the fluid, and are spatially amplified in the downstream direction while travelling in the vicinity of the coating. The forcing fields take the same form of oblique elongated waves inclined against the flow stream. On the contrary to what was observed for the T-S waves, the region where the largest forcing amplitudes occur is located farther away

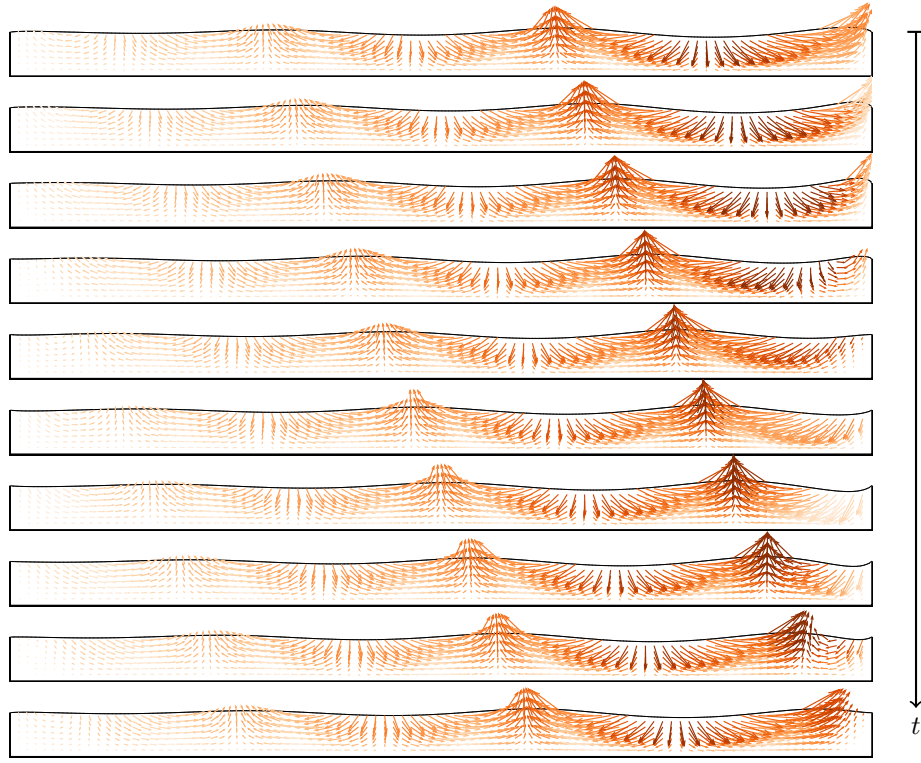


Figure 5.25 – Solid response to TSW optimal forcing. Snapshots of the solid during an oscillation period. The interface deformation is shown, while arrows indicate the displacement field, coloured by the solid perturbation velocity magnitude (darker is higher)

from the interface, close to $y = 1$, i.e. in the region where the displacement thickness is unity. The modes corresponding to the other peaks of response show very similar features.

These observations push for determining the optimal perturbation in a fully elastic framework, that is, take into account the fluid-structure interaction when determining the optimal perturbation. Before moving to this, let us clarify the mechanisms of wave attenuation/amplification.

5.4.3 Mechanism of wave attenuation/amplification

In the expression (5.4.5), the distributed forcing of the fluid momentum equation triggers the amplification of fluid waves, that also excite the viscoelastic coating, and its vibration can in return modify the amplification of the fluid waves because of the off-diagonal coupling terms. To better distinguish between these effects and thus shed light on the physical mechanism by which the viscoelastic coating mitigates the growth of Tollmien-Schlichting waves and amplifies

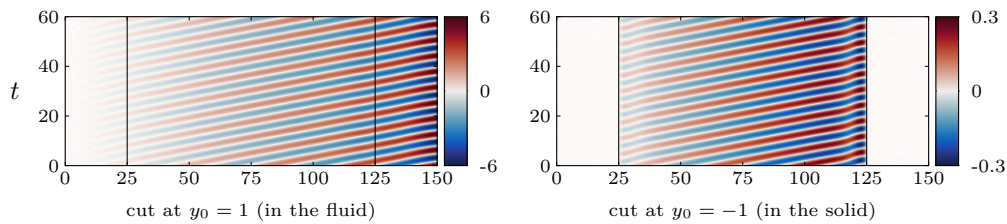


Figure 5.26 – TSW wave propagation. Plot of transverse velocity cuts $\Re\{\mathbf{u}(x, y = y_0) \exp(i\omega t)\}$ in the (x, t) plane, for $y_0 = 1$ (left) and $y_0 = -1$ (right).

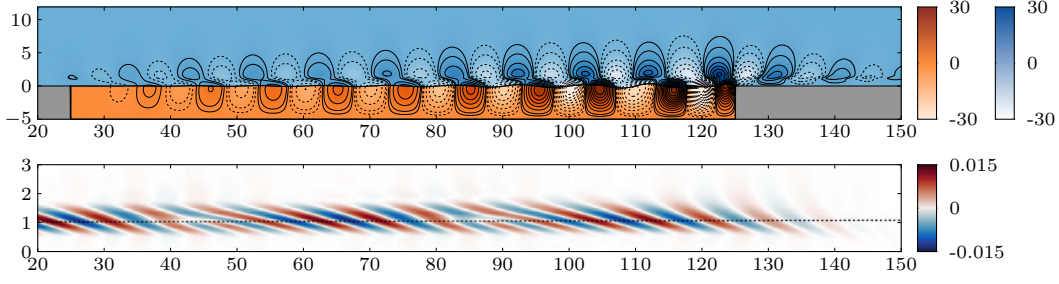


Figure 5.27 – Elastic responses to optimal fluid forcing in the TWF region. At the top, plot of the response corresponding to the point \diamond (2nd sub-optimal) in Fig. 5.23, where contour lines depict the real part of the transverse velocity (dashed negative contours) in the fluid (blue background color) and in the solid (orange background color). At the bottom, plot of the corresponding rigid-wall fluid forcing.

the travelling-flutter waves, we decompose the fluid-solid response as

$$\begin{pmatrix} \mathbf{q}_s \\ \mathbf{q}_f \end{pmatrix} = \begin{pmatrix} \mathbf{0} \\ \mathbf{q}_{f,\text{rgd}} \end{pmatrix} + \begin{pmatrix} \mathbf{q}_{s,\text{rgd}} \\ \mathbf{0} \end{pmatrix} + \begin{pmatrix} \mathbf{r}_s \\ \mathbf{r}_f \end{pmatrix} \quad (5.4.7)$$

where the first term $\mathbf{q}_{f,\text{rgd}}$ is the optimal fluid response in the rigid-wall configuration, computed from (5.4.4). The second term $\mathbf{q}_{s,\text{rgd}}$ is the solid deformation/velocity induced by the optimal fluid response, that we define as the solution of

$$(\mathbf{i}\omega\mathcal{B}_s - \mathcal{A}_s) \mathbf{q}_{s,\text{rgd}} = \mathcal{C}_{sf} \mathbf{q}_{f,\text{rgd}}. \quad (5.4.8)$$

Finally, the third term in the above decomposition is the feedback fluid-solid response, solution of the forced problem

$$\left\{ \mathbf{i}\omega \begin{pmatrix} \mathcal{B}_s & 0 \\ 0 & \mathcal{B}_f \end{pmatrix} - \begin{pmatrix} \mathcal{A}_s & \mathcal{C}_{sf} \\ \mathcal{C}_{fs} & \mathcal{A}_f(\mathbf{Q}) \end{pmatrix} \right\} \begin{pmatrix} \mathbf{r}_s \\ \mathbf{r}_f \end{pmatrix} = \begin{pmatrix} \mathbf{0} \\ \mathcal{C}_{fs} \mathbf{q}_{s,\text{rgd}} \end{pmatrix}. \quad (5.4.9)$$

This system is similar to (5.4.5) but the right-hand side forcing is the solid velocity/deformation induced by the fluid forcing instead of the fluid forcing itself. Finally, the fluid response is composed of two terms: the rigid-wall response $\mathbf{q}_{f,\text{rgd}}$ and the response \mathbf{r}_f induced by the coupling with the coating dynamics. Similarly, the solid dynamics decomposes into the external excitation by the fluid waves on the rigid-wall configuration, $\mathbf{q}_{s,\text{rgd}}$, and the self-excitation response \mathbf{r}_s generated by the coupling with the fluid. The above decomposition allows to clarify the input-output relation between the forcing and the response, that writes as

$$\mathbf{u} = \mathcal{P}_f^T \left\{ \mathcal{C}_{fs} (\mathbf{i}\omega\mathcal{B}_s - \mathcal{A}_s)^{-1} \mathcal{C}_{sf} + \mathbf{i}\omega\mathcal{B}_f - \mathcal{A}_f \right\}^{-1} \mathcal{P}_f \mathbf{f}_{\text{rgd}}.$$

Depending on the forcing frequency, we see here that different resonances (fluid or solid) are likely to be excited, resulting to the different peaks of response.

Wave-cancellation mechanism for the Tollmien-Schlichting instabilities

The attenuation of the Tollmien-Schlichting waves can be seen as a wave-cancellation process. A representation of the different components of the above decomposition is reported in Fig. 5.28. The rigid-wall pressure response (corresponding to the point \square in Fig. 5.21) is displayed in (a). The solid vertical displacement induced by this optimal fluid response is displayed in (b). As can be seen with the help of the dashed vertical lines, this component is out of phase with the fluid pressure. This can be explained as follows: the forcing term $\mathcal{C}_{sf} \mathbf{q}_{f,\text{rgd}}$ in (5.4.8) corresponds to the pressure and viscous stresses applied on the solid interface. The transverse component is dominated by the pressure. Since this pressure excitation has a frequency that is away from the solid resonances

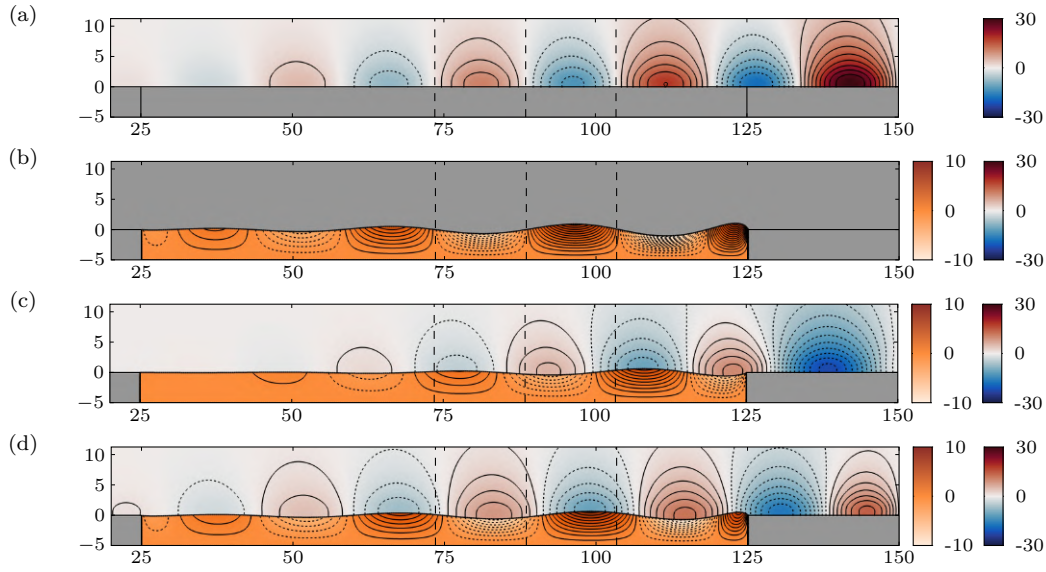


Figure 5.28 – Decomposition of the coupled response in the TSW range. For a forcing frequency $\omega = 0.06$, decomposition of the fluid-elastic response to the rigid-wall fluid forcing — displayed in (d), between (a) the rigid-wall response $\mathbf{q}_{f,rgd}$, (b) the solid excitation by the fluid waves on the rigid configuration $\mathbf{q}_{s,rgd}$ and (c) the coupling components \mathbf{r}_s and \mathbf{r}_f . Plot of the real part of the pressure in the fluid and of the transverse displacement in the solid.

(the considered frequency $\omega = 0.06$ is way below the smallest free vibration frequency in the solid that appears at a frequency of about 0.19 — see in Fig. 5.16), the resulting solid acceleration is in phase and the corresponding displacement, displayed in (b), is out of phase. Looking now at the coupling components displayed in (c), we observe that they are almost out of phase compared to the previous components. This phase delay, driven by the fluid-solid interaction and all the more pronounced as \mathcal{E}_s is small, yields to a wave cancellation effect. The superposition of (a,b) and (c) results indeed in the attenuated response (d).

This attenuation is quantified more clearly by looking at the interface shear stresses reported in Fig. 5.29. The rigid-wall stress is depicted with the solid line, while the coupling component is displayed with the dotted line. The sum of these two waves results in the attenuated fluid-elastic response.

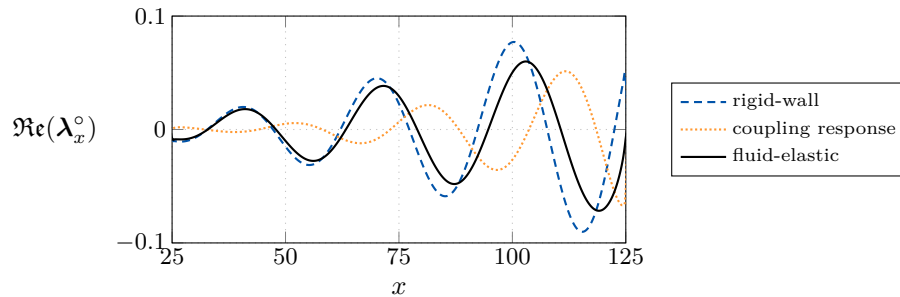


Figure 5.29 – Wave-cancellation for TSW's attenuation. For a forcing frequency $\omega = 0.06$, plot of the fluid-to-solid shear stress perturbation components at the interface (recall that $\boldsymbol{\lambda}^o = (\boldsymbol{\sigma}(\mathbf{u}^o, p^o) + \boldsymbol{\sigma}'(\mathbf{U}, P, \boldsymbol{\xi}_e^o))\mathbf{n}$) decomposed according to (5.4.7): rigid-wall stress (—) obtained from $\mathbf{q}_{f,rgd}$, stress of the coupling response (...) obtained from \mathbf{r}_f , and total stress (—) obtained from \mathbf{q}_f (sum of the two previous ones).

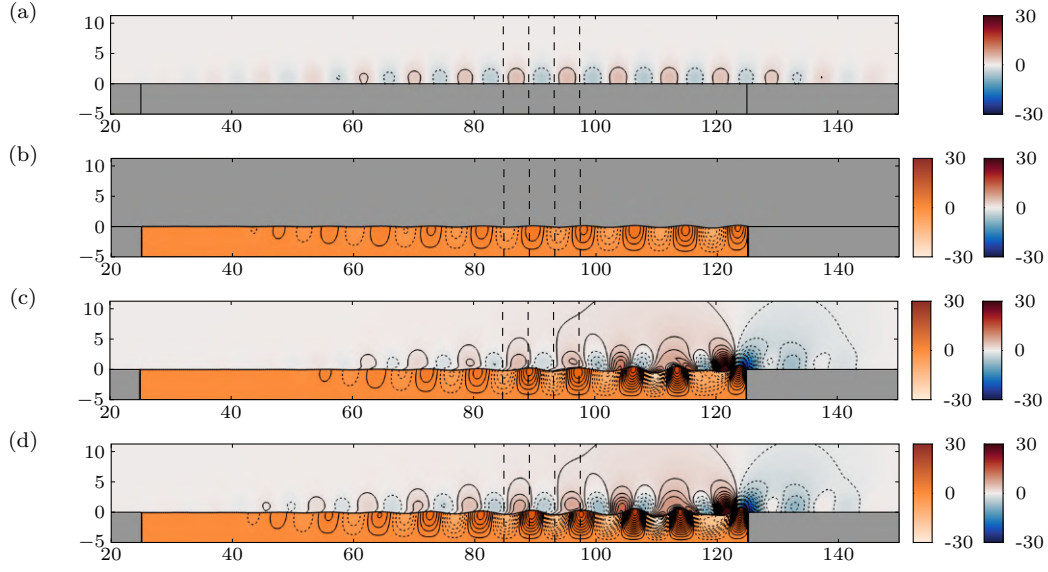


Figure 5.30 – Decomposition of the coupled response in the TWF range. For a forcing frequency $\omega = 0.45$, decomposition of the fluid-elastic response to the fluid-rigid forcing — displayed in (d), between (a) the rigid-wall response $\mathbf{q}_{f,rgd}$, (b) the solid excitation by the fluid waves on the rigid configuration $\mathbf{q}_{s,rgd}$ and (c) the coupling components \mathbf{r}_s and \mathbf{r}_f . Plot of the real part of the pressure in the fluid and of the transverse displacement in the solid.

Amplification mechanism for the Travelling-Wave Flutter instabilities

Let us now do the same analysis in the TWF range, as summarized in Fig. 5.30. At a frequency $\omega = 0.45$, the pressure response in the rigid-wall configuration is displayed in (a). The solid displacement that results from this pressure wave is displayed in (b). We see here that the displacement is no longer out of phase, a phase delay has appeared, driven by resonance effects (at the frequency $\omega = 0.45$ many solid modes might be excited). Furthermore, the coupling components (c) computed as the response to this solid excitation remain almost in phase with it. The coupling term largely dominates over the rigid-wall solid excitation responses and is the main component of the coupled response (d).

The shear stress components are reported in Fig. 5.31. We see here clearly how the coupled fluid-elastic response originates almost exclusively from the coupling term. On the contrary to what was happening in the previous case, here an amplification mechanism provoked by the fluid-solid

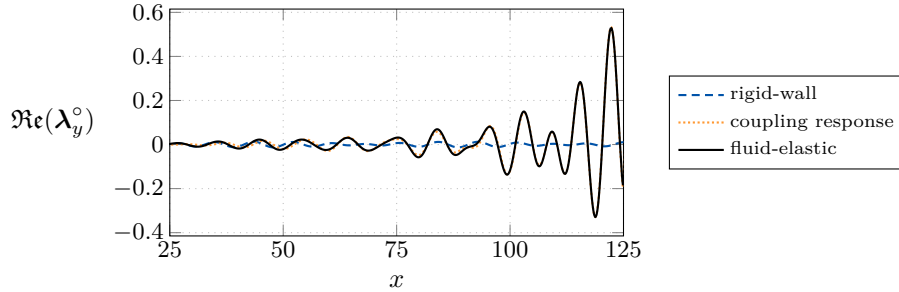


Figure 5.31 – Wave-amplification for TWF. For a forcing frequency $\omega = 0.4$, plot of the normal fluid-to-solid shear stress perturbation components at the interface (recall that $\lambda^o = (\sigma(\mathbf{u}^o, p^o) + \sigma'(U, P, \xi_e^o))\mathbf{n}$) decomposed according to (5.4.7): rigid-wall stress (—) obtained from $\mathbf{q}_{f,rgd}$, stress of the coupling response (···) obtained from \mathbf{r}_f , and total stress (—) obtained from \mathbf{q}_f (sum of the two previous ones).

coupling is at play.

5.5 Fluid-elastic resolvent analysis

5.5.1 Fully coupled resolvent analysis

As seen in §5.4.2, if the dynamics for the Tollmien-Schlichting waves interacting with the flexible coating are rather well described in terms of the response to a forcing determined in the rigid configuration, this is not as much the case for the travelling-flutter waves. We therefore consider here a combined fluid-elastic resolvent analysis. Namely, we seek for the optimal harmonic forcing

$$\mathbf{f}'(\mathbf{x}, t) = \mathbf{f}(\mathbf{x}) e^{i\omega t} + \text{c.c.}$$

of the fluid momentum equations, that produces in return a fluid-elastic response

$$\begin{pmatrix} \mathbf{q}'_s(\mathbf{x}, t) \\ \mathbf{q}'_f(\mathbf{x}, t) \end{pmatrix} = \begin{pmatrix} \mathbf{q}_s(\mathbf{x}) \\ \mathbf{q}_f(\mathbf{x}) \end{pmatrix} \exp(i\omega t) + \text{c.c.}$$

As a measure of the response, we still consider the fluid velocity like previously. This analysis gives the worst-case scenario for the development of instabilities in the fluid, since we allow the forcing to be distributed everywhere in the fluid, and measure the response everywhere in the fluid. We did not include the solid region in the forcing nor in the response, because we are primarily interested in the influence of the coating on the development of the instabilities in the fluid. Note that including a solid forcing could make sense if one aims at determining the effects of external solid vibrations on the development of the instabilities. Introducing this decomposition in the linearised problem (5.2.8), we obtain

$$\left\{ i\omega \begin{pmatrix} \mathcal{B}_s & 0 \\ 0 & \mathcal{B}_f \end{pmatrix} - \begin{pmatrix} \mathcal{A}_s & \mathcal{C}_{sf} \\ \mathcal{C}_{fs} & \mathcal{A}_f(\mathbf{Q}) \end{pmatrix} \right\} \begin{pmatrix} \mathbf{q}_s \\ \mathbf{q}_f \end{pmatrix} = \begin{pmatrix} \mathbf{0} \\ \mathcal{P}_f \mathbf{f} \end{pmatrix} \quad (5.5.1)$$

which is very similar to (5.4.5), except that the forcing is now not known. The amplification gain is now defined as

$$G_f(\omega)^2 = \max_{\|\mathbf{f}\|=1} \|\mathbf{u}\|^2 \quad \text{with} \quad \|\mathbf{q}\|^2 = \int_{\Omega_f} |\mathbf{q}|^2 d\Omega. \quad (5.5.2)$$

where $\mathbf{u} = \mathcal{P}_f^T \mathbf{q}_f$ is the fluid velocity response. Introducing the fluid-solid resolvent operator

$$\mathcal{R}_{fsi}(\omega) = \left\{ i\omega \begin{pmatrix} \mathcal{B}_s & 0 \\ 0 & \mathcal{B}_f \end{pmatrix} - \begin{pmatrix} \mathcal{A}_s & \mathcal{C}_{sf} \\ \mathcal{C}_{fs} & \mathcal{A}_f(\mathbf{Q}) \end{pmatrix} \right\}^{-1} \quad \text{and} \quad \mathcal{P}_{fsi} = \begin{pmatrix} \mathbf{0} \\ \mathcal{P}_f \end{pmatrix}$$

and following the same path as in §5.4.1, the optimal forcing is now solution of the eigenvalue problem

$$(\mathcal{P}_{fsi}^T \mathcal{R}_{fsi}(\omega)^\dagger \mathcal{P}_{fsi} \mathcal{P}_{fsi}^T \mathcal{R}_{fsi}(\omega) \mathcal{P}_{fsi}) \mathbf{f} = \sigma^2 \mathbf{f}. \quad (5.5.3)$$

5.5.2 Results

For the viscoelastic case $\mathcal{E}_s = 1$, $\mathcal{D}_s = 0.2$, the gain curve obtained by solving (5.5.3) is reported in Fig. 5.32, showing two large peaks of amplification (orange solid line), while the sub-harmonic gain reaches only a very much lower amplitude (orange dashed line). In this case, the instabilities in the TWF region are more amplified than the TSW's. In the TSW region, the fully coupled gain is almost superimposed to that of the response to the optimal fluid-rigid forcing (see Fig. 5.23). In the TWF region, the fully coupled gain has its peak centred around the different peaks previously obtained previously as a response to the fluid optimal and sub-optimum forcings.

The mode corresponding to the peak of amplification of the TSW's shows similar features (and in particular comes with the same amplification, and the same forcing/response structures) as what was previously shown, and is thus not presented here. The mode corresponding to the peak of amplification of the TWF instabilities is reported in Fig. 5.33, and shows actually only

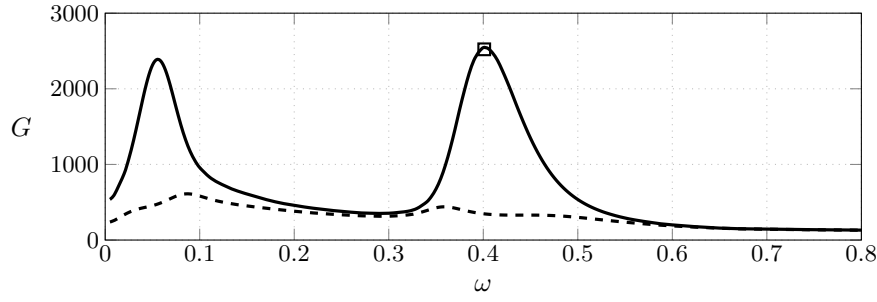


Figure 5.32 – Fully coupled gain curve for the viscoelastic configuration. Plot of the optimal (—) and sub-optimal (---) amplification gains determined in the fully coupled case, for the case with $\mathcal{E}_s = 1$ and $\mathcal{D}_s = 0.2$.

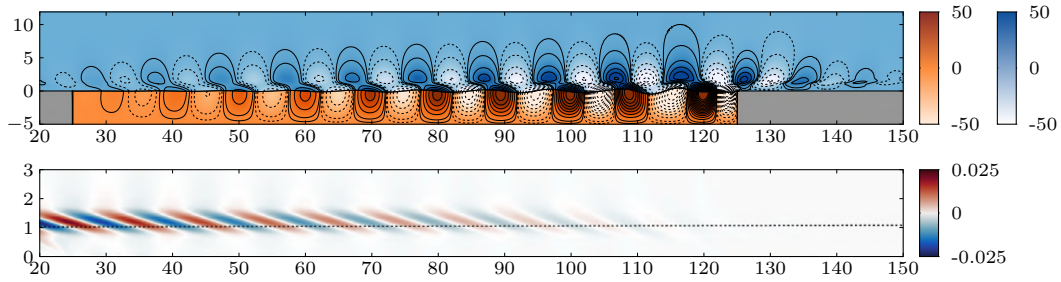


Figure 5.33 – Fully coupled optimal TWF forcing and response. Plot of the optimal forcing (blue-red gradient, bottom) and response (contour lines, dashed negative, top) corresponding to the peak of amplification for the TWF instabilities (point \square in Fig. 5.32).

little differences with the modes displayed in Fig. 5.27. The main discrepancy is a larger space separation between the region having a large forcing (located upstream) and the region having a large response (located more downstream). A comparison of the forcings computed in the fluid-rigid case and the forcing obtained in the fully coupled case is displayed in Fig. 5.34. The fully coupled case is displayed on top, while the forcings corresponding to the peaks of response to the optimal fluid forcing is displayed below.

Finally, the structure of the wave propagation in the solid, for the peak of response in the TWF range, is again visualised by taking snapshots of the solid deformation at different instants regularly spaced in one period of oscillation. This is displayed in Fig. 5.35. In the region away from the edges, we clearly see the downstream wave propagation with a constant phase speed. Edge effects are visible in the vicinity of the right clamped end, on the form of a reflected wave that is quickly damped.

5.6 Conclusion

Using an eigenvalue analysis and a resolvent analysis, the instabilities developing in a boundary-layer flow over a viscoelastic coating have been characterized. The effect of the compliance of the wall to the optimal forcing computed in a rigid-wall configuration was further investigated, showing a different behaviour between the Tollmien-Schlichting waves and travelling-flutter waves. In particular, it has been shown that the resolvent analysis should be performed in a fully coupled way if one wants to characterize properly the latter instabilities.

It remains now to investigate how to effectively attenuate the TSW/TWF instabilities. This is the object of the last chapter.

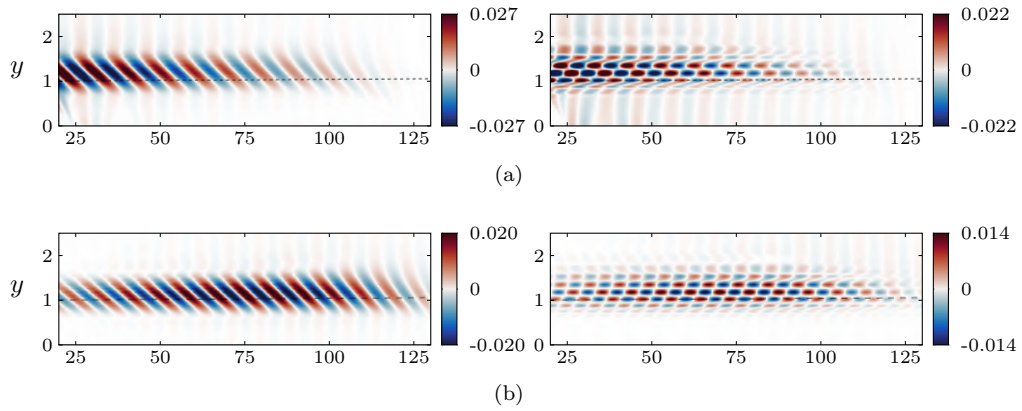


Figure 5.34 – Forcings. Plot of the forcing fields for (a) the fully coupled case, and (b) the case corresponding to the peak of response to the optimal (b) fluid forcings. The streamwise component is displayed in the left side and the transverse component in the right side.

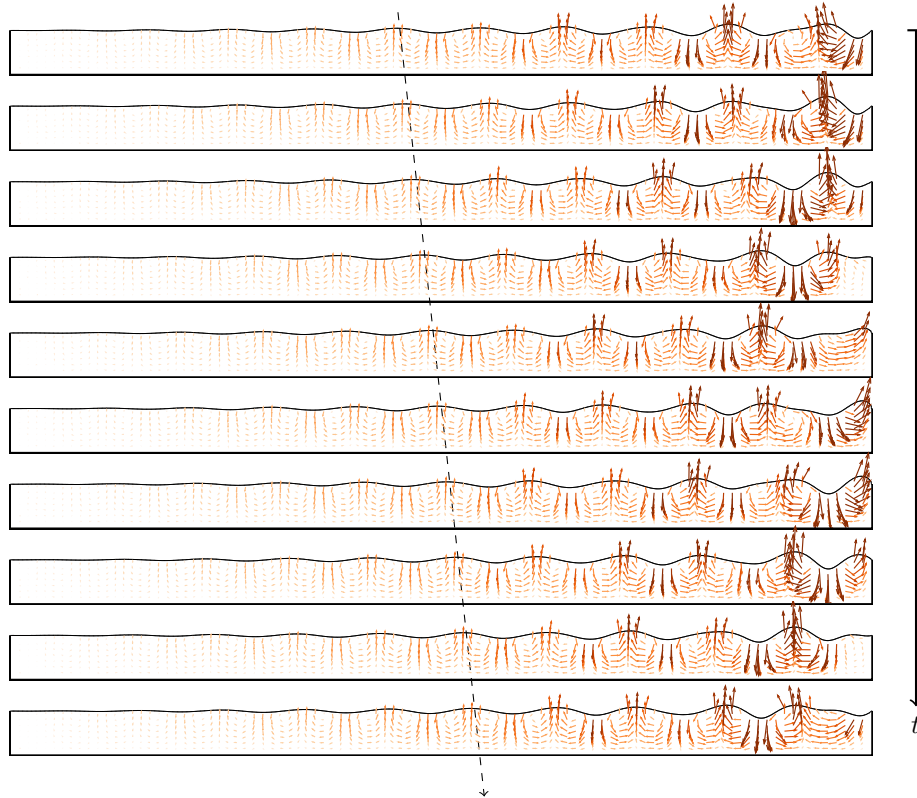


Figure 5.35 – Solid response to fluid-solid optimal forcing. Snapshots of the solid during an oscillation period. The interface deformation is shown, while arrows indicate the displacement field, coloured by the solid perturbation velocity magnitude (darker is higher)

6

COMPLIANT COATING STRUCTURE OPTIMIZATION FOR BOUNDARY-LAYER INSTABILITIES MITIGATION

Instabilities developing in a boundary-layer flow over a viscoelastic compliant coating were described in the previous chapter. We have seen that while decreasing the stiffness has a stabilizing effect on the growth of the Tollmien-Schlichting waves, this also triggers solid-based travelling-flutter instabilities. We use here an adjoint-based approach so as to design a compliant material that damps the Tollmien-Schlichting waves and at the same time mitigates the development of the travelling-flutter waves.

Contents

6.1	Introduction	170
6.2	Fully coupled resolvent analysis for the fluid-structure problem	171
6.3	Gradient of the energy gain with respect to structural parameters	172
6.3.1	Lagrangian formulation	172
6.3.2	Structural gradients	173
6.4	Optimization of the stiffness distribution	175
6.4.1	Optimisation for TWF instabilities attenuation	176
6.4.2	Combined optimization for TSW/TWF attenuation	180
6.5	Conclusion	183

6.1 Introduction

We have seen in the previous chapter that Tollmien-Schlichting waves (TSW) are damped when the stiffness of the coating is decreased. However, a solid-based instability, the travelling-wave flutter (TWF), develops if the coating becomes too soft. This tradeoff calls for an optimization approach.

Following the early attempts by [Kramer \(1960\)](#), many experimental approaches have tried to reduce the drag with compliant surfaces, both in the context of turbulent ([Choi *et al.*, 1997](#); [Bandyopadhyay *et al.*, 2005](#)) and laminar ([Gaster, 1988](#); [Gad-El-Hak *et al.*, 1984](#)) boundary-layer flows. These studies highlighted the need for highly compliant coatings (stiffness on the order of 1000 Pa to 10 MPa), often made practically as a combination of polymeric materials.

As early as in the work by [Benjamin \(1960\)](#), suggestions have been made so as to design appropriate coatings for delaying the boundary-layer transition. Based on theoretical computations relying on a modelling of the flow disturbances with the Orr-Sommerfeld equation, coupled to a one-dimensional spring-backed plate model through normal loads, [Carpenter \(1993\)](#) estimated with the e^N method ([Smith & Gamberoni, 1956](#); [van Ingen, 1956](#)) the potential benefits, in terms of transitional Reynolds number, that could be retrieved from the use of soft walls. Using $N = 7$, his best-performing compliant panel gave an increase of the transitional Reynolds number by a factor 4.6. Considering two panels mounted in series, the gain reached a factor 6. Based on this observation, he suggested that using a multi-panel wall, each tailored for a specific range of Reynolds numbers, would probably produce the largest transition delay. Furthermore, it has been observed by [Lucey & Carpenter \(1993\)](#); [Davies & Carpenter \(1997\)](#) that shorter panels are more resistant to divergence and TWF instabilities. [Carpenter & Morris \(1990\)](#) investigated the effect of material anisotropy, by adding a term that breaks the isotropy of the plate response with respect to a flow reversal. This approach was intended for mimicking a fibre-composite anisotropic compliant wall. They observed an almost ten-fold rise in transitional Reynolds number with the same value of $N = 7$ than that used by [Carpenter \(1993\)](#). Furthermore, it is found that the optimal properties of anisotropic compliant walls appear to be much less sensitive to the Reynolds number (the analysis was local, though) than those corresponding to isotropic walls.

There have also been a few approaches considering a 2d model (but homogeneous in the stream-wise direction) for the coating. Coupling an infinite-length multi-layer coating described by the Navier equations with a pressure wave modelling the action of the fluid, [Duncan \(1988\)](#) showed that a stiff upper layer delays the appearance of class A, B and C instabilities (see Fig. 5.6). Although his framework could have described an arbitrary number of layers, the study focused on the two-layer case. Using the same type of solid model but an Orr-Sommerfeld equation for describing the fluid disturbances about a Blasius profile, [Yeo \(1988\)](#) studied the two-layer case but also a four-layer case akin to the coatings from Kramer (same relative thickness for each layer). He observed that using a thin and stiff top layer tends to stabilize the TWF but to destabilize the solid-based instabilities. Furthermore, he noted that placing the stiff layer at a short distance below the surface of a softer layer helped in obtaining an overall gain in stability. Damping in the internal layer also appeared to be critical for the inhibition of TWF. Also using a 2d Navier model for the coating and applying the e^N method ($N = 7$), [Dixon *et al.* \(1994\)](#) observed an increase of the transition Reynolds number by a factor 2.5 for a single-layer coating and by a factor 5 for a two-layer panel.

The optimization approaches performed in the aforementioned papers all relied on an assumption of homogeneity in at least one direction: homogeneity in the transverse direction for 1d coatings models, or homogeneity in the streamwise direction for models using the Navier equation. For both cases, layering (in streamwise or transverse direction) showed an increase in the transition Reynolds number. From these observations, one can expect that a fully non-homogeneous optimized coating would show even greater transition-delaying properties.

We investigate here the transition-delaying properties of 2d, finite-length compliant walls, de-

signed through an adjoint-based optimization process, in the framework of the resolvent analysis presented in the previous chapter. After having briefly recalled the fully coupled resolvent analysis in section 6.2, in section 6.3 the method for computing the sensitivity of the instabilities amplification gain with respect to the solid properties is presented. This allows to compute and describe the structural gradients that indicate how to modify the solid properties so as to lower the amplification gains. Finally, a gradient-based optimization is carried out.

6.2 Fully coupled resolvent analysis for the fluid-structure problem

As mentioned above, it is reasonable to assume that the stationary flow does not deform the solid. For that reason and like in the previous chapter, it will also be assumed here that a modification of the structural parameters does not influence the stationary boundary-layer flow. This assumption is valid as long as the real material does not undergo a static divergence instability that lead to a strong static reconfiguration. We therefore consider here as a base state the boundary-layer flow over a rigid plate, and study how a modification of the structural coefficients affects the dynamic instabilities that develop in the fluid-elastic configuration over the fluid-rigid base state. More precisely, we seek for *local* variations, i.e. from now on it is assumed that $\mathcal{E}_s = \mathcal{E}_s(\mathbf{x})$, $\mathcal{D}_s = \mathcal{D}_s(\mathbf{x})$, $\mathcal{M}_s = \mathcal{M}_s(\mathbf{x})$. The forced fluid-structure problem is written under the form already described previously,

$$\begin{pmatrix} \mathbf{q}_s^\circ \\ \mathbf{q}_f^\circ \end{pmatrix} = \underbrace{\left\{ \mathbf{i}\omega \begin{pmatrix} \mathcal{B}_s & 0 \\ 0 & \mathcal{B}_f \end{pmatrix} - \begin{pmatrix} \mathcal{A}_s & \mathcal{C}_{sf} \\ \mathcal{C}_{fs} & \mathcal{A}_f(\mathbf{Q}) \end{pmatrix} \right\}^{-1}}_{\mathcal{R}_{fsi}(\omega)} \begin{pmatrix} \mathbf{0} \\ \mathcal{P}_f \mathbf{f}^\circ \end{pmatrix}$$

where $\mathcal{R}_{fsi}(\omega) = (\mathbf{i}\omega \mathcal{B}_{fsi} - \mathcal{A}_{fsi})^{-1}$ is the fluid-structure resolvent operator. In this formulation, $\mathbf{q}^\circ = (\mathbf{q}_s^\circ, \mathbf{q}_f^\circ)$ is the state vector gathering all the unknowns of the problem (fluid velocity \mathbf{u}° , fluid pressure p° , solid displacement $\boldsymbol{\xi}^\circ$ and displacement velocity \mathbf{u}_s° , solid pressure p_s° , plus extra ALE variables). The momentum forcing \mathbf{f}° is taken here as distributed in the whole fluid domain, since we have seen that this provides a worst-case scenario in terms of perturbation amplification. Recall that a prolongation operator \mathcal{P}_f is introduced, that maps the forcing space to the full problem space. By the same way, the response of the system is measured as the energy norm of the fluid velocity perturbations, \mathbf{u}° , which is deduced from the state variables by means of the extraction operator \mathcal{P}_f^T , that is,

$$\mathbf{u}^\circ = \mathcal{P}_f^T \mathbf{q}_f^\circ.$$

The optimal amplification gain G at a forcing frequency ω is defined as the maximal ratio between the norm of the response over the norm of the forcing in the forcing space (which in the present case coincides with the response space), i.e.

$$G(\omega)^2 = \max_{\|\mathbf{f}^\circ\|=1} \|\mathbf{u}^\circ\|^2, \quad \text{with} \quad \|\mathbf{q}\|^2 = \int_{\Omega_f} |\mathbf{q}|^2 d\Omega. \quad (6.2.1)$$

We have seen in §5.5.1 that the solution to (6.2.1) can be obtained by solving the eigenvalue problem

$$\left(\mathcal{P}_{fsi}^T \mathcal{R}_{fsi}^\dagger(\omega) \mathcal{P}_{fsi} \mathcal{P}_{fsi}^T \mathcal{R}_{fsi}(\omega) \mathcal{P}_{fsi} \right) \mathbf{f}_i^\circ = G_i^2 \mathbf{f}_i^\circ \quad (6.2.2)$$

that admits a set of real positive eigenvalues, since the left-hand side operator is hermitian. The eigenvectors \mathbf{f}_i° , normalized by $\|\mathbf{f}_i^\circ\|_f = 1$, form an orthonormal basis of the forcing space. The optimal gain is then the eigenvalue of largest magnitude, i.e. $G = \max G_i$.

In all what follows, we take as a reference case the viscoelastic configuration with $\mathcal{E}_s = 1$ and $\mathcal{D}_s = 0.2$, described into details in the previous chapter. Recall that compared to the case with a rigid wall, the amplification peak for the Tollmien-Schlichting waves (marked with a \square symbol in Fig. 6.1) is reduced by 22.3%. However, very large amplifications have appeared at higher frequencies, as a result of the development of travelling-wave flutter instabilities (the corresponding

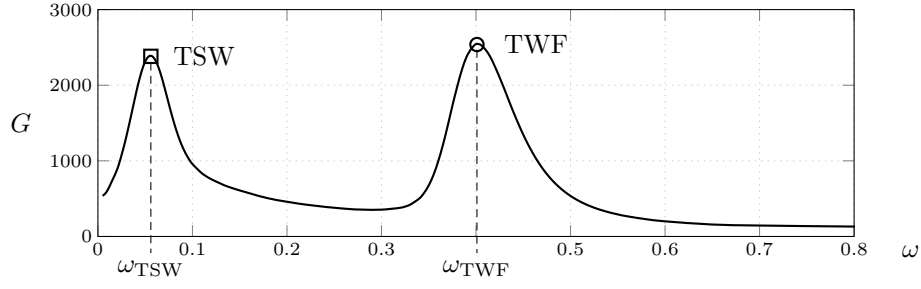


Figure 6.1 – Fully coupled gain curve for the reference viscoelastic configuration. Plot of the amplification gain G for the case with $\mathcal{E}_s = 1$ and $\mathcal{D}_s = 0.2$.

gain peak being marked with a \circ symbol). Because of the very general definition adopted for the forcing (distributed in the whole fluid region), this case is very likely to constitute the worst-case scenario for the amplification of the instabilities through perturbations in the fluid, and sets an upper bound to them.

6.3 Gradient of the energy gain with respect to structural parameters

6.3.1 Lagrangian formulation

The influence of the structural parameters (stiffness, damping,...) on the perturbation amplification gain can be determined by computing the gradient of the gain $G(\omega)$ with respect to these parameters. The optimization problem is build by introducing the cost-function

$$\mathcal{J}(\mathcal{E}_s, \mathcal{D}_s, \dots) = \left(G(\mathcal{E}_s, \mathcal{D}_s, \dots) - G_t \right)^2$$

where G_t is some target value for the gain. We derive in this section analytical expressions for the gradients, by using a Lagrangian technique first presented in the paper by [Brandt et al. \(2011\)](#) in a pure hydrodynamics context. The amplification G is taken as the objective while the constraint is given by the eigenvalue problem (6.2.2). It is then possible to apply the classical optimality results from optimisation theory ([Allaire, 2012](#)). Since no explicit expression for \mathcal{R}_{fsi} is available (the resolvent operator is defined as an *inverse* operator), a direct differentiation of (6.2.2) is not possible, therefore the problem is split between three sub-problems,

$$\begin{cases} \mathcal{R}_{\text{fsi}}(\omega) \mathcal{P}_{\text{fsi}} \mathbf{f}^\circ = \mathbf{q}^\circ \\ \mathcal{R}_{\text{fsi}}^\dagger(\omega) \mathcal{P}_{\text{fsi}} \mathcal{P}_{\text{fsi}}^\top \mathbf{q}^\circ = \mathbf{a}^\circ \\ \mathcal{P}_{\text{fsi}}^\top \mathbf{a}^\circ = G^2 \mathbf{f}^\circ \end{cases} \Rightarrow \begin{cases} \mathcal{P}_{\text{fsi}} \mathbf{f}^\circ - (\mathbf{i}\omega \mathcal{B}_{\text{fsi}} - \mathcal{A}_{\text{fsi}}) \mathbf{q}^\circ = 0 \\ \mathcal{P}_{\text{fsi}} \mathcal{P}_{\text{fsi}}^\top \mathbf{q}^\circ - (-\mathbf{i}\omega \mathcal{B}_{\text{fsi}}^\dagger - \mathcal{A}_{\text{fsi}}^\dagger) \mathbf{a}^\circ = 0 \\ \mathcal{P}_{\text{fsi}}^\top \mathbf{a}^\circ - G^2 \mathbf{f}^\circ = 0 \end{cases} \quad (6.3.1)$$

We have omitted here the subscripts “ i ”, it being understood that we consider only the largest amplification mode. The adjoint variables \mathbf{q}^\dagger , \mathbf{a}^\dagger and \mathbf{f}^\dagger are introduced so as to construct the Lagrangian function

$$\begin{aligned} \mathcal{L}(G, \mathbf{q}^\circ, \mathbf{a}^\circ, \mathbf{f}^\circ, \mathbf{q}^\dagger, \mathbf{a}^\dagger, \mathbf{f}^\dagger, \mathcal{E}_s, \mathcal{M}_s, \mathcal{D}_s) = & (G - G_t)^2 \\ & + \left\langle \mathbf{f}^\dagger, \mathcal{P}_{\text{fsi}}^\top \mathbf{a}^\circ - G^2 \mathbf{f}^\circ \right\rangle \\ & + \left\langle \mathbf{q}^\dagger, \mathcal{P}_{\text{fsi}} \mathbf{f}^\circ - (\mathbf{i}\omega \mathcal{B}_{\text{fsi}} - \mathcal{A}_{\text{fsi}}) \mathbf{q}^\circ \right\rangle \\ & + \left\langle \mathbf{a}^\dagger, \mathcal{P}_{\text{fsi}} \mathcal{P}_{\text{fsi}}^\top \mathbf{q}^\circ - (-\mathbf{i}\omega \mathcal{B}_{\text{fsi}}^\dagger - \mathcal{A}_{\text{fsi}}^\dagger) \mathbf{a}^\circ \right\rangle. \end{aligned} \quad (6.3.2)$$

In this definition, each $\langle \cdot, \cdot \rangle$ is the standard \mathcal{L}^2 scalar product on the space where the arguments are defined. Similarly to what was done in the chapter 4, the optimality conditions are obtained by setting the derivatives of the Lagrangian function \mathcal{L} to zero. Differentiating \mathcal{L} with respect to the adjoint variables \mathbf{q}^\dagger , \mathbf{a}^\dagger and \mathbf{f}^\dagger give the state equations. Differentiating \mathcal{L} with respect to the direct variables \mathbf{q}° , \mathbf{a}° and \mathbf{f}° yields to the adjoint problems

$$\begin{cases} \mathcal{P}_{\text{fsi}} \mathbf{f}^\dagger - (\mathbf{i}\omega \mathcal{B}_{\text{fsi}} - \mathcal{A}_{\text{fsi}}) \mathbf{a}^\dagger = 0 \\ \mathcal{P}_{\text{fsi}} \mathcal{P}_{\text{fsi}}^T \mathbf{a}^\dagger - (-\mathbf{i}\omega \mathcal{B}_{\text{fsi}}^\dagger - \mathcal{A}_{\text{fsi}}^\dagger) \mathbf{q}^\dagger = 0 \\ \mathcal{P}_{\text{fsi}}^T \mathbf{q}^\dagger - G^2 \mathbf{f}^\dagger = 0 \end{cases} \quad ,$$

from which obvious solutions for the adjoint fields are obtained. Provided that $\langle \mathbf{f}^\dagger, \mathbf{f}^\circ \rangle = 1$, the adjoint variables are deduced from the direct variables as follows:

$$\begin{cases} \mathbf{f}^\dagger = \left(1 - \frac{G_t}{G}\right) \mathbf{f}^\circ \\ \mathbf{a}^\dagger = \left(1 - \frac{G_t}{G}\right) \mathbf{q}^\circ \\ \mathbf{q}^\dagger = \left(1 - \frac{G_t}{G}\right) \mathbf{a}^\circ \end{cases} \quad (6.3.3)$$

6.3.2 Structural gradients

The derivatives of the Lagrangian function (6.3.2) give the gradients with respect to the parameters of interest. For this computation, we shall only retain the terms that effectively depend on the solid structural parameters, i.e. we focus on the sub-part of \mathcal{L} that depends on \mathcal{A}_{fsi} and its adjoint. Using (6.3.3) and the properties of the adjoint, we finally arrive to

$$\check{\mathcal{L}} = \langle \mathbf{q}^\dagger, \mathcal{A}_{\text{fsi}} \mathbf{q}^\circ \rangle + \langle \mathbf{q}^\circ, \mathcal{A}_{\text{fsi}}^\dagger \mathbf{q}^\dagger \rangle = 2 \Re \langle \mathbf{q}^\dagger, \mathcal{A}_{\text{fsi}} \mathbf{q}^\circ \rangle.$$

The gradients are given by differentiating $\check{\mathcal{L}}$. The stiffness and damping coefficients only appear in the solid stress tensor whereas the mass ratio is involved in the inertia term. We therefore obtain the simple expressions

$$\nabla_{\mathcal{E}_s} G = 2 \Re \left[\mathbf{D}(\boldsymbol{\xi}^\circ) : \mathbf{D}(\mathbf{u}_s^\dagger) \right], \quad (6.3.4)$$

$$\nabla_{\mathcal{D}_s} G = 2 \Re \left[\mathbf{i}\omega \mathbf{D}(\boldsymbol{\xi}^\circ) : \mathbf{D}(\mathbf{u}_s^\dagger) \right], \quad (6.3.5)$$

$$\nabla_{\mathcal{M}_s} G = 2 \Re \left[(\mathbf{i}\omega)^2 \boldsymbol{\xi}^\circ \cdot \mathbf{u}_s^\dagger \right], \quad (6.3.6)$$

where we recall that $\mathbf{D}(\mathbf{u}) = 1/2 (\nabla \mathbf{u} + \nabla \mathbf{u}^T)$. The expression of the gradients with respect to the stiffness (6.3.4) and damping (6.3.5) is related to the gradients of the displacement response $\boldsymbol{\xi}^\circ$ and adjoint solid velocity response \mathbf{u}_s^\dagger , while the gradient with respect to the density ratio (i.e. the solid density since the fluid density is constant) depends directly on \mathbf{u}_s^\dagger and $\boldsymbol{\xi}^\circ$. The spatial structure of the above gradients depends on the forcing frequency ω , because the fields \mathbf{u}_s^\dagger and $\boldsymbol{\xi}^\circ$ have spatial structures that evolve with the forcing frequency.

Remark. The derivation of the formula for the gradients is considerably simpler here compared to the case of shape optimization considered in the chapter 4. The control parameters (stiffness, mass ratio and damping) appear indeed explicitly as coefficients in the equations and differentiating with respect to them is thus straightforward. In particular, there is no need for having to determine the structure of the adjoint problem. It is therefore computed here at the discrete level, using a matrix hermitian transpose operation.

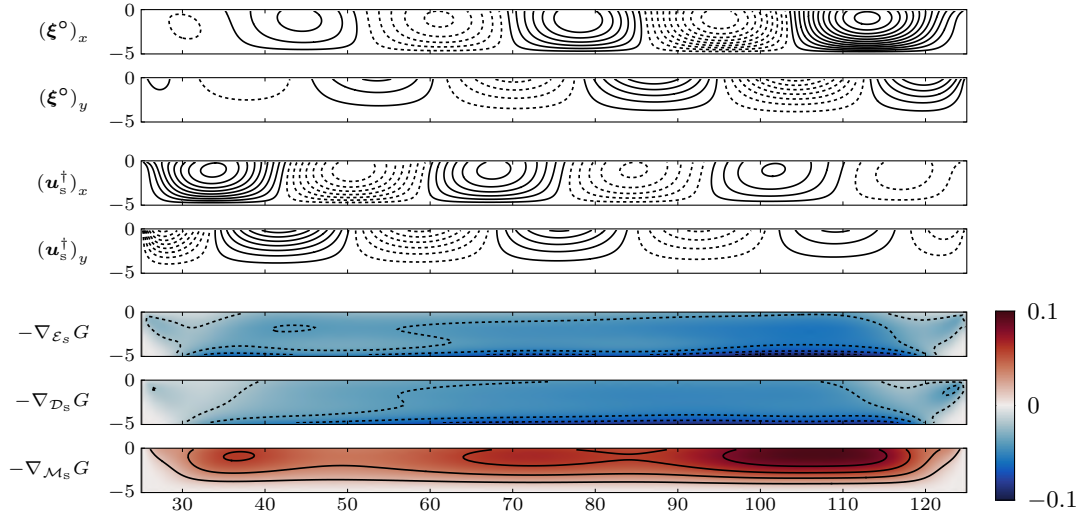


Figure 6.2 – Gradients at the TSW amplification peak ($\omega = 0.055$). The two graphs at the top display the two components of the real parts of the solid displacement response (ξ°), with 30 contours (dashed negative). The two graphs in the middle display the real parts for the adjoint solid velocity response (\mathbf{u}_s^\dagger) with 30 contours (dashed negative). The opposite of the gradients are shown at the bottom, scaled by their spatial 2-norm.

Gradients at the TSW peak

The streamwise and transverse components for the solid displacement response and adjoint solid velocity response are reported in Fig. 6.2. For each of these components, the real part is represented. The imaginary parts look similar, but out of phase. As already mentioned above, the components for the displacement response show an amplification in the downstream direction, unlike the adjoint response mode that displays an upstream amplification.

At the bottom of Fig. 6.2, the gradients with respect to a stiffness, damping and density variations are represented. Each field is normalized by its spatial 2-norm. The visualisation actually displays the opposite of the gradient, that is practically more relevant, since it shows how to modify the solid properties in order to lower the amplification gain. For instance, $-\nabla_{\epsilon_s} G$ is negative almost everywhere, in accordance with the well-known stabilizing effect of a decrease of the stiffness on the Tollmien-Schlichting waves (Carpenter & Garrad, 1985). By the same way, $-\nabla_{D_s} G$ is also negative. This also makes sense, because damping is found to have a slight destabilizing effect on Tollmien-Schlichting waves (Carpenter & Garrad, 1985). On the other hand, it is observed that the density of the solid should be globally increased for stabilizing the Tollmien-Schlichting instabilities, since $-\nabla_{M_s} G$ is positive everywhere in the coating.

Looking at the spatial distribution of the gradients, a highly non-trivial structure is observed, that displays a strong anisotropy both in the streamwise and transverse directions. In particular, no clear evolution in the streamwise direction is observed, probably because the coating extends only over a few wavelengths of the TSW's. The gradients with respect to the stiffness and damping show similar structures. In particular, the largest values are reached at the bottom of the coating, between $x \simeq 90$ and $x \simeq 120$. The structure for the gradient with respect to the density looks quite different. The largest values are reached in regions along a line $y \simeq -0.5$, with a maxima in $x \simeq 107$.

Gradients at the TWF peak

Let us now analyse the gradients obtained at the peak of amplification for the travelling-flutter waves. The streamwise and transverse components for the solid displacement response and adjoint solid velocity response are reported in Fig. 6.3. The antagonism between the direct and adjoint modes appears even more clearly than before, showing the large amplification in the downstream

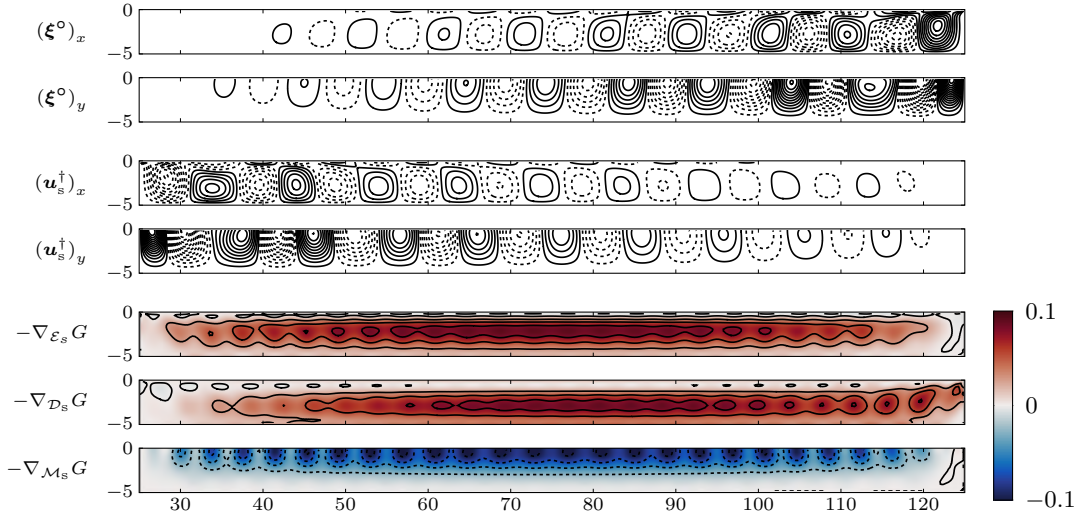


Figure 6.3 – Gradients at the TWF amplification peak ($\omega = 0.4$). The two graphs at the top display the two components of the real parts of the solid displacement response (ξ^o) , with 30 contours (dashed negative). The two graphs in the middle display the real parts for the adjoint solid velocity response (\mathbf{u}_s^\dagger) with 30 contours (dashed negative). The opposite of the gradients are shown at the bottom, scaled by their spatial 2-norm.

direction of the direct mode, and a large amplification of the adjoint mode in the upstream direction.

The opposite of the gradients are displayed at the bottom in Fig. 6.3. In contrast to what was seen before, the situation is reversed: the gradient prescribes an increase of the stiffness/damping in order to achieve a stabilization of the travelling-flutter waves, in accordance to what is reported in the literature (Carpenter & Garrad, 1985). Conversely, the density in the solid should be reduced. Like previously, important edge effects are observed, while a more regular pattern is observed between $x \simeq 60$ and $x \simeq 90$, probably because the characteristic length of the spatial structures of the direct/adjoint response in the streamwise direction is smaller than before. Because of the effect of flow advection, the structures are not exactly symmetric with respect to the mid-plane of the coating at $x = 75$.

Looking at the spatial structure for the gradient with respect to a stiffness variation, in addition to the global trend towards an increase of the stiffness, a structure organized in layers is observed, all the more marked as one is closer to the middle of the coating. The greatest variation of stiffness is prescribed along a line at $y \simeq -2.2$, then decreases above and below. Note also that the gradient changes its sign close to the fluid-solid boundary ($y \simeq -0.3$) but does not reach significantly high values in this thin layer. This is in accordance with the results obtained by Yeo (1988): using a 2d solid model composed of four layers of different stiffnesses (with homogeneity in the streamwise direction) and the Orr-Sommerfeld equation for describing the fluid disturbances about a Blasius profile, he showed that an overall stability gain for TWF instabilities can be achieved by placing a stiff layer below a softer, thinner layer, placed in the direct vicinity of the interface.

6.4 Optimization of the stiffness distribution

We focus in this section on the stiffness distribution $\mathcal{E}_s(\mathbf{x})$, keeping the other parameters \mathcal{D}_s and \mathcal{M}_s constant, with $\mathcal{D}_s = 0.2$ and $\mathcal{M}_s = 1$. In a first part, an optimization that considers only the travelling-wave flutter peak of amplification is performed. Then, a two-points optimization for both the Tollmien-Schlichting and travelling-wave flutter peaks of amplification is considered.

The approach consists in a gradient-based optimization: at each step of the algorithm, the three problems that form the system (6.3.1) are solved sequentially for each considered value of the forcing frequency, allowing to compute the gradients with respect to the stiffness distribution

using (6.3.4). Then, this distribution is updated, using a combination of the gradients computed at the different frequencies.

6.4.1 Optimisation for TWF instabilities attenuation

In this section, we focus on the optimization for damping the TWF instabilities. The maximal gain in the initial (non optimized) case reaches indeed $G_t(\omega = 0.4) = 2540$, which is greater than the maximal amplification for the TSW's, while the gain for the rigid case is only $G_{\text{rigid}}(\omega = 0.4) = 209$.

Numerical settings

The goal of the optimization naturally consists here in reaching amplifications $G(\omega = 0.4)$ that are as close as possible to the amplification in the rigid case. We use the cost-function

$$\mathcal{J}(\mathcal{E}_s) = (G(\mathcal{E}_s, \omega = 0.4) - G_t)^2 \quad (6.4.1)$$

where G_t is the target amplification gain. Note that here we kind of “optimize an optimization”, since the gain G itself is found as being the *optimal* energetic amplification at a given forcing frequency. In the present case, the optimization problem could then also be written as

$$\min_{\mathcal{E}_s(\mathbf{x})} \left\{ \max_{\substack{\|\mathbf{f}^\circ\|=1 \\ \omega=0.4}} \|\mathbf{u}^\circ\| - G_t \right\}^2.$$

The update rule for the stiffness distribution at iteration (k) of the algorithm is then defined as follows:

$$\mathcal{E}_s^{(k+1)}(\mathbf{x}) = \mathcal{E}_s^{(k)}(\mathbf{x}) - \alpha m(\mathbf{x}) \left(1 - \frac{G_t}{G^{(k)}} \right)^\beta \frac{(\nabla_{\mathcal{E}_s} G(\mathbf{x}))^{(k)}}{\|(\nabla_{\mathcal{E}_s} G)^{(k)}\|}. \quad (6.4.2)$$

The parameters α and β set the convergence properties of the optimisation procedure. Considering the curve that expresses the gain as a function of the number of iterations, α basically sets the slope at the origin (the greater α , the largest the decrease at the first iteration), while β sets the asymptotic behaviour when G gets close to the target value G_t . A mask m is applied in such a way that the stiffness remains unchanged in the top right and left corners, namely $m(x) = 1 - \exp(-1.5(x - L_w)^2 - 0.5y^2) - \exp(-1.5(x - L_w - L_c)^2 - 0.5y^2)$. The optimization loop is stopped when the deviation between G and G_t is below 0.1 %.

Remark. An other relevant definition for the optimization problem could have been

$$\min_{\substack{\mathcal{E}_s(\mathbf{x}) \\ \mathcal{E}_s \geq \mathcal{E}_s^{\min}}} \max_{\substack{\|\mathbf{f}^\circ\|=1 \\ \omega=0.4}} \|\mathbf{u}^\circ\|,$$

meaning that we simply want to find the smallest possible energy amplification under the constraint that the stiffness should be greater than some threshold \mathcal{E}_s^{\min} . Since both cases involve in any case a tuning parameter, choosing between one or another formulation is essentially a matter of taste. We have adopted the definition with the target gain because it allows to set targets that can be easily compared to the rigid case (i.e. set G_t to x % of the amplification in the rigid case).

The convergence of the algorithm is presented in Fig. 6.4.1, for $\alpha = 1$, $\beta = 1$, and some values of G_t . The convergence speed is primarily affected by the distance of the target G_t from the amplification $G_{\text{rigid}}(\omega = 0.4) = 209$ in the rigid case. As represented in the plot in Fig. 6.4.1, 9 iterations are required to converge to $G_t = 2000$ at a tolerance of 0.1 %, while it takes 180 iterations to converge to $G_t = 250$ (not represented for readability reasons). For the case $G_t = 220$ (amplification less than 5 % greater than in the rigid case) with same descent direction parameters, it takes more than 6000 iterations.

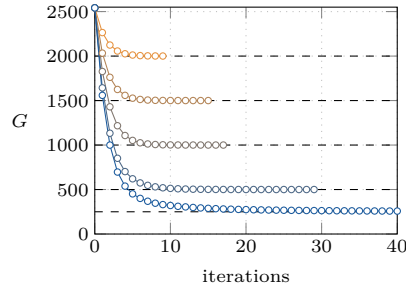


Figure 6.4 – Convergence of the optimization algorithm. Evolution of the amplification G for a forcing frequency $\omega = 0.4$, as a function of the iterations of the optimization algorithm, for different target values G_t represented by the dashed lines.

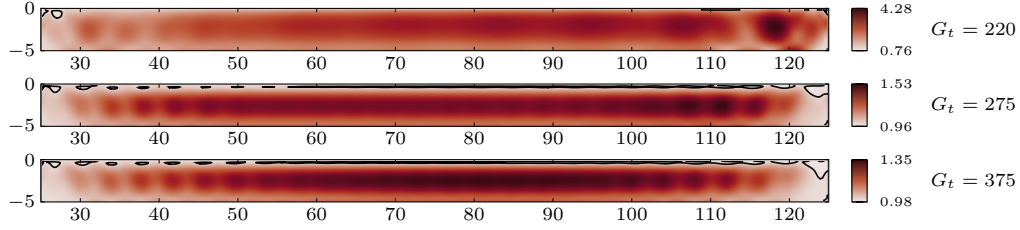


Figure 6.5 – Optimal stiffness distribution for damping the TWF peak. Plot of the stiffness distribution $\mathcal{E}_s(\mathbf{x})$ inside the coating, for optimization target gains $G_t = 220$ (top), $G_t = 275$ (middle) and $G_t = 375$ (bottom). The contour level marks the line $\mathcal{E}_s = 1$.

Optimized coatings for damping the travelling-flutter waves

Maps of the stiffness $\mathcal{E}_s(\mathbf{x})$ are reported in Fig. 6.5 for three values of the target gain G_t . In accordance with what was inferred from the gradients, it is observed that a decrease of the target gain is associated with a global increase of the stiffness in the coating: the variations of the stiffness with respect to the initial case never go below -5% , but reach more than $+400\%$ for the case $G_t = 220$. For cases $G_t = 375$ and $G_t = 275$, the structure of the stiffness actually follows what was already prescribed by the gradient $\nabla_{\mathcal{E}_s} G$. In particular, we still observe the structure in layers (as already mentioned, the favourable effect of a structure in layers was already observed for instance by Duncan (1988) or Yeo (1988) on infinite-length coatings) as well as the more complex edge effects.

We can now evaluate *a posteriori* how the coating optimized for the TWF instabilities at $\omega = 0.4$ behaves for waves at other frequencies, and especially in the frequency range of the TSW's. To that aim, we compute again the energy gain over the whole frequency range. The results are summarized in Fig. 6.6, where the amplification in the range $\omega \in [0, 0.8]$ is represented. The orange dashed line represents the initial (non-optimized) case, while the blue dashed line corresponds to the rigid case. The different circles represent the target optimal gain G_t at frequency $\omega = 0.4$ reached after the optimization loop (five target values are displayed, $G_t = 250, 500, 1000, 1500$ and 2000), while the solid lines of different colors represent the evolution of the gain in the frequency range.

In the TWF frequency region, one observes that the peak of maximum response is shifted at higher frequency. This can be interpreted as a consequence of the increased average stiffness, that also shifts the vibration frequencies to higher values. For instance, in the case $G_t = 500$, the TWF gain peak is shifted from $G(\omega = 0.4) = 2540$ to $G(\omega = 0.445) = 759$, i.e. a frequency shift by 11% . This higher-frequency peak is however in any case all the more damped as the target value G_t is low.

In the frequency range of the TSW instabilities, we observe an *increase* of the gain, as seen in the insert on the left side in Fig. 6.6. The effect is all the more marked than G_t is low. This antagonist behaviour between TSW and TWF makes sense (and is emphasized by the arrows): since the stiffness of the coating globally increases when G_t is reduced, one could have expected an increase of the gain associated to the TSW's. From $G = 2390$ in the initial case, the optimized case for $G_t = 250$ yields to a peak of amplification for the TSW's that is increased to $G_{\text{opt}} = 2518$. However, the gain in the optimized case never reach the higher gain corresponding to the rigid

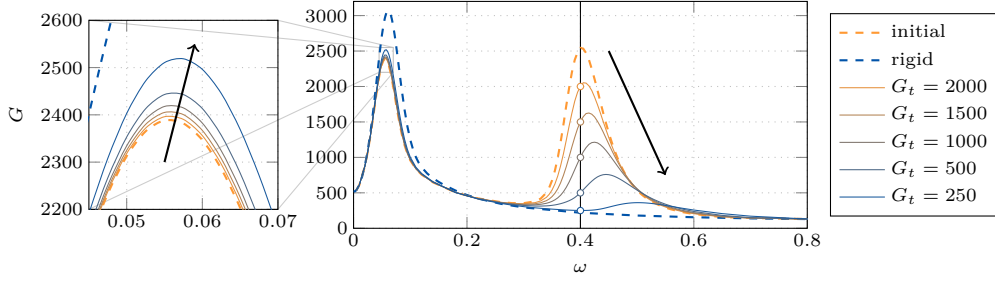


Figure 6.6 – Single-frequency TWF optimization, amplification in the frequency range. Plot of the amplification curve as a function of the forcing frequency ω , for a stiffness distribution $\mathcal{E}_s(\mathbf{x})$ obtained with a single-frequency optimization at $\omega = 0.4$. The thick solid line curve refers to the non-optimized case ($\mathcal{M}_s = 1$, $\mathcal{D}_s = 0.2$, $\mathcal{E}_s = 1$), while the thin lines correspond to different target amplifications at $\omega = 0.4$, varied between 250 and 2000. The left insert is focused on the TSW region.

case. It is thus possible to almost completely kill the travelling-wave flutter instabilities and still reduce the growth of the Tollmien-Schlichting waves compared to the rigid-wall configuration.

Comparison with an homogeneous variation of the stiffness

A natural concern is to know whether the optimized coating offers better performance than those obtained by simply varying the rigidity of a homogeneous one. This is evaluated by looking, for a given value of the peak of amplitude for the travelling-wave flutter instabilities, what is the corresponding value of the peak of amplification for the Tollmien-Schlichting waves, for both (homogeneous/optimized) cases.

We proceed here by computing the optimal forcing/responses in the whole frequency range and reporting the peaks of amplification for both instabilities, first using the optimized coatings described above, and secondly by considering homogeneous coatings having a uniform stiffness varying between $\mathcal{E}_s = 0.8$ and $\mathcal{E}_s = 2$.

These results are reported in Fig. 6.7. For both cases, the trade-off between TWF and TSW's is observed: the lower the peak of amplification for the TSW's, the higher that of the TWF instabilities. These effects are furthermore not acting in a symmetric way, as seen by the decreasing slopes of the curve as $G(\omega_{\text{TWF}})$ is increased. Let us for instance consider the reference case where $\mathcal{E}_s = 1$. A (homogeneous) decrease by 20 % of the stiffness yields to a decrease by 4.7 % of the maximal amplification gain for the TSW's, while in the same time the maximal gain for TWF instabilities undergoes a dramatic increase by more than 1000 %. In that case, we have observed that the configuration becomes actually globally unstable, and the presence of an unstable eigenvalue close to the real axis induces a very strong response peak in the gain curve (Trefethen & Embree, 2005). On the other hand, a decrease by 20 % of the stiffness (still homogeneous) yields to an increase by 3.5 % of the TSW's, while the TWF instabilities are damped by 72 %. This shows how much more stiffness-sensitive are the TWF instabilities compared to the TS instabilities.

Evaluating the gain peaks for the non-homogeneous coatings obtained after optimization result in a curve that is below that corresponding to the homogeneous coatings. This means that for a given damping of the travelling-flutter waves, the non-homogeneous coating offers a slightly smaller amplification of the Tollmien-Schlichting waves. The improvement is however rather small. This quite marginal gain pushes for a more evolved optimization in which both the TWF and TSW peaks are optimized.

Evaluation of the layering effect

Before going further, we evaluate the influence of the “layering effect”, i.e. the tendency for the optimization algorithm to generate, far from the side edges, a structure in layers aligned with the streamwise direction. Namely, we investigate here whether edge effects are relevant or not

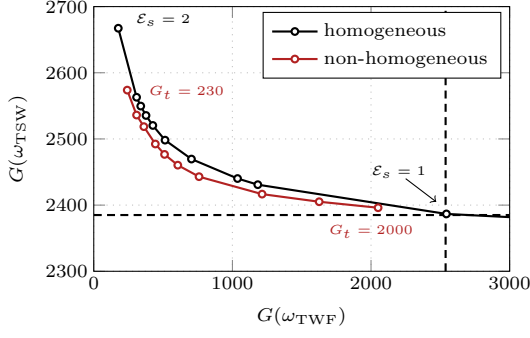


Figure 6.7 – Homogeneous *vs.* anisotropic variation of \mathcal{E}_s . Plot of the maximal amplification for the TSW peak as a function of the maximal amplification for the TWF peak, for uniform coatings with different stiffnesses \mathcal{E}_s (black solid line) and for optimized coatings with a non-uniform stiffness distribution $\mathcal{E}_s(\mathbf{x})$ (red solid line). The values of the gain peaks in the initial case ($\mathcal{E}_s = 1$) are marked with the dashed lines.

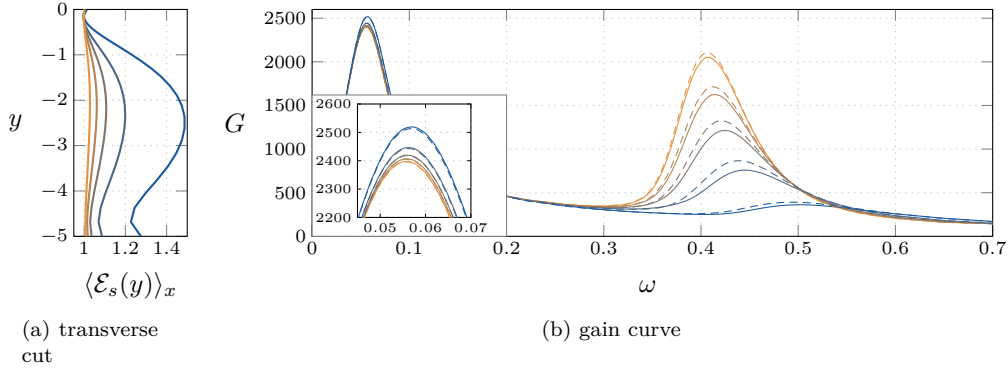


Figure 6.8 – Single-frequency TWF optimization & post-processing streamwise homogenization. For four target gains 250, 500, 1000, 1500 and 2000, (a) transverse cuts across the homogenized coatings and (b) gain curve, where solid lines indicate the results obtained with a fully non-homogeneous coating while dashed lines indicate the results for the homogenized coatings in the streamwise direction.

in the process of wave attenuation. Considering the optimized stiffness $\mathcal{E}_s(\mathbf{x})$ with respect to a given target gain, an homogenized (in the streamwise direction) repartition $\mathcal{E}_s(y) = \langle \mathcal{E}_s(\mathbf{x}) \rangle_x$ is computed, as a solution of the diffusion equation

$$\begin{aligned} \gamma \frac{d^2 \langle \mathcal{E}_s(\mathbf{x}) \rangle_x}{dx^2} &= \mathcal{E}_s(\mathbf{x}) - \langle \mathcal{E}_s(\mathbf{x}) \rangle_x & \text{in } \Omega_s \\ \frac{d \langle \mathcal{E}_s(\mathbf{x}) \rangle_x}{dx} &= 0 & \text{on } \partial\Omega_s \end{aligned}$$

where $\gamma \gg 1$ is a large diffusion parameter. The average value of the homogenized stiffness matches the average value of the initial stiffness distribution, but the minimum and maximal values are not necessarily the same.

Cuts along the y directions for homogenized materials are displayed in Fig. 6.8a. This one-dimensional view of the stiffness allows to see more clearly the evolution of the stiffness when the target amplification is decreased. Directly below the surface at $y \simeq -0.2$ the minimal stiffness is reached. It then increases monotonically until about half of the coating thickness, then globally decreases, but not as low as the minimal value at the top layer (rather at about half of the maximal stiffness). For cases with a low target gain, a slight increase of the stiffness is again found close to the bottom edge of the coating.

The effect of the streamwise homogenization on the gain curve is represented in Fig. 6.8b. While the fully anisotropic cases are displayed with solid lines, homogenized cases are displayed with dashed lines. In this latter case, the main features observed in the fully anisotropic stiffness distribution are still present. The homogenized materials perform less good than the fully anisotropic ones for the mitigation of TWF instabilities. In the insert that focuses on the TSW region, one sees that the homogenized materials performs however surprisingly slightly better. The

overall differences remain however small, and we can conclude that the damping of the travelling-flutter waves is mainly achieved by modifying the stiffness in the transverse direction. In any case, stronger streamwise effects would certainly be observed for longer coatings.

As a conclusion for this part, it is observed that an optimization run for damping the TWF amplification peak is able to eliminate completely this peak, at the price of a slight increase of the amplification of the TSW's — that remains however still below that of the rigid-wall case. The stiffness distribution that kills the travelling-wave flutter instability has essentially a structure organized in longitudinal layers. The optimized coatings are all the more stiff than the peak should be damped. The overall gain obtained with the non-homogeneous coatings is however rather small. In the next section, we will therefore go a step further and perform a two-point optimization, so as to try to damp the TWF instabilities without increasing the TSW amplification compared to the initial case.

6.4.2 Combined optimization for TSW/TWF attenuation

We now consider the case where the coating is optimized for both TSW and TWF gain peaks (recall that the maxima are found on the initial configuration with homogeneous $\mathcal{E}_s = 1$ at frequencies $\omega = 0.055$ and $\omega = 0.4$ respectively). The cost-function is then defined as

$$\mathcal{J}(\mathcal{E}_s) = \left(G(\mathcal{E}_s, \omega = 0.4) - G_t^{\text{TWF}} \right)^2 + \left(G(\mathcal{E}_s, \omega = 0.055) - G_t^{\text{TSW}} \right)^2 \quad (6.4.3)$$

where the G_t 's are target amplification gains for the peaks of response in TSW and TWF regions. The update rule for the stiffness distribution at iteration (k) of the algorithm is defined here as a weighted sum of the two individual gradients:

$$\mathcal{E}_s^{(k+1)}(\mathbf{x}) = \mathcal{E}_s^{(k)}(\mathbf{x}) - m(\mathbf{x}) \left(1 - \frac{G_t}{G^{(k)}} \right)^\beta \left\{ \alpha_1 \frac{(\nabla_{\mathcal{E}_s} G^{\text{TWF}})^{(k)}}{\|(\nabla_{\mathcal{E}_s} G^{\text{TWF}})^{(k)}\|} + \alpha_2 \frac{(\nabla_{\mathcal{E}_s} G^{\text{TSW}})^{(k)}}{\|(\nabla_{\mathcal{E}_s} G^{\text{TSW}})^{(k)}\|} \right\},$$

where the ratio between α_1 and α_2 allows to favour one or the other component. We took $\alpha_1 = 1$ and $\alpha_2 = 50$. A limiter is set on the values of the stiffness so as to prevent from reaching too low values of the rigidity: the threshold is set to $\min \mathcal{E}_s = 0.1$. During the update step in the optimization loop, the updated stiffness distribution is rescaled in such a way that the values below 0.1 lie between 0.09 and 0.1, where the actual value is determined by the departure from the threshold $\mathcal{E}_s = 0.1$.

Optimization with $G_t^{\text{TWF}} = 250$

In a first time, we set $G_t^{\text{TWF}} = 250$, i.e. at an amplification 13 % higher than the rigid case at the forcing frequency $\omega = 0.4$, or equivalently, 90 % lower than the amplification reached with the initial configuration. Then, the target G_t^{TSW} at the forcing frequency peak for the Tollmien-Schlichting waves is decreased from 2500 (approximately the best-case scenario obtained with the one-point optimization) down to 2390 (approximately the maximal gain of amplification for the Tollmien-Schlichting waves in the initial case with an homogeneous stiffness distribution with $\mathcal{E}_s = 1$).

The gain curves obtained after optimization are presented in Fig. 6.9 for (a) $G_t^{\text{TSW}} = 2450$, (b) $G_t^{\text{TSW}} = 2410$ and (c) $G_t^{\text{TSW}} = 2390$. Like previously, for comparison the initial and rigid cases are drawn with the dashed lines, while the insert in the left focuses on the TSW's region. It is observed there that it is possible to decrease the Tollmien-Schlichting amplification curve down to its initial position when G_t^{TSW} is set to 2390. The higher-frequency region however displays a less regular behaviour. As G_t^{TSW} is decreased, secondary peaks appear in the gain curve at frequencies between 0.1 and 0.3. In addition to the very damped TWF peak that is still observed at higher frequencies like in §6.4.1 (see in Fig. 6.6), three secondary amplification peaks emerge from the curve, particularly in (c). For values of G_t^{TWF} greater than about 2420, these secondary peaks are almost not visible in the gain curve. Interestingly, the shifted TWF peak at higher frequency is

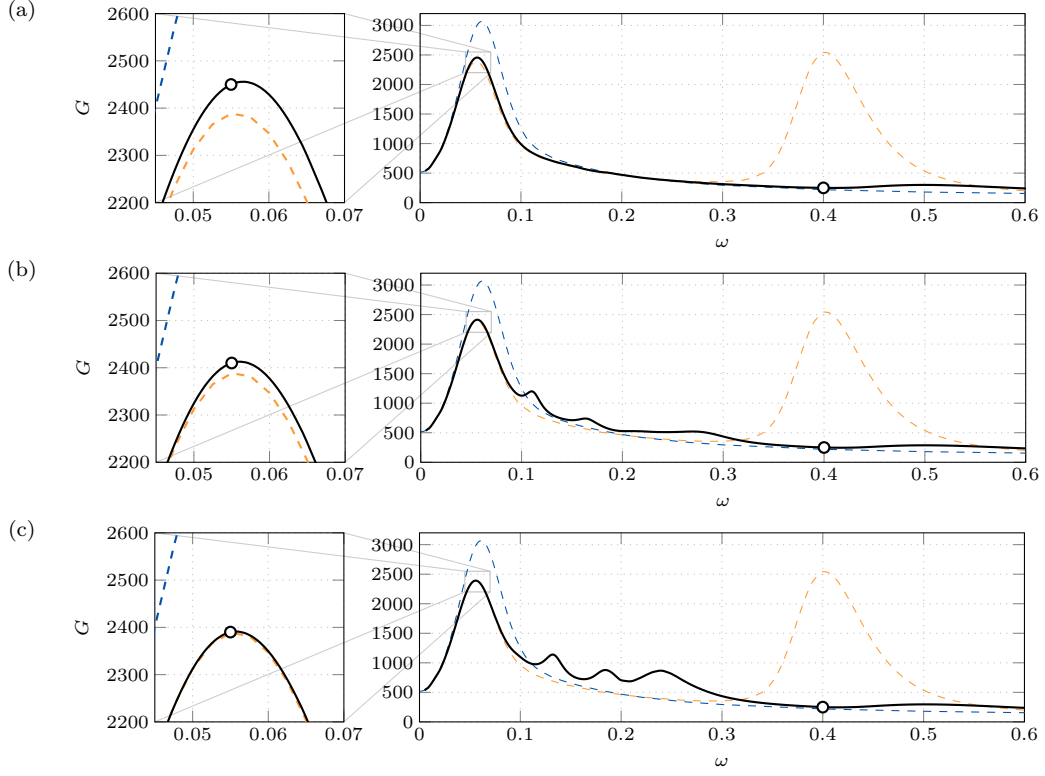


Figure 6.9 – Two-points optimization with $G_t^{\text{TWF}} = 250$, gain curves. Plot of the amplification curves as a function of the forcing frequency ω , for a stiffness distribution $\mathcal{E}_s(\mathbf{x})$ obtained with a two-frequency optimization with $G_t^{\text{TWF}} = 250$ and (a) $G_t^{\text{TSW}} = 2450$, (b) $G_t^{\text{TSW}} = 2410$ and $G_t^{\text{TSW}} = 2390$. The thick dashed orange line curve refers to the non-optimized case ($\mathcal{M}_s = 1$, $\mathcal{D}_s = 0.2$, $\mathcal{E}_s = 1$) and the thick blue line corresponds to the rigid case, while circles indicate the target gains.

even more damped than in the one-point optimization. For instance, let us consider the case (a) with $G_t^{\text{TWF}} = 2450$. The one-point optimization yields to a shifted peak for the TWF instabilities with $G(\omega \simeq 0.5) = 361$, while the two-point optimization yields to $G(\omega \simeq 0.5) = 300$.

The stiffness distribution associated to the cases (a,b,c) is reported in Fig. 6.10. In addition to the layering effect already observed previously, we also observe reminiscences from the gradient computed at the peak of amplification for the TSW's (see in Fig. 6.2), namely, zones of very low stiffness in the lower left side of the coating, especially for the cases $G_t^{\text{TSW}} = 2410$ and $G_t^{\text{TSW}} = 2390$. For each case, we also notice the softer region in the direct vicinity of the fluid/solid interface. When the value for the gain target is decreased, while the highest stiffness in the optimized coating remains approximately constant, larger low-stiffness regions are found, which are “thresholded” at $\mathcal{E}_s = 0.1$ — otherwise the algorithm eventually generates negative stiffness areas. Note that for these cases the convergence of the algorithm is altered, since we no longer follow a true gradient descent.

Optimization with $G_t^{\text{TWF}} = 400$

It turns out that allowing a slightly larger growth in the TWF region also allows a further decrease in the TSW's region. Namely, we consider here the case with $G_t^{\text{TWF}} = 400$. The corresponding results are displayed in Fig. 6.11, for (a) $G_t^{\text{TSW}} = 2390$, (b) $G_t^{\text{TSW}} = 2350$, and $G_t^{\text{TSW}} = 2310$. In the present case, decreasing the target gain is followed by the emergence of one single secondary peak located at frequencies between 0.2 and 0.3. If the target gain were to be further decreased, this peak would dramatically grow. For instance with $G_t^{\text{TSW}} = 2260$ the peak reaches an amplification

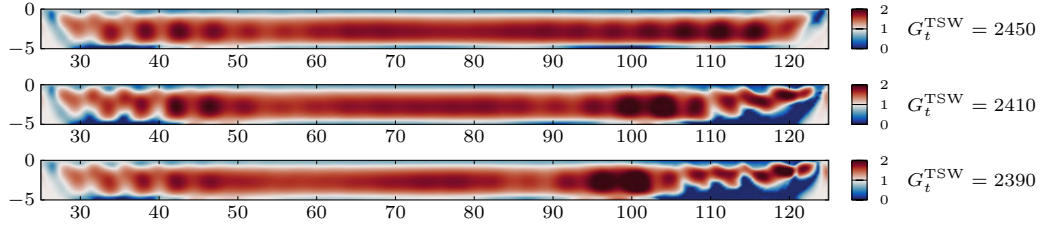


Figure 6.10 – Two-points optimization with $G_t^{\text{TWF}} = 250$, stiffness distribution. Plot of the stiffness distribution $\mathcal{E}_s(\mathbf{x})$ obtained with a two-frequency optimization with $G_t^{\text{TWF}} = 250$.

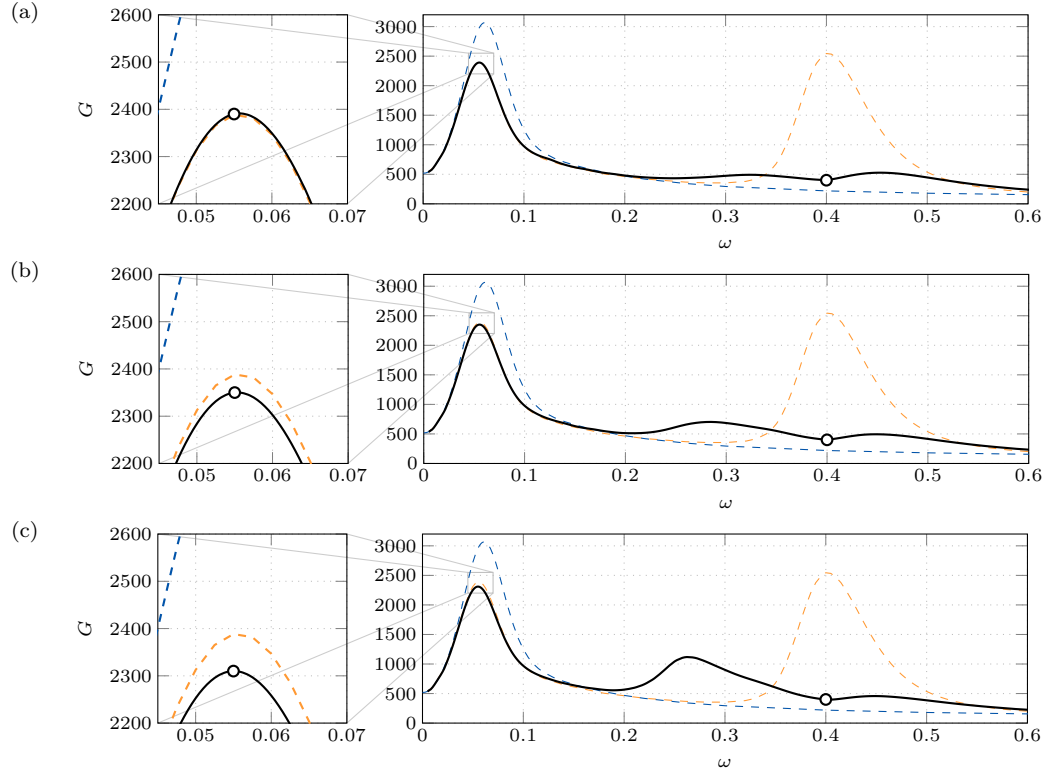


Figure 6.11 – Two-points optimization with $G_t^{\text{TWF}} = 250$, gain curves. Plot of the amplification curve as a function of the forcing frequency ω , for a stiffness distribution $\mathcal{E}_s(\mathbf{x})$ obtained with a two-frequency optimization with $G_t^{\text{TWF}} = 400$ and (a) $G_t^{\text{TSW}} = 2390$, (b) $G_t^{\text{TSW}} = 2350$. and $G_t^{\text{TSW}} = 2310$. The thick dashed orange line curve refers to the non-optimized case ($\mathcal{M}_s = 1$, $\mathcal{D}_s = 0.2$, $\mathcal{E}_s = 1$) and the thick blue line corresponds to the rigid case, while circles indicate the target gains.

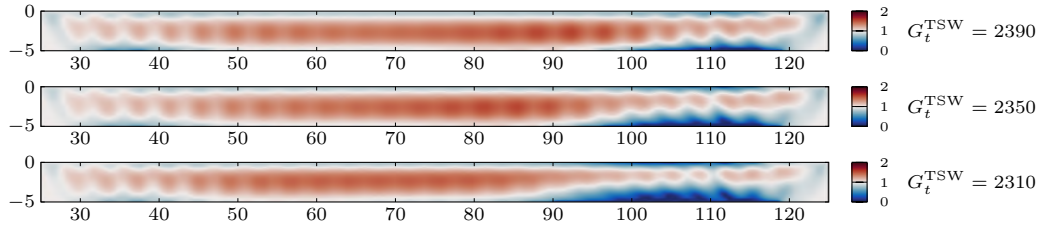


Figure 6.12 – Two-points optimization with $G_t^{\text{TWF}} = 400$, stiffness distribution. Plot of the stiffness distribution $\mathcal{E}_s(\mathbf{x})$ obtained with a two-frequency optimization with $G_t^{\text{TWF}} = 400$.

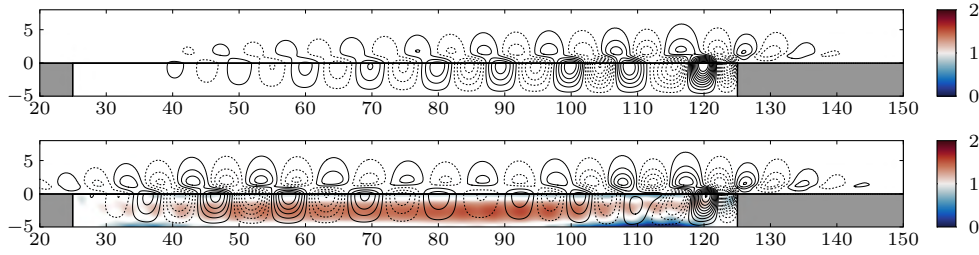


Figure 6.13 – Response field after optimization. Plot of the real part of the transverse velocity response field (lines) and of the stiffness distribution in the coating in the initial (top) and optimized case (bottom) with $G_t^{\text{TSW}} = 2390$ and $G_t^{\text{TWF}} = 400$. The same contour levels are used in both cases.

by more than 2500.

The overall aspect of the stiffness distribution still looks similar as before, as reported in Fig. 6.12. The maximal stiffness is however reduced and does not exceed 1.5. This makes sense, since we have seen before that the TWF instabilities are all the more damped that the layering effect is stronger. As the target is decreased, the low-stiffness area is found to extend more and more upstream, like what could already be observed from the gradient with respect to the stiffness in the TSW's region.

Let us finally focus more specifically on the case (a) that offers the most interesting overall performances : the amplification of the TSW's does not exceed that of the initial case, while no significant amplifications are found in the TWF region. After optimization, the structure of the Tollmien-Schlichting waves are similar to those observed in the initial case, except that the spatial growth in the streamwise direction is reduced. Let us focus on the travelling-flutter waves at the forcing frequency $\omega = 0.4$. The real part of the transverse velocity response field in this case is displayed in Fig. 6.13. The initial (non-optimized) case is shown at the top, while the optimized case is represented at the bottom. Note that a direct comparison for the two response fields is not possible, since the corresponding forcing fields are not the same. Compared to the initial case where the forcing is located upstream, in the optimized case it reaches high amplitudes over the whole length of the coating. As already evoked before, the non-optimized case displays a monotonic amplification in the streamwise direction. On the other hand, the optimized case comes with unstable waves having a noticeable amplitude as soon as the beginning of the coating is reached, but these waves are not amplified monotonically. A decrease of the amplitude is observed between $x \simeq 50$ and $x \simeq 90$, then again an increase until the end of the coating is reached, where the waves again fade out. There is actually a local growth in regions where the stiffness is reduced, and conversely a local decrease of the waves amplitude in regions where the stiffness is increased.

6.5 Conclusion

In this shorter, last chapter, we have performed an optimization of the structural parameters of the coating. In a first step we have presented the gradients of the energy gain for the Tollmien-Schlichting and travelling-flutter waves, with respect to the stiffness, damping and density. Then an optimization has been performed, focused on the distribution of stiffness in the coating.

The results obtained in the optimization part are summarized in Tab. 6.1. In every case, a balance has to be found between the damping of the TSW and the amplification of the TWF. In all cases presented in the table, the TWF peak could be damped by at least 80 % compared to the initial case. Equivalently, this corresponds to a TWF peak gain that is never increased more than a factor two compared to the rigid case at the same frequency, where there is no TWF instability at all. Focusing on the TSW maximal amplification, an homogeneous coating with $\mathcal{E}_s = 1.42$ allows for a reduction by 17.1 %. A small improvement is obtained by considering a non-homogeneous coating optimized for the TWF peak only. Finally, the best compromise between a damping of the TSW gain peak and a TWF “not-too-large” amplification results in a reduction by 22 % of the

<i>Stiffness</i>	<i>TSW max. gain</i>	<i>TWF max. gain(s)</i>
$\mathcal{E}_s \rightarrow +\infty$ (rigid)	3066	no peak
$\mathcal{E}_s = 1$ (homogeneous, reference)	2386 (−22.2 %)	2543
$\mathcal{E}_s = 1.42$ (homogeneous)	2541 (−17.1 %)	361 (−85.8 %)
$G_t^{\text{TWF}} = 250$	2518 (−17.8 %)	361 (−85.8 %)
$G_t^{\text{TWF}} = 400, G_t^{\text{TSW}} = 2390$	2401 (−22.0 %)	526 (−79.3 %)

Table 6.1 – Summary of the optimization processes. For the Tollmien-Schlichting waves, the maximal gain reduction is compared to the rigid case. For the travelling-wave flutter waves, the maximal gain reduction is compared with the initial case $\mathcal{E}_s = 1$. The best-case scenario allows to obtain the same damping of the TSW's as that provided by the homogeneous material, without increasing too much the TWF instabilities.

TSW peak, i.e. almost as good as in the initial, non optimized case that performed well for the TSW damping but went with a dramatic amplification of the TWF instabilities.

7

CONCLUSION & PERSPECTIVES

7.1 Summary and main results

This thesis represents a step towards a very high fidelity modelling and control of the linear dynamics of fluid-structure instabilities developing over stationary non-linear states.

Depending on the instability mechanisms involved, different methodologies are appropriate to characterize this fluid-solid linear dynamics. Two numerical methods have thus been developed, making it possible to investigate the long-term development of linear disturbances of a stationary state (eigenvalue analysis) as well as the frequency response to external forcings (resolvent analysis). Eigenvalue analyses are suitable for systems with an oscillator behaviour (typically, vortex-induced vibrations). On the other hand, the stability of some other systems is rather driven by the way they amplify external noise, in which case the resolvent analysis is adapted (typically, boundary layers on flexible walls). These two approaches, commonly used for the study of hydrodynamic instabilities, have been extended here to the fluid-structure case in order to be able to deal with fluid-elastic instabilities.

After the presentation and validation of the numerical methods (chapters 1 and 2), two configurations representative of the mechanisms evoked above were studied more specifically: the vortex-induced vibrations of an elastic splitter plate clamped behind a cylinder (chapter 3), and the boundary-layer instabilities developing on a finite-length compliant coating (chapter 5). For both cases, adjoint-based optimization strategies were proposed so as to control the instabilities (chapters 4 and 6).

Numerical methods

A first part of the thesis is dedicated to the development of a general approach for determining non-linear stationary equilibrium states (chapter 1) and then investigating the linear dynamics of fluid-solid perturbations developing around these steady states (chapter 2). The chosen modelling consists in the monolithic coupling between the Navier-Stokes equations and hyperelastic solid models. This approach, made without *a priori* approximations, makes it possible to determine steady fluid-solid configurations where the flow is highly heterogeneous (separation and recirculation zones, boundary layers) and the solid is possibly very deformed. The integration of all couplings in the formulation then make it possible to accurately determine the linear stability of these equilibriums, even in cases involving large added mass and strong viscous effects.

Both for eigenvalue and resolvent analyses, the key point is the derivation of an exact linearisation of the fluid-structure operator. The method used (section 2.1) consisted in rewriting the equations in a fixed reference domain, then linearising there, following a so-called “Lagrangian-based approach”. The linearised problem then includes an arbitrary extension operator whose role is to propagate the deformation of the interface into the fluid domain (non-local couplings). This approach has already been used in the past in implicit fluid-structure time solvers, where it is necessary to determine the Jacobian of the non-linear system to be solved. In these cases, however, an approximate linearisation is often sufficient, since the prevailing criterion is above all the decrease

in the non-linear residue. In the present case, a truly exact linearisation is necessary for the results of the eigenvalue or resolvent analysis to be representative.

The eigenvalue analysis derived from this formulation was tested on three test cases representative of various fluid-solid interaction phenomena: the vortex-induced vibrations of an elastic plate attached to the rear of a cylinder, the flag flutter instability, and finally the impact of the static reconfiguration of a plate on the downstream vortex shedding (section 2.3). First, it was shown that the eigenvalue analysis can robustly characterize instabilities: it reproduces the instability thresholds observed in non-linear simulations, gives the correct linear growth rate of instabilities, and makes it possible to estimate the frequency of vibration in the vicinity of the instability onset. The practical interest of the approach is that instead of having to use time-marching simulations, stability can be characterized by one single calculation of the eigenvalues of the linearised operator. Based on the data in the literature, it has been estimated that a time saving of about a factor of 10 can be achieved.

In a second step, the Lagrangian-based approach mentioned above was compared to another approach initially proposed by Fernández & Le Tallec (2003a), referred to as an “Eulerian-based approach” (section 2.4). This second approach is based on another way of linearising the fluid-structure problem, which leads to an equivalent perturbation problem — at the continuous level — to that obtained using the Lagrangian-based approach. This second formulation couples the linearised Navier-Stokes equations to the elasticity equations *via* interface terms such as a velocity transpiration and added stiffness terms: local couplings, but involving higher-order derivatives of the stationary field. The equivalence between the two formulations was tested at the discrete level in the simplified case of a Poiseuille flow between two flexible walls, for which the stationary solution can be determined analytically. On the more complex case of the flag flutter instability, it has been shown that the Eulerian-based approach poses numerical problems when a standard discretisation using Lagrange finite elements is used. More precisely, we have shown the extreme sensitivity of the results to the spatial discretization of the interface. These observations lead us to express scepticism about the practical use of the Eulerian approach in its current state: although being an *a priori* simpler formulation (that in particular does not rely on the non-local couplings via the extension operator), for some cases it gives unreliable results. On the other hand, the Lagrangian-based approach proved to be reliable in all cases considered.

Physical analysis and shape optimization of a cylinder-splitter plate configuration

A second part of the thesis deals with the physical analysis and control of a model problem consisting of a flexible splitter plate attached downstream of a cylinder. It has been shown that this configuration involves vortex-induced vibrations but also divergence instabilities, that interact non-linearly to give rise to limit cycles of different natures depending on the rigidity of the plate. The study of this problem is of interest for the understanding of some locomotion mechanisms found in nature (Lacis *et al.*, 2014), and is also a prototype for the passive control of wake instabilities (Kwon & Choi, 1996) or, conversely, of energy-harvesting devices trying to exploit the energy carried by these instabilities (Abdelkefi, 2016).

The chapter 3 focuses on the physical analysis of the system. First (section 3.3), non-linear simulations are performed. At high rigidity, the system is stable and a stationary equilibrium is observed. When the rigidity is reduced, a first unsteady regime is observed: the plate vibrates at one single characteristic frequency around an average position aligned with the incident flow, while an unsteady vortex wake develops downstream. For lower stiffness values within a certain range, much lower amplitude vibrations are observed, around a deviated mean position that comes with a non-zero mean lift. This regime ceases to exist at lower rigidities, where there are again undeflected mean oscillations. Eventually, quasi-periodic oscillations are observed for the lowest rigidity values investigated.

These non-linear results are then interpreted using the eigenvalue analysis, which allows to determine the modes that develop during the initial, linear growth of instabilities (section 3.4). First, it is shown that the rigidity threshold for which the first unsteady regime appears is perfectly identified using this analysis, which also gives an excellent estimate of the observed non-linear vibration frequency. The identification of thresholds between the different regimes with lower

rigidities is more qualitative, because several unstable modes participate in the initial growth of disturbances and give rise to different non-linear scenarios when they interact. The mechanism that leads to a deviation from the mean position of the plate with lower stiffness could be associated with unstable modes of static divergence (zero frequency modes). These bifurcations are associated with two non-linear branches of deviated stationary equilibriums. These branches are determined and the associated secondary instability is investigated. Finally, quasi-periodic oscillations are associated with the presence of two unstable, unsteady modes, at distinct frequencies.

The chapter 4 discusses the control of unstable modes by optimizing the shape of the rigid cylinder downstream of which the elastic plate is attached. The originality of the approach lies in the fact that the cost function to be minimized includes the growth rate as well as the frequency of the unstable fluid-solid mode. An analytic formula for the shape gradient of this objective function is determined using an adjoint approach, based on the derivation of the continuous fluid-structure adjoint equations. Two types of unstable modes are then studied. A first mode (F) is related to wake instabilities, while a second mode (S) is more related to the fluid-solid coupled dynamics. For these two types of modes, the shape gradients are detailed. Integrated into a descent algorithm, the successive shape gradients first allow to determine optimal shapes that suppress instabilities for modes (F) and (S). The optimal shapes are relatively similar in both cases — a flattening of the cylinder in the transverse direction, which reduces both the apparent Reynolds number (smaller section) and moderates the detachment leading to vortex shedding. More unexpected results are obtained when trying to determine shapes giving rise to unstable modes beating at a control frequency (thus designing kind of a fluid-structure oscillator): it is first shown that the structure of the mode (F), even modified by the shape of the cylinder, does not allow to obtain a mode having a frequency independent of its growth rate. On the other hand, it is possible to vary the frequency of the mode (S) within a certain range, while setting the growth rate at a slightly positive, fixed value. “D-shaped” cylinders are obtained when trying to increase the frequency, while a “C-shaped” cylinder decreases it.

Physical analysis and structure optimization of compliant coatings for laminar-turbulent transition delay

The last part of the thesis is dedicated to delaying the laminar/turbulent transition by Tollmien-Schlichting waves in a two-dimensional boundary layer by means of a viscoelastic, finite-length compliant coating, a quest that has been the subject of constant research since the 1960’s and the surprising experimental observations by [Kramer \(1960\)](#). Delaying the transition is definitely of practical interest, in that it reduces the overall drag and thus the energy spent for locomotion.

Chapter 5 deals with the physical analysis of instabilities. First, the complex dynamics of the viscoelastic patch alone, modelled as a linearised neo-Hookean incompressible material, is analysed, making it possible to identify which vibration modes are likely to interact with the waves in the flow. In particular, the dispersion relation in the case of a patch of infinite length is related to the vibration modes of a patch of finite length. The fluid-solid coupled modes are then determined for different patch stiffness and viscoelastic damping parameters. In addition to the stable low-frequency modes, traditionally associated with Tollmien-Schlichting waves, the fluid-solid interaction modifies the growth rate and frequency of the solid vibration modes located at higher frequencies in the form of the so-called travelling-flutter waves. In particular, in absence of viscoelastic damping, these modes can become globally unstable. If sufficient damping is provided, all modes are stable. Nevertheless, the noise amplifier behaviour of the boundary layer means that waves can be amplified even in absence of an unstable global mode, and the resolvent analysis is then adapted.

For the first time, this analysis is applied to the case of a 2d boundary layer flow developing over a viscoelastic patch of finite length and modelled by elasticity equations. The optimal forcings — representative of the worst-case scenario in terms of external disturbances such as noise or gusts — that lead to maximum amplification of the energy of the disturbances are first determined, in the case of a rigid configuration, that is, in the classical case of a boundary layer on a rigid wall. The fluid-elastic response to these optimal perturbations is then calculated, and highlights the extent to which the presence of the patch modifies the growth of instability waves. In the case

of Tollmien-Schlichting waves, the optimal forcing in the rigid case is also the forcing that gives the greatest response in the fluid-elastic case, while suboptimal fluid-rigid forcings also result in suboptimal responses in the fluid-elastic case. In addition, amplification in the fluid-elastic case is reduced, compared to the rigid case. On the other hand, both optimal and suboptimal forcings give high responses in the frequency range of travelling-wave flutter instabilities. This observation therefore pushes for determining both the optimal forcing and responses in the fluid-elastic case. In this latter case, the resolvent analysis clearly shows two marked response peaks, one at low frequency, related to Tollmien-Schlichting waves, and the second in the frequency range of the travelling flutter waves. The antagonist effects of the stiffness on the two types of instabilities can then be analysed quantitatively. It is shown in what extent decreasing the rigidity of the patch effectively reduces the growth of Tollmien-Schlichting waves. Large amplifications unfortunately appear in the frequency range of travelling-flutter instabilities, cancelling in practice the expected beneficial effects.

In view of these antagonistic results, it is tempting to determine an optimal material that would make it possible on the one hand to dampen Tollmien-Schlichting waves, while on the other hand preventing the development of travelling-wave flutter waves. The purpose of the last chapter is on how to do it. Again based on the adjoint formalism, the gradients of the local properties of the material (density, damping, stiffness) with respect to the energy amplification rate of the waves are determined. After having presented the different gradients, the focus is on studying the effects of a change in the distribution of rigidity. First, optimal materials are determined with respect to the growth of travelling flutter waves only. A relatively marginal gain compared to using an homogeneous material is observed. A combined optimization is then carried out, which takes into account both Tollmien-Schlichting and travelling flutter waves. In this latter case, it was possible to reduce by 22 % the growth of the Tollmien-Schlichting waves while keeping in the same time the amplification of the travelling-flutter waves at low values.

7.2 Perspectives

In order to definitely conclude this work, let us finally give some ideas of further developments. Four main topics are given, that could provide a basis for future works.

Development of an appropriate numerical discretization for the Eulerian-based linear stability approach

The Eulerian-based linearised approach initially proposed by [Fernández & Le Tallec \(2003a\)](#) was disappointing from a numerical point of view: on the benchmark cases presented in section 2.4, we have highlighted its extreme sensitivity with respect to the spatial discretization in the vicinity of the interface, and the resulting poor mesh convergence properties. Although simpler from the point of view of the formulation, its practical implementation therefore remains delicate and uncertain. However, there are situations where the Eulerian-based approach gives very satisfactory results; for example, on the case of the boundary layer developing over a flexible coating, treated in the chapters 5 and 6, we have observed that the Lagrangian-based and Eulerian-based approaches give very similar results. It would therefore be fruitful to investigate further the numerical and mathematical aspects related to this latter method (which seems actually to be an ongoing process, see [Bociu et al. \(2015\)](#)), in order to determine to what extent (e.g. through specific finite elements, or a particular spatial discretization) and at what computational cost a convergence could be guaranteed in all situations.

Compared to the Lagrangian-based method, which requires non-local couplings via the extension operator, the Eulerian method offers indeed a more natural alternative from the point of view of the physical description of the couplings. Their action at the interface *via* the transpiration velocity and the added stiffness terms makes them easier to interpret, and avoids having to use an extension operator. In addition, one can hope that the corresponding adjoint problems would also be of a simpler form than that derived in the Lagrangian-based framework.

Application of the linearised fluid-elastic formulation to the design of reduced state-space aeroelastic models

An alternative formulation of the linear stability problem was briefly mentioned in §2.1.3. It takes the form of a solid vibration problem with a second member that represents the fluid forces modified by the fluid-solid interaction, i.e. the feedback of the solid on itself, *via* the fluid. From a linear problem of fluid-solid stability, this results in a non-linear solid vibration problem that can be further reduced to a very small dimension by means of modal projection.

In the context of aeroelasticity, the special form of this feedback loop is often unknown, since the modelling relies *a priori* on simplified models. The aerodynamic forces are often determined by means of semi-empirical approaches: the fluid effect is modelled using, for instance, added mass, stiffness and damping coefficients, as well as non-linear time-delay terms (Karpel, 1982). In these models, the coefficients are unknown and must be estimated by means of fitting approaches based on time-marching simulations, or by comparison with experimental results.

The presently developed approach enables in some sense to reverse the direction of the modelling: since the exact form of the non-linear feedback loop is known, an appropriate asymptotic development of this loop allows indeed to recover the simple aeroelastic models evoked above. This approach was for instance adopted in §3.6.2 for the study of the divergence instability that develops in the cylinder-splitter plate configuration. Preliminary tests conducted on the occasion of a Master's internship (Lambrechts, 2018) have shown that this analysis can be successfully extended for analysing flutter instabilities. The practical interest of this approach appears clearly: instead of having to estimate parameters, they could be computed directly from an appropriate expansion at the desired order of the non-linear solid-to-fluid-to-solid feedback loop.

Shape optimization of deformable fluid-solid interfaces, application to the mitigation of flutter modes or to the maximization of energy transfer in energy harvesters

The most interesting and straightforward extension of the work on shape optimization would be to consider the optimization not only of the rigid part, but also of the elastic part of the object. From a practical point of view, this extension only requires to evaluate an *a priori* more complex gradient formula. Provided that the deformations remain small, it would probably not be too much of an inconvenience to rely on the approximate adjoint problem. It could even be sufficient to use the formula derived for an optimization of the rigid part, if such approximate gradient were to be a good enough approximation. For example, one can imagine an optimization case where the objective function focuses on unstable wing flutter modes. Thanks to the fully coupled approach, complex instabilities (i.e. with large detached areas) can be addressed. In an aeroelastic context where the structural displacements are usually small, the approximate-adjoint method would probably be applicable to a wide range of problems.

Finally, in the context of energy harvesting devices, shape optimization could also be used to “tune” resonance frequencies so as to maximize the energy transfer, using the same kind of approach than what was presented for the design of the “fluid-structure oscillator”. In this latter case, it should be borne in mind, however, that if non-linearities are predominant, then the linear analysis will result in unrepresentative results. In that case, one could eventually try to combine the present framework of shape optimization with non-linear approaches such as harmonic balance or time-spectral methods.

Study of the non-linear regime of the boundary-layer instabilities above the compliant coating & further optimization insights

While the optimization presented in the chapter 6 was found to be able to mitigate the development of the instabilities in the boundary-layer flow over the compliant patch, there are still many things that can be improved. First, better performances would certainly be attained by considering an optimization with more than only two frequency points. This might hopefully prevent from the emergence of secondary amplification peaks at other frequencies. In addition, the optimization

problem could also be formulated more simply as finding the minimum of amplification, with some inequality constraint on the stiffness indicating that it should remain inside some realistic range. Finally, choosing a solid model that is more representative of a real viscoelastic material would certainly add constraints between density, damping and stiffness. Since we were not aware of the precise nature of these relations that strongly depend on the material characteristics, the simplest possible case was considered, but more realistic cases would certainly be more relevant.

In addition, the analyses carried out here have only focused on the linear regime of instability. However, it is well known that the non-linear transition begins as soon as the velocity of the disturbance waves reaches on the order of a few percent of the free-stream velocity. While it is clear that the damping of Tollmien-Schlichting waves conferred by the presence of the patch can only be beneficial with regard to the non-linear transition; the effect of travelling-flutter waves is less clear: indeed, although they can give rise to very high amplification rates or even become globally unstable, these waves do not survive downstream to the patch. Therefore, one can wonder in what extent these unstable waves impact the flow more downstream. It would also be interesting to find an estimate of the transition Reynolds number corresponding to the optimized coatings, for it would give a more practical measure of the benefits that can be actually obtained.

A

RESOLVENT *vs* EIGENVALUES

Despite the apparent complexity of fluid-structure instabilities, some typical features can be observed in systems as simple as two coupled one degree of freedom oscillators. This simplicity is exploited here to present the resolvent and eigenvalue analyses, without having to cope with all the technical difficulties that come with models having many degrees of freedom. Namely, we use here a simple model inspired by the one used for instance by [Facchinetti *et al.* \(2004\)](#) for studying vortex-induced vibrations, or [Schmid & de Langre \(2002\)](#) for modelling transient energy growth in coupled-mode flutter instabilities. The “fluid” is reduced to a forced Van der Pol equation

$$\frac{d^2 q_f}{dt^2} + 2\eta_f \omega_f (1 - a q_f^2) \frac{dq_f}{dt} + \omega_f^2 q_f(t) = A q_s + B \frac{dq_s}{dt} + f(t) \quad (\text{A.0.1})$$

where q_f would be representative of an integrated lift coefficient ([Facchinetti *et al.*, 2004](#)). The real constants A and B represent respectively displacement and velocity couplings with the solid variable q_s , while the forcing $f(t)$ represents an external source of disturbance (akin to turbulence, gusts, etc.). Finally, a is a parameter that controls the non-linear effects. When the vibration amplitude is low, (A.0.1) behaves as a simple damped oscillator. When the amplitude is increased, the damping is reduced and can eventually lead to a self-sustained non-linear amplification. The “solid” is a simple harmonic oscillator

$$\frac{d^2 q_s}{dt^2} + \omega_s^2 q_s(t) = M q_f(t) \quad (\text{A.0.2})$$

that is forced by the fluid with an amplitude M whose value would be akin to the solid-to-fluid density ratio. Note that using modal projections ([de Langre, 2002](#)), the linearised solid equation derived in the section 2.1 can be turned into this very simple form.

Linear equations describing small-amplitude perturbations (q'_f, q'_s) about the obvious steady equilibrium position $(0, 0)$ are obtained here by simply neglecting the non-linear term in the “fluid” equation (A.0.1). Introducing the state vector $\mathbf{q}' = [\dot{q}_s, q_s, \dot{q}_f, q_f]^T$, the linearised problem writes on the form of a first-order differential problem

$$\begin{cases} \frac{d\mathbf{q}'}{dt} = \mathbf{A}\mathbf{q}' + \mathbf{P}f(t) & \text{for } t > 0 \\ \mathbf{q}'(0) = \mathbf{q}'_0 \end{cases} \quad (\text{A.0.3})$$

where \mathbf{q}'_0 is the initial state, and the system matrix \mathbf{A} and the prolongation matrix \mathbf{P} write as

$$\mathbf{A} = \begin{bmatrix} 0 & -\omega_s^2 & 0 & M \\ 1 & 0 & 0 & 0 \\ B & A & -2\eta_f \omega_f & -\omega_f^2 \\ 0 & 0 & 1 & 0 \end{bmatrix} \quad \text{and} \quad \mathbf{P} = \begin{bmatrix} 0 \\ 0 \\ 1 \\ 0 \end{bmatrix} \quad (\text{A.0.4})$$

The matrix \mathbf{A} can be decomposed in an upper left 2×2 block describing the solid dynamics, a lower right 2×2 block describing the fluid dynamics, plus off diagonal blocks that represent the couplings. As a measure of the perturbations, we will consider the “energy” of our simplified

fluid-structure system. Following Schmid & de Langre (2002), for sake of simplicity we define this energy as the 2-norm of the state vector. We shall then try to elucidate the behaviour of the energy gain

$$g(t)^2 = \frac{\|\mathbf{q}'(t)\|_2^2}{\|\mathbf{q}'(0)\|_2^2}, \quad (\text{A.0.5})$$

where $\|\cdot\|_2$ is the standard 2-norm for vectors, as a function of the fluid parameters ω_f and η_f , the solid parameter ω_s and the coupling parameters A , B and M , but also investigate the effect of the external forcing f . This ratio is physically relevant, because it indicates if, for a given energy input, the system amplifies or dissipates the initial energy release — an energy amplification being associated to the growth of an instability (Schmid, 2007).

Since the perturbation problem (A.0.3) is a simple first-order ordinary differential equation, its solution can be computed explicitly, as

$$\mathbf{q}'(t) = e^{t\mathbf{A}} \mathbf{q}'_0 + \int_0^t e^{(t-\tau)\mathbf{A}} \mathbf{P} f(\tau) d\tau. \quad (\text{A.0.6})$$

This general solution is composed of two terms. The first one is the response to the initial condition — and is also the only one when $f = 0$. The second part is the forced response that encloses all receptivity effects, i.e. how the system reacts to external disturbances. The linearity of the problem allows to study the two effects separately.

Remark. In problems involving incompressible flows, after space discretization of the problem the time derivative writes rather like $\mathbf{B} d\mathbf{q}'/dt$, where \mathbf{B} is a singular operator (no temporal dynamics is associated with the incompressibility constraint, which results in as many zero lines in \mathbf{B} as there are degrees of freedom to represent the continuity equation). In that case, (A.0.3) becomes a differential-algebraic equation (Brenan *et al.*, 1996) and the formula (A.0.6) no longer holds directly because it would require to compute the inverse of \mathbf{B} , which is singular. However, the problem is not fundamentally different (at least in a conceptual point of view, the story is much different when it comes to solve practically the problem), since it is possible to eliminate the pressure from the system by solving a Poisson equation. For simplicity, this case is not considered here.

A.1 Temporal, modal stability analysis

We first address the case where $f = 0$, and investigate the behaviour of the linearised system. From (A.0.6), the maximal energy gain that can be reached by the system write as

$$G(t)^2 = \max_{\mathbf{q}'(0) \neq 0} \frac{\|\exp(t\mathbf{A}) \mathbf{q}'(0)\|_2^2}{\|\mathbf{q}'(0)\|_2^2} \triangleq \|\exp(t\mathbf{A})\|^2. \quad (\text{A.1.1})$$

In the next two subsections, we analyse the time-asymptotic behaviour of this energy gain, then emphasize the transient *non-normal* effects that might occur at finite-time.

Asymptotic behaviour at large time

An upper bound to energy amplification can be derived by introducing the eigenvalue problem associated to (A.0.1) and (A.0.2), that is obtained by seeking for so-called normal modes $\mathbf{q}' = \Re\{\mathbf{q}^\circ \exp(\lambda t)\}$ in (A.0.3) with $f = 0$. We obtain an eigenvalue problem

$$\mathbf{A} \mathbf{q}_j^\circ = \lambda_j \mathbf{q}_j^\circ, \quad (\text{A.1.2})$$

where the (complex) eigenvalues λ_j determine the temporal amplification and frequency of the modes \mathbf{q}_j° . Noting $\mathbf{V} = [\mathbf{q}_1^\circ, \dots, \mathbf{q}_n^\circ]$, where $n = 4$ is the size of the problem, it holds that $\mathbf{A} = \mathbf{V} \mathbf{D} \mathbf{V}^{-1}$ where \mathbf{D} is a diagonal matrix containing the eigenvalues of \mathbf{A} , i.e.¹ $\mathbf{D} = \text{Diag}(\lambda_1, \dots, \lambda_n)$. The

¹for simplicity, we have assumed here that there are n eigenvalues with geometric multiplicity 1. When it is not the case, \mathbf{D} can only be reduced to a block-diagonal matrix where each block is a so-called Jordan block containing the degenerate eigenvalue on the diagonal and 1 in each entry of the superdiagonal. We refer the reader to the book by Trefethen & Embree (2005) for the specific treatments required in this case.

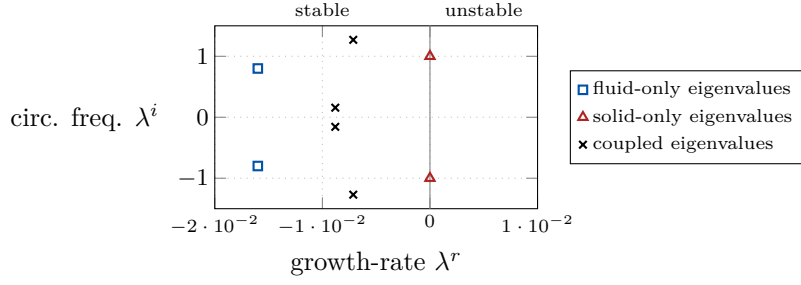


Figure A.1 – Spectrum. Eigenvalues of the fluid equation (A.0.1), of the solid equation (A.0.2) and of the coupled problem, for $\omega_s = 1$, $\omega_f = 0.8$, $\eta_f = 0.02$, $M = 3$, $A = 0.2$ and $B = 0.001$. All eigenvalues lie here in the stable region $\lambda^r < 0$.

energy gain can then be written as $G(t)^2 = \|\mathbf{V} \exp(t\mathbf{D})\mathbf{V}^{-1}\|^2$, and noting λ the eigenvalue with the largest growth-rate (i.e. the largest real part), we obtain (Trefethen & Embree, 2005)

$$G(t)^2 \leq \|\mathbf{V}\|^2 \|\mathbf{V}^{-1}\|^2 \exp(2 \Re(\lambda) t) \quad \forall t \geq 0. \quad (\text{A.1.3})$$

From this bound, we immediately notice that if $\Re(\lambda) < 0$, than an exponential decay to zero is expected for the perturbations when $t \rightarrow +\infty$, whatever the initial condition is. When on the contrary $\Re(\lambda) > 0$, another bound obtained by the same kind of arguments show that the energy gain grows exponentially to infinity.

Let us give an example with our simplified fluid-structure model. A typical spectrum with only stable eigenvalues is represented in Fig. A.1. The solid problem (A.0.2) has two pure imaginary eigenvalues $\pm i\omega_s$: there is no attenuation nor amplification mechanism in the solid, which yields to marginally stable modes oscillating at frequency ω_s . In absence of viscoelastic damping, these features are recovered in more complicated solid models — the only fundamental difference being that instead of having one single mode, elastic solids usually display a discrete set of vibration modes. The homogeneous fluid problem obtained from (A.0.1) has complex eigenvalues $\omega_f(-\eta_f \pm i(1 - \eta_f^2)^{1/2})$ with a negative real part when $\eta_f > 0$: a decay to zero of the perturbations is expected when $t \rightarrow \infty$. More realistic fluid models present a much more complicated spectra, that is composed of branches of modes as well as continuous regions when boundary conditions are set on an infinite interval (Luchini & Bottaro, 2014b). Nevertheless, for bounded wake flows for instance, the least stable mode often appear as an isolated mode. The coupled modes have a much less simple expression, and depend on the different coupling parameters. In Fig. A.1 the spectrum for $\omega_s = 1$, $\omega_f = 0.8$, $\eta_f = 0.02$, $M = 3$, $A = 0.2$ and $B = 0.001$ is represented. Four complex-conjugate, stable eigenvalues $-0.0071 \pm 1.27i$ and $-0.0088 \pm 0.157i$ are obtained, indicating that the linear response should decay to zero as time goes on. Note that a stable fluid and a marginally stable solid can also result in an unstable coupled system for values of other coupling parameters.

Non-normality and transient growth

The eigenvalue analysis overshadows an important effect. Even if the energy gain decays down to zero when $t \rightarrow \infty$, in (A.1.3) the term $\|\mathbf{V}\| \|\mathbf{V}^{-1}\|$ can still be large, thus allowing for a large linear amplification of the energy at *finite* time horizon even if $\Re(\lambda) < 0$. Since large-amplitude perturbations might trigger non-linearities present in the non-linear model, in some cases the eigenvalue analysis completely fails to predict the observed behaviour, because a non-linear transition occurred through a linear energy amplification at finite time horizon. The value that this latter term can reach depends on the *normality* of the evolution operator, i.e. whether it commutes or not with its adjoint operator. For finite-dimension problems and with the Euclidian scalar product, the adjoint \mathbf{L}^\dagger of an operator \mathbf{L} is defined by the identity

$$(\mathbf{q}'_1)^\mathbf{H} (\mathbf{L} \mathbf{q}'_2) = (\mathbf{L}^\dagger \mathbf{q}'_1)^\mathbf{H} (\mathbf{q}'_2) \quad \forall \mathbf{q}'_1, \mathbf{q}'_2 \in \mathbb{R}^n,$$

that is to say, $\mathbf{L}^\dagger = \mathbf{L}^\mathbf{H}$ where \mathbf{H} is the hermitian transpose operator (transpose-conjugate). When the system is self-adjoint, i.e. when $\mathbf{L}\mathbf{L}^\mathbf{H} = \mathbf{L}^\mathbf{H}\mathbf{L}$, then the eigenvalues of \mathbf{L} form an orthonormal

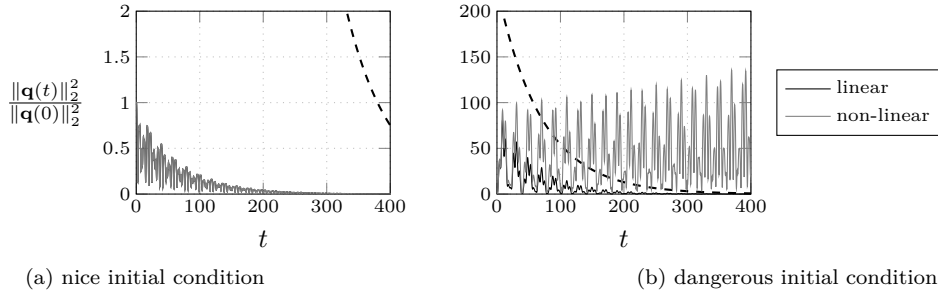


Figure A.2 – Response to initial conditions. For $\omega_s = 1$, $\omega_f = 0.8$, $\eta_f = 0.02$, $M = 3$, $A = 0.2$ and $B = 0.001$, linear response (black line) and non-linear response (gray lines, with non-linear constant $a = 0.5$) to initial conditions (a) $\mathbf{q}(0) = [0, 1, 0, 0]^T$ and (b) $\mathbf{q}(0) = [0.6, 0, -0.8, 0]^T$. The bound given by (A.1.3) is represented with the dashed line.

basis: \mathbf{V} can be taken unitary and so $\|\mathbf{V}\|\|\mathbf{V}^{-1}\| = 1$. In that case, knowing the eigenvalues is sufficient to describe the linear dynamics of the system (Trefethen & Embree, 2005). When it is not the case however, $\|\mathbf{V}\|\|\mathbf{V}^{-1}\| > 1$ and transient growth might occur.

Remark. The normality of a problem depends on the space on which it is defined and on the scalar product used. In particular, Farrell & Ioannou (1993) showed that any problem can be turned into a normal problem, provided that the scalar product is changed accordingly. However, for practical applications, the scalar product has better to be defined as a physically relevant measure of the system (typically, the corresponding norm gives the energy).

Let us now come back to our simplified model. With the Euclidian inner product chosen, the adjoint operator is simply the transpose matrix, i.e. $\mathbf{A}^\dagger = \mathbf{A}^T$. Looking at (A.0.4), we are easily convinced that the problem is non-normal, and thus transient growth might occur. An example of non-normal energy amplification is given in Fig. A.2. The plot on the left shows a case where an initial condition of norm unity $\mathbf{q}(0) = [0, 1, 0, 0]^T$ does not yield to any energy amplification, even if the energy upper bound (represented in dashed line) allows for an amplification up to by a factor 225. As a consequence of this decrease of energy, no instabilities are triggered in the non-linear problem and the curves corresponding to the linear and non-linear problems almost overlap. On the contrary, Fig. A.2b displays a case with another norm unity initial condition $\mathbf{q}(0) = [0.6, 0, -0.8, 0]^T$, that results in an appreciable transient growth (note the scale of the y axis). Shortly after $t = 0$, an energy amplification by a factor 80 is observed, that triggers the non-linearities: if the linear signal decreases down to zero as expected from the eigenvalues, the non-linear response is amplified with time. We are here in a typical case where eigenvalues completely fail to predict what is going to happen non-linearly.

A.2 Frequency response analysis

We now focus on the second term in the linear response (A.0.6). Although the formula (A.0.6) is valid whatever the temporal forcing f (time-harmonic, impulsive, stochastic, etc.), we will consider here only the case of a time-harmonic forcing. A Fourier transform for f and \mathbf{q}' ,

$$f^\circ(\omega) = \int_{-\infty}^{+\infty} f(t)e^{i\omega t}dt, \quad \mathbf{q}'^\circ(\omega) = \int_{-\infty}^{+\infty} \mathbf{q}'(t)e^{i\omega t}dt$$

yields to a formulation of (A.0.3) in the frequency space. Introducing the resolvent operator $\mathbf{R}(\omega) = (i\omega\mathbf{I} - \mathbf{A})^{-1}$, it can be written as an input-output problem,

$$\mathbf{q}^\circ = (i\omega\mathbf{I} - \mathbf{A})^{-1}\mathbf{P}f^\circ. \quad (\text{A.2.1})$$

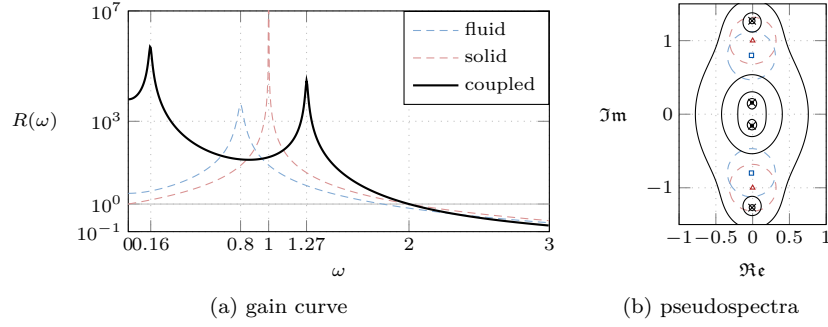


Figure A.3 – Frequency response & pseudospectra. (a) Plot of the gain curve for an harmonic forcing at frequency ω , for the fluid-alone (dashed blue), solid-alone (dashed red), and coupled operators (solid line). (b) Pseudospectra of the system in the complex plane. The isocontour $R = 10$ is represented in dashed red and blue lines for the solid and fluid-alone operators respectively. Isocontours with levels 10, 100, 1000 and 10 000 are represented for the coupled system, and the solid (red triangles), fluid (blue squares) and coupled (black cross) eigenvalues are also represented.

The receptivity processes can be quantified by evaluating the response-to-forcing gain

$$H(\omega) = \max_{f^\circ \neq 0} \frac{\|q^\circ\|_2}{|f^\circ|} = \|(\mathbf{i}\omega\mathbf{I} - \mathbf{A})^{-1}\mathbf{P}\|. \quad (\text{A.2.2})$$

On the contrary to the energy gain $G(t)$ defined in (A.1.1), $H(\omega)$ is not a ratio of root-squared energies but the ratio between response and forcing norms. Like before, computing H amounts to compute an operator norm (which is here actually the 2-norm of the vector $(\mathbf{i}\omega\mathbf{I} - \mathbf{A})^{-1}\mathbf{P}$ because \mathbf{P} is a $n \times 1$ matrix).

Several effects can contribute to an amplification in the frequency space. The most obvious effect comes from the resonance with eigenvalues: $H(\omega)$ is all the more large that $\mathbf{i}\omega\mathbf{I} - \mathbf{A}$ is close to be singular. This can be observed in Fig. A.3a, where the amplification for the solid operator alone is represented in red dashed line. When the forcing frequency approaches $\omega_s = 1$, $R(\omega) \rightarrow +\infty$ because $\mathbf{i}\omega_s$ is an eigenvalue of the block of \mathbf{A} that corresponds to the solid problem. A resonance is also observed for the fluid operator at frequency close to $\omega_f = 0.8$, but the amplitude remains finite because of the damping that shifts the eigenvalues of the fluid operator towards the left side of the complex plane. Without non-normality effects, the amplitude of the response is entirely dictated by the distance of the eigenvalues from the imaginary axis: the response should be all the more damped that they are far from it. This is not what is observed for the coupled case. Although in Fig. A.1 the low-frequency complex-conjugate eigenvalue has a smaller growth-rate than the high-frequency eigenvalue, in Fig. A.3a the response is more amplified at lower frequencies. Again, this is an effect of the non-normality of the coupled operator.

A more general overview of non-normality effects can be appreciated by looking at the *pseudospectra* of the system, i.e. the contour lines $\|(\mathbf{A} - \sigma\mathbf{I})^{-1}\| = \text{cst}$. It is represented in Fig. A.3b. Dashed lines indicate the contours for the solid-only and fluid-only problems. These contours are almost perfect circles, indicating that the system behaves as an almost perfect normal system (Trefethen & Embree, 2005). On the contrary, the fluid-structure pseudospectra exhibits a protrusion along the real axis, that is the signature for an over-amplified response. Note that the curve in Fig. A.3a is a cut along the imaginary axis of the contour plot presented in Fig. A.3b.

B

FLUID-SOLID BLOCK OPERATORS EXPRESSION

B.1 Non-linear fluid-solid equations

Three-field formulation: for $\hat{\mathbf{q}}_s = (\hat{\boldsymbol{\xi}}, \hat{\mathbf{u}}_s)$, $\hat{\mathbf{q}}_e = (\hat{\boldsymbol{\xi}}_e, \hat{\boldsymbol{\lambda}}_e)$ and $\hat{\mathbf{q}}_f = (\hat{\mathbf{u}}, \hat{p}, \hat{\boldsymbol{\lambda}})$, the three-fields formulation of the ALE fluid-structure problem reads

$$\underbrace{\begin{pmatrix} \hat{\mathcal{T}}_s & 0 & 0 \\ 0 & 0 & 0 \\ 0 & -\hat{\mathcal{T}}_{fe}(\hat{\mathbf{q}}_f, \hat{\mathbf{q}}_e) & \hat{\mathcal{T}}_f(\hat{\mathbf{q}}_e) \end{pmatrix}}_{\hat{\mathcal{T}}_{fsi}(\hat{\mathbf{q}})} \frac{\partial}{\partial t} \begin{pmatrix} \hat{\mathbf{q}}_s \\ \hat{\mathbf{q}}_e \\ \hat{\mathbf{q}}_f \end{pmatrix} = \underbrace{\begin{pmatrix} \hat{\mathcal{S}}(\hat{\mathbf{q}}_s) + \hat{\mathcal{I}}_{fs}^T \hat{\mathbf{q}}_f \\ -\hat{\mathcal{S}}_e \hat{\mathbf{q}}_e + \hat{\mathcal{I}}_{es} \hat{\mathbf{q}}_s \\ \hat{\mathcal{I}}_{fs} \hat{\mathbf{q}}_s + \hat{\mathcal{N}}_f(\hat{\mathbf{q}}_f, \hat{\mathbf{q}}_e) \end{pmatrix}}_{\hat{\mathcal{N}}_{fsi}(\hat{\mathbf{q}})} \begin{pmatrix} \hat{\mathbf{q}}_s \\ \hat{\mathbf{q}}_e \\ \hat{\mathbf{q}}_f \end{pmatrix},$$

and without the solid velocity augmentation (only the solid displacement variable),

$$\begin{pmatrix} \hat{\mathcal{M}}_s & 0 & 0 \\ 0 & 0 & 0 \\ 0 & 0 & 0 \end{pmatrix} \frac{\partial^2}{\partial t^2} \begin{pmatrix} \hat{\boldsymbol{\xi}} \\ \hat{\mathbf{q}}_e \\ \hat{\mathbf{q}}_f \end{pmatrix} + \begin{pmatrix} 0 & 0 & 0 \\ 0 & 0 & 0 \\ -\hat{\mathcal{I}}_{f\xi} - \hat{\mathcal{T}}_{fe}(\hat{\mathbf{q}}_f, \hat{\mathbf{q}}_e) & \hat{\mathcal{T}}_f(\hat{\mathbf{q}}_f) \end{pmatrix} \frac{\partial}{\partial t} \begin{pmatrix} \hat{\boldsymbol{\xi}} \\ \hat{\mathbf{q}}_e \\ \hat{\mathbf{q}}_f \end{pmatrix} = \begin{pmatrix} -\hat{\mathcal{K}}(\hat{\boldsymbol{\xi}}) + \hat{\mathcal{I}}_{f\xi}^T \hat{\mathbf{q}}_f \\ -\hat{\mathcal{S}}_e \hat{\mathbf{q}}_e + \hat{\mathcal{I}}_{e\xi} \hat{\boldsymbol{\xi}} \\ \hat{\mathcal{N}}_f(\hat{\mathbf{q}}_f, \hat{\mathbf{q}}_e) \end{pmatrix}.$$

Solid operators expression:

$$\hat{\mathcal{T}}_s = \begin{pmatrix} \hat{\mathcal{M}}_s & 0 \\ 0 & \mathcal{M}_s \cdot \hat{\mathcal{M}}_s \end{pmatrix}, \quad \hat{\mathcal{S}}(\hat{\mathbf{q}}_s) = \begin{pmatrix} \hat{\mathcal{M}}_s \hat{\mathbf{u}}_s \\ -\hat{\mathcal{K}}(\hat{\boldsymbol{\xi}}) \end{pmatrix}, \quad \hat{\mathcal{I}}_{f\xi} = \begin{pmatrix} 0 \\ 0 \\ \hat{\mathcal{I}}_s \end{pmatrix}, \quad \hat{\mathcal{I}}_{fs} = \begin{pmatrix} 0 & 0 \\ 0 & 0 \\ 0 & \hat{\mathcal{I}}_s \end{pmatrix}$$

with

$$\begin{aligned} \langle \hat{\boldsymbol{\psi}}_s^u, \hat{\mathcal{M}}_s \hat{\boldsymbol{\xi}} \rangle &= \int_{\hat{\Omega}_s} \hat{\boldsymbol{\xi}} \cdot \hat{\boldsymbol{\psi}}_s^u \, d\hat{\Omega} && \text{for } (\hat{\boldsymbol{\psi}}_s^u, \hat{\boldsymbol{\xi}}) \in \hat{\mathcal{U}}^s \times \hat{\mathcal{U}}^s, \\ \langle \hat{\boldsymbol{\psi}}_s^u, \hat{\mathcal{K}}(\hat{\boldsymbol{\xi}}) \rangle &= \int_{\hat{\Omega}_s} \hat{\mathbf{P}}(\hat{\boldsymbol{\xi}}) : \hat{\boldsymbol{\nabla}} \hat{\boldsymbol{\psi}}_s^u \, d\hat{\Omega} && \text{for } (\hat{\boldsymbol{\psi}}_s^u, \hat{\boldsymbol{\xi}}) \in \hat{\mathcal{U}}^s \times \hat{\mathcal{U}}^s, \\ \langle \hat{\boldsymbol{\psi}}^\lambda, \hat{\mathcal{I}}_s \hat{\boldsymbol{\xi}} \rangle &= \int_{\hat{\Gamma}} \hat{\boldsymbol{\psi}}^\lambda \cdot \hat{\boldsymbol{\xi}} \, d\hat{\Gamma} && \text{for } (\hat{\boldsymbol{\psi}}^\lambda, \hat{\boldsymbol{\xi}}) \in \hat{\mathcal{U}}_{\hat{\Gamma}} \times \hat{\mathcal{U}}^s. \end{aligned}$$

Extension operators expression:

$$\hat{\mathcal{S}}_e = \begin{pmatrix} \hat{\mathcal{G}} & \hat{\mathcal{I}}_e^T \\ \hat{\mathcal{I}}_e & 0 \end{pmatrix}, \quad \hat{\mathcal{I}}_{e\xi} = \begin{pmatrix} 0 \\ \hat{\mathcal{I}}_s \end{pmatrix}, \quad \hat{\mathcal{I}}_{es} = \begin{pmatrix} 0 & 0 \\ \hat{\mathcal{I}}_s & 0 \end{pmatrix},$$

with

$$\begin{aligned} \langle \hat{\psi}_e^u, \hat{\mathcal{G}} \hat{\xi}_e \rangle &= \int_{\hat{\Omega}_f} \hat{\Sigma}_e(\hat{\xi}_e) : \hat{\nabla} \hat{\psi}_e^u \, d\hat{\Omega} & \text{for } (\hat{\psi}_e^u, \hat{\xi}_e) \in \hat{\mathcal{U}}^e \times \hat{\mathcal{U}}^e \\ \langle \hat{\psi}_e^\lambda, \hat{\mathcal{I}}_e \hat{\xi}_e \rangle &= \int_{\hat{\Gamma}} \hat{\xi}_e \cdot \hat{\psi}_e^\lambda \, d\hat{\Gamma} & \text{for } (\hat{\psi}_e^\lambda, \hat{\xi}_e) \in \hat{\mathcal{U}}_{\hat{\Gamma}} \times \hat{\mathcal{U}}^e. \end{aligned}$$

Fluid operators expression:

$$\begin{aligned} \hat{\mathcal{T}}_f(\hat{\mathbf{q}}_f) &= \begin{pmatrix} \hat{\mathcal{T}}(\hat{\xi}_e) & 0 & 0 \\ 0 & 0 & 0 \\ 0 & 0 & 0 \end{pmatrix}, \quad \hat{\mathcal{T}}_{fe}(\hat{\mathbf{q}}_f, \hat{\mathbf{q}}_e) = \begin{pmatrix} \hat{\mathcal{N}}(\hat{\xi}_e, \hat{\mathbf{u}}) & 0 \\ 0 & 0 \\ 0 & 0 \end{pmatrix}, \\ \hat{\mathcal{N}}_f(\hat{\mathbf{q}}_f, \hat{\mathbf{q}}_e) &= \begin{pmatrix} -\hat{\mathcal{N}}(\hat{\xi}_e, \hat{\mathbf{u}}) \hat{\mathbf{u}} + \hat{\mathcal{B}}(\hat{\xi}_e)^T \hat{p} - \frac{2}{\mathcal{R}_e} \hat{\mathcal{D}}(\hat{\xi}_e) \hat{\mathbf{u}} - \hat{\mathcal{I}}_f^T \hat{\lambda} \\ \hat{\mathcal{B}}(\hat{\xi}_e) \hat{\mathbf{u}} \\ -\hat{\mathcal{I}}_f \hat{\mathbf{u}} \end{pmatrix}, \end{aligned}$$

with

$$\begin{aligned} \langle \hat{\psi}^u, \hat{\mathcal{T}}(\hat{\xi}_e) \hat{\mathbf{u}} \rangle &= \int_{\hat{\Omega}_f} \hat{J}(\hat{\xi}_e) \hat{\mathbf{u}} \cdot \hat{\psi}^u \, d\hat{\Omega} & \text{for } (\hat{\psi}^u, \hat{\xi}_e, \hat{\mathbf{u}}) \in \hat{\mathcal{U}}^f \times \hat{\mathcal{U}}^e \times \hat{\mathcal{U}}^f, \\ \langle \hat{\psi}^u, \hat{\mathcal{N}}(\hat{\xi}_e, \hat{\mathbf{u}}) \hat{\mathbf{w}} \rangle &= \int_{\hat{\Omega}_f} \hat{\nabla} \hat{\mathbf{u}} \hat{\Phi}(\hat{\xi}_e) \hat{\mathbf{w}} \cdot \hat{\psi}^u \, d\hat{\Omega} & \text{for } (\hat{\psi}^u, \hat{\xi}_e, \hat{\mathbf{u}}, \hat{\mathbf{w}}) \in \hat{\mathcal{U}}^f \times \hat{\mathcal{U}}^e \times \hat{\mathcal{U}}^f \times \hat{\mathcal{U}}^f, \\ \langle \hat{\psi}^u, \hat{\mathcal{D}}(\hat{\xi}_e) \hat{\mathbf{u}} \rangle &= \int_{\hat{\Omega}_f} \hat{\mathbf{D}}(\hat{\mathbf{u}}, \hat{\xi}_e) \hat{\Phi}(\hat{\xi}_e)^T : \hat{\nabla} \hat{\psi}^u \, d\hat{\Omega} & \text{for } (\hat{\psi}^u, \hat{\xi}_e, \hat{\mathbf{u}}) \in \hat{\mathcal{U}}^f \times \hat{\mathcal{U}}^e \times \hat{\mathcal{U}}^f, \\ \langle \hat{\psi}^p, \hat{\mathcal{B}}(\hat{\xi}_e) \hat{\mathbf{u}} \rangle &= \int_{\hat{\Omega}_f} \hat{\Phi}(\hat{\xi}_e)^T : \hat{\nabla} \hat{\mathbf{u}} \hat{\psi}^p \, d\hat{\Omega} & \text{for } (\hat{\psi}^p, \hat{\xi}_e, \hat{\mathbf{u}}) \in \hat{\mathcal{P}} \times \hat{\mathcal{U}}^e \times \hat{\mathcal{U}}^f, \\ \langle \hat{\psi}^\lambda, \hat{\mathcal{I}}_f \hat{\mathbf{u}} \rangle &= \int_{\hat{\Gamma}} \hat{\mathbf{u}} \cdot \hat{\psi}^\lambda \, d\hat{\Gamma} & \text{for } (\hat{\psi}^\lambda, \hat{\mathbf{u}}) \in \hat{\mathcal{U}}_{\hat{\Gamma}} \times \hat{\mathcal{U}}^f \end{aligned}$$

B.2 Linearised fluid-solid equations

Three-field formulation: for $\hat{\mathbf{q}}'_s = (\hat{\xi}', \hat{\mathbf{u}}'_s)$, $\hat{\mathbf{q}}'_e = (\hat{\xi}'_e, \hat{\lambda}'_e)$ and $\hat{\mathbf{q}}'_f = (\hat{\mathbf{u}}', \hat{p}', \hat{\lambda}')$, the three-fields formulation of the linearised ALE fluid-structure problem reads

$$\underbrace{\begin{pmatrix} \hat{\mathcal{T}}_s & 0 & 0 \\ 0 & 0 & 0 \\ 0 & -\hat{\mathcal{T}}_{fe} & \hat{\mathcal{T}}_f \end{pmatrix}}_{\hat{\mathcal{T}}_{fsi}(\hat{\mathbf{Q}})} \frac{\partial}{\partial t} \begin{pmatrix} \hat{\mathbf{q}}'_s \\ \hat{\mathbf{q}}'_e \\ \hat{\mathbf{q}}'_f \end{pmatrix} = \underbrace{\begin{pmatrix} \hat{\mathcal{J}}' & 0 & \hat{\mathcal{I}}_{fs}^T \\ \hat{\mathcal{I}}_{es} & -\hat{\mathcal{A}}_e & 0 \\ \hat{\mathcal{I}}_{fs} & \hat{\mathcal{N}}'_{fe} & \hat{\mathcal{N}}'_{ff} \end{pmatrix}}_{\hat{\mathcal{N}}'_{fsi}(\hat{\mathbf{Q}})} \begin{pmatrix} \hat{\mathbf{q}}'_s \\ \hat{\mathbf{q}}'_e \\ \hat{\mathbf{q}}'_f \end{pmatrix},$$

where all operators are evaluated on the steady variables. Without the solid velocity augmentation (only the solid displacement variable), we obtain

$$\begin{pmatrix} \hat{\mathcal{M}}_s & 0 & 0 \\ 0 & 0 & 0 \\ 0 & 0 & 0 \end{pmatrix} \frac{\partial^2}{\partial t^2} \begin{pmatrix} \hat{\xi}' \\ \hat{\mathbf{q}}'_e \\ \hat{\mathbf{q}}'_f \end{pmatrix} + \begin{pmatrix} 0 & 0 & 0 \\ 0 & 0 & 0 \\ -\hat{\mathcal{I}}_{fs} & -\hat{\mathcal{T}}_{fe} & \hat{\mathcal{T}}_f \end{pmatrix} \frac{\partial}{\partial t} \begin{pmatrix} \hat{\xi}' \\ \hat{\mathbf{q}}'_e \\ \hat{\mathbf{q}}'_f \end{pmatrix} = \begin{pmatrix} -\hat{\mathcal{K}}' & 0 & \hat{\mathcal{I}}_{fs}^T \\ \hat{\mathcal{I}}_{es} & -\hat{\mathcal{A}}_e & 0 \\ 0 & \hat{\mathcal{N}}'_{fe} & \hat{\mathcal{N}}'_{ff} \end{pmatrix} \begin{pmatrix} \hat{\xi}' \\ \hat{\mathbf{q}}'_e \\ \hat{\mathbf{q}}'_f \end{pmatrix}.$$

Linearised solid operator expression:

$$\hat{\mathcal{J}}' = \begin{pmatrix} 0 & \hat{\mathcal{M}}_s \\ -\hat{\mathcal{K}}' & 0 \end{pmatrix}$$

with

$$\left\langle \hat{\psi}_s^u, \hat{\mathcal{N}}'(\hat{\Xi}) \hat{\xi}' \right\rangle = \int_{\hat{\Omega}_s} \hat{\mathbf{P}}'(\hat{\Xi}; \hat{\xi}') : \nabla \hat{\psi}_s^u \, d\hat{\Omega} \quad \text{for } (\hat{\psi}_s^u, \hat{\xi}') \in \hat{\mathcal{U}}^s \times \hat{\mathcal{U}}^s.$$

Linearised fluid operator expression:

$$\hat{\mathcal{N}}_{\text{ff}}' = \begin{pmatrix} -\hat{\mathcal{N}}'(\hat{\Xi}_e, \hat{U}) - \frac{2}{\mathcal{R}_e} \hat{\mathcal{D}}(\hat{\Xi}_e) & \hat{\mathcal{B}}(\hat{\Xi}_e)^T & -\hat{\mathcal{I}}_f^T \\ \hat{\mathcal{B}}(\hat{\Xi}_e) & 0 & 0 \\ -\hat{\mathcal{I}}_f & 0 & 0 \end{pmatrix}$$

where the linearised bilinear advection operator reads $\hat{\mathcal{N}}'(\hat{\Xi}_e, \hat{U}) \hat{u}' = \hat{\mathcal{N}}(\hat{\Xi}_e, \hat{U}) \hat{u}' + \hat{\mathcal{N}}(\hat{\Xi}_e, \hat{u}') \hat{U}$. The shape derivative operator $\hat{\mathcal{N}}_{\text{fe}}'$ writes

$$\hat{\mathcal{N}}_{\text{fe}}' = \begin{pmatrix} -\hat{\mathcal{L}}_{\xi}'(\hat{\Xi}_e, \hat{U}, \hat{P}) - \hat{\mathcal{N}}_{\xi}'(\hat{\Xi}_e, \hat{U}) & 0 \\ \hat{\mathcal{B}}_{\xi}'(\hat{\Xi}_e, \hat{U}) & 0 \\ 0 & 0 \end{pmatrix},$$

where the different shape derivative sub-operators write

$$\begin{aligned} \left\langle \hat{\psi}^u, \hat{\mathcal{L}}_{\xi}'(\hat{\Xi}_e, \hat{U}, \hat{P}) \hat{\xi}'_e \right\rangle &= - \int_{\hat{\Omega}_f} \hat{P} \hat{\mathbf{\Phi}}'(\hat{\Xi}_e; \hat{\xi}'_e)^T : \hat{\nabla} \hat{\psi}^u \, d\hat{\Omega} \\ &\quad + \frac{2}{\mathcal{R}_e} \int_{\hat{\Omega}_f} \left[\hat{\mathbf{D}}'(\hat{U}, \hat{\Xi}_e; \hat{\xi}'_e) \hat{\mathbf{\Phi}}(\hat{\Xi}_e)^T + \hat{\mathbf{D}}(\hat{U}, \hat{\Xi}_e) \hat{\mathbf{\Phi}}'(\hat{\Xi}_e; \hat{\xi}'_e)^T \right] : \hat{\nabla} \hat{\psi}^u \, d\hat{\Omega} \quad \text{for } (\hat{\psi}^u, \hat{\xi}'_e) \in \hat{\mathcal{U}}^f \times \hat{\mathcal{U}}^e, \\ \left\langle \hat{\psi}^u, \hat{\mathcal{N}}_{\xi}'(\hat{\Xi}_e, \hat{U}) \hat{\xi}'_e \right\rangle &= \int_{\hat{\Omega}_f} \hat{\nabla} \hat{U} \hat{\mathbf{\Phi}}'(\hat{\Xi}_e; \hat{\xi}'_e) \hat{U} \cdot \hat{\psi}^u \, d\hat{\Omega} \quad \text{for } (\hat{\psi}^u, \hat{\xi}'_e) \in \hat{\mathcal{U}}^f \times \hat{\mathcal{U}}^e, \\ \left\langle \hat{\psi}^p, \hat{\mathcal{B}}_{\xi}'(\hat{\Xi}_e, \hat{U}) \hat{\xi}'_e \right\rangle &= \int_{\hat{\Omega}_f} \hat{\psi}^p \hat{\mathbf{\Phi}}'(\hat{\Xi}_e; \hat{\xi}'_e)^T : \hat{\nabla} \hat{U} \, d\hat{\Omega} \quad \text{for } (\hat{\psi}^p, \hat{\xi}'_e) \in \hat{\mathcal{P}} \times \hat{\mathcal{U}}^e. \end{aligned}$$

C

TECHNICAL FORMULAS

C.1 Transport formulas between the different configurations

We consider here two geometrical domains, a fixed (i.e. that does not evolve with time) domain $\hat{\Omega}$ and a time-dependant domain $\tilde{\Omega}_t$. They are assumed to be linked by a smooth mapping defined by the same way as in (1.1.16): for any $\hat{\mathbf{x}} \in \hat{\Omega}$,

$$\tilde{\mathbf{x}}_t = \hat{\mathcal{A}}_t(\hat{\mathbf{x}}, t) = (\text{Id} + \hat{\boldsymbol{\xi}})(\hat{\mathbf{x}}, t).$$

Given an operator acting on variables and functions $\hat{\mathbf{q}}$ defined in $\hat{\Omega}$, one want to express this operator with respect to the transported variables $\tilde{\mathbf{q}} = \hat{\mathbf{q}} \circ \hat{\mathcal{A}}_t^{-1}$ in the actual configuration $\tilde{\Omega}_t$. We use the following convention of notation: scalars are noted in lowercase roman style (q), vectors are noted in bold (\mathbf{q}) while second-order tensors are noted with uppercase bold style (\mathbf{Q}). We furthermore consider a cartesian coordinate system, so that

$$\begin{aligned} [\nabla q]_i &= \frac{\partial q}{\partial x^i} & \text{and} & & [\nabla \mathbf{q}]_{ij} &= \frac{\partial q_i}{\partial x^j}, \\ [\nabla \cdot \mathbf{q}] &= \frac{\partial q_i}{\partial x^i} & \text{and} & & [\nabla \cdot \mathbf{Q}]_i &= \frac{\partial Q_{ij}}{\partial x^j}. \end{aligned}$$

Volume and area change measures

The *Nanson's formula* (Chadwick, 1999) is an identity that relates areas in the actual configuration to areas in the reference configuration. For an infinitesimal area $d\hat{S}$ of normal $\hat{\mathbf{n}}$ in the reference configuration, their counterparts in the actual configuration are obtained with

$$\tilde{\mathbf{n}}_t d\tilde{S} = \hat{\mathbf{\Phi}}(\hat{\boldsymbol{\xi}})^T \hat{\mathbf{n}} d\hat{S}, \quad (\text{C.1.1})$$

where we recall that $\hat{\mathbf{\Phi}}(\hat{\boldsymbol{\xi}}) = \hat{J}(\hat{\boldsymbol{\xi}}) \hat{\mathbf{F}}(\hat{\boldsymbol{\xi}})^{-1}$ is the deformation operator¹, $\hat{\mathbf{F}} = \hat{\boldsymbol{\nabla}} \hat{\mathcal{A}}_t = \mathbf{I} + \hat{\boldsymbol{\nabla}} \hat{\boldsymbol{\xi}}$ is the deformation gradient and $\hat{J} = \det \hat{\mathbf{F}}$ is the Jacobian of the transformation. For 2d geometries, the deformation operator writes as follows for $\hat{\boldsymbol{\xi}} = [\hat{\xi}_x, \hat{\xi}_y]$:

$$\hat{\mathbf{\Phi}}(\hat{\boldsymbol{\xi}})^{2d} = \begin{pmatrix} 1 + \frac{\partial \hat{\xi}_y}{\partial \hat{y}} & -\frac{\partial \hat{\xi}_x}{\partial \hat{y}} \\ -\frac{\partial \hat{\xi}_y}{\partial \hat{x}} & 1 + \frac{\partial \hat{\xi}_x}{\partial \hat{x}} \end{pmatrix}.$$

In the general 3d case the expression is unfortunately much less compact. While it is does not mix components in 2d, the transformation operator does in the 3d case. Geometrically, this comes from the difference between rotations in 2d and in 3d. While 2d rotations involve only one axis

¹the transpose of this operator is sometimes referred to as the *Piola transformation*

of rotation, a general 3d rotation is the composition of two 2d rotations about different axes. The *Piola identity* (Chadwick, 1999) states that the divergence of the deformation operator is zero:

$$\hat{\nabla} \cdot \hat{\Phi}(\hat{\xi})^T = 0. \quad (\text{C.1.2})$$

From the Piola identity, an identity holding on the divergence is easily deduced,

$$\hat{\nabla} \cdot (\hat{\Phi}'(\hat{\xi})\hat{u}) = \hat{\Phi}'(\hat{\xi})^T : \hat{\nabla}\hat{u}. \quad (\text{C.1.3})$$

Another useful formula, referred to as the *Euler expansion formula* (Chadwick, 1999), relates the rate of change of the deformation Jacobian with the rate of change of the deformation field:

$$\frac{\partial \hat{J}}{\partial t} = \hat{\Phi}(\hat{\xi})^T : \hat{\nabla} \left(\frac{\partial \hat{\xi}}{\partial t} \right). \quad (\text{C.1.4})$$

An identity for the viscous dissipation in the reference configuration

The following “cosmetic” relation allows to rewrite the viscous dissipation terms of the fluid momentum equation with the following expression,

$$\hat{\mathbf{D}}(\hat{u}, \hat{\xi}_e) \hat{\Phi}(\hat{\xi}_e)^T : \hat{\nabla} \hat{u}' = \hat{J}(\hat{\xi}_e) \hat{\mathbf{D}}(\hat{u}, \hat{\xi}_e) : \hat{\mathbf{D}}(\hat{u}', \hat{\xi}_e). \quad (\text{C.1.5})$$

Proof. A direct computation gives, with $\hat{\mathbf{D}} = 1/(2\hat{J}(\hat{\xi}_e))(\hat{\nabla}\hat{u} \hat{\Phi}(\hat{\xi}_e) + \hat{\Phi}(\hat{\xi}_e)^T \hat{\nabla}\hat{u}^T)$,

$$\begin{aligned} & \hat{J}(\hat{\xi}_e) \hat{\mathbf{D}}(\hat{u}, \hat{\xi}_e) : \hat{\mathbf{D}}(\hat{u}', \hat{\xi}_e) \\ &= \frac{1}{4} \frac{1}{\hat{J}(\hat{\xi}_e)} \left(\hat{\nabla}\hat{u} \hat{\Phi}(\hat{\xi}_e) + \hat{\Phi}(\hat{\xi}_e)^T \hat{\nabla}\hat{u}^T \right) : \left(\hat{\nabla}\hat{u}' \hat{\Phi}(\hat{\xi}_e) + \hat{\Phi}(\hat{\xi}_e)^T \hat{\nabla}\hat{u}'^T \right) \\ &= \frac{1}{2} \frac{1}{\hat{J}(\hat{\xi}_e)} \left(\hat{\nabla}\hat{u} \hat{\Phi}(\hat{\xi}_e) + \hat{\Phi}(\hat{\xi}_e)^T \hat{\nabla}\hat{u}^T \right) : \left(\hat{\nabla}\hat{u}' \hat{\Phi}(\hat{\xi}_e) \right) \\ &= \frac{1}{2} \frac{1}{\hat{J}(\hat{\xi}_e)} \left(\hat{\nabla}\hat{u} \hat{\Phi}(\hat{\xi}_e) + \hat{\Phi}(\hat{\xi}_e)^T \hat{\nabla}\hat{u}^T \right) \hat{\Phi}(\hat{\xi}_e)^T : \hat{\nabla}\hat{u}' \\ &= \hat{\mathbf{D}}(\hat{u}, \hat{\xi}_e) \hat{\Phi}(\hat{\xi}_e)^T : \hat{\nabla}\hat{u}' \end{aligned}$$

□

This identity is the equivalent, in the reference domain, of the identity $\mathbf{D}(\mathbf{u}) : \mathbf{D}(\mathbf{u}) = \mathbf{D}(\mathbf{u}) : \nabla \mathbf{u}$ for $\mathbf{D}(\mathbf{u}) = 1/2 (\nabla \mathbf{u} + \nabla \mathbf{u}^T)$.

Variable change in volume and surface integrals

Let us recall two change of variable formulas (Henrot & Pierre, 2006), that are useful for writing variational formulations in one or another configuration. For sufficiently smooth fields \tilde{f} and \hat{f} , with $\hat{f} = \tilde{f} \circ \hat{\mathcal{A}}_t$ and $\tilde{\Omega}_t = \hat{\mathcal{A}}_t(\hat{\Omega})$, it holds that

$$\int_{\tilde{\Omega}_t} \tilde{f} d\tilde{\Omega}_t = \int_{\hat{\Omega}} \hat{J}(\hat{\xi}) \hat{f} d\hat{\Omega}, \quad (\text{C.1.6})$$

$$\int_{\partial \tilde{\Omega}_t} \tilde{f} d\tilde{\Gamma}_t = \int_{\partial \hat{\Omega}} \hat{J}(\hat{\xi}) \hat{f} \|\hat{\mathbf{F}}(\hat{\xi}) \hat{\mathbf{n}}\|_{\mathbb{R}^d} d\hat{\Gamma}, \quad (\text{C.1.7})$$

where $\hat{J}(\hat{\xi}) = \det(\hat{\nabla} \hat{\mathcal{A}}_t(\hat{\xi})) = \det(\mathbf{I} + \hat{\nabla} \hat{\xi}) = \det \hat{\mathbf{F}}(\hat{\xi})$ accounts for the variations of volume between the two configurations

Chain rule formulas for gradient and divergence operators

We present here the technical manipulations for transporting gradient, divergence and Laplace operators from the actual to the fixed reference configuration. All these formulas are basically obtained by applying the chain rule. The following identities hold for the gradient of a scalar and of a vector field respectively:

$$\tilde{\nabla} \tilde{q} = \hat{\mathbf{F}}(\hat{\xi})^{-\text{T}} (\hat{\nabla} \hat{q}) = \frac{1}{\hat{J}(\hat{\xi}_e)} \hat{\mathbf{F}}(\hat{\xi})^{\text{T}} (\hat{\nabla} \hat{q}) \quad (\text{C.1.8})$$

$$\tilde{\nabla} \tilde{q} = (\hat{\nabla} \hat{q}) \hat{\mathbf{F}}(\hat{\xi})^{-1} = \frac{1}{\hat{J}(\hat{\xi})} (\hat{\nabla} \hat{q}) \hat{\mathbf{F}}(\hat{\xi}) \quad (\text{C.1.9})$$

Proof. Using index notations and the chain rule, we have, noting $\hat{F}_{ij} = [\partial \tilde{x}_t / \partial \hat{x}]_{ij}$

$$[\tilde{\nabla} \tilde{q}]_i = \frac{\partial \tilde{q}}{\partial \tilde{x}^i} = \frac{\partial \hat{q}}{\partial \hat{x}^k} \frac{\partial \hat{x}^k}{\partial \tilde{x}^i} = \frac{\partial \hat{q}}{\partial \hat{x}^k} \hat{F}_{ki}^{-1} = \hat{F}_{ik}^{-\text{T}} \frac{\partial \hat{q}}{\partial \hat{x}^k}$$

from which we deduce the first identity, that can eventually be written using the deformation operator $\hat{\mathbf{F}} = \hat{J} \hat{\mathbf{F}}^{-1}$. The same path is followed to obtain the second identity,

$$[\tilde{\nabla} \tilde{q}]_{ij} = \frac{\partial \tilde{q}_i}{\partial \tilde{x}^j} = \frac{\partial \hat{q}_i}{\partial \hat{x}^k} \frac{\partial \hat{x}^k}{\partial \tilde{x}^j} = \frac{\partial \hat{q}_i}{\partial \hat{x}^k} \hat{F}_{kj}^{-1}.$$

□

By the same way, using the chain rule and the same type of indices manipulations, similar formulas are obtained for the divergence operator, namely

$$\tilde{\nabla} \cdot \tilde{q} = \frac{1}{\hat{J}(\hat{\xi})} \hat{\nabla} \hat{q} : \hat{\mathbf{F}}(\hat{\xi})^{\text{T}} = \frac{1}{\hat{J}(\hat{\xi})} \hat{\nabla} \cdot (\hat{\mathbf{F}}(\hat{\xi}) \hat{q}), \quad (\text{C.1.10})$$

$$\tilde{\nabla} \cdot \tilde{\mathbf{Q}} = \frac{1}{\hat{J}(\hat{\xi})} \hat{\nabla} \hat{\mathbf{Q}} : \hat{\mathbf{F}}(\hat{\xi})^{\text{T}} = \frac{1}{\hat{J}(\hat{\xi})} \hat{\nabla} \cdot (\hat{\mathbf{Q}} \hat{\mathbf{F}}(\hat{\xi})^{\text{T}}). \quad (\text{C.1.11})$$

The passage between the equivalent forms of the above relations are obtained using the Piola identity (C.1.2).

Linearised deformation operators

We derive here the expressions for the linearised deformation operator in the reference and steady deformed configuration. For that purpose, we use the two following properties (Chadwick, 1999): for a second-order tensor \mathbf{A} and real number ε , it holds that

$$\det(\mathbf{I} + \varepsilon \mathbf{A}) = 1 + \varepsilon \text{tr}(\mathbf{A}) + o(\varepsilon), \quad (\text{C.1.12})$$

where $\text{tr}(\mathbf{A}) = A_{ii}$ is the trace of \mathbf{A} . If ε is furthermore chosen in such a way that $\mathbf{I} + \varepsilon \mathbf{A}$ is non singular, then the inverse writes as

$$(\mathbf{I} + \varepsilon \mathbf{A})^{-1} = \mathbf{I} - \varepsilon \mathbf{A} + o(\varepsilon). \quad (\text{C.1.13})$$

Expressions in the reference configuration

We give here the derivations of the so-called *shape derivative* terms for the transformation Jacobian, the deformation operator, the viscous dissipation and the fluid stress tensor, respectively, written

for a perturbation $\hat{\xi}'_e$ about $\hat{\Xi}_e$, taken in the reference configuration:

$$\begin{aligned}\hat{J}'(\hat{\Xi}_e; \hat{\xi}'_e) &= \hat{\Phi}(\hat{\Xi}_e)^T : \hat{\nabla} \hat{\xi}'_e, \\ \hat{\Phi}'(\hat{\Xi}_e; \hat{\xi}'_e) &= \frac{1}{\hat{J}(\hat{\Xi}_e)} \left[\left(\hat{\Phi}(\hat{\Xi}_e)^T : \hat{\nabla} \hat{\xi}'_e \right) \hat{\Phi}(\hat{\Xi}_e) - \hat{\Phi}(\hat{\Xi}_e) \hat{\nabla} \hat{\xi}'_e \hat{\Phi}(\hat{\Xi}_e) \right], \\ \hat{D}'(\hat{U}, \hat{\Xi}_e; \hat{\xi}'_e) &= \frac{-1/2}{\hat{J}(\hat{\Xi}_e)^2} \left[\hat{\nabla} \hat{U} \hat{\Phi}(\hat{\Xi}_e) \hat{\nabla} \hat{\xi}'_e \hat{\Phi}(\hat{\Xi}_e) + \left(\hat{\nabla} \hat{U} \hat{\Phi}(\hat{\Xi}_e) \hat{\nabla} \hat{\xi}'_e \hat{\Phi}(\hat{\Xi}_e) \right)^T \right], \\ \hat{\Sigma}'(\hat{U}, \hat{P}, \hat{\Xi}_e; \hat{\xi}'_e) &= \hat{\sigma}(\hat{U}, \hat{P}, \hat{\Xi}_e) \hat{\Phi}'(\hat{\Xi}_e; \hat{\xi}'_e)^T + \frac{2}{\mathcal{R}_e} \hat{D}'(\hat{U}, \hat{\Xi}_e; \hat{\xi}'_e) \hat{\Phi}(\hat{\Xi}_e)^T.\end{aligned}$$

Proof. Using (C.1.12) and (C.1.13), the Taylor expansion for the Jacobian of the domain deformation writes

$$\begin{aligned}\hat{J}(\hat{\Xi}_e + \varepsilon \hat{\xi}'_e) &= \det \hat{\mathbf{F}}(\hat{\Xi}_e + \varepsilon \hat{\xi}'_e) \\ &= \det \left(\hat{\mathbf{F}}(\hat{\Xi}_e) \right) \det \left(\mathbf{I} + \varepsilon \hat{\mathbf{F}}(\hat{\Xi}_e)^{-1} \hat{\nabla} \hat{\xi}'_e \right) \\ &= \hat{J}(\hat{\Xi}_e) \left(1 + \varepsilon \operatorname{tr} \left(\hat{\mathbf{F}}(\hat{\Xi}_e)^{-1} \hat{\nabla} \hat{\xi}'_e \right) \right) + o(\varepsilon) \\ &= \hat{J}(\hat{\Xi}_e) + \varepsilon \left(\hat{\Phi}(\hat{\Xi}_e)^T : \hat{\nabla} \hat{\xi}'_e \right) + o(\varepsilon),\end{aligned}$$

where we have used the property $\operatorname{tr}(\mathbf{A}^T \mathbf{B}) = \mathbf{A} : \mathbf{B}$. The linear-order term is the tangent operator $\hat{J}'(\hat{\Xi}_e; \hat{\xi}'_e)$. We use then this identity to expand the deformation operator as follows:

$$\begin{aligned}\hat{\Phi}(\hat{\Xi}_e + \varepsilon \hat{\xi}'_e) &= \hat{J}(\hat{\Xi}_e + \varepsilon \hat{\xi}'_e) \hat{\mathbf{F}}(\hat{\Xi}_e + \varepsilon \hat{\xi}'_e)^{-1} \\ &= \hat{J}(\hat{\Xi}_e + \varepsilon \hat{\xi}'_e) \left(\mathbf{I} + \varepsilon \hat{\mathbf{F}}(\hat{\Xi}_e)^{-1} \hat{\nabla} \hat{\xi}'_e \right)^{-1} \hat{\mathbf{F}}(\hat{\Xi}_e)^{-1} \\ &= \hat{J}(\hat{\Xi}_e) \hat{\mathbf{F}}(\hat{\Xi}_e) + \varepsilon \left[\left(\hat{\Phi}(\hat{\Xi}_e)^T : \hat{\nabla} \hat{\xi}'_e \right) \hat{\mathbf{F}}(\hat{\Xi}_e)^{-1} - \hat{J}(\hat{\Xi}_e) \hat{\mathbf{F}}(\hat{\Xi}_e)^{-1} \hat{\nabla} \hat{\xi}'_e \hat{\mathbf{F}}(\hat{\Xi}_e)^{-1} \right] + o(\varepsilon) \\ &= \hat{\Phi}(\hat{\Xi}_e) + \varepsilon \frac{1}{\hat{J}(\hat{\Xi}_e)} \left[\left(\hat{\Phi}(\hat{\Xi}_e)^T : \hat{\nabla} \hat{\xi}'_e \right) \hat{\Phi}(\hat{\Xi}_e) - \hat{\Phi}(\hat{\Xi}_e) \hat{\nabla} \hat{\xi}'_e \hat{\Phi}(\hat{\Xi}_e) \right] + o(\varepsilon),\end{aligned}$$

where again the tangent, shape derivative operator $\hat{\Phi}'(\hat{\Xi}_e; \hat{\xi}'_e)$ is identified at order ε . Let us finally consider the viscous stress tensor

$$\hat{\Sigma}(\hat{U}, \hat{P}, \hat{\Xi}_e) = \left\{ -\hat{P} \mathbf{I} + \frac{1}{\mathcal{R}_e} \frac{1}{\hat{J}(\hat{\Xi}_e)} \left[\hat{\nabla} \hat{U} \hat{\Phi}(\hat{\Xi}_e) + \hat{\Phi}(\hat{\Xi}_e)^T \hat{\nabla} \hat{U}^T \right] \right\} \hat{\Phi}(\hat{\Xi}_e)^T.$$

The shape derivative of the pressure term being now clear, we focus on the viscous dissipation term,

$$\hat{D}(\hat{U}, \hat{\Xi}_e) = \frac{1}{2\hat{J}(\hat{\Xi}_e)} \left[\hat{\nabla} \hat{U} \hat{\Phi}(\hat{\Xi}_e) + \hat{\Phi}(\hat{\Xi}_e)^T \hat{\nabla} \hat{U}^T \right].$$

Using the rules for differentiating a product and using the previously established formulas, we obtain

$$\begin{aligned}\hat{D}'(\hat{U}, \hat{\Xi}_e; \hat{\xi}'_e) &= \frac{1}{2} \left\{ -\frac{\hat{J}'(\hat{\Xi}_e; \hat{\xi}'_e)}{\hat{J}(\hat{\Xi}_e)^2} \left[\hat{\nabla} \hat{U} \hat{\Phi}(\hat{\Xi}_e) + \hat{\Phi}(\hat{\Xi}_e)^T \hat{\nabla} \hat{U}^T \right] \dots \right. \\ &\quad \left. + \frac{1}{\hat{J}(\hat{\Xi}_e)} \left[\hat{\nabla} \hat{U} \hat{\Phi}'(\hat{\Xi}_e; \hat{\xi}'_e) + \hat{\Phi}'(\hat{\Xi}_e; \hat{\xi}'_e)^T \hat{\nabla} \hat{U}^T \right] \right\}.\end{aligned}$$

This expression can be further simplified. Noting that

$$-\frac{\hat{J}'(\hat{\Xi}_e; \hat{\xi}'_e)}{\hat{J}(\hat{\Xi}_e)} + \hat{\Phi}'(\hat{\Xi}_e; \hat{\xi}'_e) = -\frac{1}{\hat{J}(\hat{\Xi}_e)} \hat{\Phi}(\hat{\Xi}_e) \hat{\nabla} \hat{\xi}'_e \hat{\Phi}(\hat{\Xi}_e),$$

we finally obtain

$$\hat{\mathbf{D}}'(\hat{U}, \hat{\Xi}_e; \hat{\xi}'_e) = \frac{-1/2}{\hat{J}(\hat{\Xi}_e)^2} \left[\hat{\nabla} \hat{U} \hat{\Phi}(\hat{\Xi}_e) \hat{\nabla} \hat{\xi}'_e \hat{\Phi}(\hat{\Xi}_e) + \left(\hat{\nabla} \hat{U} \hat{\Phi}(\hat{\Xi}_e) \hat{\nabla} \hat{\xi}'_e \hat{\Phi}(\hat{\Xi}_e) \right)^T \right]$$

and from that, the shape derivative for the complete stress tensor is easily deduced. \square

Transport in the steady deformed configuration

The shape derivative operators can be recasted in the steady deformed configuration defined by $\Omega = (\text{Id} + \hat{\Xi}_e)(\hat{\Omega})$ write as follows

$$\begin{aligned} J'(\xi'_e) &= \nabla \cdot \xi'_e, \\ \Phi'(\xi'_e) &= \nabla \cdot \xi'_e \mathbf{I} - \nabla \xi'_e, \\ \mathbf{D}'(U; \xi'_e) &= -\frac{1}{2} \left(\nabla U \nabla \xi'_e + (\nabla \xi'_e)^T (\nabla U)^T \right), \\ \Sigma'(U, P; \xi'_e) &= \sigma(U, P) \Phi'(\xi'_e)^T + \frac{2}{\mathcal{R}_e} \mathbf{D}'(U; \xi'_e), \end{aligned}$$

where $\sigma(U, P) = -P \mathbf{I} + 1/\mathcal{R}_e (\nabla U + \nabla U^T)$, and are deduced from their counterparts in the stress-free reference configuration by

$$\begin{aligned} \hat{J}'(\hat{\Xi}_e; \hat{\xi}'_e) &= \hat{J}(\hat{\Xi}_e) J'(\xi'_e), \\ \hat{\Phi}'(\hat{\Xi}_e; \hat{\xi}'_e) &= \hat{\Phi}(\hat{\Xi}_e) \Phi'(\xi'_e), \\ \hat{\mathbf{D}}'(\hat{U}, \hat{\Xi}_e; \hat{\xi}'_e) &= \mathbf{D}'(U; \xi'_e) \hat{\Phi}(\hat{\Xi}_e)^T, \\ \hat{\Sigma}'(\hat{U}, \hat{P}, \hat{\Xi}_e; \hat{\xi}'_e) &= \Sigma'(U, P; \xi'_e) \hat{\Phi}(\hat{\Xi}_e)^T. \end{aligned}$$

Proof. Each gradient is transformed through the chain rule formula (C.1.9), i.e. through a multiplication by $\hat{\mathbf{F}}(\hat{\Xi}_e)$. It therefore holds that $\hat{\nabla} \hat{\xi}'_e = \nabla \xi'_e \hat{\mathbf{F}}$, $\hat{\nabla} \hat{u}' = \nabla u' \hat{\mathbf{F}}$, and $\hat{\nabla} \hat{U} = \nabla U \hat{\mathbf{F}}$. Replacing first in the expression of the deformation operator yields to

$$\begin{aligned} \hat{\Phi}'(\hat{\xi}'_e; \hat{\Xi}_e) &= \frac{1}{\hat{J}(\hat{\Xi}_e)} \left[\left(\Phi(\hat{\Xi}_e)^T : \hat{\nabla} \hat{\xi}'_e \right) \hat{\Phi}(\hat{\Xi}_e) - \hat{\Phi}(\hat{\Xi}_e) \hat{\nabla} \hat{\xi}'_e \hat{\Phi}(\hat{\Xi}_e) \right] \\ &= \left[\left(\hat{\mathbf{F}}(\hat{\Xi}_e)^{-T} : \nabla \xi'_e \hat{\mathbf{F}}(\hat{\Xi}_e) \right) \mathbf{I} - \hat{\mathbf{F}}(\hat{\Xi}_e)^{-1} \left(\nabla \xi'_e \hat{\mathbf{F}}(\hat{\Xi}_e) \right) \right] \left(\hat{J}(\hat{\Xi}_e) \hat{\mathbf{F}}(\hat{\Xi}_e)^{-1} \right) \\ &= \hat{J}(\hat{\Xi}_e) \hat{\mathbf{F}}(\hat{\Xi}_e)^{-1} \left(\text{tr}(\hat{\nabla} \hat{\xi}'_e) \mathbf{I} - \hat{\nabla} \hat{\xi}'_e \right) \\ &= \hat{\Phi}(\hat{\Xi}_e) \left(\nabla \cdot \xi'_e \mathbf{I} - \nabla \xi'_e \right) \end{aligned}$$

which is the desired relation. By the same way, still using (C.1.9) the linearised Jacobian writes as

$$\begin{aligned} \hat{J}'(\hat{\Xi}_e; \hat{\xi}'_e) &= \hat{\Phi}(\hat{\Xi}_e)^T : \hat{\nabla} \hat{\xi}'_e \\ &= \hat{J}(\hat{\Xi}_e) \hat{\Phi}(\hat{\Xi}_e)^T : \nabla \xi'_e \hat{\Phi}(\hat{\Xi}_e)^{-1} \\ &= \hat{J}(\hat{\Xi}_e) \mathbf{I} : \nabla \xi'_e \end{aligned}$$

which is the expected formula, since $\mathbf{I} : \nabla \xi'_e = \nabla \cdot \xi'_e$. The procedure is in any point the same for changing the variables in the viscous stress tensor. \square

The linearised deformation operator is again significantly different whether the geometry is 2d or 3d, namely, in a cartesian frame,

$$\hat{\Phi}'(\hat{\xi})^{2d} = \begin{pmatrix} \frac{\partial \hat{\xi}_y}{\partial \hat{y}} & -\frac{\partial \hat{\xi}_x}{\partial \hat{y}} \\ -\frac{\partial \hat{\xi}_y}{\partial \hat{x}} & \frac{\partial \hat{\xi}_x}{\partial \hat{x}} \end{pmatrix} \quad \text{and} \quad \hat{\Phi}'(\hat{\xi})^{3d} = \begin{pmatrix} \frac{\partial \hat{\xi}_y}{\partial \hat{y}} + \frac{\partial \hat{\xi}_z}{\partial \hat{z}} & -\frac{\partial \hat{\xi}_x}{\partial \hat{y}} & -\frac{\partial \hat{\xi}_x}{\partial \hat{z}} \\ -\frac{\partial \hat{\xi}_y}{\partial \hat{x}} & \frac{\partial \hat{\xi}_x}{\partial \hat{x}} + \frac{\partial \hat{\xi}_z}{\partial \hat{z}} & -\frac{\partial \hat{\xi}_y}{\partial \hat{z}} \\ -\frac{\partial \hat{\xi}_z}{\partial \hat{x}} & -\frac{\partial \hat{\xi}_z}{\partial \hat{y}} & \frac{\partial \hat{\xi}_x}{\partial \hat{x}} + \frac{\partial \hat{\xi}_y}{\partial \hat{y}} \end{pmatrix}.$$

Transport of the fluid-structure equations

Using the transport formulas derived above, it is possible to write the fluid-structure equations in one or the other configuration, either by applying the chain-rule formulas to the local equations or by changing the variables in the variational formulations. We present here the two approaches, applied to the linearised continuity equation — the way of reasoning being the same for the other equations. Namely, we have

$$\begin{aligned} \hat{\nabla} \cdot [\hat{\Phi}(\hat{\Xi}_e) \hat{u}' + \hat{\Phi}'(\hat{\Xi}_e; \hat{\xi}'_e) \hat{U}] &= 0 & \text{in } \hat{\Omega}_f, \\ \nabla \cdot u' - \nabla \cdot (\Phi'(\xi'_e) U) &= 0 & \text{in } \Omega_f = (\text{Id} + \hat{\Xi}_e)(\hat{\Omega}_f). \end{aligned}$$

The local point of view

We use the chain rule formula for the divergence and the transport formula for the deformation operator to get in the first equation

$$\begin{aligned} &\hat{\nabla} \cdot [\hat{\Phi}(\hat{\Xi}_e) \hat{u}' + \hat{\Phi}'(\hat{\Xi}_e; \hat{\xi}'_e) \hat{U}] \\ &= \hat{J}(\hat{\Xi}_e) \nabla \cdot [\hat{\Phi}(\hat{\Xi}_e)^{-1} (\hat{\Phi}(\hat{\Xi}_e) u' + \hat{\Phi}(\hat{\Xi}_e) \Phi'(\xi'_e) U)] \\ &= \hat{J}(\hat{\Xi}_e) \nabla \cdot (u' + \Phi'(\xi'_e) U), \end{aligned}$$

from which the second equation is deduced.

The variational point of view

Using (C.1.3), the variational equivalent of the continuity equation in the reference configuration writes as follows,

$$\int_{\hat{\Omega}_f} \left(\hat{\Phi}(\hat{\Xi}_e)^T : \hat{\nabla} \hat{u}' + \hat{\Phi}'(\hat{\Xi}_e; \hat{\xi}'_e)^T : \hat{\nabla} \hat{U} \right) \hat{\psi} \, d\hat{\Omega} = 0 \quad \forall \hat{\psi} \in \mathcal{L}^2(\hat{\Omega}).$$

Changing the variables in the above formula with $\psi = \hat{\psi} \circ (\text{Id} + \hat{\Xi}_e)^{-1}$, $U = \hat{U} \circ (\text{Id} + \hat{\Xi}_e)^{-1}$ and $u' = \hat{U}' \circ (\text{Id} + \hat{\Xi}_e)^{-1}$ yields to

$$\begin{aligned} &\int_{\Omega_f} \left\{ \hat{\Phi}^T : (\hat{J} \nabla u' \hat{\Phi}^{-1}) + (\hat{\Phi} \Phi'(\xi'_e))^T : (\hat{J} \nabla U \hat{\Phi}^{-1}) \right\} \psi \frac{1}{\hat{J}} \, d\Omega \\ &= \int_{\Omega_f} \left\{ \hat{\Phi}^T : (\nabla u' \hat{\Phi}^{-1}) + (\Phi'(\xi'_e)^T \hat{\Phi}^T) : (\nabla U \hat{\Phi}^{-1}) \right\} \psi \, d\Omega \\ &= \int_{\Omega_f} \left\{ (\hat{\Phi}^{-T} \hat{\Phi}) : \nabla u' + (\Phi'(\xi'_e)^T \hat{\Phi}^T \hat{\Phi}^{-T}) : (\nabla U) \right\} \psi \, d\Omega \\ &= \int_{\Omega_f} \left\{ \mathbf{I} : \nabla u' + \Phi'(\xi'_e)^T : \nabla U \right\} \psi \, d\Omega \end{aligned}$$

Eventually using that $\mathbf{I} : \nabla u' = \nabla \cdot u'$ and again (C.1.3), we have arrived to a variational formulation for the continuity equation in the steady deformed configuration.

C.2 From Lagrangian-based to Eulerian-based perturbation equations

We show here the equivalence between the two formulations of the stability equations, provided sufficiently smooth velocity, pressure and displacement fields. More precisely, using the variable decomposition (2.1.28), we derive the Eulerian-based momentum equation (2.1.29) and continuity equation (2.1.30) from the momentum and continuity equations of the Lagrangian-based linearised equations in the problem (2.1.2).

Fluid mass conservation equation

Let us consider first the continuity equation. In index notations, introducing the decomposition (2.1.28) into the linearised, Lagrangian-based continuity equation, and using the continuity equation for the stationary solution, $\nabla \cdot \mathbf{U} = 0$, we have for $i = \{1, 2, 3\}$:

$$\begin{aligned} & \nabla \cdot (\tilde{\mathbf{u}}' + \nabla \mathbf{U} \xi_e) + \nabla \mathbf{U} : \Phi'(\xi_e)^T \\ &= \frac{\partial}{\partial x^i} \left(\tilde{u}'_i + \frac{\partial U_i}{\partial x^j} \xi'_{ej} \right) + \frac{\partial U_i}{\partial x^j} \left(\frac{\partial \xi'_{ek}}{\partial x^k} \delta_{ij} - \frac{\partial \xi'_{ej}}{\partial x^i} \right) \\ &= \frac{\partial \tilde{u}'_i}{\partial x^i} + \underbrace{\frac{\partial^2 U_i}{\partial x^i \partial x^j} \xi'_{ej}}_{=0} + \frac{\partial U_i}{\partial x^j} \frac{\partial \xi'_{ej}}{\partial x^i} + \underbrace{\frac{\partial U_i}{\partial x^i} \frac{\partial \xi'_{ek}}{\partial x^k}}_{=0} - \frac{\partial U_i}{\partial x^j} \frac{\partial \xi'_{ej}}{\partial x^i} \\ &= \frac{\partial \tilde{u}'_i}{\partial x^i}. \end{aligned}$$

This last line corresponds to the Eulerian-based linearised continuity equation (2.1.30).

Fluid momentum conservation equation

We now consider the Lagrangian-based momentum equation. Injecting the Eulerian-based decomposition (2.1.28), we notice that the fluid domain velocity cancels and we obtain

$$\frac{\partial \tilde{\mathbf{u}}'}{\partial t} + \nabla \mathbf{U} \tilde{\mathbf{u}}' + \nabla \tilde{\mathbf{u}}' \mathbf{U} - \nabla \cdot \sigma(\tilde{\mathbf{u}}', \tilde{p}') + \mathbf{r}(\mathbf{U}, P, \xi'_e) = 0$$

which is the momentum stability equation written with the Eulerian decomposition, plus extra terms $\mathbf{r}(\mathbf{U}, P, \xi'_e)$ that write as

$$\begin{aligned} \mathbf{r}(\mathbf{U}, P, \xi'_e) &= \nabla \mathbf{U} \nabla \mathbf{U} \xi'_e + \nabla (\nabla \mathbf{U} \xi'_e) \mathbf{U} + \nabla \mathbf{U} \Phi'(\xi'_e) \mathbf{U} \\ &\quad - \nabla \cdot [\sigma(\nabla \mathbf{U} \xi'_e, \nabla P \cdot \xi'_e) + \Sigma'(\mathbf{U}, P, \xi'_e)]. \end{aligned}$$

We can show that these terms are actually identically zero. We first note that $\sigma(\nabla \mathbf{U} \xi'_e, \nabla P \cdot \xi'_e) = \nabla \sigma(\mathbf{U}, P) \xi'_e - 1/\mathcal{R}_e (\nabla \mathbf{U} \nabla \xi'_e + \nabla \xi'^T_e \nabla \mathbf{U}^T)$, where $\nabla \sigma(\mathbf{U}, P)$ is the third-order tensor already obtained in the interface condition in the Eulerian stability formulation. Using (2.1.21) to express $\Sigma'(\mathbf{U}, P, \xi'_e)$, we obtain

$$\begin{aligned} \mathbf{r}(\mathbf{U}, P, \xi'_e) &= \nabla \mathbf{U} \nabla \mathbf{U} \xi'_e + \nabla (\nabla \mathbf{U} \xi'_e) \mathbf{U} + \nabla \mathbf{U} \Phi'(\xi'_e) \mathbf{U} \\ &\quad - \nabla \cdot [\nabla \sigma(\mathbf{U}, P) \xi'_e + \sigma(\mathbf{U}, P) \Phi'^T(\xi'_e)]. \end{aligned}$$

Then, we use the relations $\nabla \mathbf{U} \nabla \mathbf{U} = \nabla (\nabla \mathbf{U} \mathbf{U}) - \nabla (\nabla \mathbf{U}) \mathbf{U}$ and $\nabla (\nabla \mathbf{U} \xi'_e) = \nabla (\nabla \mathbf{U}) \xi'_e + \nabla \mathbf{U} \nabla \xi'_e$ obtained by the rule of derivation of a product, and $\Phi'(\xi'_e) = \nabla \cdot \xi'_e \mathbf{I} - \nabla \xi'_e$, to transform the first line above in $\nabla \mathbf{U} \nabla \mathbf{U} \xi'_e + \nabla (\nabla \mathbf{U} \xi'_e) \mathbf{U} + \nabla \mathbf{U} \Phi'(\xi'_e) \mathbf{U} = \nabla (\nabla \mathbf{U} \mathbf{U}) + (\nabla \cdot \xi'_e) \nabla \mathbf{U} \mathbf{U}$, noting that $\nabla (\nabla \mathbf{U}) \mathbf{U} \xi'_e = \nabla (\nabla \mathbf{U}) \xi'_e \mathbf{U}$. We use the stationary equation

$$\nabla \mathbf{U} \mathbf{U} - \nabla \cdot \sigma(\mathbf{U}, P) = 0$$

to express the advection term $\nabla U U$. Finally an expression involving only the stress tensor and the extension displacement field is obtained,

$$\mathbf{r} = \nabla(\nabla \cdot \boldsymbol{\sigma}) \boldsymbol{\xi}'_e + (\nabla \cdot \boldsymbol{\xi}'_e)(\nabla \cdot \boldsymbol{\sigma}) - \nabla \cdot \left[\nabla \boldsymbol{\sigma} \boldsymbol{\xi}'_e + (\nabla \cdot \boldsymbol{\xi}'_e) \boldsymbol{\sigma} - \boldsymbol{\sigma} \nabla \boldsymbol{\xi}'_e{}^T \right],$$

where we did not precise $\mathbf{r} = \mathbf{r}(U, P, \boldsymbol{\xi}'_e)$ and $\boldsymbol{\sigma} = \boldsymbol{\sigma}(U, P)$ for conciseness. Using now index notations, we have for $i = \{1, 2, 3\}$

$$r_i = \frac{\partial}{\partial x^j} \left(\frac{\partial \sigma_{ik}}{\partial x^k} \right) \xi'_{ek} + \frac{\partial \xi'_{ek}}{\partial x^k} \frac{\partial \sigma_{ij}}{\partial x^j} - \frac{\partial}{\partial x^j} \left[\frac{\partial \sigma_{ij}}{\partial x^k} \xi'_{ek} + \frac{\partial \xi'_{ek}}{\partial x^k} \sigma_{ij} - \sigma_{ik} \frac{\partial \xi'_{ej}}{\partial x^k} \right].$$

Expanding all the derivatives involved in the expression above, we observe that the terms cancel two-by-two. As a result, we obtain

$$\mathbf{r}(U, P, \boldsymbol{\xi}'_e) = 0.$$

By the same type of operations, it is possible to show that the interface conditions are equivalent as well.

C.3 Lagrange identities for adjoint ALE equations

In this section, the formulas used to derive the adjoint linearised fluid-structure problem are derived. All the derivations are performed for convenience in the steady deformed configuration. The formulas derived in section C.1 allow to express these identities in other configurations.

Self-adjointness of the linearised STVK stress

We establish in this section a Lagrange identity for the linearised stress in the perturbation elasticity equation written in the steady deformed configuration. In the steady deformed configuration, integrating twice by parts the linearised Saint-Venant Kirchhoff stress (2.1.6), it holds that whatever \mathbf{u}_s^\dagger and $\boldsymbol{\xi}'$ that

$$\begin{aligned} \int_{\Omega_s} \left(\nabla \cdot \mathbf{P}'(\boldsymbol{\Xi}; \boldsymbol{\xi}') \right) \cdot \mathbf{u}_s^\dagger d\Omega &= \int_{\Omega_s} \left(\nabla \cdot \hat{\mathbf{P}}'(\boldsymbol{\Xi}; \mathbf{u}_s^\dagger) \right) \cdot \boldsymbol{\xi}' d\Omega \dots \\ &+ \int_{\partial\Omega_s} \left(\mathbf{P}'(\boldsymbol{\Xi}; \boldsymbol{\xi}') \mathbf{n}_s \cdot \mathbf{u}_s^\dagger - \mathbf{P}'(\boldsymbol{\Xi}; \mathbf{u}_s^\dagger) \mathbf{n}_s \cdot \boldsymbol{\xi}' \right) d\Gamma. \end{aligned} \quad (\text{C.3.1})$$

Proof. The formula written above holds provided that the algebraic identity (used after integration by parts)

$$\mathbf{P}'(\boldsymbol{\Xi}; \boldsymbol{\xi}') : \nabla \mathbf{u}_s^\dagger = \mathbf{P}'(\boldsymbol{\Xi}; \mathbf{u}_s^\dagger) : \nabla \boldsymbol{\xi}'$$

holds, that we shall prove now. From (2.1.16) the linearised first Piola-Kirchhoff stress is split between its two components, namely

$$\hat{\mathbf{P}}'(\boldsymbol{\Xi}; \boldsymbol{\xi}') : \nabla \mathbf{u}_s^\dagger = \frac{1}{J(\boldsymbol{\Xi})} \left\{ \nabla \boldsymbol{\xi}' \mathbf{F}(\boldsymbol{\Xi}) \mathbf{S}(\boldsymbol{\Xi}) + \mathbf{F}(\boldsymbol{\Xi}) \mathbf{S}'(\boldsymbol{\xi}'; \boldsymbol{\Xi}) \right\} \mathbf{F}(\boldsymbol{\Xi})^T : \nabla \mathbf{u}_s^\dagger.$$

For the first term, using the symmetry of the tensor $(\mathbf{F} \mathbf{S} \mathbf{F}^T)(\boldsymbol{\Xi})$, it is easy to show that $\nabla \boldsymbol{\xi}' \mathbf{F} \mathbf{S} \mathbf{F}^T : \nabla \mathbf{u}_s^\dagger = \nabla \mathbf{u}_s^\dagger \mathbf{F} \mathbf{S} \mathbf{F}^T : \nabla \boldsymbol{\xi}'$ — for conciseness of the notations, we will omit in the following to systematically write the dependency of the different tensors on the steady deformation $\boldsymbol{\Xi}$. For the second term, we further decompose \mathbf{S}' using (2.1.7) and (2.1.8). Then, still using manipulations on the trace operator (recall that $\mathbf{A} : \mathbf{B} = A_{ij} B_{ij}$), we get

$$\begin{aligned} &\mathbf{F} \mathbf{S}'(\boldsymbol{\xi}') \mathbf{F}^T : \nabla \mathbf{u}_s^\dagger \\ &= \mathbf{F} \left\{ \lambda_s \text{tr}(\mathbf{E}'(\boldsymbol{\xi}')) \mathbf{I} + 2\mu_s \mathbf{E}'(\boldsymbol{\xi}') \right\} \mathbf{F}^T : \nabla \mathbf{u}_s^\dagger \end{aligned}$$

$$\begin{aligned}
&= \mathbf{F} \left\{ \frac{\lambda_s}{2} \operatorname{tr} \left(\mathbf{F}^T \left(\nabla \boldsymbol{\xi}' + \nabla \boldsymbol{\xi}'^T \right) \mathbf{F} \right) \mathbf{I} + \mu_s \mathbf{F}^T \left(\nabla \boldsymbol{\xi}' + \nabla \boldsymbol{\xi}'^T \right) \mathbf{F} \right\} \mathbf{F}^T : \nabla \mathbf{u}_s^\dagger \\
&= \frac{\lambda_s}{2} \operatorname{tr} \left(\mathbf{F}^T \left(\nabla \boldsymbol{\xi}' + \nabla \boldsymbol{\xi}'^T \right) \mathbf{F} \right) (\mathbf{F} \mathbf{F}^T : \nabla \mathbf{u}^\dagger) + \mu_s \mathbf{F} \mathbf{F}^T \left(\nabla \boldsymbol{\xi}' + \nabla \boldsymbol{\xi}'^T \right) \mathbf{F} \mathbf{F}^T : \nabla \mathbf{u}_s^\dagger \\
&= \lambda_s (\mathbf{F} \mathbf{F}^T : \nabla \boldsymbol{\xi}') (\mathbf{F} \mathbf{F}^T : \nabla \mathbf{u}_s^\dagger) + \mu_s \left[\mathbf{F} \mathbf{F}^T \left(\nabla \boldsymbol{\xi}' + \nabla \boldsymbol{\xi}'^T \right) \right] : \left[\mathbf{F} \mathbf{F}^T \left(\nabla \mathbf{u}_s^\dagger + \nabla \mathbf{u}_s^{\dagger T} \right) \right].
\end{aligned}$$

From the symmetry in the last line, we are easily convinced that the positions of $\boldsymbol{\xi}'$ and \mathbf{u}_s^\dagger can be switched, i.e. that $\mathbf{F} \mathbf{S}'(\boldsymbol{\xi}') \mathbf{F}^T : \nabla \mathbf{u}_s^\dagger = \mathbf{F} \mathbf{S}'(\mathbf{u}_s^\dagger) \mathbf{F}^T : \nabla \boldsymbol{\xi}'$. \square

The above relation shows in particular that the linearised solid stress operator is self-adjoint, for \mathbf{u}_s^\dagger and $\boldsymbol{\xi}'$ can be switched without changing the structure of the operator.

Self-adjointness of the Stokes operator

Using integration by parts, one can easily show (Luchini & Bottaro, 2014a) that the Stokes operator is self-adjoint. Whatever (\mathbf{u}', p') and $(\mathbf{u}^\dagger, p^\dagger)$, the following relation holds, with $\boldsymbol{\sigma}(\mathbf{u}, p) = -p \mathbf{I} + 1/\mathcal{R}_e (\nabla \mathbf{u} + \nabla \mathbf{u}^T)$:

$$\begin{aligned}
&\int_{\Omega_f} \left\{ \nabla \cdot \boldsymbol{\sigma}(\mathbf{u}', p') \cdot \mathbf{u}^\dagger + \nabla \cdot \mathbf{u}' p^\dagger \right\} d\Omega \dots \\
&= \int_{\Omega_f} \left\{ \nabla \cdot \boldsymbol{\sigma}(\mathbf{u}^\dagger, p^\dagger) \cdot \mathbf{u}' + \nabla \cdot \mathbf{u}^\dagger p' \right\} d\Omega \\
&+ \int_{\partial\Omega_f} (\boldsymbol{\sigma}(\mathbf{u}', p') \mathbf{n}_f \cdot \mathbf{u}^\dagger - \boldsymbol{\sigma}(\mathbf{u}^\dagger, p^\dagger) \mathbf{n}_f \cdot \mathbf{u}') d\Omega.
\end{aligned} \tag{C.3.2}$$

Note that the self-adjointness property is obtained only when the term $\nabla \cdot \mathbf{u}'$ in the above relation, coming from the continuity equation, is taken with a positive sign. Otherwise, the adjoint Stokes operator has an opposite sign in the adjoint continuity equation.

Adjoint of the linearized Navier-Stokes advection

It is well-known that the linearised Navier-Stokes equations are *not* self-adjoint (Luchini & Bottaro, 2014a), because of the advection term: if the diffusion/pressure terms can be transposed by still keeping the same structure (see §C.3), it is not the case of the advection terms. Namely, considering a smooth, divergence-free velocity field \mathbf{U} in the steady deformed configuration, for sufficiently smooth fields \mathbf{u}' and \mathbf{u}^\dagger we have the relation

$$\begin{aligned}
&\int_{\Omega_f} \left\{ \nabla \mathbf{U} \mathbf{u}' + \nabla \mathbf{u}' \mathbf{U} \right\} \cdot \mathbf{u}^\dagger d\Omega \dots \\
&= \int_{\Omega_f} \left\{ \nabla \mathbf{U}^T \mathbf{u}^\dagger - \nabla \mathbf{u}^\dagger \mathbf{U} \right\} \cdot \mathbf{u}' d\Omega + \int_{\partial\Omega_f} (\mathbf{U} \cdot \mathbf{n}_f) (\mathbf{u}' \cdot \mathbf{u}^\dagger) d\Gamma.
\end{aligned} \tag{C.3.3}$$

Its derivation can be found for instance in the Appendix of the paper by Luchini & Bottaro (2014a), and relies on an integration by parts and indices manipulation.

Adjoint for the shape derivatives terms

In the linearised ALE framework, non-standard adjoint terms arise from the presence of the shape derivatives terms. In the following, we establish the formulas used to derive these terms of sensitivity with respect to a variation of the domain.

Advection term

A first formula is related to the shape derivative term that appears in the advection term of the linearised Navier-Stokes equations. Considering a smooth velocity field \mathbf{u} such that $\nabla \cdot \mathbf{U} = 0$ in Ω_f , it holds that, whatever ξ'_e and \mathbf{u}^\dagger ,

$$\begin{aligned} \int_{\Omega_f} \nabla \mathbf{U} \Phi'(\xi'_e) \mathbf{U} \cdot \mathbf{u}^\dagger \, d\Omega &= \int_{\partial\Omega_f} \nabla \mathbf{U} [\mathbf{U} (\xi'_e \cdot \mathbf{n}_f) - \xi'_e (\mathbf{U} \cdot \mathbf{n}_f)] \cdot \mathbf{u}^\dagger \, d\Gamma \dots \\ &- \int_{\Omega_f} \left\{ \nabla \mathbf{U}^T (\nabla \mathbf{U}^T \mathbf{u}^\dagger - \nabla \mathbf{u}^\dagger \mathbf{U}) + (\nabla \mathbf{u}^\dagger)^T \nabla \mathbf{U} \mathbf{U} \right\} \cdot \xi'_e \, d\Omega. \end{aligned} \quad (\text{C.3.4})$$

Proof. Using (2.1.19), the deformation operator is written explicitly. Then using index notations and, since there is no ambiguity, omitting the subscript identifying the domain, we get

$$\begin{aligned} &\int_{\Omega_f} \nabla \mathbf{U} \Phi'(\xi'_e) \mathbf{U} \cdot \mathbf{u}^\dagger \, d\Omega \dots \\ &= \int_{\Omega_f} \frac{\partial U_i}{\partial x^k} \left(\frac{\partial \xi'_l}{\partial x^l} \delta_{kj} - \frac{\partial \xi'_k}{\partial x^j} \right) U_j u_i^\dagger \, d\Omega \\ &= \int_{\Omega_f} \left\{ \left(\frac{\partial U_k}{\partial x^j} U_j u_k^\dagger \right) \frac{\partial \xi'_i}{\partial x^i} - \left(\frac{\partial U_k}{\partial x^i} U_j u_k^\dagger \right) \frac{\partial \xi'_i}{\partial x^j} \right\} \, d\Omega \\ &\stackrel{\text{i.b.p.}}{=} \int_{\partial\Omega_f} \left(\frac{\partial U_k}{\partial x^j} n_i - \frac{\partial U_k}{\partial x^i} n_j \right) U_j u_k^\dagger \xi'_i \, d\Gamma \dots \\ &\quad - \int_{\Omega_f} \left\{ \frac{\partial U_k}{\partial x^j} \frac{\partial U_j}{\partial x^i} u_k^\dagger + \frac{\partial U_k}{\partial x^j} \frac{\partial u_k^\dagger}{\partial x^i} U_j - \frac{\partial U_k}{\partial x^i} \frac{\partial U_j}{\partial x^j} u_k^\dagger - \frac{\partial U_k}{\partial x^i} \frac{\partial u_k^\dagger}{\partial x^j} U_j \right\} \xi'_i \, d\Omega. \end{aligned}$$

Using the incompressibility condition $\partial_j U_j = 0$ to simplify this expression, we arrive to the expected formula by identifying back the operators. \square

Diffusion-pressure term

Let us now consider the identity used for handling the shape derivative terms of the viscous stress tensor and incompressibility condition in the linearised ALE equations. Considering a smooth velocity field \mathbf{U} and a pressure field P , it holds that, whatever ξ'_e , \mathbf{u}^\dagger and p^\dagger ,

$$\begin{aligned} &\int_{\Omega_f} \left\{ \nabla \cdot \Sigma'(U, P; \xi'_e) \cdot \mathbf{u}^\dagger + \Phi'(\xi'_e)^T : \nabla \mathbf{U} p^\dagger \right\} d\Omega = \dots \\ &\int_{\Omega_f} \nabla \cdot \Sigma^\dagger(U, P, \mathbf{u}^\dagger, p^\dagger) \cdot \xi'_e \, d\Omega - \int_{\partial\Omega_f} \Sigma^\dagger(U, P, \mathbf{u}^\dagger, p^\dagger) \mathbf{n}_f \cdot \xi'_e \, d\Gamma \dots \\ &+ \int_{\partial\Omega_f} \Sigma'(U, P; \xi'_e) \mathbf{n}_f \cdot \mathbf{u}^\dagger \, d\Gamma, \text{ with} \\ &\Sigma^\dagger(U, P, \mathbf{u}^\dagger, p^\dagger) = - \left(P \Phi'(\mathbf{u}^\dagger)^T + P^\dagger \Phi'(U)^T \right) \dots \\ &\quad + \frac{2}{\mathcal{R}_e} \left\{ - \left((\nabla \mathbf{u}^\dagger)^T \mathbf{D}(U) + (\nabla U)^T \mathbf{D}(\mathbf{u}^\dagger) \right) + \left(\mathbf{D}(U) : \mathbf{D}(\mathbf{u}^\dagger) \right) \mathbf{I} \right\} \end{aligned} \quad (\text{C.3.5})$$

Proof. The formula is obtained by integration by parts and then algebraic manipulations. Recall that we have $\Sigma'(U, P; \xi'_e) = \sigma(U, P) \Phi'(\xi'_e)^T - 1/\mathcal{R}_e (\nabla \mathbf{U} \nabla \xi'_e + (\nabla \xi'_e)^T (\nabla \mathbf{U})^T)$. Integrating by parts, we obtain

$$\begin{aligned} &\int_{\Omega_f} \left\{ \nabla \cdot \Sigma'(U, P; \xi'_e) \cdot \mathbf{u}^\dagger + \Phi'(\xi'_e)^T : \nabla \mathbf{U} p^\dagger \right\} d\Omega = \int_{\partial\Omega_f} \Sigma'(U, P; \xi'_e) \mathbf{n}_f \cdot \mathbf{u}^\dagger \, d\Gamma \dots \\ &+ \int_{\Omega_f} \left\{ - \Sigma'(U, P; \xi'_e) : \nabla \mathbf{u}^\dagger + \Phi'(\xi'_e)^T : \nabla \mathbf{U} p^\dagger \right\} d\Omega. \end{aligned}$$

Three algebraic identities are then used to exchange the position of the direct and adjoint variables, namely

$$\begin{aligned} (\nabla U \nabla \xi + (\nabla \xi)^T (\nabla U)^T) : \nabla u &= \nabla U^T (\nabla u + \nabla u^T) : \nabla \xi, \\ \Phi'(\xi)^T : \nabla u &= \Phi'(u)^T : \nabla \xi, \\ \mathbf{A} \Phi'(\xi)^T : \nabla u &= \left[(\mathbf{A} : \nabla u) \mathbf{I} - (\nabla u)^T \mathbf{A} \right] : \nabla \xi. \end{aligned}$$

The first and second identities are derived by simple manipulations on the “:” operator. The last one (where \mathbf{A} is an arbitrary second-order tensor) is less straightforward to figure out but can be checked by term-by-term identification. These identities gives allows in particular to write

$$-\Sigma'(U, P; \xi'_e) : \nabla u^\dagger + \Phi'(\xi'_e)^T : \nabla U p^\dagger = -\Sigma^\dagger(U, P, u^\dagger, p^\dagger) : \nabla \xi'_e.$$

Replacing in the above expression and integrating again by parts gives the expected result. \square

D

DERIVATION OF THE FLUID-ELASTIC SHAPE GRADIENT

We give here a sketch of the proof for the formula (4.3.19) that give the shape gradient, as well as the related equations. The derivation presented here gives hopefully also some keys for computing the shape gradient on a flexible surface.

D.1 Lagrangian formulation with C  a’s method

We use the Lagrangian approach proposed by C  a (1986) to derive the fluid-elastic shape gradient. Two groups of *adjoint variables* $\hat{\mathbf{Q}}^\dagger$ and $\hat{\mathbf{q}}^\dagger$ are introduced. These additional variables are Lagrange multipliers used to enforce the state equations (4.2.3) and (4.2.4). Using the expressions for the variational formulations (1.1.35), (2.1.4) and (1.1.36), the following Lagrangian function for the shape optimization problem is introduced — Eq. (4.3.3),

$$\begin{aligned} \mathcal{L}(\hat{\Omega}, \hat{\mathbf{Q}}, \hat{\mathbf{Q}}^\dagger, \hat{\mathbf{q}}^\circ, \hat{\mathbf{q}}^\dagger, \lambda^r, \lambda^i) = & \lambda \\ & - \langle \hat{\mathbf{Q}}^\dagger, -\hat{\mathcal{N}}_{\text{fsi}}(\hat{\mathbf{Q}}) \rangle \\ & - \langle \hat{\mathbf{q}}^\dagger, (\lambda \hat{\mathcal{T}}_{\text{fsi}}(\hat{\mathbf{Q}}) - \hat{\mathcal{N}}'_{\text{fsi}}(\hat{\mathbf{Q}})) \hat{\mathbf{q}}^\circ \rangle. \end{aligned}$$

The real-valued state and adjoint variables corresponding to the stationary part are

$$\hat{\mathbf{Q}} = [\hat{\mathbf{U}}_s = \mathbf{0}, \hat{\mathbf{\Xi}}, \hat{\mathbf{\Xi}}_e, \hat{\mathbf{\Lambda}}_e, \hat{\mathbf{U}}, \hat{\mathbf{P}}, \hat{\mathbf{\Lambda}}]^\text{T} \quad \text{and} \quad \hat{\mathbf{Q}}^\dagger = [\hat{\mathbf{U}}_s^\dagger, \hat{\mathbf{\Xi}}^\dagger, \hat{\mathbf{\Xi}}_e^\dagger, \hat{\mathbf{\Lambda}}_e^\dagger, \hat{\mathbf{U}}^\dagger, \hat{\mathbf{P}}^\dagger, \hat{\mathbf{\Lambda}}^\dagger]^\text{T},$$

where $[\hat{\mathbf{U}}_s, \hat{\mathbf{\Xi}}]$ is the solid variable (velocity and displacement), $[\hat{\mathbf{\Xi}}_e, \hat{\mathbf{\Lambda}}_e]$ is the extension variable and $[\hat{\mathbf{U}}, \hat{\mathbf{P}}, \hat{\mathbf{\Lambda}}]$ is the fluid variable. Recall that following Babuřka (1973), $\hat{\mathbf{\Lambda}}_e$ and $\hat{\mathbf{\Lambda}}$ are additional variables associated to the interface Lagrange multipliers $\hat{\mathbf{\Lambda}}_e^\dagger$ and $\hat{\mathbf{\Lambda}}^\dagger$ introduced to enforce the Dirichlet interface conditions. Note that by “interface” we mean here $\Gamma_{\text{rgd}} \cup \hat{\Gamma}$, that is, the interface with the rigid cylinder plus the flexible, fluid-elastic interface.

Remark. In C  a’s approach, this weak formulation of Dirichlet boundary conditions is actually mandatory for the variables in the Lagrangian function to be truly independent (Allaire & Schoenauer, 2007). If Dirichlet boundary conditions on Γ_{rgd} were to be embedded into some functional space defined on $\hat{\Omega}$, then by construction they would depend on the domain $\hat{\Omega}$ that itself is a variable of the problem. In this case, the variables are no longer independent.

By the same way, the complex-valued direct and adjoint eigenmodes corresponding to the unsteady part are written as

$$\hat{\mathbf{q}}^\circ = [\hat{\mathbf{u}}_s^\circ, \hat{\mathbf{\xi}}^\circ, \hat{\mathbf{\xi}}_e^\circ, \hat{\mathbf{\lambda}}_e^\circ, \hat{\mathbf{u}}^\circ, \hat{\mathbf{p}}^\circ, \hat{\mathbf{\lambda}}^\circ]^\text{T} \quad \text{and} \quad \hat{\mathbf{q}}^\dagger = [\hat{\mathbf{u}}_s^\dagger, \hat{\mathbf{\xi}}^\dagger, \hat{\mathbf{\xi}}_e^\dagger, \hat{\mathbf{\lambda}}_e^\dagger, \hat{\mathbf{u}}^\dagger, \hat{\mathbf{p}}^\dagger, \hat{\mathbf{\lambda}}^\dagger]^\text{T}$$

where the same sub-decomposition as above between the solid, extension and fluid parts holds.

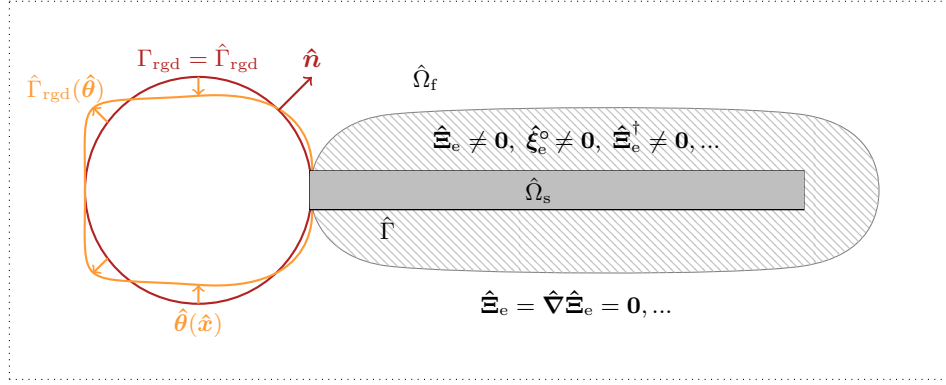


Figure D.1 – Physical domain and extension domain. All extension displacements as well as their derivatives are assumed to be zero outside from the hatched region.

In the above notation, the problem is written in the reference domain, but for convenience we will sometimes recast it (or parts of it) in the steady deformed domain. Noting $\Omega_f = (\text{Id} + \hat{\Xi}_e)(\hat{\Omega}_f)$ the steady deformed domain, we introduce for that purpose the transported variables

$$\begin{aligned} Q &= \hat{Q} \circ (\text{Id} + \hat{\Xi})^{-1} \\ Q^\dagger &= \hat{Q}^\dagger \circ (\text{Id} + \hat{\Xi})^{-1} \\ q^\circ &= \hat{q}^\circ \circ (\text{Id} + \hat{\Xi})^{-1} \\ q^\dagger &= \hat{q}^\dagger \circ (\text{Id} + \hat{\Xi})^{-1} \end{aligned}$$

The introduction of these transported variables is convenient, for it allows to write the volume integrals arising from the fluid momentum and continuity equations with a simpler expression (an expression in the stress-free reference configuration would have involved the stationary displacement $\hat{\Xi}_e$ in each gradient, see §2.1.2).

We assume here that the extension displacements (both steady, unsteady, adjoint steady and adjoint unsteady) are non-zero only in some sub-region of $\hat{\Omega}_f$ that encloses the solid, as represented (hatched region) in the Fig. D.1. Outside from this region, the displacements are assumed to be zero, as well as the displacement derivatives. The extension region can indeed be defined only in the region where the solid actually deforms. This allows to obtain a simpler expression for the gradient computed on the **rigid** boundary Γ_{rgd} , because all the terms related to the ALE geometric transformation then vanish. For conciseness of the presentation, we do not distinguish between these two regions, but the reader should keep in mind that the displacement fields as well as their gradients are identically zero outside from the hatched region.

As detailed in §4.3.1, once the Lagrangian is formed with independent variables, its variations with the different variables give the different equations needed for computing the shape gradient, namely:

$$\begin{aligned} \mathcal{L}'_{\hat{Q}^\dagger}(\delta \hat{Q}^\dagger) &= 0 & \forall \delta \hat{Q}^\dagger & \quad (\text{non-linear stationary equation}), \\ \mathcal{L}'_{\hat{Q}}(\delta \hat{Q}) &= 0 & \forall \delta \hat{Q} & \quad (\text{linear stationary adjoint equation}), \\ \mathcal{L}'_{\hat{q}^\dagger}(\delta \hat{q}^\dagger) &= 0 & \forall \delta \hat{q}^\dagger & \quad (\text{direct eigenvalue problem}), \\ \mathcal{L}'_{\hat{q}^\circ}(\delta \hat{q}^\circ) &= 0 & \forall \delta \hat{q}^\circ & \quad (\text{adjoint eigenvalue problem}), \\ \mathcal{L}'_\lambda(\delta \lambda) &= 0 & \forall \delta \lambda & \quad (\text{direct/adjoint modes normalization}), \\ \mathcal{L}'_{\hat{\Omega}}(\delta \hat{\Omega}) &= \lambda'(\hat{\Omega})(\hat{\theta}) & & \quad (\text{shape sensitivity of } \lambda). \end{aligned}$$

Non-linear stationary problem

Varying the Lagrangian function with respect to the adjoint stationary variable and looking for zero solutions gives the variational problem $\langle \delta \hat{\mathbf{Q}}^\dagger, -\hat{\mathcal{N}}_{\text{fsi}}(\hat{\mathbf{Q}}^\dagger) \rangle = 0$ whatever the variation $\delta \hat{\mathbf{Q}}^\dagger$. From (1.1.36), we have

$$\begin{aligned} \langle \delta \hat{\mathbf{Q}}^\dagger, -\hat{\mathcal{N}}_{\text{fsi}}(\hat{\mathbf{Q}}^\dagger) \rangle &= \int_{\hat{\Omega}_s} \left\{ \hat{\mathbf{P}}(\hat{\boldsymbol{\Xi}}) : \hat{\boldsymbol{\nabla}}(\delta \hat{\mathbf{U}}_s^\dagger)^* - \hat{\mathbf{U}}_s \cdot (\delta \hat{\boldsymbol{\Xi}}^\dagger)^* \right\} d\hat{\Omega} \\ &\quad + \int_{\hat{\Omega}_f} \left\{ \hat{\boldsymbol{\Sigma}}_e(\hat{\boldsymbol{\Xi}}_e) : \hat{\boldsymbol{\nabla}}(\delta \hat{\boldsymbol{\Xi}}_e^\dagger)^* \right\} d\hat{\Omega} \\ &\quad + \int_{\hat{\Omega}_f} \left\{ (\hat{\boldsymbol{\nabla}}\hat{\mathbf{U}})\hat{\boldsymbol{\Phi}}(\hat{\boldsymbol{\Xi}}_e)\hat{\mathbf{U}} \cdot (\delta \hat{\mathbf{U}}^\dagger)^* + \frac{2}{\mathcal{R}_e} \hat{\mathbf{D}}(\hat{\mathbf{U}}, \hat{\boldsymbol{\Xi}}_e) \hat{\boldsymbol{\Phi}}(\hat{\boldsymbol{\Xi}}_e)^T : \hat{\boldsymbol{\nabla}}(\delta \hat{\mathbf{U}}^\dagger)^* \right\} d\hat{\Omega} \\ &\quad - \int_{\hat{\Omega}_f} \left\{ \hat{\boldsymbol{\Phi}}(\hat{\boldsymbol{\Xi}}_e)^T : \left(\hat{P} \hat{\boldsymbol{\nabla}}(\delta \hat{\mathbf{U}}^\dagger)^* + \delta \hat{P}^\dagger (\hat{\boldsymbol{\nabla}}\hat{\mathbf{U}})^* \right) \right\} d\hat{\Omega} \\ &\quad + \int_{\hat{\Gamma}} \left\{ \hat{\boldsymbol{\Lambda}} \cdot (\delta \hat{\mathbf{U}}^\dagger - \delta \hat{\mathbf{U}}_s^\dagger)^* + \hat{\mathbf{U}} \cdot (\delta \hat{\boldsymbol{\Lambda}}^\dagger)^* + \hat{\boldsymbol{\Lambda}}_e \cdot (\delta \hat{\boldsymbol{\Xi}}_e^\dagger)^* + (\hat{\boldsymbol{\Xi}}_e - \hat{\boldsymbol{\Xi}}) \cdot (\delta \hat{\boldsymbol{\Lambda}}_e^\dagger)^* \right\} d\hat{\Gamma} \\ &\quad + \int_{\Gamma_{\text{rgd}}} \left\{ \hat{\boldsymbol{\Lambda}} \cdot (\delta \hat{\mathbf{U}}^\dagger)^* + \hat{\mathbf{U}} \cdot (\delta \hat{\boldsymbol{\Lambda}}^\dagger)^* \right\} d\hat{\Gamma} \end{aligned}$$

Using integration by parts in the above relation and requiring that the resulting integral vanish gives the steady fluid-structure equilibrium equations already introduced in §2.1.1, and the associated boundary conditions. This non-linear problem, once solved, gives an expression for the steady flow $\hat{\mathbf{Q}}$, and writes as follows (Eq. (4.3.4)):

$$\begin{aligned} -\hat{\boldsymbol{\nabla}} \cdot \hat{\mathbf{P}}(\hat{\boldsymbol{\Xi}}) &= \mathbf{0} && \text{in } \hat{\Omega}_s, \\ -\hat{\boldsymbol{\nabla}} \cdot \hat{\boldsymbol{\Sigma}}_e(\hat{\boldsymbol{\Xi}}_e) &= \mathbf{0} && \text{in } \hat{\Omega}_f, \\ (\hat{\boldsymbol{\nabla}}\hat{\mathbf{U}})\hat{\mathbf{U}} - \hat{\boldsymbol{\nabla}} \cdot \hat{\boldsymbol{\Sigma}}(\hat{\mathbf{U}}, \hat{P}, \hat{\boldsymbol{\Xi}}_e) &= \mathbf{0} && \text{in } \hat{\Omega}_f, \\ -\hat{\boldsymbol{\nabla}} \cdot (\hat{\boldsymbol{\Phi}}(\hat{\boldsymbol{\Xi}}_e)\hat{\mathbf{U}}) &= \mathbf{0} && \text{in } \hat{\Omega}_f, \\ \hat{\mathbf{U}} &= \mathbf{0} && \text{on } \hat{\Gamma} \cup \Gamma_{\text{rgd}}, \\ \hat{\boldsymbol{\Xi}} - \hat{\boldsymbol{\Xi}}_e &= \mathbf{0} && \text{on } \hat{\Gamma}, \\ \hat{\mathbf{P}}(\hat{\boldsymbol{\Xi}})\hat{\mathbf{n}} - \hat{\boldsymbol{\Sigma}}(\hat{\mathbf{U}}, \hat{P}, \hat{\boldsymbol{\Xi}}_e)\hat{\mathbf{n}} &= \mathbf{0} && \text{on } \hat{\Gamma}. \end{aligned}$$

These equations are completed with fluid-solid interface conditions on $\hat{\Gamma}$, namely $\hat{\mathbf{U}} = \mathbf{0}$ (no-slip velocity), $\hat{\boldsymbol{\Xi}} - \hat{\boldsymbol{\Xi}}_e = \mathbf{0}$ (displacement continuity) and $\hat{\mathbf{P}}(\hat{\boldsymbol{\Xi}})\hat{\mathbf{n}} = \hat{\boldsymbol{\Sigma}}(\hat{\mathbf{U}}, \hat{P}, \hat{\boldsymbol{\Xi}}_e)\hat{\mathbf{n}}$ (stress continuity). The (fixed) farfield boundary Γ_∞ is composed of an inflow boundary Γ_{in} , an outflow boundary Γ_{out} and lateral boundaries Γ_{lat} . We take the inflow condition $\hat{\mathbf{U}} = \mathbf{u}_\infty$ on Γ_{in} , the outflow condition $\hat{\boldsymbol{\Sigma}}(\hat{\mathbf{U}}, \hat{P}, \hat{\boldsymbol{\Xi}}_e = \mathbf{0})\hat{\mathbf{n}} = \mathbf{0}$ on Γ_{out} , the zero extension displacement $\hat{\boldsymbol{\Xi}}_e = \mathbf{0}$ on $\partial\hat{\Omega}_f \setminus (\hat{\Gamma} \cup \Gamma_{\text{rgd}})$ and solid displacement $\hat{\boldsymbol{\Xi}} = \mathbf{0}$ on $\partial\hat{\Omega}_s \setminus \hat{\Gamma}$, and a zero normal velocity condition on the lateral boundary Γ_{lat} . On the rigid boundary Γ_{rgd} , the no-slip velocity condition $\hat{\mathbf{U}} = \mathbf{0}$ is enforced. Recall that the interface Lagrange multipliers on $\hat{\Gamma}$ take the following expression,

$$\hat{\boldsymbol{\Lambda}} = \hat{\mathbf{P}}(\hat{\boldsymbol{\Xi}})\hat{\mathbf{n}} = \hat{\boldsymbol{\Sigma}}(\hat{\mathbf{U}}, \hat{P}, \hat{\boldsymbol{\Xi}}_e)\hat{\mathbf{n}} \quad \text{and} \quad \hat{\boldsymbol{\Lambda}}_e = \hat{\boldsymbol{\Sigma}}_e(\hat{\boldsymbol{\Xi}}_e)\hat{\mathbf{n}},$$

these relations being also deduced from the variations of the Lagrangian function. On the rigid boundary Γ_{rgd} , $\hat{\boldsymbol{\Lambda}} = \boldsymbol{\Lambda}$ and reduces to

$$\boldsymbol{\Lambda} = \boldsymbol{\sigma}(\mathbf{U}, P)\mathbf{n}. \quad (\text{D.1.1})$$

Since the boundary Γ_{rgd} is rigid, there is indeed no solid stress term to consider there.

Direct eigenvalue problem

Computing the variations of the Lagrangian function (4.3.3) with respect to the adjoint mode and looking for zero solutions gives the condition

$$\left\langle \delta \hat{\mathbf{q}}^\dagger, (\lambda \hat{\mathcal{T}}_{\text{fsi}}(\hat{\mathbf{Q}}) - \hat{\mathcal{N}}'_{\text{fsi}}(\hat{\mathbf{Q}})) \hat{\mathbf{q}}^\circ \right\rangle = 0 \quad \forall \delta \hat{\mathbf{q}}^\dagger,$$

while the normalization (4.3.6) is set for the amplitude of the modes. Like in §2.1.2, it is convenient to change the variables in the above formulation, so as to transport it in the steady deformed domain Ω deduced from $\hat{\Omega}$ through a deformation by the steady displacement fields $\hat{\mathbf{\Xi}}_e$ and $\hat{\mathbf{\Xi}}$ previously determined. From (2.1.14) and (2.1.15), the developed expression for this problem then writes as follows in the steady deformed configuration:

$$\begin{aligned} \left\langle \delta \mathbf{q}^\dagger, (\lambda \mathcal{T}_{\text{fsi}}(\mathbf{Q}) - \mathcal{N}'_{\text{fsi}}(\mathbf{Q})) \mathbf{q}^\circ \right\rangle = & \dots \quad (\text{D.1.2}) \\ \lambda \left[\int_{\Omega_s} \left\{ \boldsymbol{\xi}^\circ \cdot \delta \boldsymbol{\xi}^{\dagger*} + \frac{\mathcal{M}_s}{J(\boldsymbol{\Xi})} \mathbf{u}_s^\circ \cdot \delta \mathbf{u}_s^{\dagger*} \right\} d\Omega + \int_{\Omega_f} \left(\mathbf{u}^\circ - (\nabla \mathbf{U}) \boldsymbol{\xi}_e^\circ \right) \cdot \delta \mathbf{u}^{\dagger*} d\Omega \right] \\ & - \int_{\Omega_s} \left\{ \mathbf{u}_s^\circ \cdot \delta \boldsymbol{\xi}^{\dagger*} - \mathbf{P}'(\boldsymbol{\Xi}; \boldsymbol{\xi}^\circ) : \nabla \delta \mathbf{u}_s^{\dagger*} \right\} d\Omega + \int_{\Omega_f} \left\{ \boldsymbol{\Sigma}_e(\boldsymbol{\xi}_e^\circ) : \nabla \delta \boldsymbol{\xi}_e^{\dagger*} \right\} d\Omega \\ & + \int_{\Omega_f} \left\{ (\nabla \mathbf{U}) \mathbf{u}^\circ + (\nabla \mathbf{u}^\circ) \mathbf{U} + (\nabla \mathbf{U}) \boldsymbol{\Phi}'(\boldsymbol{\xi}_e^\circ) \mathbf{U} \right\} \cdot \delta \mathbf{u}^{\dagger*} d\Omega \\ & + \frac{2}{\mathcal{R}_e} \int_{\Omega_f} \left\{ \mathbf{D}(\mathbf{u}^\circ) + \mathbf{D}(\mathbf{U}) \boldsymbol{\Phi}'(\boldsymbol{\xi}_e^\circ)^T + \mathbf{D}'(\mathbf{U}, \boldsymbol{\xi}_e^\circ) \right\} : \nabla \delta \mathbf{u}^{\dagger*} d\Omega \\ & - \int_{\Omega_f} \left\{ p^\circ \nabla \cdot \delta \mathbf{u}^{\dagger*} + \delta p^{\dagger*} \nabla \cdot \mathbf{u}^\circ + \boldsymbol{\Phi}'(\boldsymbol{\Xi}_e, \boldsymbol{\xi}_e^\circ)^T : \left(P \nabla \delta \mathbf{u}^{\dagger*} + \delta p^{\dagger*} \nabla \mathbf{U} \right) \right\} d\Omega \\ & + \int_{\Gamma} \left\{ \boldsymbol{\lambda}^\circ \cdot (\delta \mathbf{u}^\dagger - \delta \mathbf{u}_s^\dagger)^* + \boldsymbol{\lambda}_e^\circ \cdot \delta \boldsymbol{\xi}_e^{\dagger*} + (\boldsymbol{\xi}_e^\circ - \boldsymbol{\xi}^\circ) \cdot \delta \boldsymbol{\lambda}_e^{\dagger*} + (\mathbf{u}^\circ - \lambda \boldsymbol{\xi}^\circ) \cdot \delta \boldsymbol{\lambda}^{\dagger*} \right\} d\Gamma \\ & + \int_{\Gamma_{\text{rgd}}} \left\{ \boldsymbol{\lambda}^\circ \cdot \delta \mathbf{u}^{\dagger*} + \mathbf{u}^\circ \cdot \delta \boldsymbol{\lambda}^{\dagger*} \right\} d\Gamma = 0. \end{aligned}$$

Since this relation should be satisfied whatever the variations of the δ 's functions, using integration by parts, one finally arrive to the local equations for the state modal problem (Eq. (4.3.7)):

$$\begin{aligned} \lambda^2 \left(\mathcal{M}_s / J(\boldsymbol{\Xi}) \right) \boldsymbol{\xi}^\circ - \nabla \cdot \mathbf{P}'(\boldsymbol{\Xi}, \boldsymbol{\xi}^\circ) &= \mathbf{0} & \text{in } \Omega_s, \\ -\nabla \cdot \boldsymbol{\Sigma}_e(\boldsymbol{\xi}_e^\circ) &= \mathbf{0} & \text{in } \hat{\Omega}_f, \\ \lambda \mathbf{u}^\circ + (\nabla \mathbf{U}) \left(\mathbf{u}^\circ - \lambda \boldsymbol{\xi}_e^\circ \right) + (\nabla \mathbf{u}^\circ) \mathbf{U} + (\nabla \mathbf{U}) \boldsymbol{\Phi}'(\boldsymbol{\xi}_e^\circ) \mathbf{U} \dots \\ & - \nabla \cdot (\boldsymbol{\sigma}(\mathbf{u}^\circ, p^\circ) + \boldsymbol{\Sigma}'(\mathbf{U}, P; \boldsymbol{\xi}_e^\circ)) = \mathbf{0} & \text{in } \Omega_f, \\ -\nabla \cdot \mathbf{u}^\circ - \nabla \cdot (\boldsymbol{\Phi}'(\boldsymbol{\xi}_e^\circ) \mathbf{U}) &= 0 & \text{in } \Omega_f, \\ \mathbf{u}^\circ - \lambda \boldsymbol{\xi}_e^\circ &= \mathbf{0} & \text{on } \Gamma, \\ \mathbf{u}^\circ &= \mathbf{0} & \text{on } \Gamma_{\text{rgd}}, \\ \boldsymbol{\xi}_e^\circ - \boldsymbol{\xi}^\circ &= \mathbf{0} & \text{on } \Gamma, \\ (\boldsymbol{\sigma}(\mathbf{u}^\circ, p^\circ) + \boldsymbol{\Sigma}'(\mathbf{U}, P, \boldsymbol{\xi}_e^\circ)) \mathbf{n} - \mathbf{P}'(\boldsymbol{\Xi}; \boldsymbol{\xi}^\circ) \mathbf{n} &= \mathbf{0} & \text{on } \Gamma. \end{aligned}$$

These equations are completed by zero extension displacement farfield conditions, $\boldsymbol{\xi}_e^\circ = \mathbf{0}$ on $\partial\Omega_f \setminus \Gamma$, zero solid displacement $\boldsymbol{\xi}^\circ = \mathbf{0}$ on $\partial\Omega_s \setminus \Gamma$, and the outflow condition $(\boldsymbol{\sigma}(\mathbf{u}^\circ, p^\circ) + \boldsymbol{\Sigma}'(\mathbf{U}, P, \boldsymbol{\xi}_e^\circ)) \mathbf{n} = \mathbf{0}$ on Γ_{out} . A zero condition holds for the velocity on Γ_{rgd} , Γ_{in} and Γ , and the slip condition on Γ_{lat} . The Lagrange multipliers on Γ write as

$$\boldsymbol{\lambda}^\circ = \mathbf{P}'(\boldsymbol{\Xi}, \boldsymbol{\xi}^\circ) \mathbf{n} = (\boldsymbol{\sigma}(\mathbf{u}^\circ, p^\circ) + \boldsymbol{\Sigma}'(\mathbf{U}, P; \boldsymbol{\xi}_e^\circ)) \mathbf{n} \quad \text{and} \quad \boldsymbol{\lambda}_e^\circ = \boldsymbol{\Sigma}_e(\boldsymbol{\xi}_e^\circ) \mathbf{n},$$

and on the rigid boundary Γ_{rgd} , the interface stress $\boldsymbol{\lambda}^\circ$ reduces to the fluid component

$$\boldsymbol{\lambda}^\circ = \boldsymbol{\sigma}(\mathbf{u}^\circ, p^\circ) \mathbf{n}. \quad (\text{D.1.3})$$

Adjoint eigenvalue problem

Computing the variations of the Lagrangian function (4.3.3) with respect to the direct mode and looking for zero solutions gives the condition

$$\langle \hat{\mathbf{q}}^\dagger, (\lambda \hat{\mathcal{T}}_{\text{fsi}}(\hat{\mathbf{Q}}) - \hat{\mathcal{N}}_{\text{fsi}}'(\hat{\mathbf{Q}})) \delta \hat{\mathbf{q}}^\circ \rangle = 0 \quad \forall \delta \hat{\mathbf{q}}^\circ,$$

Like previously, it is also convenient to change the variables in the above formulation, so as to transport it in the steady deformed domain Ω deduced from $\hat{\Omega}$ through a deformation by the steady displacement fields $\hat{\mathbf{\Xi}}_e$ and $\hat{\mathbf{\Xi}}$. Then, adjoint identities are used so as to isolate the variation $\delta \mathbf{q}^\circ$,

$$\langle \mathbf{q}^\dagger, (\lambda \mathcal{T}_{\text{fsi}}(\mathbf{Q}) - \mathcal{N}_{\text{fsi}}'(\mathbf{Q})) \delta \mathbf{q}^\circ \rangle = \langle (\lambda^* \mathcal{T}_{\text{fsi}}^\dagger(\mathbf{Q}) - \mathcal{N}_{\text{fsi}}'^\dagger(\mathbf{Q})) \mathbf{q}^\dagger, \delta \mathbf{q}^\circ \rangle = 0 \quad \forall \delta \mathbf{q}^\circ.$$

The above operation is practically achieved using integration by parts and the technical formulas reported in Appendix C.3, that allow to identify the adjoint operators (marked with the \dagger symbol). Using the developed forms (2.1.14) and (2.1.15), we have

$$\begin{aligned} & \langle \mathbf{q}^\dagger, (\lambda \mathcal{T}_{\text{fsi}}(\mathbf{Q}) - \mathcal{N}_{\text{fsi}}'(\mathbf{Q})) \delta \mathbf{q}^\circ \rangle = \dots \\ & \lambda \left[\int_{\Omega_s} \left\{ \delta \boldsymbol{\xi}^\circ \cdot \boldsymbol{\xi}^{\dagger*} + \frac{\mathcal{M}_s}{J(\boldsymbol{\Xi})} \delta \mathbf{u}_s^\circ \cdot \mathbf{u}_s^{\dagger*} \right\} d\Omega + \int_{\Omega_f} \left(\delta \mathbf{u}^\circ - (\nabla \mathbf{U}) \delta \boldsymbol{\xi}_e^\circ \right) \cdot \mathbf{u}^{\dagger*} d\Omega \right] \\ & - \int_{\Omega_s} \left\{ \delta \mathbf{u}_s^\circ \cdot \boldsymbol{\xi}^{\dagger*} - \mathbf{P}'(\boldsymbol{\Xi}; \delta \boldsymbol{\xi}^\circ) : \nabla \mathbf{u}_s^{\dagger*} \right\} d\Omega + \int_{\Omega_f} \left\{ \boldsymbol{\Sigma}_e(\delta \boldsymbol{\xi}_e^\circ) : \nabla \boldsymbol{\xi}_e^{\dagger*} \right\} d\Omega \\ & + \int_{\Omega_f} \left\{ (\nabla \mathbf{U}) \delta \mathbf{u}^\circ + (\nabla \delta \mathbf{u}^\circ) \mathbf{U} + (\nabla \mathbf{U}) \boldsymbol{\Phi}'(\delta \boldsymbol{\xi}_e^\circ) \mathbf{U} \right\} \cdot \mathbf{u}^{\dagger*} d\Omega \\ & + \frac{2}{\mathcal{R}_e} \int_{\Omega_f} \left\{ \mathbf{D}(\delta \mathbf{u}^\circ) + \mathbf{D}(\mathbf{U}) \boldsymbol{\Phi}'(\delta \boldsymbol{\xi}_e^\circ)^T + \mathbf{D}'(\mathbf{U}, \delta \boldsymbol{\xi}_e^\circ) \right\} : \nabla \mathbf{u}^{\dagger*} d\Omega \\ & - \int_{\Omega_f} \left\{ \delta p^\circ \nabla \cdot \mathbf{u}^{\dagger*} + p^{\dagger*} \nabla \cdot \delta \mathbf{u}^\circ + \boldsymbol{\Phi}'(\boldsymbol{\Xi}_e, \delta \boldsymbol{\xi}_e^\circ)^T : (P \nabla \mathbf{u}^{\dagger*} + p^{\dagger*} \nabla \delta \mathbf{U}) \right\} d\Omega \\ & + \int_{\Gamma} \left\{ \delta \boldsymbol{\lambda}^\circ \cdot (\mathbf{u}^\dagger - \mathbf{u}_s^\dagger)^* + \delta \boldsymbol{\lambda}_e^\circ \cdot \boldsymbol{\xi}_e^{\dagger*} + (\delta \boldsymbol{\xi}_e^\circ - \delta \boldsymbol{\xi}^\circ) \cdot \boldsymbol{\lambda}_e^{\dagger*} + (\delta \mathbf{u}^\circ - \lambda \delta \boldsymbol{\xi}^\circ) \cdot \boldsymbol{\lambda}^{\dagger*} \right\} d\Gamma \\ & + \int_{\Gamma_{\text{rgd}}} \left\{ \delta \boldsymbol{\lambda}^\circ \cdot \mathbf{u}^{\dagger*} + \delta \mathbf{u}^\circ \cdot \boldsymbol{\lambda}^{\dagger*} \right\} d\Gamma = 0. \\ & = \\ & \int_{\Omega_s} \left\{ \lambda \boldsymbol{\xi}^{\dagger*} \cdot \delta \boldsymbol{\xi}^\circ + \mathbf{P}'(\boldsymbol{\Xi}; \mathbf{u}_s^{\dagger*}) : \nabla \delta \boldsymbol{\xi}^\circ \right\} d\Omega_s + \int_{\Omega_s} \left\{ \frac{\mathcal{M}_s}{J(\boldsymbol{\Xi})} \mathbf{u}_s^{\dagger*} - \boldsymbol{\xi}^{\dagger*} \right\} \cdot \delta \mathbf{u}_s^\circ d\Omega \\ & + \int_{\Omega_f} \left\{ (\lambda \mathbf{u}^{\dagger*} + \nabla \mathbf{U}^T \mathbf{u}^{\dagger*} - \nabla \mathbf{u}^{\dagger*} \mathbf{U}) \cdot \delta \mathbf{u}^\circ + \boldsymbol{\sigma}(\mathbf{u}^\dagger, p^\dagger)^* : \nabla \delta \mathbf{u}^\circ - \delta p^\circ \nabla \cdot \mathbf{u}^{\dagger*} \right\} d\Omega \\ & + \int_{\partial \Omega_f} \left\{ (\mathbf{U} \cdot \mathbf{n}_f) \delta \mathbf{u}^\circ + \nabla \mathbf{U} \left[\mathbf{U} (\delta \boldsymbol{\xi}_e^\circ \cdot \mathbf{n}_f) - \delta \boldsymbol{\xi}_e^\circ (\mathbf{U} \cdot \mathbf{n}_f) \right] \right\} \cdot \mathbf{u}^{\dagger*} d\Gamma \\ & - \int_{\Omega_f} \left\{ \nabla \mathbf{U}^T (\lambda \mathbf{u}^{\dagger*} + \nabla \mathbf{U}^T \mathbf{u}^{\dagger*} - \nabla \mathbf{u}^{\dagger*} \mathbf{U}) + (\nabla \mathbf{u}^{\dagger*})^T \right\} \cdot \delta \boldsymbol{\xi}_e^\circ d\Omega \\ & + \int_{\Omega_f} \left\{ \boldsymbol{\Sigma}_e(\boldsymbol{\xi}_e^{\dagger*}) + \boldsymbol{\Sigma}_e^\dagger(\mathbf{U}, P; \mathbf{u}^{\dagger*}, p^{\dagger*}) \right\} : \nabla \delta \boldsymbol{\xi}_e^\circ d\Omega \\ & + \int_{\Gamma} \left\{ \delta \boldsymbol{\lambda}^\circ \cdot (\mathbf{u}^{\dagger*} - \mathbf{u}_s^{\dagger*}) - \delta \boldsymbol{\xi}^\circ \cdot (\boldsymbol{\lambda}_e^{\dagger*} + \lambda \boldsymbol{\lambda}^{\dagger*}) + \delta \boldsymbol{\xi}_e^\circ \cdot \boldsymbol{\lambda}_e^{\dagger*} + \delta \mathbf{u}^\circ \cdot \boldsymbol{\lambda}^{\dagger*} + \delta \boldsymbol{\lambda}_e^\circ \cdot \boldsymbol{\xi}_e^{\dagger*} \right\} d\Gamma \\ & + \int_{\Gamma_{\text{rgd}}} \left\{ \delta \boldsymbol{\lambda}^\circ \cdot \mathbf{u}^{\dagger*} + \delta \mathbf{u}^\circ \cdot \boldsymbol{\lambda}^{\dagger*} \right\} d\Gamma = 0, \end{aligned}$$

A last integration by parts allow to identify the local adjoint equations. The expression for $\boldsymbol{\Sigma}_e^\dagger(\mathbf{U}, P, \mathbf{u}^\dagger, p^\dagger)$ is given by (C.3.5). In particular, cancelling the interface terms on Γ results

in the relations

$$\begin{aligned} \mathbf{P}'(\Xi; \mathbf{u}_s^\dagger) \mathbf{n}_s - \lambda_e^\dagger - \lambda^* \lambda^\dagger &= \mathbf{0} && \text{on } \Gamma, \\ \lambda_e^\dagger + \left(\Sigma_e(\xi_e^\dagger) + \Sigma_e^\dagger(\mathbf{U}, P; \mathbf{u}^\dagger, p^\dagger) \right) \mathbf{n}_f &= \mathbf{0} && \text{on } \Gamma, \\ \sigma(\mathbf{u}^\dagger, p^\dagger) \mathbf{n}_f + \lambda^\dagger &= \mathbf{0} && \text{on } \Gamma. \end{aligned}$$

Eventually, eliminating the solid adjoint velocity with the relation $\xi_s^\dagger = (\mathcal{M}_s/J(\Xi)) \mathbf{u}_s^\dagger$, the adjoint eigenvalue problem writes, in the steady deformed configuration, as follows (Eq. 4.3.9):

$$\begin{aligned} (\lambda^*)^2 \left(\mathcal{M}_s/J(\Xi) \right) \mathbf{u}_s^\dagger - \nabla \cdot \mathbf{P}'(\Xi; \mathbf{u}_s^\dagger) &= \mathbf{0} && \text{in } \Omega_s, \\ -\nabla \mathbf{U}^T \left(\lambda^* \mathbf{u}^\dagger + (\nabla \mathbf{U})^T \mathbf{u}^\dagger - (\nabla \mathbf{u}^\dagger) \mathbf{U} \right) - (\nabla \mathbf{u}^\dagger)^T \nabla \mathbf{U} \mathbf{U} \dots \\ -\nabla \cdot \left(\Sigma_e(\xi_e^\dagger) + \Sigma_e^\dagger(\mathbf{U}, P, \mathbf{u}^\dagger, p^\dagger) \right) &= \mathbf{0} && \text{in } \Omega_f, \\ \lambda^* \mathbf{u}^\dagger + (\nabla \mathbf{U})^T \mathbf{u}^\dagger - (\nabla \mathbf{u}^\dagger) \mathbf{U} - \nabla \cdot \sigma(\mathbf{u}^\dagger, p^\dagger) &= \mathbf{0} && \text{in } \Omega_f, \\ -\nabla \cdot \mathbf{u}^\dagger &= 0 && \text{in } \Omega_f, \\ \mathbf{u}^\dagger - \mathbf{u}_s^\dagger &= \mathbf{0} && \text{on } \Gamma, \\ \mathbf{u}^\dagger &= \mathbf{0} && \text{on } \Gamma_{\text{rgd}}, \\ \xi_e^\dagger &= \mathbf{0} && \text{on } \Gamma, \\ \lambda^* \sigma(\mathbf{u}^\dagger, p^\dagger) \mathbf{n} + \left(\Sigma_e(\xi_e^\dagger) + \Sigma_e^\dagger(\mathbf{U}, P, \mathbf{u}^\dagger, p^\dagger) \right) \mathbf{n} - \mathbf{P}'(\Xi; \mathbf{u}_s^\dagger) \mathbf{n} &= \mathbf{0} && \text{on } \Gamma. \end{aligned}$$

The other boundary conditions are the zero extension displacement farfield conditions, $\xi_e^\dagger = \mathbf{0}$ on $\partial\Omega_f \setminus \Gamma$, the zero solid displacement $\xi_s^\dagger = \mathbf{0}$ on $\partial\Omega_s \setminus \Gamma$, and finally the outflow condition $\sigma(\mathbf{u}^\dagger, p^\dagger) \mathbf{n} + (\mathbf{U} \cdot \mathbf{n}) \mathbf{u}^\dagger = \mathbf{0}$ on Γ_{out} . A zero condition holds for the velocity on Γ_{rgd} , Γ_{in} and Γ , and the slip condition on Γ_{lat} . On the rigid interface, the Lagrange multiplier for the velocity Dirichlet boundary condition writes as

$$\lambda^\dagger = \sigma(\mathbf{u}^\dagger, p^\dagger) \mathbf{n}. \quad (\text{D.1.4})$$

The normalization condition (4.3.11) — obtained from the variation with respect to the eigenvalue — is used to set the amplitude for the adjoint modes.

Adjoint stationary problem

It remains to differentiate the Lagrangian function with respect to the steady solution so as to obtain the adjoint stationary problem. In the most general case both the steady and unsteady parts, in the Lagrangian function (4.3.3), depend on the steady flow, especially from the steady displacement fields. The weak form of the equation reads (Eq. (4.3.12))

$$\left\langle \hat{\mathbf{Q}}^\dagger, \mathcal{N}'_{\text{fsi}}(\hat{\mathbf{Q}}) \delta \mathbf{Q} \right\rangle = \left\langle \hat{\mathbf{q}}^\dagger, \left(\lambda \frac{\partial \hat{\mathcal{F}}_{\text{fsi}}}{\partial \hat{\mathbf{Q}}} \Big|_{\hat{\mathbf{Q}}} \delta \hat{\mathbf{Q}} - \frac{\partial \hat{\mathcal{N}}'_{\text{fsi}}}{\partial \hat{\mathbf{Q}}} \Big|_{\hat{\mathbf{Q}}} \delta \hat{\mathbf{Q}} \right) \hat{\mathbf{q}}^\circ \right\rangle \quad \forall \delta \hat{\mathbf{Q}}.$$

We treat separately the left-hand (i) and right-hand (ii) sides of the above equation.

The (i) left-hand side of (4.3.13) is obtained by the very same approach as the one used to derive the adjoint eigenvalue problem: after having differentiated with respect to the steady variables, the habitual variable change allows to express the problem in the steady deformed domain. Then, adjoint identities result in the transposed variational formulation, from which local equations are deduced. Namely, in the steady deformed configuration,

$$\begin{aligned} \left\langle \mathbf{Q}^\dagger, \mathcal{N}'_{\text{fsi}}(\mathbf{Q}) \delta \mathbf{Q} \right\rangle &= \int_{\Omega_s} \left\{ \delta \mathbf{U}_s \cdot \Xi^{\dagger*} - \mathbf{P}'(\Xi; \delta \Xi) : \nabla \mathbf{U}_s^{\dagger*} \right\} d\Omega - \int_{\Omega_f} \left\{ \Sigma_e(\delta \Xi_e) : \nabla \Xi_e^{\dagger*} \right\} d\Omega \\ &\quad - \int_{\Omega_f} \left\{ (\nabla \mathbf{U}) \delta \mathbf{U} + (\nabla \delta \mathbf{U}) \mathbf{U} + (\nabla \mathbf{U}) \Phi'(\delta \Xi_e) \mathbf{U} \right\} \cdot \mathbf{U}^{\dagger*} d\Omega \end{aligned}$$

$$\begin{aligned}
& -\frac{2}{\mathcal{R}_e} \int_{\Omega_f} \left\{ \mathbf{D}(\delta \mathbf{U}) + \mathbf{D}(\mathbf{U}) \Phi'(\delta \Xi_e)^T + \mathbf{D}'(\mathbf{U}; \delta \Xi_e) \right\} : \nabla \mathbf{U}^{\dagger*} \, d\Omega \\
& + \int_{\Omega_f} \left\{ \delta P \nabla \cdot \mathbf{U}^{\dagger*} + P^{\dagger*} \nabla \cdot \delta \mathbf{U} + \Phi'(\delta \Xi_e)^T : (P \nabla \mathbf{U}^{\dagger*} + P^{\dagger*} \nabla \mathbf{U}) \right\} \, d\Omega \\
& - \int_{\Gamma} \left\{ \delta \Lambda \cdot (\mathbf{U}^\dagger - \mathbf{U}_s^\dagger)^* + \delta \mathbf{U} \cdot \Lambda^{\dagger*} + \delta \Lambda_e \cdot \Xi_e^{\dagger*} + (\delta \Xi_e - \delta \Xi) \cdot \Lambda_e^{\dagger*} \right\} \, d\Gamma \\
& - \int_{\Gamma_{\text{rgd}}} \left\{ \delta \Lambda \cdot \mathbf{U}^{\dagger*} + \delta \mathbf{U} \cdot \Lambda^{\dagger*} \right\} \, d\Gamma.
\end{aligned}$$

Using the adjoint identities in Appendix C.3 and taking into account the boundary conditions for the stationary flow, this expression is rewritten as

$$\begin{aligned}
\langle \mathbf{Q}^\dagger, \mathcal{N}'_{\text{fsi}}(\mathbf{Q}) \delta \mathbf{Q} \rangle &= \int_{\Omega_s} \left\{ \Xi^{\dagger*} \cdot \delta \mathbf{U}_s - \mathbf{P}'(\Xi; \mathbf{U}_s^{\dagger*}) : \nabla \delta \Xi \right\} \, d\Omega - \int_{\Omega_f} \left\{ \Sigma_e(\Xi_e^{\dagger*}) : \nabla \delta \Xi_e \right\} \, d\Omega \\
& - \int_{\Omega_f} \left\{ (\nabla \mathbf{U}^T \mathbf{U}^{\dagger*} - \nabla \mathbf{U}^{\dagger*} \mathbf{U}) \cdot \delta \mathbf{U} + \sigma(\mathbf{U}^\dagger, P^\dagger)^* : \nabla \delta \mathbf{U} - \delta P \nabla \cdot \mathbf{U}^{\dagger*} \right\} \, d\Omega \\
& - \int_{\partial \Omega_f} (\mathbf{U} \cdot \mathbf{n})(\mathbf{U}^{\dagger*} \cdot \delta \mathbf{U}) \, d\Gamma \\
& + \int_{\Omega_f} \left\{ \nabla \mathbf{U}^T (\nabla \mathbf{U}^T \mathbf{U}^{\dagger*} - \nabla \mathbf{U}^{\dagger*} \mathbf{U}) + (\nabla \mathbf{U}^{\dagger*})^T (\nabla \mathbf{U}) \mathbf{U} \right\} \cdot \delta \Xi_e \, d\Omega \\
& - \int_{\Omega_f} \left\{ \Sigma_e(\Xi_e^{\dagger*}) + \Sigma_e^\dagger(\mathbf{U}, P, \mathbf{U}^{\dagger*}, P^{\dagger*}) \right\} : \nabla \delta \Xi_e \, d\Omega \\
& - \int_{\Gamma} \left\{ \delta \Lambda \cdot (\mathbf{U}^\dagger - \mathbf{U}_s^\dagger)^* + \delta \mathbf{U} \cdot \Lambda^{\dagger*} + \delta \Lambda_e \cdot \Xi_e^{\dagger*} + (\delta \Xi_e - \delta \Xi) \cdot \Lambda_e^{\dagger*} \right\} \, d\Gamma \\
& - \int_{\Gamma_{\text{rgd}}} \left\{ \delta \Lambda \cdot \mathbf{U}^{\dagger*} + \delta \mathbf{U} \cdot \Lambda^{\dagger*} \right\} \, d\Gamma.
\end{aligned}$$

If we further make the assumption that the steady deformed and stress-free reference configurations coincide, the variations with respect to the displacements are zero. An integration by parts then allows to recover the local equations corresponding to the left-hand side of (4.3.16), Eq. (4.3.16).

Let us now (ii) consider the second term in (4.3.12), from which the right-hand side of (4.3.13) is deduced. The complete expression — before differentiating with respect to the steady fields — writes as follows:

$$\begin{aligned}
& \langle \hat{\mathbf{q}}^\dagger, (\hat{\mathcal{T}}_{\text{fsi}}(\hat{\mathbf{Q}}) - \hat{\mathcal{N}}'_{\text{fsi}}(\hat{\mathbf{Q}})) \hat{\mathbf{q}}^\circ \rangle = \dots \\
& \lambda \left[\int_{\Omega_s} \left\{ \hat{\xi}^\circ \cdot \hat{\xi}^\dagger + \mathcal{M}_s \hat{\mathbf{u}}_s^\circ \cdot \hat{\mathbf{u}}_s^\dagger \right\} \, d\hat{\Omega} \int_{\Omega_f} \left\{ \hat{J}(\hat{\Xi}_e) \hat{\mathbf{u}}^\circ - (\hat{\nabla} \hat{\mathbf{U}}) \hat{\Phi}(\hat{\Xi}_e) \hat{\xi}_e^\circ \right\} \cdot \hat{\mathbf{u}}^\dagger \, d\hat{\Omega} \right] \\
& - \int_{\Omega_s} \left\{ \hat{\mathbf{u}}_s^\circ \cdot \hat{\xi}^\dagger - \hat{\mathbf{P}}'(\hat{\Xi}; \hat{\xi}^\circ) : \hat{\nabla} \hat{\mathbf{u}}_s^\dagger \right\} \, d\hat{\Omega} + \int_{\Omega_f} \left\{ \hat{\Sigma}_e(\hat{\xi}_e^\circ) : \hat{\nabla} \hat{\xi}_e^\dagger \right\} \, d\hat{\Omega} \\
& + \int_{\Omega_f} \left\{ (\hat{\nabla} \hat{\mathbf{U}}) \hat{\Phi}(\hat{\Xi}_e) \hat{\mathbf{u}}^\circ + (\hat{\nabla} \hat{\mathbf{u}}^\circ) \hat{\Phi}(\hat{\Xi}_e) \hat{\mathbf{U}} + (\hat{\nabla} \hat{\mathbf{U}}) \hat{\Phi}'(\hat{\Xi}_e, \hat{\xi}_e^\circ) \hat{\mathbf{U}} \right\} \cdot \hat{\mathbf{u}}^\dagger \, d\hat{\Omega} \\
& + \frac{2}{\mathcal{R}_e} \int_{\Omega_f} \left\{ \hat{\mathbf{D}}(\hat{\mathbf{u}}^\circ, \hat{\Xi}_e) \hat{\Phi}(\hat{\Xi}_e)^T + \hat{\mathbf{D}}(\hat{\mathbf{U}}, \hat{\Xi}_e) \hat{\Phi}'(\hat{\Xi}_e, \hat{\xi}_e^\circ)^T + \hat{\mathbf{D}}'(\hat{\mathbf{U}}, \hat{\Xi}_e; \hat{\xi}_e^\circ) \hat{\Phi}(\hat{\Xi}_e)^T \right\} : \hat{\nabla} \hat{\mathbf{u}}^\dagger \, d\hat{\Omega} \\
& - \int_{\Omega_f} \left\{ \hat{\Phi}(\hat{\Xi}_e)^T : (\hat{p}^\circ \hat{\nabla} \hat{\mathbf{u}}^\dagger + \hat{p}^\dagger \hat{\nabla} \hat{\mathbf{u}}^\circ) + \hat{\Phi}'(\hat{\Xi}_e, \hat{\xi}_e^\circ)^T : (\hat{P} \hat{\nabla} \hat{\mathbf{u}}^\dagger + \hat{p}^\dagger \hat{\nabla} \hat{\mathbf{U}}) \right\} \, d\hat{\Omega} \\
& + \int_{\hat{\Gamma}} \left\{ \hat{\lambda}^\circ \cdot (\hat{\mathbf{u}}^\dagger - \hat{\mathbf{u}}_s^\dagger) + (\hat{\mathbf{u}}^\circ - \lambda \hat{\xi}^\circ) \cdot \hat{\lambda}^\dagger + \hat{\lambda}_e^\circ \cdot \hat{\xi}_e^\dagger + (\hat{\xi}_e^\circ - \hat{\xi}^\circ) \cdot \hat{\lambda}_e^\dagger \right\} \, d\hat{\Gamma}. \tag{D.1.5}
\end{aligned}$$

The terms related to the steady displacements are emphasized by the red color. Their variations should be considered as well as those for \hat{P} and $\hat{\mathbf{U}}$ in order to obtain an exact adjoint equation, but

in the present case we rely on an approximate version where all these displacements are neglected, which amounts to consider in this expression that $\hat{\Omega} \simeq \hat{\Omega}_t$. Taking then the variations with respect to the velocity and the pressure, we get in the steady deformed configuration

$$\begin{aligned} & \left\langle \hat{q}^\dagger, \left(\lambda \frac{\partial \hat{\mathcal{J}}_{\text{fsi}}}{\partial \hat{\mathbf{Q}}} \bigg|_{\hat{\mathbf{Q}}} \hat{\mathbf{q}}^\circ - \frac{\partial \hat{\mathcal{N}}'_{\text{fsi}}}{\partial \hat{\mathbf{Q}}} \bigg|_{\mathbf{Q}} \hat{\mathbf{q}}^\circ \right) \delta \hat{\mathbf{Q}} \right\rangle \simeq \\ & - \lambda \int_{\Omega_f} (\nabla \delta \mathbf{U}) \boldsymbol{\xi}_e^\circ \cdot \mathbf{u}^{\dagger*} \, d\Omega \\ & + \int_{\Omega_f} \left\{ (\nabla \delta \mathbf{U}) \mathbf{u}^\circ + (\nabla \mathbf{u}^\circ) \delta \mathbf{U} + (\nabla \delta \mathbf{U}) \boldsymbol{\Phi}'(\boldsymbol{\xi}_e^\circ) \mathbf{U} + (\nabla \mathbf{U}) \boldsymbol{\Phi}'(\boldsymbol{\xi}_e^\circ) \delta \mathbf{U} \right\} \cdot \mathbf{u}^{\dagger*} \, d\Omega \\ & + \frac{2}{\mathcal{R}_e} \int_{\Omega_f} \left\{ \mathbf{D}(\delta \mathbf{U}) \boldsymbol{\Phi}'(\boldsymbol{\xi}_e^\circ)^T + \mathbf{D}'(\delta \mathbf{U}, \boldsymbol{\xi}_e^\circ) \right\} : \nabla \mathbf{u}^{\dagger*} \, d\Omega \\ & - \int_{\hat{\Omega}_f} \left\{ \boldsymbol{\Phi}'(\boldsymbol{\xi}_e^\circ)^T : (\delta P \nabla \mathbf{u}^{\dagger*} + p^{\dagger*} \nabla \delta \mathbf{U}) \right\} \, d\Omega. \end{aligned}$$

This expression is again transformed so as to switch the position of the variations $\delta \mathbf{U}$, δP and that of the adjoint perturbation variables. Using integrations by parts, the continuity equation of the direct eigenvalue problem and Piola's identity, we have first the identity

$$\begin{aligned} & \int_{\Omega_f} \nabla \delta \mathbf{U} (\mathbf{u}^\circ - \lambda \boldsymbol{\xi}_e^\circ + \boldsymbol{\Phi}'(\boldsymbol{\xi}_e^\circ) \mathbf{U}) \cdot \mathbf{u}^{\dagger*} \, d\Omega = \int_{\partial \Omega_f} (\delta \mathbf{U} \cdot \mathbf{u}^{\dagger*}) (\mathbf{u}^\circ - \lambda \boldsymbol{\xi}_e^\circ + \boldsymbol{\Phi}'(\boldsymbol{\xi}_e^\circ) \mathbf{U}) \cdot \mathbf{n}_f \, d\Gamma \\ & + \int_{\Omega_f} \left\{ \lambda (\nabla \mathbf{u}^{\dagger*} \boldsymbol{\xi}_e^\circ + (\nabla \cdot \boldsymbol{\xi}_e^\circ) \mathbf{u}^{\dagger*}) - \nabla \mathbf{u}^{\dagger*} \mathbf{u}^\circ - \nabla \mathbf{u}^{\dagger*} \boldsymbol{\Phi}'(\boldsymbol{\xi}_e^\circ) \mathbf{U} \right\} \cdot \delta \mathbf{U} \, d\Omega \end{aligned}$$

Using then the properties of the double contraction, the diffusion-pressure term can also be rewritten as $\boldsymbol{\Sigma}'(\mathbf{u}^{\dagger*}, p^{\dagger*}; \boldsymbol{\xi}_e^\dagger)$. Taking eventually into account the boundary conditions for the steady variables, the direct and adjoint modes, and integrating again by parts, ones finally arrives to

$$\begin{aligned} & \left\langle \hat{q}^\dagger, \left(\lambda \frac{\partial \hat{\mathcal{J}}_{\text{fsi}}}{\partial \hat{\mathbf{Q}}} \bigg|_{\hat{\mathbf{Q}}} \hat{\mathbf{q}}^\circ - \frac{\partial \hat{\mathcal{N}}'_{\text{fsi}}}{\partial \hat{\mathbf{Q}}} \bigg|_{\mathbf{Q}} \hat{\mathbf{q}}^\circ \right) \delta \hat{\mathbf{Q}} \right\rangle \simeq \dots \\ & \int_{\Omega_f} \left\{ (\nabla \mathbf{u}^{\circ*})^T \mathbf{u}^\dagger - \nabla \mathbf{u}^\dagger \mathbf{u}^{\circ*} + \boldsymbol{\Phi}'(\boldsymbol{\xi}_e^{\circ*})^T \nabla \mathbf{U}^T \mathbf{u}^\dagger - \nabla \mathbf{u}^\dagger \boldsymbol{\Phi}'(\boldsymbol{\xi}_e^{\circ*}) \mathbf{U} \right\}^* \cdot \delta \mathbf{U} \, d\Omega \\ & + \int_{\Omega_f} \left\{ \lambda^* (\nabla \mathbf{u}^\dagger \boldsymbol{\xi}_e^{\circ*} + \nabla \cdot \boldsymbol{\xi}_e^{\circ*} \mathbf{u}^\dagger) \right\}^* \cdot \delta \mathbf{U} \, d\Omega \\ & - \int_{\Omega_f} \left\{ \nabla \cdot \boldsymbol{\Sigma}'(\mathbf{u}^\dagger, p^\dagger; \boldsymbol{\xi}_e^{\circ*}) \right\}^* \cdot \delta \mathbf{U} \, d\Omega \\ & - \int_{\Omega_f} \delta P \left\{ (\boldsymbol{\Phi}'(\boldsymbol{\xi}_e^{\circ*})^T : \nabla \mathbf{u}^\dagger) \right\}^* \, d\Omega \\ & + \int_{\Gamma_{\text{out}}} \left\{ (\mathbf{u}^{\circ*} \cdot \mathbf{n}_f) \mathbf{u}^\dagger + \boldsymbol{\sigma}(\mathbf{u}^\dagger, p^\dagger) \mathbf{n}_f \right\}^* \cdot \delta \mathbf{U} \, d\Gamma. \end{aligned} \tag{D.1.6}$$

We identify there the sensitivities $\nabla_U(\lambda)$ and $\nabla_P(\lambda)$ that constitute the right-hand side of the adjoint equation:

$$\begin{aligned} \nabla_U(\lambda) &= -(\nabla \mathbf{u}^{\circ*})^T \mathbf{u}^\dagger + \nabla \mathbf{u}^\dagger \mathbf{u}^{\circ*} \\ &\quad - \boldsymbol{\Phi}'(\boldsymbol{\xi}_e^{\circ*})^T \nabla \mathbf{U}^T \mathbf{u}^\dagger + \nabla \mathbf{u}^\dagger \boldsymbol{\Phi}'(\boldsymbol{\xi}_e^{\circ*}) \mathbf{U} \\ &\quad - \lambda^* (\nabla \mathbf{u}^\dagger \boldsymbol{\xi}_e^{\circ*} + \nabla \cdot \boldsymbol{\xi}_e^{\circ*} \mathbf{u}^\dagger) \\ &\quad + \nabla \cdot \boldsymbol{\Sigma}'(\mathbf{u}^\dagger, p^\dagger; \boldsymbol{\xi}_e^{\circ*}), \\ \nabla_P(\lambda) &= \boldsymbol{\Phi}'(\boldsymbol{\xi}_e^{\circ*})^T : \nabla \mathbf{u}^\dagger. \end{aligned}$$

Combining (i) and (ii), we arrive to the adjoint stationary equation with the approximate right-hand side, that writes as follows:

$$\begin{aligned}
-\nabla \cdot \mathbf{P}'(\mathbf{U}_s^\dagger, \hat{\Xi}) &= \mathbf{0} && \text{in } \Omega_s, \\
(\nabla \mathbf{U})^T \left((\nabla \mathbf{U}^\dagger) \mathbf{U} - (\nabla \mathbf{U})^T \mathbf{U}^\dagger \right) - (\nabla \mathbf{U}^\dagger)^T (\nabla \mathbf{U}) \mathbf{U} \dots \\
-\nabla \cdot \left(\Sigma_e(\Xi_e^\dagger) + \Sigma_e^\dagger(\mathbf{U}, P, \mathbf{U}^\dagger, P^\dagger) \right) &= \mathbf{0} && \text{in } \Omega_f, \\
(\nabla \mathbf{U})^T \mathbf{U}^\dagger - (\nabla \mathbf{U}^\dagger) \mathbf{U} - \nabla \cdot \sigma(\mathbf{U}^\dagger, P^\dagger) &= \nabla_U(\lambda) && \text{in } \Omega_f, \\
-\nabla \cdot \mathbf{U}^\dagger &= \nabla_P(\lambda) && \text{in } \Omega_f, \\
\mathbf{U}^\dagger - \mathbf{U}_s^\dagger &= \mathbf{0} && \text{on } \Gamma, \\
\mathbf{U}^\dagger &= \mathbf{0} && \text{on } \Gamma_{\text{rgd}}, \\
\Xi_e^\dagger &= \mathbf{0} && \text{on } \Gamma, \\
\left(\Sigma_e(\Xi_e^\dagger) + \Sigma_e^\dagger(\mathbf{U}, P, \mathbf{U}^\dagger, P^\dagger) \right) \mathbf{n} - \mathbf{P}'(\mathbf{U}_s^\dagger, \hat{\Xi}) \mathbf{n} &= \mathbf{0} && \text{on } \Gamma,
\end{aligned}$$

completed by a zero velocity and extension displacement farfield condition $\mathbf{U}^\dagger = \Xi_e^\dagger = \mathbf{0}$ on $\partial\Omega_f \setminus \Gamma$, a zero solid displacement condition $\xi^\dagger = \mathbf{0}$ on $\partial\Omega_s \setminus \Gamma$, and the outflow condition $(\mathbf{U} \cdot \mathbf{n}_f) \mathbf{U}^\dagger + \sigma(\mathbf{U}^\dagger, P^\dagger) \mathbf{n}_f - \sigma^\dagger(\mathbf{u}^\dagger, p^\dagger, \xi_e^\circ) \mathbf{n} = \mathbf{0}$ on Γ_{out} . Furthermore, the interface Lagrange multipliers for the velocity and displacement continuity write as follows,

$$\begin{aligned}
\Lambda &= \mathbf{P}(\Xi_e) \hat{\mathbf{n}} = \Sigma(\mathbf{U}, P) \mathbf{n} && \text{and} && \Lambda^\dagger = \left(\Sigma(\mathbf{U}^\dagger, P^\dagger) - \sigma^\dagger(\mathbf{u}^\dagger, p^\dagger, \xi_e^\circ) \right) \mathbf{n}, \\
\Lambda_e &= \Sigma_e(\Xi_e) \hat{\mathbf{n}} && \text{and} && \Lambda_e^\dagger = (\Sigma_e + \Sigma_e^\dagger) \mathbf{n} = \mathbf{P}'(\Xi_e, \mathbf{U}_s^\dagger) \mathbf{n}.
\end{aligned}$$

The equation (4.3.16) corresponds to the above equations where the displacements have been neglected also in the left-hand side.

D.2 Explicit formula for the shape gradient

Differentiation of integrals with respect to the domain

The path for obtaining the identity (4.3.17) might be useful to be recalled. We give here the intuitive idea, the reader is referred to [Henrot & Pierre \(2006\)](#) where the proofs are given together with more precise regularity hypotheses.

Volume integral

Given f an arbitrary smooth function, let us first consider the case of an arbitrary surface integral

$$\mathcal{L}_v = \int_{\hat{\Omega}(\hat{\theta})} f(\hat{\mathbf{x}}) d\hat{\Omega}.$$

The variations of \mathcal{L} when the domain is modified by the Lagrangian mapping (4.3.1) write as

$$\begin{aligned}
\mathcal{L}_v(\hat{\theta} + \varepsilon \delta \hat{\theta}) - \mathcal{L}_v(\hat{\theta}) &= \int_{\hat{\Omega}(\hat{\theta} + \varepsilon \delta \hat{\theta})} f(\hat{\mathbf{x}}) d\hat{\Omega} - \int_{\hat{\Omega}(\hat{\theta})} f(\hat{\mathbf{x}}) d\hat{\Omega} \\
&= \int_{\hat{\Omega}(\hat{\theta})} \left(f \circ (\text{Id} + \varepsilon \delta \hat{\theta}) | \det(\mathbf{I} + \varepsilon \hat{\nabla} \hat{\theta}) | - f \right) (\hat{\mathbf{x}}) d\hat{\Omega}
\end{aligned}$$

after changing the variables. We recover in particular the Jacobian of the transformation $\det(\mathbf{I} + \varepsilon \hat{\nabla} \hat{\theta})$. Expanding the terms inside the integral yields to

$$f \circ (\text{Id} + \varepsilon \delta \hat{\theta}) | \det(\mathbf{I} + \varepsilon \hat{\nabla} \hat{\theta}) | = f + \varepsilon \left(\hat{\nabla} f \cdot \delta \hat{\theta} + f \hat{\nabla} \cdot \delta \hat{\theta} \right) d\hat{\Omega} + o(\varepsilon)$$

$$= f + \hat{\nabla} \cdot (f \delta \hat{\boldsymbol{\theta}}) d\hat{\Omega} + o(\varepsilon)$$

so that the variations of the integral write as

$$\mathcal{L}_v(\hat{\boldsymbol{\theta}} + \varepsilon \delta \hat{\boldsymbol{\theta}}) - \mathcal{L}_v(\hat{\boldsymbol{\theta}}) = \varepsilon \int_{\hat{\Omega}(\hat{\boldsymbol{\theta}})} \hat{\nabla} \cdot (f \delta \hat{\boldsymbol{\theta}}) d\hat{\Omega} + o(\varepsilon),$$

and finally using the divergence theorem (Chadwick, 1999) one arrives to an expression that allows to identify the derivative in the first-order term, that writes

$$\mathcal{L}'_v(\hat{\Omega})(\delta \hat{\boldsymbol{\theta}}) = \int_{\partial \hat{\Omega}} f (\delta \hat{\boldsymbol{\theta}} \cdot \hat{\mathbf{n}}) d\hat{\Gamma} \quad (\text{D.2.1})$$

Surface integral

Let us now consider some function g defined on a border $\partial \hat{\Omega}$. The case of the surface integral is treated by coming back to the case of a volume integral. From the divergence theorem,

$$\mathcal{L}_b = \int_{\partial \hat{\Omega}(\hat{\boldsymbol{\theta}})} g(\hat{\mathbf{x}}) d\hat{\Gamma} = \int_{\partial \hat{\Omega}(\hat{\boldsymbol{\theta}})} g(\hat{\mathbf{x}}) \hat{\mathbf{n}} \cdot \hat{\mathbf{n}} d\hat{\Gamma} = \int_{\hat{\Omega}(\hat{\boldsymbol{\theta}})} \hat{\nabla} \cdot (g(\hat{\mathbf{x}}) \hat{\mathbf{n}}) d\hat{\Omega}.$$

Note that special requirements are required for the expression in the right side to make sense (Henrot & Pierre, 2006), since, for instance, the normal has to be extended by any means onto the domain. This last formula allows to use the result for volume integrals, that gives

$$\mathcal{L}'_b(\hat{\Omega})(\delta \hat{\boldsymbol{\theta}}) = \int_{\partial \hat{\Omega}} \hat{\nabla} \cdot (g(\hat{\mathbf{x}}) \hat{\mathbf{n}}) (\delta \hat{\boldsymbol{\theta}} \cdot \hat{\mathbf{n}}) d\hat{\Gamma} \quad \text{and} \quad \hat{\nabla} \cdot (g(\hat{\mathbf{x}}) \hat{\mathbf{n}}) = \frac{\partial g}{\partial \hat{\mathbf{n}}} + g \hat{\nabla} \cdot \hat{\mathbf{n}},$$

where we note $H = \hat{\nabla} \cdot \hat{\mathbf{n}}$ the interface mean curvature. Finally, the following formula is obtained,

$$\mathcal{L}'_b(\hat{\Omega})(\delta \hat{\boldsymbol{\theta}}) = \int_{\partial \hat{\Omega}} \left(\frac{\partial g}{\partial \hat{\mathbf{n}}} + Hg \right) (\delta \hat{\boldsymbol{\theta}} \cdot \hat{\mathbf{n}}) d\hat{\Gamma}. \quad (\text{D.2.2})$$

Shape gradient computation

Shape gradient for the steady part

We can now differentiate the Lagrangian function with respect to the domain. The fact that the derivative is taken on a rigid boundary considerably simplifies the result, since all the terms related to the displacements (as well as their derivatives, see the Fig. D.1) vanish. Using (4.3.17), we obtain

$$\begin{aligned} \langle \hat{\mathbf{Q}}^\dagger, \hat{\mathcal{N}}_{\text{fsi}}(\hat{\mathbf{Q}}) \rangle'(\hat{\Omega})(\hat{\boldsymbol{\theta}}) &= - \frac{2}{\mathcal{R}_e} \int_{\hat{\Gamma}_{\text{rgd}}} \left\{ \hat{\mathbf{D}}(\hat{\mathbf{U}}) : (\hat{\nabla} \hat{\mathbf{U}}^\dagger)^* \right\} (-\hat{\boldsymbol{\theta}} \cdot \hat{\mathbf{n}}) d\hat{\Gamma} \\ &\quad + \int_{\hat{\Gamma}_{\text{rgd}}} \left(\hat{P} \hat{\nabla} \cdot (\hat{\mathbf{U}}^\dagger)^* + (\hat{P}^\dagger)^* \hat{\nabla} \cdot \hat{\mathbf{U}} \right) (-\hat{\boldsymbol{\theta}} \cdot \hat{\mathbf{n}}) d\hat{\Gamma} \\ &\quad - \int_{\hat{\Gamma}_{\text{rgd}}} \frac{\partial}{\partial(-\hat{\mathbf{n}})} \left\{ \hat{\boldsymbol{\Lambda}} \cdot (\hat{\mathbf{U}}^\dagger)^* + \hat{\mathbf{U}} \cdot (\hat{\boldsymbol{\Lambda}}^\dagger)^* \right\} (-\hat{\boldsymbol{\theta}} \cdot \hat{\mathbf{n}}) d\hat{\Gamma}, \end{aligned}$$

where we have already simplified the fluid advection term which is zero thanks to the no-slip condition, and all the terms in factor of the interface curvature H that are also zero (but not their derivatives). The integrals are zero on $\hat{\Gamma}$, Γ_{in} , Γ_{lat} and Γ_{out} because we have enforced $\hat{\boldsymbol{\theta}} = \mathbf{0}$ on this boundary. Finally, recall that the normal $\hat{\mathbf{n}}$ is pointing *in* the fluid domain (Fig. D.1) — for which reason we find the $-\hat{\mathbf{n}}$ in the above formula — and $\hat{\mathbf{D}}(\hat{\mathbf{U}}) = 1/2(\hat{\nabla} \hat{\mathbf{U}} + \hat{\nabla} \hat{\mathbf{U}}^T)$ on the rigid boundary $\hat{\Gamma}_{\text{rgd}}$. We can now replace the expression for the Lagrange multipliers at the rigid interface, namely from (D.1.3) and (D.1.4) we have

$$\hat{\boldsymbol{\Lambda}} = \hat{\boldsymbol{\sigma}}(\hat{\mathbf{U}}, \hat{P}) \hat{\mathbf{n}} \quad \text{and} \quad \hat{\boldsymbol{\Lambda}}^\dagger = \hat{\boldsymbol{\sigma}}(\hat{\mathbf{U}}^\dagger, \hat{P}^\dagger) \hat{\mathbf{n}},$$

where $\hat{\sigma}(\hat{U}, \hat{P}) = -\hat{P}\mathbf{I} + 2/\mathcal{R}_e (\hat{\nabla}\hat{U} + \hat{\nabla}\hat{U}^T)$ on $\hat{\Gamma}_{\text{rgd}}$ and the same for the adjoint stresses. Then, using the fact that the tangential gradient of a vanishing field on the interface is zero (Gao & Ma, 2008) and tensor indices manipulations, we have

$$\begin{aligned} \frac{\partial}{\partial \hat{\mathbf{n}}} \left(\hat{\Lambda} \cdot (\hat{U}^\dagger)^* \right) &= \frac{\partial \hat{\Lambda}}{\partial \hat{\mathbf{n}}} \cdot \underbrace{(\hat{U}^\dagger)^*}_{=0} + \frac{\partial (\hat{U}^\dagger)^*}{\partial \hat{\mathbf{n}}} \cdot \hat{\Lambda} \\ &= -\hat{P} \underbrace{\frac{\partial (\hat{U}^\dagger)^*}{\partial \hat{\mathbf{n}}} \cdot \hat{\mathbf{n}}}_{=\hat{\nabla} \cdot (\hat{U}^\dagger)^*} + \frac{2}{\mathcal{R}_e} \underbrace{\frac{\partial (\hat{U}^\dagger)^*}{\partial \hat{\mathbf{n}}}}_{(\hat{\nabla} \hat{U}^\dagger)^* \hat{\mathbf{n}}} \cdot (\hat{\mathbf{D}}(\hat{U})\hat{\mathbf{n}}) \\ &= -\hat{P} (\hat{\nabla} \cdot \hat{U}^\dagger)^* + \frac{2}{\mathcal{R}_e} \hat{\mathbf{D}}(\hat{U}^\dagger)^* : \hat{\mathbf{D}}(\hat{U}) \end{aligned}$$

Putting all these pieces together, we obtain the following expression for the shape gradient of the steady part,

$$\left\langle \hat{Q}^\dagger, \hat{\mathcal{N}}_{\text{fsi}}(\hat{Q}) \right\rangle'(\hat{\Omega})(\hat{\theta}) = \frac{2}{\mathcal{R}_e} \int_{\hat{\Gamma}} \hat{\mathbf{D}}(\hat{U}^\dagger)^* : \hat{\mathbf{D}}(\hat{U}) (-\hat{\theta} \cdot \hat{\mathbf{n}}) d\hat{\Omega}.$$

Remark – stationary part of the gradient on a deformable interface. Let us use (4.3.17) for the case where $\hat{\theta} \neq \mathbf{0}$ on $\hat{\Gamma}$ and is zero everywhere else. A formula for the shape gradient on the deformable (by the fluid-structure interaction) interface $\hat{\Gamma}$ would then be given by the expression

$$\begin{aligned} \left\langle \hat{Q}^\dagger, \hat{\mathcal{N}}_{\text{fsi}}(\hat{Q}) \right\rangle'(\hat{\Omega})(\hat{\theta}) &= \dots \\ &- \int_{\hat{\Gamma}} \left\{ \hat{\mathbf{P}}(\hat{\Xi}) : (\hat{\nabla} \hat{U}_s^\dagger)^* \text{bigg} \right\} (\hat{\theta} \cdot \hat{\mathbf{n}}) d\hat{\Gamma} - \int_{\hat{\Gamma}} \left\{ \hat{\Sigma}_e(\hat{\Xi}_e) : (\hat{\nabla} \hat{\Xi}_e^\dagger)^* \right\} (-\hat{\theta} \cdot \hat{\mathbf{n}}) d\hat{\Gamma} \\ &- \frac{2}{\mathcal{R}_e} \int_{\hat{\Gamma}} \left\{ \hat{\mathbf{D}}(\hat{U}, \hat{\Xi}_e) \Phi(\hat{\Xi}_e)^T : (\hat{\nabla} \hat{U}^\dagger)^* \right\} (-\hat{\theta} \cdot \hat{\mathbf{n}}) d\hat{\Gamma} \\ &+ \int_{\hat{\Gamma}} \left\{ \hat{\Phi}(\hat{\Xi}_e)^T : \left(\hat{P} (\hat{\nabla} \hat{U}^\dagger)^* + (\hat{P}^\dagger)^* \hat{\nabla} \hat{U} \right) \right\} (-\hat{\theta} \cdot \hat{\mathbf{n}}) d\hat{\Gamma} \\ &- \int_{\hat{\Gamma}} \left(H + \frac{\partial}{\partial \hat{\mathbf{n}}} \right) \left\{ \hat{\Lambda} \cdot (\hat{U}^\dagger - \hat{U}_s^\dagger)^* + \hat{U} \cdot (\hat{\Lambda}^\dagger)^* + \hat{\Lambda}_e \cdot (\hat{\Xi}_e^\dagger)^* + (\hat{\Xi}_e - \hat{\Xi}) \cdot (\hat{\Lambda}_e^\dagger)^* \right\} (\hat{\theta} \cdot \hat{\mathbf{n}}) d\hat{\Gamma}, \end{aligned}$$

but in this case the further simplifications of the expression are less straightforward. For instance, the “cosmetic” results used above does not hold anymore for terms involving the displacement fields, that do not vanish anymore on the interface. We see again the need for the continuous approach, since the expression for the adjoint interface stresses $\hat{\Lambda}_e^\dagger$ appear in this expression.

Shape gradient for the unsteady part

We use again the identity (4.3.17) to compute the unsteady part of the gradient. The procedure is exactly the same as previously. Using the vanishing displacement/displacement gradients property on Γ_{rgd} , as well as the no-slip velocity condition, we obtain an expression that involves the Lagrange multipliers on Γ_{rgd} (Eq.(D.1.3) and Eq.(D.1.4))

$$\hat{\lambda}^\circ = \hat{\sigma}(\hat{u}^\circ, \hat{p}^\circ) \hat{\mathbf{n}} \quad \text{and} \quad \hat{\lambda}^\dagger = \hat{\sigma}(\hat{u}^\dagger, \hat{p}^\dagger) \hat{\mathbf{n}},$$

and replacing in the obtained expression and using the same “cosmetic” properties as before, we finally obtain the unsteady part of the gradient,

$$-\left\langle \hat{q}^\dagger, (\lambda \hat{\mathcal{T}}_{\text{fsi}}(\hat{q}) - \hat{\mathcal{N}}_{\text{fsi}}'(\hat{Q})) \hat{q}^\circ \right\rangle'(\hat{\Omega})(\hat{\theta}) = \frac{2}{\mathcal{R}_e} \int_{\hat{\Gamma}_{\text{rgd}}} \hat{\mathbf{D}}(\hat{u}^\circ) : \hat{\mathbf{D}}((\hat{u}^\dagger)^*) (-\hat{\theta} \cdot \hat{\mathbf{n}}) d\hat{\Gamma}.$$

BIBLIOGRAPHY

- ABDELKEFI, A. 2016 Aeroelastic energy harvesting: a review. *International Journal of Engineering Science* **100**, 112–135.
- AGHAJARI, N. & SCHÄFER, M. 2015 Efficient shape optimization for fluid–structure interaction problems. *Journal of Fluids and Structures* **57**, 298–313.
- ÅKERVIK, E., EHRENSTEIN, U., GALLAIRE, F. & HENNINGSON, D. S. 2008 Global two-dimensional stability measures of the flat plate boundary-layer flow. *European Journal of Mechanics-B/Fluids* **27** (5), 501–513.
- ALEYEV YU, G. 1977 *Nekton*. Junk, The Hague.
- ALLAIRE, G. 2012 *Analyse numérique et optimisation: une introduction à la modélisation mathématique et à la simulation numérique*, 2nd edn. Éditions de l'École polytechnique, Palaiseau.
- ALLAIRE, G. & PANTZ, O. 2006 Structural optimization with FreeFem++. *Structural and Multidisciplinary Optimization* **32** (3), 173–181.
- ALLAIRE, G. & SCHOENAUER, M. 2007 *Conception optimale de structures*. *Mathématiques et applications* 58. Springer.
- ALLANDRIEU, R. 2018 Experimental study of fluid-structure interactions using a soap film channel. Master's thesis, Delft University of Technology.
- AMANDOLESE, X., HÉMON, P. & MANZOOR, S. 2013 The transient temporal response of a flexible bridge deck subjected to a single gust. *Journal of Computational and Applied Mathematics* **246**, 153–160.
- AMESTOY, P., BUTTARI, A., GUERMOUCHE, A., L'EXCELLENT, J.-Y. & UCAR, B. 2013 MUMPS: a multifrontal massively parallel sparse direct solver.
- ANDERSON, W. K. & BONHAUS, D. L. 1999 Airfoil design on unstructured grids for turbulent flows. *AIAA Journal* **37** (2), 185–191.
- ANSYS 2016 Shape optimization for aerodynamic efficiency using adjoint methods. White paper. ANSYS Inc.
- APELT, C. & WEST, G. 1974 The effect of wake splitter plates on bluff-body flow in the range $10^4 < Re < 5 \times 10^5$. *Journal of Fluid Mechanics* **71**, 145–160.
- ARIS, R. 1989 *Vectors, tensors and the basic equations of fluid mechanics*. Dover Books on Mathematics.
- ARNOLDI, W. E. 1951 The principle of minimized iterations in the solution of the matrix eigenvalue problem. *Quarterly of applied mathematics* **9** (1), 17–29.
- ASSI, G. R., BEARMAN, P. & KITNEY, N. 2009 Low drag solutions for suppressing vortex-induced vibration of circular cylinders. *Journal of Fluids and Structures* **25** (4), 666–675.
- AUDOLY, B. & POMEAU, Y. 2010 *Elasticity and geometry: from hair curls to the non-linear response of shells*. Oxford University Press.

- BABENKO, V. V. & CARPENTER, P. W. 2003 Dolphin hydrodynamics. In *Flow Past Highly Compliant Boundaries and in Collapsible Tubes*, pp. 293–323. Springer.
- BABUŠKA, I. 1973 The finite element method with lagrangian multipliers. *Numerische Mathematik* **20** (3), 179–192.
- BADIA, S., NOBILE, F. & VERGARA, C. 2008 Fluid-structure partitioned procedures based on Robin transmission conditions. *Journal of Computational Physics* **227** (14), 7027–7051.
- BAGHERI, S., MAZZINO, A. & BOTTARO, A. 2012 Spontaneous symmetry breaking of a hinged flapping filament generates lift. *Physical Review Letters* **109**, 154502.
- BALE, R., HAO, M., BHALLA, A. P. S., PATEL, N. & PATANKAR, N. A. 2014 Gray's paradox: a fluid mechanical perspective. *Nature Scientific Reports* **4**, 5904.
- BANDYOPADHYAY, P., HENoch, C., HRUBES, J., SEMENOV, B., AMIROV, A., KULIK, V., MALYUGA, A., CHOI, K.-S. & ESCUDIER, M. 2005 Experiments on the effects of aging on compliant coating drag reduction. *Physics of Fluids* **17** (8), 085104.
- BANDYOPADHYAY, P. R. & HELLMUM, A. M. 2014 Modeling how shark and dolphin skin patterns control transitional wall-turbulence vorticity patterns using spatiotemporal phase reset mechanisms. *Nature Scientific Reports* **4**, 6650.
- BARBOSA, H. & HUGHES, T. 1991 The finite element method with Lagrange multipliers on the boundary: circumventing the Babuška-Brezzi condition. *Computer Methods in Applied Mechanics and Engineering* **85**, 109–128.
- BARKLEY, D. 1996 Three-dimensional Floquet stability analysis of the wake of a circular cylinder. *Journal of Fluid Mechanics* **322**, 215–241.
- BARKLEY, D. 2006 Linear analysis of the cylinder wake mean flow. *Europhysics Letters* **75**, 750–756.
- BARRETT, D., TRIANTAFYLLOU, M., YUE, D., GROSENBAUGH, M. & WOLFGANG, M. 1999 Drag reduction in fish-like locomotion. *Journal of Fluid Mechanics* **392**, 183–212.
- BAZILEVS, Y., CALO, V., HUGHES, T. & ZHANG, Y. 2008 Isogeometric fluid-structure interaction: theory, algorithms, and computations. *Computational Mechanics* **43**, 3–37.
- BAZILEVS, Y. & HUGHES, T. J. 2005 Weak imposition of Dirichlet boundary conditions in fluid mechanics. *Computers & Fluids* **36** (1), 12–26.
- BAZILEVS, Y., TAKIZAWA, K. & TEZDUYAR, T. E. 2013 *Computational Fluid-Structure Interaction: Methods and Applications*. Wiley.
- BEHR, M. A., FRANCA, L. P. & TEZDUYAR, T. E. 1993 Stabilized finite element methods for the velocity-pressure-stress formulation of incompressible flows. *Computer Methods in Applied Mechanics and Engineering* **104** (1), 31–48.
- BEKKA, N., SELLAM, M. & CHPOUN, A. 2015 Aeroelastic stability analysis of a flexible over-expanded rocket nozzle using numerical coupling by the method of transpiration. *Journal of Fluids and Structures* **56**, 89–106.
- BENJAMIN, T. B. 1960 Effects of a flexible boundary on hydrodynamic stability. *Journal of Fluid Mechanics* **9** (4), 513–532.
- BENJAMIN, T. B. 1963 The threefold classification of unstable disturbances in flexible surfaces bounding inviscid flows. *Journal of Fluid Mechanics* **16** (3), 436–450.
- BENZI, M. 2002 Preconditioning techniques for large linear systems: a survey. *Journal of Computational Physics* **182** (2), 418–477.

-
- BENZI, M., GOLUB, G. H. & LIESEN, J. 2005 Numerical solution of saddle point problems. *Acta Numerica* **14**, 1–137.
- BENZI, M. & OLSHANSKII, M. A. 2006 An augmented Lagrangian-based approach to the Oseen problem. *SIAM Journal on Scientific Computing* **28** (6), 2095–2113.
- BISPLINGHOFF, R. L., ASHLEY, H. & HALFMAN, R. L. 1955 *Aeroelasticity*. Addison-Wesley Publishing Company.
- BOCIU, L., TOUNDYKOV, D. & ZOLÉSIO, J.-P. 2015 Well-posedness analysis for a linearization of a fluid-elasticity interaction. *SIAM Journal on Mathematical Analysis* **47** (3), 1958–2000.
- BODENSCHATZ, E., PESCH, W. & AHLERS, G. 2000 Recent developments in Rayleigh-Bénard convection. *Annual Review of Fluid Mechanics* **32** (1), 709–778.
- BOKAIAN, A. 1990 Natural frequencies of beams under tensile axial loads. *Journal of Sound and Vibration* **142** (3), 481–498.
- BRANDT, L., SIPP, D., PRALITS, J. O. & MARQUET, O. 2011 Effect of base-flow variation in noise amplifiers: the flat-plate boundary layer. *Journal of Fluid Mechanics* **687**, 503–528.
- BRENAN, K. E., CAMPBELL, S. L. & PETZOLD, L. R. 1996 *Numerical solution of initial-value problems in differential-algebraic equations*. Society for Industrial and Applied Mathematics.
- BREUER, M., DE NAYER, G., MÜNSCH, M., GALLINGER, T. & WÜCHNER, R. 2012 Fluid–structure interaction using a partitioned semi-implicit predictor–corrector coupling scheme for the application of large-eddy simulation. *Journal of Fluids and Structures* **29**, 107–130.
- BUSHNELL, D. M. & MOORE, K. 1991 Drag reduction in nature. *Annual Review of Fluid Mechanics* **23** (1), 65–79.
- CARINI, M., PFISTER, J.-L. & MARQUET, O. 2017 Passive control of fluid-structure instabilities by means of piezo-electric shunts. In *16th European Turbulence Conference, Stockholm, Sweden*.
- CARLSON, D. R., WIDNALL, S. E. & PEETERS, M. F. 1982 A flow-visualization study of transition in plane Poiseuille flow. *Journal of Fluid Mechanics* **121**, 487–505.
- CARPENTER, P. & GARRAD, A. 1985 The hydrodynamic stability of flow over Kramer-type compliant surfaces. Part 1. Tollmien-Schlichting instabilities. *Journal of Fluid Mechanics* **155**, 465–510.
- CARPENTER, P. & GARRAD, A. 1986 The hydrodynamic stability of flow over Kramer-type compliant surfaces. Part 2. Flow-induced surface instabilities. *Journal of Fluid Mechanics* **170**, 199–232.
- CARPENTER, P. W. 1993 Optimization of multiple-panel compliant walls for delay of laminar-turbulent transition. *AIAA Journal* **31** (7), 1187–1188.
- CARPENTER, P. W., DAVIES, C. & LUCEY, A. D. 2000 Hydrodynamics and compliant walls: does the dolphin have a secret? *Current Science* pp. 758–765.
- CARPENTER, P. W., LUCEY, A. D. & DAVIES, C. 2001 Progress on the use of compliant walls for laminar-flow control. *Journal of Aircraft* **38** (3), 504–512.
- CARPENTER, P. W. & MORRIS, P. J. 1990 The effect of anisotropic wall compliance on boundary-layer stability and transition. *Journal of Fluid Mechanics* **218**, 171–223.
- CAUSIN, P., GERBEAU, J.-F. & NOBILE, F. 2005 Added-mass effect in the design of partitioned algorithms for fluid-structure problems. *Computer Methods in Applied Mechanics and Engineering* **194** (42), 4506–4527.
- CHADWICK, P. 1999 *Continuum mechanics: concise theory and problems*. Dover.

- CHAN, T. F. & KELLER, H. 1982 Arc-length continuation and multigrid techniques for nonlinear elliptic eigenvalue problems. *SIAM Journal on Scientific and Statistical Computing* **3** (2), 173–194.
- CHANG, Y.-C., HOU, T., MERRIMAN, B. & OSHER, S. 1996 A level set formulation of Eulerian interface capturing methods for incompressible fluid flows. *Journal of Computational Physics* **124** (2), 449–464.
- CHARRU, F. 2007 *Instabilités hydrodynamiques*. EDP Sciences.
- CHOI, K.-S., YANG, X., CLAYTON, B., GLOVER, E., ATLAR, M., SEMENOV, B. & KULIK, V. 1997 Turbulent drag reduction using compliant surfaces. *Proceedings of the Royal Society of London A: Mathematical, Physical and Engineering Sciences* **453**, 2229–2240.
- CHRISTENSEN, R. 2012 *Theory of viscoelasticity: an introduction*. Academic Press.
- CIARLET, P. G. 1980 A justification of the von Kármán equations. *Archive for Rational Mechanics and Analysis* **73** (4), 349–389.
- CIARLET, P. G. 2013 *Linear and nonlinear functional analysis with applications*. Society for Industrial and Applied Mathematics.
- CIMBALA, J. & CHEN, K. 1994 Supercritical Reynolds number experiments on a freely rotatable cylinder/splitter plate body. *Physics of Fluids* **6** (7), 2440–2445.
- CIMBALA, J. & GARG, S. 1991 Flow in the wake of a freely rotatable cylinder with splitter plate. *AIAA Journal* **29** (6), 1001–1003.
- CIMBALA, J., GARG, S. & PARK, W. 1988 The effect of a non-rigidly mounted splitter plate on the flow over a circular cylinder. *Bulletin of the American Physical Society* **33**, 2249.
- CISONNI, J., LUCEY, A. D., ELLIOTT, N. S. & HEIL, M. 2017 The stability of a flexible cantilever in viscous channel flow. *Journal of Sound and Vibration* **396**, 186–202.
- COURT, S., FOURNIÉ, M. & LOZINSKI, A. 2010 A fictitious domain approach for the Stokes problem based on the extended finite element method. *International Journal for Numerical Methods in Fluids* **74** (2), 73–99.
- CROSETTO, P., DEPARIS, S., FOURESTY, G. & QUARTERONI, A. 2011 Parallel algorithms for fluid-structure interaction problems in haemodynamics. *SIAM Journal on Scientific Computing* **33** (4), 1598–1622.
- CÉA, J. 1986 Conception optimale ou identification de formes, calcul rapide de la dérivée directionnelle de la fonction coût. *RAIRO-Modélisation mathématique et analyse numérique* **20** (3), 371–402.
- DAPOGNY, C., FREY, P., OMNÈS, F. & PRIVAT, Y. 2017 Geometrical shape optimization in fluid mechanics using FreeFem++.
- DAVIES, C. & CARPENTER, P. W. 1997 Numerical simulation of the evolution of Tollmien-Schlichting waves over finite compliant panels. *Journal of Fluid Mechanics* **335**, 361–392.
- DAWSON, P. 1978 Viscoplastic finite element analysis of steady-state forming processes including strain history and stress flux dependence. *Tech. Rep.*. Sandia Labs.
- DELFOUR, M. C. & ZOLÉSIO, J.-P. 2011 *Shapes and geometries : metrics, analysis, differential calculus, and optimization*. Society for Industrial and Applied Mathematics.
- DEPARIS, S., FERNÁNDEZ, M. A. & FORMAGGIA, L. 2003 Acceleration of a fixed point algorithm for fluid-structure interaction using transpiration conditions. *ESAIM: Mathematical Modelling and Numerical Analysis* **37** (4), 601–616.

-
- DEPARIS, S., FORTI, D., GRANDPERRIN, G. & QUARTERONI, A. 2016 FaCSI: a block parallel preconditioner for fluid–structure interaction in hemodynamics. *Journal of Computational Physics* **327**, 700–718.
- DEPARIS, S., GRANDPERRIN, G. & QUARTERONI, A. 2014 Parallel preconditioners for the unsteady Navier–Stokes equations and applications to hemodynamics simulations. *Computers & Fluids* **92**, 253–273.
- DETTMER, W. G. & PERIĆ, D. 2008 On the coupling between fluid flow and mesh motion in the modelling of fluid–structure interaction. *Computational Mechanics* **43** (1), 81–90.
- DIXON, A. E., LUCEY, A. D. & CARPENTER, P. W. 1994 Optimization of viscoelastic compliant walls for transition delay. *AIAA Journal* **32** (2), 256–267.
- DONEA, J., HUERTA, A., PONTOT, J.-P. & RODRIGEZ-FERRAN, A. 2004 Arbitrary Lagrangian-Eulerian methods. *Encyclopedia of Computational Mechanics*.
- DOWELL, E. 1970 A review of the aeroelastic stability of plates and shells. *AIAA Journal* **8** (3), 385–399.
- DOWELL, E. H. 1971 Generalized aerodynamic forces on a flexible plate undergoing transient motion in a shear flow with an application to panel flutter. *AIAA Journal* **9** (5), 834–841.
- DOWELL, E. H., CLARK, R., COX, D. & OTHERS 2004 *A modern course in aeroelasticity. Solid Mechanics and Its Applications* 217. Springer.
- DRAZIN, P. G. & REID, W. H. 2004 *Hydrodynamic stability*, 2nd edn. Cambridge University Press.
- DUNCAN, J. 1988 The dynamics of waves at the interface between a two-layer viscoelastic coating and a fluid flow. *Journal of Fluids and Structures* **2** (1), 35–51.
- DUNCAN, J., WAXMAN, A. & TULIN, M. 1985 The dynamics of waves at the interface between a viscoelastic coating and a fluid flow. *Journal of Fluid Mechanics* **158**, 177–197.
- DUNNE, T., RANNACHER, R. & RICHTER, T. 2010 Numerical simulation of fluid-structure interaction based on monolithic variational formulations. *Fundamental Trends in Fluid-Structure Interaction* **1**, 1–75.
- EHRENSTEIN, U. & GALLAIRE, F. 2005 On two-dimensional temporal modes in spatially evolving open flows: the flat-plate boundary layer. *Journal of Fluid Mechanics* **536**, 209–218.
- EMMONS, H. 1951 The laminar-turbulent transition in a boundary layer – Part I. *Journal of the Aeronautical Sciences* **18** (7), 490–498.
- ERRICO, R. M. 1997 What is an adjoint model? *Bulletin of the American Meteorological Society* **78** (11), 2577–2592.
- ESSAPIAN, F. S. 1955 Speed-induced skin folds in the bottle-nosed porpoise *tursiops truncatus*. In *Library of the Museum of Comparative Zoology*. Harvard University.
- ETIENNE, S. & PELLETIER, D. 2005 An updated Lagrangian monolithic formulation for steady-state fluid-structure interaction problems. In *43rd AIAA Aerospace Sciences Meeting and Exhibit*, p. 2005.
- FACCHINETTI, M. L., DE LANGRE, E. & BIOLLEY, F. 2004 Coupling of structure and wake oscillators in vortex-induced vibrations. *Journal of Fluids and Structures* **19** (2), 123–140.
- FAILER, L., MEIDNER, D. & VEXLER, B. 2016 Optimal control of a linear unsteady fluid-structure interaction problem. *Journal of Optimization Theory and Applications* pp. 1–27.

- FARHAT, C. 2017 CFD-based nonlinear computational aeroelasticity. *Encyclopedia of Computational Mechanics* pp. 1–21.
- FARHAT, C., VAN DER ZEE, K. G. & GEUZAIN, P. 2006 Provably second-order time-accurate loosely-coupled solution algorithms for transient nonlinear computational aeroelasticity. *Computer Methods in Applied Mechanics and Engineering* **195** (17–18), 1973–2001.
- FARHLOUL, M. & FORTIN, M. 2002 Review and complements on mixed-hybrid finite element methods for fluid flows. *Journal of Computational and Applied Mathematics* **140** (1–2), 301–313.
- FARRELL, B. F. & IOANNOU, P. J. 1993 Stochastic forcing of the linearized Navier–Stokes equations. *Physics of Fluids* **5** (11), 2600–2609.
- FEDOROV, A. 2011 Transition and stability of high-speed boundary layers. *Annual Review of Fluid Mechanics* **43**, 79–95.
- FEPPON, F., ALLAIRE, G., BORDEU, F., CORTIAL, J. & DAPOGNY, C. 2018 Shape optimization of a coupled thermal fluid-structure problem in a level set mesh evolution framework.
- FERNÁNDEZ, M. Á. 2011 Coupling schemes for incompressible fluid-structure interaction: implicit, semi-implicit and explicit. *SeMA Journal* **55** (1), 59–108.
- FERNÁNDEZ, M. Á., GERBEAU, J.-F. & GRANDMONT, C. 2007 A projection semi-implicit scheme for the coupling of an elastic structure with an incompressible fluid. *International Journal for Numerical Methods in Engineering* **69** (4), 794–821.
- FERNÁNDEZ, M. Á. & LE TALLEC, P. 2003a Linear stability analysis in fluid-structure interaction with transpiration. Part I: formulation and mathematical analysis. *Computer Methods in Applied Mechanics and Engineering* **192**, 4805–4835.
- FERNÁNDEZ, M. Á. & LE TALLEC, P. 2003b Linear stability analysis in fluid-structure interaction with transpiration. Part II: numerical analysis and applications. *Computer Methods in Applied Mechanics and Engineering* **192**, 4837–4873.
- FERNÁNDEZ, M. Á. & MOUBACHIR, M. 2005 A newton method using exact jacobians for solving fluid-structure coupling. *Computers & Structures* **83** (2), 127–142.
- FISH, F. E. 2006 The myth and reality of Gray’s paradox: implication of dolphin drag reduction for technology. *Bioinspiration & biomimetics* **1** (2), R17.
- FISH, F. E. & ROHR, J. 1999 Review of dolphin hydrodynamics and swimming performance. *Tech. Rep.*. Space and naval warfare systems command, San Diego (CA).
- FISHER, C. & ARENA, A. 1996 On the transpiration method for efficient aeroelastic analysis using an Euler solver. *AIAA Paper* pp. 96–3436.
- FORMAGGIA, L. & NOBILE, F. 1999 A stability analysis for the Arbitrary Lagrangian Eulerian formulation with finite elements. *East-West Journal of Numerical Mathematics* **7**, 105–132.
- GAD-EL-HAK, M. 1996 Compliant coatings: a decade of progress. *Applied Mechanics Reviews* **49** (10S), S147–S157.
- GAD-EL-HAK, M. 2000 *Flow control: passive, active, and reactive flow management*. Cambridge University Press.
- GAD-EL-HAK, M., BLACKWELDER, R. F. & RILEY, J. J. 1984 On the interaction of compliant coatings with boundary-layer flows. *Journal of Fluid Mechanics* **140**, 257–280.
- GADELHA, H., GAFFNEY, E., SMITH, D. & KIRKMAN-BROWN, J. 2010 Nonlinear instability in flagellar dynamics: a novel modulation mechanism in sperm migration? *Journal of The Royal Society Interface*.

-
- GALLAIRE, F. 2019 Commentaire de lecture du présent manuscrit, « ça n'est pas infiniment digeste, mais ça a le mérite d'être précis ». Soutenance de thèse.
- GAO, Z. & MA, Y. 2008 Shape gradient of the dissipated energy functional in shape optimization for the viscous incompressible flow. *Applied Numerical Mathematics* **58** (11), 1720–1741.
- GASTER, M. 1988 Is the dolphin a red herring? *Turbulence management and relaminarisation* pp. 285–304.
- GEE, M. W., KÜTTLER, U. & WALL, W. A. 2011 Truly monolithic algebraic multigrid for fluid-structure interaction. *International Journal for Numerical Methods in Engineering* **85** (8), 987–1016.
- GERBEAU, J.-F., VIDRASCU, M. & FREY, P. 2003 Fluid-structure interaction in blood flows on geometries coming from medical imaging. Research Report RR-5052. INRIA.
- GHATTAS, O. & LI, X. 1995 A variational finite element method for stationary nonlinear fluid-solid interaction. *Journal of Computational Physics* **121** (2), 347–356.
- GIANNETTI, F. & LUCHINI, P. 2006 Structural sensitivity of the first instability of the cylinder wake. *Journal of Fluid Mechanics* **581**, 167–197.
- GIRAULT, V. & RAVIART, P. 1985 *Finite Element Methods for Navier-Stokes Equations*. Springer Series in Computational Mathematics 5. Springer.
- GLOWINSKI, R., PAN, T., HESLA, T., JOSEPH, D. & PERIAUX, J. 2001 A fictitious domain approach to the direct numerical simulation of incompressible viscous flow past moving rigid bodies: application to particulate flow. *Journal of Computational Physics* **169** (2), 363–426.
- GLOWINSKI, R., PAN, T.-W. & PERIAUX, J. 1994a A fictitious domain method for Dirichlet problem and applications. *Computer Methods in Applied Mechanics and Engineering* **111** (3-4), 283–303.
- GLOWINSKI, R., PAN, T.-W. & PERIAUX, J. 1994b A fictitious domain method for external incompressible viscous flow modeled by Navier-Stokes equations. *Computer Methods in Applied Mechanics and Engineering* **112** (1-4), 133–148.
- GLOWINSKI, R. & PIRONNEAU, O. 1976 Towards the computation of minimum drag profiles in viscous laminar flow. *Applied Mathematical Modelling* **1** (2), 58–66.
- GOLUB, G. H. & VAN LOAN, C. F. 2013 *Matrix computations*, 4th edn. Johns Hopkins University Press.
- GOMES, J. P., YIGIT, S., LIENHART, H. & SCHÄFER, M. 2011 Experimental and numerical study on a laminar fluid-structure interaction reference test case. *Journal of Fluids and Structures* **27** (1), 43–61.
- GRAY, J. 1936 Studies in animal locomotion: VI. The propulsive powers of the dolphin. *Journal of Experimental Biology* **13** (2), 192–199.
- GU, F., WANG, J., QIAO, X. & HUANG, Z. 2012 Pressure distribution, fluctuating forces and vortex shedding behavior of circular cylinder with rotatable splitter plates. *Journal of Fluids and Structures* **28**, 263–278.
- HADAMARD, J. 1908 *Mémoire sur le problème d'analyse relatif à l'équilibre des plaques élastiques encastrées, Mémoires présentés par divers savants à l'Académie des sciences de l'Institut de France*, vol. 33. Imprimerie nationale.
- HAFTKA, R. T. 1977 Optimization of flexible wing structures subject to strength and induced drag constraints. *AIAA Journal* **15** (8), 1101–1106.

- HECHT, F. 2012 New development in FreeFem++. *Journal of Numerical Mathematics* **20** (3-4), 251–265.
- HEIL, M. 2004 An efficient solver for the fully coupled solution of large-displacement fluid-structure interaction problems. *Computer Methods in Applied Mechanics and Engineering* **193** (1), 1–23.
- HEIL, M., HAZEL, A. L. & BOYLE, J. 2008 Solvers for large-displacement fluid-structure interaction problems: segregated versus monolithic approaches. *Computational Mechanics* **43** (1), 91–101.
- HEISTER, T. & RAPIN, G. 2013 Efficient augmented Lagrangian-type preconditioning for the Oseen problem using Grad-Div stabilization. *International Journal for Numerical Methods in Fluids* **71** (1), 118–134.
- HELENBROOK, B. T. 2003 Mesh deformation using the biharmonic operator. *International Journal for Numerical Methods in Engineering* **56** (7), 1007–1021.
- HELGASON, E. & KRAJNOVIĆ, S. 2015 Optimization using Arbitrary Lagrangian–Eulerian Formulation of the Navier–Stokes equations. *Journal of Fluids Engineering* **137** (6), 061202.
- HENERS, J., RADTKE, L., HINZE, M. & DÜSTER, A. 2018 Adjoint shape optimization for fluid–structure interaction of ducted flows. *Computational Mechanics* **61** (3), 259–276.
- HENROT, A. & PIERRE, M. 2006 *Variation et optimisation de formes: une analyse géométrique. Mathématiques et applications* 48. Springer Science & Business Media.
- HEUVELINE, V. & STRAUSS, F. 2009 Shape optimization towards stability in constrained hydrodynamic systems. *Journal of Computational Physics* **228** (4), 938–951.
- HEYWOOD, J. G., RANNACHER, R. & TUREK, S. 1996 Artificial boundaries and flux and pressure conditions for the incompressible Navier–Stokes equations. *International Journal for Numerical Methods in Fluids* **22**, 325–352.
- HILL, D. 1992 A theoretical approach for analyzing the restabilization of wakes. In *30th Aerospace Sciences Meeting and Exhibit*, p. 67.
- HOU, G., WANG, J. & LAYTON, A. 2012 Numerical methods for fluid-structure interaction. *Communications in Computational Physics* **12**, 337 – 377.
- HRON, J. & TUREK, S. 2006 A monolithic FEM/multigrid solver for an ALE formulation of fluid-structure interaction with applications in biomechanics. In *Fluid-structure interaction*, pp. 146–170. Springer.
- HUERRE, P. & MONKEWITZ, P. A. 1990 Local and global instabilities in spatially developing flows. *Annual Review of Fluid Mechanics* **22**, 473–537.
- HUGHES, T., LIU, W. & ZIMMERMANN, T. 1981 Lagrangian-Eulerian finite element formulation for incompressible viscous flows. *Computer Methods in Applied Mechanics and Engineering* **29**, 329–349.
- HUR, J., BERAN, P., HUTTSELL, L., SNYDER, R., SONI, B. & THORNBURG, H. 2004 Parametric mesh deformation for sensitivity analysis and design of a joined-wing aircraft. *42nd AIAA Aerospace Sciences Meeting and Exhibit. Reston: AIAA*.
- HÜBNER, B., WALHORN, E. & DINKLER, D. 2004 A monolithic approach to fluid-structure interaction using space-time finite elements. *Computer Methods in Applied Mechanics and Engineering* **193** (23), 2087–2104.
- VAN INGEN, J. 1956 A suggested semi-empirical method for the calculation of the boundary layer transition region. *Tech. Rep.*. Delft University of Technology.

-
- ITO, M., TAMANO, S., IGUCHI, R., YOKOTA, K., AKINO, N., HINO, R. & KUBO, S. 2006 Turbulent drag reduction by the seal fur surface. *Physics of Fluids* **18** (6), 065102.
- JAMESON, A. 1988 Aerodynamic design via control theory. *Journal of Scientific Computing* **3** (3), 233–260.
- JAMESON, A., MARTINELLI, L. & PIERCE, N. 1998 Optimum aerodynamic design using the Navier–Stokes equations. *Theoretical and Computational Fluid Dynamics* **10** (1), 213–237.
- JAMESON, A. & OU, K. 2011 50 years of transonic aircraft design. *Progress in Aerospace Sciences* **47** (5), 308–318.
- JIA, L.-B. & YIN, X.-Z. 2009 Response modes of a flexible filament in the wake of a cylinder in a flowing soap film. *Physics of Fluids* **21** (10), 101704.
- JUNIPER, M. P., HANIFI, A. & THEOFILIS, V. 2014 Modal stability theory, lecture notes from the FLOW-NORDITA summer school on advanced instability methods for complex flows, Stockholm. *Applied Mechanics Reviews* **66** (2), 024804.
- KACHANOV, Y. S. 1994 Physical mechanisms of laminar-boundary-layer transition. *Annual Review of Fluid Mechanics* **26** (1), 411–482.
- KARPEL, M. 1982 Design for active flutter suppression and gust alleviation using state-space aeroelastic modeling. *Journal of Aircraft* **19** (3), 221–227.
- KASSIOTIS, C., IBRAHIMBEGOVIC, A., NIEKAMP, R. & MATTHIES, H. G. 2011 Nonlinear fluid–structure interaction problem. Part I: implicit partitioned algorithm, nonlinear stability proof and validation examples. *Computational Mechanics* **47** (3), 305–323.
- KATO, T. 1995 *Perturbation theory for linear operators*, 2nd edn. *Grundlehren der mathematischen Wissenschaften* 132. Springer.
- KAY, D., LOGHIN, D. & WATHEN, A. 2002 A preconditioner for the steady-state Navier–Stokes equations. *SIAM Journal on Scientific Computing* **24** (1), 237–256.
- KENWAY, G. K., KENNEDY, G. J. & MARTINS, J. R. 2014 Scalable parallel approach for high-fidelity steady-state aeroelastic analysis and adjoint derivative computations. *AIAA Journal* .
- KIM, H., KANG, S. & KIM, D. 2017 Dynamics of a flag behind a bluff body. *Journal of Fluids and Structures* **71**, 1–14.
- KRAMER, M. O. 1960 Boundary layer stabilization by distributed damping. *Naval Engineers Journal* **72** (1), 25–34.
- KRAMER, M. O. 1961 The dolphin’s secret. *Naval Engineers Journal* **73** (1), 103–108.
- KWON, K. & CHOI, H. 1996 Control of laminar vortex shedding behind a circular cylinder using splitter plates. *Physics of Fluids* **8** (2), 479–486.
- LACIS, U., BROSSE, N., INGREMEAU, F., MAZZINO, A., LUNDELL, F., KELLAY, H. & BAGHERI, S. 2014 Passive appendages generate drift through symmetry breaking. *Nature* .
- LADD, A. J. 1994 Numerical simulations of particulate suspensions via a discretized Boltzmann equation. Part 1. Theoretical foundation. *Journal of Fluid Mechanics* **271**, 285–309.
- LAMBRECHTS, R. 2018 Méthodes pour l’analyse de stabilité linéaire de systèmes couplés fluide-structure. Master’s thesis, École Nationale Supérieure d’Arts et Métiers.
- LANDAHL, M. T. 1962 On the stability of a laminar incompressible boundary layer over a flexible surface. *Journal of Fluid Mechanics* **13** (4), 609–632.
- LANDAU, L. & LIFCHITZ, E. 1967 *Physique théorique : Théorie de l’élasticité*. MIR.

- DE LANGRE, E. 2002 *Fluides et Solides*. Éditions de l'École polytechnique, Palaiseau.
- DE LANGRE, E. 2006 Frequency lock-in is caused by coupled-mode flutter. *Journal of Fluids and Structures* **22** (6), 783–791.
- DE LANGRE, E. 2008 Effects of wind on plants. *Annual Review of Fluid Mechanics* **40**, 141–168.
- LE TALLEC, P. & MOURO, J. 2001 Fluid structure interaction with large structural displacements. *Computer Methods in Applied Mechanics and Engineering*.
- LECLERCQ, T. & DE LANGRE, E. 2018 Vortex-induced vibrations of cylinders bent by the flow. *Journal of Fluids and Structures* **80**, 77–93.
- LEE, J. & YOU, D. 2013 Study of vortex-shedding-induced vibration of a flexible splitter plate behind a cylinder. *Physics of Fluids* **25**, 110811.
- LEE, J. H., HUANG, W.-X. & SUNG, H. J. 2014 Flapping dynamics of a flexible flag in a uniform flow. *Fluid Dynamics Research* **46** (5), 055517.
- LEHOUCQ, R., SORENSEN, D. & YANG, C. 1997 *ARPACK Users' guide: solution of large scale eigenvalue problems with implicitly restarted Arnoldi methods*.
- LESOINNE, M. & FARHAT, C. 1993 Stability analysis of dynamic meshes for transient aeroelastic computations. In *11th Computational Fluid Dynamics Conference*, p. 3325.
- LESOINNE, M. & FARHAT, C. 1998 Higher-order subiteration-free staggered algorithm for nonlinear transient aeroelastic problems. *AIAA Journal* **36** (9), 1754–1757.
- LI, X. S. 2005 An overview of SuperLU: algorithms, implementation, and user interface. *ACM Transactions on Mathematical Software (TOMS)* **31** (3), 302–325.
- LIGHTHILL, M. 1945 A new method of two-dimensional aerodynamics design. In *R&M1111, Aeronautical Research Council*. Citeseer.
- LIGHTHILL, M. 1958 On displacement thickness. *Journal of Fluid Mechanics* **4** (04), 383–392.
- LIONS, J. L. 1971 *Optimal control of systems governed by partial differential equations*. Grundlehren der mathematischen Wissenschaften 170. Springer Verlag.
- LU, L., GUO, X.-L., TANG, G.-Q., LIU, M.-M., CHEN, C.-Q. & XIE, Z.-H. 2016 Numerical investigation of flow-induced rotary oscillation of circular cylinder with rigid splitter plate. *Physics of Fluids* **28** (9), 093604.
- LUCEY, A. & CARPENTER, P. 1993 The hydroelastic stability of three-dimensional disturbances of a finite compliant wall. *Journal of Sound and Vibration* **165** (3), 527–552.
- LUCEY, A. & CARPENTER, P. 1995 Boundary layer instability over compliant walls: comparison between theory and experiment. *Physics of Fluids* **7** (10), 2355–2363.
- LUCEY, A. D. & CARPENTER, P. W. 1992 A numerical simulation of the interaction of a compliant wall and inviscid flow. *Journal of Fluid Mechanics* **234**, 121–146.
- LUCHINI, P. & BOTTARO, A. 2014a Adjoint equations in stability analysis. *Annual Review of Fluid Mechanics* **46** (1), 493.
- LUCHINI, P. & BOTTARO, A. 2014b An introduction to adjoint problems – supplemental appendix to ADJOINTS EQUATIONS IN STABILITY ANALYSIS. *Annual Review of Fluid Mechanics* **46** (1), 493.
- LUND, E., MØLLER, H. & JAKOBSEN, L. A. 2003 Shape design optimization of stationary fluid-structure interaction problems with large displacements. *Structural and Multidisciplinary Optimization* **25** (5-6), 383–392.

-
- MADIGOSKY, W., LEE, G., HAUN, J., BORKAT, F. & KATAOKA, R. 1986 Acoustic surface wave measurements on live bottlenose dolphins. *The Journal of the Acoustical Society of America* **79** (1), 153–159.
- MANZONI, A. & PONTI, L. 2016 An adjoint-based method for the numerical approximation of shape optimization problems in presence of fluid-structure interaction.
- MARCKMANN, G. & VERRON, E. 2006 Comparison of hyperelastic models for rubber-like materials. *Rubber chemistry and technology* **79** (5), 835–858.
- MARQUET, O. & LARSSON, M. 2015 Global wake instabilities of low aspect-ratio flat-plates. *European Journal of Mechanics-B/Fluids* **49**, 400–412.
- MARQUET, O., SIPP, D. & JACQUIN, L. 2008 Sensitivity analysis and passive control of cylinder flow. *Journal of Fluid Mechanics* **615**, 221–252.
- MARSDEN, J. E. & HUGHES, T. J. 1994 *Mathematical foundations of elasticity*. Dover Books on Mathematics.
- MARTINS, P., NATAL JORGE, R. & FERREIRA, A. 2006 A comparative study of several material models for prediction of hyperelastic properties: application to silicone-rubber and soft tissues. *Strain* **42** (3), 135–147.
- MAT ALI, M. S., DOOLAN, C. J. & WHEATLEY, V. 2011 Low Reynolds number flow over a square cylinder with a splitter plate. *Physics of Fluids* **23** (3), 033602.
- MATTHIES, H. G. & STEINDORF, J. 2002 Partitioned but strongly coupled iteration schemes for nonlinear fluid-structure interaction. *Computers & Structures* **80** (27), 1991 – 1999.
- MAXEY, M. R. & RILEY, J. J. 1983 Equation of motion for a small rigid sphere in a nonuniform flow. *The Physics of Fluids* **26** (4), 883–889.
- MELIGA, P. & CHOMAZ, J.-M. 2010 An asymptotic expansion for the vortex-induced vibrations of a circular cylinder. *Journal of Fluid Mechanics* pp. 137–167.
- MICHELIN, S., SMITH, S. G. L. & GLOVER, B. J. 2008 Vortex shedding model of a flapping flag. *Journal of Fluid Mechanics* **617**, 1–10.
- MITTAL, S. & SINGH, S. 2005 Vortex-induced vibrations at subcritical Re. *Journal of Fluid Mechanics* **534**, 185–194.
- MORTCHELEWICZ, G. 1997 Application of the linearized Euler equations to flutter. *Office National d'Études et de Recherches Aéropatiales (ONERA)*.
- MOULIN, J., JOLIVET, P. & MARQUET, O. 2019 Augmented Lagrangian preconditioner for large-scale hydrodynamic stability analysis. *Computer Methods in Applied Mechanics and Engineering* **351**, 718–743.
- NADARAJAH, S. K. & JAMESON, A. 2007 Optimum shape design for unsteady flows with time-accurate continuous and discrete adjoint method. *AIAA Journal* **45** (7), 1478–1491.
- NAKAJIMA, N. & HARRELL, E. 2001 Rheology of PVC plastisol: formation of immobilized layer in pseudoplastic flow. *Journal of Colloid and Interface Science* **238** (1), 116–124.
- NAKAJIMA, N., ISNER, J. & HARRELL, E. 1981 Gelation and fusion mechanism of PVC plastisols observed by changes of morphology, viscoelastic properties, and ultimate mechanical properties. *Journal of Macromolecular Science, Part B: Physics* **20** (3), 349–364.
- NAKAZAWA, T. & AZEGAMI, H. 2016 Shape optimization of flow field improving hydrodynamic stability. *Japan Journal of Industrial and Applied Mathematics* **33** (1), 167–181.

- NAVROSE & MITTAL, S. 2016 Lock-in in vortex-induced vibration. *Journal of Fluid Mechanics* **794**, 565–594.
- NEMEC, M., ZINGG, D. W. & PULLIAM, T. H. 2004 Multipoint and multi-objective aerodynamic shape optimization. *AIAA Journal* **42** (6).
- NOBILE, F. 2001 Numerical approximation of fluid-structure interaction problems with application to haemodynamics. PhD thesis, EPFL.
- OGDEN, R. W. 1997 *Non-linear elastic deformations*. Dover.
- OLSHANSKII, M. A. & BENZI, M. 2008 An augmented Lagrangian approach to linearized problems in hydrodynamic stability. *SIAM Journal on Scientific Computing* **30** (3), 1459–1473.
- ORSZAG, S. A. 1971 Accurate solution of the Orr-Sommerfeld stability equation. *Journal of Fluid Mechanics* **50** (4), 689–703.
- PATANKAR, S. & SPALDING, D. 1972 A calculation procedure for heat, mass and momentum transfer in three-dimensional parabolic flows. *International Journal of Heat and Mass Transfer* **15**, 1787–1972.
- PATANKAR, S. V. 1981 A calculation procedure for two-dimensional elliptic situations. *Numerical heat transfer* **4** (4), 409–425.
- PAVLOV, V. 2006 Dolphin skin as a natural anisotropic compliant wall. *Bioinspiration & biomimetics* **1** (2), 31.
- PELLEGRINI, F. 2008 Scotch and libscotch 5.1 user's guide.
- PESKIN, C. S. 1977 Numerical analysis of blood flow in the heart. *Journal of Computational Physics* **25** (3), 220–252.
- PESKIN, C. S. 2002 The immersed boundary method. *Acta Numerica* **11**, 479–517.
- PIPERNO, S. & FARHAT, C. 2001 Partitioned procedures for the transient solution of coupled aeroelastic problems – Part II: energy transfer analysis and three-dimensional applications. *Computer Methods in Applied Mechanics and Engineering* **190** (24–25), 3147–3170.
- PIRONNEAU, O. 1973 On optimum profiles in Stokes flow. *Journal of Fluid Mechanics* **59** (1), 117–128.
- PIRONNEAU, O. 2012 *Optimal shape design for elliptic systems*. Springer Science & Business Media.
- PITMAN, M. W. & LUCEY, A. D. 2009 On the direct determination of the eigenmodes of finite flow–structure systems. *Proceedings of the Royal Society of London A: Mathematical, Physical and Engineering Sciences* **465**, 257–281.
- PLACZEK, A., SIGRIST, J.-F. & HAMDOUNI, A. 2009 Numerical simulation of an oscillating cylinder in a cross-flow at low Reynolds number: forced and free oscillations. *Computers & Fluids* **38** (1), 80–100.
- RAJ, P. & HARRIS, B. 1993 Using surface transpiration with an Euler method for cost-effective aerodynamic analysis. In *1993 AIAA 11th Applied Aerodynamics Conference*.
- RAVIART, P.-A. & THOMAS, J.-M. 1977 A mixed finite element method for 2-nd order elliptic problems. In *Mathematical aspects of finite element methods*, pp. 292–315. Springer.
- RAYLEIGH, L. 1885 On waves propagated along the plane surface of an elastic solid. *Proceedings of the London Mathematical Society* **1** (1), 4–11.
- REDDY, S. C., SCHMID, P. J. & HENNINGSON, D. S. 1993 Pseudospectra of the Orr–Sommerfeld operator. *SIAM Journal on Applied Mathematics* **53** (1), 15–47.

-
- REUTHER, J., JAMESON, A., FARMER, J., MARTINELLI, L. & SAUNDERS, D. 1996 Aerodynamic shape optimization of complex aircraft configurations via an adjoint formulation. In *34th Aerospace Sciences Meeting and Exhibit*, p. 94.
- RICHTER, T. 2015 A monolithic geometric multigrid solver for fluid-structure interactions in ALE formulation. *International Journal for Numerical Methods in Engineering* **104** (5), 372–390.
- RICHTER, T. 2017 *Fluid-structure Interactions: Models, Analysis and Finite Elements*, vol. 118. Springer.
- RICHTER, T. & WICK, T. 2010 Finite elements for fluid-structure interaction in ALE and fully Eulerian coordinates. *Computer Methods in Applied Mechanics and Engineering* **199** (41), 2633–2642.
- RICHTER, T. & WICK, T. 2015 On time discretizations of fluid-structure interactions. In *Multiple Shooting and Time Domain Decomposition Methods*, pp. 377–400. Springer.
- ROSHKO, A. 1954 On the drag and shedding frequency of bluff cylinders. *Tech. Rep.*. National Advisory Committee for Aeronautics.
- ROSHKO, A. 1993 Perspectives on bluff body aerodynamics. *Journal of Wind Engineering and Industrial Aerodynamics* **49** (1-3), 79–100.
- SAAD, Y. 2003 *Iterative methods for sparse linear systems*. Society for Industrial and Applied Mathematics.
- SAAD, Y. 2011 *Numerical methods for large eigenvalue problems*. Society for Industrial and Applied Mathematics.
- SAAD, Y. & SCHULTZ, M. H. 1986 Gmres: A generalized minimal residual algorithm for solving nonsymmetric linear systems. *SIAM Journal on scientific and statistical computing* **7** (3), 856–869.
- SARIC, W. S., REED, H. L. & KERSCHEN, E. J. 2002 Boundary-layer receptivity to freestream disturbances. *Annual Review of Fluid Mechanics* **34** (1), 291–319.
- SCHENK, O. & GÄRTNER, K. 2004 Solving unsymmetric sparse systems of linear equations with PARDISO. *Future Generation Computer Systems* **20** (3), 475–487.
- SCHLICHTING, H. 1933 Zur entstehung der turbulenz bei der platenstromung. *Nach. Ges. Wiss. Göttingen Math. Phys. Klasse* **182**.
- SCHLICHTING, H. 1979 *Boundary-Layer Theory*. McGraw-Hill.
- SCHMID, P. & DE LANGRE, E. 2002 Transient growth before coupled-mode flutter. In *ASME 2002 International Mechanical Engineering Congress and Exposition*, pp. 1055–1064. American Society of Mechanical Engineers.
- SCHMID, P. J. 2007 Nonmodal stability theory. *Annual Review of Fluid Mechanics* **39**, 129–162.
- SCHMID, P. J. & HENNINGSON, D. S. 2012 *Stability and transition in shear flows*. *Applied Mathematical Sciences* 142. Springer.
- SCHUBAUER, G. B. & SKRAMSTAD, H. K. 1947 Laminar boundary-layer oscillations and stability of laminar flow. *Journal of the Aeronautical Sciences* **14** (2), 69–78.
- SCHWARTZ, M., MANZOOR, S., HÉMON, P. & DE LANGRE, E. 2009 By-pass transition to airfoil flutter by transient growth due to gust impulse. *Journal of Fluids and Structures* **25** (8), 1272–1281.
- SEN, P. & ARORA, D. 1988 On the stability of laminar boundary-layer flow over a flat plate with a compliant surface. *Journal of Fluid Mechanics* **197**, 201–240.

- SHOELE, K. & MITTAL, R. 2016 Flutter instability of a thin flexible plate in a channel. *Journal of Fluid Mechanics* **786**, 29–46.
- SHUKLA, S., GOVARDHAN, R. & ARAKERI, J. 2013 Dynamics of a flexible splitter plate in the wake of a circular cylinder. *Journal of Fluids and Structures* **41**, 127–134.
- SIPP, D. & LEBEDEV, A. 2007 Global stability of base and mean flows: a general approach and its applications to cylinder and open cavity flows. *Journal of Fluid Mechanics* **593**, 333–358.
- SIPP, D. & MARQUET, O. 2013 Characterization of noise amplifiers with global singular modes: the case of the leading-edge flat-plate boundary layer. *Theoretical and Computational Fluid Dynamics* **27** (5), 617–635.
- SIPP, D., MARQUET, O., MELIGA, P. & BARBAGALLO, A. 2010 Dynamics and control of global instabilities in open-flows: a linearized approach. *Applied Mechanics Reviews* **63** (3), 030801.
- SLOTNICK, J., KHODADOUST, A., ALONSO, J., DARMOFAL, D., GROPP, W., LURIE, E. & MAVRIPLIS, D. 2014 CFD vision 2030 study: a path to revolutionary computational aerosciences.
- SMITH, A. & GAMBERONI, N. 1956 Transition, pressure gradient, and stability theory. *Tech. Rep.* Douglas Aircraft & Co.
- SOKOLOWSKI, J. & ZOLESIO, J.-P. 1992 *Introduction to shape optimization. Springer series in Computational Mathematics* 16. Springer.
- SØRENSEN, J. N. 2011 Aerodynamic aspects of wind energy conversion. *Annual Review of Fluid Mechanics* **43**, 427–448.
- SREENIVASAN, K., STRYKOWSKI, P. & OLINGER, D. 1987 Hopf bifurcation, landau equation, and vortex shedding behind circular cylinders. In *Forum on Unsteady Flow Separation* (ed. American Society of Mechanical Engineers), pp. 1–13.
- STANFORD, B. K. & BERAN, P. S. 2010 Analytical sensitivity analysis of an unsteady vortex-lattice method for flapping-wing optimization. *Journal of Aircraft* **47** (2), 647–662.
- STEIN, K., TEZDUYAR, T. & BENNEY, R. 2003 Mesh moving techniques for fluid-structure interactions with large displacements. *ASME Journal of Applied Mechanics* **70**, 58–63.
- STEWART, E. C., PATIL, M. J., CANFIELD, R. A. & SNYDER, R. D. 2016 Aeroelastic shape optimization of a flapping wing. *Journal of Aircraft* pp. 636–650.
- STEWART, P. S., WATERS, S. L. & JENSEN, O. E. 2009 Local and global instabilities of flow in a flexible-walled channel. *European Journal of Mechanics-B/Fluids* **28** (4), 541–557.
- STRYKOWSKI, P. & SREENIVASAN, K. 1990 On the formation and suppression of vortex shedding at low Reynolds numbers. *Journal of Fluid Mechanics* **218**, 71–107.
- TAKIZAWA, K. & TEZDUYAR, T. E. 2012 Computational methods for parachute fluid–structure interactions. *Archives of Computational Methods in Engineering* **19** (1), 125–169.
- TEZDUYAR, T., BEHR, M. & LIOU, J. 1992 A new strategy for finite element computations involving moving boundaries and interfaces—the deforming-spatial-domain/space-time procedure: I. The concept and the preliminary numerical tests. *Computer Methods in Applied Mechanics and Engineering* **94** (3), 339–351.
- THEODORSEN, T. 1949 General theory of aerodynamic instability and the mechanism of flutter. *Tech. Rep.* National Advisory Committee for Aeronautics.
- THEOFILIS, V. 2011 Global linear instability. *Annual Review of Fluid Mechanics* **43**, 319–352.
- THEVENIN, D. & JANIGA, G. 2008 *Optimization and Computational Fluid Dynamics*. Springer.

- TIMOSHENKO, S. P. & GERE, J. M. 1961 *Theory of elastic stability*. McGraw Hill.
- TOLLMIE, W. 1929 Über die entstehung der turbulenz. *Vorträge aus dem Gebiete der Aerodynamik und verwandter Gebiete* pp. 18–21.
- TREFETHEN, L. N. & EMBREE, M. 2005 *Spectra and pseudospectra: the behavior of nonnormal matrices and operators*. Princeton University Press.
- TREFETHEN, L. N., TREFETHEN, A., REDDY, S., DRISCOLL, T. & OTHERS 1993 Hydrodynamic stability without eigenvalues. *Science* **261** (5121), 578–584.
- TRELOAR, L. 1943 The elasticity of a network of long-chain molecules — ii. *Transactions of the Faraday Society* **39**, 241–246.
- TRITTON, D. 1959 Experiments on the flow past a circular cylinder at low Reynolds numbers. *Journal of Fluid Mechanics* **6**, 547–567.
- TRUESDELL, C. & NOLL, W. 1992 *The non-linear field theories of mechanics*. Springer.
- TSIGKLIFIS, K. & LUCEY, A. D. 2017 The interaction of Blasius boundary-layer flow with a compliant panel: global, local and transient analyses. *Journal of Fluid Mechanics* **827**, 155–193.
- TUCKERMAN, L. S. & BARKLEY, D. 2000 Bifurcation analysis for timesteppers. In *Numerical methods for bifurcation problems and large-scale dynamical systems*, pp. 453–466. Springer.
- TUREK, S. & HRON, J. 2006 Proposal for numerical benchmarking of fluid-structure interaction between an elastic object and laminar incompressible flow. In *Fluid-structure interaction*. Springer.
- TUREK, S., HRON, J., RAZZAQ, M., WOBKER, H. & SCHÄFER, M. 2011 Numerical benchmarking of fluid-structure interaction: A comparison of different discretization and solution approaches. In *Fluid Structure Interaction*, pp. 413–424. Springer.
- VAN DYKE, M. 1982 *An Album of Fluid Motion*. Parabolic Press.
- WALSH, M. & LINDEMANN, A. 1984 Optimization and application of riblets for turbulent drag reduction. In *22nd Aerospace Sciences Meeting*, p. 347.
- WICK, T. 2011 Fluid-structure interactions using different mesh motion techniques. *Computers & Structures* **89** (13), 1456–1467.
- WICK, T. 2013a Solving monolithic fluid-structure interaction problems in Arbitrary Lagrangian–Eulerian coordinates with the deal.II library. *Archive of Numerical Software* **1** (1), 1–19.
- WICK, T. 2013b Stability estimates and numerical comparison of second order time-stepping schemes for fluid-structure interactions. In *Numerical Mathematics and Advanced Applications 2011*, pp. 625–632. Springer.
- WILLIAMS, T. M., DAVIS, R., FUIMAN, L., FRANCIS, J., LE, B., HORNING, M., CALAMBOKIDIS, J., CROLL, D. & OTHERS 2000 Sink or swim: strategies for cost-efficient diving by marine mammals. *Science* **288** (5463), 133–136.
- WILLIAMSON, C. 1996 Vortex dynamics in the cylinder wake. *Annual Review of Fluid Mechanics* **28**, 477–539.
- WILLIAMSON, C. & GOVARDHAN, R. 2004 Vortex-induced vibrations. *Annual Review of Fluid Mechanics* **36**, 413–455.
- WIPLIER, O. & EHRENSTEIN, U. 2001 On the absolute instability in a boundary-layer flow with compliant coatings. *European Journal of Mechanics-B/Fluids* **20** (1), 127–144.

- WRIGHT, S. & NOCEDAL, J. 1999 *Numerical optimization*, 2nd edn. *Springer Series in Operations Research and Financial Engineering* 35. Springer.
- WU, J., QIU, Y. & ZHAO, N. 2014 Flow control of a circular cylinder by using an attached flexible filament. *Physics of Fluids* **26**, 103601.
- WU, T. Y. 2011 Fish swimming and bird/insect flight. *Annual Review of Fluid Mechanics* **43**, 25–58.
- XU, J. C., SEN, M. & GAD-EL HAK, M. 1990 Low-reynolds number flow over a rotatable cylinder-splitter plate body. *Physics of Fluids A: Fluid Dynamics* **2** (11), 1925–1927.
- YEO, K. 1988 The stability of boundary-layer flow over single-and multi-layer viscoelastic walls. *Journal of Fluid Mechanics* **196**, 359–408.
- YEO, K. 1992 The three-dimensional stability of boundary-layer flow over compliant walls. *Journal of Fluid Mechanics* **238**, 537–577.
- YEO, K., KHOO, B. & CHONG, W. 1994 The linear stability of boundary-layer flow over compliant walls: effects of boundary-layer growth. *Journal of Fluid Mechanics* **280**, 199–225.
- YEO, K., KHOO, B. & ZHAO, H. 1996 The absolute instability of boundary-layer flow over viscoelastic walls. *Theoretical and Computational Fluid Dynamics* **8** (4), 237–252.
- VAN DER ZEE, K., VAN BRUMMELEN, E., AKKERMAN, I. & DE BORST, R. 2011 Goal-oriented error estimation and adaptivity for fluid–structure interaction using exact linearized adjoints. *Computer Methods in Applied Mechanics and Engineering* **200** (37), 2738–2757.
- ZEL'DOVICH, Y. B. & RAIZER, Y. P. 2012 *Physics of shock waves and high-temperature hydrodynamic phenomena*. Dover.
- ZHANG, J., CHILDRESS, S., LIBCHABER, A. & SHELLEY, M. 2000 Flexible filaments in a flowing soap film as a model for one-dimensional flags in a two-dimensional wind. *Nature* **408** (6814), 835–839.
- ZHANG, W., LI, X., YE, Z. & JIANG, Y. 2015 Mechanism of frequency lock-in in vortex-induced vibrations at low Reynolds numbers. *Journal of Fluid Mechanics* **783**, 72–102.

Titre: Instabilités et optimisation de structures élastiques en interaction avec des écoulements laminaires

Mots clés: interaction fluide-structure ; analyse de stabilité linéaire ; optimisation de forme et de structure

Résumé: L'interaction entre solides élastiques et écoulements visqueux peut conduire à de grandes déformations. Outre les simulations non linéaires instationnaires, des approches modales linéarisées sont utiles pour identifier les instabilités hydro-élastiques à l'origine de ces vibrations, et peuvent également être utilisés pour concevoir des stratégies de contrôle. Les objectifs de cette thèse sont de développer et d'appliquer des méthodes, d'abord pour décrire la dynamique linéaire fluide-solide, puis la contrôler en optimisant la forme ou les propriétés élastiques du solide.

La première partie présente les méthodes développées pour étudier la dynamique linéaire des perturbations fluide-solide fortement couplées. La dynamique des fluides est régie par les équations de Navier-Stokes incompressibles, tandis que le solide est décrit par des modèles hyperélastiques. Un couplage Arbitrairement Lagrangien-Eulérien est choisi. Une linéarisation exacte de cette formulation est dérivée, et l'analyse modale qui en résulte est validée.

La deuxième partie est consacrée à l'analyse et au contrôle des vibrations de plaques élastiques fixées en aval d'un cylindre circulaire rigide, et immergées dans un

écoulement entrant uniforme. Des modes propres fluide-solide sont identifiés au moyen d'une analyse aux valeurs propres de l'opérateur linéarisé, et des simulations temporelles sont effectuées pour expliciter les interactions non linéaires. En second lieu, une optimisation de forme par état adjoint est proposée pour contrôler les modes instables. La stabilisation des modes est réalisée, ainsi qu'une modification des fréquences instables.

La dernière partie est consacrée au délai de la transition laminaire/turbulent de couche limite grâce à des revêtements visco-élastiques. Une analyse de résolvant de l'opérateur fluide-solide est utilisée pour quantifier l'atténuation des ondes de Tollmien-Schlichting lorsque la rigidité du revêtement est réduite. D'autre part, l'analyse aux valeurs propres montre que des modes à haute fréquence, liés à la dynamique du solide, sont déstabilisés lorsque l'amortissement visqueux solide est trop faible. Une stratégie pour optimiser la répartition de la rigidité du revêtement vis-à-vis de l'amplification énergétique des deux instabilités est finalement proposée. Les revêtements optimisés permettent à la fois d'atténuer les ondes de Tollmien-Schlichting et de limiter le développement des instabilités à plus haute fréquence.

Title: Instabilities and optimization of elastic structures interacting with laminar flows

Keywords: fluid-structure interaction; linear stability analysis; adjoint-based structure and shape optimization

Abstract: The interaction between elastic solids and viscous flows can lead to large deformations. In addition to unsteady non-linear simulations, linearised modal approaches are useful to identify the hydro-elastic instabilities at the origin of these vibrations, and can also be used to design control strategies. The objectives of this thesis are to develop and apply methods, first to describe fluid-solid linear dynamics, then to control it by optimizing the shape or elastic properties of the solid.

The first part presents the methods developed to study the linear dynamics of strongly coupled fluid-solid disturbances. Fluid dynamics is governed by incompressible Navier-Stokes equations, while the solid is described by hyperelastic models. An Arbitrary Lagrangian-Eulerian coupling is chosen. An exact linearization of this formulation is derived, and the resulting modal analysis is validated.

The second part is devoted to the analysis and control of the vibrations of elastic plates fixed downstream of a rigid circular cylinder, and immersed in a uniform incoming flow. Fluid-solid eigenmodes are identified by means

of an eigenvalue analysis of the linearised operator, and time-marching simulations are performed to clarify non-linear interactions. Secondly, an adjoint-based shape optimization is proposed to control unstable modes. A stabilization of the modes is achieved, as well as a modification of unstable frequencies.

The last part is devoted to the delay of the laminar/turbulent transition of a boundary-layer flow thanks to viscoelastic coatings. A resolvent analysis of the linearised fluid-solid operator is used to quantify the attenuation of unstable Tollmien-Schlichting waves when the stiffness of the coating is reduced. On the other hand, the eigenvalue analysis shows that high-frequency modes, linked to the dynamics of the solid, are destabilised when the solid viscous damping is too low. A strategy to optimize the distribution of the coating's rigidity with respect to the energetic amplification of both instabilities is finally proposed. Optimized coatings both reduce the growth of Tollmien-Schlichting waves and limit the development of higher frequency instabilities.